Investigating the role of *DIAPH1* in double strand break repair as the underlying cause of a novel DNA repair syndrome in humans

By Beth Louise Woodward

A thesis submitted to the University of Birmingham for the degree of DOCTOR OF PHILOSOPHY



UNIVERSITY OF BIRMINGHAM



CANCER RESEARCH UK CLINICAL ACADEMIC TRAINING PROGRAMME

Institute of Cancer and Genomic Sciences
College of Medical and Dental Scienced
University of Birmingham
May 2024

UNIVERSITY OF
BIRMINGHAM

University of Birmingham Research Archive

e-theses repository

This unpublished thesis/dissertation is copyright of the author and/or third parties. The intellectual property rights of the author or third parties in respect of this work are as defined by The Copyright Designs and Patents Act 1988 or as modified by any successor legislation.

Any use made of information contained in this thesis/dissertation must be in accordance with that legislation and must be properly acknowledged. Further distribution or reproduction in any format is prohibited without the permission of the copyright holder.

Abstract

DNA double-strand break (DSB) repair is crucial for maintaining genome stability and preventing disease. The cell cycle phase and chromatin context largely determine which DSB repair pathway is used to restore damaged DNA. Several human diseases are associated with defective DSB repair and often arise from inherited variations in genes with critical roles in DSB repair pathways. One of the most well characterised human DSB repair deficiency disorders is Nijmegen Breakage Syndrome (NBS), which is caused by biallelic mutations in the *NBN/NBS1* gene. Typically, NBS patients display a range of neurodevelopmental defects that include microcephaly, short stature, dysmorphic facial features, intellectual disability and immunodeficiency. Moreover, affected patients also have an increased risk of developing tumours, particularly those of lymphoid origin.

Recently, it has been shown that nuclear actin filaments play an important role in clustering DSBs to facilitate repair by homologous recombination (HR). However, the specific mechanism with which nuclear actin and various actin nucleating factors regulate HR remains unclear. Interestingly, patients with biallelic mutations in the actin nucleating factor *DIAPH1* exhibit clinical features that significantly overlap with those typically associated with NBS, such as microcephaly, short stature, intellectual disability, immunodeficiency and tumour predisposition. This indicates that DIAPH1 may play a role in regulating HR, and that some of the clinical deficits associated with *DIAPH1* mutations could stem from a DSB repair defect.

Consistent with this clinical similarity, this study demonstrates that cells derived from patients with biallelic mutations in *DIAPH1* have a HR repair defect comparable to loss of Nbs1. Notably, this DSB repair defect is observed in a subset of patients with Baraitser-Winter Cerebrofrontofacial (BWCFF) Syndrome caused by *de novo* mutations in *ACTG1* (γ-actin) but not *ACTB* (β-actin). Lastly, this study shows that DIAPH1 and γ-actin support HR-dependent repair by facilitating the relocalisation of the MRE11/RAD50/NBS1 (MRN) complex to sites of DNA damage to initiate DNA-end resection. Consequently, loss of DIAPH1 protein compromises the entire HR pathway, which inevitably gives rise to genome instability. These findings offer a novel mechanistic explanation for the overlapping clinical symptoms observed in patients with biallelic *DIAPH1* mutations, BWCFF Syndrome, and NBS, and provides further insight into the role of actin and actin-nucleating factors in DSB repair.

Dedication



For my Mom and Dad

“So Beth, what is it that you are doing in the lab again?”

Acknowledgements

"In the laboratory, there are no failures, only unexpected results... and occasional broken centrifuges."

"What is meant for you will not pass you by."

The above quote encompasses why I had to do this PhD, the circumstances around how it came about felt too much like it was an opportunity that was not meant to pass me by. It feels strange to finally be writing my acknowledgements because I remember thinking when I was starting my PhD journey how far away it felt to be in the position to be thanking people and I wondered who those people would be, knowing at that stage some of them I had not even met yet. However, I cannot begin this start without thanking my supervisor, Professor Grant Stewart. Despite his annoyance every time I played Radio 1 in his lab, he has been the most incredible scientific supervisor, pushing me beyond what I ever thought was capable. His passion for science is something to be admired and what a privilege to be taught by someone with such skill and who's knowledge is somewhat of an encyclopaedia of DNA repair. I feel forever grateful to Grant for not only training me to become the best scientist I can be, with the most stunning western blots, but for instilling a work ethic in me that meant I generated more data for this thesis in less time than most. The Stewart lab motto of "Why do one experiment when you can do 15?" has served me well even if at the time I identified as a lab octopus, doing multiple experiments alongside each other and I thought I might implode. Thank you Grant for our inspiring scientific conversations, your constant unwavering support, problem solving and trouble shooting and for being the lab fairy and making up all my buffers even if it is most certainly below your pay grade. I am also very grateful for you to introducing me to possibly one of the most valuable additions to my life going forward, Snowdonia Cheese Company's Black Bomber vintage mature cheddar cheese!

Thank you to my clinical supervisor, Professor Gary Middleton, for seeing something in me and selecting me to embark on this journey to do the MBPhD and for inspiring me with your passion for academic medicine and being willing to move mountains to keep me happy and on track. I would also like to thank my second supervisor, Angelo for being so kind to me in times of need, having my back and keeping 'Beth's back street blood clinic' open for regular business so I could maintain some level of clinical skills before returning to Medical School. Thank you to CRUK for funding my work and supporting me in my journey into academic medicine.

Next, I would like to thank the members of the Stewart lab who have supported me through this journey, provided great lunch time chat and being friendly faces with coffee and treats (particularly Charlotte's fantastic brownies and Sati bringing Samosa man's famous samosas on QE farmer's market Wednesdays) when I have been

overwhelmed by life. Thank you particularly to Sati, Anoop, Marcos and Charlotte for being these people, you are all wonderful human beings. Sati and Grant, I will now always be on the hunt for appropriate (or inappropriate if you're a prude) phrases suitable for the 'title of your sex tape" game. Thank you to everyone in the Rothenberg lab at New York University for one of the best 2 months of my life, particularly to Eli, Sudipta, Nastia, Dipika and George. Thank you also to Tanja and Malcolm for their support and many valuable pieces of advice on how to survive the Stewart lab experience and words of wisdom that will keep me in good stead for many years to come. I would also like to thank my mentor of the last 10 years and now a very good friend, Linda, for buying me every single Costa Coffee at every one of our meetings for the last decade. You have been instrumental in supporting me through my studies both academically but also mentally and emotionally and I am very grateful to you.

I would next like to thank the wonderful people who have helped generate some of the data for this thesis. Firstly, to Sudipta Lahiri in the Rothenberg lab for finishing off my STORM experiments. To Tom Clarke at Harvard Medical School for performing the resection assay in Chapter 4 and to the incredibly talented Summer Internship Student, Lucy Goodley, for helping me finish a mammoth lot of analysis for the actin chapter of this thesis. Thank you to Grant Stewart for performing the GFP-Trap and Co-IP experiments. Thank you to the Houlden lab at University College London and to Peter Arkwright at the University of Manchester for providing patient samples for this project and to all the collaborators on this project who have either provided reagents or ideas to try. Thank you to Anil in the Stewart lab for teaching me how to do molecular biology and making a lot of the plasmids used in this study.

Now, next on my list of people to thank is my fiancé, Ant. You have been my rock during my PhD, present for all the tears, the celebrations, the good times and the bad and always with open arms and a silly phrase ready to me make me laugh. Thank you for letting me practise all my talks to you, for always knowing what to say and suggesting just the right thing at the right time (Poking your head around the door when I am deep into a thesis writing flow with "Wanna go for a milkshake at Parky's Farm?"). You are one of life's angels and I am so grateful to have you and I love you beyond words could ever explain. I am so happy with the life we have built together, our cosy house, our dog Nellie, our hens, Polly and Ada and my beloved pony Applejack. I am so excited to get to do life with you and for all our exciting adventures.

Thank you to all of my amazing friends who have been the lights of my life. I feel like an absolute millionaire in love and friendship, and I love every single one of you. Kate, you are my ride or die and I will now forever be known as Dr Bob, even if I made you wait an extra 4 years before you could start calling it me officially. Thank you for your support on this wild journey, right from getting A-level results with your bottle of celebratory 80% Absinthe to this point now 10 years later. I know we'll always be there for each other through various life milestones, and I hope for your sake I don't ever do another degree. Thank you, my beautiful friends, Fiona, Emily, Louise, Emily and Sophie. You have all been my cheerleaders through various challenging and happy times and you are all so special to me and I cherish the time we spend together. I cannot wait for more girls holidays to make it out of the '5 doctors and a wedding planner' group chat. I will be drawing upon all of you to help me get through the final year of medicine after a 4-year break! Thank you to my two longest friendships from

my two high schools, Eilish and Jo, for our lunch time phone calls as a welcome break from the lab and anytime we spend together always being the most wholesome and energising time. Fiona, Ben and Eilish, thank you for flying across the Atlantic for me. You do not realise how grateful I am that I got to share some of my NYC experience with all of you, having you there was a highlight, and I will cherish those memories forever.

Thank you to the friends I made very serendipitously during my PhD, especially to James, who has become a friend for life, blossoming from our shared love of RuPaul's Drag Race. Also, to Kelly and Jack for making the commute on the cross-country service a lot more bearable with our gossip sessions on the 16.39 train. My last friendship thank you goes to one of the most amazing communities I become part of whilst in the lab, the Badgers running club, which I honestly believe is what has kept me going and able to produce so much work. I am so grateful to my running girls, Amber, Millie, and Hannah for our long run therapy sessions during the final phase of my PhD. Amber, we were always meant to be sat opposite each other at that wedding, and from that I cannot believe how rapidly we became such close friends. I am honoured to have got to train and run London Marathon 2024 with you whilst writing this thesis, your infectious and boundless positivity was a welcome break from staring at my computer.

The last round of thank you's is to my family. Amy, thank you for always being my hype woman and for your little pick me up treats. I am so grateful and proud to have my sister as one of my best friends. Thank you to my Nanny Dolly for always being so interested in my research and my career even into your 90s. Your zest for life is inspiring and I am glad I have been able to make you proud. Thank you to my very special aunties, Sue and Sandra, for making me a roast dinner and copious amounts of tea every Sunday without fail. Thank you, Mary and Terry, for all your love and support for Ant and I to be able to be where we are now, we love you both so much. Dave and Charlene, thank you to you both for our Sunday afternoon 'putting the world to rights' over a cup of tea (or three). An extra thank you to Dave for your coaching and support when I am having a running-related melt down. A final thank you goes to the two people whom my thesis is dedicated to, my mom and dad, Jackie and Richard. You two have championed me and everything I do for my entire life. Without you, none of what I have achieved or the experiences I have had would have been possible. For someone completely lacking in common sense, I didn't turn out too badly! I love you both more than all the leaves on all the trees and this thesis is a product of your love and support. The bank of mom and dad is very near to being able to recoup some of its funds! You are legendary, thank you!

That was very long, but this is a girl who doesn't do brief.

Table of Contents

	Page
1.0 Introduction	**1**
1.1 Diaphanous-related formin	2
1.1.1 Background	2
1.1.2 Structure and functions of Diaphanous related formins	3
1.1.3 DIAPH1 function in microtubule dynamics	8
1.1.4 DIAPH1 function in the RAGE axis	8
1.1.5 Nuclear functions of DIAPH1	9
1.2 Human diseases associated with variants in DIAPH1	11
1.2.1 Heterozygous variants in DIAPH1 and associated human disorders	11
1.2.2 Homozygous variants in DIAPH1 and associated human disorders	12
1.2.3 5q chromosome deletions and myelodysplastic syndrome	12
1.2.4 DIAPH1 and its association with cancer	14
1.3 Actin	16
1.3.1 Actin structure and function	17
1.3.2 Actin binding proteins	20
1.3.3 The ARP2/3 Complex	20
1.3.4 Spire family actin nucleators	23
1.4 Human diseases associated with actin and actin nucleators	26
1.4.1 ATCB and ACTG1 gene variants and human disease	26
1.4.2 Variants in actin nucleator genes and associated human diseases	27
1.5 The DNA Damage Response	32
1.5.1 Background	32
1.5.2 Repair of DNA double-strand breaks	35
1.5.3 Key kinases in DDR signalling	36
1.5.3.1 DNA-PKcs	37
1.5.3.2 ATM	38
1.5.3.3 ATR	40
1.5.4 DSB signal transduction: The MRN complex	42
1.6 Non-homologous end joining	45
1.6.1 Classical non-homologous end joining	45
1.6.2 Alternate-end joining	50
1.7 Homologous recombination	51
1.7.1 Background	51
1.7.2 The HR pathway and sub-pathways	52
1.7.3 Single strand annealing	58
1.8 The role of HR proteins in replication	59
1.8.1 Background: DNA replication	59
1.8.2 Replication stress	61
1.8.3 HR proteins with a role in replication stress	61

1.9 The Actin network in DNA repair	63
1.9.1 Actin in the nucleus	63
1.9.2 Actin and actin nucleators in double strand break repair and replication stress	64
1.10 Human diseases associated with DNA repair	67
1.11 Aims for this thesis	71
2.0 Materials and methods	**72**
2.1 General Equipment	73
2.2 Mammalian Cell Culture	74
2.2.1 Cell lines	74
2.2.2 Maintenance of mammalian cell lines	81
2.3 siRNA mediated protein knockdown	83
2.3.1 Preparation of cells for siRNA knockdown	83
2.3.2 siRNA knockdown	83
2.4 Generation of plasmid DNA constructs	84
2.4.1 Plasmid DNA constructs and vectors	84
2.4.2 Amplification and isolation of plasmid DNA constructs from bacterial cultures	85
2.4.3 Quantification of DNA in solution	87
2.4.4 Agarose gel electrophoresis of DNA fragments	87
2.4.5 Amplification of plasmid DNA constructs	87
2.4.6 DNA restriction enzyme digestion	89
2.4.7 Ligation of DNA fragments	90
2.5 Immunofluorescence	90
2.5.1 Micronuclei and γ-H2AX/53BP1 foci formation in patient-derived fibroblasts	90
2.5.2 Micronuclei and γ-H2AX/53BP1 foci formation in siRNA depletion of DIAPH1 in HeLa cells	91
2.5.3 RAD51, RPA and BRCA1 foci formation in adherent cells	92
2.5.6 Native BrdU foci in siRNA depleted HeLa cells	92
2.5.7 ER-mCherry-LacI-FokI-DD nuclease system double strand break repair assay in U2-O-S LacO-FokI mCherry expressing cells	93
2.5.8 Mitotic defects in adherent cells	93
2.5.9 Cell harvesting for immunofluorescence	93
2.5.10 Immunofluorescence	94
2.6 GFP-Trap affinity purification	96
2.7 Western Blotting	97
2.7.1 Preparation of whole cell extracts	97
2.7.2 Bradford protein determination assay	98
2.7.3 SDS-PAGE Electrophoresis	98
2.7.4 Western Blotting	99
2.8 Metaphase Spread analysis	102
2.8.1 Preparation of patient derived LCLs for metaphase spread analysis	102
2.8.2 Preparation of patient derived fibroblasts for metaphase spread analysis	103
2.8.3 Preparation of HeLa cells for metaphase spread analysis	103

2.8.4 Harvesting cells for metaphase spread analysis	104
2.8.5 Dropping and visualisation of metaphases	104
2.9 Sister chromatid exchange (SCE) analysis	105
2.9.1 Preparation of patient derived LCLs for SCE analysis	105
2.9.2 Preparation of HeLa cells for SCE analysis	105
2.9.3 Harvesting cells for SCE analysis	106
2.9.4 Dropping of mitotic cells	106
2.10 CRISPR-based homologous recombination assay	107
2.10.1 Preparation of HeLa cells for plasmid transfection	107
2.10.2 Plasmid transfection	108
2.10.3 Harvesting and analysis	108
2.11 Stochastic Optical Reconstruction Microscopy (STORM)	109
2.11.1 Preparation of patient-derived fibroblast cells for STORM	109
2.11.2 Harvesting of cells for STORM	109
2.11.3 EdU Click-iT Chemistry	110
2.11.4 Antibody staining	110
2.11.5 Sample preparation	111
2.11.6 STORM Imaging	111
2.11.7 Region of interest selection and analysis	113
2.12 DNA fibre analysis	114
2.12.1 Thymidine label preparation	114
2.12.2 Assessment of exposure to replication stress agents	115
2.12.3 Assessment of replication fork restart	115
2.12.4 Assessment of fork stability	116
2.12.5 Harvesting cells for DNA fibre analysis	116
2.12.6 DNA fibre immunostaining	117
2.13 AsiSI real-time PCR DNA resection assay	119
2.13.1 siRNA transfection	119
2.13.2 AsiSI real-time PCR DNA resection assay	119
2.14 Statistical Analysis	120
2.14.1 Mann-Whitney U test	120
2.14.2 Student t-test	121
3.0 Identification and cellular characterisation of genome instability in cells from patients with variants in DIAPH1	122
3.1 Introduction	123
3.2 Aims of this chapter	125
3.3 Results	128
3.3.1 Identification of patients with homozygous variants in DIAPH1	128
3.3.2 Western blot analysis of ATM-dependent DNA damage response in DIAPH1 patient cells	137
3.3.3 Loss of DIAPH1 leads to an increase in genomic stability following DNA damage	144
3.3.4 Complementation of WT-DIAPH1 in patient-derived cells lacking DIAPH1 rescues genomic instability	152
3.3.5 Loss of DIAPH1 leads to an increase in chromosomal instability following exposure to DNA damaging agents	157

3.4 Concluding remarks	167
4.0 Characterisation of the role of DIAPH1 in double strand break repair	172
4.1 Introduction	173
4.2 Aims of this chapter	174
4.3 Results	175
4.3.1 Analysis of γ-H2AX/53BP1 foci formation following DNA damage in DIAPH1 patient-derived cells	175
4.3.2 Loss of DIAPH1 reduces efficiency of homologous recombination	183
4.3.3 Loss of DIAPH1 leads to reduced localisation and foci formation of HR factors RPA2, BRCA1 and Rad51 following CPT-induced DNA damage	194
4.3.4 DIAPH1 plays a role in MRN complex localisation to DSBs and interacts with components of the MRN complex	203
4.3.5 Loss of DIAPH1 leads to reduced resection following DSBs	213
4.4 Concluding remarks	219
5.0 Chapter 5: Characterisation of the role of *ACTB* and *ACTG1* in double strand break repair	224
5.1 Introduction	225
5.2 Aims of this chapter	227
5.3 Results	228
5.3.1 Clinical and genetic information of patients with variants in *ACTB, ACTG1* and components of the ARP2/3 complex	228
5.3.2 Analysis of genome instability following DNA damage in *ACTB, ACTG1* and ARP2/3 complex component patient cells	233
5.3.3 Analysis of γ-H2AX/53BP1 foci formation following DNA damage in *ACTB, ACTG1* and ARP2/3 complex component patient-derived cells	243
5.3.4 Loss of ACTG1 leads to reduced localisation of HR factors BRCA1, RPA2, RAD51 and MRE11 following CPT-induced DNA damage	253
5.3.5 DIAPH1, γ-actin and the ARP2/3 complex function within the same HR pathway	261
5.3.6 Actin-binding defective DIAPH1 gives rise to a DSB repair defect and DIAPH1 preferentially interacts with γ-actin	268
5.4 Concluding remarks	275
6.0 Loss of DIAPH1 lead to defects in DNA replication and mitosis	282
6.1 Introduction	283
6.2 Aims of this chapter	283
6.3 Results	286
6.3.1 Loss of DIAPH1 causes defects in DNA replication and the DNA replication stress response	286
6.3.2 Loss of DIAPH1 causes defects in mitosis	295
6.4 Concluding remarks	298
7.0 Discussion	300
7.1 Introduction	301
7.2 The actin network and genome stability	303
7.3 The future applications of this study	311
7.4 Final conclusion	313
8.0 References	316
Appendices	340

List of Figures

- Figure 1.1 - Schematic diagram of the structure of DIAPH1 protein **(Page 6)**
- Figure 1.2 – Schematic of DIAPH1's function in actin **(Page 7)**
- Figure 1.3 – Schematic diagram of β-actin and γ-actin structure and function **(Page 19)**
- Figure 1.4 - Schematic diagram of C-terminal WCA region of WASP, WASH, SCAR and WHAMM **(Page 22)**
- Figure 1.5 – Schematic diagram of actin nucleation **(Page 25)**
- Figure 1.6 – Types and sources of DNA damage and the cellular pathways that exist to repair them **(Page 34)**
- Figure 1.7 - Schematic Diagram of the Components of the MRN Complex **(Page 44)**
- Figure 1.8 – Different types of DNA ends repaired by NHEJ **(Page 49)**
- Figure 1.9 – Homologous recombination pathway and sub-pathways **(Page 57)**
- Figure 3.1 – Schematic to show different ways DSBs can be induced by exogenous DNA-damaging agents **(Page 127)**
- Figure 3.2 – Schematic of DIAPH1 protein variants resulting from variants in the DIAPH1 gene **(Page 134)**
- Figure 3.3 – Clinical photographs to show physical manifestations of patients harbouring homozygous variants in *DIAPH1* **(Page 135)**
- Figure 3.4 - Western blot analysis of patient-derived cell lines **(Page 136)**
- Figure 3.5 - Western blot analysis of DIAPH1-P5 derived LCLs exposed to 2 Gy IR **(Page 140)**
- Figure 3.6 - Western blot analysis of DIAPH1-P 5 LCLs exposed to DNA damaging agents **(Page 141)**
- Figure 3.7 - Western blot analysis of DIAPH1-P5 derived LCLs exposed to 1 mM HU **(Page 143)**
- Figure 3.8 - Western blot analysis of hTERT immortalised patient derived fibroblasts and siDIAPH1 HeLa cells exposed to 5 Gy IR **(Page 146)**
- Figure 3.9 – Schematic diagram to show micronuclei analysis **(Page 149)**
- Figure 3.10 - Formation of micronuclei in DIAPH1-P1, P2, P3-1, P4-2, P5 hTERT immortalised fibroblasts following exogenous DNA damage **(Page 150)**
- Figure 3.11 Formation of micronuclei in siDIAPH1 HeLa cells following exogenous DNA damage **(Page 151)**

- Figure 3.12 – *Western blot analysis of hTERT immortalised patient derived* **(Page 154)**
- Figure 3.13 - Formation of micronuclei in P1+Vector and P1+DIAPH1 hTERT immortalised fibroblasts following exogenous DNA damage **(Page 156)**
- Figure 3.14 – Schematic diagram of metaphase spread analysis **(Page 159)**
- Figure 3.15 - Quantification of chromosomal aberrations in DIAPH1-P 5 LCLs exposed to IR **(Page 160)**
- Figure 3.16 - Quantification of chromosomal aberrations in siRNA depleted HeLa cells **(Page 161)**
- Figure 3.17 - Quantification of chromosomal aberrations in DIAPH1-P 5 LCLs exposed to DNA damage **(Page 164)**
- Figure 3.18 - Quantification of chromosomal aberrations in siRNA depleted HeLa cells **(Page 165)**
- Figure 3.19 - Quantification of chromosomal aberrations in P1+Vector and P1+DIAPH1 hTERT immortalised fibroblasts following exogenous DNA damage **(Page 166)**
- Figure 4.1- Schematic representation of immunofluorescence techniques **(Page 177)**
- Figure 4.2 - Quantification of γ-H2AX/53BP1 foci formation in DIAPH1-P1, P2, P3-1, P4-2, P5 hTERT immortalised fibroblasts following exogenous DNA damage **(Page 178)**
- Figure 4.3 Quantification of γ-H2AX/53BP1 foci formation in siRNA mediated DIAPH1 depleted HeLa cells following exogenous DNA damage **(Page 179)**
- Figure 4.4 Quantification of γ-H2AX/53BP1 foci formation in P1+Vector and P1+DIAPH1 fibroblasts following exogenous DNA damage **(Page 180)**
- Figure 4.5 Quantification of γ-H2AX/53BP1 foci formation in DIAPH1 depleted HeLa cells following exogenous DNA damage **(Page 181)**
- Figure 4.6 Quantification of γ-H2AX/53BP1 foci formation in P1+Vector and P1+DIAPH1 fibroblasts following exogenous DNA damage **(Page 182)**
- Figure 4.7 Quantification of individual γ-H2AX/53BP1 foci per CENPF positive P1+Vector and P1+DIAPH1 fibroblasts following exogenous DNA damage **(Page 187)**
- Figure 4.8 – Schematic representation of sister chromatid exchange **(Page 188)**
- Figure 4.9 Quantification of sister chromatid exchanges in DIAPH1-P 5 LCLs exposed to DNA damaging agents **(Page 189)**
- Figure 4.10 Quantification of sister chromatid exchanges in DIAPH1 depleted HeLa cells exposed to DNA damaging agents **(Page 191)**
- Figure 4.11– Schematic representation of CRISPR Homologous recombination assay **(Page 192)**

- Figure 4.12 Quantification of Lamin-GFP positive nuclei in RFP positive siDIAPH1 HeLa cells **(Page 193)**
- Figure 4.13 Quantification of BRCA1 foci intensity in P1+DIAPH1 and P1+vector hTERT immortalised fibroblasts following CPT treatment **(Page 198)**
- Figure 4.14 Quantification of RPA2 foci intensity in P1+DIAPH1 and P1+vector hTERT immortalised fibroblasts following CPT treatment **(Page 199)**
- Figure 4.15 Quantification of Rad51 foci formation P1+DIAPH1 and P1+vector hTERT immortalised fibroblasts following CPT treatment **(Page 200)**
- Figure 4.16 - Schematic diagram of STORM **(Page 201)**
- Figure 4.17 Quantification of average local density of BRCA1 and RPA2 detected around individual EdU molecules in P1+DIAPH1 and P1+vector cells **(Page 202)**
- Figure 4.18 Quantification of average local density of MRE11 detected around individual EdU molecules in P1+DIAPH1 and P1+vector cells **(Page 207)**
- Figure 4.19 Quantification of average local density of CtIP detected around individual EdU molecules in P1+DIAPH1 and P1+vector cells **(Page 209)**
- Figure 4.20 – Schematic diagram of mCherry-LacI-FokI-DD nuclease system **(Page 210)**
- Figure 4.21 – Quantification of MRE11 signal intensity as mCherry-LacO-FokI-induced DSB sites **(Page 211)**
- Figure 4.22 – GFP-DIAPH1 nuclear localisation and binding to HR proteins **(Page 212)**
- Figure 4.23 – Native BrdU foci intensity in DIAPH1 depleted HeLa cells **(Page 216)**
- Figure 4.24 – Schematic diagram of AsiSI-end resection assay **(Page 217)**
- Figure 4.25– Quantification of DNA end resection using AsiSI-ER U-2-OS reporter **(Page 218)**
- Figure 5.1 – Location of mutations in ACTB and ACTG1 protein in patient cohort **(Page 232)**
- Figure 5.2 - Formation of micronuclei in ACTB and ACTG1 patient-derived hTERT immortalised fibroblasts following treatment with CPT **(Page 237)**
- Figure 5.3 - Formation of micronuclei in ARPC1B, ARPC4 and ARPC5 patient-derived hTERT immortalised fibroblasts following treatment with CPT **(Page 238)**
- Figure 5.4 - Formation of micronuclei in ACTB, ACTG1 and ARPC1B patient-derived hTERT immortalised fibroblasts following exposure to DNA damage **(Page 239)**
- Figure 5.5 - Quantification of micronuclei formation in A375 cells following DNA damage **(Page 240)**

- Figure 5.6 - Quantification of chromosomal aberrations in A375 cells following DNA damage **(Page 242)**
- Figure 5.7 - Quantification of γ-H2AX/53BP1 foci formation in ACTB and ACTG1 patient hTERT immortalised fibroblasts following treatment with CPT **(Page 246)**
- Figure 5.8 - Quantification of γ-H2AX/53BP1 foci formation in ARPC1B, ARPC4 and ARPC5 patient hTERT immortalised fibroblasts following treatment with CPT **(Page 247)**
- Figure 5.9 - Quantification of γ-H2AX/53BP1 foci formation ACTB-P2, ACTB-P3, ACTG1-P1, ACTG1-P2, ARPC4-P1.1, ARPC4-P.14 hTERT immortalised fibroblasts following treatment with IR **(Page 248)**
- Figure 5.10 - Quantification of γ-H2AX/53BP1 foci formation ACTB-P2, ACTB-P3, ACTG1-P1, ACTG1-P2, ARPC4-P1.1, ARPC4-P.14 hTERT immortalised fibroblasts following treatment with ETOP **(Page 250)**
- Figure 5.11 - Quantification of γ-H2AX/53BP1 foci formation in A375 cells following DNA damage **(Page 251)**
- Figure 5.12 - Quantification of γ-H2AX/53BP1 foci formation in A375 cells following exposure to IR **(Page 251)**
- Figure 5.13 - Quantification of BRCA1 foci intensity A375 cell lines following CPT treatment **(Page 256)**
- Figure 5.14 - Quantification of RPA2 foci intensity A375 cell lines following CPT treatment **(Page 257)**
- Figure 5.15 - Quantification of Rad51 foci intensity A375 cell lines following CPT treatment **(Page 258)**
- Figure 5.16 - Quantification of Rad51 foci in ACTB, ACGT1, ARPC1B, ARPC4 and APRC5 hTERT immortalised fibroblasts following CPT treatment **(Page 259)**
- Figure 5.17 – Quantification of Mre11 signal intensity as mCherry-LacO-FokI-induced DSB sites **(Page 260)**
- Figure 5.18 - Quantification of Lamin-GFP positive nuclei in RFP positive siRNA depleted HeLa cells **(Page 265)**
- Figure 5.19 - Quantification of Rad51 foci intensity siRNA depleted HeLa cells following CPT treatment **(Page 266)**
- Figure 5.20 – Native BrdU foci intensity in siRNA depleted HeLa cells **(Page 267)**
- Figure 5.21 - Formation of micronuclei in DIAPH1-P1 patient hTERT immortalised fibroblasts following exposure to DNA damage **(Page 271)**
- Figure 5.22 - Quantification of γ-H2AX/53BP1 foci formation in DIAPH1-P1 hTERT immortalised fibroblasts following DNA damage **(Page 272)**
- Figure 5.23 - Quantification of Rad51 foci intensity in DIAPH1-P1 hTERT immortalised fibroblasts following DNA damage **(Page 273)**

- Figure 5.24 – GFP-DIAPH1 binding to actin isoforms **(Page 274)**
- Figure 6.1 – Schematic representation of DNA fibre analysis to assess replication dynamics **(Page 285)**
- Figure 6.2 - Quantification of DNA fibre structures in HU treated DIAPH1 P1 hTERT fibroblasts **(Page 289)**
- Figure 6.3 - Quantification of DNA fibre structures in HU treated siRNA depleted U-2-OS cells **(Page 290)**
- Figure 6.4 - Ratio of IdU and CldU tract length in DIAPH1 P1 fibroblasts after release from HU treatment **(Page 291)**
- Figure 6.5 - Ratio of IdU and CldU tract length in siDIAPH1 U-2-OS after release from HU treatment **(Page 292)**
- Figure 6.6 - Quantification of replication fork stability in siDIAPH1 U-2-OS after 5 h HU treatment **(Page 293)**
- Figure 6.7 - Ratio of IdU and CldU tract length in siDIAPH1 U-2-OS in the presence of replication stress **(Page 294)**
- Figure 6.8 - Quantification of mitotic defects in P1+DIAPH1 and P1+Vector hTERT immortalised fibroblasts **(Page 297)**
- Figure 7.1 - *Figure 7.1* – Schematic diagram of the working model of actin's role in DSB repair proposed by this study **(Page 310)**

List of Tables

- Table 1.1 - Summary of actin nucleator classes **(Page 24)**
- Table 1.2 - Comparison of clinical features of ARPC1B, ARPC4, ARPC5 and WASP patients **(Page 31)**
- Table 1.3 - Summary of human diseases associated with DNA repair **(Page 69)**
- Table 1.4 – Human mutation nomenclature **(Page 70)**
- Table 2.1 - Cell lines used and generated for this study **(Page 75)**
- Table 2.2 - siRNA used in this study **(Page 84)**
- Table 2.3 - Plasmids used in this study **(Page 85)**
- Table 2.4 - PCR reaction components **(Page 88)**
- Table 2.5 - PCR Thermocycler settings **(Page 88)**
- Table 2.6 - Primers for amplification of DNA constructs **(Page 89)**
- Table 2.7 - Components of pre-extraction buffer (**Page 94)**
- Table 2.8 - Primary antibodies used for IF **(Page 95)**
- Table 2.9 - Secondary fluorophore coupled antibodies used for IF **(Page 95)**
- Table 2.10 - Components of lysis buffer for GFP-Trap affinity purification (**Page 96)**
- Table 2.11 - Components of wash buffer for GFP-Trap affinity purification (**Page 96)**
- Table 2.12 - Components of SDS-Page gel **(Page 99)**
- Table 2.13 - Components of running buffer **(Page 99)**
- Table 2.14 - Antibodies used for Western Blotting **(Page 101)**
- Table 2.15 - Antibodies used for STORM **(Page 110)**
- Table 2.16 - Primary antibodies used for DNA fibre analysis **(Page 118)**
- Table 2.17 - Secondary fluorophore coupled antibodies used for DNA fibre analysis **(Page 118)**
- Table 2.18 - Primers for AsiSI real-time PCR DNA resection assay (**Page 120)**
- Table 3.1 - Clinical features of patients with DIAPH1 variants and comparisons to known DNA repair disorders (**Page 133)**
- Table 5.1 - Clinical features of patients with *ACTB, ACTG1, ARPC1B, ARPC4 and ARPC5* gene variants (**Page 231)**

List of Abbreviations

A - Adenine

ABP - Actin-binding protein

ADP - Adenosine diphosphate

Ala (A) - Alanine

ALL - Acute lymphoblastic leukaemia

alt-EJ - Alternate end-joining

AML - Acute myeloid leukaemia

AMP - Adenosine monophosphate

APC - Adenomatous polyposis coli

APLF - Aprataxin and PNK-like factor

APTX - Aprataxin

Arg (R) - Arginine

ARP - Actin-related protein

Asn (N) - Asparagine

AT - Ataxia Telangiectasia

ATLD - Ataxia Telangiectasia-like disorder

ATM - Ataxia telangiectasia mutated

ATP - Adenosine triphosphate

ATR - Ataxia telangiectasia and Rad3-related

ATRIP - ATR-interacting protein

BER - Base excision repair

BIR - Break induced replication

BLM - Bloom syndrome protein

Bp - Base pair

BRCA1 - Breast cancer type 1 susceptibility protein

BRCA2 - Breast cancer type 2 susceptibility protein

BRCT - BRCA1 C-terminal domain

BrdU - Bromodeoxyuridine

BSA - Bovine serum albumin

BWCFF - Baraitser-Winter Cerebrofrontalfacial syndrome

C- Cytosine

C-terminus – Carboxy-terminus

c. - Coding

C. *Elegans* - *Caenorhabditis elegans*

CAPU - Cappucino

CC - Coiled-coil

CD4 - Cluster of differentiation 4

CD8 - Cluster of differentiation 8

CDC[number] - Cell division cycle [number]

CDC25A - Cell division cycle 25A

CDC42 - Cell division control protein 42

CDC7 - Cdk2-Cyclin E, Dbf4/Drf10-dependent cell cycle 7

CDK - Cyclin-dependent kinase

CDNA - Coding DNA

CDR - Complementarity-determining region

Cdt1 - Chromatin licensing and DNA replication factor 1

CENPF - Centromere protein F

CIN - Chromosomal instability

CldU - Chlorodeoxyuridine

COBL - Cordon-bleu

CPT - Camptothecin

CRC - Colorectal cancer

CRIB - Cdc42/Rac/GTPase interactive binding region

CRISPR - Clustered regularly interspaced short palindromic repeats

CRL1 - Cullin-RING Ligase 1

CtIP - C-terminal binding protein-interacting protein

ctRAGE - Cleaved receptor for advanced glycation end-products

Cys (C) - Cysteine

DAAM - Dishevelled-associated activator of morphogenesis

DAD - Diaphanous autoregulatory domain

DAPI - 4',6-diamidino-2-phenylindole

DBSCAN - Density-based spatial clustering of applications with noise

DCLRE1C – DNA Cross-link repair 1C (Artemis)

DD - Dimerisation domain

DDR - DNA damage response

DDT - DNA damage tolerance

dHJ - Double Holliday junction

DIAPH[number] - Diaphanous-related formin[number]

DID - Diaphanous inhibitory domain

DNA - Deoxyribonucleic acid

DNA-PKcs - DNA-dependent protein kinase catalytic subunit

DNA2 - DNA replication ATP-dependent helicase/nuclease DNA2

DONSON - Protein downstream neighbour of Son

DOX - Doxycycline

DRF - Diaphanous-related formin

DRF1 - Diaphanous related formin 1

DSB - Double-strand break

ECL - Enhanced chemiluminescence

EDTA - Ethylenediaminetetraacetic acid

EEA1 - Early endosomal Rab5 effector protein

EGR1 - Early growth response protein 1

ERCC1 - Excision repair cross-complementation group 1

ERG1 - Early Growth Response 1

ETAA1 - Ewing tumour-associated antigen 1

ETOP - Etoposide

EXO1 - Exonuclease 1

F-actin - Filamentous actin

FA - Fanconi anaemia

FANC - Fanconi anaemia complementation group

FAS - Fryns-Aftimos syndrome

FAT - FRAP, ATM, and TRRAP domain

FATC - FAT C-terminal domain

FBS – Foetal bovine serum

FH - Formin Homology

FHA - Forkhead-associated domain

FHOD - Formin homology 2 domain-containing proteins

FMN - Formin

FRL - Fused in rhabdomyosarcoma-like protein

Fwd - Forward

G - Guanine

G-actin - Globular / monomeric actin

G_1 - Gap 1 phase

G_2 - Gap 2 phase

GBD - GTPase binding domain

GBP - GTPase-binding protein

GEN1 - GEN1 Holliday Junction 5' Flap Endonuclease

GINS - Japanese go-ichi-ni-san meaning 5-1-2-3

GLU - Glutamic acid

Glu (E) - Glutamic acid

GTPase - Nucleotide guanosine triphosphate hydrolase

H2A - Histone H2A

HCT-116 - Human colorectal carcinoma cell line

HDAC - Histone deacetylase

hDia1 - Human diaphanous 1

HDR - Homology-directed repair

HEAT - Huntingtin, elongation factor 3, protein phosphatase 2A, TOR1

HHR - Homologous recombination repair

His (H) - Histidine

HJ - Holliday junction

HP1 - Heterochromatin protein 1

HPC - Haematopoietic progenitor cell

HR - Homologous recombination

HSC - Haematopoietic stem cell

H. sapiens – Homo sapiens

HT29 - Human colorectal adenocarcinoma cell line

HU - Hydroxyurea

HUS1 - HUS1 checkpoint clamp component

ICL - Interstrand crosslink

IdU - Iododeoxyuridine

Indel - Insertion / deletion

INF - Inverted formins

Ile (I) – Isoleucine

IQGAP1 - Ras GTPase-activating-like protein

IR - Ionising radiation

JAK-STAT - Janus kinase/signal transduction and transcription activation

JMY - Junction-mediating and regulatory protein

JNK - Jun N-terminal kinase

KAP1 - KRAB-associated protein 1

kb - Kilobase

KCl - Potassium chloride

kDa - Kilodalton

LFHL - Low frequency hearing loss

LCL – Lymphoblastoid cell line

LSCC - Lung squamous cell carcinoma

Lys (K) - Lysine

M - Mitosis

M phase - Mitotic phase

MAL - Megakaryocyte acute leukaemia

MCM[number] – Mini chromosome maintenance[number]

MDC1 - Mediator of DNA damage checkpoint 1

mDia1 - Mouse diaphanous 1

MDS - Myelodysplastic syndrome

MMD - Moyamoya disease

MMR - Mismatch repair

MRE11 - Meiotic recombination 11

MT1-MMP - Membrane type 1-matrix metalloproteinase

MTBP - MDM Two Binding Protein

MTOC - Microtubule organizing centre

N-terminus – Amino acid-terminus

NBS - Nijmegen Breakage Syndrome

NBS1 - Nijmegen breakage syndrome protein 1

NBSLD - Nijmegen Breakage Syndrome-like disorder

NHEJ - Non-homologous end joining

NK - Natural killer

NLS - Nuclear localisation signal

NND – Nearest-neighbouring distance

NPF - Nucleation promoting factors

nWASP - Neural Wiskott-Aldrich syndrome protein

O/N - Overnight

ORC - Origin recognition complex

p. - Protein

PALB2 - Partner and localizer of BRCA2

PARP1 - Poly(ADP-ribose) polymerase 1

PAXX - Paralog of XRCC4 and XLF

PBS - Phosphate buffered saline

PCNA - Proliferating cell nuclear antigen

PIKK - Phosphoinositide 3-kinase-related kinase

PIPES - Piperazine-N,N′-bis(2-ethanesulfonic acid)

PI3K - Phosphoinositide 3-kinases

PNPK - Polyribonucleotide nucleotidyltransferase

POL - DNA polymerase

POLθ - DNA polymerase theta

Pro (P) – Proline

PSF - Point spread function

R loop - RNA-DNA hybrid

RAD[number] - **Rad**iation sensitive protein [number]

RAGE - Receptor for advanced glycation end-products

RAS – Rat sarcoma virus

RBBP8 - Retinoblastoma-binding protein 8

RecQ - RecQ Family of DNA Helicases

RER - Ribonucleotide excision repair

Rev - Reverse

RhoA - Raf homolog family member A

RIF1 - Rap1-interacting factor 1

RNA - Ribonucleic acid

RNF[number] - Ring finger protein [number]

ROS - Reactive oxygen species

RPA - Replication protein A

RPA-P - Phosphorylated replication protein A

RPM - Revolutions per minute

RPS14 - 40S Ribosomal protein S14

RT – Room temperature

Sc - Supercoil

SCAR - Suppressor of cAR

SCBMS - Seizures, cortical blindness, and microcephaly syndrome

SDSA - Synthesis dependent strand annealing

seDSB – Single-ended double strand break

Ser (S) - Serine

siRNA - Small interfering RNA

SMARCAD1 - SWI/SNF-related matrix-associated actin-dependent regulator of chromatin subfamily A containing DEAD/H box 1

SRF - Serum response factor

SSA - Single-strand annealing

SSB - Single strand break

ssDNA – Single-stranded DNA

STORM - Stochastic optical reconstruction microscopy

T - Thymine

TAR – Transcription-associated replication

TCR - T-cell receptor

TDP - TAR DNA-binding protein

Ter - Termination

Thr (T) - Threonine

TMB - Tandem-monomer-binding nucleators

TOP111A - Topoisomerase III alpha

TOPBP1 - Topoisomerase (DNA) II binding protein 1

TOPI - Topoisomerase I

TOPII - Topoisomerase II

TS – Trans-lesion synthesis

TSG - Tumour suppressor gene

UV - Ultraviolet

v/v - Volume per volume

w/v - Weight per volume

WABS - Warsaw Breakage Syndrome

WAS - Wiskott-Aldrich Syndrome

WASH - WAS protein family homologue

WASP - Wiskott-Aldrich Syndrome protein

WAVE - WASP family Verprolin-homologous protein

WES – Whole exome sequencing

WH2 - Wiskott-Aldrich Syndrome homology 2

WHAMM - WAS protein homologue associated with actin golgi membranes and microtubules

XLF - XRCC4-like factor

XP - Xeroderma Pigmentosum

XPF - Xeroderma pigmentosum complementation group F

XRCC[number] - X-Ray Repair Cross Complementing[number]

XPF - Xeroderma pigmentosum complementation group F

XRCC[number] - X-Ray Repair Cross Complementing[number]

Chapter 1: Introduction

1.0 Introduction

1.1 Diaphanous-related formin 1

1.1.1 Background

Diaphanous-related formin 1 (DIAPH1) is the human homologue of the Drosophila gene, Diaphanous, and was first identified in 1997 by Watanabe et al. DIAPH1 is located on chromosome 5q31.3 and contains 28 exons which encode the DIAPH1 protein (other names include mDia1, hDia1, DRF1, DFNA1, LFHL, SCBMS, diaphanous-related formin 1, and protein diaphanous homologue 1), which is approximately 180 kDa in size. DIAPH1 is an abundant cytoskeletal protein expressed in a wide range of tissue types and is a member of the Diaphanous-related formin (DRF) family of actin-nucleating factors (Watanabe *et al.*, 1997; Breitsprecher and Goode, 2013). It is a known canonical effector for the RhoA (Raf Homology family member A) family of GTPases and functions as a nucleator of unbranched actin filaments, binds microtubules with high affinity, and is also a regulator of the receptor of advanced glycation end products (RAGE) intracellular signalling cascade (Pan *et al.*, 2014; Ramasamy *et al.,* 2022). DIAPH1 has several implications in human diseases, including myelodysplastic syndrome, non-syndromic sensorineural hearing loss, microcephaly, and tumorigenesis, which will be explored further in sections below.

1.1.2 Structure and functions of Diaphanous-related formins

There are currently 15 known mammalian formin genes and 7 subfamilies, including the most well-studied subfamily, the Diaphanous-related formins (DRFs) (Table 1.1). DIAPH1 is a member of the DRF sub-family, with its most well-characterised cellular function being actin nucleation. In mammals, the DRF family consists of 3 formin paralogues; DIAPH1, 2 and 3, that are specifically required for the nucleation of unbranched actin filaments (Breitsprecher and Goode, 2013; Ueyama, Ninoyu, S.-Y. Nishio, *et al.*, 2016; Zhang *et al.*, 2022). DRF proteins contain highly conserved regions spanning the entire protein: an N-terminal GTPase binding domain (GBD) adjacent to a Diaphanous inhibitory domain (DID; also known as FH3 domain), a Formin homology 1 and 2 (FH1 and FH2 respectively) domain and a C-terminal Diaphanous autoregulatory domain (DAD), as shown in Figure 1.1A. Interaction between the DID and DAD, within the protein, results in auto-inhibition and an inactive/'closed' protein conformation as shown in Figure 1.1B. Crystallographic structures and single-particle electron microscopy studies have demonstrated that the DID-DAD interaction results in a protein conformation that physically obstructs the protein's ability to polymerise actin (Breitsprecher and Goode, 2013). The N-terminal GBD binds to Rho GTPases to counteract this auto-inhibitory conformation and results in an active protein confiormation. However, additional factors can also target DRFs to influence their activity (Ueyama, Ninoyu, S.-Y. Nishio, *et al.*, 2016).

DRFs specifically nucleate unbranched actin structures to facilitate the formation of actin filaments, stress fibres and filaments required for cell divisions and plasma membrane protrusions. DRF proteins are activated by Rho GTPases and are required for the regulation of a number of cellular processes such as actin elongation and/or

nucleation, cytoskeletal organisation, cilia function, regulation of cellular morphology, cytokinetic contractile rings, formation of stress fibres and cables, endocytosis and formation of lamellipodia, filopodia and microtubules (Campellone and Welch, 2010; Weston *et al.,* 2012; Nishimura *et al.*, 2019; Chen *et al.*, 2021). The formins also have non-redundant roles within the same pathways, such as during mitosis; DIAPH1 is situated at the cortex of the dividing cell, facilitating the assembly of γ-actin filaments to control the positioning of the furrow and the pace of membrane ingression while activation of DIAPH3 acts at the cytokinetic furrow to initiate the generation of a β-actin contractile ring at the cell's midpoint (Chen *et al.*, 2021; Jeruzalska and Mazur, 2023). In addition to their cytoplasmic roles, some members of the DRF family have been reported to accumulate in the nucleus and function in the nucleus, which is discussed in more detail in Section 1.1.5 and 1.9.

Structurally, DIAPH1-3 are very similar, and all 3 proteins share a similar Rho-dependent mechanism of activation. However, DIAPH1 binds specifically to, and is activated by RhoA, B and C, whereas DIAPH2 and DIAPH3 can also be activated by other Rho homologues such as RhoD, Rac1 and CDC42. These differences, in mice, have been attributed to a motif of three asparagine (Asn) residues (N-N-N) in DIAPH1 which is substituted for a Threonine-Serine-Histidine (T-S-H) motif in DIAPH2 and 3 (Lammers *et al.*, 2008). Other formin protein families include formin-related proteins in leukocytes (FRLs), dishevelled-associated activators of morphogenesis (DAAMs) and formin homology 2 domain-containing proteins (FHODs), inverted formins (INFs) and delphilin (Higgs, 2005).

In the active Rho GTPase-bound state, DRFs exist as dimeric multi-domain proteins and the FH1 and FH2 domains interact with actin filaments and microtubules. The FH1 domain of DRFs interacts with actin monomers via profilin, an abundant protein that binds to ATP-actin monomers. The predicted structure of the FH1 domain is an extended and unstructured region containing multiple proline-rich motifs to enable recruitment of profilin-bound ATP-actin monomers. FH2 domains form a dimeric anti-parallel ring-shaped structure that binds to the barbed end of actin filaments with high affinity. The two halves of the FH2 dimer are held in place through interactions between the 'lasso' and 'post' segments to generate a flexible but tethered dimer (Figure 1.2). Within the FH2 region there are three separate highly conserved actin binding sites; isoleucine (Ile) residues, I143 and I862 and a lysine (Lys) residue, K1601 which are conserved from Bni1 (a formin in Saccharomyces cerevisiae) to DIAPH1 in humans. Mutating these specific residues results in a strong reduction in actin nucleation and elongation *in vivo*, suggesting the importance for these residues in actin-related functions (Goode and Eck, 2007; Breitsprecher and Goode, 2013; Chen *et al.*, 2021)

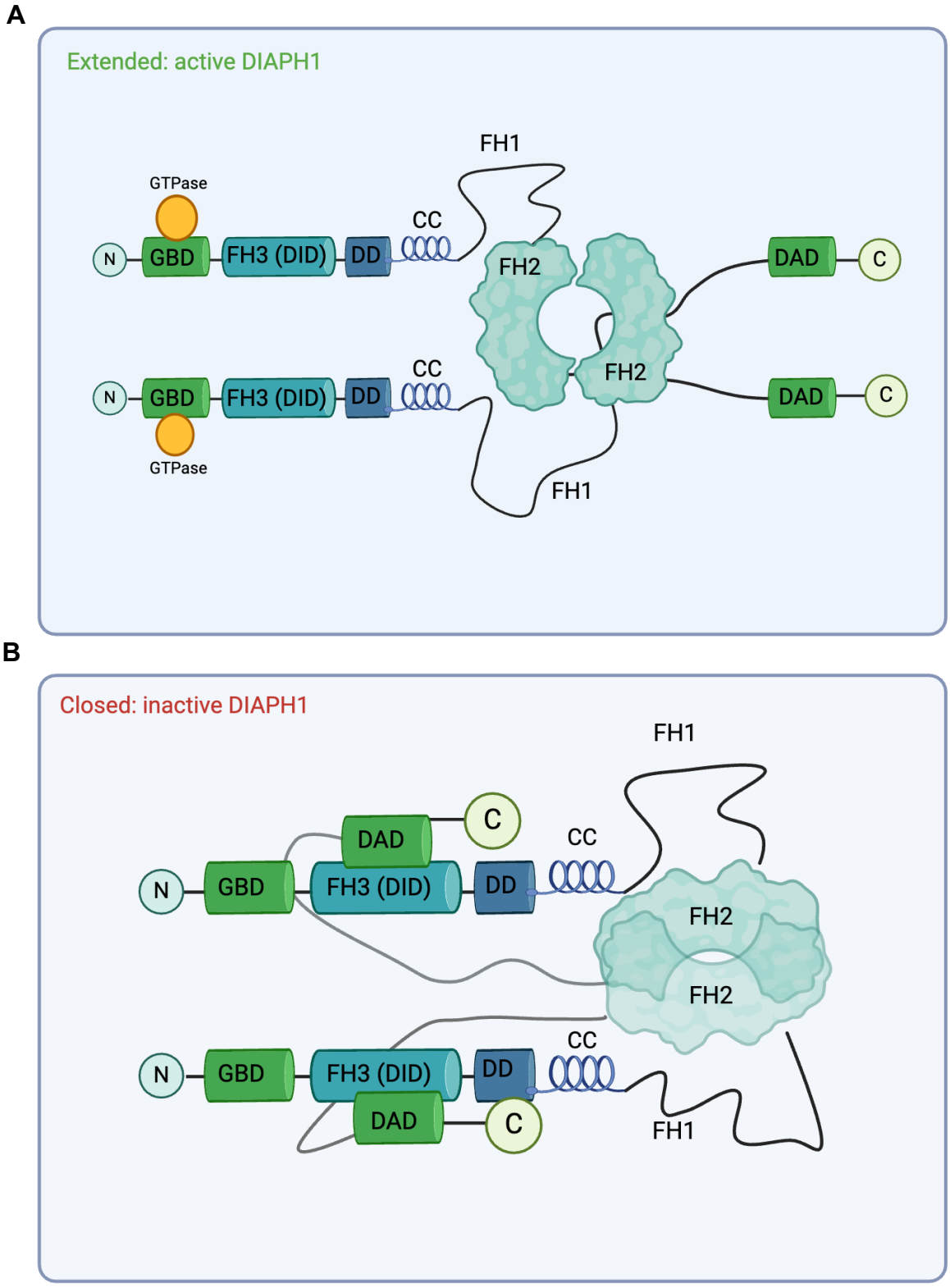


Figure 1.1 - Schematic diagram of the structure of DIAPH1 protein *– **A** - Schematic representation of DIAPH1 bound to a Rho GTPase at the N-terminal GTPase Binding Domain (GBP) resulting in DIAPH1 being in its active/open conformation where it forms a dimer via the FH2 domain. **B** - Representation of DIAPH1 in a closed conformation. The C-terminal DAD region interacts with the FH3/DID region. GBP – GTPase binding domain, FH(1-3) – formin homology (1-3), DAD – Diaphanous autoregulatory domain, DID – Diaphanous inhibitory domain, DD-dimerisation domain, CC- coiled-coil. Created with BioRender.com.*

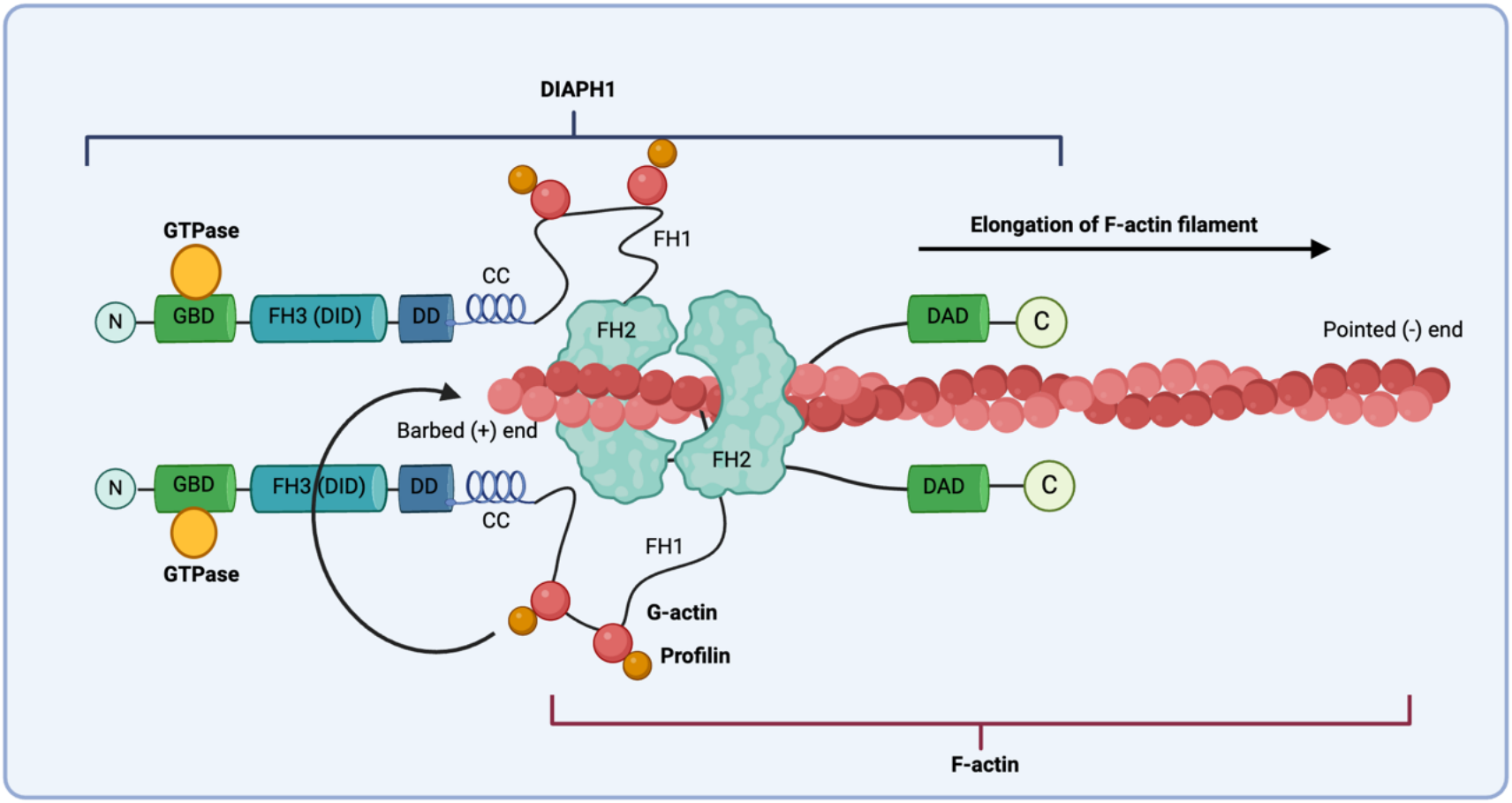


Figure 1.2 – Schematic of DIAPH1's function in actin nucleation *– When in the active, GTPase bound-conformation, the dimeric DIAPH1 FH2 domains encircle the barbed (+) end of the F-actin filament. The FH1 domain binds profilin bound G-actin and adds monomers onto the growing F-actin filament and the filament elongates towards the pointed (-) end. Abbreviations: Coiled-coil (CC), Diaphanous autoregulatory domain (DAD), dimerisation domain (DD), Diaphanous inhibitory domain (DID), formin homology (1-3) (FH(1-3)), filamentous actin (F-actin), globular actin (G-actin), and GTPase binding domain (GBP). Created with BioRender.com.*

1.1.3 DIAPH1 function in microtubule dynamics

In addition to regulating the actin cytoskeleton, DIAPH1 also plays a role in microtubule dynamics. DIAPH1 induces selective stabilisation of the head (polar end) of microtubules, which has implications for certain diseases. Microtubules are an integral part of the cytoskeleton and are hollow tubes made up of tubulin, arranged in linear strands called protofilaments. Microtubules are assembled from head to tail in arrangements of α/β tubulin heterodimers. Microtubules have multiple roles in the cell, including during mitosis, and work in coordination with the actin cytoskeleton (Gudimchuk and McIntosh, 2021). Microtubules can assemble in many ways depending on the required function, making them dynamic cytoskeletal proteins with multiple roles. In specific cell types, microtubules are of pivotal importance for specialised functions such as in T cell migration. The importance of DIAPH1 in T cell migration has been highlighted in some studies, which have shown it is required for reorientation of the microtubule organising centre (MTOC) downstream of T cell receptor (TCR) engagement in cytotoxic T cells. This process has been shown to be regulated by Rho GTPases (Eisenmann *et al.*, 2007; Sakata *et al.*, 2007; Dong *et al.*, 2013).

1.1.4 DIAPH1 function in the RAGE axis

The receptor for advanced glycation end-products (RAGE) axis responds to advanced glycation end-products (AGE), such as methylglyoxal, glyoxal and carboxymethyl-lysine and plays a role in regulating pathological processes such as inflammation and oxidative stress (Chavakis, Bierhaus and Nawroth, 2004; Bhattacharya *et al.*, 2023).

RAGE has crucial roles in regulating metabolic processes associated with the development of obesity and associated metabolic disorders, including diabetes and atherosclerosis (Ruiz *et al.*, 2021; Ramasamy *et al.,* 2022; Senatus *et al.*, 2023). DIAPH1 binds to the intracellular domain of RAGE and contributes to RAGE signalling through binding to the cytoplasmic tail of RAGE (ctRAGE). Silencing of DIAPH1 blocks RAGE ligand-mediated activation of CDC42 and Rac1 (both Rho GTPases) and prevents cell migration mediated through RAGE ligands (Hudson *et al.*, 2008). It has also been shown that blocking the interaction between DIAPH1 and RAGE prevents adipocyte glucose uptake, and DIAPH1 is a modulator in the response to ischemia in myocardial tissue and regulates vascular remodelling and microvascular hyperpermeability (Strieder-Barboza et al., 2019; Zhou et al., 2018; Toure et al., 2012; O'Shea et al., 2017). Furthermore, the DIAPH1-RAGE axis has also been implicated in neuroinflammation associated with neurodegenerative diseases, where DIAPH1 binding to RAGE has been shown to activate four major signalling pathways; JAK-STAT, JNK, RAS and PI3K (Bhattacharya *et al.*, 2023). Whilst the role of DIAPH1 in the RAGE axis is not fully understood, and is an emerging area of research, it highlights the diversity of functions of DIAPH1 and the potential for therapeutic interventions that are independent of actin.

1.1.5 Nuclear functions of DIAPH1

The cytoplasmic function of DIAPH1 in actin elongation and microtubule dynamics is well characterised, but its nuclear function remains poorly understood. In recent years, formins have been detected in the nucleus and have been shown to have nuclear functions. Both DIAPH1 and DIAPH2 have been detected in the nucleus and provide

an important contribution to controlling nuclear actin dynamics, which was shown by siRNA-mediated knockdown of both proteins resulting in a significant decrease in basal levels of actin polymerisation in nuclear extracts (Baarlink and Grosse, 2014). A study by Baarlink et al. showed that DIAPH1 plays a role in the activation of serum response factor (SRF), which promotes the release of megakaryocyte acute leukaemia (MAL) protein from G-actin monomers, which in turn stimulates SRF-dependent expression of genes required for cytoskeletal processes (Baarlink *et al.*, 2017). Before this study, the role of formins in the nucleus was unclear, but it is now understood that DIAPH1 and DIAPH2 promote the assembly of nuclear F-actin networks, which then result in MAL-SRF-dependent transcription. Furthermore, cells expressing a dominant negative form of DIAPH2 were not able to initiate a response to serum when compared to control cells (Baarlink, Wang and Grosse, 2013).

It is not yet clear how DIAPH1 is imported into the nucleus, but DIAPH1 has been shown to co-precipitate with exportin-6, a protein critically required for the nuclear export of actin and profilin-actin complexes, as well as the transcriptional regulator HAN11 (Stüven, Hartmann and Görlich, 2003; Morita *et al.*, 2006; Baarlink and Grosse, 2014). Moreover, DIAPH1 contains a nuclear localisation signal (NLS) within its C-terminus, and C-terminal fragments of DIAPH1 (containing FH1, FH2, and DAD) have been shown to predominantly localize to the nucleus. It has not yet been tested if the NLS functions in full-length DIAPH1 and if N-terminal domains have any impact on its cellular localisation (Copeland *et al.*, 2007). At present, the impact of cytosolic functions of formins, including the DRFs and DIAPH1, on nuclear actin dynamics is not yet clear.

1.2 Human diseases associated with variants in *DIAPH1*

DIAPH1 variants have been associated with several human diseases. Most notably, non-syndromic sensorineural hearing loss, 5q-Myelodysplastic syndrome, and Seizures, cortical blindness, and microcephaly syndrome (SCBMS). DIAPH1 has also been linked to cancer as well as other pathologies including diabetes and Moyamoya disease (MMD) (Kundishora *et al.*, 2021; Zglejc-Waszak *et al.,* 2021; Ramasamy *et al.,* 2022). The outcomes of dysregulation of DIAPH1 function either through gene mutation, epigenetic alteration, and/or overexpression are varied, highlighting many of the diverse functions of DIAPH1 within the cytoplasm via the actin network or through the RAGE-DIAPH1 axis. However, most strikingly, the clinical features between patients harbouring mono-allelic and bi-allelic mutations (outlined in further detail in Sections 1.2.1 and 1.2.2 respectively) are very different and suggests that DIAPH1 has additional functions that are not currently known. This section outlines the most well-characterised human diseases associated with DIAPH1. However, the role of DIAPH1 in MMD pathogenesis and the RAGE-DIAPH1 axis in the pathogenesis of diabetes and diabetic complications is not discussed.

1.2.1 Heterozygous variants in *DIAPH1* and associated human disorders

The first human disease to be associated with the *DIAPH1* gene was autosomal dominant non-syndromic sensorineural hearing loss caused by an underlying heterozygous variant in *DIAPH1* (Ueyama, Ninoyu, S.-Y. Nishio, *et al.*, 2016). This association was first made in 1997 in a Costa Rican family presenting with delayed low-frequency deafness, beginning at around 10 years of age (Lynch *et al.*, 1997). This

variant in *DIAPH1* was c.3634+1G>T, whereby the canonical splicing donor sequence is disrupted and moved the splice donor site to a cryptic site four base pairs (bp) downstream. This results in a 4bp insertion (ttaa), causing a frameshift close to the DAD in the 3′ end of the gene. This frameshift truncates the DIAPH1 protein by removing the DAD, which gives rise to a constitutively active DIAPH1 protein (Lynch *et al.*, 1997). In 2016, another heterozygous mutation (c.3610C>T) was identified in patients with autosomal dominant non-syndromic sensorineural hearing loss, which gives rise a p.R1204Ter mutant form of DIAPH1. This mutation causes an early translation termination site just before the C-terminal basic motif ($RRKR^{1204-1207}$), where the DAD is located. Again, this mutation would be predicted to result in the formation of a constitutively active protein due to loss of the DAD domain. The p.R1204Ter mutation was identified in two unrelated Japanese families, whereby affected individuals had autosomal dominant sensorineural hearing loss (Ueyama, Ninoyu, S.-Y. Nishio, *et al.*, 2016). A further novel variant has been identified in a Korean family; c.1589T > G; p.I530S, located in the coiled-coil domain also giving rise to the same clinical features (Kang *et al.*, 2016).

Another heterozygous *DIAPH1* variant, c.3637C>T; p.R1213Ter, has also been identified by three different groups. This mutation results in a truncated DIAPH1 protein, which is again, constitutively active. The clinical features of this mutant not only cause sensorineural hearing loss, but macrothrombocytopaenia (abnormally large platelets) and neutropenia (low neutrophils) (Stritt *et al.*, 2016; Ganaha *et al.*, 2017; Neuhaus *et al.*, 2017). p.R1213Ter DIAPH1 results in a reduction in the formation of proplatelets, abnormal actin filament formation and compromised cell clustering (Stritt *et al.*, 2016).

1.2.2 Homozygous variants in *DIAPH1* and associated human disorders

Homozygous variants in *DIAPH1* give rise to a very different clinical presentation to those with heterozygous variants discussed in Section 1.2.1. The main features of this disorder include microcephaly, seizures, dysmorphic facial features, and immunodeficiency (Low CD4+/low CD8+ T cells and high NK cells). However, other clinical features have been reported e.g. cortical blindness, developmental delay and recurrent respiratory disease (Ercan-Sencicek *et al.*, 2015; Al-Maawali *et al.*, 2016). Whilst the underlying mechanism giving rise of this clinical phenotype is currently unknown, it is strikingly similar to other disorders associated with a defective DNA damage response (discussed in Section 1.10) suggestive that they might be caused, in part, by a DNA repair deficiency.

1.2.3 5q chromosome deletions and myelodysplastic syndrome

DIAPH1 mutations have also been linked to macrothrombocytopaenia and myelodysplastic syndromes (MDS) (Eisenmann et al., 2009; Keerthivasan et al., 2014; Stritt et al., 2016). MDS encompasses a range of haematopoietic disorders stemming from defects in haematopoietic stem cell and/or haematopoietic progenitor cell (HSC/HPC) differentiation and control. Clinical manifestations of MDS span from anaemias, thrombocytopaenia, and leukopenia to more severe pancytopenia, with patients facing an increased risk of developing acute myeloid leukaemia (AML) (Malcovati and Nimer, 2008). Macrothrombocytopaenia, characterised by thrombocytopenia alongside significantly larger platelets, typically presents asymptomatically or with minor bleeding disorders (Ghosh et al., 2018).

Located on chromosome 5q,31.3, *DIAPH1* resides within a region associated with MDS when deleted. Deletions of this chromosome arm are the most common karyotypic abnormality in MDS, predisposing patients to AML and other myeloproliferative malignancies. This location contains known tumour suppressor genes (TSGs) involved in the growth of haematopoietic stem cells (HSCs), including *ERG1/Krox20, RPS14, and α-catenin/CTNNA1.* Despite the identification of these TSGs, the mechanisms underlying deficits in patients with 5q deletions, and their propensity for malignancies, remains unclear. Microarray gene profiling of MDS patient samples has revealed reduced *DIAPH1* expression, akin to other candidate genes like *ERG1, CTNNA1*, and *RPS14*. Murine models of *DIAPH1* knockout (Drf1$^{-/-}$) have shown age-dependent myelodysplasia development, similar to other gene knockouts in the 5q common deleted regions, suggesting that DIAPH1 loss contributes to the MDS pathogenesis associated with 5q deletions. However, the mechanism for this is not yet understood (Peng et al., 2007).

1.2.4 DIAPH1 and its association with cancer

The hallmarks of cancer serve as a valuable framework for categorising the intricate characteristics of cancer genotypes and phenotypes into ten fundamental principles. These hallmarks encapsulate the dysregulation of crucial cellular processes such as the cell cycle, DNA repair pathways, and mitosis, which facilitate the evasion of growth suppressors, maintenance of proliferative signals, and genomic instability, leading to the emergence of mutations (Hanahan and Weinberg, 2011). Given the dynamic nature of these processes, the actin cytoskeleton and microtubules play pivotal roles in ensuring accurate cell division, assembly of the mitotic spindle, and intracellular

trafficking (Heng and Koh, 2010; Forth and Kapoor, 2017). Additionally, cytoskeletal reorganisation is closely associated with the invasion and metastasis of tumours. DIAPH1, known for its involvement in cytoskeletal organisation through actin nucleation and microtubule dynamics, has emerged as a significant player in various tumour types, contributing to cell cycle dysregulation, apoptosis, microtubule dysregulation, cell migration, invasion, and metastasis.

In colorectal cancer (CRC) cell lines, HCT-116 and HT29 cells, depletion of DIAPH1 lead to decreased mitotic spindle dynamics and increases chromosomal instability in both cell lines (Miao *et al.*, 2021) An earlier study showed that DIAPH1 is downregulated in inflammatory bowel disease-associated CRC transformation (Kanaan et al., 2010). These studies indicate that downregulation of DIAPH1 may be important for tumourigenesis in CRC. Further to this, laryngeal squamous cell carcinoma (LSCC) exhibits altered DIAPH1 expression. Knockdown experiments in LSCC cell lines demonstrate DIAPH1 has a role in LSCC tumour growth, which was further supported by *in vivo* studies in mice whereby the tumour weight of DIAPH1 knockdown mice was significantly reduced compared to the negative control mice (Yang et al., 2019; Yang et al., 2021).

In contrast to these studies, the upregulation of DIAPH1 has been observed in various other solid tumours, including ovarian, breast, high-grade malignant glioma, kidney and prostate cancers, where it is thought to promote invasion, proliferation, migration, and metastasis (Yamana *et al.*, 2006; Li *et al.*, 2014; Kim *et al.*, 2016) (Kim and Rhee, 2016; Yamana *et al*., 2006; Li *et al*., 2014). Knockdown of DIAPH1 in breast cancer cell lines reduced colocalisation of membrane type 1-matrix metalloproteinase (MT1-MMP) and

EEA1 to the cell surface in invasion, and DIAPH1 loss also reduced MT1-MMP interaction with microtubules (Kim *et al.*, 2016). Conversely, in ovarian cancer, high DIAPH1 expression correlates with improved survival, possibly due to increased responsiveness to chemotherapeutic agents targeting highly proliferative cells (Schiewek *et al*., 2018). In haematological malignancies, DIAPH1 expression is dysregulated through a mechanism that remains unclear (Thompson *et al*., 2018). However, the fact DIAPH1 expression is dysregulated in many tumour types, suggests it may be functioning In tumourigenesis, but the precise mechanism for this remains poorly understood. Given DIAPH1 functions in multiple cellular processes, the role of DIAPH1 in tumourigenesis is likely to be content- and cell type-dependent.

In summary, DIAPH1 emerges as a potential therapeutic target and/or biomarker across multiple tumour types, although specific clinically inhibitors are currently unavailable. Further research is warranted, to elucidate its precise roles, mechanisms and potential as a prognostic marker or therapeutic target.

1.3 Actin

Sections 1.1 and 1.2 outlined the known functions of DIAPH1 and the associated human diseases. As discussed, DIAPH1 is an actin nucleating factor in the Formin family nucleators. This next section summarises what is known about actin and other key actin nucleator families in the cytoplasm and human disease associated with them.

1.3.1 Actin structure and function

Actin is a 42 kDa 375 amino acid-long protein that forms a major component of the cytoskeleton, performing a wide range of cellular functions such as cell migration, adhesion, intracellular transport, and cell signalling. Actin is conserved with a high degree of sequence homology from *C. elegans* to *H. sapiens* and is one of the most abundant proteins in eukaryotic cells (Gupta, Ambaru and Bajaj, 2020). There are 6 actin paralogues in the mammalian genome; *ACTA1, ACTA2, ACTC1, ACTB, ACTG1* and *ACTG2* each encoding a different isoform of actin (Dugina, Shagieva and Kopnin, 2022). Recently an actin-like protein has also been reported, β-actin-like protein 2 (*ACTBL2*) (Malek *et al.*, 2021). The 3 α-actin genes (*ACTA1, ACTC1, ACTA2; located on chromosomes 1, 10 and 15 respectively)* are classed as muscle actin, being required for contractile structures, such as muscle fibres (α-smooth muscle, α-cardiac muscle and α-smooth muscle) (Vandekerckhove and Weber, 1978; Dugina, Shagieva and Kopnin, 2022). The two main non-muscle, class of actin proteins are β-actin and γ-actin; and ACTBL2 has also been categorised within this class. *ACTB* located on chromosome 7 and containing 6 exons, is the only β-actin gene and is required for β-cytoplasmic actin filament formation, and it is the most abundant protein in the cytoplasm. β-actin functions in cellular scaffolding and is required for stress fibre formation to provide tension and contractility within the cytoplasm, as well as the formation of filopodia and lamellipodia. There are two genes that encode γ-actin, however their functions differ. *ACTG1*, located on chromosome 17, encodes cytoplasmic γ-actin and is required for γ-cytoplasmic actin filaments, stress fibres in lamellipodia and cortical networks during cell motility and mitosis. Whereas *ACTG2,* located on chromosome 2 encodes γ-2-actin which is expressed in smooth muscle

cells such as those in walls of the gastrointestinal tract, blood vessels and the uterus (Dugina *et al.*, 2009; Shagieva *et al.*, 2020; Dugina, Shagieva and Kopnin, 2022; Miyoshi *et al.*, 2022). Interestingly, the two cytoplasmic actin proteins β-actin and γ-actin, despite their distinct cytoplasmic functions, differ only by 4 amino acids in the N-terminal region of the protein (Figure 1.3A). β-actin contains 3 aspartic acid (Asp) residues in position 2-4 and a valine (Val) at position 10 whereas γ-actin contains glutamic acid (Glu) in residues 2-4 and isoleucine (Ile) at position 10, the remainder of the two proteins are identical (Figure 1.3A) (Jeruzalska and Mazur, 2023).

For actin to carry out its function, it exists in two forms; globular monomers (G-actin) or as filaments (F-actin), as shown in Figure 1.3B-D, and is regulated by a large range of actin-binding proteins (ABPs) (discussed in more detail in Sections 1.3.2-1.3.4). Within cells, G-actin is ATP-bound, and F-actin is ADP-bound. The polymerisation of actin occurs with the addition of G-actin monomers onto F-actin filaments (Figure 1.3C-D). This polymerisation process consists of three distinct steps: Step 1, the “lag phase”, which is the formation of an actin dimer. These actin dimers are unstable molecules and can revert to monomers rapidly. Step 2 is the formation of a trimer, which increases the stability of the molecule and allows for further monomers to be added to facilitate Step 3, the “elongation phase” (Figure 1.5A). The elongation phase comprises rapid binding of ATP-bound-G-actin to the ‘polar’ or ‘barbed’ end of the filament, which is termed actin ‘nucleation’. The ATP-bound to the actin molecule is hydrolysed into ADP + phosphate as the filament matures. ADP-bound actin is then released from the ‘pointed’ end of the filament and ADP is exchanged for ATP so the actin monomer can be used again. This process is facilitated by the presence of divalent cations and after

the filament is formed, it remains in a dynamic equilibrium with continuing association and dissociation of actin monomers (Cooper, 2000).

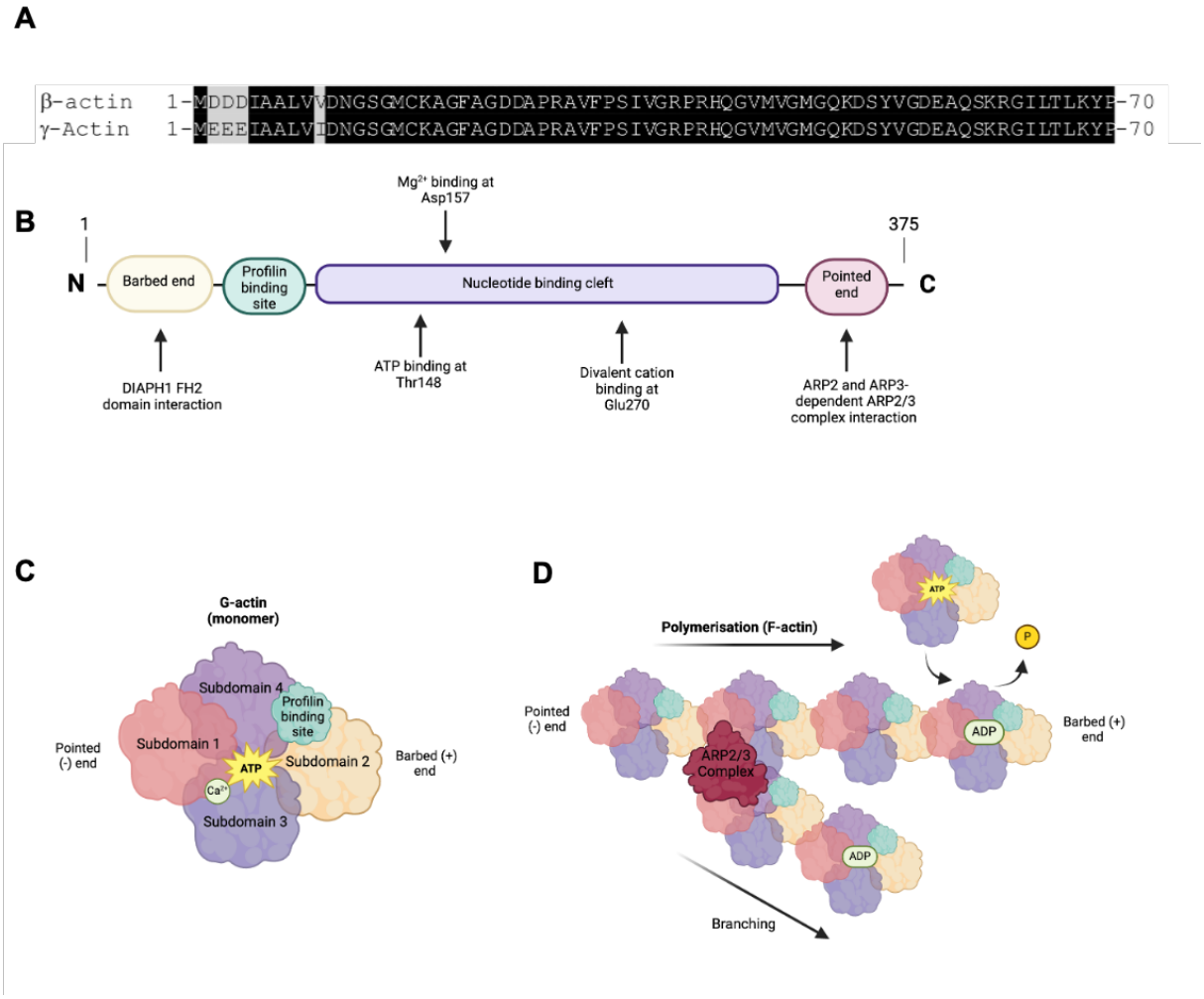


Figure 1.3 – Schematic diagram of* β-actin *and* γ-actin *structure and function – A *- The first 70 amino acids of* β-actin *and* γ-actin*, which are 375 amino acids long. The structures of both proteins are identical other than 4 amino acids in the N-terminus;* β-actin *has D at positions 2-4 and a valine at position 10, whereas* γ-actin *has an E at positions 2-4 and an isoleucine at position 10.* ***B*** *– Actin does not have specific domain and bounds to many proteins. The N-terminus of the protein is the barbed (+) end, which is the site exposed at the growing end of a filament of actin and where the globular actin monomer would be added onto the polymer. DIAPH1 FH2 domain interacts with this region to facilitate filament nucleation. The profilin binding site is located near the barbed end. The C terminus is the pointed (-) which is the region that binds to other monomers barbed end to facilitate filament extension. The remainder of the protein has various binding sites for ATP, divalent cations (examples shown) and proteins, such as the ARP2/3 complex and DIAPH1, that facilitates various functions of actin including polymerisation, depolymerisation and branching.* ***C*** *– A schematic diagram to show a globular monomer of actin with an ATP binding cleft at the center and the pointed and barbed and at either end of the folded protein.* ***D*** *– schematic to show monomers of actin being added onto a straight and branching filament. G-actin is ATP bound and F-actin is ADP bound. Colours in C-D signify distinct subdomains 1-4 of actin monomers, subdomain 1 being the pointed (-) end and subdomain 2 being the barbed (+) end. Profilin binding site is shown to demonstrate its proximity to the barbed (+) end. Created with Biorender.com.*

1.3.2 Actin binding proteins

Due to the diverse range of cellular processes that actin is involved in, over 150 proteins associate with or regulate its function. ABPs fall into a wide range of categories, defined by their functions, including nucleation, elongation, severing, capping, crosslinking, bundling, de-polymerising and sequestering activities. Actin nucleators are of particular importance due to the unfavourable kinetics of initial actin polymerisation and the need for rapid polymerisation of F-actin to respond to many different cellular stimuli (Dos Remedios *et al.*, 2003). The 3 major classes of actin nucleators that function in the cytoplasm are the Class I ARP2/3 complex, Class II Formins and Class III Spire-family (also known as tandem-monomer-binding (TMBs) nucleators) (Table 1.1; Figure 1.5). Formins have been discussed in Section 1.2 but the ARP2/3 complex and Spire-family are discussed in more detail below.

1.3.3 The ARP2/3 complex

ARP2/3 was the first major actin nucleator to be identified, which is a 220 kDa complex of 7 stable polypeptides (Goley and Welch, 2006). The 7 subunits consist of ARP2, ARP3 and 5 further subunits ARPC1, ARPC2, ARPC3, ARPC4 and ARPC5. ARPC1 is expressed in 2 isoforms in humans; ARPC1A and ARPC1B (Brigida *et al.*, 2018). This complex is unique in that it can nucleate actin whilst also organising filaments into branched networks (Figure 1.5B) (Campellone and Welch, 2010). The ARP2/3 complex requires nucleation-promoting factors (NPFs) to carry out its function, of which there are four types (all class I NPFs): Wiskott-Aldrich Syndrome (WAS) family proteins (which includes WASP, neuronal-WASP (N-WASP), WASH (WAS protein family

homologue), SCAR (suppressor of cAMP receptor, also known as WASP-family verprolin homologous protein (WAVE)) and WHAMM (WAS protein homologue associated with actin golgi membranes and microtubules). Each of these actin nucleator families and ARP2/3 NPFs function in different contexts to nucleate actin filaments (Caridi *et al.*, 2019). WASP is expressed specifically in haematopoietic cells whereas N-WASP is ubiquitously expressed and required for a range of cellular processes. WASH on the other hand has an essential role in the facilitation of microtubule fission through activating the ARP2/3 complex for endosome sorting. WASH also functions in concert with the formin Cappuccino (CAPU) and Spire, in the control of microtubules and actin dynamics (Weston, Coutts and La Thangue, 2012). NPFs that function with the ARP2/3 complex are activated through different mechanisms, for example, SCAR and N-WASP are selectively activated by the Rho GTPases (Haga and Ridley, 2016). Rac and CDC42 activate N-WASP via binding to its CDC42/Rac/GTPase interactive binding region (CRIB). WASP and WAVE recruit 1-3 G-actin monomers to promote a conformational change in the ARP2/3 complex, which in turn promotes its stabilisation and activation (Goley and Welch, 2006; Dominguez, 2009). WASP, WASH, SCAR and WHAMM all possess a C-terminal WCA region; 'W' motif for Wiskott-Aldrich syndrome protein homology 2 (WH2) domain binding, 'C' for connecting/central motif and 'A' for acidic. The W motif of the WCA region has a short sequence required for ARP2/3 complex activation whereby the WH2 domain binds to the actin monomer at the end of a new actin filament (Figure 1.4). The C and A motifs interact with various subunits within the ARP2/3 complex to promote its stabilisation. The actin-bound W motif, together with ARP2 and ARP3, form a trimeric seed to enable nucleation of a branch off the main actin filament, that emerges at a 70° angle off the side, with ARP2 and ARP3 being the two subunits at the pointed (-)

end of the growing filament (Figure 1.5B) (Robinson *et al.*, 2001; Dominguez, 2009; Tyler, Allwood and Ayscough, 2016).

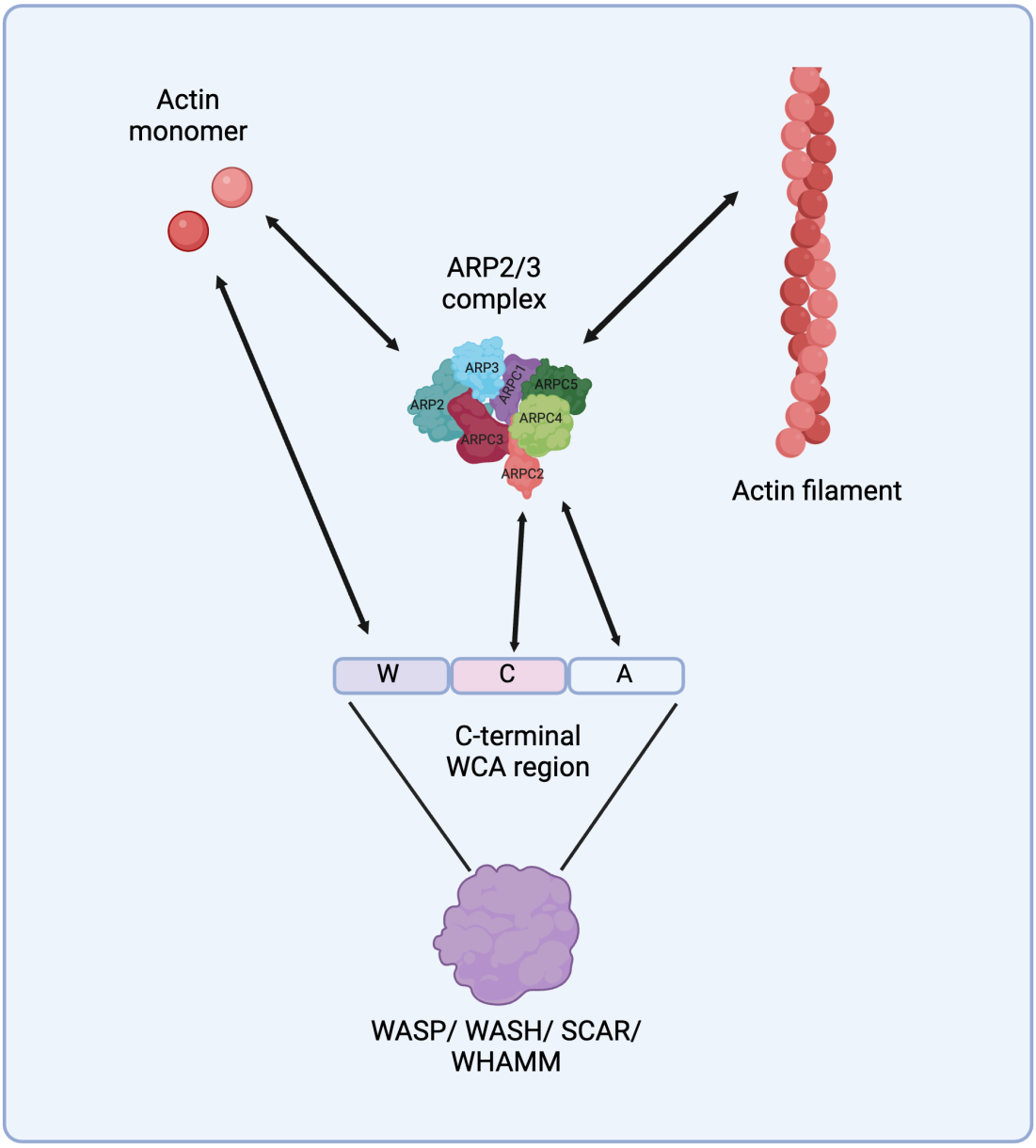


Figure 1.4 – Schematic diagram of C-terminal WCA region of WASP, WASH, SCAR and WHAMM – *The WCA motif of ARP2/3 activators, WASP, WASH, SCAR and WHAMM is required for ARP2/3 actin nucleation function. The W motif of the WCA region is required for ARP2/3 complex activation whilst also binding to actin monomers to aid in the formation of an actin filament. The C and A motifs of the region interact with the ARP2/3 complex to promote its stabilisation. Actin monomers bound to the W region in combination with ARP2 and ARP3 of the ARP2/3 complex form a trimer of actin molecules to enable the ARP2/3 complex to form branches off of an existing actin filament. Abbreviations: W - Wiskott-Aldrich syndrome protein homology 2 (WH2) domain binding, C – connecting/central motif, A – acidic motif, WASP- Wiskott-Aldrich Syndrome protein, WASH - WAS protein family homologue, SCAR, WHAMM - WAS protein homologue associated with actin golgi membranes and microtubules. Black arrows indicate an interaction. Adapted from Higgs et al., 2001. Created with Biorender.com.*

1.3.4 Spire family actin nucleators

The Class III Spire family nucleators includes Spire, Cordon-bleu, junction-mediating and regulatory protein (JMY) and the most recently identified in this group; adenomatous polyposis coli (APC) (Table 1.1). This unique group of actin nucleators all share the commonality of a tandem G-actin binding motif, such as a WH2 domain. This domain is 17-27 amino acid long and enables these nucleators to gather actin monomers into a nucleation complex with each WH2 domain able to bind 1 actin monomer, the confirmation of which varies depending on the nucleator. Spire WH2 domain is in the N-terminus and is an intrinsically disordered region that adopts an α-helical structure upon binding to actin and has the potential to form a string of 4 actin monomers through interaction between the four WH2 domains (Figure 1.5D) (Goode and Eck, 2007; Sitar *et al.*, 2011). The exception in this group is APC which does not contain a WH2 domain and recruits actin monomers via a currently unknown mechanism (Weston *et al*., 2012). APC is a tumour suppressor protein linked to colorectal cancer which forms a homodimer to recruit four actin monomers to generate unbranched actin filaments. Interestingly, APC synergises with the formin nucleator DIAPH1 to promote actin assembly (Okada *et al.*, 2010).

Table 1.1: Summary of actin nucleator classes		
Class I	**Function**	**Protein**
ARP2/3 Complex	Nucleators of branched actin filaments	ARP2
		ARP3
		ARPC1A
		ARPC1B
		ARPC2
		ARPC3
		ARPC4
		ARPC5
	Nucleation promoting factors; activators of ARP2/3 complex	WASP
		N-WASP
		WASH
		SCAR/WAVE
		WHAMM
Class II	**Function**	**Protein**
Formins	Nucleators of linear actin filaments and elongation, Microtubule binding, actin filament bundling, actin filament disassembly	DIAPH1
		DIAPH2
		DIAPH3
		DAAM1
		DAAM2
		FMNL1
		FMNL2
		FMNL3
		INF1
		FHOD1
		FHOD3
		Delphilin
		FMN1
		FMN2
		CAPU
Class III	**Function**	**Protein**
Spire family / tandem monomer binding nucleators	Protects pointed end from disassembly and bring filaments together	Spire
		Cordon-bleu (COBL)
		JMY
		APC

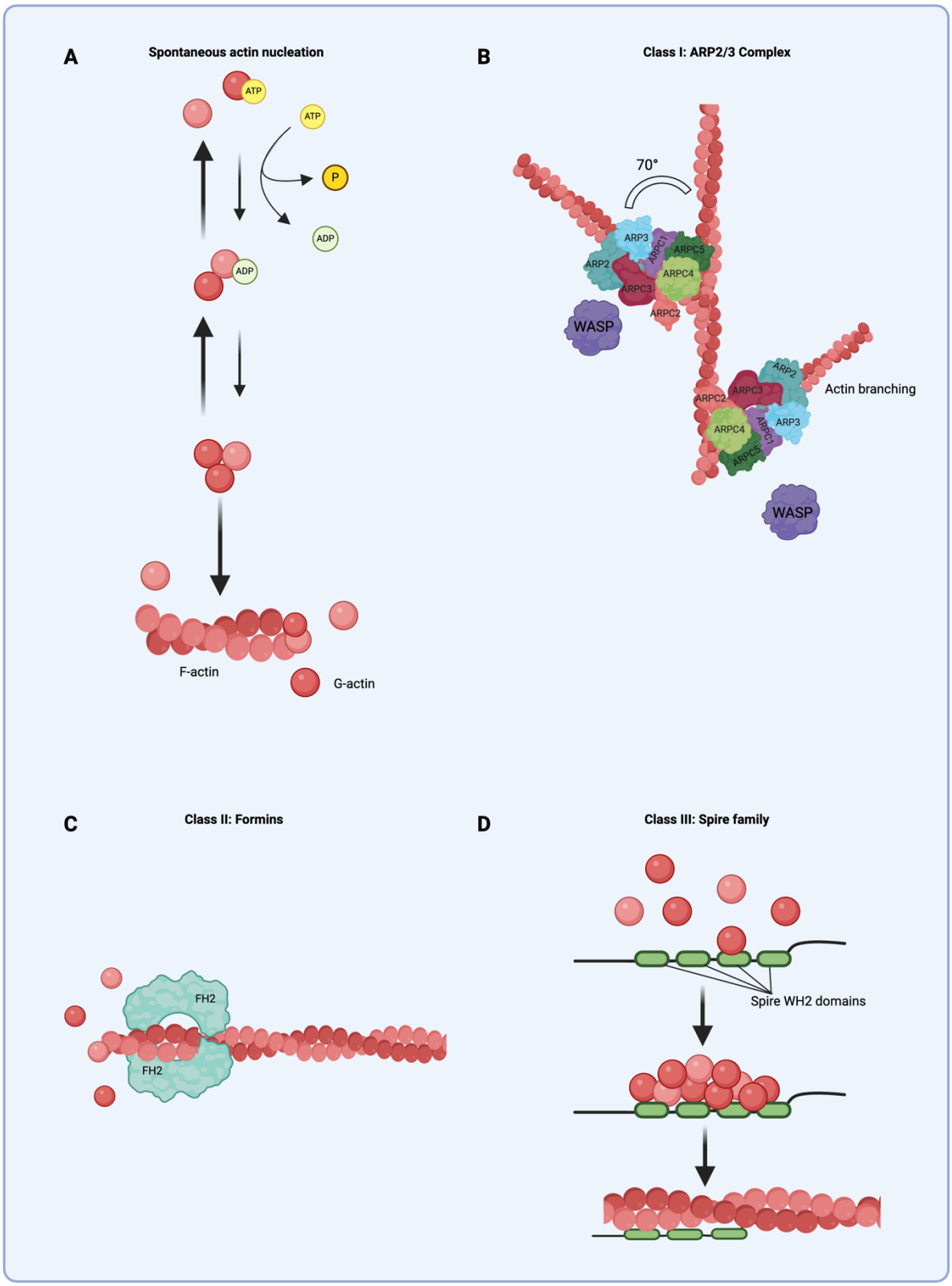


Figure 1.5 – Schematic diagram of actin nucleation *– **A** - Spontaneous actin nucleation from single monomers (G-actin) to dimers and trimers, which are highly unstable and rapidly dissociate back into monomers. The arrow thickness indicates which reaction is energetically favoured. **B** - Class I actin nucleators is the ARP2/3 complex and associated activators (WASP shown). The ARP2/3 is required for forming branched chains of actin from an already existing filament, which branch at a 70° angle from the main filament.. **C** - Class II actin nucleators are the formins which bind to the growing end of an actin filament via the FH2 domain of Formin family proteins. **D** - Class III actin nucleators are the Spire family, which all feature 4 WH2 domains, each capable of binding one actin monomer and bring monomers in close proximity to catalyse the formation of an actin filament. Abbreviations: G-actin – globular actin, F-actin – filamentous actin, FH2 – formin homology, WH2 domain – Wiskott-Aldrich Syndrome protein homology 2 domain. Created with BioRender.com.*

1.4 Human diseases associated with actin and actin nucleators

1.4.1 *ATCB* and *ACTG1* gene variants and human disease

ACTB and *ACTG1* gene variants are most commonly associated with the disease Barsaitser-Winter Cerebrofrontalfacial syndrome (BWCFF; also known as Barsaitser-Winter Syndrome or BRWS). BWCFF syndrome is a rare genetic disease with defined clinical features including distinct facial features, hearing loss, ocular colobomas, developmental disability, heart and renal defects, muscle wasting and defects in neuronal migration (Rivière *et al.*, 2012). In 1999 a single clinical case of an individual carrying an *ACTB* variant with clinical features distinct from BWCFF was identified by Nunoi et al. This patient possessed a *de novo c.G1174A; p.E364K ACTB* missense mutation in exon 6, which gave rise to an abnormal white blood cell count, moderate intellectual disability and thrombocytopenia (Nunoi *et al.*, 1999). More recently, several studies have identified patients with *de novo* variants in both *ACTB* and *ACTG1* with a heterogeneous clinical phenotype including features not previously defined by BWCFF syndrome such as microcephaly, thrombocytopenia and developmental disability (Rivière *et al.*, 2012; Di Donato *et al.*, 2014; Verloes *et al.*, 2015; Cuvertino *et al.*, 2017; Zech *et al.*, 2017; Cabanillas *et al.*, 2018; Latham *et al.*, 2018; Miyajima *et al.*, 2020). Di Donato et al., proposed that patients with *ACTB* variants were more severely affected than *ACTG1* variants, with a more diverse clinical phenotype than BWCFF syndrome. These patients were originally diagnosed with Fryns-Aftimos syndrome (FAS) but were reclassified as BWCFF syndrome. This study suggested that the diagnostic classification for this disease should be expanded to encompasses a wider range of clinical features with some *ACTB* variants resulting in more severe clinical

deficits than *ACTG1* (Di Donato *et al.*, 2014). Whilst there is a great deal of clinical heterogeneity of BCWFF syndrome and actin gene variants, there is some overlap of symptoms with patients harbouring both heterozygous and homozygous variants in *DIAPH1* discussed in Section 1.2. These features include microcephaly, developmental delay, seizures, and hearing loss. This may be explained by the gene products functioning in the same pathway whilst also reflecting the wide array of cellular processes that actin is involved in.

In addition to BCWFF syndrome, *ACTB* has also been associated with Dystonia-Deafness Syndrome combined with Parkinson's disease as well as Becker's Nevus Syndrome which is characterised by non-cancerous cutaneous hamartomas forming usually on the shoulders and upper trunk (Cai *et al.*, 2017; Straccia *et al.*, 2022).

1.4.2. Variants in actin nucleator genes and associated human diseases

DIAPH1 has been identified as a disease-causing gene since it was first reported in 1997 by Lynch et al. and again in 2015 by Ercan-Sencicek et al., but in more recent years, components of the ARP2/3 complex have been also identified as human disease causing genes (Lynch *et al.*, 1997; Ercan-Sencicek *et al.*, 2015). Out of the 7 components of the ARP2/3 complex, *ARPC4, ARPC1B and ARPC5* are associated with human disease (Table 1.2). Cintron et al. reported 7 individuals with a novel *de novo* variant in *ARPC4* c.472C>T; p.R158C associated with the presence of microcephaly and developmental delays (motor and speech). Some affected patients also exhibited visual impairments including strabismus, central vision impairments and congenital cataracts. The ARPC4 protein along with ARPC2 form the site that directly

interacts with F-actin and as such, are critical for actin nucleation. Interestingly, R158 is a critical residue for this process and is predicted to directly interact with F-actin, suggesting that the clinical phenotype in the affected patients with the p.R158C may arise directly from an inability to nucleate branched actin chains (Cintron *et al.*, 2022).

Several studies have identified homozygous recessive variants in *ARPC1B* as a underlying cause of severe combined immunodeficiency, thrombocytopenia, autoimmunity and radiosensitivity in 33 individuals (Table 1.2) (Kahr *et al.*, 2017; Kuijpers *et al.*, 2017; Somech *et al.*, 2017; Brigida *et al.*, 2018; Volpi *et al.*, 2019; Antala *et al.*, 2021; Papadatou *et al.*, 2021; Chiriaco *et al.*, 2022; Sefer *et al.*, 2023). Primary Immunodeficiencies, arising from pathogenic genetic variations in immune genes, can be divided into T-cell deficiencies, B-cell deficiencies, combined (B- and T-cell deficiency), complement deficiencies, phagocyte deficiencies and IgA deficiencies. Severe combined immunodeficiency arising in *ARPC1B* patients indicates both B- and T-cell immunodeficiency indicated ARPC1B is required for normal function in both B- and T-cell development (Justiz Vaillant and Qurie, 2024). In all reported cases across all studies, all patients have homozygous mutations that result in loss or reduced expression of ARPC1B, which destabilises the ARP2/3 complex entirely. ARPC1B is highly expressed in immune cells, which cannot be compensated for by ARPC1A. A proposed mechanism is that ARPC1B is specifically activated by WASP to activate the ARP2/3 complex within the immune system.

Linking with this, the activating factor of the ARP2/3 complex, WASP is associated with the human disease, Wiskott-Aldrich Syndrome (WAS). WAS is a rare X-linked primary severe combined immunodeficiency syndrome typified by the presence of

macrothrombocytopaenia, eczema and immunodeficiency with additional clinical features including autoimmune diseases and development of lymphoma. WASP is primarily expressed in nonerythroid haematopoietic cells and deficiency results in disruption of many cellular processes (Buchbinder, Nugent and Fillipovich, 2014). The underlying molecular mechanisms of mutations in WAS are complex, and there are currently 300 unique disease-associated mutations in WAS resulting in 3 distinct clinical conditions (classical WAS, X-linked thrombocytopenia and X-linked neutropenia (Moulding *et al.*, 2013). Interestingly, WAS and ARPC1B deficiency in humans shares many clinical features, demonstrating the proteins likely function together within the same pathways in the immune system (Leung *et al.*, 2021).

More recently, *ARPC5* has also been identified as a disease causing gene by one study which identified homozygous variants in two unrelated patients exhibiting recurring severe infections, autoimmunity and dysmorphisms (Nunes-Santos *et al.*, 2023). One patient had a homozygous nonsense c.23C>A; p.S8Ter *ARPC5* and the other had a homozygous frameshift c.11_12insTG; p.T5AfsTer47 *ARPC5* mutation. Both mutations lead to undetectable ARPC5 protein in LCLs and fibroblasts and reduced expression of ARPC1A and ARPC1B. These patients share many overlapping features with WAS and ARPC1B. Intriguingly, despite being part of the same complex, ARPC4 patient variants display a different clinical phenotype, but this may be because the pattern of inheritance of mutations have different effects on the protein function, as demonstrated with the striking difference between heterozygous and homozygous DIAPH1 mutations outlined in Section 1.2. However, the clinical deficits present in these patients highlight that ARP2/3 complex plays an important role in neurodevelopment and immune function. Given there are shared features with

BWCFF syndrome, it is likely some of these deficits arise due to actin-dependent dysfunction. Taken together, the clinical deficits present in patients with variants in *ARPC4*, *ARPC1B*, *ARPC5* and *WASP* demonstrates the importance of actin cytoskeletal functions in immune cell and platelet cell function but also strongly suggest the actin network plays role in neurodevelopment.

Table 1.2 - Comparison of clinical features of ARPC1B, ARPC4, ARPC5 and WASP patients

ARPC1B				Clinical features				
No. of individuals	**Gene mutation**	**Inheritance**	**Protein expression**	**Immune dysfunction**	**Platelet dysfunction**	**Neurodevelopmental defects**	**Other**	**Reference**
1	c.269_270dupCT; p.Val91Trpfs*30	*Homozygous*	*No protein*	Eosinophilia and inflammatory bowel disease	Microthrombocytopenia	N/A		Kahr et al., 2017
2	c.314C>T and c.712G>A; p.A105V	*Homozygous*	*Reduced expression*	Eosinophilia, eczema and leukocytoclastic vasculitis	Microthrombocytopenia	N/A		Kuijpers et al., 2017
1	c.491_495TCAAGdelCCTGCCCins	*Homozygous*	*No protein*	Combined immunodeficiency	Bleeding disorder, leukocytoclastic vasculitis	N/A		Kuijpers et al., 2018
2	c.G623DEL-TC; p.V208VfsX20	*Homozygous*	*No protein*	Recurrent chest infections , peri-anal abscess, lymphadenitis and CMV pneumonitis, colitis, an eczematous rash, papulovesicular lesions on the scalp	Severe thrombocytopenia	N/A		Somech et al., 2017
1	c.64+1G>C (P1)	*Homozygous*	*Low/absent protein*	Autoimmunity, immunodeficinecy	Thrombocytopenia	N/A		Brigida et al., 2017
1	c.622G>T (P2)	*Homozygous*	*Low/absent protein*	Autoimmunity, immunodeficinecy	Thrombocytopenia	N/A		Brigida et al., 2017
1	c.1087dup; p.E363GfsTer95 (P3)	*Homozygous*	*Low/absent protein*	Autoimmunity, immunodeficinecy	Thrombocytopenia	N/A		Brigida et al., 2017
1	c.258G>A;p.W86Ter (P4)	*Homozygous*	*Low/absent protein*	Autoimmunity, immunodeficinecy	Thrombocytopenia	N/A		Brigida et al., 2017
1	c.64+1G>A (P6)	*Homozygous*	*Low/absent protein*	Autoimmunity, immunodeficinecy	Thrombocytopenia	N/A		Brigida et al., 2017
1	c.318del; p.N107TfsTer13 (P5)	*Homozygous*	*Low/absent protein*	Autoimmunity, immunodeficinecy	Thrombocytopenia	N/A		Brigida et al., 2017
14	See Supplementary Table 2 in Volpi et al., 2019 for detailed genetic information of patient cohort	*All homozygous*	*Low/absent protein*	Immunodeficinecy	Bleeding disorders	N/A	Bronchiecastasis, pulmonary cystic lesions, gastrointestinal bleeding	Volpi et al., 2019
1	Information not avaiable	Information not avaiable	Information not avaiable	N/A	N/A	N/A	Hematemesis	Antala et al., 2021
3	c.783G>A, p.A261A	*Homozygous*	Information not avaiable	Recurrent bronchiolitis, pneumonia, skin abcesses, recurrent viral upper respitatirt tract infection, allergy, eczema, autoimmune hypothyroidism	N/A	N/A	Failure to thrive	Papadatou et al., 2021
1	c.212_226del	*Homozygous*	*No protein*	Combined immunodeficiency, recurrent infections	Thrombocytopenia	N/A	Radiosensitvitiy	Chiriaco et al., 2022
2	Information not avaiable	*Homozygous*	Information not avaiable	Inflammatory bowel disease, bronchiolitis, pneumonia, asthma, lymphopenia, eosinophilia,		N/A	Growth retardartion	Sefer et al., 2023
ARPC4				**Clinical features**				
No. of individuals	**Gene mutation**	**Inheritance**	**Protein expression**	**Immune dysfunction**	**Platelet dysfunction**	**Neurodevelopmental defects**	**Other**	**Reference**
7	c.472C>T; p.R158C	*De novo heterozygous*	Information not avaiable	N/A	N/A	Microcephaly, mild motor delay, speech delay	N/A	Cintron et al., 2022
ARPC5				**Clinical features**				
No. of individuals	**Gene mutation**	**Inheritance**	**Protein expression**	**Immune dysfunction**	**Platelet dysfunction**	**Neurodevelopmental defects**	**Other**	**Reference**
1	c.23C>A; p.S8Ter	*Homozygous*	No protein	Combined immunodeficiency	Bleeding disorder	N/A	N/A	Nunes-Santos et al., 2023
1	c.11_12insTG; p.T5AfsTer47	*Homozygous*	Information not avaiable	Combined immunodeficiency	Bleeding disorder	N/A	N/A	Nunes-Santos et al., 2024
WASP				**Clinical features**				
No. of individuals	**Gene mutation**	**Inheritance**	**Protein expression**	**Immune dysfunction**	**Platelet dysfunction**	**Neurodevelopmental defects**	**Other**	**Reference**
1 in 100000 live births	Variable; can be X-linked	*X-linked*	Variable	Immunodeficinecy, eczema	Thrombocytopenia	N/A	N/A	N/A

1.5 The DNA Damage Response

DIAPH1 and the actin network have been extensively discussed in Sections 1.1-1.4. The clinical features of some of the human diseases associated with these genes overlap with a subset of rare human diseases linked to the DNA damage response (DDR). This suggests that individuals may have an underlying DNA repair deficiency, specifically a defect in DNA double-strand break repair (DSBs). The following sections outline, in detail, the DNA damage response, with a particular focus on DSB repair, highlighting the clinical features of known human diseases associated with these cellular processes and ones that significantly overlap with homozygous variants in *DIAPH1*.

1.5.1 Background

Every day, in healthy mammalian cells, DNA is continuously exposed to damage from both exogenous and endogenous sources. There are numerous types of DNA damage that can impede both DNA replication and transcription, leading to mutations or cell death if not accurately repaired. Unrepaired DNA damage poses a risk to the faithful transmission of genetic material to daughter cells and threatens cell viability. To counter this constant threat, cells have evolved a plethora of sophisticated mechanisms, collectively termed the DDR. The DDR encompasses numerous pathways, each recognising specific DNA lesions. Specialised proteins in each pathway carry out functions to identify the lesion, signal its presence, and orchestrate halting of the cell cycle for repair to occur, followed by restart of the cell cycle. Some DDR proteins carry out multiple functions across various repair pathways such as

Ataxia Telangiectasia and Rad3-related protein (ATR) (discussed in Section 1.5.3.3) (Hakem, 2008; Jackson and Bartek, 2009). The different types of DNA damage, along with examples of how they arise, and the DDR pathways responsible for their repair, are outlined in Figure 1.6.

Endogenous sources of DNA damage often arise from normal physiological processes and cannot always be avoided. Reactive oxygen species (ROS), which are by-products of oxidative respiration, redox cycling, and the activity of macrophages and neutrophils at sites of infection, can result in DNA damage. DNA mismatches occasionally occur during DNA replication, and DNA strand breaks can result from the abortive activity of topoisomerase I and II. Other sources of endogenous DNA damage include hydrolytic reactions, non-enzymatic methylation, and situations where two single-stranded breaks (SSBs) occur in close proximity, or the replication machinery encounters an SSB, leading to the formation of a double-strand break (DSB) (Jackson and Bartek, 2009). Additionally, exogenous sources of DNA damage may arise from exposure to environmental factors such as ultraviolet (UV) light, chemical agents found in tobacco and contaminated food products, exposure to specific sources including ionising radiation (IR), and chemotherapeutic agents (e.g., Etoposide, Topotecan, and Cisplatin) (Chatterjee and Walker, 2017). The importance of the DDR is evidenced by the devastating impact that inherited mutations in DDR genes has on embryonal development, which will be discussed in Section 1.10.

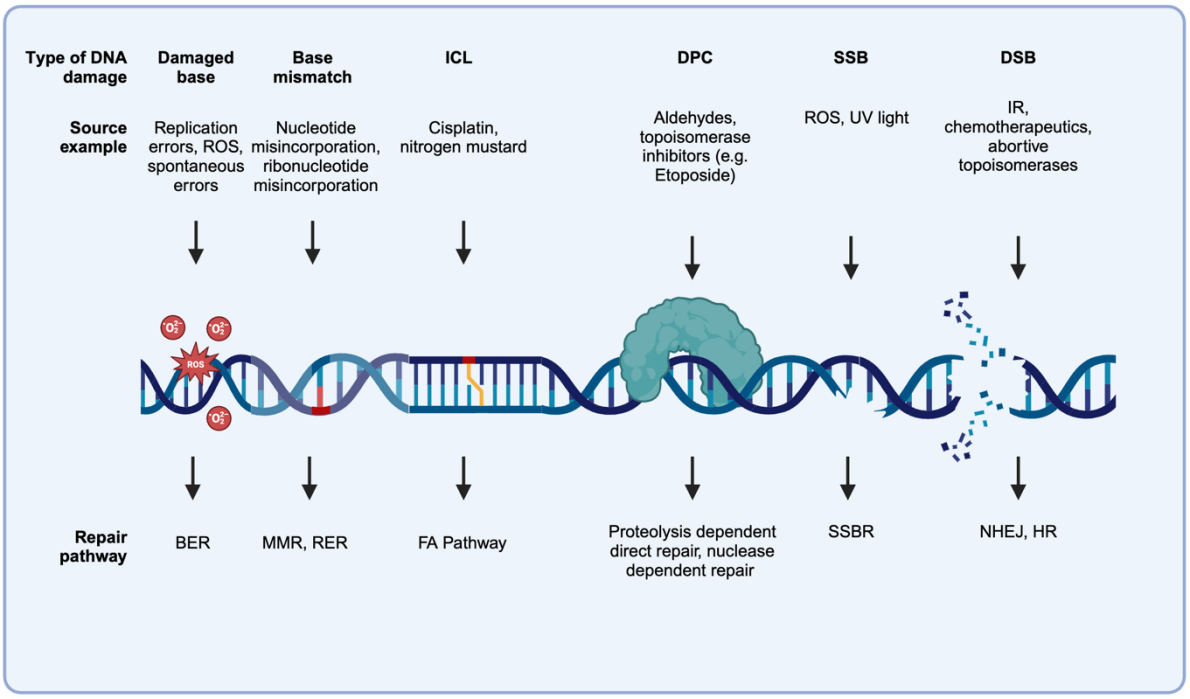


Figure 1.6 – Types and sources of DNA damage and the cellular pathways that exist to repair them – *There are various sources and types of DNA damage. A damaged base can arise through endogenous replication errors, ROS generated as a biproduct of aerobic respiration and spontaneous errors in processing of DNA including transcription. These lesions are repaired by base-excision repair. Base mismatch can arises= during replication and transcription through spontaneous errors in DNA and RNA polymerases. These errors are repaired by MMR and RER repair pathways. ICLs are induced through exposure to ICL-inducing agents such as the chemotherapeutic platinum-based agent, cisplatin and nitrogen mustard derivatives. DPCs are induced by exposure to endogenous aldehyde compounds or exogenously through exposure to topoisomerase I inhibitors (e.g. Topotecan) and topoisomerase I inhibitors (e.g. Etoposide). SSBs arise through exposure to ROS and damage induced exogenously by UV light. DSBs arise endogenously if replication fork collides with an unrepaired SSB and exogenously through exposure to IR and other agents such topoisomerase inhibitors that result in abortive topoisomerase activity. Abbreviations: Base excision repair (BER), DNA-protein crosslink (DPC), double strand break (DSB), Fanconi anaemia pathway (FA pathway), homologous recombination (HR), interstrand crosslink (ICL), ionising radiation (IR), mismatch repair (MMR), non-homologous end joining (NHEJ), reactive oxygen species (ROS), ribonucleotide excision repair (RER), single strand break (SSB), and single strand break repair (SSBR). Created with BioRender.com.*

1.5.2 Repair of DNA double strand breaks

DNA DSBs are formed when both strands of the DNA are broken. They arise much less frequently than other types of DNA damage but are the most toxic; potentially leading to chromosomal translocations or cell death if not repaired correctly. They can arise exogenously (e.g. exposure to ionising radiation and chemotherapeutic agents such as etoposide) and endogenously during DNA replication through collapsed replication forks colliding with unrepaired DNA lesions or through abortive topoisomerase I/II activity. Despite their potential toxicity to the cell, DSBs also serve an important function in health. They are induced under controlled conditions during B and T cell antigen receptor assembly and class-switch recombination to generate receptor diversity, and increase the repertoire of antigens the immune system is able to recognise (Blundred and Stewart, 2011). DSBs are also induced in meiosis during meiotic recombination of parental chromosomes to generate unique combinations of parental alleles thus increasing genetic diversity (Murakami and Keeney, 2008).

There are four pathways that can repair DSBs. The choice of which pathway is selected is highly dependent on cell cycle phase, chromatin environment and the specific type of DSB induced. The two major repair pathways are classical non-homologous end joining (NHEJ) and homologous recombination repair (HR; HRR, also known as homology directed repair; HDR). The less prominent repair pathways are alternative end-joining (alt-EJ) and single strand annealing (SSA) (Grand and Reynolds, 2018; Scully *et al.*, 2019).

1.5.3 Key kinases in DDR signalling

To orchestrate the complex signalling pathways that occurs following the induction of DNA damage, there are three pivotal kinases that coordinate the DDR depending on the type of damage induced: Ataxia-Telangectasia Mutated (ATM), Ataxia-Telangiectasia mutated and Rad3 related (ATR) and DNA-dependent protein kinase, catalytic subunit (DNA-PKcs). All three serine/threonine kinases are members of the phosphatidylinositol-3-kinase-like kinase family (PIKKs). (Lempiäinen and Halazonetis, 2009; Lovejoy and Cortez, 2009). Members of the PIKK family share similar domains and organisation. The kinase domains are located at the C-terminal end of the proteins, flanked by a highly conserved FAT (FRAP-ATM-TRRAP) and FAT C-terminal (FATC) domain. The PIKKs also contain numerous α-helical HEAT (Huntington-elongation factor 3 protein phosphatase 2A-TOR1) repeats flanking the FAT domain which are thought to mediate protein-protein interactions. (Perry and Kleckner, 2003; Maréchal and Zou, 2013; Blackford and Jackson, 2017).

Activation of these three kinases must be tightly regulated to prevent aberrant activation leading to undesired cell-cycle arrest, unwarranted DNA repair, senescence, or apoptosis. Therefore, each kinase requires a specific protein co-factor for recruitment to a specific DNA lesion. DNA-PKcs activation requires the Ku70/Ku80 heterodimer bound to a double-stranded DNA end. NBS1, a component of the MRN complex, is required to recruit ATM to sites of DNA DSBs (further details outlined in Section 1.5.3.2), whereas ATR requires its obligate binding partner, ATR-interacting protein (ATRIP), bound to replication protein A (RPA)-coated single-stranded DNA to be activated. All three of the recruiting factors share a PIKK binding domain located in

their C-terminus, which interacts with the PIKK HEAT domains (Blackford and Jackson, 2017).

1.5.3.1 DNA-PKcs

DNA-PKcs, along with the Ku70/80 complex, forms the DNA-PK serine-threonine kinase, with DNA-PKcs acting as its catalytic component. This complex plays a crucial role in promoting classical non-homologous end joining (NHEJ) repair of DSBs, which accounts for approximately 80% of DSB repairs and is known as "fast NHEJ" due to minimal processing needed before DNA end ligation. DNA-PKcs is recruited and activated by the Ku70/Ku80 complex bound to the ends of a DNA DSB. DNA-PKcs binds strongly to the Ku70/80-DNA end structure, inducing conformational changes in both the Ku70/Ku80 heterodimer and DNA-PKcs itself, which changes into a ring-like structure with an extended arm of HEAT repeats (Gell and Jackson, 1999; Singleton *et al.*, 1999; Maréchal and Zou, 2013). This facilitates DNA-end tethering and recruitment of additional NHEJ factors, such as Artemis, a critical nuclease utilised during NHEJ to trim DNA DSB ends or remove DNA hairpins (further details outlined in Section 1.5.4) (Blackford and Jackson, 2017; Valikhani *et al.*, 2021). Phosphorylation sites of downstream targets occur in clusters and autophosphorylation patterns of DNA-PKcs itself correspond to distinct downstream reactions (Goodarzi *et al.*, 2006). The significance of DNA-PKcs autophosphorylation patterns becomes evident in knock-in mouse models where phosphorylation sites are mutated to Alanine (Ala), leading to bone marrow failure. Autophosphorylation is crucial for releasing DNA-PKcs from DNA ends (Ding *et al.*, 2003). Mutating these sites traps DNA-PKcs, hindering downstream NHEJ processes and adversely affecting other repair pathways,

including HR (Neal *et al.*, 2011). Although most DSBs repaired by NHEJ are repaired faithfully, the more difficult to repair breaks that require end processing are at risk of incurring small (1-4bp) insertions or deletions (indels) and as such, NHEJ has been labelled an error-prone repair pathway.

1.5.3.2 ATM

Ataxia Telangiectasia Mutated (ATM), is a large protein (370 kDa) crucial in the response to DSBs. It exists as an inactive dimer in unperturbed conditions and becomes an active monomer upon autophosphorylation on S1981 when recruited to DSBs by the MRN complex (Falck, Coates and Jackson, 2005; So, Davis and Chen, 2009). Activated ATM then phosphorylates thousands of downstream targets to regulate cell cycle checkpoint activation (G_1/S, intra-S and G_2/M checkpoint), senescence, DSB repair, apoptosis and other functions including altering chromatin structure (Falck, Coates and Jackson, 2005). Examples of phosphorylation targets of ATM include CHK2 on T68, leading to cell cycle arrest and apoptosis and p53 on S15, activating G_1 checkpoint, senescence, or apoptosis (Matsuoka, Huang and Elledge, 1998; Ahn *et al.*, 2000; Matsuoka *et al.*, 2000; Melchionna *et al.*, 2000; Shiloh, 2003; Rashi-Elkeles *et al.*, 2011; Blackford and Jackson, 2017). While MRN enhances ATM activation, oxidative stress can activate ATM independently but the active ATM in both cases differ. In response to a DSB, the MRN complex results in inactive ATM dimers to dissociate into active monomers (Lee and Paull, 2004, 2005). In the case of ATM being exposed to H_2O_2, the active form of ATM is dimer crosslinked with two more disulphide bonds (Guo *et al.*, 2010). Following activation after a DSB, ATM phosphorylates the histone variant H2AX (γ-H2AX), initiating a cascade which results

in recruitment of mediator of DNA damage checkpoint 1 (MDC1), then the RING finger ubiquitin E3 ligases RNF8 and RNF168, which ubiquitylate H2A/H2AX on K13/15 to stimulate recruitment of p53 binding protein (53BP1) and the BRCA1-A complex (Isono *et al.*, 2017; Shibata and Jeggo, 2021).

Most ionising radiation (IR)-induced DSBs outside of S-phase (around 80%) are repaired by NHEJ independently of ATM. However, ATM is crucial for repairing DSBs located within regions of heterochromatin (Hakem, 2008; Bohgaki *et al.,* 2010; Shibata and Jeggo, 2021). ATM therefore has downstream substrates that remodel chromatin such as KRAB-associated protein 1 (KAP-1), heterochromatin protein 1 (HP1) and histone deacetylase 1/2 (HDAC1/2). KAP1 phosphorylation promotes chromatin relaxation at DSB sites located within regions of heterochromatin via recruitment of the nucleosome remodeller chromodomain helicase DNA-binding 3 (CHD3) (Goodarzi *et al.*, 2006). In addition to heterochromatic breaks, ATM is also critical for repairing DSBs with blocked ends that require processing. These breaks require longer periods of time to repair and have been labelled ‘slow repair’. Both types of DSB requiring ATM-dependent functions account for the remaining 20% of breaks in G_1-phase not repaired by NHEJ (discussed in further detail in Section 1.6) (Shibata and Jeggo, 2021).

In S/G_2-phase of the cell cycle, ATM is active primarily at unresected DNA ends and is involved in repairing approximately 20% of breaks (Shibata and Jeggo, 2021). In G_2-phase of the cell cycle, ATM phosphorylates similar targets as in G_1-phase (e.g. γ-H2AX, 53BP1, MDC1) and functions to regulate the balance between NHEJ- and HR-dependent repair mechanisms (Shibata and Jeggo, 2021). Following ATM-dependent 53BP1-hyperphosphorylation, HR suppressing factors such as replication regulatory

factor 1 (RIF1) and the Shieldin complex are recruited. Shieldin recruits Polα primase, which has been proposed to fill in single-stranded DNA (ssDNA) gaps and promote a pro-NHEJ environment (Setiaputra and Durocher, 2019; Mirman and de Lange, 2020; Shibata and Jeggo, 2021).

To oppose NHEJ and promote a pro-HR environment, BRCA1 directs protein phosphatase 4 catalytic subunit (PP4C) to dephosphorylates 53BP1 (Isono *et al.*, 2017). ATM can also phosphorylate BRCA1, which was first identified in 1999 but more recently it has been shown that ATM promotes HR via BRCA1 T1394 phosphorylation (Cortez *et al.*, 1999; Foo *et al.*, 2021). Interestingly, ATM is also thought to facilitate HR, by phosphorylating CtIP on eight SQ/TQ motifs after a DSB (Wang *et al.*, 2013; Shibata and Jeggo, 2021). However currently, the precise circumstances determining whether ATM enhances or limits HR remains unclear (Wang *et al.*, 2013; Isono *et al.*, 2017; Shibata and Jeggo, 2021).

1.5.3.3 ATR

ATR is the key kinase regulating the cellular response to replication stress. Replication stress is considered to be anything which slows or stalls the progression of DNA replication (Zeman and Cimprich, 2014). ATR responds to a much wider range of DNA damage/genotoxic stresses than ATM and DNA-PKcs, as both are specific to DSBs (Zeman and Cimprich, 2014). In contrast to ATM and DNA-PKcs, ATR is also essential for proliferating cells, as *Atr* knock-out in mice is embryonic lethal (Brown and Baltimore, 2000).

At the site of a stressed/stalled replication fork, whatever the cause, adjacent to the blockage, ssDNA is generated through helicase-polymerase uncoupling, which is rapidly coated in RPA. ATR is rapidly recruited to RPA coated ssDNA via ATRIP, whereby it becomes activated following binding to one of two activating proteins that contain an ATR activation domain (AAD): Topoisomerase binding protein 1 (TOPBP1) and ETAA1. TOPBP1 interacts with the phosphorylated C-terminal tail of RAD9 of the RAD9-RAD1-HUS1 (9-1-1) complex, which is a PCNA-like heterotrimeric clamp that is loaded onto RPA-coated DNA at ssDNA/dsDNA junctions by the RAD17-RFC clamp-loading complex (Zou, Cortez and Elledge, 2002; Zhou *et al.*, 2013; Blackford and Jackson, 2017; Williams and Zhang, 2021). The TOPBP1-RAD9 interaction is important for ATR activation. Conversely, ETAA1 is recruited to RPA-ssDNA through direct binding to RPA (Bass *et al.*, 2016; Feng *et al.*, 2016; Haahr *et al.*, 2016). It is not clear under which circumstances either TOPBP1 or ETAA1 are recruited to damaged DNA to activate ATR.

One of the key downstream targets of ATR is CHK1. When CHK1 becomes phosphorylated and activated by ATR, it promotes the proteasomal degradation of CDC25A, a phosphatase that removes inhibitory phosphorylation from Cyclin-dependent kinases (CDKs) (Walworth and Bernards, 1996; Liu *et al.*, 2000; Lopez-Girona *et al.*, 2001). This action slows/arrests the cell cycle and allows time for repair or promotes apoptosis if the damage cannot be repaired (Saldivar, Cortez and Cimprich, 2017).

ATR phosphorylates a lot of the same substrates as ATM to mediate the DDR, but in addition has additional targets for controlling normal replication progression and origin

firing as well as those involved in the response to replication stress, which is discussed further in Section 1.8. Furthermore, ATR has a role in activating the Fanconi Anaemia (FA) pathway, which is required for the repair of DNA intra-/inter-strand crosslinks (ICLs) (Blackford and Jackson, 2017; Williams and Zhang, 2021).

1.5.4 DSB signal transduction: the MRN complex

The MRN complex consists of MRE11, RAD50 and NBS1 in a stoichiometric arrangement of $MRE11_2$:$RAD50_2$:$NBS1_1$ and is a key sensor for DSBs (Figure 1.7A) (Schiller *et al.*, 2012; Bian *et al.*, 2019). The MRN complex plays a pivotal role in the initiation of DNA end resection to promote HR (which is discussed in more detail in Sections 1.7), but also is involved in cell cycle checkpoint activation, telomere maintenance, meiosis and normal DNA replication (Figure 1.7) (Porter-Goff and Rhind, 2009; Qiu and Huang, 2021). MRE11 can bind directly to DSB ends and possesses both endo- and 3′-5′ exonuclease activity against different dsDNA substrates.

Stable formation of the complex requires an MRE1111 dimer binding to two RAD50 molecules between RAD50's globular and coiled-coil domain (Figure 1.7A). The MRE11 dimer binds DNA ends in short range synapsis, whereas RAD50 has the capacity for long range tethering of two DNA molecules due to dimerisation via its zinc hook and coiled-coil flexible "arms" that can project away from the DNA (Figure 1.7B). The spatial organisation of the complex allows for MRE11 DNA binding, DSB tethering and nuclease activity along with the DNA-binding and termini unwinding of RAD50 (Lamarche, Orazio and Weitzman, 2010). The third component of the complex, NBS1, contains an FHA domain, and two BRCT domains within its N-terminal domain. The C-

terminal domain of NBS1 contains an MRE11 interacting domain and an ATM binding domain (Figure 1.7A). The FHA and BRCT domains all have important phospho-dependent interactions which are required for the recruitment of checkpoint and repair proteins to DNA break sites. The FHA domain recognises phosphorylated threonine residues and BRCT domains recognise pS-X-X-F motifs that occur in target DNA damage proteins (Durocher *et al.*, 1999; Manke *et al.*, 2003; Yu *et al.*, 2003; Clapperton *et al.*, 2004). MDC1 is recruited to damage sites by γ-H2AX (Stucki *et al.*, 2005). The interaction between MDC1 and γ-H2AX regulates the response to DSBs when it is constitutively phosphorylated at these sites (located in its N-terminus) it is required for the retention of the MRN complex on chromatin at damage sites to potentiate DNA damage signalling (Stucki *et al.*, 2005; Spycher *et al.*, 2008) Through the interaction of NBS1 with MRE11 and its NLS, NBS1 recruits the MRN complex to the nucleus.

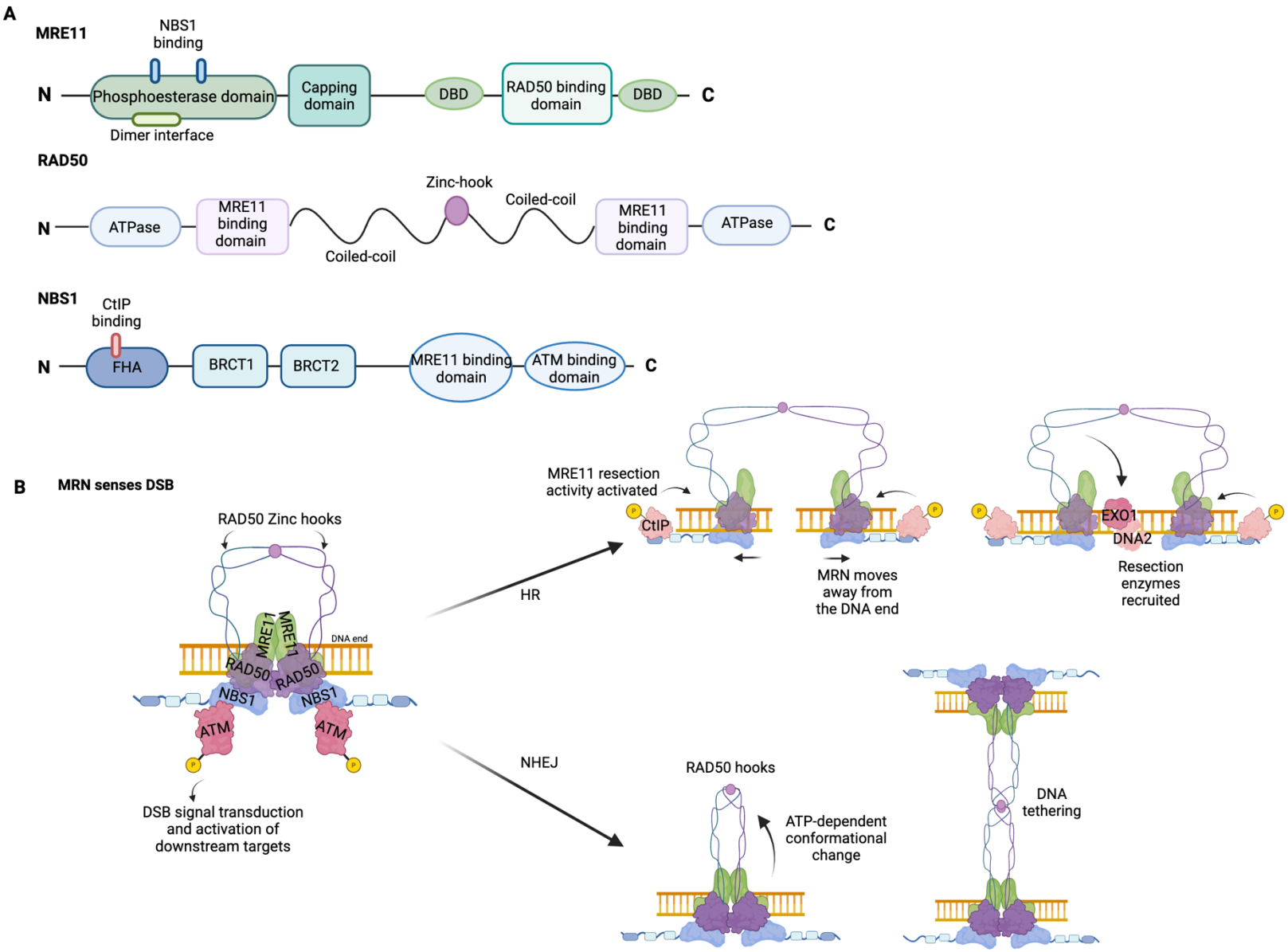

A
MRE11
NBS1 binding
N
Phosphoesterase domain
Dimer interface
Capping domain
DBD
RAD50 binding domain
DBD
C
RAD50
Zinc-hook
Coiled-coil
N
ATPase
MRE11 binding domain
Coiled-coil
MRE11 binding domain
ATPase
C
NBS1
CtIP binding
N
FHA
BRCT1
BRCT2
MRE11 binding domain
ATM binding domain
C
B
MRN senses DSB
RAD50 Zinc hooks
DNA end
MRE11
MRE11
RAD50
RAD50
NBS1
NBS1
ATM
ATM
DSB signal transduction and activation of downstream targets
HR
MRE11 resection activity activated
CtIP
MRN moves away from the DNA end
EXO1
DNA2
Resection enzymes recruited
NHEJ
RAD50 hooks
ATP-dependent conformational change
DNA tethering

Figure 1.7 - Schematic Diagram of the Components of the MRN Complex - ***A*** *- Key Domains of the 3 Components of the MRN Complex: MRE11: Contains a phosphoesterase domain with 2 NBS1 binding motifs. This domain possesses ssDNA endonuclease and dsDNA exonuclease activity. RAD50: Features an antiparallel coiled-coil domain extending from the globular domain of the protein, with a zinc hook facilitating dimer formation. NBS1: Includes a CtIP binding motif within the FHA domain.* ***B*** *- The MRN Complex Sensing a DSB and Recruiting ATM: The MRN complex binds to the end of a double-strand break (DSB) and recruits ATM. ATM undergoes autophosphorylation and then phosphorylates downstream targets for DSB repair signal transduction and cell cycle checkpoint activation. The MRN complex functions in both homologous recombination (HR) and non-homologous end joining (NHEJ). In HR, CtIP is recruited and activates endonuclease activity to create a cut in the DNA. Mre11 then performs 3' to 5' resection via its exonuclease activity towards the DSB end. This interaction also alters its conformation to allow for the recruitment of further exonucleases, including EXO1 and DNA2, to perform resection from 5' to 3'. In NHEJ, the role of the MRN complex is less clear, but the DNA tethering function of Rad50 plays a role. The coiled-coil domains undergo an ATP-dependent conformation change to enable the tethering of two DNA ends. Abbreviations: ATM – Ataxia Telangiectasia mutated, CtIP - CtBP-interacting protein, DNA2 - DNA replication helicase/nuclease 2, DSB – double-strand break, EXO1 – exonuclease 1, FHA domain - forkhead-associated domain, HR – homologous recombination, NHEJ – non-homologous end joining. Figure adapted from Lefrance-Vanasse et al., 2015. Created with BioRender.com*

1.6 Non-homologous end-joining

1.6.1 Classical Non-homologous end joining

Classical NHEJ (NHEJ) repairs the majority of DSBs and is active throughout the cell cycle, predominately in G_1-phase of the cell cycle. At its core, NHEJ promotes the ligation of two DNA ends back together, sometimes in an error-prone fashion, which may result in small insertions, deletions, or substitutions at the break site. In rare cases, NHEJ can also result in translocations, if DSBs from different parts of the genome are ligated together (Stinson and Loparo, 2021). There are numerous DNA DSB-ends that can be repaired by NHEJ with varying degrees of end processing required before ligation can take place. From blunt ends (termed fast NHEJ) which can be directly ligated with minimal processing, through to more complex and difficult to repair ends requiring resection and nucleotide synthesis prior to ligation (Slow NHEJ), examples of which are shown in Figure 1.7 (Ensminger and Löbrich, 2020). The other type of NHEJ is termed alternative-end joining (alt-EJ) which requires regions of

microhomology for effective repair and repairs DSBs when NHEJ cannot be used, such as during S-phase and in NHEJ deficient cells (Chang *et al.*, 2017).

The Ku70/80 heterodimer senses DSBs with free DNA ends or DNA ends which require minimal processing. The MRN complex also senses the presence of DSBs, as described in Section 1.5.4 but is favoured at blocked DNA ends requiring resection prior to repair (Chang *et al.*, 2017; Ackerson *et al.*, 2021). Histone variant H2AX is targeted for phosphorylation at the site of a DSB, thereafter termed γ-H2AX, which can occur on chromatin spanning >1 megabases of DNA surrounding the break site .Once loaded onto DNA ends, Ku70/80 undergoes allosteric changes to expose the C-terminal end of the Ku80 protein and rotates the complex inwards, which allows recruitment of DNA-PK catalytic subunit (DNA-PKcs), the key kinase in NHEJ signalling (Section 1.5.3.1) as well as other core NHEJ factors including PAXX and the XLF-XRCC4 complex. At this point, DNA-PKcs tethers the DNA ends together (end synapsis) and recruits several nucleases to the DNA break for processing as most DSBs have incompatible DNA ends for direct ligation (Figure 1.8A-B) (Chang *et al.*, 2017). DNA end synapsis is facilitated by the XLF-XRCC4 filaments which allow for proximity alignment by being in contact with the DNA. XLF-XRCC4 is stabilised on the DNA by PAXX, which also binds to Ku70/80, and the DNA ends are protected from any undesired enzymatic activity. This allows for controlled DNA end processing to take place. PAXX is a paralogue of XRCC4 and is one of the newest NHEJ factors to have been identified in recent years, sharing homology with XRCC4 and XLF (Craxton *et al.*, 2015; Ochi *et al.*, 2015; Xing *et al.*, 2015). PAXX directly interacts with Ku70/80

and it does not directly bind to DNA itself. It is thought to play a role in the assembly of the NHEJ complex (Ochi *et al.*, 2015; Grand and Reynolds, 2018).

For DNA end-processing to take place, the NHEJ core complex permits removal of end blocking groups. End processing entails ‘cleaning’ (removal of ligation blocking proteins) and ‘processing’ (filling in gaps or trimming of flaps of DNA into a ligatable DNA configuration). The XRCC4/Ligase IV complex then senses the generation of a 5’ phosphate group and the DNA ends are then ligated back together. XRCC4 is a dimer that functions as a scaffold protein in NHEJ complex assembly and serves as a chaperone to Ligase IV (Figure 1.8A-E). Ligase IV contains a DNA-binding and catalytic domains in its N-terminal region and two BRCT domains in its C-terminus. The sequence between the two BRCT domains binds to the C-terminal region of the XRCC4 coiled coil domain (Sibanda *et al.*, 2001). Ligase IV catalytic domain functions to adenylate DNA ends (Ochi, Gu and Blundell, 2013). During the ligation of DNA ends, an AMP group is transferred to 5’ phosphate of one DNA end by DNA ligase IV. This allows the 3’ hydroxy group of the second DNA end to undergo nucleophilic attack by the adenylated 5´ end and release of the AMP molecule which yields the final ligation product (Lieber, 2010). Ligase IV is a versatile enzyme which can perform a wide range of ligation reactions on incompatible DNA ends using ssDNA present at the DNA ends. This action is important as SSBs are much easier to repair so results in a mechanistically simpler route to repair. In addition to this role, other roles of XRCC4 include phospho-dependent interactions with APLF, PNKP and APTX (aprataxin) (accessory proteins in NHEJ), which is mediated by phosphorylation of a short C-

terminal motif by casein kinase II (CK2) on XRCC4 (Chang *et al.*, 2017; Grand and Reynolds, 2018).

Another factor involved in NHEJ is DCLRE1C (Artemis), which is one of the key nucleases in NHEJ in both pathological contexts and physiologically induced DSBs in class-switch recombination. It possesses intrinsic 5' exonuclease activity and endonuclease activity on both 5' and 3' DNA overhangs (generated from DNA hairpins formed during V(D)J recombination and at pathological breaks) and the N-terminus contains a catalytic metallo-β-lacatamse (MBL) domain, a region shared with many nucleases (Allerston *et al.*, 2015; Chang *et al.*, 2017). Following the induction of a DSB, Artemis is phosphorylated on many sites in its C-terminal region, which contains a DNA-PKcs interaction site and a Ligase IV binding site. Artemis is a downstream phosphorylation substrate of both DNA-PKcs and ATM kinase in response to DSBs. Artemis and DNA-PKcs interact to form a complex possessing endonuclease activity that cleaves structures such as DNA hairpins, flaps and overhangs, which are all ssDNA-dsDNA transition structures (Figure 1.8B-E) (Chang and Lieber, 2016; Grand and Reynolds, 2018). Additional NHEJ end processing factors include the Pol X family of DNA polymerases e.g. Polμ, Polλ and TdT (terminal deoxynucleotide transferase), which insert nucleotides at DSB sites, as well as APTX/Aprataxin, PNPK, TDP1 and TDP2 (Tyrosyl-DNA-phosphodiesterases) and APLF/Aprataxin and PNKP-like factor (Waters *et al.*, 2014; Pryor *et al.*, 2015; Chang *et al.*, 2017).

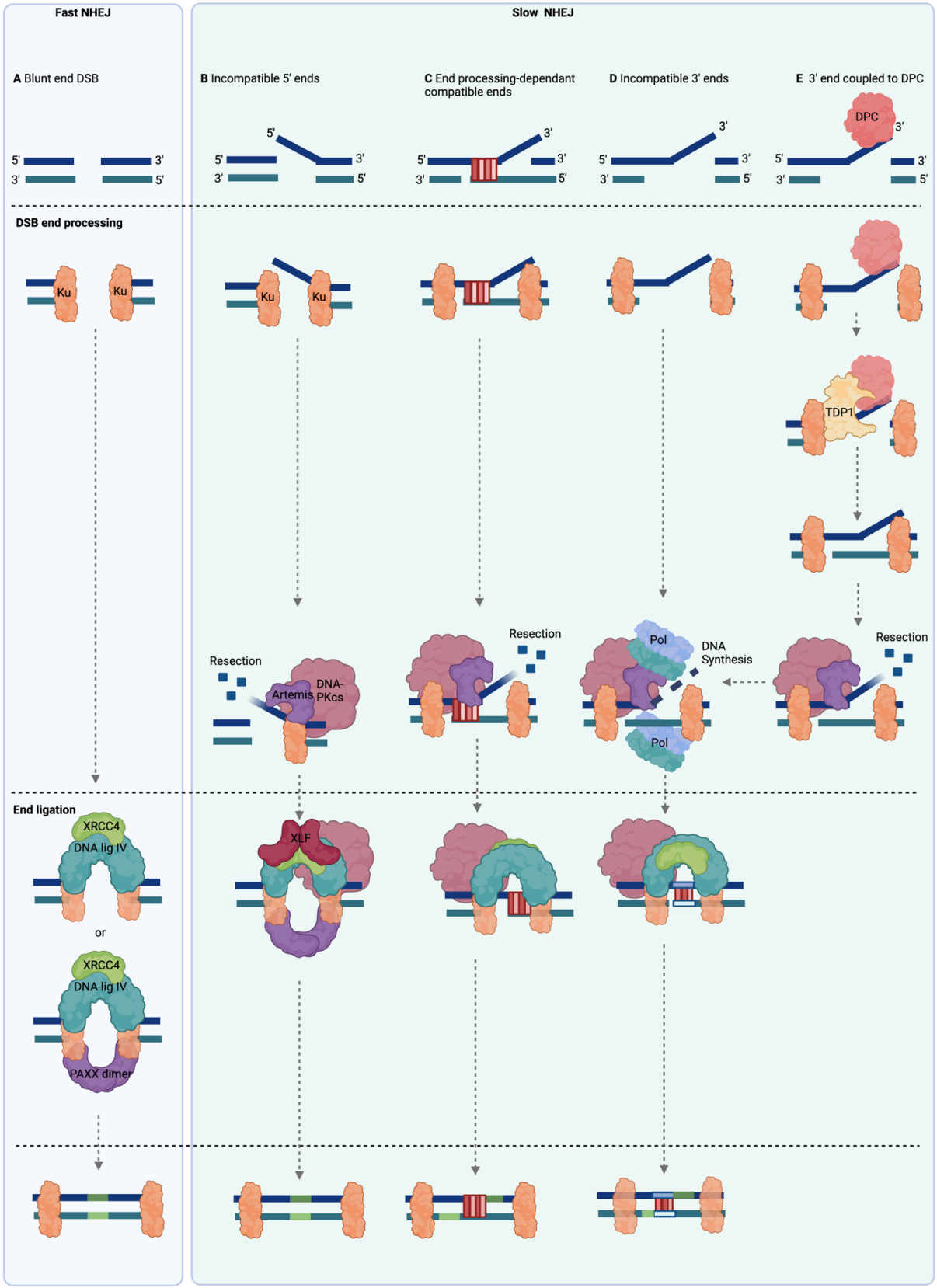

Fast NHEJ
Slow NHEJ
A Blunt end DSB
B Incompatible 5' ends
C End processing-dependant compatible ends
D Incompatible 3' ends
E 3' end coupled to DPC
DPC
DSB end processing
Ku
TDP1
Resection
Artemis
DNA-PKcs
Pol
DNA Synthesis
End ligation
XRCC4
DNA lig IV
XLF
or
PAXX dimer

Figure 1.8 – Different types of DNA ends repaired by NHEJ – *There are many proteins involved in NHEJ processes depending on the type of DNA end. A) Fast NHEJ occurs when the two ends of a DSB are blunt ends that can be ligated back together without processing. Ku binds to the two DNA ends and are then ligated back together by DNA Ligase IV which is stimulated by XRCC4 or PAXX. B-E are DNA end types that require processing and are therefore termed slow NHEJ. B) A DSB with an incompatible 5' overhang is processed primarily by endonuclease activity of Artemis which is recruited to the site by DNA-PKcs. C) End processing-dependent ends have a short region of microhomology along with a 3' overhand, which is resected and cleaved off by Artemis-DNA-PKcs before ligation can take place. D) Incompatible 3' overhands are first processed by resection followed by nucleotide synthesis by DNA polymerases which generates a short region of base pairing (pink/red lines) before end ligation. E) 3' ends coupled to a DPC can form on either blunt ends or overhangs which can be processed by TDP1 which cleaves the DPC before resection/ nucleotide synthesis if required. Abbreviations: DPC – DNA-protein crosslink, Pol – DNA polymerase, XRCC4 - X-ray repair cross-complementing protein 4, XLF – XRCC4-like factor, , PAXX - Paralogue of XRCC4 and XLF. TDP1 - Tyrosyl-DNA-phosphodiesterase 1. Figure has been adapted from figure 3 Chang et al., 2017, created on Biorender.com.*

1.6.2 Alternate-end joining

Canonical NHEJ is one of the two major pathways used to repair DSBs. In contrast, alternative end joining (alt-EJ or microhomology-mediated end-joining; MMEJ) is thought to represent a backup pathway for NHEJ (Boulton and Jackson, 1996; Decottignies, 2013). Alt-EJ involves error-prone repair mechanisms using microhomology sequences, leading to deletions/insertions (Sfeir and Symington, 2015). When mice lacking essential NHEJ factors such as DNA-PKcs, Ku80 and XRCC4 are crossed with p53 KO mice (to permit lymphocyte survival), the offspring develop oncogenic translocations in lymphoid cells due to the use of alt-EJ to repair physiological DSBs generated during V(D)J recombination (Gao *et al.*, 2000). NHEJ predominates over alt-EJ and only a small number of DSBs are repaired by it, which has made studying this pathway challenging. However, factors with known roles in Alt-EJ include PARP1, MRN, CtIP and DNA ligases I and III (Chiruvella, Liang and Wilson, 2013).

Recently, POLθ (POLQ), a unique polymerase with distinct N-terminal helicase and C-terminal polymerase domains has been identified to play a key role in alt-EJ (Kent *et al.*, 2015). POLθ repairs DSB using a two-step mechanism: microhomology independent DNA synapse formation followed by microhomology-dependent annealing (Kent *et al.*, 2015). In the alt-EJ process, PARP1 mediates the rapid recruitment of the MRN complex and CtIP. The MRN complex endonuclease activity induces a SSB within the 5' strand, a process enhanced by CtIP. Following this, short complimentary regions, ranging from 2-20 nucleotides, are exposed. DNA ends are then aligned via short microhomologies whereby both POLθ and the MRN complex are thought to be required for end alignment (Sallmyr and Tomkinson, 2018). Following this, non-homologous 3' DNA tails are removed, then POLθ facilitates error-prone gap-filling DNA synthesis. Finally, both strands are ligated by LigIIIA-XRCC1 complex (Mateos-Gomez *et al.*, 2015; Wyatt *et al.*, 2016; Sallmyr and Tomkinson, 2018). Interestingly, inhibition of POLθ is being explored as a therapeutic strategy for HR-deficient tumours (Barszczewska-Pietraszek et al., 2022).

1.7 Homologous recombination

1.7.1 Background

Homologous recombination (HR) repair is a highly accurate genome maintenance pathway that repairs DSBs accurately in S- and G_2-phase of the cell cycle, where an undamaged homologous sister chromatid is present to act as a repair template. HR processes are also used extensively at perturbed replication forks during S phase, at

sites of ssDNA gaps, during meiosis to mediate crossover formation and also to repair ICLs (Li and Heyer, 2008). HR is a highly regulated process as recombination has the potential to induce chromosomal rearrangements, particularly in higher eukaryotes with repetitive regions of DNA (Rothkamm *et al.*, 2003). HR repairs around 20% of DSBs and is favoured at breaks that arise at replication forks or in transcriptionally active chromatin.

1.7.2 The HR pathway and sub-pathways

The central enzyme to HR is the recombinase RAD51 (RecA in bacteria). RAD51 binds to ssDNA and searches for homologous sequences in the genome, then catalyses the invasion of a homologous strand to initiate repair (Figure 1.8). RAD51 is loaded onto 3' overhangs of ssDNA, which must first be generated by processing of the DNA DSB ends by exonucleases which resect the ends of the DNA breaks. This end processing is restricted to S- and G_2-phase of the cell cycle and as such, requires high levels of Cyclin-dependent kinases (CDK) activity (Grand and Reynolds, 2018).

During DNA end processing, the MRN complex is a key factor involved in carrying out 3'-5' short-range DNA end resection prior to the initiation of recombination. CtIP and the E3 ubiquitin ligase, BRCA1, are essential for short-range DNA resection to take place (Sartori *et al.*, 2007; Cruz-García, López-Saavedra and Huertas, 2014; Shibata *et al.*, 2014; Anand *et al.*, 2016). Following short range resection, long-range resection is then carried out by 5'-3' exonucleases activity of EXO1 and DNA2, which is stimulated by the presence of the DNA helicase BLM and RPA-bound ssDNA (Garcia

et al., 2011; Nimonkar *et al.*, 2011; Shibata *et al.*, 2014; Zheng *et al.*, 2020). Additional factors with a role in resection are the WRN helicase, which possesses both 3'-5' exonuclease and helicase activity, and SMARCAD1, which facilitates BRCA1 recruitment (Figure 1.8A-C) (Chen *et al.*, 2003; Chakraborty *et al.*, 2018).

MRE11 (component of the MRN complex, Section 1.5.4) endonuclease activity is promoted by CDK-dependent CtIP phosphorylation on T874, whereby the interaction between phosphorylated CtIP and NBS1 promotes MRE11 to make an initial nick in the DNA and to generate a 3' overhang by 3'-5' resection (Figure 1.9C) (Sartori *et al.*, 2007; Panier and Boulton, 2014; Anand *et al.*, 2016; Qiu and Huang, 2021). If this initial nick is not made due to inhibition of MRE11 with mirin or EXO1/BLM exonuclease activity, repair is directed towards NHEJ (Shibata *et al.*, 2014). BRCA1 co-localises with the MRN complex and directly interacts with phosphorylated CtIP through its BRCT domain, which is a central factor in the initiation of DNA resection (Sartori *et al.*, 2007; Chen *et al.*, 2008). Additional CtIP phosphorylation sites, S664, 679 and 745, which are targets of ATM, are also required for resection and HR to take place (Shibata and Jeggo, 2021). BRCA1 promotes HR over NHEJ by mediating the dephosphorylation and subsequent removal of 53BP1 and the release of RIF1 from the DNA break (both pro-NHEJ factors). This enables CtIP-dependent 5'-3' long-range resection of DNA by DNA2 and EXO1 (Ceppi *et al.*, 2020). In the absence of BRCA1, HR is blocked and 53BP1 accumulates at sites of DSBs (Bouwman *et al.*, 2010; Bunting *et al.*, 2010).

After DNA-end processing, RPA is loaded on to ssDNA ends to protect the ssDNA from further processing and to preventing the formation of secondary structures, prior to displacement with RAD51 for homologous strand invasion and recombination to take place (Figure 1.9D) (Dueva and Iliakis, 2020). RPA is a heterotrimeric protein complex consisting of RPA14, RPA32 and RPA70 and contains multiple oligonucleotide binding (OB)-folds to enable interaction with ssDNA and other repair proteins (Yates *et al.*, 2018). RAD51 competes for binding to ssDNA with RPA, which has a higher affinity for ssDNA and therefore, for RAD51 to displace RPA and be effectively loaded onto the ssDNA, several mediators are required to promote this interaction. One of the most important factors in this displacement is BRCA2 (also known as FANCD1), which is a large scaffold protein that binds multiple RAD51 molecules via its BRC repeats and stabilises RAD51 multimers and filaments. BRCA1 recruits PALB2 which in turn promotes the localisation of BRCA2 to chromatin, forming a BRCA1/PALB2/BRCA2 complex (Figure 1.9E) (Zhang *et al.*, 2009; Prakash *et al.*, 2015). Monoallelic pathogenic variants in *BRCA1* and *BRCA2* predispose women to ovarian and breast cancer, whereas biallelic variants in either *BRCA1*, *PALB2* or *BRCA2* give rise to Fanconi Anaemia (FA) (Shibata and Jeggo, 2021). Other important mediating factors include the RAD51 paralogues XRCC2, XRCC3, RAD51B, RAD51C and RAD51D. The function of these meditating proteins is also to ensure that RAD51 is loaded specifically onto 3'-ssDNA overhangs and to stabilise RAD51 filaments once formed (Grand and Reynolds, 2018).

The loaded RAD51 nucleofilament then catalyses the homology sequence search, strand invasion and D-loop formation (Figure 1.9F-G). The presence of cohesin to hold

sister chromatids together and cell cycle regulated resection, ensures that the homologous sequence is on the sister chromatid rather than occurring on a homologous chromosome. Once this has been identified, the D-loop is formed, whereby one strand of the double helix is displaced by the RAD51 filaments to form a loop of ssDNA. A short tract of DNA is synthesised then the strands are annealed back together. Ideally, the outcome of the repair is that it occurs without any crossovers of genetic material between the sister chromatids. (Elbakry and Löbrich, 2021). Once the sister chromatid has been identified, there are multiple sub-pathways within HR that can occur depending on the DNA-end type. The first being synthesis dependent strand annealing (SDSA), which occurs at 2-ended DSBs (Figure 1.9H). An alternative sub-pathway involves the formation of an intermediate structure from the D-loop called a Holliday junction (HJ) (Daley *et al.*, 2014). The HJ arises through annealing of the non-invading DNA strand to the displaced D-loop in the second end capture step within the process but has also been reported to occur via simultaneous invasion of the resected ends into the donor strand. Copying of genetic material from the homologous sequence takes place from priming the 3' end of the D-loop for DNA synthesis, followed by the second 3' end annealing to the displaced strand of the D-loop, providing a template for more DNA synthesis (Figure 1.9G-I). Following this step, the 3' end of the D-loop gets reannealed to its original partner to generate a second HJ structure (double HJ; dHJ). This four-way junction generated in a dHJ must be segregated and resolved. The HJ structures are resolved by HJ dissolution by topoisomerase III alpha (TOP3A) in complex with BLM helicase and RMI1/RMI2 (Figure 1.9I) (Wu and Hickson, 2003; Mankouri, Ashton and Hickson, 2011). The way in which these structures are resolved can result in two outcomes: non-crossover and crossover products and the pathway

choice may also be dependent on the function of structure specific nucleases including MUS81/EME1, GEN1 and SLX1/SLX4 (Elbakry and Löbrich, 2021). The third sub-pathway in which HR can proceed is non-canonical break induced replication (BIR). BIR is a more error-prone sub-pathway and occurs from long-range DNA synthesis from the invading DSB end without engagement of the second DNA end, therefore is the repair pathway of choice for the repair of one-ended DSBs (Kramara, Osia and Malkova, 2018). The fourth sub-pathway utilising homologous DNA is single strand annealing (SSA), which is discussed in further detail in Section 1.7.3.

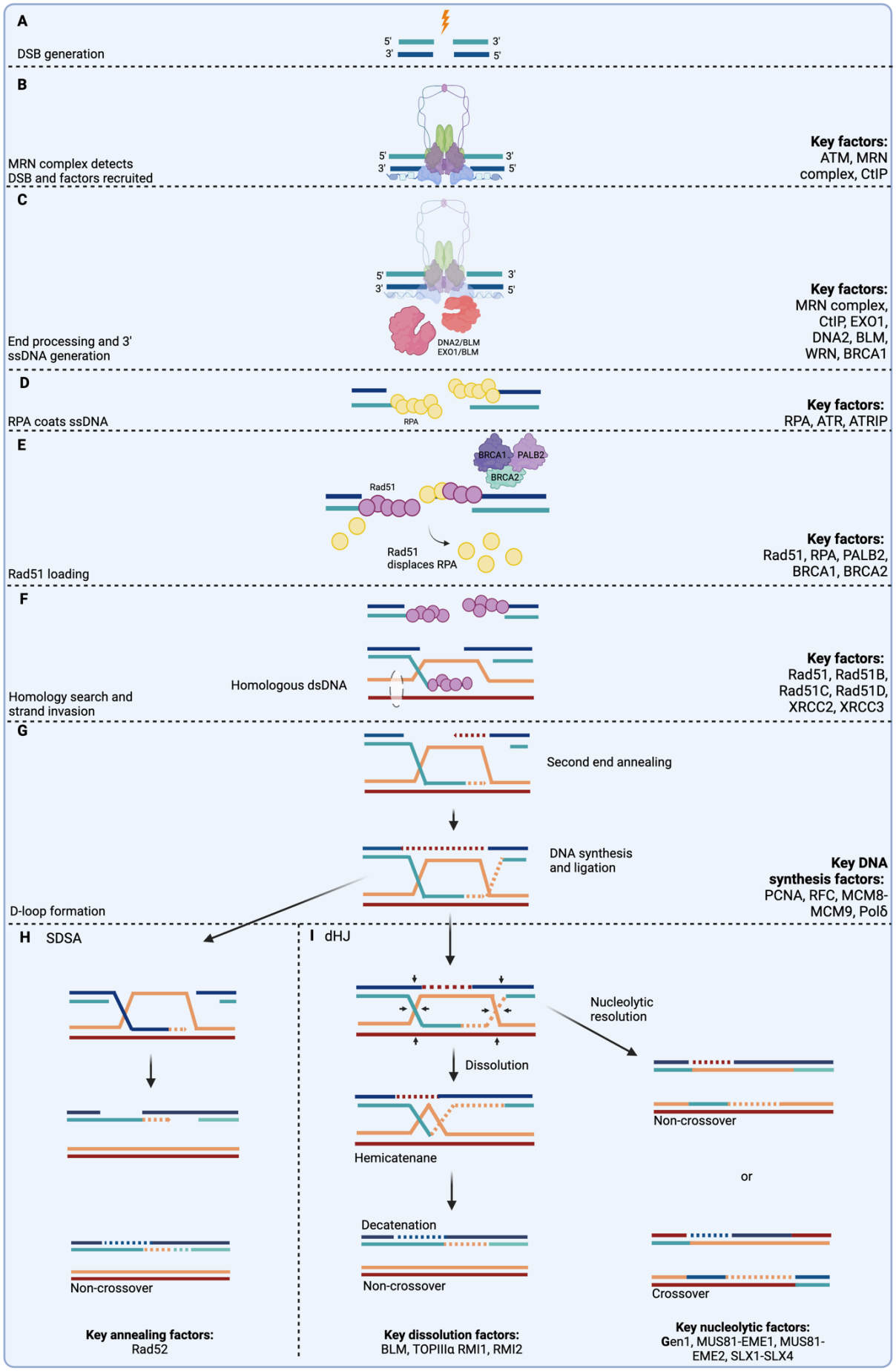

A
DSB generation
5'
3'
3'
5'
B
MRN complex detects
DSB and factors recruited
Key factors:
ATM, MRN
complex, CtIP
C
End processing and 3'
ssDNA generation
DNA2/BLM
EXO1/BLM
Key factors:
MRN complex,
CtIP, EXO1,
DNA2, BLM,
WRN, BRCA1
D
RPA coats ssDNA
RPA
Key factors:
RPA, ATR, ATRIP
E
Rad51 loading
BRCA1
PALB2
BRCA2
Rad51
Rad51
displaces RPA
Key factors:
Rad51, RPA, PALB2,
BRCA1, BRCA2
F
Homology search and
strand invasion
Homologous dsDNA
Key factors:
Rad51, Rad51B,
Rad51C, Rad51D,
XRCC2, XRCC3
G
Second end annealing
DNA synthesis
and ligation
D-loop formation
Key DNA
synthesis factors:
PCNA, RFC, MCM8-
MCM9, Polδ
H SDSA
I dHJ
Nucleolytic
resolution
Dissolution
Hemicatenane
Decatenation
Non-crossover
Non-crossover
or
Crossover
Key annealing factors:
Rad52
Key dissolution factors:
BLM, TOPIIIα RMI1, RMI2
Key nucleolytic factors:
Gen1, MUS81-EME1, MUS81-
EME2, SLX1-SLX4

Figure 1.9 – Homologous recombination pathway and sub-pathways *– **A-B** - When a DSB arises, the MRN complex rapidly detects it and binds to the DNA ends, initiating an ATM-dependent signalling cascade. In breaks in S/G_2 the predominant repair pathway is HR. **C** - CtIP is recruited and Mre11 endonuclease activity generates a nick in the DNA and exonuclease activity resects the DNA generating a 3' overhang of ssDNA. **D** - RPA binds to ssDNA. **E** - RAD51 displaces RPA and is loaded into the ssDNA forming a nucleofilament. The loading of RAD51 is mediated by BRCA2, which is recruited to the site by BRCA1-mediated recruitment of PALB2, forming the BRCA1/PALB2/BRCA2 complex. This complex ensures RAD51 only binds 3' ssDNA. **F** - The RAD51-ssDNA nucleofilament searches for a homologous DNA sequence, usually the sister chromatid, it then invades the strand. **G** - A D-loop is formed by the invading strand and the majority go on to be repaired by SDSA (H). **H** - SDSA occurs when the D-loop is disrupted, and newly synthesised DNA is annealed with the second broken DNA end and the result is a non-crossover product. **I** -Alternatively, to SDSA, the D-loop can from a HJ and if the second end also forms a D-loop, a dHJ junction is formed as shown. This either results in a non-crossover product by dissolution by factors including BLM, TOPIIIα, RMI1 and RMI2. If resolved by nucleases, the product can either be crossover or non-crossover. To simplify the diagram from D-I, the 3' ssDNA end generated on the light blue strand in C has been flipped such that the 3' overhang is now the bottom strand. Solid line indicates DNA strand, dotted lines indicate DNA synthesis. Abbreviations: DSB – double strand break, HJ – Holliday junction, dHJ – double Holliday junction, HR – homologous recombination, SDSA – synthesis dependent strand annealing. Created with Biorender.com.*

1.7.3 Single strand annealing

Single-strand annealing (SSA) is a minor DNA DSB repair pathway utilising homologous repeats to link DNA ends. SSA is error-prone with the potential to induce deletions and chromosomal rearrangements due to the involvement of repetitive sequences flanking the DSB. A crucial SSA step is generating 3' ssDNA overhangs, likely dependent on the MRN complex and CtIP. Suppressors of SSA include RNF168, 53BP1, RIF1, and H2AX (Bennardo *et al.*, 2008; Muñoz *et al.*, 2012; Bhargava, Onyango and Stark, 2016). Post-end resection, flanking repeats are annealed followed by removal of non-homologous 3' ssDNA overhangs, mediated by Rad52 and ERCC1. Rad52 facilitates ssDNA annealing, while ERCC1, in complex with XPF, cleaves 3' ssDNA overhangs (Symington, 2002; Motycka *et al.*, 2004; Rothenberg *et al.*, 2008; Bhargava, Onyango and Stark, 2016). The polymerases and ligases specific to SSA remain largely unknown. SSA is highly mutagenic but the context in which SSA may be important is to restore broken chromosomes whereby the DSB ends have undergone extensive resection and cannot be repaired by HR or alt-EJ. The cell cycle phase, absence of a sister chromatid and the length of sequence with uninterrupted

homology are scenarios in which SSA may be favoured, but the precise conditions for SSA are not well understood (Bhargava *et al.,* 2016).

1.8 The role of HR proteins in replication

1.8.1 Background: DNA replication

DNA replication is essential for cellular survival, ensuring accurate transmission of genetic material. Errors in replication, such as under-replication or re-replication, can lead to loss or amplification of genetic material, compromising cellular health (Takisawa, Mimura, & Kubota, 2000; Green, Finn, & Li, 2010). Replication occurs in S-phase of the cell cycle and has three distinct steps: initiation, elongation, and termination (Leonard & Méchali, 2013).

Step 1 is initiation, which is further divided into 3 steps: replication origin selection, origin licensing and origin firing. Origin selection occurs when the origin recognition complex (ORC), a 6-subunit complex comprising of ORC1-6, along with CDC6 and CDT1 are recruited to DNA, which then orchestrates formation of the pre-replicative complex (pre-RC) along with initiator proteins facilitating DNA replication (Duncker, Chesnokov, & McConkey, 2009). Once an origin has been selected, it is licensed by loading of the MCM2-7 hexamer, which form the core of the replicative machinery. Following licensing, origin firing ensues. Origins fire sequentially, with early origins activating in early S-phase and late origins in late S-phase (Masai *et al*., 2010). Essential factors for this to occur are Cdk2-Cyclin E, Dbf4/Drf10-dependent cell cycle

7 (CDC7) kinase (DDK), Treslin/TICRR-MTBP, TOPBP1, DONSON, RecQL4, CDC45, DNA polymerase ε, GINS and MCM10 (Yeeles *et al*., 2015; Grand and Reynolds, 2018).

Step 2 in replication is elongation, with replication forks forming and replisomes unwinding DNA, synthesizing leading and lagging strands (Georgescu *et al*., 2017; Grand & Reynolds, 2018). DNA polymerases, including polα, polδ, and polε, synthesize nascent DNA, facilitated by sliding clamp structures like PCNA (Kelman, 1997; Moldovan, Pfander, & Jentsch, 2007). Topoisomerases I/II relieve topological stress ahead and behind replication forks, a crucial process for replication progression (Pommier *et al*., 2016).

Step 3 is termination, which occurs when replication forks converge, requiring completion of DNA synthesis and efficient decatenation (Dewar *et al*., 2017). MCM7 ubiquitylation by RNF8 and CRL1 (Cullin-RING Ligase 1) complex and p97/VCP/CDC48 segregase facilitate replisome disassembly (Dewar, Budzowska and Walter, 2015; Jang *et al.*, 2020; Sun *et al.*, 2021). Termination remains the most poorly understood part of replication, with many questions still remaining (Grand & Reynolds, 2018).

1.8.2 Replication stress

Replication stress refers to any obstacle that impedes ongoing replication fork progression and/or DNA synthesis (Zeman & Cimprich, 2014). It encompasses a variety of challenges, including DNA nicks, gaps, lesions, and conflicts with transcription. When replication forks stall, they may generate ssDNA stretches, potentially leading to fork collapse and DSB formation.

To mitigate stalled replication forks, a cellular pathway mediated by the kinase ATR (Section 1.5.3.3) can activate dormant origins, re-prime replication, or remodel and reverse stalled forks. Failure to stabilize a stalled fork can result in fork collapse, where replisome components dissociate, leading to generation of broken ssDNA and DSBs (Magdalou *et al.*, 2014). This collapse may occur through multiple mechanisms, including unresolved structures and persistent ssDNA gaps (Zeman and Cimprich, 2014). Various factors work to prevent fork collapse, aiming to resolve replication stress and restart the replication fork. These factors can be broadly categorized as fork protection factors, which stabilize or remodel the fork, or factors involved in fork degradation (Zeman and Cimprich, 2014; Saxena and Zou, 2022). HR proteins play an important role in this process, which is discussed in further detail below.

1.8.3 HR proteins with a role in replication stress

HR plays a vital role in responding to DSBs as previously outlined, but also acts at stalled replication forks, protecting them from collapse and aiding in their repair and

restart (Ait Saada, Lambert, & Carr, 2018). RAD51, a key HR protein, facilitates homology search and strand invasion for DNA synthesis during replication stress. BRCA2 also plays critical roles in replication fork restart, fork regression, prevention of excessive resection, and normal fork progression, alongside RAD51 (Lambert *et al.*, 2010; Petermann *et al.*, 2010; Ray Chaudhuri *et al.*, 2012; Neelsen and Lopes, 2015; Kolinjivadi *et al.*, 2017). They prevent excessive nuclease resection and promote normal replication fork progression (Somyajit *et al*., 2015). The Fanconi anaemia (FA) pathway, related to HR, also participates in the replication stress response, repairing damaged forks alongside canonical HR proteins (Pichierri *et al*., 2004). Moreover, they protect replication forks from collisions with transcription machinery and RNA:DNA hybrids (R-loops), known as transcription-associated recombination (TAR) (Schwab *et al*., 2015).

In the context of replication blockage, HR-mediated DNA damage tolerance (DDT) pathways are activated. These include error-free pathways, such as template switching (TS), and fork reversal, which prevent accumulation of ssDNA gaps. HR-mediated DDT involves TS to the sister chromatid and operates behind the replication fork, ensuring error-free replication (Giannattasio et al., 2014). However, further research is needed to fully understand these mechanisms (Grand & Reynolds, 2018).

To summarise, HR proteins have multifaceted roles in maintaining genome integrity and ensuring faithful DNA replication under various stress conditions as well as a pivotal role in the repair of DSBs.

1.9 The Actin network in DSB repair

1.9.1 Actin in the nucleus

Over recent years, nuclear actin has gained attention, facilitated by advancements in staining methods and the development of fluorescently tagged F-actin probes with a nuclear localisation signal (NLS). Identified roles for nuclear actin include maintenance of nuclear structure, chromatin remodelling, transcription, and DNA repair, while aberrant nuclear actin function has been associated with diseases such as cancer, immune dysfunction, and neurodegenerative diseases (Caridi *et al*., 2019; Hyrskyluoto and Vartiainen, 2020).

Early reports of nuclear actin date back to the 1960s in bovine thymus cells and Triturus viridescens oocytes (Kelpsch and Tootle, 2018). Since then, it is has been shown that actin filaments respond to cellular stressors and stimuli such as serum treatment, cell-spreading, and mitotic exit (Baarlink *et al*., 2017; Hyrskyluoto and Vartiainen, 2020). Various actin-binding proteins (ABPs) influence nuclear F-actin formation under different conditions. Studies in Xenopus oocytes have highlighted the role of F-actin, formed by Wave1 polymerisation, in nuclear organisation and mechanical stability, as well as transcriptional reprogramming induced by somatic cell nucleus transplantation (Caridi et al., 2019; Hyrskyluoto and Vartiainen, 2020).

1.9.2 Actin and actin nucleators in double strand break repair and replication stress

Recent studies suggest a role for F-actin in regulating DNA DSB repair and the replication stress response. F-actin polymerisation, induced by replication stress, is regulated by ATR through various proteins, including the ARP2/3 complex, WASP, and IQGAP1 (Lamm *et al.*, 2020). In support of this, two further studies implicating actin in the replication stress response also showed this is primarily dependent on the ARP2/3 complex and WASP, with Nieminuszczy et al., also showing that DIAPH1 has a role in regulating this process (Nieminuszczy *et al.*, 2023; Palumbieri *et al.*, 2023). Similar roles for F-actin in the replication stress response have been observed in yeast and mouse cells (Nagai *et al*., 2008; Johnson *et al*., 2013; Su *et al*., 2019). Interestingly, myosin VI, which is an actin based motor protein and the only minus end-directed myosin (moves towards the minus/barbed end of an actin filament) is required in replication fork stability (Shi *et al.*, 2023).

Actin and actin nucleators translocate to the nucleus following damage, interacting with DNA repair proteins including BRCA1 and BRCA2 (Yuan and Shen, 2001; Velkova *et al.*, 2010). Nuclear F-actin plays a crucial role in chromatin remodelling, histone modification, and recruitment of repair proteins to DNA damage sites (Caridi *et al*., 2019). It has been suggested that actin promotes the recruitment of ATR to damage sites and is essential for efficient repair following exposure to various DNA-damaging agents, such as methyl methanesulfonate (MMS). In Drosophila, F-actin and myosins aid in repairing DNA DSBs by relocalising them from heterochromatic to euchromatic

regions. F-actin polymerisation, facilitated by ARP2/3 and myosins, promotes DSB relocalisation to the nuclear periphery for HR repair, reducing the risk of aberrant recombination (Caridi *et al.*, 2018; Dialynas, Delabaere and Chiolo, 2019). Defects in this process lead to genomic instability and chromosomal rearrangements (Caridi *et al.*, 2018).

Additionally, F-actin assists in clustering DSBs in euchromatic regions, favouring HR repair over NHEJ (Caridi *et al.*, 2018; Schrank *et al.*, 2018). DSB clustering, which has been shown to be dependent on the MRN complex and the formin domain-containing protein FMN2, enhances HR repair efficiency, particularly during G_1-phase of the cell cycle, despite HR typically occurring in S- and G_2-phases (Aymard *et al.*, 2014; Schrank *et al.*, 2018). F-actin and the LINC complex are also involved in clustering DSBs in ribosomal DNA (rDNA) in human cells (Marnef *et al.*, 2019). One study has shown actin plays a role in NHEJ, where filaments are required for stabilising NHEJ proteins, such as Ku80, at sites of DNA damage (Andrin *et al.*, 2012).

Distinct actin nucleators are responsible for DNA damage-induced nuclear F-actin polymerisation across different organisms and cell cycle phases. For example, euchromatic DSB clustering in human G_1-phase cells requires FMN-2, while HR-prone DSBs in S/G_2-phase cells depend on ARP2/3 and WASP. The role of F-actin in DSB repair has only recently been discovered so further studies are needed to fully understand the mechanisms underlying these processes and their implications for disease pathology (Belin, Lee, & Mullins, 2015). Additionally, which isoform of actin are functioning in specific nuclear context also needs to be elucidated.

Interestingly, despite DIAPH1 being a key player in nuclear actin dynamics, it has often been overlooked in prior studies with most studies focusing on ARP2/3 complex family. However, a study conducted by Baarlink *et al*. in 2013 demonstrated that depletion of DIAPH1 using siRNA disrupted the formation of nuclear F-actin filaments, particularly in the context of SRF-induced F-actin (Baarlink, Wang and Grosse, 2013). Conversely, a two separate studies by Belin *et al*. in 2015 and Caridi *et al*. 2018 actively ruled out DIAPH1 having a role in DSB repair. Caridi *et al*. showed no increase in γ-H2AX foci following DIAPH depletion with RNA interference (RNAi) in drosophila (Caridi *et al*., 2018). However, drosophila only have one DIAPH gee as opposed to three in humans. Belin *et al*. utilised shRNA to knock down DIAPH1 protein expression but found no discernible impact on the formation of DNA damage-induced F-actin (Belin, Lee and Mullins, 2015). It's worth noting that in the latter study, the method of DIAPH1 protein knockdown only resulted in 50% knockdown of the endogenous protein, as confirmed by western blot analysis..

In summary, while the role of actin and actin nucleators in DSB repair is becoming increasingly recognised, much remains unknown. Elucidating these mechanisms could provide insights into disease mechanisms, particularly cancer, and inform future therapeutic strategies.

1.10 Human diseases associated with DNA repair

A functional DDR is crucial for human health and physiological processes. When repair pathways are impaired due to genetic variations, DNA repair syndromes emerge. These syndromes, though rare, are severe and life-limiting, affecting multiple tissues and organ systems. Many clinical manifestations observed in patients with DNA repair gene variations stem from the inability of cells to repair DNA damage.

Clinical features of DNA repair syndromes include neurodevelopmental defects like microcephaly and developmental delays, along with short stature, skeletal abnormalities, organ malformations, immunodeficiency, and susceptibility to tumours. Although these symptoms can resemble those of other diseases, they often indicate an underlying cellular DNA repair defect. The variable presentation of these syndromes underscores their complexity, with overlapping clinical features even among patients with the same gene variant.

A lot of knowledge about the identity of the proteins that regulate the DDR and how they function has come from studying these rare DNA repair deficiency syndromes. The identification of chromosomal instability disorders, such as Ataxia Telangiectasia (A-T syndrome), arising from variants in *ATM* (Section 1.5.3.2), DNA Ligase IV Syndrome, DNA-PK and Xeroderma Pigmentosum (XP syndrome; arising from variants in genes such as *DDB2, ERCC1*, *ERCC2*, *ERCC3*, *ERCC4*, *ERCC5*, *POLH*, *XPA* and *XPC*), has greatly contributed to our understanding of DDR pathways and the consequences of unrepaired DNA damage (Boder and Sedgwick, 1958; Cleaver,

1968; O'Driscoll *et al.*, 2001; Burg *et al.*, 2009; Hanawalt, 2015). The key clinical features of some well characterised DNA repair syndromes have been summarised in Table 1.3, with the focus being on disorders of ATM and the MRN complex. A summary of common human mutation nomenclature has been included in Table 1.4 as a reference for the mutations discussed throughout this thesis (den Dunnen *et al.*, 2016).

Table 1.3 - Human diseases associated with DNA repair										
			Clinical features							
Disease	**Gene**	**Function**	**Neurodegeneration**	**Microcephaly**	**Immunodeficiency**	**Telangectasia**	**Tumours**	**Short stature**	**Developmental delay and intellectual disability**	**Hearing loss**
Ataxia Telangesctasia (AT; classical)	*ATM*	Key kinase in DSB repair signalling	++	-	+	+	++	-	-	-
Ataxia Telangesctasia Like Disorder (ATLD)	*MRE11*	Part of the MRN complex; key sesnor and effector of DSB repair signalling	++	+ / -	+ / -	-	+	+	+	-
Nijmegen Breakage Syndrome (NBS)	*NBN*	Part of the MRN complex; key sesnor and effector of DSB repair signalling	-	+	+	-	+	+	+	-
Nijmegen Breakage Syndrome-like disorder (NBSLD)	*RAD50*	Part of the MRN complex; key sesnor and effector of DSB repair signalling	-	+	?	-	?	+	+	-
Warsaw Breakage Sydnrome (WABS)	*DDX11*	DNA helicase with role in DNA replication, sister chromatid cohesion and chromosome artchitecture	-	+	-	-	?	+	+	+

Table 1.4: Human mutation nomenclature			
Notation	**Type of mutation**	**Example**	**Explaination**
c.	Coding DNA	c.76A>T	Refers to changes in the coding DNA sequence (cDNA).
g.	Genomic DNA	g.123G>A	A nucleotide change at position 123 in the genomic sequence from G to A.
p.	Protein	p.Val600Glu	A substitution of valine (Val) with glutamic acid (Glu) at position 600 in the protein.
n.	Non-coding DNA	n.1020G>C	Nucleotides of the non-coding reference sequence.
m.	Mitochondrial DNA	m. 2817T>A	Nucleotides of the mitochondrial DNA reference sequence.
r.	RNA	r. 123U>A	Nucleotide of the translation start codon of the RNA reference sequence.
>	Substituion	c.76A>T	Refers to a substition of one nucleotide for another. c.76A>T refers to a substitution at position 76 from A to T in the coding sequence.
del	Deletion	g.3664_3769del	A change where one or more nucleotides are deleted. _ refers to between nucleotides 3664 and 3769 has been delected in the genomic DNA. g.3664_3769del refers to a deletion of nucleotides between 3664 and 3769.
inv	Inversion	c.76_100inv	A change where more than one nucleotide replaces the original sequence and is the reverse compliment of the original sequence (e.g. CTCGA to TCGAG). c.76_100inv indicates an inversion of nucleotides from positions 76 to 100.
ins	Insertion	c.4372_4376insACCT	A change where one or more nucleotides has been inserted in a sequence where the inseetion is not a copy of the seqeuence immediately 5'. c.4372_4376insACCT denotes an ACCT inserted between positions c.4372 and c.4376
con	Conversion	c.500_569con1844_2101con	A specific type of deletion-insertion where a range of nucleotides replace the orginal seqeuence and are a copy of a seqeuence from another site in the genome. A conversion event between positions 500-569 and 1844-2101.
dup	Duplication	c.123_127dup	A change where one or more nucleotides are inserted directly 3' of the orginal copy of the sequence 5' to it. c.123_127dup is a duplication of nucleotides 123 to 127 immediately after the original sequence.
delins/indel	Deletion-Insertion	c.76_78delinsTT	A change where one or more nucleotides are replaced by one or more other nucleotides, which is not a substituion, inversion or conversion. c.76_78delinsTT denotes a deletion of nucleotides 76 to 78, replaced with two thymine (TT) residues.
[number]	Repeitive stretch	g.24_51[25]	Describes how many times a sequence is repeated. g.24_51[25] denotes the sequence between nucleotide 24-51 is reepated 25 times in the genomic DNA.
mosaic	Mosaicism	c.76A>T (mosaic)	The mutation c.76A>T is present in some cells, but not all.
fs	Frameshift	p. Pro660Thrfs	Describes when a mutation results in a frameshift in the protein. p.Pro660Thrfs indicates proline at position 660 has been changed to a Threonine, resulting in a frameshift.
Ter / *	Termination	p. Pro660Thrfs*32 / p. Pro660Thrfs_Ter32	Describes a premature termination in the protein. p. Pro660Thrfs*32 denotes a premature stop codon 32 amino acids downstream of the frameshift resulting from the amino acid change at posistion 660.
+	Cryptic Splice Site	c.89+1G>T (cryptic)	The G>T mutation at the +1 position activates a cryptic splice site, leading to an aberrant mRNA.
	Splice Site Mutation	c.92+1G>A (splice)	Mutation at the +1 position of an intron, likely affecting splicing.
Hom	Homozygous	c.76A>T (Hom)	Mutation occurs on both alleles.
Het	Heterozygous	c.76A>T (Het)	Mutation occurs on one allele.
[ ];[ ]	Compound Heterozygous (Cis configuration)	c.[76A>T];[89C>G]	Two separate mutations occuring on the same allele, denoting a compound heterozygous mutation. The individual has one allele with c.76A>T and c.89C>G.
trans	Trans configuration of compound heterozygoys mutations	c.[76A>T];[89C>G] (trans)	Two separate mutations occuring on different alleles, denoting a compound heterozygous mutation. The individual has one allele with c.76A>T and another with c.89C>G.

1.11 Aims for this thesis

Individuals with homozygous variants in *DIAPH1* exhibit a disease with significant clinical overlap to human syndromes associated with defective DNA repair and replication (Section 1.10). Strikingly, these clinical features overlap significantly with one particular disorder: Nijmegen Breakage Syndrome (NBS). As such, NBS was considered as a potential clinical diagnosis for patients with homozygous *DIAPH1* variants prior to identification of the underlying genetic cause of disease. These similarities suggest that DIAPH1 may function to repair DNA DSBs in a manner similar to NBS1. Therefore, the overall aim of this study is to determine whether DIAPH1 plays a role in regulating actin-dependent DNA DSB repair and identify the potential mechanism with which DIAPH1 regulates DNA DSB repair and its relationship to other actin nucleating factors.

Chapter 2: Materials and methods

2.0 Materials and methods

2.1 General Equipment

All non-proprietary chemicals and reagents were ordered from Sigma-Aldrich-Aldrich or Fisher Scientific unless otherwise indicated. Enzymes used for the cloning of plasmids were obtained from Addgene unless otherwise indicated.

All cell culture plastics were obtained from Corning unless otherwise stated. Invitrogen's Gibco tissue culture medium pre-supplemented with glutamine and Foetal bovine serum (FBS) were used for all tissue culture unless otherwise indicated. For plating out cells for experiments, cell concentrations were determined using the Applied Biosystems Countess II automated cell counter. When centrifugation was performed, an Eppendorf 5810 benchtop centrifuge with A-4-62 swing bucket rotor and appropriate adapters for the tubes were used.

All centrifugation of microfuge tubes was carried out using an Eppendorf 5417C benchtop centrifuge. If samples required refrigeration, an Eppendorf 5424R benchtop centrifuged was used. For larger sample volumes, a Beckman Allegra X-30R benchtop centrifuge with SX4400 swing bucket rotor or FO630 fixed angle rotor with appropriate adapters were used. PCR reactions were performed using the Applied Biosystems Veriti 96 well Thermocyter.

2.2 Mammalian Cell Culture

2.2.1 Cell lines

Cell lines generated and used in the preparation of this thesis are summarised in the table 2.1.

Table 2.1 - Cell lines used and generated for this study			
Cell line	Source	Cell Type	Genotype
Qin HeLa	ATCC	Cervical cancer (epithelial)	
U2-O-S	ATCC	Sarcoma (epithelial)	
U2-O-S for FOK1-mCherry	Supplied by R. Greenberg (University of Pennsylvania); originally generated by Shanbhag and Greenberg, 2013	Sarcoma (epithelia)	
293FT	Thermofisher Scientific	Human embryonal kidney cells transformed with the SV40 large T antigen	
A375 Melanoma, CRISPR WT Cl.5, Cl.7, Cl10	Kindly supplied by A.J. Mazur (University of Wroclaw); originally published in Malek N, *et al*., 2020	Melanoma (epithelial)	
A375 Melanoma, CRISPR KO *ACTB-/-* Cl.10, Cl.17, Cl.21	Kindly supplied by A.J. Mazur (University of Wroclaw); originally published in Malek N, *et al*., 2020	Melanoma (epithelial)	*ACTB*$^{-/-}$ KO
A375 Melanoma, CRISPR KO ACTG1$^{-/-}$, Cl.10, Cl.11 Cl. 16	Kindly supplied by A.J. Mazur (University of Wroclaw); originally published in Malek N, *et al*., 2020	Melanoma (epithelial)	*ACTG1*$^{-/-}$ KO
WT1	Kindly supplied by A. Jackson (University of Oxford)	hTERT immortalised Fibroblast	Wildtype
WT (SC)	Healthy laboratory donor	Lymphoblastoid cell line	Wildtype
HD1-LCL	Peripheral blood mononucleocytes isolated from peripheral venous blood sample supplied by healthy volunteer	Lymphoblastoid cell line	Wildtype

NBS-P1 (EL)	Generated in the Stewart lab	hTERT immortalised Fibroblast	*NBN* mutant c.657_661delACAAA; p.Lys219fs (Hom)
AT1BR	Kindly supplied by P. Jeggo (University of Sussex)	hTERT immortalised Fibroblast	*ATM*$^{-/-}$
NBS-P1 (EL)	Peripheral blood mononucleocytes isolated from peripheral venous blood sample supplied by P. Arkwright (University of Manchester)	Lymphoblastoid cell line	*NBN* mutant c.657_661delACAAA; p.Lys219fs (biallelic)
DIAPH1-P1	Skin biopsy from patient originating from Pakistan, generated in-house	hTERT immortalised Fibroblast	*DIAPH1* mutant c.2101dupC; p. P701fs (Hom)
DIAPH1-P1 + Vector	Skin biopsy from patient originating from Pakistan transduced with empty lentiviral vector	hTERT immortalised Fibroblast	*DIAPH1* mutant c.2101dupC; p. P701fs (Hom)
DIAPH1-P1+I862A DIAPH1	Skin biopsy from patient originating from Pakistan transduced with lentiviral vector expressing I862A mutant DIAPH1, generated in house	hTERT immortalised Fibroblast	*DIAPH1* mutant c.2101dupC; p. P701fs (Hom)
DIAPH1-P1+ DIAPH1	Skin biopsy from patient originating from Pakistan transduced with lentiviral vector expressing WT DIAPH1	hTERT immortalised Fibroblast	*DIAPH1* mutant c.2101dupC; p. P701fs (Hom)
DIAPH1-P2	Skin biopsy from patient originating from Egypt, generated in-house	hTERT immortalised Fibroblast	*DIAPH1* mutant c.2305C>T; p.Q769Ter (Hom)
DIAPH1-P3-1	Skin biopsy from patient kindly supplied by H. Houlden (University College London)	hTERT immortalised Fibroblast	*DIAPH1* mutant c.1976dup; p.P660fs (Hom)

DIAPH1-P4-2	Skin biopsy from patient kindly supplied by H. Houlden (University College London)	hTERT immortalised Fibroblast	*DIAPH1* mutant c.76C>CA; p.P27fs (Hom)
DIAPH1-P5	Peripheral blood mononucleocytes isolated from peripheral venous blood sample kindly supplied by P. Arkwright (University of Manchester)	Lymphoblastoid cell line	*DIAPH1* mutant c.2582-3C>A (Hom)
DIAPH1-P6-1	Peripheral blood mononucleocytes isolated from peripheral venous blood sample kindly supplied by H. Houlden (University College London)	Lymphoblastoid cell line	*DIAPH1* mutant c.3569_3574+2delins18 (Hom)
DIAPH1-P7	Skin biopsy from patient kindly supplied by H. Houlden (University College London)	hTERT immortalised Fibroblast	*DIAPH1* mutant c.752del; p.F251Sfs (Hom)
ACTB-P1	Skin biopsy from patient kindly supplied from N. DiDonato (MHH Hannover Medical School)	hTERT immortalised Fibroblast	*ACTB* mutant c.474_475DupGG; p.Val159fs (*De novo*)
ACTB-P2	Skin biopsy from patient kindly supplied from N. DiDonato (MHH Hannover Medical School); originally published in Verloes *et al*., 2015.	hTERT immortalised Fibroblast	*ACTB* mutant c.587G>A; p.Arg196His (*De novo*)
ACTB-P3	Skin biopsy from patient kindly supplied from N. DiDonato (MHH Hannover Medical School)	hTERT immortalised Fibroblast	*ACTB* mutant c.547C>T; p.Arg183Trp (*De novo*)

ACTB-P4	Skin biopsy from patient kindly supplied from N. DiDonato (MHH Hannover Medical School); originally published in Zech *et al*., 2017	hTERT immortalised Fibroblast	*ACTB* mutant c.547C>T; p.Arg183Trp (*De novo*)
ACTB-P5	Skin biopsy from patient kindly supplied from N. DiDonato (MHH Hannover Medical School); originally published in Latham *et al*., 2018	hTERT immortalised Fibroblast	*ACTB* mutant c.992_1008del; p.Ala331Valfs (*De novo*)
ACTB-P6	Skin biopsy from patient kindly supplied from N. DiDonato (MHH Hannover Medical School); originally published in Di Donato *et al*., 2014 and Verloes *et al*.. 2015	hTERT immortalised Fibroblast	*ACTB* mutant c.220G>A; p.Gly74Ser (*De novo*)
ACTG1-P1	Skin biopsy from patient kindly supplied from N. DiDonato (MHH Hannover Medical School)	hTERT immortalised Fibroblast	*ACTG1* mutant c.608C>T; p.Thr203Met (*De novo*)
ACTG1-P2	Skin biopsy from patient kindly supplied from N. DiDonato (MHH Hannover Medical School)	hTERT immortalised Fibroblast	*ACTG1* mutant c.611C>G; p.Ala204Gly (*De novo*)
ACTG1-P3	Skin biopsy from patient kindly supplied from N. DiDonato (MHH Hannover Medical School); originally published in Cabanillas *et al*., 2018	hTERT immortalised Fibroblast	*ACTG1* mutant c.548G>A; p.Arg183Gln (*De novo*)
ACTG1-P4	Skin biopsy from patient kindly supplied from N. DiDonato (MHH Hannover Medical School)	hTERT immortalised Fibroblast	*ACTG1* mutant c.221G>T; p.Gly74Val (*De novo*)

ACTG1-P6	Skin biopsy from patient kindly supplied from N. DiDonato (MHH Hannover Medical School)	hTERT immortalised Fibroblast	*ACTG1* mutant c.760C>T; p.Arg254Trp (*De novo*)
ARPC4-P1	Skin biopsy from patient kindly supplied from H. Mefford (St Jude Children's Research Hospital); originally published in Laboy Cintron *et al*., 2021	hTERT immortalised Fibroblast	*ARPC4* mutant c.472C>T; p.Arg158Cys (*De novo*)
ARPC4-P2	Skin biopsy from patient kindly supplied from H. Mefford (St Jude Children's Research Hospital); originally published in Laboy Cintron *et al*., 2021	hTERT immortalised Fibroblast	*ARPC4* mutant c.472C>T; p.Arg158Cys (*De novo*)
ARPC1B-P1	Skin biopsy from patient kindly supplied from S. Volpi (University of Genoa); originally published in Brigida *et al*., 2018	hTERT immortalised Fibroblast	*ARPC1B* mutant c.622G>T; p.Val208Phe (Hom)
ARPC1B-P2	Skin biopsy from patient kindly supplied from S. Volpi (University of Genoa); Originally published in Chiriaco *et al*., 2022	hTERT immortalised Fibroblast	*ARPC1B* mutant c.212_226del; p.Gly71_Asn75del (Hom)
ARPC1B-P3	Skin biopsy from patient kindly supplied from S. Volpi (University of Genoa); originally published in Brigida *et al.,* 2018	hTERT immortalised Fibroblast	*ARPC1B* mutant c.64+1G>A (Hom)

ARPC5-P1	Skin biopsy from patient kindly supplied from S. D. Rosenzweig (National Institutes of Health, Bethesda); originally published in Nunes-Santos *et al*., 2023	hTERT immortalised Fibroblast	*ARPC5* mutant c.23C>A; p.Ser8Ter (Hom)

2.2.2 Maintenance of Mammalian cell lines

All mammalian cell lines were maintained at 37 °C humidified 5 % CO_2 incubators. Cell lines derived from fibroblast were cultured in Gibco DMEM media (Cat: 41966-029) supplemented with 20% (v/v) FBS (cat: F9664), 100units/ml penicillin and 100 ng/ml streptomycin (Sigma-Aldrich cat: P4333-100ml). Fibroblast were grown in monolayers and maintained at 80-90% confluence.

HeLa cell lines, U2-O-S *Fok1*-mCherry and HEK293FT cells were cultured in Gibco DMEM media (Cat: 41966-029) supplemented with 10% (v/v) FBS (cat: F9664), 100units/ml penicillin and 100 ng/ml streptomycin (Sigma-Aldrich car: P4333-100ml) and were grown in monolayers and maintained at 80-90% confluence. U2-O-S cells were maintained in Gibco McCoys 5A media (cat: 16600082) supplemented with 10% (v/v) FBS (cat: F9664), 100units/ml penicillin and 100 ng/ml streptomycin (Sigma-Aldrich car: P4333-100ml) and were grown in monolayers and maintained at 80-90 % confluence.

For cell passaging, adherent cells were washed first using sterile tissue culture grade Gibco phosphate buffered saline (PBS) (Gibco, cat: 14190-094) and incubated with an appropriate volume of Gibco 1 x trypsin-EDTA (0.05 % trypsin and 0.53 mM EDTA). Once cells were detached, they were resuspended into a final volume of 15 ml in fresh media and diluted at the appropriate cell concentration every 3-4 days.

Human lymphoblastoid cell lines (LCLs) were maintained in suspension cultures in RPMI-1640 (Gibco, cat: 21875-034) medium supplemented with 20 % (v/v) FBS (cat:

10270-106) and 100 units/ml penicillin and 100 ng/ml streptomycin (Sigma-Aldrich, cat: P4333-100ml). Suspension cells were passaged every 3 days by diluting cells in fresh medium at a 1:1 ratio. Cells were transferred into fresh flasks and topped up with a suitable volume of media in the tissue culture vessel.

All cells were stored in liquid phase nitrogen for long term storage. To prepare cells for storage, adherent cells were grown to confluence, trypsinised then re-suspended in 10 ml of appropriate media. Suspension cells were grown to confluence then re-suspended in a total volume of 10 ml medium. Re-suspended cells were centrifuged at 1400 rpm for 4 min, the supernatant removed then cells were re-suspended in 1 ml of freezing medium (10 % DMSO, 90 % FBS). Cell suspension was then transferred to a cryotube and slowly cooled to -80 °C using a Nalgene cryo freezing container (cat: 5100-001) before being transferred to liquid nitrogen.

To recover cells from liquid nitrogen, cells were quickly thawed in a 37 °C water bath before re-suspending in 10 ml of appropriate medium. Cells were spun at 1400 rpm for 4 min, the supernatant was removed and replaced with fresh media. The cell suspension was then transferred to a fresh tissue culture vessel and topped up with a suitable volume of medium.

2.3 siRNA-mediated protein knockdown

2.3.1 Preparation of cells for siRNA knockdown

8 h prior to addition of siRNA reagents, HeLa cells were seeded into 6 cm dishes at a density of 5 x 10^5 cells per dish and incubated with complete DMEM supplemented with 10 % FBS and 100 units/ml penicillin and 100 ng/ml streptomycin. U2-O-S cells were seeded in 6 cm dishes at a density of 2.5 x 10^5 cells per dish the evening before siRNA knockdown reagents were added.

2.3.2 siRNA knockdown

In 1.5 ml sterile RNAase free tubes (Ambion, cat: AM12400), 20 µl of oligofectamine (Thermofisher cat: 12252011) for HeLa cells and 12 µl for U-2-O-S cells were added to 1 ml of Gibco optiMEM (Thermofisher cat: 31985070) and mixed by gentle pipetting. To the mix, 100 nM of siRNA was added and gently mixed by pipetting and incubated for 30 min at RT. A list of all siRNAs used are listed in Table 2.2. Before the addition of siRNA to cells, cells were washed in 2 ml of optiMEM two times, then 1 ml of optiMEM was added to cells. The additional 1 ml siRNA containing solution was added to cells in a dropwise fashion and mixed gently by agitation. HeLa cells were incubated with siRNA overnight at 37 °C 5 % CO_2. U2-O-S cells were incubated with siRNA for 4-6 h. Cells were rescued by removal of siRNA and addition of 2 ml antibiotic-free DMEM (HeLa cells) or McCoys 5A (U2-OS cells) containing 20 % FBS and incubated for 24 h. The next day, cells were trypsinised and plated at cell densities appropriate for specific experimental techniques. For siRNA depletion of ACTB and ACTG1, a

second siRNA depletion was carried out 24 h after the first to adequately deplete these abundant proteins. These cells were then trypsinised and plated at cell densities appropriate for specific experimental techniques.

Table 2.2 - siRNA used in this study

siRNA target	Description	Concentration added to cells	Company
ACTB	Human ACTB ON-TARGET plus siRNA Smartpool	20 μM	Dharmacon Horizon Discovery
ACTG1	Human ACTG1 ON-TARGET plus siRNA Smartpool	20 μM	Dharmacon Horizon Discovery
ARPC4	Human ARPC4 ON-TARGET plus siRNA Smartpool	20 μM	Dharmacon Horizon Discovery
BRCA2	Human BRCA2 ON-TARGET plus siRNA Smartpool	20 μM	Dharmacon Horizon Discovery
DIAPH1	Human DIAPH1 ON-TARGET plus siRNA Smartpool	20 μM	Dharmacon Horizon Discovery
Luciferase (Non-targeting control)	Custom siRNA to LacZ (Higgs *et al*., 2015)	20 μM	Custom made
NBS1	Human NBN ON-TARGET plus siRNA Smartpool	20 μM	Dharmacon Horizon Discovery

2.4 Generation of Plasmid DNA constructs

Generation of plasmid DNA constructs was completed with the assistance of Anil Ganesh, the Stewart Group laboratory technician.

2.4.1 Plasmid DNA constructs and vectors:

A list of plasmids used in this study are outlined in the below Table 2.3.

Table 2.3 - Plasmids used in this study		
Plasmid name	**Use**	**Source**
pLVX-IRES-Neo-2xHA-WT DIAPH1 lentiviral vector	Add back WT-DIAPH1 to patient fibroblast	Takara Bio
pLX330-LMNA-gRNA-1	Homologous recombination assay	Addgene
pCR2.1-Clover-LMNA-Donor	Homologous recombination assay	Addgene
piRFP670-N1	Homologous recombination assay	Addgene
GFP-tagged DIAPH1 pcDNA5/FRT/TO	GFP-Trap	Thermofisher, GFP-DIAPH1 addition generated in the Stewart Lab
2xHA-tagged pLVX-IRES-Neo-HA-WT DIAPH1 I862A	Add back mutant DIAPH1 to patient fibroblast	Generated in the Stewart lab via site-directed mutagenesis
psPAX2	To make lentivirus to add back WT-DIAPH1 to patient fibroblast	Addgene
pMD.G	To make lentivirus to add back WT-DIAPH1 to patient fibroblast	Addgene

2.4.2 Amplification and isolation of Plasmid DNA constructs from bacterial cultures

Amplification of plasmid DNA was done by transformation of chemically competent NEB stable *E.coli* (NEB, cat: C3010L). A dilution of approximately 100 ng of DNA for transformation was made and 1 µl of this stock was added a vial containing 50 µl of competent cells, which were thawed for 10 min on ice prior to adding DNA. DNA and bacterial mixture were incubated on ice for 30 min then heat shocked at 42 °C for 42 s followed by incubation on ice for a further 2 min. The heat shocked bacteria were then

recovered by addition of 950 µl of room temperature outgrowth media/NEB 10-β (cat: B9035S) and incubated horizontally at 37 °C in a 250 rpm shaking incubator for 1 h. Recovered cells were plated on LB agar plates, containing the appropriate antibiotic selection at a concentration of 100 µg/ml, then incubated overnight at 37 °C. Plasmid DNA was then extracted by selection of single colonies of transformed bacteria which were then placed in 5 ml of LB medium supplemented with the appropriate antibiotic selection at a concentration of 100 µg/ml, and incubated overnight at 37 °C in a 250 rpm shaking incubator. The following day, plasmid DNA was extracted from the culture via alkaline lysis using a Qiaprep mini kit (Qiagen, cat: 27106) as per manufacturer's instructions. To extract large quantities of plasmid DNA, bacteria was transformed as above and single colonies were selected and added to 5 ml of LB medium supplemented with the appropriate antibiotic, then incubated overnight at 37 °C in a 250 rpm shaking incubator. The starter culture was then used to inoculate flasks containing 250 ml of LB medium supplemented with appropriate antibiotic. Cultures were grown overnight, and plasmids extracted via alkaline lysis using an Invitrogen PureLink HiPure plasmid filter maxiprep kit (Invitrogen, cat: K210017). Plasmid DNA preps were re-suspended in appropriate volumes of TE Buffer - Ambion nuclease-free water (Ambion, cat: AM9939).

2.4.3 Quantification of DNA in solution

For quantification of plasmid DNA preps, a Metler-Toledo UV5Nano micro volume spectrophotometer was used. DNA concentration was determined by placing 3 µl of solution on the micro-volume measuring platform. DNA purity was quantified using 260/280 absorbance ratio and ratios of 1.8 and above indicated the DNA was of high purity.

2.4.4 Agarose gel electrophoresis of DNA fragments

DNA fragments and plasmids were separated by 0.8 % - 1 % (w/v) agarose gel electrophoresis. Agarose gels were prepared by dissolving agarose (Sigma-Aldrich, cat: A9539) in 1 x TBE (cat: 15581044). To visualise DNA, 1 x Invitrogen SyberSafe DNA gel stain (10,000 X stock, cat: S33102) was added to the agarose before polymerisation once cooled to approximately 50 °C. To assist with loading samples, 6 x purple gel loading dye was used (New England Biolabs, cat: B7024S). The gel was run at a voltage between 75-100 V. To estimate the DNA fragment size, a Bio-line Hyper Ladder 1 kb (Merdian Bioscience, cat: BIO-33053) was loaded alongside the DNA samples. To visualise DNA in the gel, a FastGene blue light LED trans-illuminator was used.

2.4.5 Amplification of plasmid DNA constructs

The pLVX-IRES-Neo-HA-WT-DIAPH1 lentiviral vector (used to complement P1-fibroblasts) and GFP-tagged *DIAPH1* pcDNA5/FRT/TO vector was generated with the

DIAPH1 open reading frame (ORF) amplified from cDNA with PCR using NEB Q5 PCR reaction components (New England Biolabs, cat: M0491). The total PCR reaction mixture was 25 µl (Table 2.4) and run as described in Table 2.5. Forward and reverse primers for these plasmids are outlined in Table 2.6. The I862A mutant of pLVX-IRES-Neo-HA-WT-DIAPH1 was generated using the Q5 Site-directed mutagenesis Kit (NEB, E0554S) according to manufacturer's instructions using the primers outlined in Table 2.6.

Table 2.4 - PCR reaction components

Component	Volume	Final concentration
DNA template 10ng/ml	2 µl	10ng/ml
10 µM Forward primer	1 µl	0.5 µM
10 µM Reverse primer	1 µl	0.5 µM
5X Q5 Reaction buffer	5 µl	1 X
Q5 DNA polymerase	0.25 µl	0.02 U/ µL
10 mM dNTPs	0.5 µl	200 µM
Nuclease free water	16.25 µl	

Table 2.5 - PCR Thermocycler settings

Step	Temperature	Time
Initial Denaturation	98 °C	30 s
25-35 cycles	50 - 60 °C	10 - 30 s
Final Extension	72 °C	2 min
Hold	4-10 °C	

Table 2.6 - Primers for amplification of DNA constructs		
Target	**Strand**	**Oligo sequence**
pLVX-IRES-Neo-HA-WT-DIAPH1	Forward (DIAPH1-LVX-XhoI-Fwd)	5'-GTTGTTCTCGAGATGGAGCCGCCCGGCGGGAG-3'
	Reverse (DIAPH-LVX-NotI-Rev)	5'-GTTGTTGCGGCCGCTTAGCTGCACGCCCAACCAACTCCTTG-3'
Site-directed mutagenesis I862A mutant of pLVX-IRES-Neo-HA-WT-DIAPH1	Forward (DIAPH-LVX-I862A-Fwd)	5'-GAATCTCTCAGCGTTTTTGGGTTCCTTCC-3'
	Reverse (DIAPH-LVX-I862A-Rev)	5'-TGGGCTGTCTTTGAATC-3'
GFP-tagged DIAPH1 pcDNA5/FRT/TO	Forward (DIAPH-GFP-NotI-Fwd)	5'-GTTGTTGCGGCCGCATGGAGCCGCCCGGCGGGAG-3'
	Reverse (DIAPH-GFP-XhoI-Rev)	5'-GTTGTTCTCGAGTTAGCTGCACGCCCAACCAACTCCTTG-3'.

2.4.6 DNA restriction enzyme digestion

Prior to restriction digest, PCR products were purified using QIAquick PCR purification kit (Qiagen, cat: 28104). Restriction digest was carried out by adding 1 µg of PCR product and 2 units of appropriate restriction enzymes EcoR1 (NEB, cat: R3101) and Not1 (NEB, cat: #R3189) buffered in 1 X rCutSmart buffer suppled with restriction enzymes. Samples were digested for 1 h at 37 °C in a heat block. Following digestion of vectors, the product was de-phosphorylated with 1 unit of Calf intestinal

phosphatase (NEB, cat: M0290) by incubating for 30 min at 37 °C. Digestion of DNA was confirmed with agarose gel electrophoresis and uncut DNA was used as a control.

2.4.7 Ligation of DNA fragments

Ligation of purified PCR products were set up such that insert:vector ratio was 3:1. For each preparation of vector DNA, an empty vector only ligation reaction was also set up to determine the efficiency of the reaction and de-phosphorylation of the vector DNA. Reactions were set up in 0.5 ml tubes. T4 DNA ligase reactions were set up according to manufacturer's instructions (NEB, cat: M0202L). 10 x ligase buffer (1 X concentration components; 50 mM Tris-HCl, 10 mM $MgCl_2$, 1 mM ATP, 10 mM DTT) was diluted 1:10 and used for the ligation to take place. Reactions were mixed by gentle pipetting and left O/N at RT. Ligated DNA was transformed as per Section 2.4.6. Plasmid DNA was extracted from multiple single colonies by alkaline lysis using Qiagen Miniprep kits (Qiagen, cat: 27104) following manufactures instructions. Confirmation of ligation was confirmed through Sanger sequencing by Source Biosciences using standard primers.

2.5 Immunofluorescence

2.5.1 Micronuclei and γ-H2AX/53BP1 foci formation in patient derived fibroblasts

24 h prior to treatment of cells with either IR, 10 μM etoposide (ETOP; Selleckchem cat: S1225) or 10 μM camptothecin (CPT; Selleckchem cat: S1288), cells were seeded into 10 cm dishes containing 6 sterile coverslips then incubated at 37 °C, 5 % CO_2.

Untreated control cells and cells harvested at 1 h post-treatment were seeded at 1.2 x 10^6 cells/dish, 24 h post-treatment were seeded at 0.8 x 10^5 cells/dish and cells harvested at 48 h post-treatment were seeded at 0.4 x 10^5 cells/dish.

On the day of treatment, coverslips were transferred to 6 cm with 3-4 ml of appropriate media. Cells treated with IR were irradiated using CellRad (Precision X-ray irradiation) at the appropriate dose (Gy) then incubated at 37 °C, 5 % CO_2 until harvesting. Cells that were treated 10 uM ETOP were incubated with drug for 30 min, cells treated 100 nM CPT were incubated with the drug for 1 h. The media containing drug was then removed and coverslips were washed 3 times with warmed drug-free media and left in the third wash followed by incubation at 37 °C, 5 % CO_2 until harvesting. Coverslips were harvested at 1 h, 24 h and 48 h time points.

2.5.2 Micronuclei and γ-H2AX/53BP1 foci formation in siRNA depletion of DIAPH1 in HeLa cells

Following siRNA depletion outlined in Section 2.3. 24 h prior to treatment of cells with either IR, cells were seeded into 10 cm dishes containing 6 sterile coverslips then incubated at 37 °C, 5 % CO_2. Untreated control cells and cells harvested at 1 h post-treatment were seeded at 1.2 x 10^6 cells/dish, 24 h post-treatment were seeded at 1.0 x 10^5 cells/dish and cells harvested at 48 h post-treatment were seeded at 0.8 x 10^5 cells/dish.

2.5.3 RAD51, RPA and BRCA1 foci formation in adherent cells

For cells treated with CPT, 24 h prior to treatment, cells were seeded into 10 cm dishes containing 6 sterile coverslips at a density of 1.2 x 10^6 cells for fibroblasts and 1 x 10^6 for HeLa cells and A375 cells, then incubated at 37 °C, 5 % CO_2. HeLa cells were siRNA depleted prior to treatment outlined in Section 2.3. On day of treatment, coverslips were transferred to sterile 6 cm dishes and treated with 100 nM CPT for 1 h. After 1 h, CPT containing media was removed and cells were washed three times with DMEM supplemented with 20 % FBS and 100 units/ml penicillin and 100 ng/ml streptomycin. Cells were harvested at 1 h and 4 h post-CPT washout and pre-extracted/fixed as outlined in Section 2.5.9.

2.5.6 Native BrdU foci in siRNA depleted HeLa cells

HeLa cells were subject to siRNA depletion described in in Section 2.3. 24 h prior to treatment with IR, cells were seeded into individual wells of a 6 well plate onto sterile glass coverslips at a density of 2.5 x 10^5 cells per well with 25 μM BrdU added directly to the media and mixed by agitation. Cells were then incubated at 37 °C, 5 % CO_2 for 24 h. On day of treatment, cells were treated with 50 μM mirin (Selleckchem, cat: S8096) for 1 h prior to treatment with 10 Gy IR. 1 h post-IR, cells were harvested and pre-extracted/fixed as outlined in Section 2.5.9.

2.5.7 ER-mCherry-LacI-FokI-DD nuclease system double strand break repair assay in U2-O-S LacO-FokI mCherry expressing cells

U2-O-S LacO-*Fok1* mCherry expressing cells were subject to siRNA protein depletion as per Section 2.3. 24 h post-siRNA depletion, cells were seeded at a density of 2.5 x 10^5 per well of a 6 well plate onto sterile glass coverslips and incubated at 37 °C, 5 % CO_2 for 24 h. On the day of treatment, cells were incubated with 1 μM Shield1 ligand (Takara Bio, cat: 632189) and 1 μM 4-Hydroxytamoxifen (4-OHT, Merck, cat: H6278-10MG) for 4 h. After 4 h incubation, cells were pre-extracted/fixed as outlined in Section 2.5.9.

2.5.8 Mitotic defects in adherent cells

48 h prior to harvesting, cells were seeded into 10 cm dishes containing 6 sterile Poly-L-Lysine coverslips (Corning, cat: 354086) then incubated at 37 °C, 5 % CO_2. Fibroblast cells were seeded at 0.4 x 10^5 cells/dish and HeLa cells were seeded at 1 x 10^6 cells/dish. On day of harvesting, all coverslips were transferred to a fresh 6 cm dish and incubated with 4 ml of ice-cold methanol for 15 min to fix cells. Following fixing, coverslips were washed three times in PBS and stored at 4 °C in 10 % FBS/PBS containing 0.05 % sodium azide until antibody staining.

2.5.9 Cell harvesting for immunofluorescence

On day of harvesting cells at appropriate time-points for each experiment, two coverslips per time point were incubated with 3 ml of ice-cold pre-extraction buffer

(Table 2.7, pH 7.2) for 5 min. For native BrdU foci analysis, cells were incubated with pre-extraction buffer for 2 x 3 min. Extraction buffer was removed then the coverslips were fixed by incubating with 3 ml of ice-cold 3.6 % paraformaldehyde (PFA) in PBS for 10 min. Following fixation, coverslips were washed three times in PBS and stored at 4 °C in 10 % FBS/PBS containing 0.05 % sodium azide.

Table 2.7 - Components of pre-extraction buffer

Component	Final concentration
Triton-X	0.5 % (v/v)
PIPES	10 mM
Sucrose	300 mM
NaCl	20 mM
$MgCl_2$	3 mM

2.5.10 Immunofluorescence

Coverslips with PFA fixed cells (described in Section 2.5.9) or methanol fixed cells (described in Section 2.5.8) were washed once in PBS and then incubated in the dark with the primary antibodies outlined in Table 2.8, diluted in 2 % FBS in PBS for 1 h at RT. The coverslips were washed three times in PBS and then incubated, in the dark, with the secondary antibodies coupled to a fluorophore outlined in Table 2.9 diluted in 2 % FBS in PBS for 1 h at RT. The coverslips were again washed three times in PBS and mounted facedown onto slides with 10 µl of VectaShield-containing DAPI (4', 6'-Diamidino-2-phenylindole, Vector Laboratories cat: H-1200). Poly-L-lysine coverslips were mounted with 5 µl of DAPI. Excess VectaShield was carefully dabbed from the edges of the coverslips before sealing with clear nail varnish and left to dry in the dark for 30 min. Slides were stored in the dark, at 4 °C and visualised with Nikon

fluorescence microscopy and images captured with Volocity software. Fluorescence intensity was analysed using ImageJ software.

Table 2.8 - Primary antibodies used for IF						
Antigen	**Species**	**Dilution**	**Dilution medium**	**Incubation condition**	**Company**	**Cat. no**
α-tubulin	Mouse	1 in 5000	2 % FBS in PBS	1 h at RT	Sigma-Aldrich-Aldrich	T6199
γ-H2AX (pSer139)	Mouse	1 in 1000	2 % FBS in PBS	1 h at RT	Millipore	05-636
BRCA1	Mouse	1 in 200	2 % FBS in PBS	1 h at RT	Santa Cruz Biotechnology	sc6954
BrdU	Rat	1 in 100	2 % FBS in PBS	1 h at RT	Abcam	ab6326
CENPF	Rabbit	1 in 1000	2 % FBS in PBS	1 h at RT	Antibody Atlas	HPA052382
CDK5/RAP2	Rabbit	1 in 1000	2 % FBS in PBS	1 h at RT	Bethyl	IHC-00063
Mitosin	Mouse	1 in 1000	2 % FBS in PBS	1 h at RT	BD Biosciences	610768
MRE11	Mouse	1 in 1000	2 % FBS in PBS	1 h at RT	Abcam	ab214
RAD51	Rabbit	1 in 500	2 % FBS in PBS	1 h at RT	Millipore	ABE257
RPA2	Rabbit	1 in 250	2 % FBS in PBS	1 h at RT	Abcam	ab10359
53BP1	Rabbit	1 in 1000	2 % FBS in PBS	1 h at RT	Novus	NB100-304

Table 2.9 - Secondary fluorophore coupled antibodies used for IF						
Company	**Antigen**	**Fluorophor**	**Colour**	**Dilution**	**Dilution medium**	**Incubation condition**
Invitrogen	Polyclonal donkey anti-rabbit IgG	Alexa 488	Green	1 in 1000	2 % FBS in PBS	1 h at RT in the dark
Invitrogen	Polyclonal donkey anti-mouse IgG	Alexa 488	Green	1 in 1000	2 % FBS in PBS	1 h at RT in the dark

Invitrogen	Polyclonal goal anti-mouse IgG	Alexa 594	Red	1 in 1000	2 % FBS in PBS	1 h at RT in the dark
Invitrogen	Polyclonal goat anti-rat IgG	Alexa 555	Red	1 in 500	2 % FBS in PBS	1 h at RT in the dark

2.6 GFP-Trap affinity purification

293FT cells were transfected with plasmids (Table 2.3) using Lipofectamine 2000 and harvested 36 h post-transfection. Cells were incubated in GFP-trap lysis buffer (Table 2.10) for 2 h with rotation at 4 °C. The cellular lysates were subsequently pre-cleared by centrifugation at 44,000 rpm at 4 °C for 30 mins. For GFP-Trap, 3-5 mg of lysate was then incubated with 20 µl of GFP-Trap agarose beads (ChromoTek) for 5 hours at 4 °C. The resulting complexes formed by GFP-Trap were pelleted at 3,000 rpm for 30 secs and subjected to three washes using GFP-trap wash buffer (Table 2.11) Subsequently, all residual wash buffer was removed from the bead pellet using a syringe needle, and the beads were resuspended in 30 µl of 2 x Bio-Rad Laemmli buffer supplemented with 5 % β-mercaptoethanol, followed by boiling for 5 min. The resultant samples were either preserved at -80 ºC or loaded onto an SDS–PAGE gel (Section 2.7.3-2.7.4) for further analysis.

Table 2.10 - Components of lysis buffer for GFP-Trap affinity purification	
Component	**Final concentration**
NaCl	150 mM
Tris HCl (pH 7.5)	50 mM
$MgCl_2$	2 mM
NP40	1% (v/v)
Bezonase (Novagen)	90 U/ml
EDTA-free protease inhibitor cocktail (Roche)	

Table 2.11 - Components of wash buffer for GFP-Trap affinity purification	
Component	**Final concentration**
NaCl	150 mM
Tris HCl (pH 7.5)	50 mM
NP40	0.5% (v/v)
Bezonase (Novagen)	90 U/ml
EDTA-free protease inhibitor cocktail (Roche)	

2.7 Western Blotting

2.7.1 Preparation of whole cell extracts

Whole cell lysates were harvested by removing media and washing cells in pre-chilled PBS. Cells were pelleted by centrifugation at 1400 rpm for 5 min, the supernatant was discarded, and the pellet washed in PBS and centrifuged again for 5 min, three times. As much PBS as possible was removed by aspiration with care taken not to disturb the pellet.

To Western blot for all proteins outlined in this study, cell pellets were lysed in UTB buffer (8 M Urea, 50 mM Tris-HCl pH 7.5, 150 mM β-mercaptoethanol). Microfuge tubes were pre-chilled on ice, cell pellets were re-suspended in 200 µl - 300 µl of UTB buffer and immediately sonicated for 10 seconds twice. To clear cell debris from the lysate, re-suspended pellets were then centrifuged at 13000 rpm at 4 °C for 20 min. Samples were aliquoted and snap frozen in liquid nitrogen and stored at -80 °C.

2.7.2 Bradford protein determination assay

Protein concentration of whole cell lysates was determined using the Bradford Assay A protein standard was made using a set of 6 concentrations of bovine serum albumin (BSA; Fisher Scientific cat: 10711454001) ranging 0-500 µg/ml, which was prepared using 1 mg/ml BSA stock solution with distilled water. 10 µl of cell extract (diluted 1 in 10 in water) and BSA standard were loaded in quadruplet into a flat-bottom 96-well plate. 200 µl of dilute Bradford Reagent (Bio-Rad 1:5 in water, Bio-Rad cat 500-0006) was added to each well containing cell extract or BSA standard. The reagent and sample were mixed by gentle trituration. The absorbance of samples was measured on a Bio-Rad iMark Microplate reader set to read at 595 nm wavelength. A linear standard curve was constructed by plotting absorbance readings of the BSA standards. Concentrations of protein were calculated using the BSA protein standard curve. 50 µg of cell extracts were typically loaded per lane on an SDS-Page gel.

2.7.3 SDS-PAGE Electrophoresis

Proteins were separated by size on 6 %, or 10 % polyacrylamide slab gels, components of gels are outlined in Table 2.12. All gels were run using a Heofer SE400 Vertical protein electrophoresis apparatus constructed to the manufacturer's instructions. Prior to loading, an appropriate volume of 4 x Bio-Rad Laemmli buffer plus 5 % β-mercaptoethanol was added to 50 µg of cell extracts and incubated for 5 min at 90 °C in a head block. Samples were briefly centrifuged before loading with a Hamilton glass syringe. A rainbow full range molecular marker (Cytiva, cat: RPN800E) was run alongside the cell lysates to provide a visual marker of protein size. Gels were run in a

buffer composed of 100 mM Tris-Bicine and 1 % SDS, recipe summarised below in Table 2.13. Gels were run at 30 mA per gel. Once the gel front had reached the bottom edge of the glass plate proteins were transferred to nitrocellulose.

Table 2.12 - Components of SDS-Page gel				
	6 %		10 %	
Component	**1 Gel**	**2 Gel**	**1 Gel**	**2 Gel**
H_2O	27.4 ml	54.8 ml	22.04 ml	44.08 ml
1 M Tris/Bicine	4 ml	8 ml	4 ml	8 ml
30 % Acrylamide	8 ml	16 ml	13.36 ml	26.72 ml
10 % SDS	400 µl	800 µl	400 µl	800 µl
TEMED	80 µl	160 µl	80 µl	160 µl
10 % APS	200 µl	400 µl	200 µl	400 µl

Table 2.13 - Components of running buffer	
Component	Volume
H_2O	890 ml
1M Tris-Bicine	10 ml
10 % SDS	100 ml

2.7.4 Western Blotting

Proteins were transferred to Bio Trace N Pure nitrocellulose membrane (Pall Corporation cat: 66485) before visualising with antibodies. All transfers carried out using a Hoefer TE62 transfer tank as per manufacture instructions. Transfer buffer composed of 20 % methanol, 50 mM Tris base, 190 mM glycine was used for transfer of all proteins onto nitrocellulose membrane. Proteins were left to transfer for 18 h at room temperature using a constant 200 mA current. Successful transfer was confirmed

by staining the membrane with Ponceau S solution (Sigma-Aldrich cat: SLCB3855). Excess unbound Ponceau S was washed off the membrane with three washes of deionised water. Excess nitrocellulose membrane was trimmed before cutting membrane into horizontal strips based on the size of the protein to be visualised. Ponceau S was washed off by incubating the membrane with agitation in 1 X TBS-T (20 mM Tris-HCl, 150 mM NaCl, 0.1 % Tween pH 7.6).

Nitrocellulose membranes were blocked in 5 % milk powder dissolved in TBS-T for 2 h at RT with agitation. Primary antibodies were diluted in 5 % milk in TBS-T, or 5 % BSA in TBS-T for phospho-specific antibodies (Table 2.14), and membranes incubated overnight at 4 °C on a rocker. Primary antibodies were washed off the membrane with 3 x 10 min washes of TBS-T with gentle agitation. The membranes were then incubated with the appropriate anti-species horseradish peroxidase-conjugated secondary antibody (Table 2.14) diluted in milk block for 1 h with gentle agitation. Secondary antibodies were washed off the membrane with a further three x 10 min washes of TBS-T with gentle agitation. Protein bands were visualised by incubation of membranes for 1 min with enhanced chemiluminescence reagent (GE Healthcare cat RPM2106V2) and visualised on GE Healthcare hyperfilm ECL film (cat: 28906846).

Table 2.14 - Antibodies used for western blotting						
Company	**Antigen**	**Antibody**	**Species**	**Dilution**	**Dilution medium**	**Incubation conditions**
Sigma-Aldrich Aldrich	β-actin	Anti-β-actin (AC-74)	Mouse	1 in 100,000	5 % BSA in TBS-T	1 h at 4 °C
Sigma-Aldrich Aldrich	γ-actin	Anti-γ-actin	Mouse	1 in 100,000	5 % BSA in TBS-T	1 h at 4 °C
Thermofisher	ARP2	Anti-ARP2 (E-12)	Mouse	1 in 500	5 % BSA in TBS-T	ON at 4 °C
Abcam	ARPC4	Anti-ARPC4	Rabbit	1 in 2000	5 % BSA in TBS-T	ON at 4 °C
Bethyl Laboratories	ATM	Anti-ATM	Mouse	1 in 1000	5 % BSA in TBS-T	ON at 4 °C
Bethyl Laboratories	ATM S1981-P	Anti-pATM	Mouse	1 in 1000	5 % BSA in TBS-T	ON at 4 °C
Millipore	BRCA2	Anti-BRCA2	Mouse	1 in 200	5 % BSA in TBS-T	ON at 4 °C
Cell Signalling	CHK2	Anti-CHK2	Rabbit	1 in 1000	5 % BSA in TBS-T	ON at 4 °C
Cell Signalling	CHK2 T68-P	Anti-pCHK2	Rabbit	1 in 1000	5 % BSA in TBS-T	ON at 4 °C
Bethyl Laboratories	DIAPH1	Anti-DIAPH1	Rabbit	1 in 2000	5 % BSA in TBS-T	ON at 4 °C
Abcam	GFP	Anti-GFP	Mouse	1 in 1000	5 % BSA in TBS-T	ON at 4 °C
Sigma-Aldrich Aldrich	HA	Anti-HA	Mouse	1 in 1000	5 % BSA in TBS-T	ON at 4 °C
Millipore	H2AX	Anti-H2AX	Rabbit	1 in 1000	5 % BSA in TBS-T	ON at 4 °C
Millipore	γ-H2AX	Anti-γ-H2AX	Mouse	1 in 1000	5 % BSA in TBS-T	ON at 4 °C
Bethyl Laboratories	KAP-1	Anti-KAP1	Rabbit	1 in 3000	5 % BSA in TBS-T	ON at 4 °C
Bethyl Laboratories	KAP1 S824-P	Anti-pKAP1	Rabbit	1 in 3000	5 % BSA in TBS-T	ON at 4 °C

Genetex	NBS1	Anti-NBS	Rabbit	1 in 10000	5 % BSA in TBS-T	ON at 4 °C
Abcam	NBS1 S343-P	Anti-pNBS	Rabbit	1 in 1000	5 % BSA in TBS-T	ON at 4 °C
Calbiochem	RPA2	Anti-RPA2	Mouse	1 in 1000	5 % BSA in TBS-T	ON at 4 °C
Bethyl Laboratories	RPA2 S4/8-P	Anti-pRPA2	Rabbit	1 in 1000	5 % BSA in TBS-T	ON at 4 °C
Bethyl Laboratories	SMC1	Anti-SMC1	Rabbit	1 in 1000	5 % BSA in TBS-T	ON at 4 °C
Bethyl Laboratories	SMC1 S966-P	Anti-pSMC1	Rabbit	1 in 3000	5 % BSA in TBS-T	ON at 4 °C
ProteinTech	Vinculin	Anti-Vinculin	Rabbit	1 in 5000	5 % BSA in TBS-T	ON at 4 °C
Dako laboratories	Polyclonal swine anti-mouse IgG HRP conjugated	Anti-mouse	Swine	1 in 1000	5 % BSA in TBS-T	1 h at RT
Dako laboratories	Polyclonal goat anti-rabbit IgG HRP conjugated	Anti-rabbit	Goat	1 in 3000	5 % BSA in TBS-T	1 h at RT

2.8 Metaphase Spread Analysis

2.8.1 Preparation of patient derived LCLs for metaphase spread analysis

24 h prior to treatment and harvesting of cells, 7.5 x 10^5 / ml of patient-derived LCLs were seeded into T25 tissue culture flasks with appropriate cell culture medium and in the presence of 50 nM ETOP (Selleckchem, cat: S1225) or 5 nM CPT (Selleckchem, cat: S1288). Cells were prepared for harvesting by adding 10 µg/ml Colcemid (Gibco Kyromax, cat: 15212-012) for 3 h before harvesting. For IR treated cells, 1 h prior to

irradiation, cells were treated with 3 μM APH (Sigma-Aldrich-Aldrich, cat: A4487) then irradiated with 2 Gy IR. IR treated cells were harvested 12 h post-treatment and 10 μg/ml Colcemid was added 4 h prior to harvesting.

2.8.2 Preparation of patient derived fibroblasts for metaphase spread analysis

48 h prior to treatment and harvesting of cells, 1 x 10^6 / ml of patient-derived fibroblasts were seeded into 10 cm dishes with appropriate cell culture medium and incubated at 37 °C 5 % CO_2 for 24 h. 24 h prior to harvesting, 50 nM ETOP or 5 nM CPT were added to the appropriate dishes and incubated at 37 °C 5 % CO_2. Cells were prepared for harvesting by adding 10 μg/ml Colcemid for 3 h before harvesting.

2.8.3 Preparation of HeLa cells for metaphase spread analysis

24 h prior to treatment and harvesting of cells, 5 x 10^5 cells per 10 cm dish of siRNA treated HeLa cells (Section 2.3) were seeded into 10 cm dishes with appropriate cell culture medium and in the presence of 50 nM ETOP or 5 nM CPT. Cells were prepared for harvesting by adding 10 μg/ml Colcemid for 3 h before harvesting. For IR treated cells, 1 h prior to treatment, cells were treated with 3 uM APH then irradiated with 2 Gy IR. For IR treated cells, 1 h prior to treatment, cells were treated with 3 uM APH then irradiated with 2 Gy IR. IR treated cells were harvested 12 h post-treatment and 10 μg/ml Colcemid was added 4 h prior to harvesting.

2.8.4 Harvesting cells for metaphase spread analysis

Suspension cells were transferred to 30 ml tubes and centrifuged at 1200 rpm for 4 min. Adherent cells were harvested by removing media, washing 1 X in sterile PBS then trypsinising for 5 min. All media and washes were retained as mitotic cells detach easily. Then the pellet was washed in 10 ml PBS and centrifuged at 1200 rpm for 4 min, twice before resuspension with 1 ml of fresh PBS. 10 ml of pre-warmed hypotonic buffer (1:1:5 ratio of FBS, 75 mM KCl and 18.2 MΩ H_2O) was then added to the cells dropwise with gentle agitation. Cells were then incubated at 37 °C for 25 min. Following incubation, cells in hypotonic buffer were transferred to polypropylene tubes (Corning) to prevent cells sticking to the sides of the tube. 1 ml of fixation buffer (3:1 ethanol: acetic acid) was then added to the cells in hypotonic buffer before centrifugation at 1400 rpm for 4 min. 1 ml of supernatant was retained in the bottom of the tube and the pellet re-suspended by gently flicking the tube. Cells were then fixed in 9 ml of fixation buffer, added dropwise to the cells with gentle agitation. Cells were spun as before and 1 ml of supernatant retained. This was repeated once more, followed by storage of tubes at -20 °C.

2.8.5 Dropping and visualisation of metaphases

For each experimental condition, 2 slides were used. Slides were prepared by dipping into acetic acid followed by air drying. Cells were dropped on to the slide from a height of 1 m. Slides were placed at a 45 ° angle and 20 µl of cell suspension was dropped onto slides. Excess liquid was flicked off the slide and the slides were then dried horizontally in a fume cupboard overnight. After overnight drying, the slides were

incubated with Giesma (diluted 1:20 in 18.2 MΩ H_2O, Sigma-Aldrich-Aldrich, cat: GS500-500ML) in Coplin jars for 15 min. Slides were then transferred to clean Coplin jars and bathed in 18.2 MΩ H_2O for 5 min. Slides were then air dried overnight before mounting a coverslip over the metaphases with Entellan New mounting medium (Merck, cat: 10709610100). Metaphases were visualised on a Nikon Brightfield microscope with a 100 X lens and scored for aberrations.

2.9 Sister chromatid exchange (SCE) analysis

2.9.1 Preparation of patient derived LCLs for SCE analysis

48 h prior to treatment and harvesting of cells, 5 x 10^5 / ml of patient derived LCLs were seeded into T25 tissue culture flasks with appropriate cell culture medium with 10 µM BrdU. 24 h prior to harvesting, either 10 nM ETOP (Selleckchem, cat: S1225) or 0.5 nM CPT (Selleckchem, cat: S1288) were added to cells. 3 h before harvesting, cells were prepared by adding 10 µg/ml Colcemid (Gibco Kyromax, cat: 15212-012).

2.9.2 Preparation of HeLa cells for SCE analysis

48 h prior to treatment and harvesting of cells, 2.5 x 10^5 of HeLa cells were seeded into 10 cm dishes with appropriate cell culture medium made up to a total volume of 10 ml. 10 µM BrdU was added to the cells at the time of seeding. 24 h prior to harvesting, either 10 nM ETOP or 0.5 nM CPT were added to cells. 3 h before harvesting, cells were prepared by adding 10 µg/ml Colcemid (Gibco Kyromax, cat: 15212-012).

2.9.3 Harvesting cells for SCE analysis

Suspension cells were transferred to 30 ml tubes and centrifuged at 1200 rpm for 4 min. The pellet was washed in 10 ml PBS and centrifuged at 1200 rpm for 4 min, twice before resuspension with 1 ml of fresh PBS. Adherent cells were harvested by removing media, washing once in sterile PBS then trypsinising for 5 min. All media and washes were retained as mitotic cells detach easily. 10 ml of pre-warmed hypotonic buffer (75 mM KCl in 18.2 MΩ H_2O for LCLs, 0.3 M Sodium Citrate for HeLa cells) was then added to the cells dropwise with gentle agitation. Cells were then incubated at 37 °C for 25 min. Following incubation, cells in hypotonic buffer were transferred to polypropylene tubes (Corning) to prevent cells sticking to the sides of the tube. 1 ml of fixation buffer (3:1 methanol: acetic acid) was then added to the cells in hypotonic buffer before centrifugation at 1400 rpm for 4 min. 1 ml of supernatant was retained in the bottom of the tube and the pellet re-suspended by gently flicking the tube. Cells were then fixed in 9 ml of fixation buffer, added dropwise to the cells with gentle agitation. Cells were spun as before, and 1 ml of supernatant retained. This was repeated once more, followed by storage of tubes at -20 °C.

2.9.4 Dropping of mitotic cells

For each experimental condition, 2 slides were used. Slides were prepared by dipping the slides into acetic acid followed by air drying. Cells were dropped on to the slide from a height of 1 m. Slides were placed at a 45 ° angle and 20 µl of cells were dropped. Excess liquid was flicked off the slide and the slides were dried horizontally in a fume cupboard overnight. The following day, slides were incubated with 10 µg/ml Hoescht

for 20 min in the dark. Slides containing metaphases from LCLs were then incubated in 2 x SSC buffer (A 20 x SSC buffer: 2M NaCl, 0.3M sodium citrate in 18.2 MΩ H_2O, pH 7, was diluted 1:10) and metaphases from HeLa cells were incubated with 20 x SSC buffer for 5 min. 1 ml of 2 x SSC (LCLs; 20 x SSC buffer for HeLa cells) was then added to slides and a long coverslip was placed over the top of the slides to prevent drying. Cells were irradiated under a 355 nm UV-lamp for 1 h then incubated at 60 °C in 2 x SSC (LCLs; 20 x SSC buffer for HeLa cells) buffer for 1 h. The slides were then washed once in 18.2 MΩ H_2O and incubated with Giesma (diluted 1 in 20 in 18.2 MΩ H_2O, Sigma-Aldrich cat: GS500-500ML) in Coplin jars for 15 min. Slides were then transferred to clean Coplin jars and bathed in 18.2 MΩ H_2O for 5 min. Slides were then air dried overnight before mounting a coverslip over the cells with Entellan new mounting medium (Merck cat: 10709610100) and left to dry overnight. SCEs were visualised on a Nikon Brightfield microscope with a 100 X lens and scored for number of SCEs per chromosome.

2.10 CRISPR-mediated homologous recombination assay

2.10.1 Preparation of HeLa cells for plasmid transfection

HeLa cells were treated with siRNA outlined in Section 2.3, as per manufacturer's instructions. 8 h prior to plasmid transfection, siRNA treated HeLa cells were seeded into wells of a 6 cm dish with a single glass coverslip at a density of 6 x 10^5 cells per well, with 2 ml of complete DMEM supplemented with 20 % FBS and no antibiotic. Remaining cells were seeded into 10 cm dishes and harvested 24 h later for western

blotting (Section 2.7) to access siRNA knockdown efficiency. An extra coverslip was seeded per condition to act as an untransfected control.

2.10.2 Plasmid transfection

In 1.5 ml sterile RNAase free tubes (Ambion cat: AM12400), 2 ug of plasmids outlined in Tale 2.3 and 5 µl of Lipofectamine 2000 (Thermofisher cat: 11668027) were added to 200 µl of OptiMEM (Gibco cat: 31985070) and incubated for 20 min at RT. 1 tube was used per coverslip. 8 h after seeding cells onto coverslips, the plasmid complex was added to the cells and incubated for 48 h at 37 °C, 5 % CO_2.

2.10.3 Harvesting and analysis

48 h after the addition of plasmids to cells, coverslips were harvested by removing media and incubating cells with 3 ml of 3.6 % PFA for 10 min at RT. The PFA was then removed, and cells were incubated for 5 min with 0.5 % v/v TritonX-100 in PBS at RT. Cells were then blocked in 10 % FBS in PBS and mounted onto microscope slides with DAPI. Coverslips were sealed with clear nail varnish and analysed by quantifying the presence of GFP-Lamin rings around DAPI positive nuclei, normalised to RFP expression.

2.11 Stochastic Optical Reconstruction Microscopy (STORM)

2.11.1 Preparation of patient-derived fibroblast cells for STORM

24 h prior to drug treatment, patient-derived fibroblast cell lines were plated onto glass coverslips in wells of a 6-well plate at a density of 2.5 x 10^5 cells per well. On the day of drug treatment, cells were treated with 100 nM CPT for 1 h. 30 mins prior to removal of CPT treatment, 10 μM EdU was added to the media and incubated for 30 min. After 1 h of incubation with CPT and 30 min with EdU, the media was aspirated and cells were washed three times in warm drug-free media and then incubated at 37 °C, 5 % CO_2 until harvesting at specific time-points (1 h and 4 h post CPT-washout).

2.11.2 Harvesting of cells for STORM

At 1 h and 4 h post-CPT washout, drug-free media was aspirated off and coverslips were washed three times PBS. Cells were then incubated in CSK buffer (10 mM PIPES, 300 mM Sucrose, 100 mM NaCl, 3 mM $MgCl_2$, 0.5 % v/v Triton-X-100) for 5 min before aspirating off followed by three washes in PBS. Cells were then incubated in PFA (4 % v/v in PBS) for 15 min before aspiration and a further three washes in PBS. Cells were then incubated in STORM blocking buffer (PBS, 2 % Glycine (w/v), 2 % BSA (w/v), 0.2 % gelatine (w/v), 0.267 % NH_4Cl) for three x 5 min washes before being stored in blocking buffer at 4 °C until EdU click-iT chemistry.

2.11.3 EdU Click-iT Chemistry

Following extraction and fixation, cells were washed twice in PBS then incubated with EdU Click-iT EdU AlexaFluor 647 imaging kit (Thermofisher, cat: C10640) and labelled with Janelia Fluor 549-aizde (Tocris Biosciences, cat; 6501) for 30 min at RT as per manufactures instructions. Cells were then washed three times in STORM blocking buffer, for 5 min per wash. After washes, cells were stored overnight in STORM blocking buffer at 4 °C in the dark. Cells can be imaged up to 3 days after Click-iT chemistry reaction before photobleaching.

2.11.4 Antibody staining

Following Click-iT chemistry (Section 2.11.3), on the day of STORM imaging, cells were incubated with antibodies outlined in Table 2.15.

Table 2.15 – Antibodies used for STORM

Antigen	Anti-body	Species	Dilution	Incubation conditions	Company	Cat. No
BRCA1	Anti-BRCA1 Alexafluor (B) 488	Mouse	1 in 1000	1 h at RT in the dark	Novus Biologicals	NB100 598
CtIP	Anti-CtIP (D-4) Alexafluor (B) 488	Mouse	1 in 1000	1 h at RT in the dark	Santa Cruz Biotechnol ogies	SC-271339 A
MRE11	Anti-MRE11 Alexafluor I 647	Mouse	1 in 3000	1 h at RT in the dark	Novus Biologicals	NB100 473
RPA70	Anti-RPA70 AlexaflulR) 647	Rabbit	1 in 3000	2 h at RT in the dark	Abcam	ab1992 40

2.11.5 Sample preparation

Prior to imaging cells, two 1 mm holes were drilled in the centre of glass microscope slides, then cleaned with 18.2 MΩ H_2O and dried. Slides were then held in place on a flat surface with double-sided tape. Coverslips were mounted onto pre-drilled microscope slides with holes situated at the centre of the coverslip to create a microfluidics chamber. 100 µl of PBS was pipetted under the coverslip to prevent cells from drying, then coverslips were sealed around the edged with Epoxy (Devcon, cat: 14250) and left to dry for 10 min in the dark. Meanwhile, super-resolution buffer (PBS, 10 % glucose, 100 mM mercaptoethylamine (Fisher bioreagents, cat: BP2664100), 10 % w/v Poly(ethylene glycol) PEG-200) was made up fresh. Prior to imaging each slide, pre-made 100 X Gloxy stock (PBS, 10 % Catalase (Sigma-Aldrich, cat: C301G), 10 % w/v glucose oxidase (Gloxy, Sigma-Aldrich, cat: G2133) was thawed. 1 µl of Gloxy was added to 100 µl aliquots of super-resolution buffer prior to imaging of each individual slide. Super-resolution buffer with added gloxy was pipetted carefully into the 1 mm hole in the microscope slide, ensuring flow through the other hole.

2.11.6 STORM Image capture

Prior to imaging samples on the STORM instrument, a TetraSpeck microsphere 0.1 µM fluorescent bead (Thermofisher, cat: T7279) slide was prepared as per manufacturer's instructions. The bead was used to create a normalised mapping file for reconstruction of 2 or 3 channel (Green, Blue, Red; GBR) images into one compressed file for analysis of localisation of proteins of interest to nascent DNA and to each other. After bead mapping, samples were imaged within 30 min of super

resolution buffer being added to the microfluidics chamber and 8-10 images per condition (in GBR channels) were captured of suitable S-phase nuclei with visibly blinking EdU fluorophores. Distinct fluorophores were stimulated by varying laser lines, specifically the 488 nm, 561 nm, and 639 nm laser lines, which were employed for sample excitation under Highly Inclined and Laminated Optical sheet (HILO) illumination mode. Photons emitted from the different fluorophores were sequentially captured for multi-colour imaging. The imaging sequence adhered to a consistent pattern: green (EdU; JF549), blue (BRCA1/CtIP; AF488 conjugated), and red (MRE11/RPA70; AF647 conjugated). Additionally, a 405 nm laser line (Applied Scientific Pro., SL-405 nm-150 mW) was introduced to induce photo-switching of Alexa Fluor 647 fluorophores, promoting their return to the ground state. To broaden the emission profile, a 2 X lens tube was employed, followed by chromatic aberration correction utilizing a correction lens (Thorlabs, AC254-300-A), before the emissions were finally captured using an sCMOS camera (Photometrics, Prime 95B). Each colour channel was comprised of 2000 frames acquired at a rate of 33 Hz using Micro-Manager software (Version 2.0). During the imaging process, each frame was stacked, and all samples were equally weighted within a square region of the image with a box size set at four times the Full width at half maximum of a 2D Gaussian Point Spread Function (PSF). The Maximum likelihood estimation algorithm was employed for 2D-Gaussian single-PSF fitting on a GPU (Nvidia GTX 1060, CUDA 8.0), with fitting accuracy evaluated using the Cramér-Rao lower bound, as detailed in (Yin and Rothenberg, 2016; Yin, Lee and Rothenberg, 2019). After imaging all samples, image files were reconstructed using a Rothenberg lab algorithm written in MatLab coding software.

2.11.7 Region of interest selection and analysis

Regions of interest (ROIs), defined as approximately 4 × 4 μm² squares within the 3-colour STORM image of a nucleus, were created and subjected to Auto-PC function and fraction analysis, as outlined in (Yin, Lee and Rothenberg, 2019; Lee *et al.*, 2021; Yin *et al.*, 2021; Coleman *et al.*, 2022). To assess the degree of colocalisation, cross-correlation between nascent DNA and the target protein of interest (MRE11/BRCA1/CtIP/RPA70) was calculated. Subsequently, the amplitude for the cross-correlation values was multiplied by the local density of the coordinates (i.e., the number of coordinates per ROI) for nascent DNA, providing an average likelihood of finding the target protein molecule around nascent DNA. The difference between the average distribution of all ROIs in drug-treated versus non-treated samples was normalised to the non-treated condition for each sample and was subjected to a two-sample t-test to obtain p-value scores.

For the fraction analysis, each nucleus was manually outlined to generate an ROI for independent analysis. The single molecule localisations of both targets (nascent DNA and protein of interest) were initially processed using the Density-based spatial clustering of applications with noise (DBSCAN) algorithm for foci segmentation. The minimum number of points forming a focus was set to 20, and the thresholding distance was set at 15. Following DBSCAN segmentation, the Nearest-neighbouring distance (NND) (edge-to-edge) between the two targets was calculated. Clusters maintaining an NND ≤ 5 nm were identified as co-localised clusters. To account for the non-random nature of the detected colocalisations, a comparison was made between the levels of colocalisation and random distributions by randomly repositioning and orienting the

clusters. Data generated was then imported into GraphPad and represented in graphical format.

2.12 DNA Fibre Analysis

DNA fibre analysis was used as a way of determining alterations in replication DNA replication dynamics in patient-derived cell lines and isogenic cell systems. This single molecule technique utilised dual labelling of cells with two subsequent thymidine analogues CldU (5'-Chloro-2'-deoxyuridine, Sigma-Aldrich cat: C6891-100MG) and IdU (5'-Iodo-2'-deoxyuridine, Sigma-Aldrich cat: I17125-5G). These analogues were used in combination with different treatments to determine changes in replication dynamics.

2.12.1 Thymidine label preparation

Stock solutions of CldU and IdU were prepared prior to DNA labelling. A 2.5 mM stock solution of each label was made by dissolving the thymidine analogue in the appropriate cell culture medium for the cells being treated. The medium was pre-warmed to 37 °C, then 660 µg/ml of CldU and 890 µg/ml of IdU were dissolved separately and vortexed. IdU was heated to 60 °C and vortexed every 1 h over a 6-8 h period until it fully dissolved into solution. Stock solutions of each label were then stored at -20 °C until required.

24 h prior to labelling, IdU stock solution was thawed at 60 °C, then a 250 µM stock solutions of IdU in appropriate cell culture medium was prepared in a tissue culture

flask, then stored at 37 °C in a 5 % CO_2 incubator overnight to equilibrate the IdU solution.

2.12.1 Labelling of DNA with thymidine analogues

48 h prior to staining, patient-derived fibroblasts were seeded into 10 cm dishes at a density of 25 x 10^5 cells / 10 cm dish. 24 h prior to staining, U-2-O-S were seeded into 6 cm dishes at a density of 25x10^5 cells / 10 cm dish.

2.12.2 Assessment of exposure to replication stress agents

To assess the impact of exposure to ETOP and CPT on replication, cells were treated with 100nM ETOP or 100nM CPT during the second label. On the day of treatment, cells were incubated with 25 µM of CldU for 30 min at 37 °C. After CldU incubation, cells were washed three times in warm media containing second label (IdU 250 µM) then incubated with 250 µM IdU in the presence of either CPT 100 nM or ETOP 100 nM for 30 min at 37 °C. To harvest cells, IdU containing media was then aspirated followed by two washes in cold PBS to heat shock the cells and arrest replication.

2.12.3 Assessment of replication fork restart

To assess the ability of cells to restart replication after replication arrest, cells were treated with 2 µM Hydroxyurea (HU, Sigma-Aldrich, cat: H8624-25G) between the first and second label. On the day of treatment, cells were incubated with 25 µM of CldU for 30 min at 37 °C. After CldU incubation, cells were treated with 2 µM HU for 2 h at

37 °C. Cells were then washed three times in warm media containing second label (IdU 250 μM) then incubated with 250 μM IdU for 30 min at 37°C. To harvest cells, IdU containing media was then aspirated followed by two washes in cold PBS to heat shock the cells and arrest replication.

2.12.4 Assessment of fork stability

To assess fork stability/degradation, cells were subsequently incubated with CldU and IdU labels then treated with 4 mM HU after the second label. On the day of treatment, cells were incubated with 25 μM of CldU for 30 min at 37 °C. After CldU incubation, cells were washed three times in warm media containing second label (IdU 250 μM) then incubated with 250 μM IdU for 30 min at 37 °C. Cells were then washed three times in media containing 4 mM HU and then were treated with HU for 5 h. After HU treatment, media was then aspirated followed by two washes in cold PBS to heat shock the cells and arrest replication.

2.12.5 Harvesting cells for DNA fibre analysis

Following heat shock with cold PBS, cells were trypsinised and spun down at 1400 rpm for 4 min. The supernatant was removed, and cells were resuspended in 250 μl of cold PBS and transferred to a pre-chilled Eppendorf tube. Cell number was counted, and the volume of PBS adjusted so that cell number was roughly 0.5 x 10^6 cells / ml. 2 μl of cell suspension was then aliquoted onto a glass slide and left to dry for 2-4 min. Once dry, 9 μl of spreading buffer (200 mM Tris-HCl pH 7.4, 50 mM EDTA, 0.5 % SDS) was mixed with the dried droplet and incubated for 2 min. Slides were then tilted to

encourage migration of the droplet down the slide. Once the droplet had reached the bottom, excess liquid was dabbed off and slides were air dried for 2 min. The location of the migration of the droplet was marked on the frosted end of the glass slide. DNA was fixed to the slide by incubating slides with 3:1 methanol: acetic acid in Coplin jars for 10 min. Slides were then air dried before storage at 4 °C.

2.12.6 DNA fibre immunostaining

Slides stored at 4 °C were protected from light during immunostaining to preserve the signal from thymidine analogues. Slides were washed twice in 18.2 MΩ H_2O and then washed once in 2.5 M HCl. Following washes, slides were incubated with 2.5 M HCl for 1 h 15 min to denature the DNA. HCl was then washed off and slides were washed two times with non-sterile PBS. Slides were then blocked in 1 % BSA blocking buffer (1% Bovine serum albumin, 0.01 % Tween-20 in PBS) fo– 0.5 - 1 h. Primary antibodies (Table 2.16) were diluted in 1 % BSA blocking buffer and slides were incubated in 200 ul of primary antibody solution for 1 h at RT, protected from light. To equally distribute the antibody, a long coverslip was placed over the slide during antibody incubation. Following incubation with primary antibody, slides were washed three times in PBS-T (1 x PBS, 0.01% Tween 20) then washed once in 1 % BSA blocking buffer. Slides were incubated with secondary antibody (Table 2.17) diluted in blocking buffer for 1.5 h as described above. Slides were then washed twice in PBS-T, then two washes with blocking buffer, followed by two further washes in PBS. Excess liquid was dabbed off the slides with tissue paper. Two drops of Fluoroshield mounting medium (Sigma-Aldrich, cat: F6182-20ml) were spotted onto each slide and a long coverslip placed on top. Gentle pressure was applied over the coverslip with tissue paper to remove excess

liquid. The coverslip was then sealed with clear nail varnish. Slides were stored in the dark at 4 °C until visualisation on a Nikon fluorescent microscope and images were analysed using ImageJ software.

Table–2.16 - Primary antibodies used for DNA fibre analysis

Company	Antigen	Species	Dilution	Dilution medium	Incubation condition
Invitrogen	Rat IgG	Goat	1 in 500	1 % BSA in PBS, 0.01 % Tween	1 h at RT
Invitrogen	Mouse IgG	Goat	1 in 500	1 % BSA in PBS, 0.01 % Tween	1 h at RT

Table–2.17 - Secondary fluorophore coupled antibodies used for DNA fibre analysis

Company	Antigen	Fluorophor	Colour	Dilution	Dilution medium	Incubation condition
Invitrogen	Polyclonal goal anti-mouse IgG	Alexa 594	Red	1 in 500	1 % BSA in PBS, 0.01 % Tween	1.5 h at RT in the dark
Invitrogen	Polyclonal donkey anti-rabbit IgG	Alexa 488	Green	1 in 500	1 % BSA in PBS, 0.01 % Tween	1.5 h at RT in the dark

2.13 AsiSI real-time PCR DNA resection assay

2.13.1 siRNA Transfection

siRNA transfections (90 nM / transfection) were carried out using Lipofectamine RNAi Max (Invitrogen, cat:13778030) according to the manufacturer's instructions, with total siRNA not exceeding 90 nM. siRNA cocktail in Opti-MEM was added to 6 ml of fresh DMEM and removed after 8 h, followed by replenishment with complete DMEM. All experiments were performed at least 48 h after knockdown. Assessment of siRNA-knockdown by immunoblotting (Section 2.7).

2.13.2 AsiSI real-time PCR DNA resection assay

U2OS *AsiSi* cells were transfected with 90 nM siRNA as described above in Section 2.13.1. 48 h after transfection, cells were treated with 300 nM 4-OHT for 4 h in DMEM, 10 % FBS, 100units/ml Penicillin and 100 ng/ml Streptomycin (Sigma-Aldrich car: P4333-100ml), to induce DNA double-strand breaks. Cells were washed twice with PBS and harvested in 1 ml of PBS using a cell scraper. Cells were pelleted by centrifugation and DNA extracted using DNAeasy kit as per manufacturer's instructions (Qiagen), followed by elution in 50 µl of nuclease-free water. Extracted genomic DNA was treated with 5 units RNAse H for 15 min at 37 °C. 5 µl of DNA (approximately 0.5-1 µg DNA) was used for each condition (BsrG1 digestion and matched undigested sample). DNA digests were carried out in 30 µl, with 20 units of BsrG1 enzyme in CUTSMART digestion buffer (NEB), at 37 °C overnight. BsrG1 enzyme was heat-inactivated according to the manufacturer's instructions (80 °C for 20 min). 20 ml of

nuclease-free water was added to each sample and 2 ml of sample was used directly for RT-PCR. Primers used for RT-PCR are outlined in Table 2.18. The percentage of ssDNA (ssDNA %) generated by resection at selected sites was determined as previously described (Zhou *et al.*, 2014). Briefly, for each sample, a ΔCt was calculated by subtracting the Ct value of the mock-digested sample from the Ct value of the digested sample. The undigested sample serves as a loading control for genomic DNA for each experimental condition. The ssDNA % was calculated with the following equation: ssDNA % =1/(2^(ΔCt-1) +0.5) *100.

Table–2.18 - Primers for AsiSI real-time PCR DNA resection assay	
Strand	**Oligo sequence**
AsiSI Bsrg1 335bp –Forward	5'-GAATCGGATGTATGCGACTGATC-3'
AsiSI Bsrg1 335bp -Reverse	5'- TTCCAAAGTTATTCCAACCCGAT-3'
AsiSI Bsrg1 1618bp-Forward	5'-TGAGGAGGTGACATTAGAACTCAGA-3'
AsiSI Bsrg1 1618bp-Reverse	5'-AGGACTCACTTACACGGCCTTT-3'

2.14 Statistical Analysis

2.14.1 Mann-Whitney U test

Statistics for RAD51 foci, RPA2 foci intensity, native BrdU foci intensity, Fok1 foci intensity, SCEs, replication fork speed, ratio of CldU to IdU incorporation and fork asymmetry were calculated using a 2 tailed Mann-Whitney U test. All data points collected were used to generate graphs and for statistical analysis. Statistical analysis and graphs were generated using the GraphPad Prism 10.1.1 software package. The

calculated *p* values were expressed as asterisks (*, *p* = ≤0.05; **, *p* = ≤0.01; ***, *p* = ≤0.001; ****, *p* = ≤0.0001) or non-significant (ns) within the figure.

2.14.2 Student t-test

The unpaired student t-test was used to calculate the statistical significance of data generated for micronuclei formation, γ-H2AX/53BP1 formation, chromosomal aberrations, BRCA1 foci formation, STORM and DNA fibre structure quantification. Experiments were repeated a minimum of three times, unless otherwise stated. For each experimental repeat, the mean was calculated for the categories stated in the figure and denoted by a red dot on bar charts, this information was used to generate the graphs presented. An unpaired 2-tailed student t-test was performed using GraphPad Prism 10.1.1. *P* values were calculated using this software and expressed as asterisks (*, *p* = ≤0.05; **, *p* = ≤0.01;***, *p* = ≤0.001, **** p=≤0.0001) or non-significant (ns) within the figure.

Chapter 3: Identification and cellular characterisation of genome instability in cells from patients with variants in *DIAPH1*

3.0 Results

3.1 Introduction

DNA repair is a highly regulated process in which cells must rapidly detect damage and accurately repair it. If this does not happen and cells undergo genome duplication or continue the cell cycle with unrepaired DNA damage, the consequences can be extremely detrimental. The most harmful type of DNA damage is the double strand break (DSB) and whilst all DNA damage has the potential to be very detrimental to human health, the DSB is particularly toxic due to how difficult it is to repair accurately. DSBs have the potential for loss or gain of genetic material leading to mutations, tumourigenesis and cell death.

How harmful DSBs can be to human health is evidenced by the clinical deficits exhibited by patients who have an underlying genetic variation in a gene involved in DSB repair. The known human syndromes associated with defective DSB repair exhibit common clinical features such as neurodevelopmental defects including microcephaly, developmental delays, and intellectual disability, immunodeficiency, growth retardation, and a predisposition to tumour development (particularly those of lymphoid origin). Whilst DNA repair is essential for the viability of every cell, the underlying basis for why a DSB repair deficiency causes specific clinical deficits is more obvious than others. For example, in the case of immunodeficiency, this arises if the DSBs induced under controlled conditions in the B- and T- lymphocyte antigen receptors during V(D)J recombination and class switch recombination are not repaired. This triggers apoptosis and a progressive loss of B and T cells.

One well-known example of a DSB repair disorder is Nijmegen Breakage Syndrome (NBS). NBS is caused by deleterious variants in *NBN* which encodes for NBS1, a component of the MRN complex, which plays a crucial role in the sensing, signalling and repair of DSBs, as well as functioning within the replication stress response. The typical features of NBS include microcephaly and growth restriction, dysmorphic facial features, immunodeficiency and lymphoid tumour predisposition. The diverse and complex role of the MRN complex in maintaining genome stability underpins why individuals with NBS display clinical deficits affecting numerous organ systems.

The repair of DSBs is complex, aId it is likely that there are many potential novel proteins that are yet to be identified that play a key role in this process. One way in which novel DNA repair genes are often found is through the identification of patients with clinical features indicative of a DSB repair defect harbouring variants in genes not previously associated with DNA repair. To support this notion, 28 individuals with homozygous variants in *DIAPH1* have been identified. These patients all display clinical features that strongly overlap with NBS including the neurodevelopmental defects (microcephaly, developmental delay and intellectual disability), short stature, facial dysmorphism, recurrent respiratory infections and the development of tumours of lymphoid origin. The affected patients have additional clinical features, such as seizures and cortical blindness, which are not typically observed in NBS patients. *DIAPH1* is a formin family gene with well-characterised roles in mediating nucleation of actin filaments and regulation of microtubule dynamics in the cytoplasm. DIAPH1 also has an additional role in the RAGE signalling axis, a cellular signalling pathway involved in the cellular stress response, but this process is less well understood. However, *DIAPH1* has been shown to be present in the nucleus and recently has been

implicated in regulating the actin-dependent replication stress response. Despite this, DIAPH1 has not been previously linked to DSB repair (Baarlink and Grosse, 2014; Nieminuszczy *et al.*, 2023). Given the clinical similarities caused by mutations in *NBN* and *DIAPH1*, this strongly suggests that DIAPH1 may play a role in maintaining genome stability by promoting DSB repair.

3.2 Aims of this chapter

A role for *DIAPH1* in maintaining genome stability has not been previously identified. Therefore, the aim of this chapter is to confirm the pathogenicity of the identified homozygous variants in *DIAPH1* and to investigate whether these lead to an inability of cells to repair DNA DSBs induced by different genotoxins. To achieve this, patient-derived lymphoblastoid cell lines (LCLs) and hTERT immortalised fibroblast cell lines, were exposed to three different DSB-inducing agents: ionising radiation (IR), camptothecin (CPT) and etoposide (ETOP). Where possible, any defects in DNA DSB repair observed in the patient-derived cell lines were validated using siRNA-mediated depletion of DIAPH1 in HeLa cells. DNA repair following exposure to these agents was monitored by Western blotting, immunofluorescence, and chromosome breakage analysis. The rationale for using three separate DSB-inducing agents was to determine whether DIAPH1 responds to all types of DSBs or specific types of DSBs that arise either in defined cell cycle phases and/or are associated with blocked DNA ends.

IR is a potent inducer of DSBs, as well as other forms of DNA damage. IR induces breaks by exposing DNA to high-energy γ-radiation, and indirectly through the ionisation of H_2O to produce hydroxyl free radicals that also damage the DNA

backbone (Figure 3.1A). IR induces DSB in all cell cycle phases and as such these are predominantly repaired by NHEJ (Mahaney, Meek and Lees-Miller, 2009). CPT is a 5-ring heterocyclic alkaloid that inhibits topoisomerase I (TOPI). TOPI is required for relaxing topological tension (specifically positive supercoils (Sc^+) during replication) in DNA by inducing a transient single stranded nick in the DNA backbone to provide a swivel point in which DNA can be rotated around ahead of DNA replication machinery (Figure 3.1B). The intermediate structure generated by TOPI is termed the TOPI cleavage complex (TOPIcc). The TOPIcc is vulnerable to inhibitors during this step and CPT blocks the release of the cleavage complex from DNA, trapping it on DNA creating a DNA protein crosslink (DPC) coupled to a single strand break (SSB). When replication machinery encounters this structure, it is converted to a single-ended DSB (seDSB or replication-associated DSB). The nature of this type of DSB means it can only be repaired by HR as it lacks a ligatable end which is required for NHEJ (Pommier, 2006; Xu, Wu and Her, 2015).

ETOP induces DSBs through the inhibition of Topoisomerase II (TOPII). TOPII has two isoforms (TOPIIα and TOPIIβ) and induces transient DSBs in DNA to relax supercoils. During replication, like TOPI, TOPIIα functions to relax Sc^+. When the replisome swivels due to torsional tension, the Sc diffuses behind the replisome to generate a precatenane. This structure is removed by TOPIIα (McClendon and Osheroff, 2007; Keszthelyi, Minchell and Baxter, 2016; Pommier *et al.*, 2022). ETOP traps TOPII enzymes on DNA, generating a DPC-coupled to a DSB (generated by TOPII action), which is a 2-ended DSB. ETOP-induced DSBs are induced primarily in S-phase if inhibiting TOPIIα and can be repaired by both HR and NHEJ due to having two ends, making ligation possible (Figure 3.1B) (Nitiss, 2009; Tammaro *et al.*, 2013).

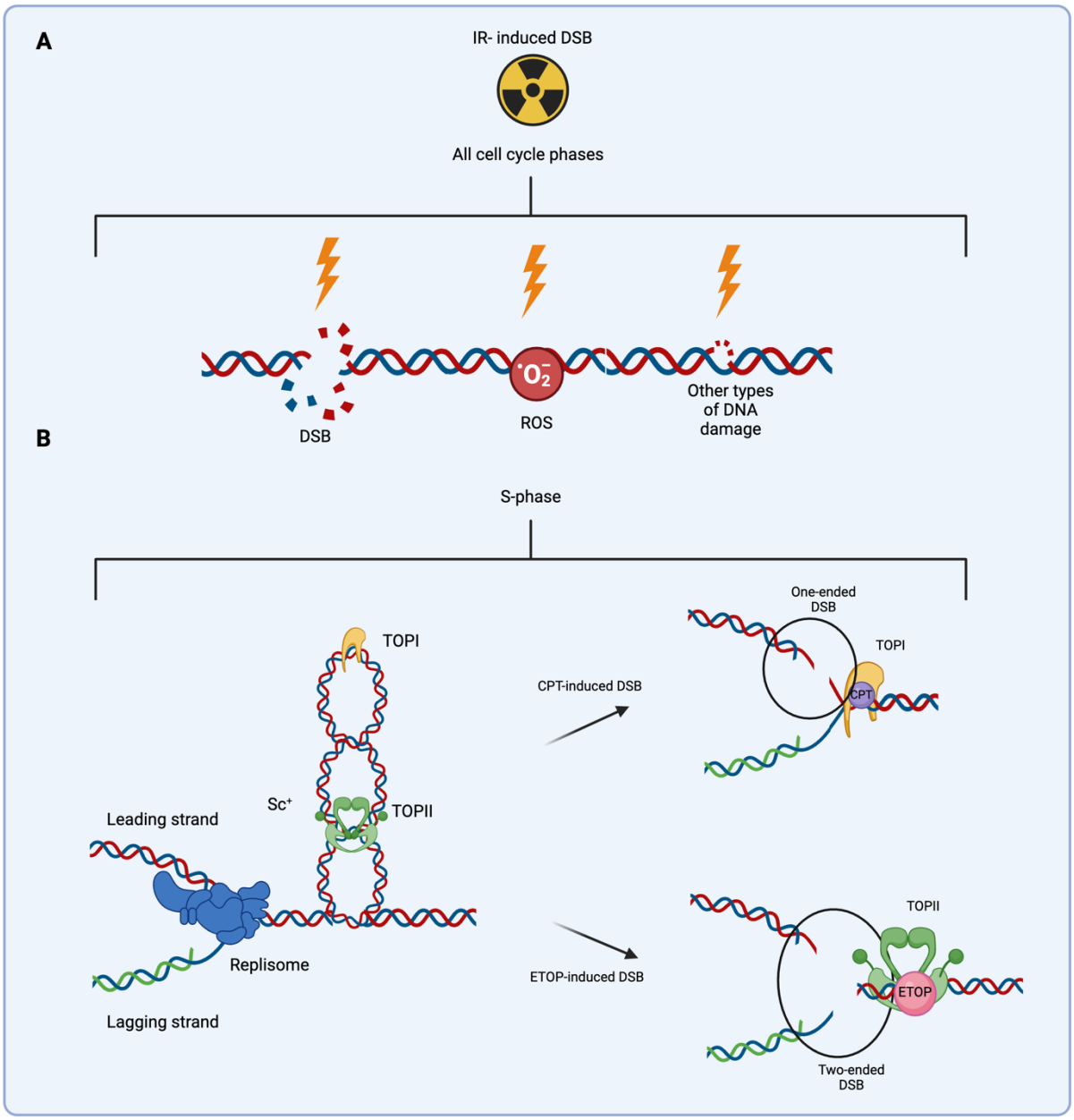


Figure 3.1 – Schematic to show different ways DSBs can be induced by exogenous DNA-damaging agents - A – *IR induces DSB in all cell cycle phases. It does this through exposing DNA to high energy γ-radiation which breaks the DNA backbone. It can also cause DSBs indirectly though reactive oxygen species such as hydroxyl free radicals from H_2O ionisation attacking DNA. Other types of DNA damage are also induced by IR.* ***B -*** *CPT and ETOP induce DSBs specifically in S-phase. During replication, torsional tension ahead of a replication fork is relaxed by TOPI and TOPII. TOPI induces a SSB and TOPII induces DSBs. CPT is a TOPI inhibitor that traps TOPI on DNA generating a DPC. When the replication machinery encounters the SSB couped to a DPC, a one-ended DSB is generated, that can only be repaired by HR. ETOP is a TOPII inhibitor that traps TOPII on the DNA also generating a DPC-coupled to a DSB. When the replication machinery encounters this block, a two-ended DSB coupled to a DPC is generated, which can be repaired by both HR and NHEJ. Abbreviations – CPT – Camptothecin, DSB – double strand break, ETOP – etoposide, IR – ionising radiation, SSB – single strand break, S – phase – Synthesis phase, TOPI/II – topoisomerase I/II. Created with Biorender.com.*

3.3 Results

3.3.1 Identification of patients with homozygous variants in *DIAPH1*

DIAPH1 was first linked to human disease by Lynch et al., who identified a heterozygous variant in *DIAPH1* containing a single nucleotide change resulting in a *ttaa* insertion near the penultimate exon during mRNA processing. This variant was identified as the underlying cause of non-syndromic sensorineural hearing loss in a single family from Costa Rica (Table 3.1) (Lynch *et al.*, 1997). This mutation results in a truncation that removes the C-terminal Diaphanous autoregulatory domain (DAD), which normally bind to the FH3/ diaphanous inhibitory domain (DID) to maintain the protein in an inhibited state. Consequently, this truncating mutation gives rise to a constitutively active protein (Figure 3.1). The specific mechanism with which constitutively active DIAPH1 triggers hearing loss is not clear. However, it is thought that within the inner ear, sensory hair cells with actin-dependent cilial structures detect sound vibrations. Disruption to the actin network surrounding the cilia prevents sound vibrations being accurately converted into intra-cellular signalling. However, since actin and DIAPH1 are critically involved in development and maintenance of the auditory system, other proposed mechanisms including aberrant cellular organisation of the cochlea and/or the surrounding microenvironment could also play a role in the sensory-neural hearing loss observed in patients with dominant acting *DIAPH1* mutations. (Chiereghin *et al.*, 2022). Subsequent to this initial report, two more studies also identified novel heterozygous variants in *DIAPH1* associated with non-syndromic sensorineural hearing loss. Notably however, these patients also developed macrothrombocytopaenia. Surprisingly, these variants were also located within the

same DAD domain and again caused a C-terminal truncation leading to a constitutively active DIAPH1 protein (Table 3.1) (Ueyama, Ninoyu, S. Nishio, *et al.*, 2016; Ganaha *et al.*, 2017).

In contrast to the studies linking heterozygous mutations in *DIAPH1* to hearing loss, homozygous variants in *DIAPH1* have also been identified in a small cohort of patients displaying microcephaly, growth retardation, blindness and seizures (Ercan-Sencicek *et al.*, 2015; Al-Maawali *et al.*, 2016; Kaustio *et al.*, 2021). However, these studies did not provide any insight into the underlying cellular mechanism to explain the features displayed by the affected individuals.

Our interest in *DIAPH1* originated when the Stewart lab was sent a skin biopsy sample from a patient suspected of having NBS (P1, Family 1) (Table 3.1). The presenting features of this patient were microcephaly, facial dysmorphia, immunodeficiency, severe developmental delay, intellectual disability, blindness and seizures (age of onset at 6 m). Since this individual did not have any variants in the *NBN* gene, whole exome sequencing (WES) was performed. WES identified a homozygous variant in *DIAPH1 (c.2108dupC; p.Pro701Thrfs)* (Figure 3.2). Following this, a collaboration was established with Prof. Henry Houlden's lab (UCL) to identify additional patients with biallelic mutations in *DIAPH1*. As part of this collaboration, 19 families have been identified, with 28 affected individuals with biallelic mutations in *DIAPH1*. The location of DIAPH1 mutations are shown in Figure 3.2A. Interestingly, all bar one of the affected individuals have homozygous mutations, whereas patient 12 (P12) has a heterozygous c.934-2A>G *(paternal) DIAPH1* variant and a *de novo* c.1051C>T, p.Arg351Ter *(de novo) DIAPH1* variant (Figure 3.2). Whilst the variants within this cohort are all

different, and they span across the gene resulting in varying degrees of truncation of the DIAPH1 protein, the clinical phenotypes are all very similar. The key clinical features of these patients are outlined in Table 3.1 and whilst not all the patients display all the features, overall, the clinical features are fairly ubiquitous. Of the patients where detailed clinical information has been documented, 23/28 individuals have microcephaly, all patients are affected by motor developmental delays and intellectual disability and nearly all patients have seizures, dysmorphic facial features, and visual impairments. Clinical photographs of some of the patients have been captured to show microcephaly and dysmorphic facial features, short stature can also be observed in P2-2 and P13 (Figure 3.3). The features that are a more variable between patients are recurrent respiratory infections and immunodeficiency. Two patients within this cohort have developed lymphoid tumours, P11-2 developed Hodgkin lymphoma and P11-3 developed EBV-associated large B-cell lymphoma.

The clinical features of"this'cohort highlight thIt DIAPH1 is critical for neurodevelopment, the visual system and neuronal function and/or synaptic activity. The fact some patients also have recurrent respiratory infections and immunodeficiency also suggests DIAPH1 may play a role in immune function. Whilst only 2 patients have developed tumours, this also supports a role for DIAPH1 as a tumour suppressor gene (TSG). It is interesting how distinct the clinical features are between heterozygous and homozygous variants in *DIAPH1*, which most likely can be accounted for by the presence of a constitutively active protein versus not having any protein at all. For comparison, in Table 3.1, a summary of clinical features of 3 known DNA repair syndromes are shown, and it is striking how closely the patients in this cohort overlap with NBS, which suggests that DIAPH1 has a role in maintaining

genome stability and DSB repair. It should also be noted that heterozygous variants in *DIAPH1* share an over-lapping clinical feature with Warsaw Breakage Syndrome (WABS); both syndromes give rise to microcephaly, growth retardation, seizures, intellectual disability, hearing loss and tumour predisposition. WABS is caused by biallelic inherited mutations in *DDX11,* which gives rise to cohesion defects, DNA repair defects and replication abnormalities (van Schie *et al.*, 2020). However, whether DIAPH1 and DDX11 function together to regulate sister chromatin cohesion, DNA repair or replication is unknown.

Next, the aim was to investigate how a selection of these variants impacted the expression of DIAPH1 protein. To do this, western blot analysis was performed on patient-derived LCLs and fibroblast whole cell lysates. The whole cell lysates from asynchronous cell cultures in both cell types were resuspended in Urea Tris Buffer (UTB) and sonicated to extract proteins. The whole cell lysates were then immunoblotted with an antibody raised against DIAPH1 (Figure 3.4). KAP1 was used as a loading control to show an equal concentration of protein was loaded into each well and whole cell extracts derived from a healthy wild-type (WT) individual were used as an experimental control (F–gure 3.4A - C, Lane 1 in all blots 3.4C Lane 6). LCL whole cell lysates derived from an individual with NBS was used as another control to assess endogenous DIAPH1 expression in cells lacking the NBS1 protein, which was expressed at WT levels (Figure 3.4B; lane 2). In the *DIAPH1* patient-derived cell lines tested, all the patients expressed either no DIAPH1 protein or a very small amount of truncated DIAPH1 which was only visible on the immunoblot after a higher exposure time (Figure 3.–A; lane 2 - 3, 3.–B; lane 3 - 5, 3.–C; lane 2 - 4 and lane 7 – 9). These findings confirm that in the cell lines tested, the homozygous variants identified lead to

a total loss of DIAPH1 protein expression or expression of a very small amount of truncated DIAPH1 protein.

In summary, the clinical features of the DIAPH1 patient cohort are severe, with the main features being neurodevelopmental defects, blindness and seizures. In addition, the impact of these gene variants results in cells derived from affected individuals being null for DIAPH1 protein. The clinical features resemble NBS, which may indicate DIAPH1 and NBS1 could be functioning in the same cellular pathway.

Table 3.1: Clinical features of patients with *DIAPH1* variants and comparison to known DNA repair disorders

		Ancestry	*DIAPH1* variant	Microcephaly	Motor developmental delay	Intelleuctual disability	Dysmorphic facial features	Visual impairment	Seizures	Recurrent respiratory infections	immunodeficiency	Cancer	Hearing impairment	Thrombocytopenia
		Costa Rica	c.3661+1G>T; IVS27dsG-T+1; p.Ala1212ValfsTer22 *(Het.)*	No	No	No	No	No	No	No	No	No	Yes	No
		Japan	c.3637C>T, p.Arg1213Ter *(Het.)*	No	No	No	No	No	No	No	No	No	Yes	Yes
		Germany	c.3624_3625delAG; p.Ala1219SerfsTer32 *(Het.)*	No	No	No	No	No	No	No	No	No	Yes	Yes
Family	**Individual**	**Ancestry**	***DIAPH1* variant**	**Microcephaly**	**Motor developmental delay**	**Intelleuctual disability**	**Dysmorphic facial features**	**Visual impairment**	**Seizures**	**Recurrent respiratory infections**	**immunodeficiency**	**Cancer**	**Hearing impairment**	**Thrombocytopenia**
1	P1	Pakistan	c.2108dupC; p.Pro704Thrfs *(Hom.)*	Yes	Yes	Yes	Yes	Impaired	Yes	Not known	Yes	Not known	Not known	No
2	P2-1	Egypt	c.1976dup; p.Pro660Thrfs *(Hom.)*	Yes	Yes	Not known	Yes	Impaired	Yes	No	Yes	Not known	No	No
	P2-2	Egypt	c.1976dup; p.Pro660Thrfs *(Hom.)*	Yes	Yes	Severe	Yes	Impaired	Yes	No	Yes	Not known	No	No
	P2-3	Egypt	c.1976dup; p.Pro660Thrfs *(Hom.)*	Yes	Yes	Severe	Yes	Impaired	Yes	No	Yes	Not known	No	No
3	P3-1	Egypt	c.75insA; p.Leu26Hisfs9Ter *(Hom.)*	Yes	Yes	Severe	Yes	Mild impairment	Yes	Yes	Yes	Not known	No	No
	P3-2	Egypt	c.75insA; p.Leu26Hisfs9Ter *(Hom.)*	Yes	Yes	Severe	Yes	Mild impairment	Yes	Yes	Not known	Not known	No	No
4	P4	Pakistan	c.2582-3C>A *(Hom.)*	Yes	Yes	Severe	Not known	Blind	Yes	Yes	Not known	Not known	No	No
5	P5-1	Pakistan	c.3569_3574+2 delins 18 *(Hom.)*	Yes	Yes	Severe	Not known	Blind	Yes	Yes	Not known	Not known	No	No
	P5-2	Pakistan	c.3569_3574+2 delins 19 *(Hom.)*	Yes	Yes	Severe	Not known	Blind	Yes	Yes	Not known	Not known	No	No
6	P6	Pakistan	c.752del; p.Phe251SerfsTer8 *(Hom.)*	Yes	Yes	Severe	No	Impaired	Yes	Yes	Not known	Not known	No	No
7	P7	Jordan	c.1051C>T; p. Arg351Ter *(Hom.)*	Yes	Yes	Severe	Yes	Impaired	Yes	No	Not known	Not known	No	No
8	P8	Pakistan	c.3353T>G; p.Leu1118Arg *(Hom.)*	Yes	Yes	Moderate	No	Impaired	Yes	No	Yes	Not known	No	No
9	P9-1	Egypt	c.3463C>T; p.Arg1155Trp *(Hom.)*	Yes	Yes	Severe	Yes	Mild impairment	Yes	Yes	Not known	Not known	No	No
	P9-2	Egypt	c.3463C>T; p.Arg1155Trp *(Hom.)*	Yes	Yes	Severe	Yes	Impaired	Yes	Yes	Not known	Not known	No	No
	P9-3	Egypt	c.3463C>T; p.Arg1155Trp *(Hom.)*	Yes	Yes	Moderate	Yes	Blind	Yes	No	Not known	Not known	No	No
	P9-4	Egypt	c.3463C>T; p.Arg1155Trp *(Hom.)*	Yes	Yes	Moderate	Yes	Mild impairment	No	No	Not known	Not known	No	No
10	P10	Germany	c.1768g>T; p.Gly590Val *(Hom.)*	No	Yes	Moderate	No	Normal	Yes	No	Not known	Not known	No	No
11	P11-1	Saudi Arabia	c.2332C>T; p.Gln778Ter *(Hom.)*	Yes	Yes	Severe	Yes	Blind	Yes	No	Not known	Not known	No	No
	P11-2	Saudi Arabia	c.2332C>T; p.Gln778Ter *(Hom.)*	Yes	Yes	Severe	No	Blind	Yes	No	Not known	Yes	No	No
	P11-3	Saudi Arabia	c.2332C>T; p.Gln778Ter *(Hom.)*	Yes	Yes	Not known	Yes	Not known	Yes	Yes	Yes	Yes	No	No
12	P12	Netherlands	c.934-2A>G *(paternal)* ; c.1051C>T, p.Arg351Ter *(de novo)*	Yes	Yes	Moderate	Not known	Blind	Yes	Yes	Yes	Not known	No	Yes
13	P13	Iran	c.537C>A; p.Tyr209Ter *(Hom.)*	No	Yes	Moderate	No	Impaired	Yes	Yes	Not known	Not known	Yes	No
14	P14	Iran	c.1277_1280+5del *(Hom.)*	No	Yes	Not known	No	Blind	Yes	No	No	Not known	No	No
15	P15	India	c.1483C>t; p.Arg495Ter *(Hom.)*	No	Yes	Moderate	Yes	Impaired	Yes	No	Not known	Not known	No	No
16	P16	Palestine	c.3011T>A; p.Leu1004His *(Hom.)*	No	Yes	Not known	Yes	Impaired	Yes	No	Not known	Not known	No	No
17	P17	Morocco	c.2108dupC; p.Pro704Thrfs *(Hom.)*	Yes	Not known	Not known	Not known	Impaired	No	No	Not known	Not known	Not known	No
18	P18		c.1169_1170del; p.Phe390Ter *(Hom.)*										Not known	No
19	P19		c.2332C>T; p.Gln778Ter *(Hom.)*										Not known	No
Known DNA Repair Syndromes				**Clinical features**										
				Microcephaly	**Motor developmental delay**	**Intelleuctual disability**	**Dysmorphic facial features**	**Visual impairment**	**Seizures**	**Recurrent respiratory infections**	**Immunodeficinecy**	**Cancer**	**Hearing impairment**	**Thrombocytopenia**
Nigmegen Breakage Syndrome				Yes	Yes	Yes	Yes	No	No	Yes	Yes	Yes	Yes	Yes
Ataxia Telangectasia				No	Yes	Mild	No	No	No	Mild	Yes	Yes	No	No
Warsaw Breakage Syndrome				Yes	Yes	Yes	Yes	No	No	Moderate	Yes	Unknown	Yes	No

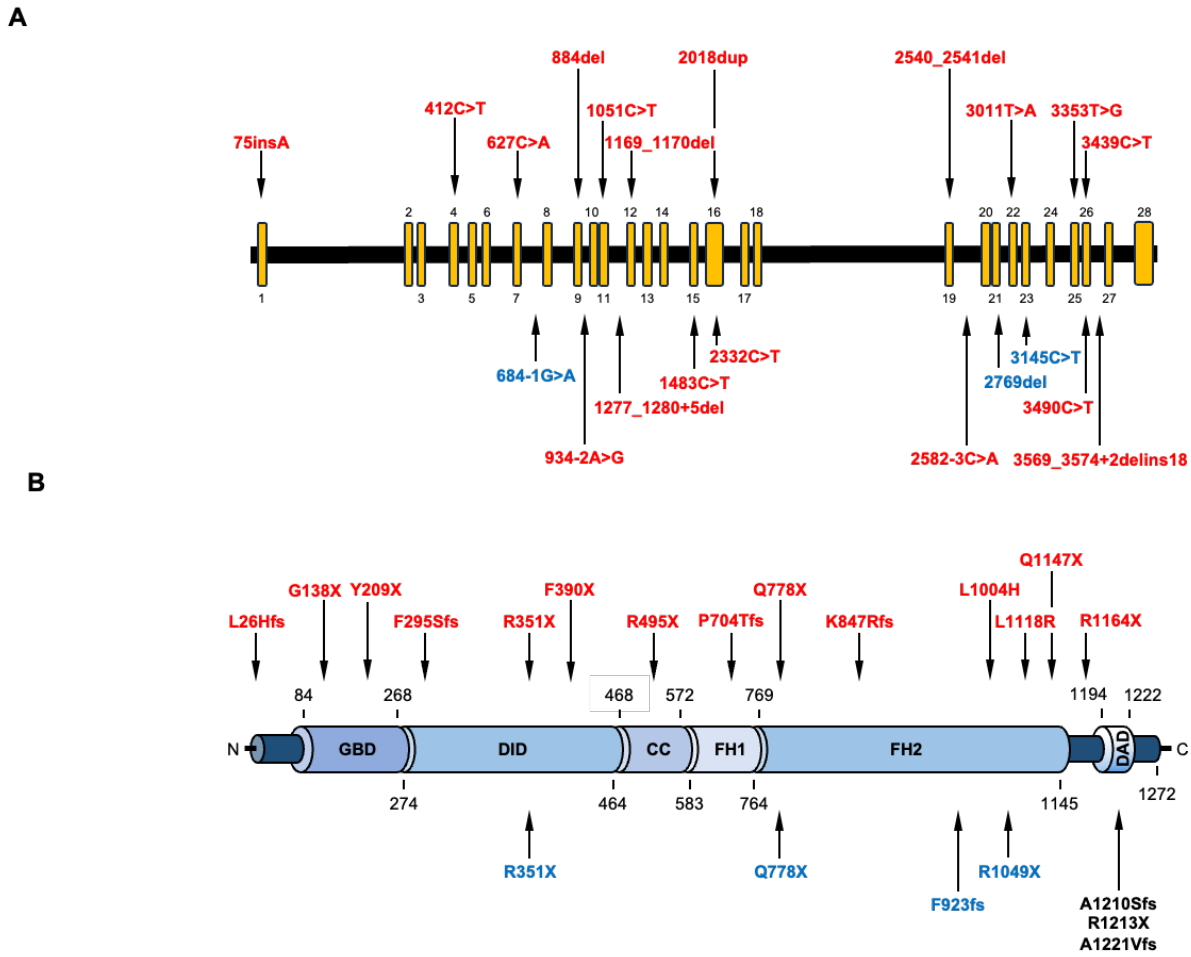


Figure 3.2 – Schematic of DIAPH1 variant locations on DIAPH1 gene and protein – A – *Location of homozygous gene variants on DIAPH1 gene. Yellow represents exons, black line represents intronic regions of gene.* ***B*** *- The functional domains of DIAPH1 are marked and arrows indicate the location of variants identified within the patient cohort. Homozygous variants are highlighted in red. Previously reported autosomal recessive variants in DIAPH1 associated with SCBMS are shown in blue. The variants highlighted in black are heterozygous variants previously identified which give rise to a distinct clinical phenotype and occur specifically in the C-terminal autoregulatory domain. Abbreviations: DAD – Diaphanous autoregulatory domain, DID – Diaphanous inhibitory domain, GBD – GTPase binding domain, FH – formin homology.*



Figure 3.3 – Clinical photographs to show physical manifestations of patients harbouring homozygous variants in DIAPH1 – *A selection of the DIAPH1 patient cohort. Patients exhibit microcephaly, dysmorphic facial features and short stature can be seen in P2-2 and P13. Other clinical manifestations of these patients include developmental delays, intellectual disability seizures and blindness. P denotes patient identifier.*

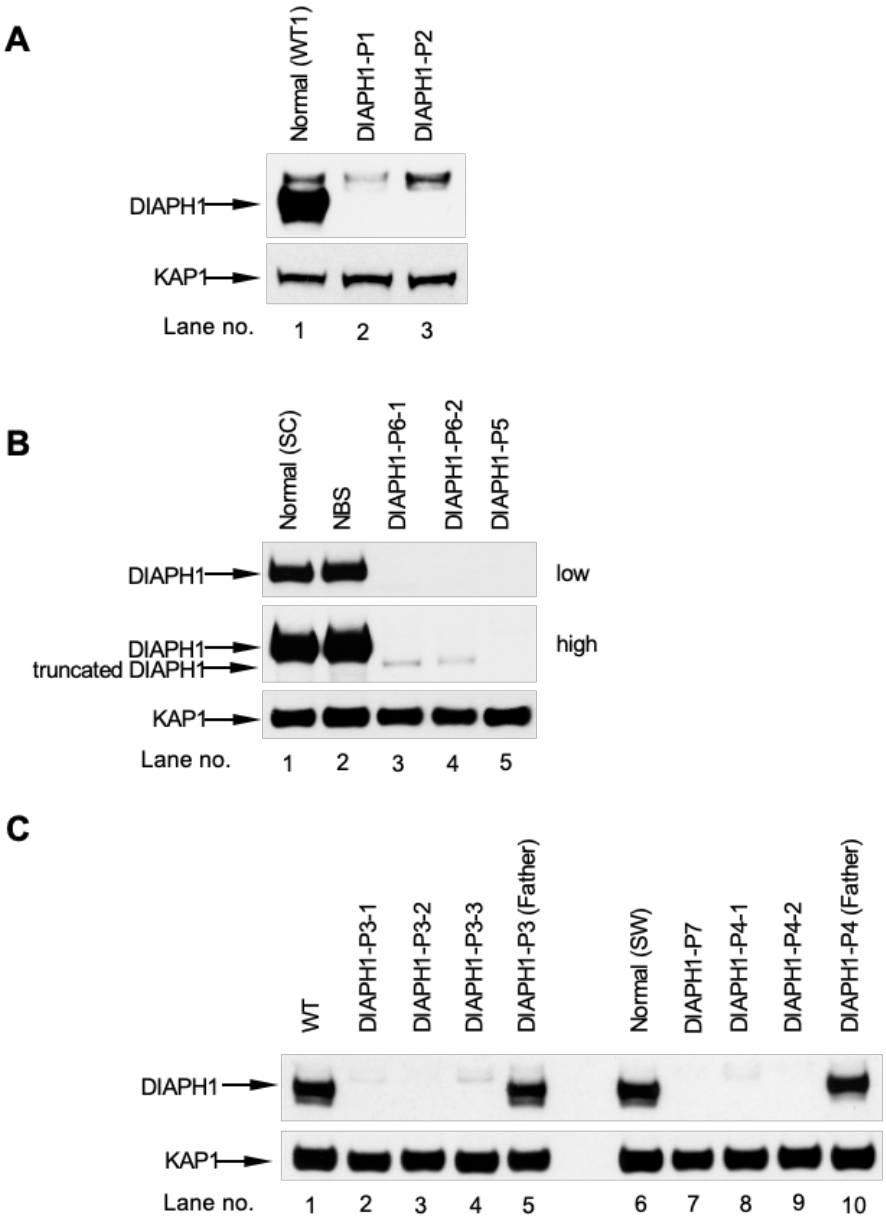


Figure 3.4 Western blot analysis of patient-derived cell lines – *Western blots on cell extracts derived from DIAPH1 patients indicating the level of DIAPH1 protein expression. Cells were cultured in asynchronous cell culture methods then harvested, and protein was extracted with UTB buffer. 50 µg of protein was loaded per lane and samples were subject to SDS-PAGE and western blotting using the indicated antibodies. KAP1 was used as a loading control.* ***A*** *- (Fibroblasts) DIAPH1-P1 and DIAPH1-P2 fibroblasts. WT1 are fibroblasts from unrelated healthy control.* ***B*** *- (Lymphoblastoid cell lines (LCLs) from DIAPH1 P6-1, P6-2 and P5. SC and NBS are LCLs from a healthy control and a patient with Nijmegen Breakage Syndrome (NBS) carrying a homozygous p.657del5 mutation in NBS1 respectively. KAP1 was used as a loading control in all blots.* ***C*** *- (Fibroblasts) DIAPH1-P3-1, P3-2, P3-3, P7, P4-1 and P4-2 fibroblasts. WT are fibroblasts from unrelated healthy control. Low and high indicates the length of the exposure time.*

3.3.2 Western blot analysis of ATM-dependent DNA damage response in DIAPH1 patient cells

Section 3.3.1 provided an overview of the clinical features of the DIAPH1 patient cohort and demonstrated that in the patient derived cell lines analysed, all variants resulted in absence of full length DIAPH1 expression. The clinical features of the patients, particularly their severe neurodevelopmental defects, imply an underlying defect in maintaining genome stability. Genomic instability arises from three main sources; DNA damage, replication stress and mitotic defects (Ovejero, Bueno and Sacristán, 2020). DNA damage and replication stress signalling are vital cellular pathways in maintaining genome stability in the nervous system. The two key kinases responding to these threats, as discussed in Chapter 1, Section 1.5.3.2-1.5.3.2, are ATM which responds to DSBs and ATR which primarily responds to various types of replication stress. Both unrepaired DSBs and unresolved replication stress are sources of genomic instability leading to clinical deficits in neurodevelopment or, in the case of *ATM* and *MRE11A* variants, neurodegeneration (McKinnon, 2013). Therefore, as a starting point in this study, ATM and ATR signalling was investigated in LCLs derived from DIAPH1-P5, following to DNA damage. To do this, Western blot analysis was used to study the activation of ATM and ATR signalling cascades by immunoblotting for well-known downstream substrates of both kinases.

To analyse the ATM signalling pathway, P5 LCLs were exposed to three DSB-inducing agents: IR, CPT and ETOP. Western blot analysis was used to assess the ATM-dependent activation of DSB repair signalling. To do this, asynchronous cell cultures of P5 LCLs were exposed to 2 Gy IR and harvested/lysed at 1 h and 24 h post-IR to

assess activation and resolution of the ATM-dependent DNA damage response (Figure 3.5; Lane 10-12). Phospho-specific antibodies to known phosphorylation sites on downstream targets of ATM, such as SMC1, KAP1, NBS1 and CHK2 were used to assess the activation of ATM (Ahn *et al.*, 2000; Zhao *et al.*, 2000; Kitagawa *et al.*, 2004; White *et al.*, 2006). A healthy WT control LCL cell line (Normal HC; Figure 3.5; Lane 1-3) was used as a negative experimental control and cell lines from LCLs derived from patients with a confirmed diagnosis of either Ataxia Telangiectasia (A-T) (Figure 3.5; Lane 4-6) or NBS (Figure 3.5; Lane 7-9) were used as positive controls for defective ATM-signalling.

Notably, cells from DIAPH1 patient P5 did not display a defect in the IR-induced activation of ATM (Figure 3.5; Lane 3-6), when compared to the IR-induced activation of ATM in cells with WT DIAPH1 (Figure 3.5; Lane 11-12). The NBS LCLs show an absence of endogenous NBS1 and therefore no NBS1 phosphorylation and a reduction in the phosphorylation of SMC1 at 1 h post-IR (Figure 3.5; Lane 5). The A-T LCLs show a complete absence of endogenous ATM and no increased phosphorylation of any of the downstream targets at 1 h post-IR (Figure 3.5; Lane 8). At 24 h post-IR there is an increase in the phosphorylation of CHK2 and NBS1 (Figure 3.5; Lane 9), suggesting a delay in this signalling pathway is due to absence of ATM.

Overall, this analysis confirms that absence of DIAPH1 in DIAPH1 patient P5 LCLs does not lead to any defects in ATM-dependent DSB repair signalling following IR. To confirm this finding, DIAPH1 patient P5 LCLs were also exposed to both CPT and ETOP to investigate if DIAPH1 functions to promote ATM activation in response to protein-coupled blocked DNA DSBs arising from the inhibition of topoisomerase I or II.

DIAPH1 P5 LCLs were incubated with either 100 nM CPT for 1 h or 10 μM ETOP for 30 min. The drugs were then washed off and cells were harvested and lysed at 1 h and 24 h post-treatment (Figure 3.6 A-B). The same positive and negative control cell lines as Figure 3.5 were used in this analysis (Figure 3.6 A; Lane 1-9 and Figure 3.6 B; Lane 1-9). Due to the nature of both CPT and ETOP inducing DSBs in S-phase at sites of replication, RPA2 S4/S8 phosphorylation was also blotted for to assess DSB-end resection and whether replication stress signalling may be defective when DIAPH1 is lost. ATM, ATR and DNA-PKcs can phosphorylate this site so whilst it is not specific to ATM-dependent signalling, and is in fact primarily phosphorylated by DNA-PKcs, it would provide insight into whether replication stress signalling is affected by loss of DIAPH1 (Liu *et al.*, 2012).

As with IR-induced ATM-signalling being unaffected, in response to either CPT and ETOP, DIAPH1 patient P5 LCLs displayed normal ATM activation (Figure 3.6A; Lane 10-12 and Figure 3.6B; Lane 10-12). Both the NBS LCLs (Figure 3.6 A-B; Lane 4-6) and A-T LCLs (Figure 3.6 A-B; Lane 7-9) exhibited a reduction in the phosphorylation of the downstream ATM targets as expected.

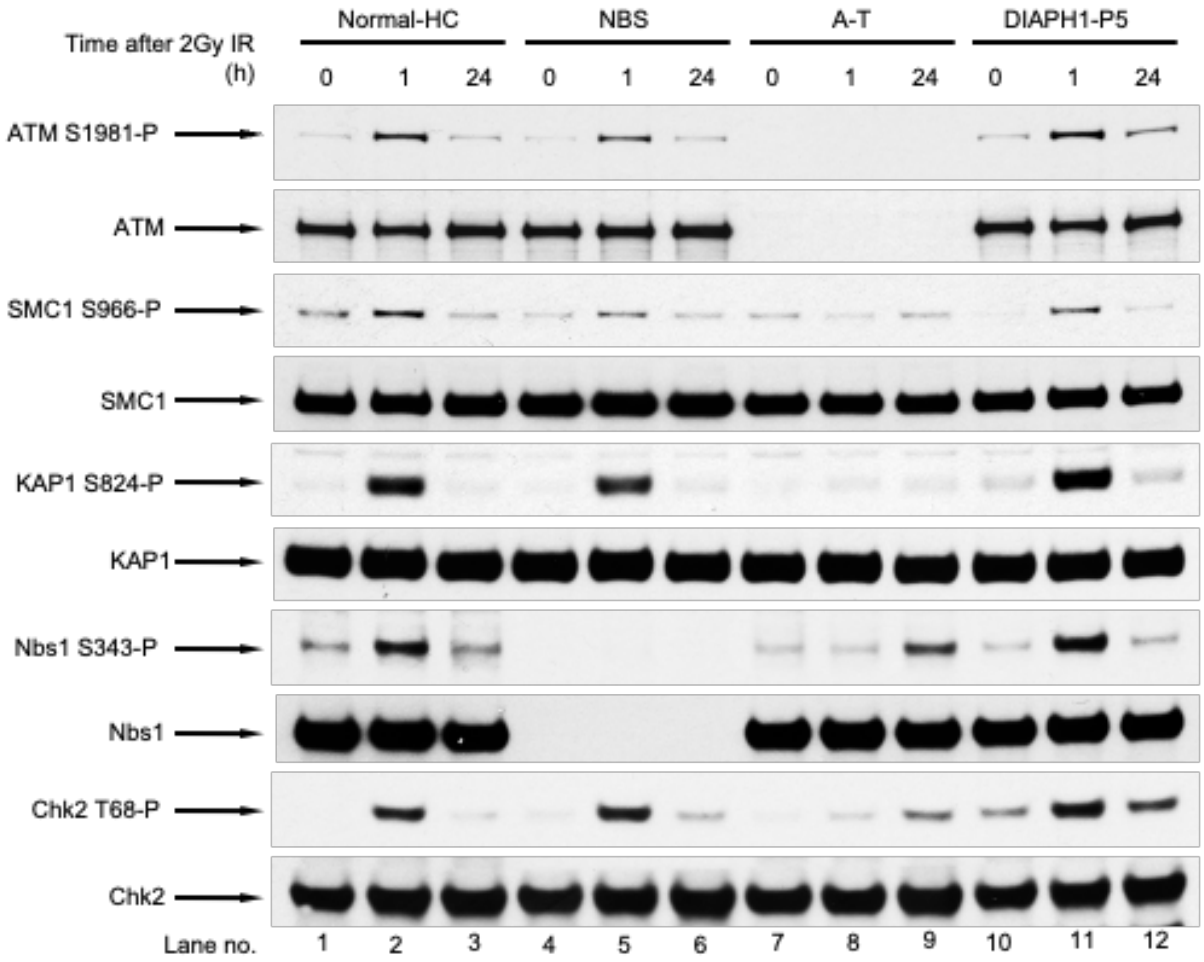


Figure 3.5 Western blot analysis of DIAPH1-P5 derived LCLs exposed to 2 Gy IR *– LCLs were either untreated (0 h) or exposed to 2 Gy of IR and harvested at specific time points post IR (1 h, 24 h). Cells were then harvested, and protein was extracted with UTB buffer. 50 µg of protein was loaded per lane and samples were subject to SDS-PAGE and western blotting using the indicated antibodies. Endogenous protein expression was blotted for and used as a loading control. Specific antibodies to phosphor-specific forms of proteins indicated were used as markers of ATM-dependent protein phosphorylation. Normal HC – normal donor cells, NBS- cells from individual with a confirmed diagnosis of NBS, A-T – cells from individual with a confirmed diagnosis of A-T. P-denotes antibody was specific to the phosphorylated form of the protein.*

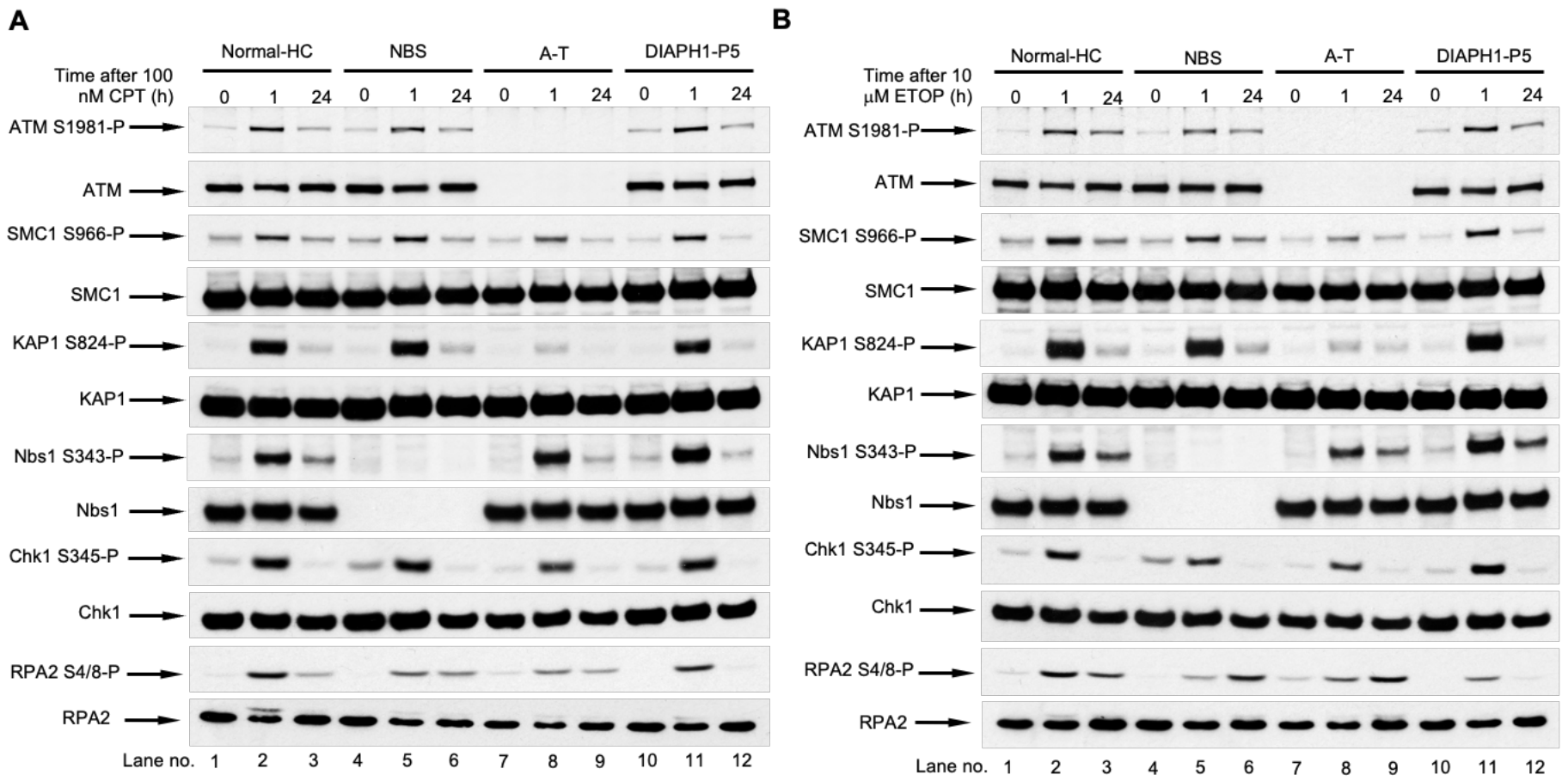


Figure 3.6 - Western blot analysis of DIAPH1-P 5 LCLs exposed to DNA damaging agents – *Western blots on cell extracts derived from DIAPH1 patients indicating activation of ATM-dependent signalling pathway. Cells were cultured in asynchronous cell culture methods then harvested, and protein was extracted with UTB buffer specific time points post treatment (1 h, 24 h). 50 µg of protein was loaded per lane and samples were subject to SDS-PAGE and western blotting using the indicated antibodies. Endogenous protein expression was blotted for and used as a loading control. Specific antibodies to phosphor-specific forms of proteins indicated were used as markers of ATM-dependent protein phosphorylation.* ***A*** *- LCLs were exposed to 100 nM Camptothecin (CPT) for 1 h.* ***B*** *- 10 µM Etoposide (ETOP) for 30 min. Normal HC – normal donor cells, NBS- cells from individual with a confirmed diagnosis of NBS, A-T – cells from individual with a confirmed diagnosis of A-T. P-denotes antibody was specific to the phosphorylated form of the protein.*

Next, whether DIAPH1 is required to facilitate the activation of the ATR-dependent signalling pathway was analysed. To investigate this, both a WT LCL and DIAPH1 patient P5 LCLs were treated with 1 mM hydroxyurea (HU) and whole cell lysates were subject to Western blotting with phospho-specific antibodies to sites of phosphorylation on known ATR substrates (Zhao *et al.*, 2000; Olson *et al.*, 2007; So *et al.*, 2011) (Figure 3.7). HU is a selective inhibitor of ribonucleoside reductase (RNR) that inhibits the production of deoxyribonucleotides (dNTPs). As a result HU causes the cellular dNTP pool to become depleted, which stalls the replicative DNA polymerase leading to helicase-polymerase uncoupling and the generation of long regions of ssDNA (Musiałek and Rybaczek, 2021). In response to HU-treatment, DIAPH1 patient P5 LCLs did not show any defects in the activation of ATR at 2 h and 24 h post-HU treatment (Figure 3.7; Lane 4-6). Notably however, RPA2 pS4/S8 was slightly reduced at 24 h compared to the WT cell line (Figure 3.7; Lane 3 and 6) and in untreated cells there was a slight increase in γ-H2AX signalling when DIAPH1 is lost (Figure 3.7; Lane 4).

Overall, these data suggest that DIAPH1 is not a key component of the ATM- or ATR-dependent DDR induced by exposure to IR, CPT or ETOP (DSB signalling) or HU (replication stress response). However, the minimally reduced RPA2 pS4/S8 signal and basal increase in γ-H2AX signal suggests the presence of spontaneous genome instability.

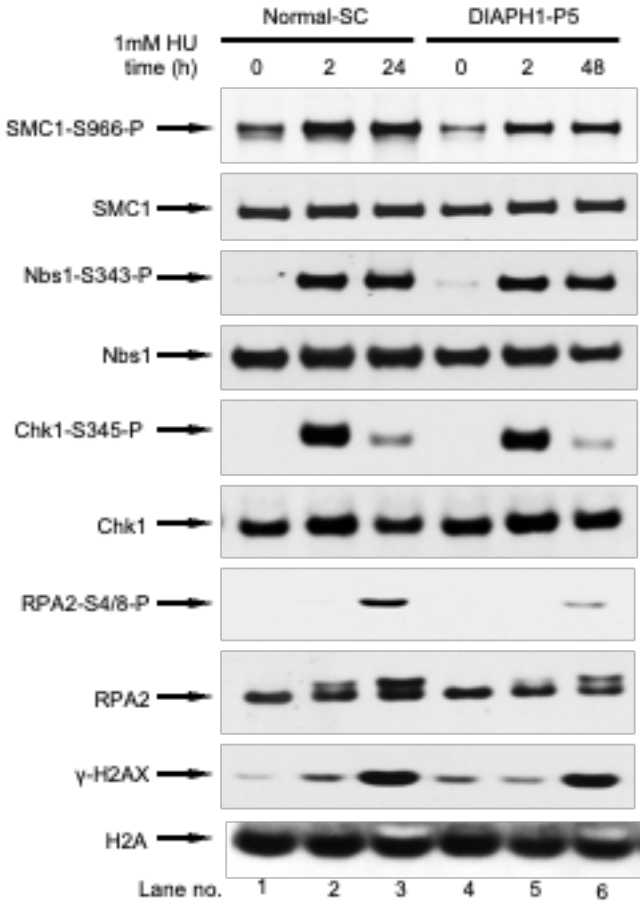


Figure 3.7 Western blot analysis of DIAPH1-P5 derived LCLs exposed to 1 mM HU *– Cells were either untreated (0 h) or exposed to 1 mM HU and harvested at specific time points post IR (2 h, 24 h). Cells were then harvested, and protein was extracted with UTB buffer. 50 µg of protein was loaded per lane and samples were subject to SDS-PAGE and western blotting using the indicated antibodies. Endogenous protein expression was blotted for and used as a loading control. Specific antibodies to phosphor-specific forms of proteins indicated were used as markers of ATR-dependent protein phosphorylation. Normal SC – normal donor cells, P-denotes antibody was specific to the phosphorylated form of the protein.*

3.3.3 Loss of DIAPH1 leads to an increase in genomic stability following DNA damage

To investigate whether loss of DIAPH1 affects the repair of DNA DSBs, Western blotting in conjunction with an antibody recognising H2AX phosphorylated on S139 (γ-H2AX) was used to examine the kinetics of DNA repair over time following the induction of DNA damage. DIAPH1 patient P1 fibroblasts and a fibroblast from a healthy individual (WT1) were treated with 5 Gy IR and harvested and lysed at specific time points post-irradiation (0 h, 1 h, 4 h, 8 h and 24 h). Following irradiation, the γ-H2AX signal was similar between the WT cell line and the DIAPH1 patient P1 cell line at the 1 h, 4 h and 8 h timepoints post-exposure to IR (Figure 3.8A; Lanes 2-4 and 7-9). However, at 24 h post-irradiation the DIAPH1 patient P1 cell line displayed an elevated γ-H2AX signal when compared to the WT cell line, suggesting a loss of DIAPH1 compromises the repair of IR-induced DSBs (Figure 3.8A; Lane 10). Notably, a low level of γ-H2AX signal in the untreated DIAPH1 patient P1 cell line was also observed (Figure 3.8A; Lane 6), suggesting the loss of DIAPH1 results in increased spontaneous genomic instability even in the absence of exposure to exogenous DNA damage. This was a similar observation to the findings in Section 3.2.2.

To validate the DNA repair defect caused by loss of DIAPH1 in patient-derived fibroblasts, HeLa cells depleted of DIAPH1 with siRNA were used. To do this, a SMARTpool siRNA, specifically targeted to depleting DIAPH1, was transfected into an asynchronous HeLa cell culture before treating the cells with 5 Gy IR and harvesting/lysing cells at the same time points (0 h, 1 h, 4 h, 8 h and 24 h). Non-

targeting siRNA to luciferase was used as a transfection control. γ-H2AX was then immunoblotted for, as well as DIAPH1, to confirm successful depletion of endogenous protein expression (Figure 3.8B). SMC1 and H2A were both used as protein loading controls. Reassuringly, siRNA mediated depletion of DIAPH1 in HeLa cells confirmed the observations in the patient fibroblasts. In the untreated DIAPH1 depleted HeLa cells, a low level of γ-H2AX signal can be observed when compared to the control siRNA (Figure 3.8B; Lane 1 and Lane 6). Following treatment with IR, at 1 h, both DIAPH1 depleted HeLa cells and non-targeting siRNA treated HeLa cells display an elevated signal in response the treatment (Figure 3.8B; Lane 2 and Lane 7). Interestingly, at the time-points from 4 h – 24 h, the DIAPH1 depleted HeLa cells display an elevated and prolonged γ-H2AX response, confirming that loss of DIAPH1 leads to elevated markers of genome instability and unresolved DNA damage at the later time point (24 h) (Figure 3.8B; Lane 3-5 and Lane 8-10).

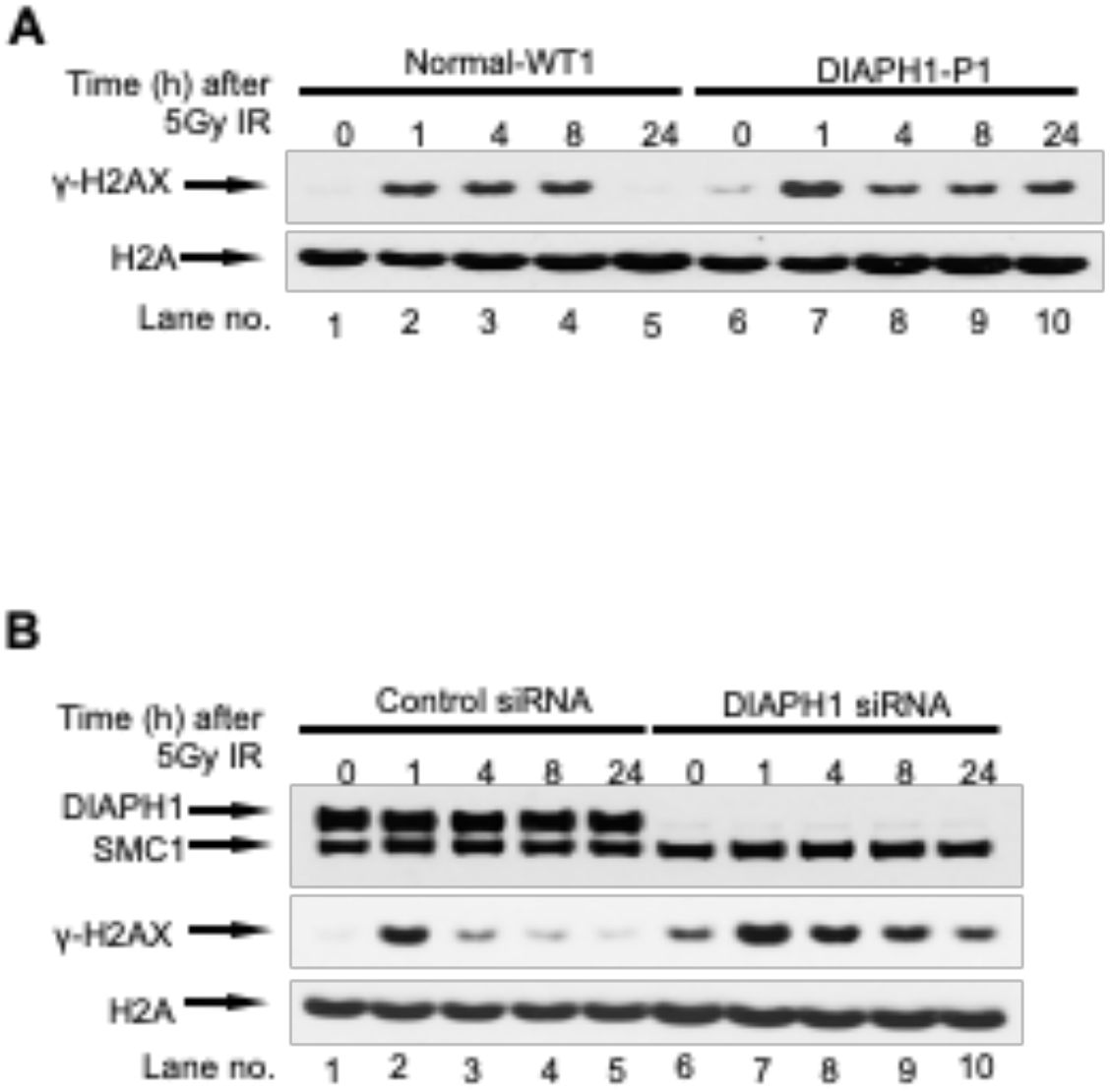


Figure 3.8 Western blot analysis of hTERT immortalised patient derived fibroblasts and siDIAPH1 HeLa cells exposed to 5 Gy IR *- Western blots on cell extracts derived from WT1 and DIAPH1-P1 hTERT fibroblasts and HeLa cells depleted of DIAPH1 Cells were cultured in asynchronous cell culture methods then treated with 5 Gy IR harvested and the indicated time points (0 h, 1 h, 4 h, 8 h, 24 h), and protein was extracted with UTB buffer. 50 µg of protein was loaded per lane and samples were subject to SDS-PAGE and western blotting using the indicated antibodies. H2A and SMC1 (B only) was used as loading control.* ***A*** *– Western blot of cell extracts derived WT1 and DIAPH1-P1 hTERT immortalised fibroblasts.* ***B*** *– Western blot of cell extracts derived from siRNA to either DIAPH1 or a non-targeting luciferase control. Successful complemented of DIAPH1 or empty vector in DIAPH1-P1 is indicated in A.*

Next, genomic instability was investigated through another method to validate the unrepaired DNA damage observed in patient fibroblasts and DIAPH1 depleted HeLa cells. One such method was the quantification of micronuclei formation. Micronuclei are extra-nuclear structures that are enclosed within their own nuclear membrane and can be easily visualised by fluorescence microscopy using DAPI. Micronuclei contain either whole or fragments of chromosomes that have been separated from the nucleus during mitosis and arise due to defects in DNA repair such as unresolved DSBs as well as defects in mitosis and DNA replication. As such, they are a well-established marker of genomic instability (Figure 3.9) (Jiang, Panda and Gekara, 2019). To examine micronuclei formation, several DIAPH1 patient fibroblasts (P1, P2, P3.1, P4 and P7) were either left untreated or exposed to 3 Gy IR, to induce DSBs before harvesting 24 h post-IR (Figure 3.9). When compared to the WT cell line, all of the fibroblasts derived from DIAPH1 patients, as well as the NBS control, displayed a statistically significant elevation of micronuclei in the absence of exogenous DNA damage, suggesting spontaneous genomic instability (Figure 3.10A, C). After IR exposure, the levels of micronuclei in all of the DIAPH1 patient fibroblasts were elevated when compared to the WT fibroblast cell line, but interestingly, this increase was lower than the level of micronuclei observed in NBS cell line (Figure 3.10B, C). This finding confirms that loss of DIAPH1 results in increased markers of genomic instability before and after exposure to IR.

Reassuringly, the elevated levels of micronuclei seen in the DIAPH1 patient fibroblasts was confirmed utilising siRNA in HeLa cells to deplete DIAPH1. Loss of DIAPH1 in HeLa cells was confirmed by Western blotting (Figure 3.11A). DIAPH1 depleted HeLa

cells were then either left untreated or exposed to 3 Gy IR and harvested/fixed 24 h post-treatment. In untreated cells, there was no difference in the level of micronuclei between HeLa cells transfected with siDIAPH1 or control siRNA (Figure 3.11B, D, G). However, following irradiation, DIAPH1 depleted HeLa cells displayed significantly elevated levels of micronuclei when compared to the non-targeting control (Figure 3.11C, G). The next investigation was to test if this phenotype was specific to IR-induced DSBs or could be observed following treatment with other DSB inducing agents, CPT and ETOP. Thus, DIAPH1 depleted HeLa cells were treated with either 100 nM CPT for 1 h or 10 μM ETOP for 30 min then harvested/fixed in PFA at 48 h and stained with DAPI. A later time-point was used to analyse micronuclei formation with CPT and ETOP than for IR to allow for cells to go through at least two cell cycles following exposure to TOPI/II inhibitors (Nitiss, 2009; Pommier *et al.*, 2022). In response to both CPT and ETOP, DIAPH1 depleted HeLa cells displayed significantly elevated levels of micronuclei formation when compared to the non-targeting control suggesting the increase in genomic instability is not specific to IR and arises due to a failure to repair all types of DSB (Figure 3.11E-G).

Taken together, these findings show that a loss of DIAPH1 resulting from either biallelic mutations or siRNA-mediated knockdown gives rise to genome instability following exposure to a variety of genotoxins that induce DNA DSBs.

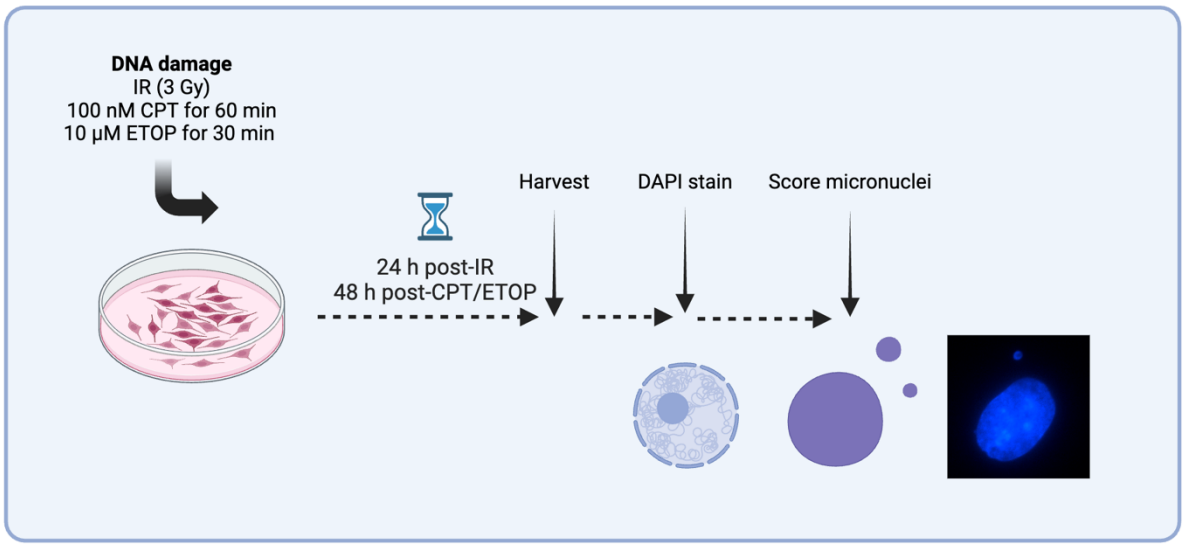


Figure 3.9 – Schematic diagram to show micronuclei analysis – *Asynchronous cell cultured were treated with DNA damaging agents (3 Gy ionising radiation (IR), 100 nM camptothecin (CPT) for 60 min or 10 µM etoposide (ETOP) for 30 min. After treatment, cells were cultured for either 24 h (IR) or 48 h (CPT and ETOP) then harvested by 5 min incubation with pre-extraction buffer followed by 10 min incubation with 3.6% paraformaldehyde (PFA). FPA-fixed cells were then stained with DAPI and micronuclei scored on a fluorescent microscope.*

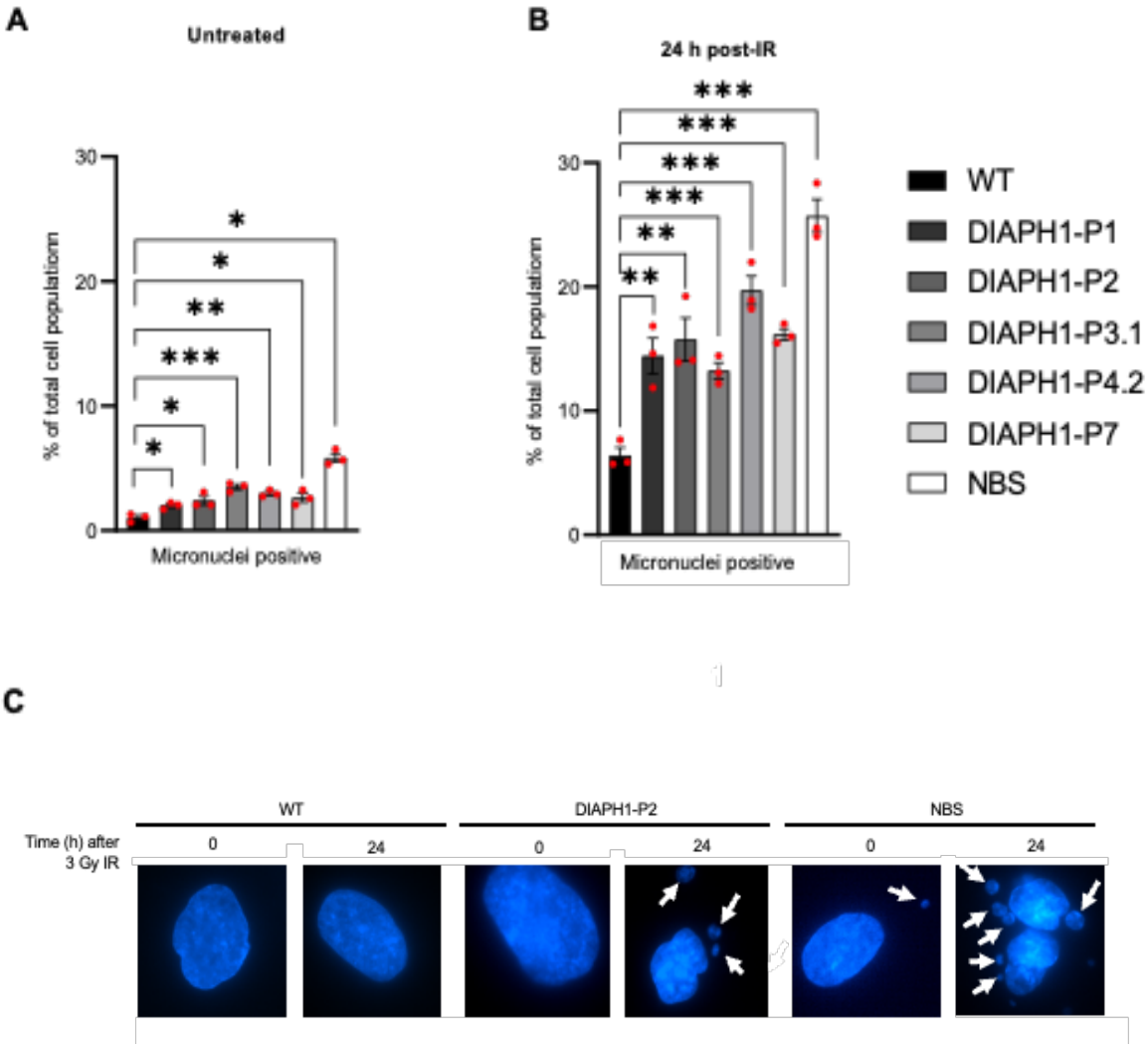


Figure 3.10 - Formation of micronuclei in DIAPH1-P1, P2, P3-1, P4-2, P5 hTERT immortalised fibroblasts following exogenous DNA damage – *Fibroblasts were seeded onto glass coverslips and left untreated or treated with either 3 Gy IR. Coverslips were harvested at specific time-points post treatment (1 h, 24 h) and fixed with paraformaldehyde (PFA).* ***A*** *- Quantification of micronuclei in the absence of exogenous DNA damage.* ***B*** *- Quantification of micronuclei 24 h post-3 Gy IR.* ***C*** *- Representative images of DAPI positive cells from quantification in (A-B). Data from 3 independent repeats, a minimum of 500 cells counted per condition per repeat. Error bars represent standard error of the mean. * Indicates statistical significance (p=<0.05), ** indicates statistical significance (p=<0.01), *** indicates statistical significance (p=<0.001) calculated using an unpaired Students T-test. Statistical significance was calculated using GraphPad Prism software.*

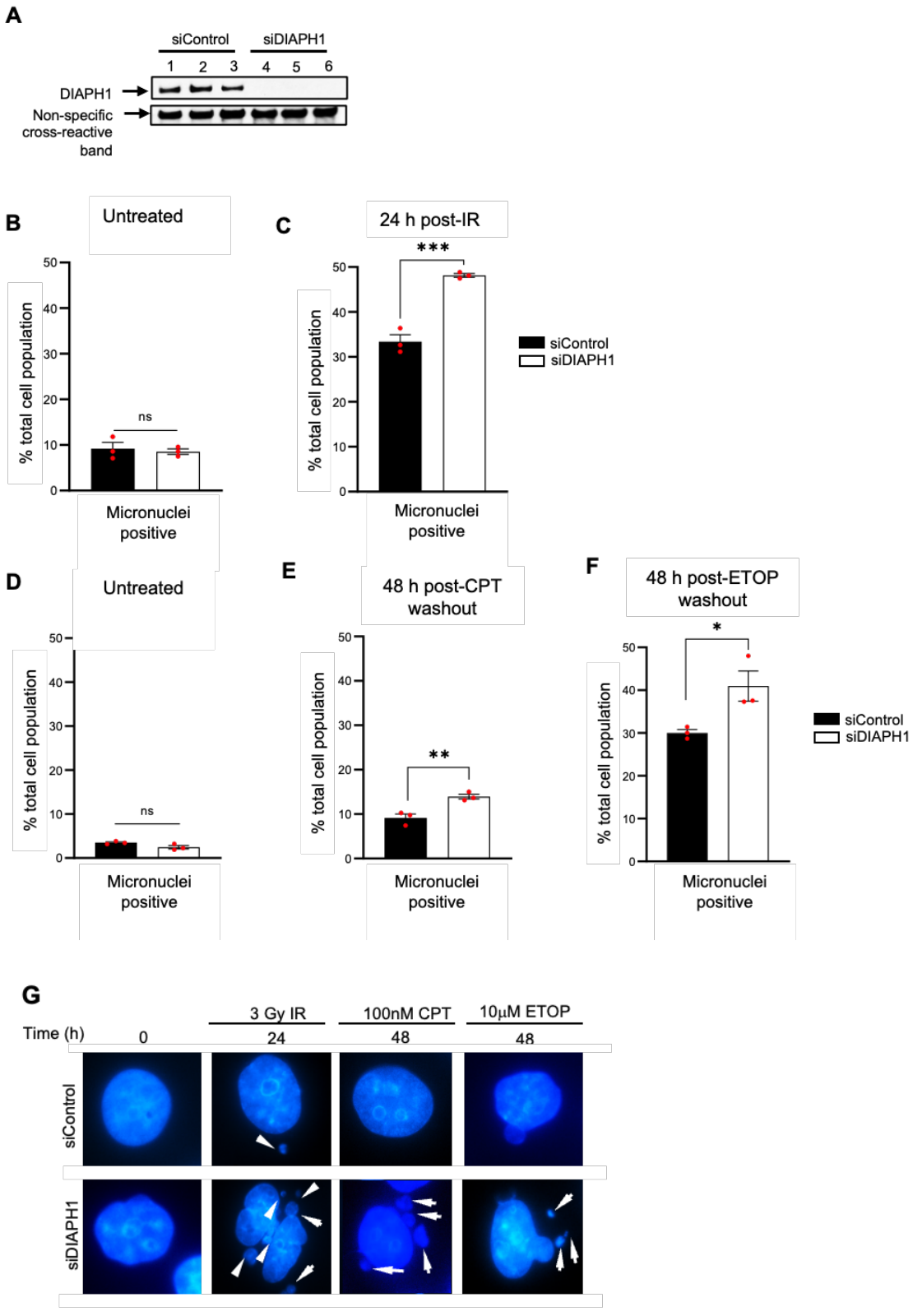

A
siControl
siDIAPH1
1 2 3 4 5 6
DIAPH1
Non-specific cross-reactive band
B
Untreated
% total cell population
ns
Micronuclei positive
C
24 h post-IR
***
siControl
siDIAPH1
D
Untreated
E
48 h post-CPT washout
**
F
48 h post-ETOP washout
*
G
Time (h)
0
3 Gy IR
24
100nM CPT
48
10μM ETOP
48
siControl
siDIAPH1

Figure 3.11 - Formation of micronuclei in siDIAPH1 HeLa cells following exogenous DNA damage – *HeLa cells transfected with siRNA to DIAPH1 or a non-targeting luciferase control were seeded onto glass coverslips and left untreated or treated with either 3 Gy IR, 100 nM CPT for 1 h or 10 μM ETOP for 30 min. Coverslips were harvested at specific time-points post treatment (24 h for IR and 48 h for ETOP and CPT) and fixed with paraformaldehyde (PFA).* ***A*** *- Western blot of whole cell lysates derived from siRNA depleted HeLa cells showing successful knockdown of DIAPH1. A non-specific cross-reactive band was used as a loading control.* ***B*** *- Quantification of micronuclei in the absence of exogenous DNA damage used as the experimental control for IR treatment only.* ***C*** *- Quantification of micronuclei 24 h post-3 Gy IR.* ***D*** *- Quantification of micronuclei in the absence of exogenous DNA damage used as the experimental control for CPT and ETOP treatments.* ***E*** *- Quantification of micronuclei 48 h post 100 nM CPT. F - Quantification of micronuclei 48 h-post 10 μM ETOP.* ***G*** *- Representative images of DAPI positive cells from quantification in (B-F). Data from 3 independent repeats, a minimum of 500 cells counted per condition per repeat. Error bars represent standard error of the mean. * Indicates statistical significance (p=<0.05), ** indicates statistical significance (p=<0.01), *** indicates statistical significance (p=<0.001) calculated using an unpaired Students T-test. Statistical significance was calculated using GraphPad Prism software.*

3.3.4 Complementation of WT-DIAPH1 in patient-derived cells lacking DIAPH1 rescues genomic instability

To validate the observation that inherited mutations in *DIAPH1* result in increased genome instability following the induction of DNA DSBs (Section 3.3.2-3.3.3), was specifically due to loss of DIAPH1, it was then investigated if this DNA damage phenotype could be rescued by complementing DIAPH1 patient P1 fibroblasts with wild-type *DIAPH1* (WT-DIAPH1). DIAPH1 patient P1 fibroblasts were transduced with a lentivirus expressing either WT-DIAPH1 with an N-terminal HA-Tag or an empty vector as a control, to generate an isogenic pair of cell lines (subsequently referred to as P1+DIAPH1 and P1+Vector throughout this thesis). Once re-expression of WT-DIAPH1 had been confirmed by Western blot (Figure 3.12A), it was then investigated if the presence of DIAPH1 could rescue the increased and prolonged γ-H2AX response seen in both the P1 fibroblasts and the DIAPH1 depleted HeLa cells.

To do this, P1+DIAPH1 and P1+Vector cell lines were either left untreated or exposed to 5 Gy IR and harvested at 0 h, 1 h and 24 h post-irradiation. Cell lysates were

immunoblotted using specific antibodies to γ-H2AX, as well as H2A, as a non-phosphorylated loading control. Reassuringly, the P1+DIAPH1 cell line displayed a reduced γ-H2AX signal at both 1 h and 24 h when compared to the P1+Vector cell line (Figure 3.12B; Lane 2-3 and 5-6) indicating that the elevated DNA damage-induced γ-H2AX signal observed in patient-derived cell lines with mutations in *DIAPH1* is specifically caused by a loss of DIAPH1 and is not due to inherited variants in other genes.

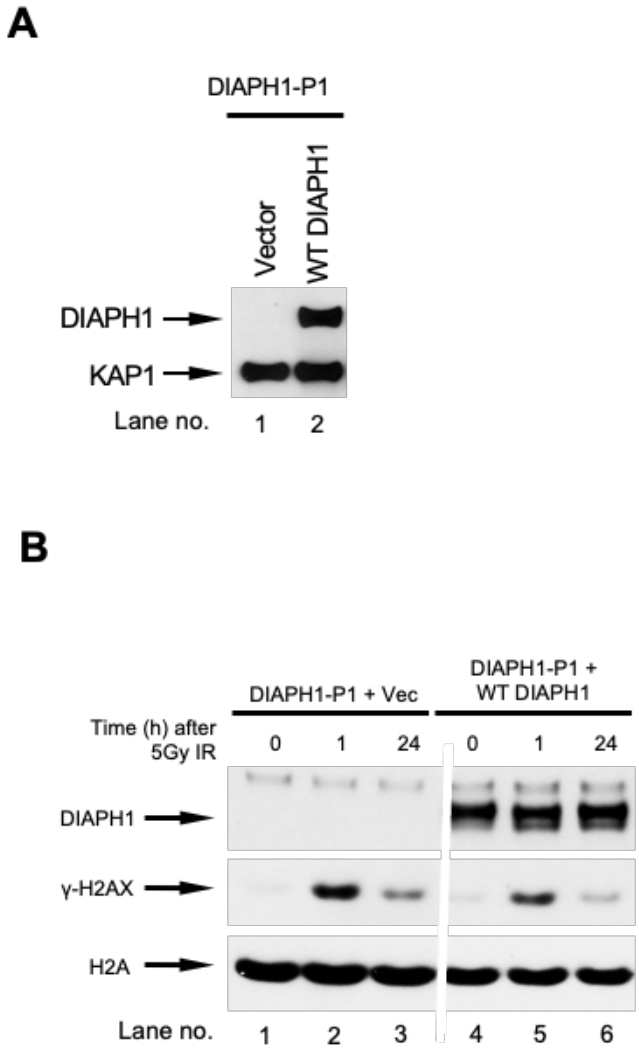


Figure 3.12 - *Western blot analysis of hTERT immortalised patient derived fibroblasts -* Western *blots on cell extracts derived from DIAPH1 patients expressing either WT-DIAPH1 or an empty vector. Cells were cultured in asynchronous cell culture methods then harvested, and protein was extracted with UTB buffer. 50 µg of protein was loaded per lane and samples were subject to SDS-PAGE and western blotting using the indicated antibodies.* ***A*** *- DIAPH1 protein expression of P1+DIAPH1 and P1+Vector fibroblasts. KAP1 was used as a loading control.* ***B*** *- P1+DIAPH1 and P1+Vector fibroblasts exposed to 5 Gy of IR and harvested at specific time points post IR (0 h, 4 h, 8 h, 24 h). H2A was used as a loading control.*

To confirm that re-expression of *DIAPH1* in P1 fibroblasts rescues the elevation in ionising radiation-induced micronuclei, micronuclei were then analysed in the patient-derived isogenic cell lines (P1+DIAPH1 and P1+Vector). No difference in the levels of micronuclei between P1+DIAPH1 or P1+Vector cells in untreated conditions were observed (Figure 3.13A, E). However, 24 h after IR exposure, there was a significant increase in the number of micronuclei in P1+Vector cells when compared to P1+DIAPH1 cells (Figure 3.13B, E), suggesting that loss of DIAPH1 gives rise to increase in genomic instability following exposure to IR. Moreover, in response to either CPT or ETOP, P1+Vector cells also displayed a significant elevation in micronuclei formation when compared to P1+DIAPH1 (Figure 3.13C-E).

To summarise, this section demonstrates that complementing P1 fibroblasts expressing WT-DIAPH1 rescues the genomic instability phenotype observed in patient-derived cell lines with mutations in *DIAPH1* arising from exposure to IR, CPT and ETOP.

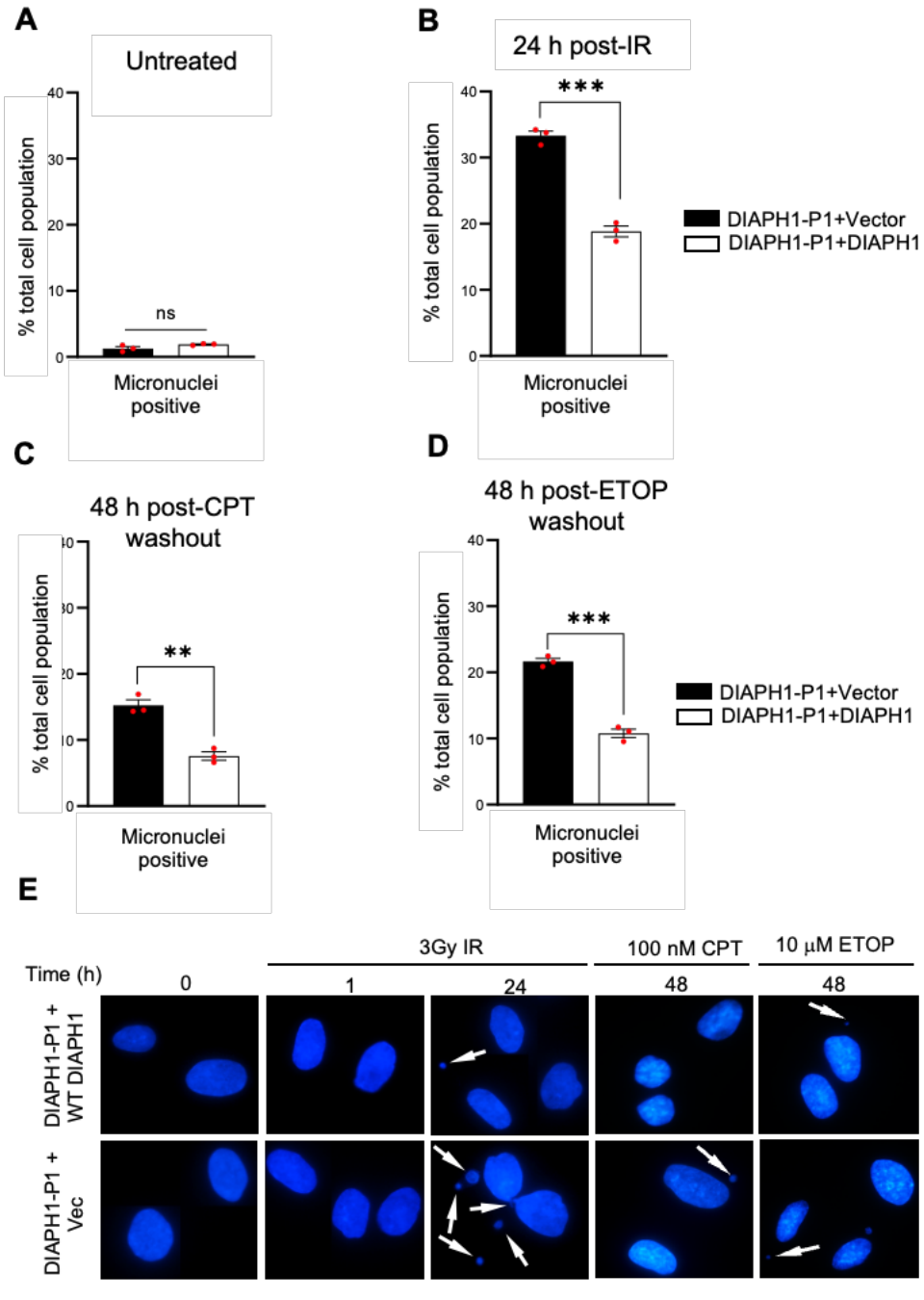


Figure 3.13 - Formation of micronuclei in P1+Vector and P1+DIAPH1 hTERT immortalised fibroblasts following exogenous DNA damage – *fibroblasts were seeded onto glass coverslips and left untreated or treated with either 3 Gy IR, 100 nM CPT for 1 h or 10 µM ETOP for 30 min. Coverslips were harvested at specific time-points post treatment and fixed with paraformaldehyde (PFA).* ***A*** *- Quantification of micronuclei in the absence of exogenous DNA damage.* ***B*** *- Quantification of micronuclei 24 h post-3 Gy IR* ***C*** *- Quantification of micronuclei 48 h post 100 nM CPT* ***D*** *- Quantification of micronuclei 48 h-post 10 µM ETOP.* ***E*** *- Representative images of DAPI positive cells from quantification in (A-D). Data from 3 independent repeats, a minimum of 500 cells counted per condition per repeat. Error bars represent standard error of the mean. * Indicates statistical significance (p=<0.05), ** indicates statistical significance (p=<0.01), *** indicates statistical significance (p=<0.001) calculated using an unpaired Students T-test. Statistical significance was calculated using GraphPad Prism software.*

3.3.5 Loss of DIAPH1 leads to an increase in chromosomal instability following exposure to DNA damaging agents

To further investigate the genomic instability caused by loss of DIAPH1, the metaphase spread technique was utilised to analyse chromosomal aberrations. This technique allows for visualisation and analysis of condensed chromosomes through brightfield microscopy (Figure 3.14A). Different types of chromosomal aberrations can be visualised and quantified, which includes chromatid or chromosome gaps or breaks, chromosome fragments, chromosome fusions and radial chromosomes (Figure 3.14B). Cells for metaphase spread analysis were prepared by treating cycling cells with colcemid, a mitotic spindle poison, for 3 h. Colcemid is used to inhibit polymerisation of the mitotic spindle, which prevents chromosomes from aligning at the nuclear axis prior during metaphase (Brinkley, Stubblefield and Hsu, 1967). This treatment produces a metaphase-like state where it is possible to observe individual chromatids using microscopy. Initially, asynchronous DIAPH1 patient P5-derived LCLs were treated with 3 μM aphidicolin (APH) 1 h prior to irradiation with 2 Gy. APH was added to prevent damaged G_1-phase and S-phase cells progressing into mitosis, which ensures that only damaged G_2-phase cells enter mitosis, as damaged G_1-phase and S-phase cells complicates this analysis. A WT LCL and an NBS patient LCL were used as positive and negative controls respectively. LCLs were incubated with APH and harvested 12 h post-irradiation. The 12 h time point is sufficient for WT cells to repair most of the damage induced by low dose IR. In untreated conditions, there was no significant difference between WT and DIAPH1 patient P5 LCLs. However, in contrast, the NBS LCL displayed a slight elevation in spontaneous chromosomal aberrations

(Figure 3.15A, C). Following treatment with IR, DIAPH1 patient P5 LCLs displayed elevated levels of chromosomal aberrations which was comparable to the NBS LCL (Figure 3.15B, C). To confirm this observation, the same phenotype was observed in HeLa cells depleted of DIAPH1, when compared to a non-targeting siRNA control (Figure 3.16A-C).

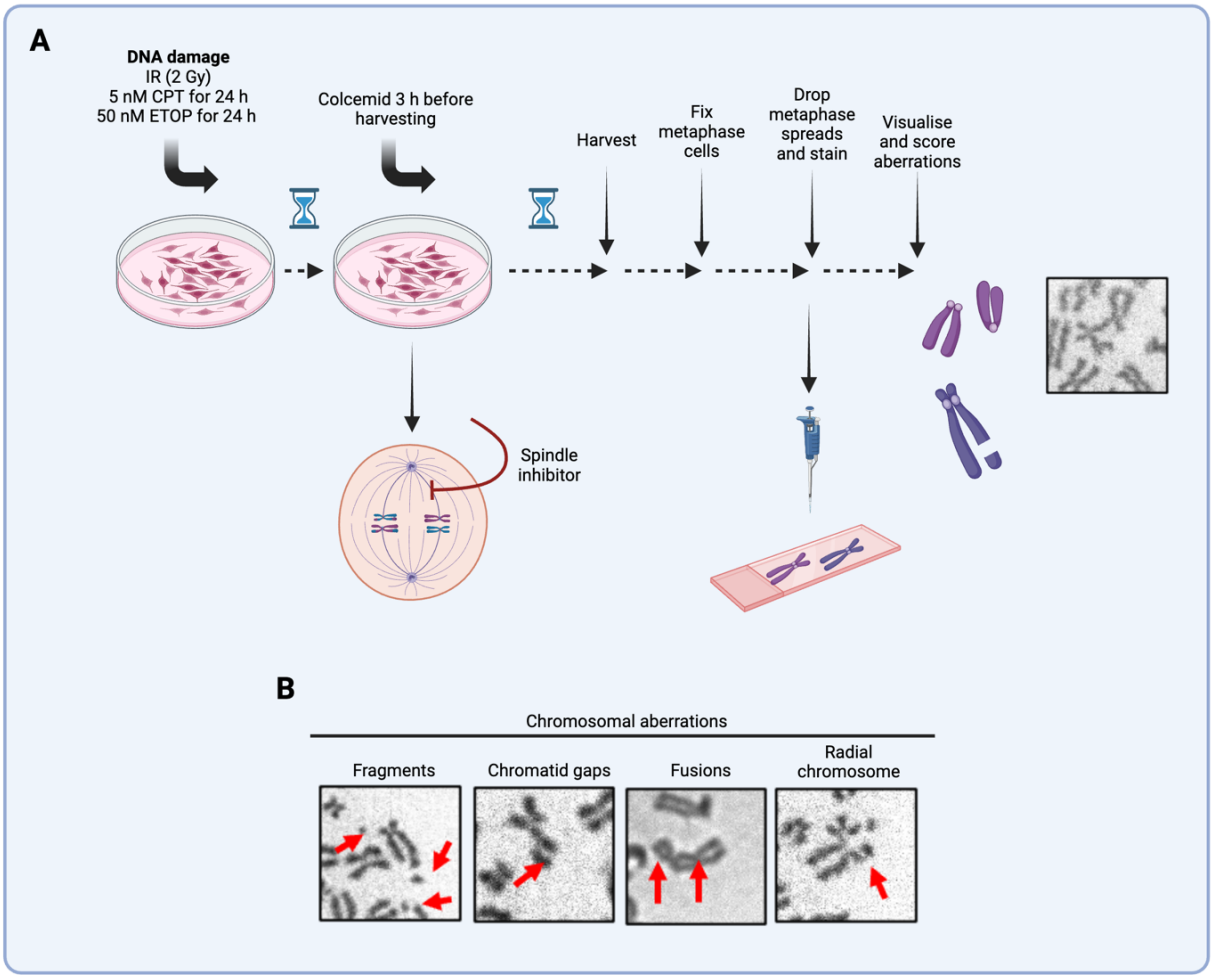


Figure 3.14 – Schematic diagram of metaphase spread analysis – A - *Asynchronous cell cultures were treated with DNA damaging agents (2 Gy ionising radiation (IR), 5 nM camptothecin (CPT) for 24 h or 50 nM etoposide (ETOP) for 24 h. 3 h prior to treatment cells were treated with colcemid to inhibit the spindle and trap cells in metaphase. Cells were harvested at 12 h post-IR and 24 h post CPT or ETOP and fixed in 3:1 ethanol: acetic acid. Fixed cells were dropped onto microscope slides from a 1 m height to spread metaphases. Chromosomes were stained with Giemsa stain and visualised by Brightfield microscopy and scored for aberrations shown.* ***B*** *– examples of chromosome aberrations analysed. Created in Biorender.com.*

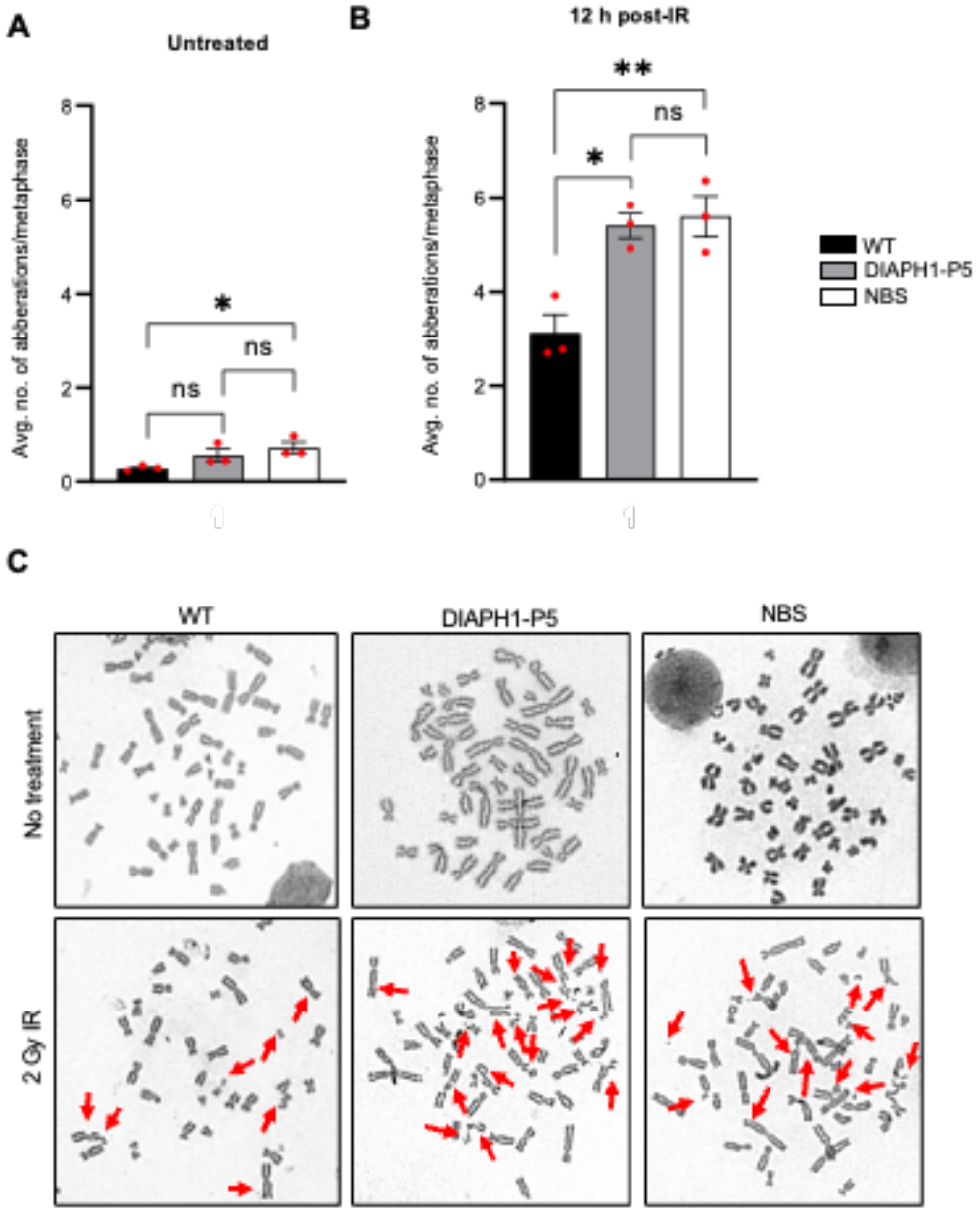


Figure 3.15 - Quantification of chromosomal aberrations in DIAPH1-P5 LCLs exposed to IR – *LCLs were cultured in flasks and 1 h prior to IR, 3 uM APH was added to cells 1 h prior to IR, followed by treatment with 2 Gy IR. Cells were then left for 12 h before harvesting. 4 h prior to harvesting, colcemid was added to the cells. Cells were then harvested at 12 h post-IR, dehydrated and fixed in 3:1 ethanol:acetic acid and dropped onto slides before staining with Giemsa.* ***A*** *- Quantification of chromosomal aberrations in the absence of exogenous DNA damage.* ***B*** *- Quantification of chromosomal aberrations 12 h post-IR treatment.* ***C*** *- Representative images metaphase spreads quantified in A-B. Data from 3 independent repeats, a minimum of 50 metaphase spreads counted per condition per repeat. Error bars represent standard error of the mean. * Indicates statistical significance (p=<0.05), ** indicates statistical significance (p=<0.01), *** indicates statistical significance (p=<0.001) calculated using an unpaired Students T-test. Statistical significance was calculated using GraphPad Prism software.*

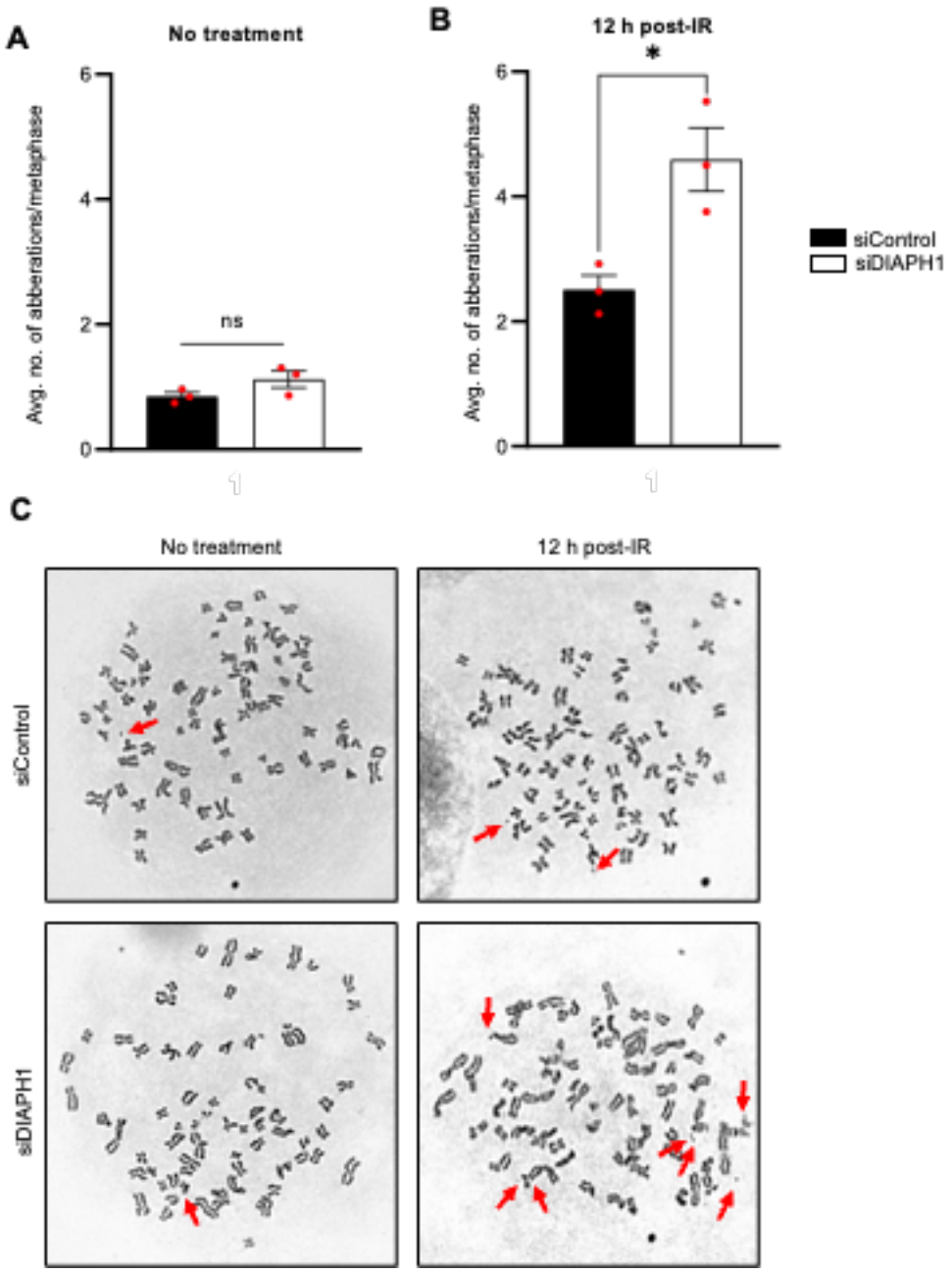


Figure 3.16 - Quantification of chromosomal aberrations in siRNA depleted HeLa cells- *Asychronous HeLa cell cultures transfected with siRNA to DIAPH1 or a non-targeting luciferase control were plated into dishes and 1 h prior to IR, 3 uM APH was added to cells followed by treatment with 2 Gy IR. Cells were then left for 12 h. 4 h prior to harvesting, colcemid was added, then cells were harvested at 12 h post-IR, dehydrated and fixed in 3:1 ethanol:acetic acid and dropped onto slides before staining with Giemsa.* ***A*** *- Quantification of chromosomal aberrations in the absence of exogenous DNA damage.* ***B*** *- Quantification of chromosomal aberrations 12 h post-IR treatment.* ***C*** *- Representative images metaphase spreads quantified in A-B. Data from 3 independent repeats, a minimum of 50 metaphase spreads counted per condition per repeat. Error bars represent standard error of the mean. * Indicates statistical significance (p=<0.05), ** indicates statistical significance (p=<0.01), *** indicates statistical significance (p=<0.001) calculated using an unpaired Students T-test. Statistical significance was calculated using GraphPad Prism software.*

Next, the aim was to assess whether treatment with CPT or ETOP lead to an increase in chromosomal aberrations when DIAPH1 is absent. To do this, asynchronous DIAPH1 patient P5 LCLs were either left untreated or cultured in the presence of 5 nM CPT or 50 nM ETOP for 24 h. 3 h prior to harvesting, colcemid was added to arrest cells in metaphase. APH was not added to the cells this time, since both CPT and ETOP induce DSBs during S-phase. Consistent with the increased chromosomal radiosensitivity observed in DIAPH1 patient P5 LCLs, these cells also displayed an elevated level of chromosomal aberrations following both CPT and ETOP treatment (Figure 3.17B-D). Importantly, these findings could be recapitulated in DIAPH1 depleted HeLa cells, further confirming that DIAPH1 loss results in defects in the repair of DNA DSBs induced by IR, CPT and ETOP (Figure 3.18A-D).

To ensure that the elevated level of chromosomal aberrations following IR, CPT and ETOP observed in P5 LCLs was caused by DIAPH1 loss, the P1+DIAPH1 and P1+Vector isogenic cell lines were used. However, due to the very low mitotic index of fibroblasts and the fact that IR induces a very potent G_2/M checkpoint response, it was not possible to assess chromosomal aberrations in response to IR in these cells. Therefore, only low dose CPT and ETOP were used to induce DSBs in the fibroblasts. Reassuringly, following treatment with CPT and ETOP, the re-expression of WT in DIAPH1 patient P1 cells was able to significantly reduce the level of unrepaired chromosome breaks observed in the empty vector complemented cells, providing further evidence that the chromosome breakage phenotype in patient-derived cell lines is specifically due to DIAPH1 loss (Figure 3.19B-D).

Collectively, the results in this section further demonstrate that loss of DIAPH1 gives rise to genomic instability, evidenced by an increase in chromosomal aberrations following DNA damage. This phenotype is rescued by complementation with DIAPH1 highlighting these observations are directly due to the loss of DIAPH1 both in the patient LCLs, DIAPH1 depleted HeLa cells and P1+Vector fibroblasts. These data strongly support a role for DIAPH1 in maintaining genome/chromosomal stability.

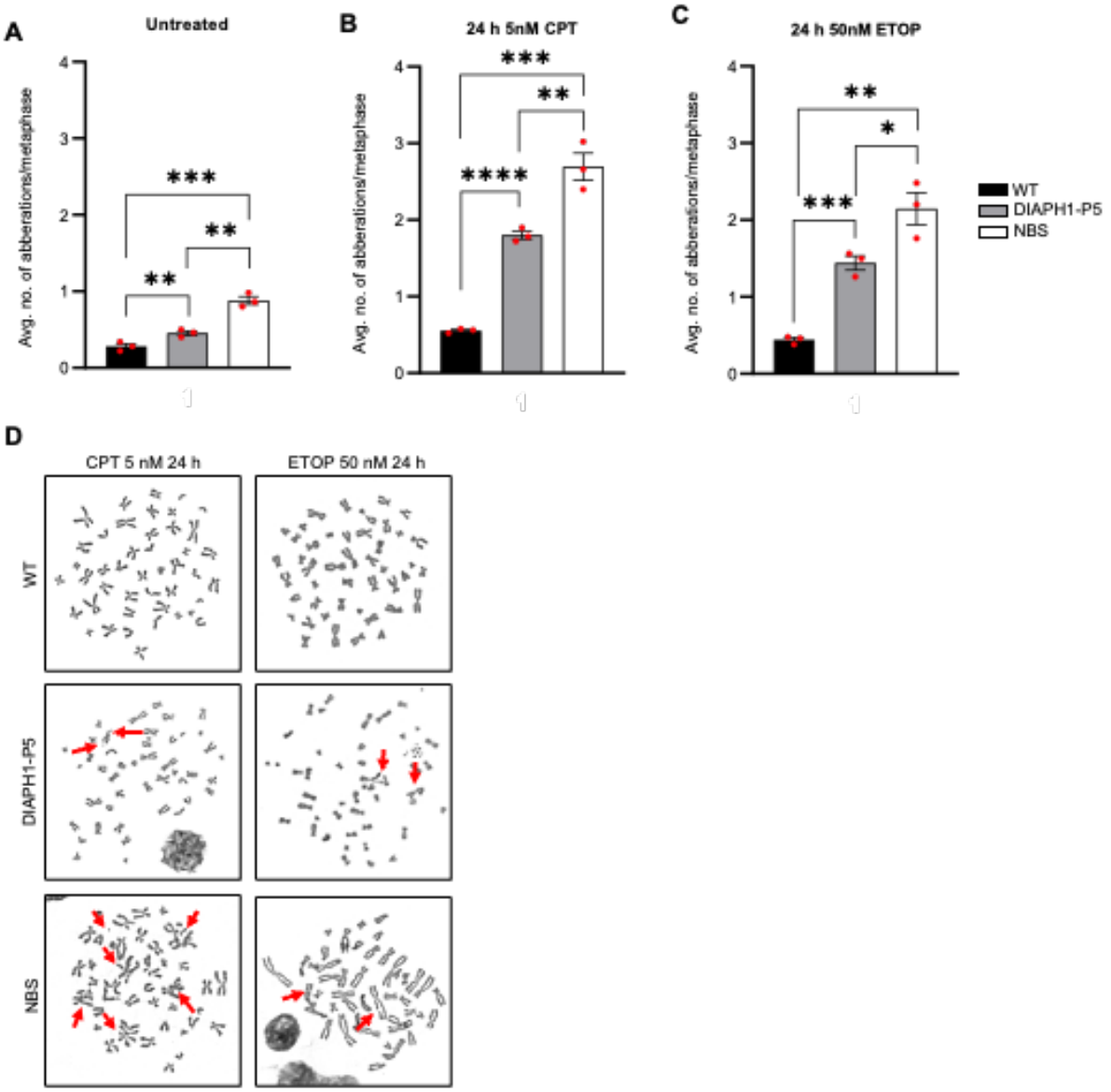


Figure 3.17 - Quantification of chromosomal aberrations in DIAPH1-P5 LCLs exposed to DNA damage– *LCLs were cultured in flasks and either left untreated or treated with 5 nM camptothecin (CPT) or 50 nM etoposide (ETOP) for 24 h. 3 h prior to harvesting, colcemid was added, then cells were harvested at 24 h post-CPT/ETOP, dehydrated and fixed in 3:1 ethanol:acetic acid and dropped onto slides before staining with Giemsa.* ***A*** *- Quantification of chromosomal aberrations in the absence of exogenous DNA damage.* ***B*** *- Quantification of chromosomal aberrations 24 h post-CPT.* ***C*** *- Quantification of chromosomal aberrations 24 h post-ETOP.* ***D*** *- Representative images metaphase spreads quantified in A-C. Data from 3 independent repeats, a minimum of 50 metaphase spreads counted per condition per repeat. Error bars represent standard error of the mean. * Indicates statistical significance (p=<0.05), ** indicates statistical significance (p=<0.01), *** indicates statistical significance (p=<0.001) calculated using an unpaired Students T-test. Statistical significance was calculated using GraphPad Prism software.*

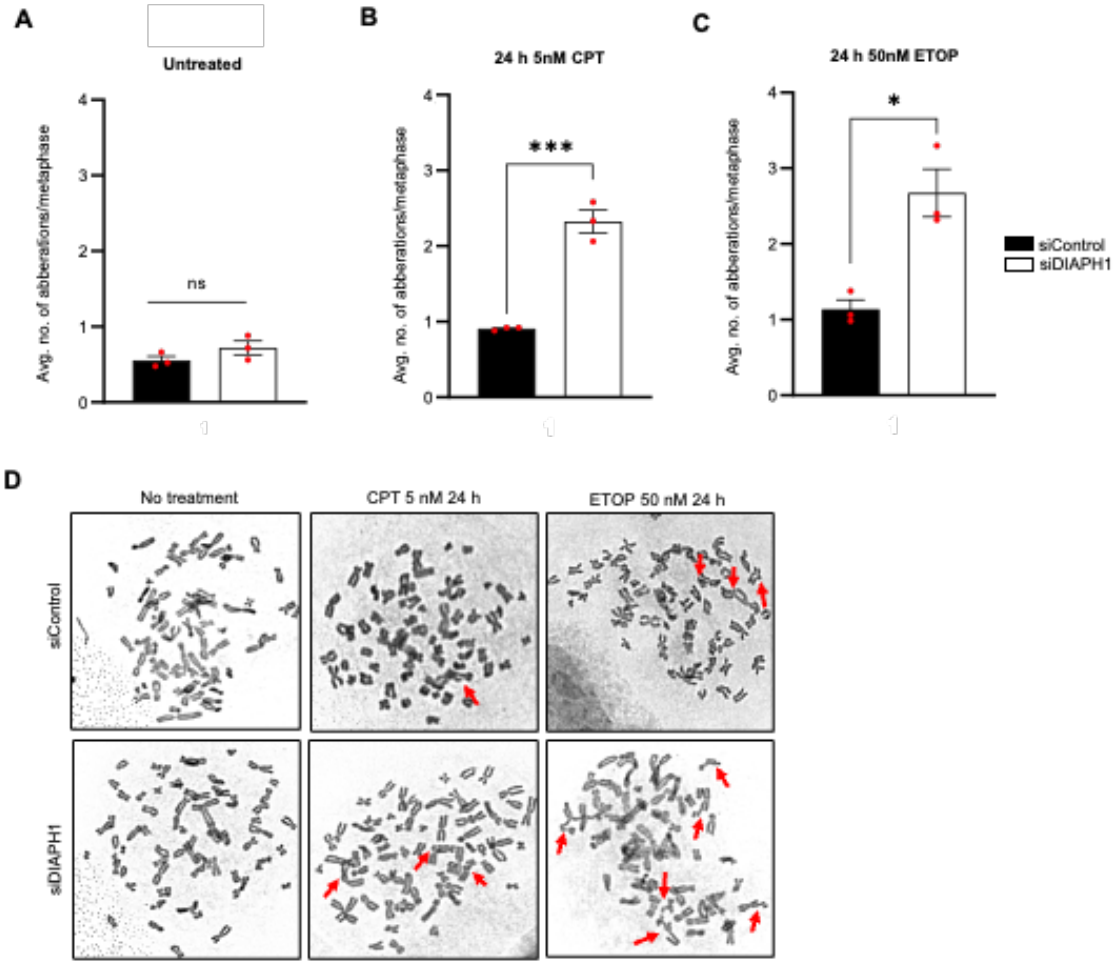


Figure 3.18 - Quantification of chromosomal aberrations in siRNA depleted HeLa cells*- Asychronous HeLa cell cultures transfected with siRNA to DIAPH1 or a non-targeting luciferase control were plated into dishes and either left untreated or treated with 5 nM camptothecin (CPT) or 50 nM etoposide (ETOP) for 24 h. 3 h prior to harvesting, colcemid was added, then cells were harvested at 24 h post-CPT/ETOP, dehydrated and fixed in 3:1 ethanol:acetic acid and dropped onto slides before staining with Giemsa.* ***A*** *- Quantification of chromosomal aberrations in the absence of exogenous DNA damage.* ***B*** *- Quantification of chromosomal aberrations 24 h post-CPT.* ***C*** *- Quantification of chromosomal aberrations 24 h post-ETOP.* ***D*** *- Representative images metaphase spreads quantified in A-C. Data from 3 independent repeats, a minimum of 50 metaphase spreads counted per condition per repeat. Error bars represent standard error of the mean. * Indicates statistical significance (p=<0.05), ** indicates statistical significance (p=<0.01), *** indicates statistical significance (p=<0.001) calculated using an unpaired Students T-test. Statistical significance was calculated using GraphPad Prism software.*

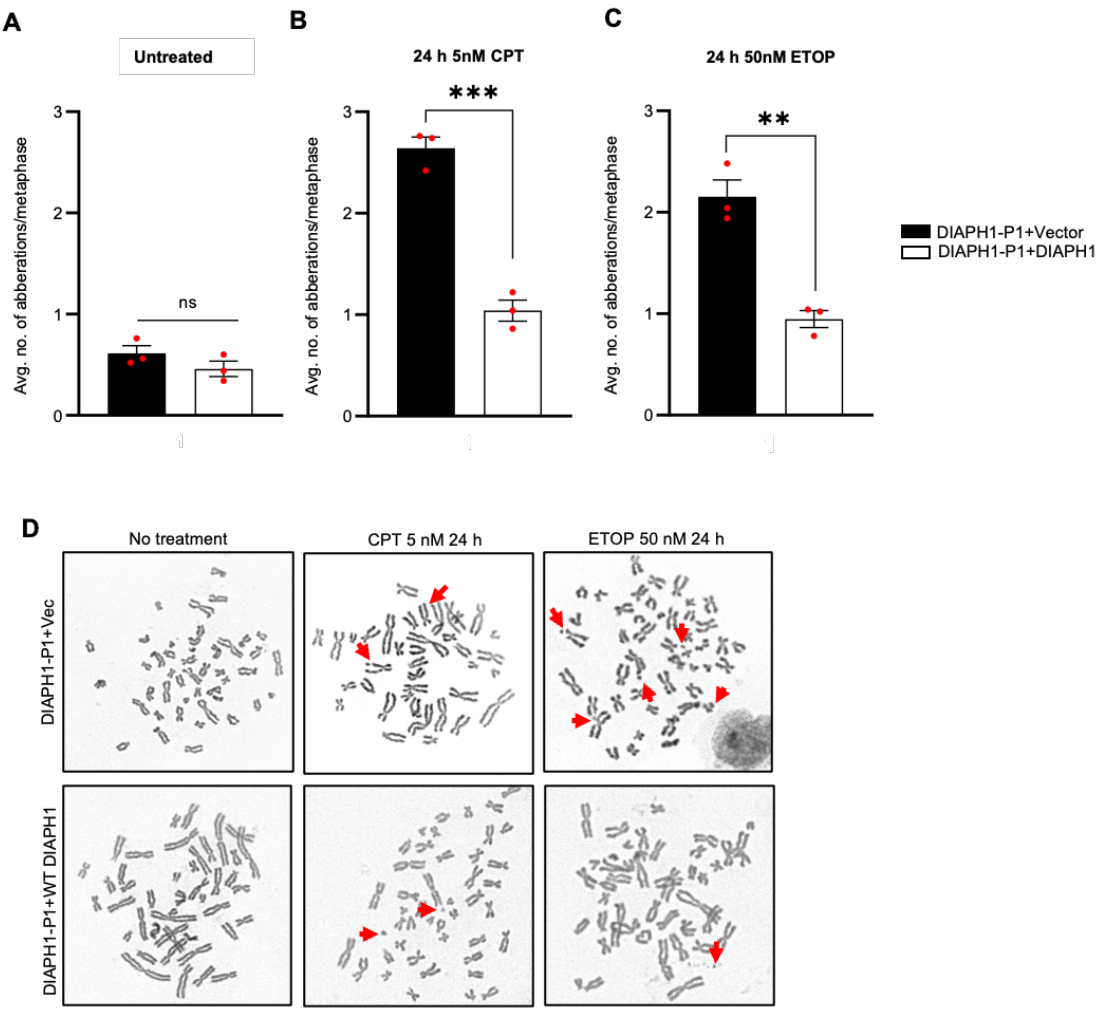


Figure 3.19 - Quantification of chromosomal aberrations in P1+Vector and P1+DIAPH1 hTERT immortalised fibroblasts following exogenous DNA damage – *Asychronous fibroblasts were cultured in flasks and either left untreated or treated with 5 nM camptothecin (CPT) or 50 nM etoposide (ETOP) for 24 h. 3 h prior to harvesting, colcemid was added, then cells were harvested at 24 h post-CPT/ETOP, dehydrated and fixed in 3:1 ethanol:acetic acid and dropped onto slides before staining with Giemsa.* ***A*** *- Quantification of chromosomal aberrations in the absence of exogenous DNA damage.* ***B*** *- Quantification of chromosomal aberrations 24 h post-CPT.* ***C*** *- Quantification of chromosomal aberrations 24 h post-ETOP.* ***D*** *- Representative images metaphase spreads quantified in A-C. Data from 3 independent repeats, a minimum of 50 metaphase spreads counted per condition per repeat. Error bars represent standard error of the mean. * Indicates statistical significance (p=<0.05), ** indicates statistical significance (p=<0.01), *** indicates statistical significance (p=<0.001) calculated using an unpaired Students T-test. Statistical significance was calculated using GraphPad Prism software.*

3.4 Concluding remarks

The data in this chapter demonstrates that homozygous variants in *DIAPH1* in our cohort of 28 patients give rise to a range of clinical deficits that overlap with the DNA DSB repair deficiency disorder, Nijmegen Breakage Syndrome (NBS). These include microcephaly and growth retardation, immunodeficiency, and a predisposition for developing lymphoid tumours. These clinical similarities indicate that DIAPH1 has a role in maintaining genome stability and could function together with the MRN complex in promoting DSB repair. Interestingly, the patients also exhibited clinical features not observed with NBS patients, such as seizures and cortical blindness. This suggests that DIAPH1 has additional roles outside of a possible role in DNA repair.

Whilst there is some variation in the clinical phenotypes of the patients within our cohort, it should be noted that the majority of patients, apart from P12, have inherited homozygous loss-of-function mutations and for those patients where cell lines were available this resulted in a complete lack of DIAPH1 protein expression. Therefore, it is not clear to what extent the clinical phenotype will vary when some mutant DIAPH1 protein is expressed. Interestingly, patient P16 in this cohort was the only individual to inherit a homozygous missense variant (p.Leu1004His), which is located within the FH2 actin nucleating domain of DIAPH1. Notably, this patient did exhibit a milder phenotype, i.e. they displayed visual impairment, seizures, dysmorphic facial features and delayed motor development, they did not exhibit microcephaly or recurrent infections. Unfortunately, due to cell lines from this patient being unavailable for testing, the protein stability of DIAPH1 and the cellular phenotype could not be investigated. However, it is tempting to speculate that the DNA repair deficiency present in cells

expressing the mutant p.Leu1004His DIAPH1 protein might be milder than that observed in cells completely lacking DIAPH1 protein expression.

In contrast to the patients in our cohort, heterozygous variants identified in *DIAPH1* tend to result in a constitutively active DIAPH1 protein, which gives rise to an entirely different clinical phenotype. These patients exhibit sensorineural hearing loss and thrombocytopenia (Lynch *et al.*, 1997; Stritt *et al.*, 2016; Ueyama, Ninoyu, S. Nishio, *et al.*, 2016). Why the loss of DIAPH1 versus it's hyper-activation affect neurodevelopment so differently is not clear. Given the importance of DIAPH1 during neurodevelopment, it is evident that its absence is a lot more detrimental to this process than the presence of a constitutively active protein. Conversely, with respect to development and function of the auditory system, overactive DIAPH1 is more deleterious than a total loss of the protein, since all bar one of the patients within our cohort did not exhibit any hearing loss. Again, the underlying reasons for this are not known, but could be explained by functional redundancy and compensatory mechanisms from other Diaphanous-related formins, such as from DIAPH3. Interestingly, a homozygous point mutation that hyperactivates DIAPH3 has been identified in 2 individuals with auditory neuropathy (Schoen *et al.*, 2010). This suggests that both DIAPH1 and DIAPH3 both have important functions in the auditory system and that dominant activating mutations could block the function of both DIAPH1 and DIAPH3, whereas individual loss of either DIAPH1 or DIAPH3 can be compensated for by the other, at least in the auditory system. Notably, whilst microcephaly has not been associated with *DIAPH3* mutations in humans, a complete loss of *Diaph3* in mice gives rise to microcephaly, suggesting both proteins are required for neurodevelopment in

mammals (Damiani *et al.*, 2016; Labat-de-Hoz and Alonso, 2021; Lau *et al.*, 2021). Thus, in different tissues both DIAPH1 and DIAPH3 may have functional redundancy under certain circumstances, providing a possible explanation for the distinct clinical phenotypes between homozygous loss of DIAPH1 and heterozygous constitutively active DIAPH1.

Since 23/28 patients within our cohort exhibit microcephaly, this highlights the importance of DIAPH1 during neurodevelopment. Microcephaly can either arise during foetal development (primary microcephaly) or develop postnatally (secondary microcephaly) and is caused by any genetic or acquired defect that slows the cell cycle (Passemard, Kaindl and Verloes, 2013). As such, microcephaly has been linked with defects in a diverse array of cellular processes such as DNA replication, DNA repair, cell cycle checkpoint activation, transcription and mitosis (Jean, Stuart and Tarailo-Graovac, 2020). Since a balance between DNA replication, cell cycle progression and the orientation of mitotic division are critically linked to neuronal stem cell renewal and differentiation, any perturbations that affect this balance during neurogenesis result in fewer neurons. This may occur via an increase in neuronal cell death, an imbalance between neuronal progenitor stem cell renewal and differentiation, abnormal differentiation and/or a reduction in the proliferative capacity of the neuronal stem cells. In addition to this, the brain is extremely sensitive to DNA damage, due to the rapid rate of proliferation that occurs *in utero* and during early childhood. Any genetic/epigenetic event that increases genomic instability during this time can be extremely detrimental in terms of producing enough different types of neuronal cells to allow the brain to develop properly (Schär, 2001; Ribeiro *et al.*, 2023).

Given the extent of the neurodevelopmental defects present in our DIAPH1 mutant patient cohort and the overlap with other syndromes known to be caused by a DNA DSB repair defect e.g. NBS, it was reasonable to assume that DIAPH1 plays a role in DNA repair and that loss of this function may contribute the onset of the neurodevelopment abnormalities exhibited by the affected patients. Notably, cells from patients with mutations in the MRN complex exhibit defects in the ability to activate ATM in response to DSBs, which has been proposed to contribute to the underlying DSB repair defect (Uziel *et al.*, 2003). Interestingly however, despite the clinical overlap with NBS, no gross defects in the activation of the ATM-dependent DNA damage response pathway following treatment with DSB-inducing agents IR, CPT and ETOP were identified in patient-derived cell lines lacking DIAPH1. In addition, no gross defects in ATR-dependent signalling after inducing replication stress with HU were observed in cells lacking DIAPH1. This is in stark contrast to cells lacking NBS1, which have also been reported to exhibit defects in activating ATR in response to replication stress (Li *et al.*, 2012). Notably however, cells lacking DIAPH1 do display elevated levels of spontaneous γ-H2AX, which is usually caused by problems during DNA replication. Consistent with this, cells lacking DIAPH1 did exhibit a reduction in HU-induced RPA2 phosphorylation when compared to a healthy control cell line. Therefore, whilst DIAPH1 does not play a major role in activating ATR in response to replication stress, this observation may suggest that DIAPH1 could have a role in signalling replication damage.

Whilst the data presented within this chapter strongly support a role for DIAPH1 in regulating DSB repair, the analysis of genotoxin-induced micronuclei and chromosomal aberrations do not offer much insight into the exact mechanism of how this arises. What is clear however is that these markers of genome instability were elevated following treatment with all three DSB inducing agents used, which indicates DIAPH1 may be required to repair DSBs induced by IR, CPT and ETOP. Notably, IR- and ETOP-induced DSBs can be repaired via NHEJ and HR, but CPT-induced DSBs can only be repaired by HR. This implies DIAPH1 is most likely required for HR repair. As DIAPH1 is an actin nucleating factor, this would be consistent with previous reports documenting that actin, the ARP2/3 complex and its activator WASP are required for HR (Caridi *et al.*, 2018; Schrank *et al.*, 2018). Despite this, there is preliminary evidence that nuclear F-actin also forms during NHEJ-dependent DSB repair (Andrin *et al.*, 2012). As such, it is not clear from this data whether DIAPH1 is required for both NHEJ- and HR-dependent DSB repair and that its role in either pathway is dictated by the type of DNA break, the chromatin context of the DSB and/or the stage of the cell cycle within which the DSB occurs.

Taken together, whilst DIAPH1 is not required for activation of the ATM- and ATR-dependent DNA damage response, the data presented in this chapter provides evidence that loss of DIAPH1 results in increased genome instability following the induction of DSBs. The next chapter focusses on addressing which DSB repair pathway is regulated by DIAPH1 and the mechanism with which it regulates DNA repair.

Chapter 4: Characterisation of the role of DIAPH1 in double strand break repair

4.0 Results

4.1 Introduction

Data presented in Chapter 3 showed that homozygous frameshift variants in *DIAPH1* lead to a loss of DIAPH1 protein expression in patient-derived cell lines. Subsequently, this loss of DIAPH1 leads to an increase in genomic instability following treatment with agents that induce DSBs. The increase in markers of genome instability, namely an elevated and prolonged γ-H2AX response, increased micronuclei and higher levels of chromosomal aberrations after treatment with IR, CPT and ETOP, indicates that loss of DIAPH1 leads to defects in the repair of DSBs. These three agents induce DSBs in different ways and the repair pathways favoured in each context differ (Chapter 3, Figure 3.1). DIAPH1 has not been previously associated with DSB repair and these data strongly suggest that it plays an important role in this process following damage induced by all three genotoxins. Excitingly, this provides evidence that loss of DIAPH1 gives rise to a novel double strand break repair syndrome.

DIAPH1 functions as a nucleator of linear actin filaments in the cytoplasm (Labat-de-Hoz and Alonso, 2021). This function is important for several cellular processes including cell migration, adhesion and intracellular transport. Recently, a role for actin in DSB repair is emerging, and it has been shown to play a role in both Non-homologous end-joining (NHEJ) and Homologous recombination (HR) (Andrin *et al.*, 2012; Caridi *et al.*, 2018; Huang, Zhang and Park, 2022). In NHEJ, Andrin et al showed that a mutant of actin is unable to form filaments, and chemical inhibition of actin

filament formation, affected the retention of Ku80 at DSB ends, but not its recruitment to DSB sites (Andrin *et al.*, 2012). In human cells, it has been proposed that actin facilitates clustering of euchromatic DSBs, promotes DNA end resection and the movement of heterochromatic DSBs to the nuclear periphery (Caridi *et al.*, 2018; Schrank *et al.*, 2018; Nieminuszczy *et al.*, 2023; Palumbieri *et al.*, 2023). Most of the studies examining actin in DSB repair have used chemical inhibitors that interfere with polymerisation, making it difficult to study the impact of the loss of individual factors (Andrin *et al.*, 2012; Pfitzer *et al.*, 2019) . However, recently it has been shown that these processes are dependent on the ARP2/3 complex, WASP and myosins I and V (Caridi *et al.*, 2018; Schrank *et al.*, 2018). However, DIAPH1 has not been implicated in these processes and one study even ruled out a role for DIAPH1 in actin-dependent DSB repair (Belin *et al.*, 2013).

4.2 Aims of this chapter

The data included in Chapter 3 indicates that DIAPH1 is required for DSB repair, as cells derived from patients harbouring variants in *DIAPH1* displayed increased genome instability following DSB induction. To assess this more thoroughly, the aim of this chapter was to investigate how loss of DIAPH1 impacts DSB repair efficiency. To do this, patient-derived cell lines were utilised to assess the impact of DIAPH1 loss on DSB repair kinetics and if complementation with WT-DIAPH1 could rescue the phenotype. Additionally, the next aim was to recapitulate the patient phenotype by depleting DIAPH1 in HeLa cells. The final aims of this chapter was to investigate the recruitment of repair proteins to DSB sites in P1+Vector and P1+DIAPH1 isogenic cell

lines and analysis of DNA end resection following DSB in cells depleted of DIAPH1 with siRNA.

4.3 Results

4.3.1 Analysis of γ-H2AX / 53BP1 foci formation following DNA damage in DIAPH1 patient-derived cells

To investigate the cellular response to DSBs in the absence of DIAPH1, immunofluorescence (IF) techniques were carried out without treatment, or following exposure to IR, in patient-derived hTERT immortalised fibroblasts. Fibroblast cell lines derived from a healthy wildtype (WT) control cell line and an NBS cell line were used as a negative and positive experimental control. Fibroblasts were either left untreated or exposed to 3 Gy IR and harvested at 1 h and 24 h post-IR then stained with antibodies to γ-H2AX and 53BP1 as markers of DSBs (Figure 4.1).

In unperturbed conditions, there was no significant difference in the number of γ-H2AX /53BP1 foci between WT and the DIAPH1 patient fibroblasts (Figure 4.2A, D). At 1 h post-IR, all cell lines had 100% of cells with >10 γ-H2AX/53BP1 foci (Figure 4.2B, D). However, at 24 h post-IR, when compared to WT, the DIAPH1 patient cohort had statistically elevated levels of cells with >10 γ-H2AX/53BP1 foci, indicating loss of DIAPH1 leads to unresolved DSBs at late-time points post-IR (Figure 4.2C-D). Notably, this was not as elevated as the NBS patient cell line. To confirm this finding, the same experimental technique with the same time-points post-IR was carried out in HeLa cells

depleted of DIAPH1 with siRNA along with a non-targeting luciferase control cell line (Figure 4.3). Similarly, in unperturbed conditions and at 1 h post-IR, there was no difference between HeLa cells depleted of DIAPH1 and the control (Figure 4.3 A-B, D). However, at 24 h post-IR, DIAPH1 depleted HeLa cells had a significantly elevated number of cells with >10 γ-H2AX/53BP1 at 24 h when compared to control (Figure 4.3C-D). To confirm this effect was specifically due to DIAPH1 loss, analysis of γ-H2AX/53BP1 foci was performed in P1+DIAPH1 and P1+Vector fibroblasts (Figure 4.4A-D). Reassuringly, at 24 h post-IR, P1+Vector had elevated levels of >10 γ-H2AX /53BP1 foci when compared to P1+DIAPH1 fibroblasts (Figure 4.4C-D). This finding confirms that the DSB repair defect is specifically due to DIAPH1 loss as it can be rescued by complementation with WT DIAPH1 protein.

Next, to investigate if this effect could be recapitulated with other DSB inducing agents, the same experimental technique was performed in the presence of CPT or ETOP. First, DIAPH1 depleted HeLa cells, as well as a non-targeting luciferase control were treated with either 100 nM CPT for 1 h or 10 μM ETOP for 30 min (Figure 4.5A-F). The drugs were washed out then cells were permeabilised and fixed in 3.6% PFA at 1 h and 24 h post-treatment. Strikingly, in response to both CPT and ETOP, DIAPH1 depleted HeLa cells displayed a statistically significant increase in cells with >10 γ-H2AX/53BP1 at 24 h post-treatment (Figure 4.5C, E, F). Showing that loss of DIAPH1 results in unresolved DSBs at late-time points following DSBs induced by not only IR, but also CPT and ETOP. To confirm these findings, the same experiment was performed in P1+Vector and P1+DIAPH1 fibroblasts (Figure 4.6). P1+Vector cells also

displayed elevated γ-H2AX/53BP1 foci at 24 h after both CPT and ETOP, when compared with P1+DIAPH1 (Figure 4.6C, E, G, F)

Taken together, the results of this section provide evidence that loss of DIAPH1 gives rise to genome instability, which may be due to unresolved DSBs. Therefore suggesting that DIAPH1 may be required to promote DSB repair. However, the exact role for DIAPH1 in this process is unclear.

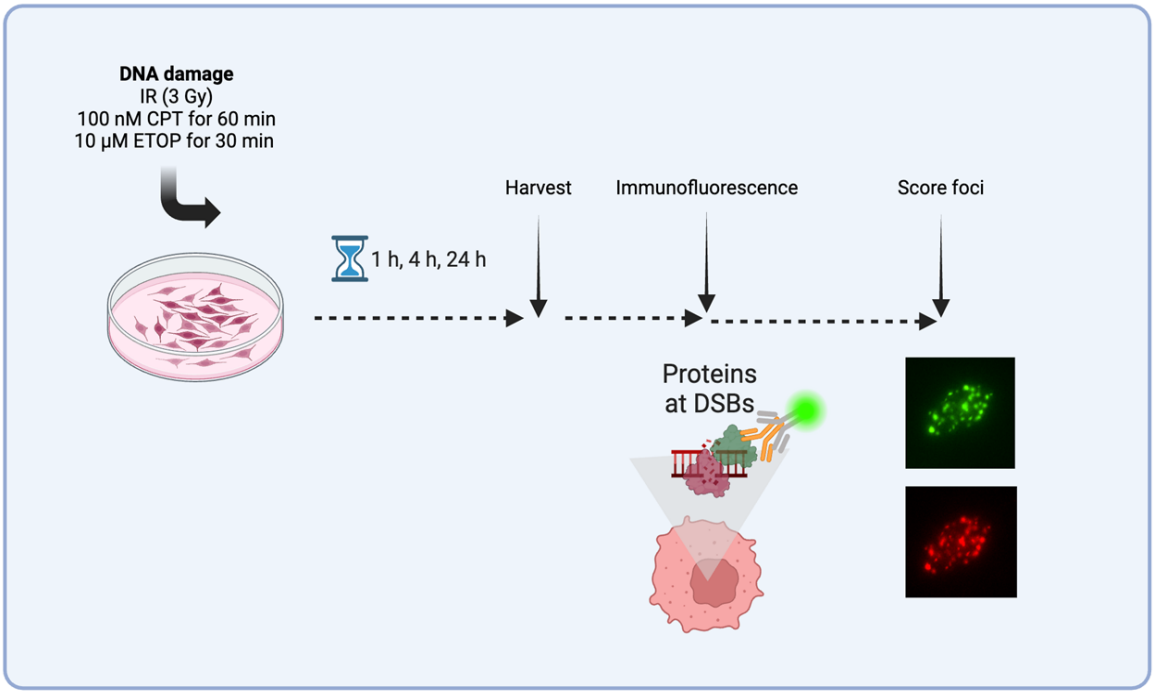


Figure 4.1 – Schematic representation of immunofluorescence techniques – *For all immunofluorescence (IF) based techniques, cells were seeded onto glass coverslips in dishes and cultured for at least 24 h. On day of treatment, cells were subject to DNA damage including ionising radiation (IR), camptothecin (CPT) and etoposide (ETOP). Cells were then harvested and fixed in 3.6 % PFA at specific time points post treatment, examples including 1 h, 4 h and 24 h post-treatment. Cells were then incubated with specific antibodies raised against targets of interest and incubated again with a secondary antibody coupled to a fluorophore (either red or green). The fluorescence signal was then visualised by fluorescence microscopy and analysis performed as appropriate. Created with Biorender.com.*

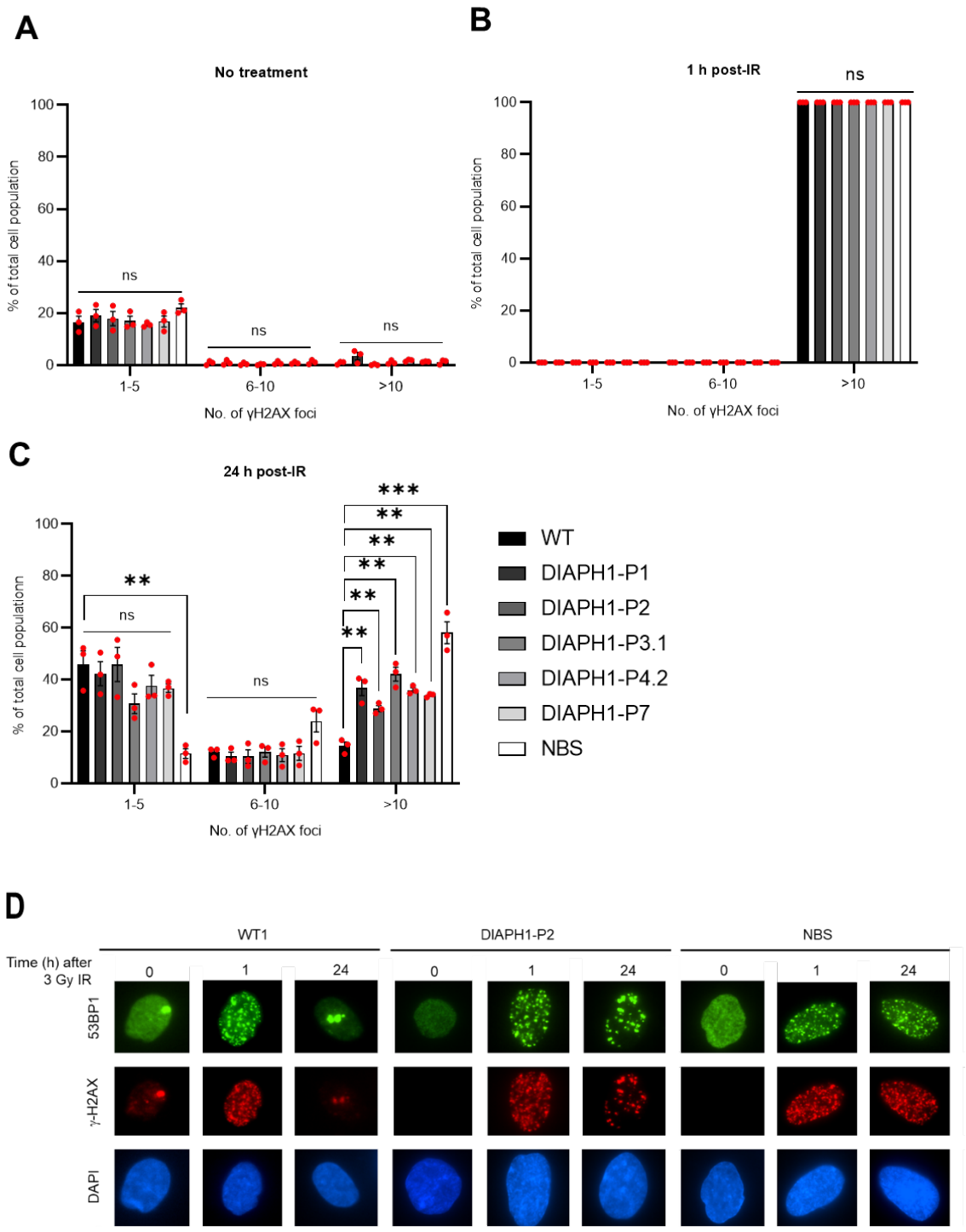


Figure 4.2 - Quantification of γ-H2AX/53BP1 foci formation in DIAPH1-P1, P2, P3-1, P4-2, P5 hTERT immortalised fibroblasts following exogenous DNA damage – *Fibroblasts were seeded onto glass coverslips and left untreated or treated with 3 Gy IR. Coverslips were harvested at specific time-points post treatment (1 h, 24 h) and fixed with 3.6 % paraformaldehyde (PFA).* ***A*** *- Quantification of γ-H2AX/53BP1 foci in the absence of exogenous DNA damage.* ***B*** *- Quantification of γ-H2AX/53BP1 foci 1 h post-3 Gy IR.* ***C*** *- Quantification of γ-H2AX/53BP1 foci 24 h post-3 Gy IR.* ***D*** *- Representative images of DAPI positive nuclei from quantification in (A-C). Data from 3 independent repeats, a minimum of 500 cells counted per condition per repeat. Error bars represent standard error of the mean. * Indicates statistical significance (p=<0.05), ** indicates statistical significance (p=<0.01), *** indicates statistical significance (p=<0.001) calculated using an unpaired Students T-test. Statistical significance was calculated using GraphPad Prism software.*

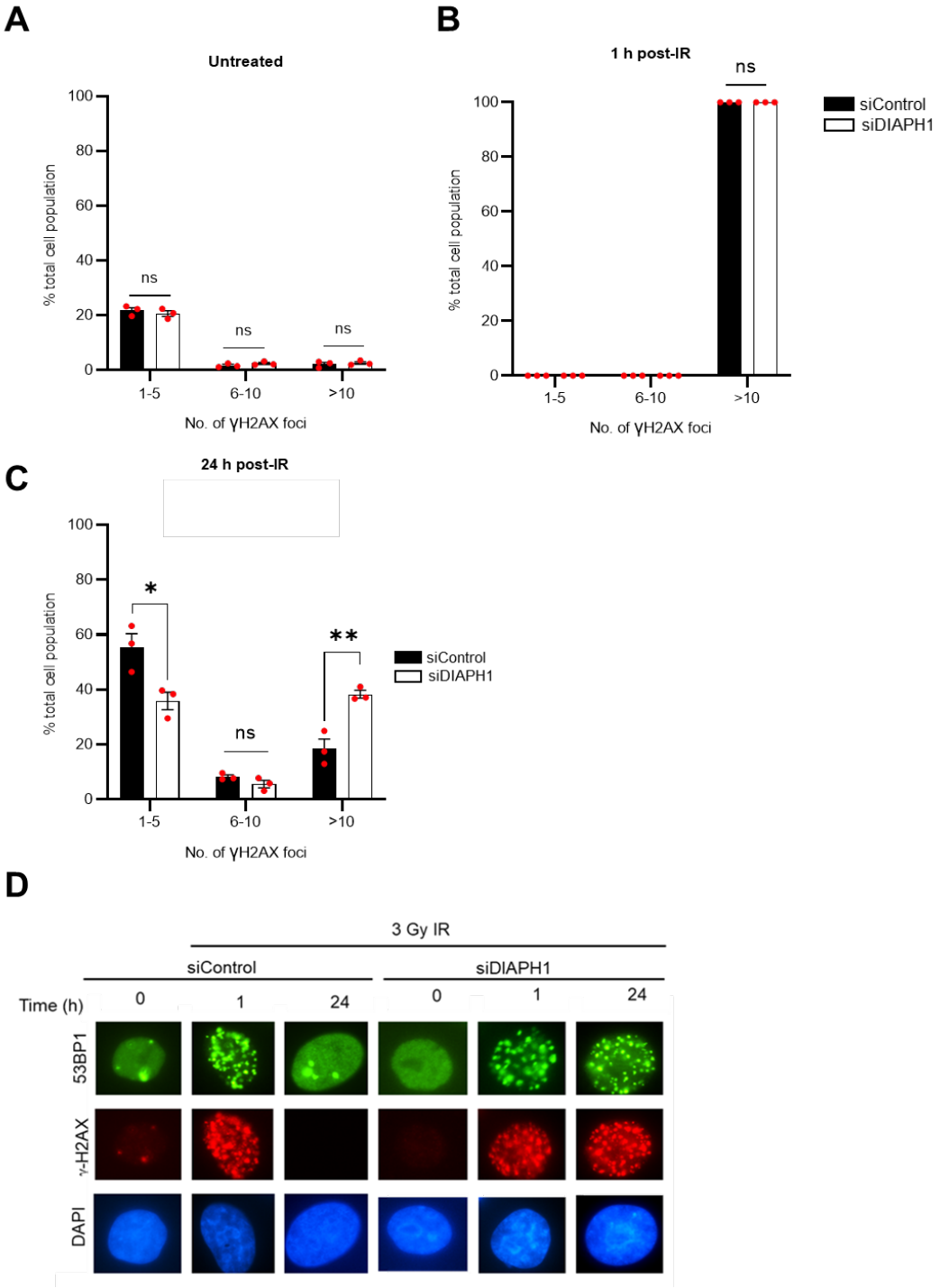


Figure 4.3 - Quantification of γ-H2AX/53BP1 foci formation in siRNA mediated DIAPH1 depleted HeLa cells following exogenous DNA damage – *HeLa cells were subject to siRNA depletion of either non-targeting luciferase control or DIAPH1 and were seeded onto glass coverslips and left untreated or treated with 3 Gy IR. Coverslips were harvested at specific time-points post treatment (1 h, 24 h) and fixed with 3.6 % paraformaldehyde (PFA).* ***A*** *- Quantification of γ-H2AX/53BP1 foci in the absence of exogenous DNA damage.* ***B*** *- Quantification of γ-H2AX/53BP1 foci 1 h post-3 Gy IR.* ***C*** *- Quantification of γ-H2AX/53BP1 foci 24 h post-3 Gy IR.* ***D*** *- Representative images of DAPI positive nuclei from quantification in (A-C). Data from 3 independent repeats, a minimum of 500 cells counted per condition per repeat. Error bars represent standard error of the mean. * Indicates statistical significance (p=<0.05), ** indicates statistical significance (p=<0.01), *** indicates statistical significance (p=<0.001) calculated using an unpaired Students T-test. Statistical significance was calculated using GraphPad Prism software.*

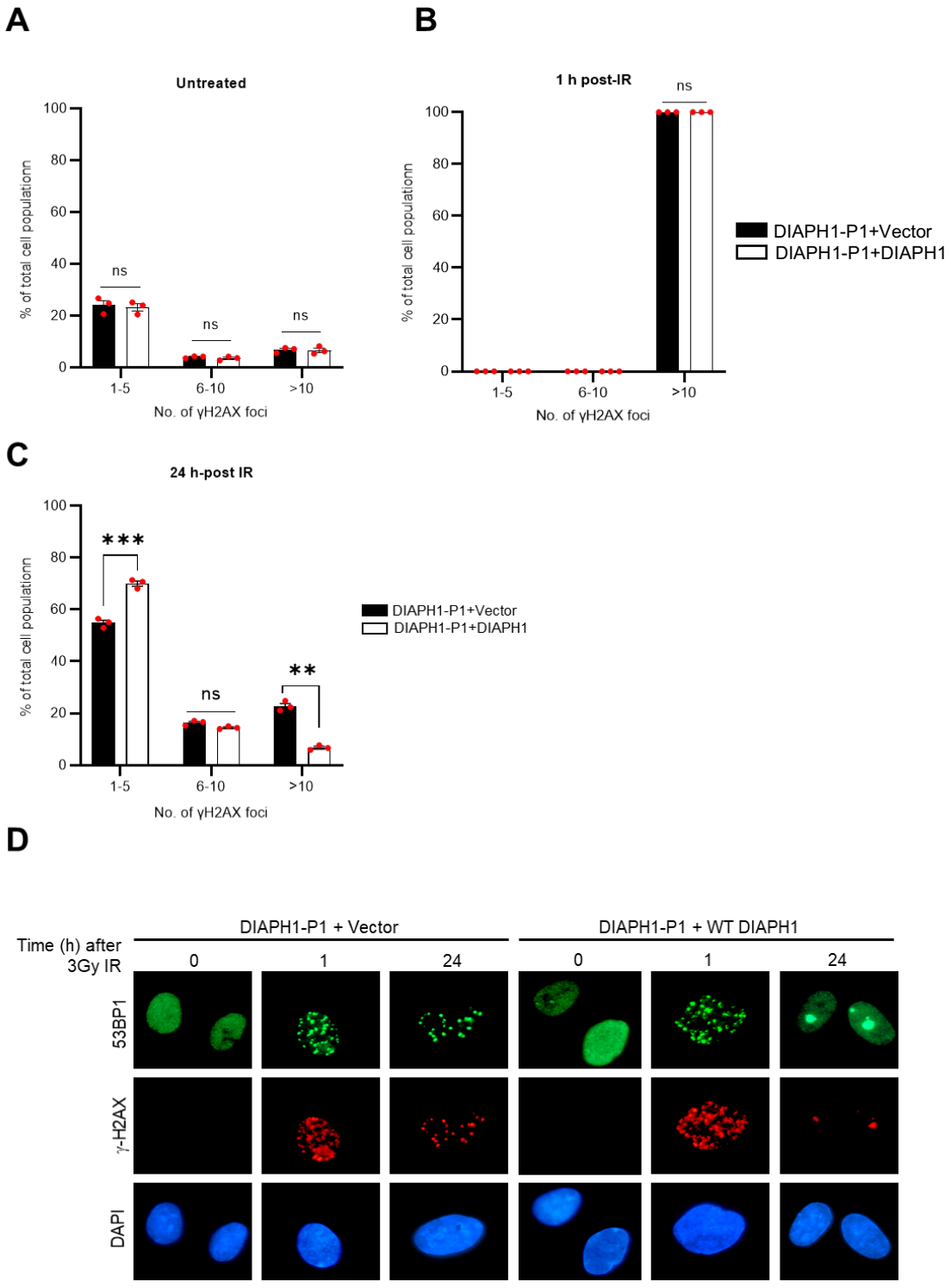


Figure 4.4 - Quantification of γ-H2AX/53BP1 foci formation in P1+Vector and P1+DIAPH1 fibroblasts following exogenous DNA damage *– P1+Vector and P1+DIAPH1 fibroblast cell lines were seeded onto glass coverslips and left untreated or treated with 3 Gy IR. Coverslips were harvested at specific time-points post treatment (1 h, 24 h) and fixed with 3.6 % paraformaldehyde (PFA).* ***A*** *- Quantification of γ-H2AX/53BP1 foci in the absence of exogenous DNA damage.* ***B*** *- Quantification of γ-H2AX/53BP1 1 h post-3 Gy IR.* ***C*** *- Quantification of γ-H2AX/53BP1 foci 24 h post-3 Gy IR.* ***D*** *- Representative images of DAPI positive nuclei from quantification in (A-C). Data from 3 independent repeats, a minimum of 500 cells counted per condition per repeat. Error bars represent standard error of the mean. * Indicates statistical significance (p=<0.05), ** indicates statistical significance (p=<0.01), *** indicates statistical significance (p=<0.001) calculated using an unpaired Students T-test. Statistical significance was calculated using GraphPad Prism software.*

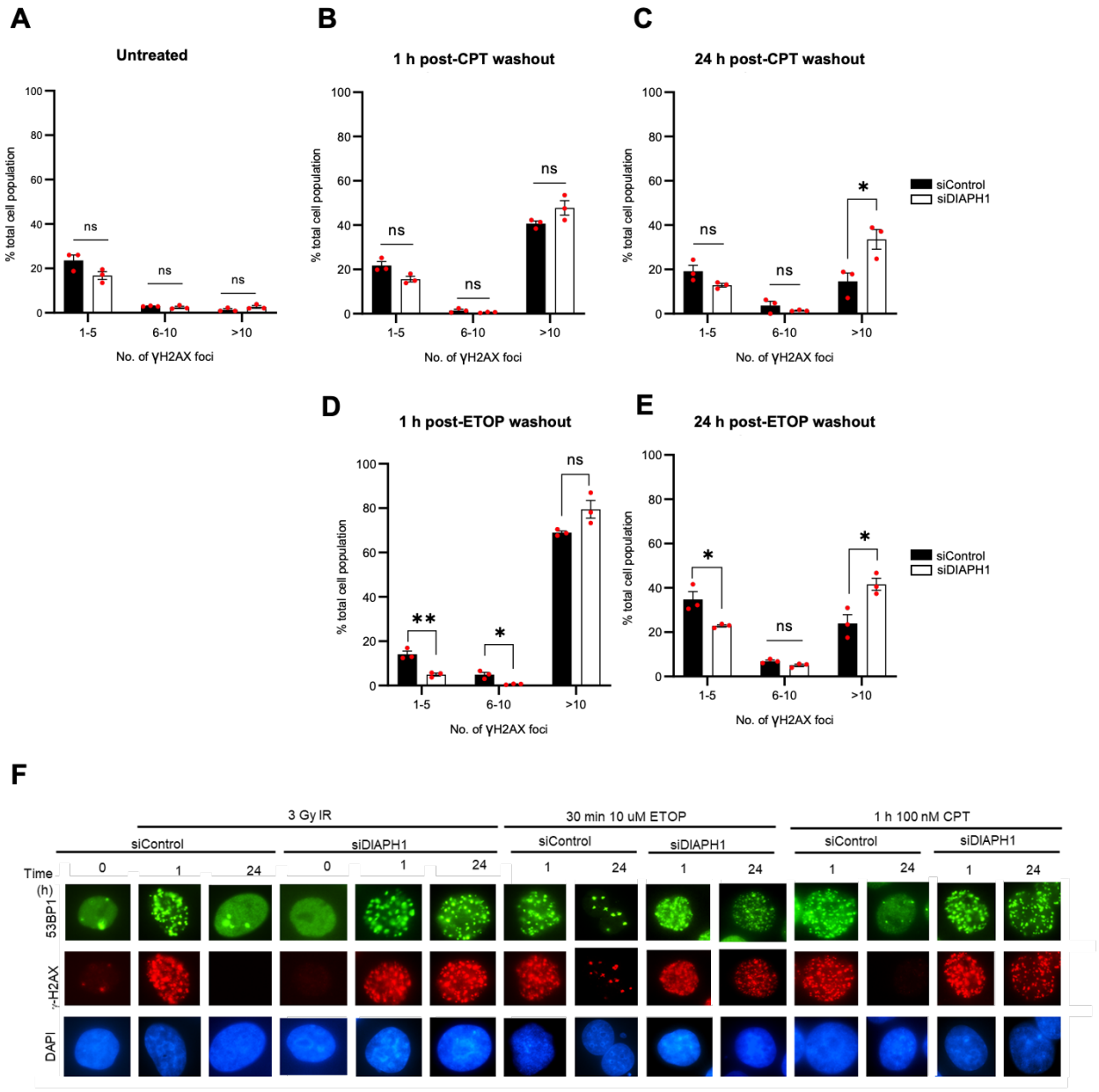


Figure 4.5 - Quantification of γ-H2AX/53BP1 foci formation in DIAPH1 depleted HeLa cells following exogenous DNA damage – *HeLa cells were subject to siRNA depletion of either non-targeting luciferase control or DIAPH1 and were seeded onto glass coverslips and left untreated or treated with 100 nM CPT for 1 h or 10 μM ETOP for 30 min then incubated in drug-free media. Coverslips were harvested at specific time-points post treatment (1 h, 24 h) and fixed with 3.6 % paraformaldehyde (PFA).* ***A*** *- Quantification of γ-H2AX/53BP1 foci in the absence of exogenous DNA damage.* ***B*** *- Quantification of γ-H2AX/53BP1 foci 1 h post-CPT.* ***C*** *- Quantification of γ-H2AX/53BP1 foci 24 h post-CPT.* ***D*** *- Quantification of γ-H2AX/53BP1 foci 1 h post-ETOP.* ***E*** *- Quantification of γ-H2AX/53BP1 foci 24 h post-ETOP. F - Representative images of DAPI positive nuclei from quantification in (A-C). Data from 3 independent repeats, a minimum of 500 cells counted per condition per repeat. Error bars represent standard error of the mean. * Indicates statistical significance (p=<0.05), ** indicates statistical significance (p=<0.01), *** indicates statistical significance (p=<0.001) calculated using an unpaired Students T-test. Statistical significance was calculated using GraphPad Prism software.*

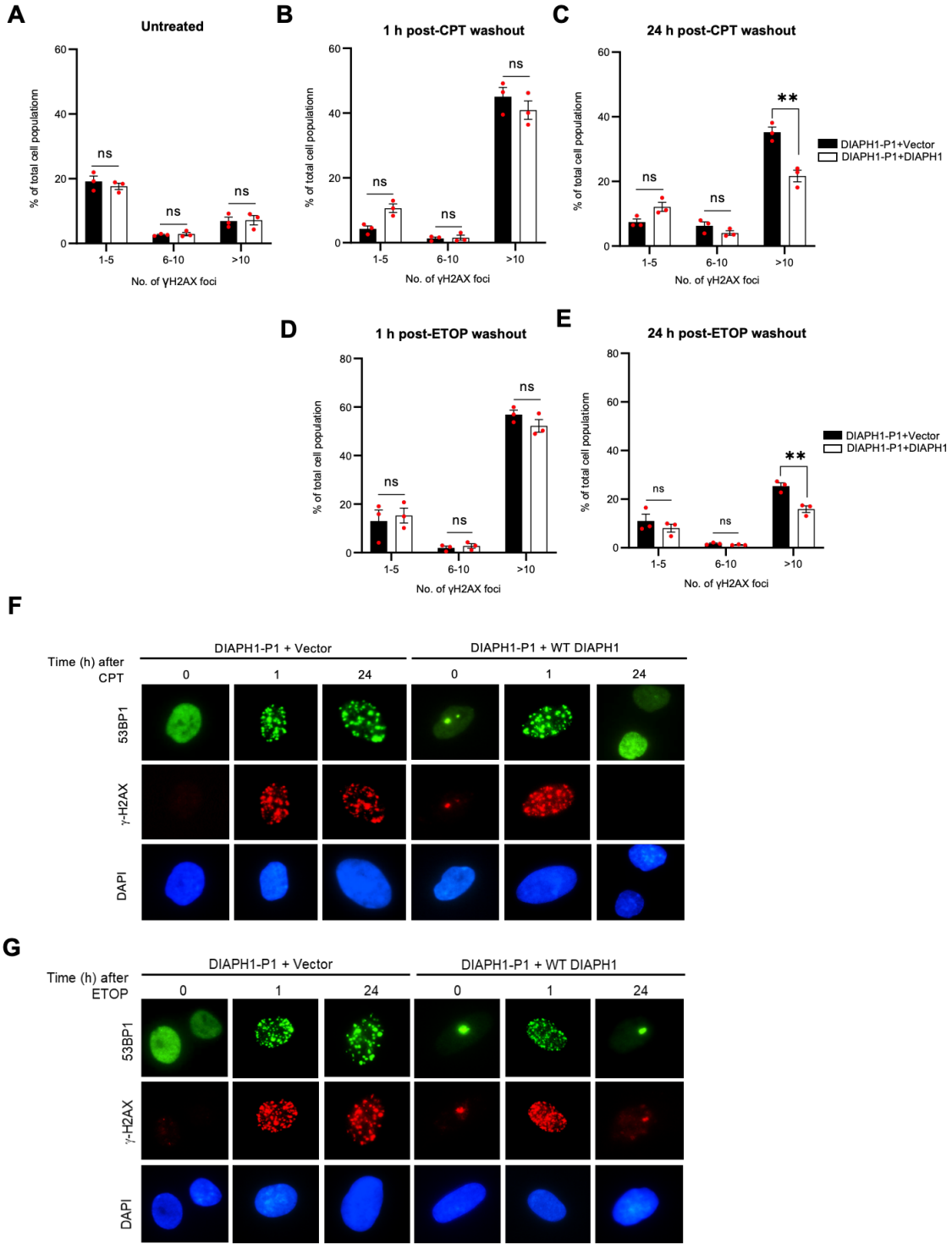

A
Untreated
B
1 h post-CPT washout
C
24 h post-CPT washout
D
1 h post-ETOP washout
E
24 h post-ETOP washout
% of total cell populationn
No. of γH2AX foci
1-5
6-10
>10
ns
**
DIAPH1-P1+Vector
DIAPH1-P1+DIAPH1
F
Time (h) after CPT
DIAPH1-P1 + Vector
DIAPH1-P1 + WT DIAPH1
0
1
24
53BP1
γ-H2AX
DAPI
G
Time (h) after ETOP

Figure 4.6 Quantification of γ-H2AX/53BP1 foci formation in P1+Vector and P1+DIAPH1 fibroblasts following exogenous DNA damage – *P1+Vector and P1+DIAPH1 fibroblast cell lines were seeded onto glass coverslips and left untreated or treated with 100 nM CPT for 1 h or 10 μM ETOP for 30 min then incubated in drug-free media. Coverslips were harvested at specific time-points post treatment (1 h, 24 h) and fixed with 3.6 % paraformaldehyde (PFA).* ***A*** *- Quantification of γ-H2AX/53BP1 foci in the absence of exogenous DNA damage.* ***B*** *- Quantification of γ-H2AX/53BP1 1 h post-CPT.* ***C*** *- Quantification of γ-H2AX/53BP1 foci 24 h post-CPT.* ***D*** *- Quantification of γH2AX foci 1 h post-ETOP.* ***E*** *- Quantification of γ-H2AX/53BP1 foci 24 h post-ETOP. F - Representative images of DAPI positive nuclei from quantification in (A-C).* ***G*** *- Representative images of DAPI positive nuclei from quantification in (A, D-E). Data from 3 independent repeats, a minimum of 500 cells counted per condition per repeat. Error bars represent standard error of the mean. * Indicates statistical significance (p=<0.05), ** indicates statistical significance (p=<0.01), *** indicates statistical significance (p=<0.001) calculated using an unpaired Students T-test. Statistical significance was calculated using GraphPad Prism software.*

4.3.2 Loss of DIAPH1 reduces efficiency of homologous recombination

The two major pathways that repair DSBs, NHEJ and HR, operate in different contexts. NHEJ ligates the broken DSB ends together and is active throughout the cell cycle. In contrast, HR is only active during S- and G_2-phase of the cell cycle due to the requirement for a homologous sister chromatid which is used as the repair template (Chapter 1, Figure 1.8). In order to dissect the exact role that DIAPH1 plays in DSB repair and whether it functions in NHEJ, HR or both, the resolution of IR-induced γ-H2AX foci between G_1- and S/G_2-phase cells was analysed. P1+Vector and P1+DIAPH1 cells were treated 3 μM aphidicolin (APH) 1 h prior to 1 Gy IR. APH was added to prevent damaged G_1-phase cells progressing into S-phase and damaged S-phase cells progressing into G2-phase. Cells were then harvested at 1 h and 8 h post-IR. To distinguish between cells in G_1- and S/G_2-phase, cells were incubated with a specific antibody raised against Centromere protein F (CENPF)/Mitosin. CENPF is a cell cycle regulated protein, expressed at low levels during G_1-phase that increases as cell move into S/G_2-phase (Rattner *et al.*, 1993; Liao *et al.*, 1995). It should also be noted that in G_2-phase cells, roughly double the amount of DSBs were induced due to an increase in DNA content.

As expected, there was no difference in the number of γ-H2AX foci at 1 h post-IR (Figure 4.7A). However, at 8 h post-IR, P1+Vector cells in G_2- but not G_1-phase displayed significantly elevated levels of γ-H2AX foci when compared to P1+DIAPH1 cell in the same cell cycle phase (Figure 4.7B). This finding indicates that the loss of DIAPH1 gives rise to a defect in the repair of DSBs in G_2-phase of the cell cycle, and therefore implicates a role for DIAPH1 in promoting HR. To specifically assess HR-dependent DSB repair in cells lacking DIAPH1, the sister chromatid exchange (SCE) assay was performed. This assay quantifies the level of HR-dependent cross-overs between differentially labelled sister chromatids before and after exposure to exogenous DNA damaging agents (Figure 4.8) (Tumini and Aguilera, 2021). As shown in Figure 4.8, cells were incubated with BrdU for 48 h. This time point was used so that BrdU was intercalated into the DNA backbone for two cycles of DNA replication, with one chromatid containing twice the concentration of BrdU than the other. 24 h into the BrdU labelling, either CPT or ETOP was added to induce DSBs. 3 h prior to harvesting, colcemid was added to arrest metaphase cells for analysis, then cells were dehydrated and fixed in 3:1 methanol: acetic acid. Fixed metaphases were incubated with a UV-sensitive dye, Hoechst, which binds to BrdU, and then UV irradiated. Since sister chromatids contain differing amounts of BrdU/Hoechst, they are differentially damaged by the UV radiation. As such, each sister chromatid takes up different amounts of Giemsa stain, with the more damaged sister taking up lower amounts of Giemsa that the other. This creates a ‘dark’ and ‘light’ chromatid allowing crossovers between the two sisters to be visualised. First, SCEs in DIAPH1 P5 LCLs in unperturbed conditions and in the presence of either 0.5 nM CPT or 10 nM ETOP were assessed. Both CPT and ETOP were selected for this analysis over IR as both drugs are S-phase

dependent agents and are strong inducers of SCEs. CPT is a more potent inducer of SCEs than ETOP, because CPT-induced DSBs can only be repaired by HR (Zhao, Tohda and Oikawa, 1992; Fantini *et al.*, 1998; Conrad, Künzel and Löbrich, 2011). A healthy donor WT LCL was used as a negative control and an NBS LCL was used a positive control for this assay.

In untreated conditions, there was no significant differences in SCEs between the WT cell line and either the NBS LCL or P5 LCL (Figure 4.9A, D). However, there was a striking reduction in SCEs in DIAPH1 P5 LCLs after treatment with both CPT and ETOP, which was similar to the reduction observed in the NBS LCL control (Figure 4.9B-D). This result indicates that loss of DIAPH1 reduces efficiency of HR following DSB induction. To validate this observation, the same analysis was performed in HeLa cells depleted of DIAPH1 by siRNA (Figure 4.10). Importantly, HeLa cells depleted of DIAPH1 displayed a significant reduction in the number of SCEs induced by exposure to CPT and ETOP, when compared to HeLa cells transfected with a non-targeting control siRNA (Figure 4.10B-D). Therefore, suggesting DIAPH1 is required to promote efficient HR following DNA damage.

To substantiate these observations HR efficiency was investigated utilising a CRISPR-based homologous recombination assay (Figure 4.11). This assay utilises CRISPR to induce a DSB in the *LMNA/C* locus that can be repaired by HR using template DNA containing the mClover gene flanked by regions of homology to *LMNA/C* gene where the DSB is induced. If HR is used to repair the Cas9-induced DSB, mClover is inserted in-frame into the 5' end of the *LMNA/C* gene thus giving rise to cells with green nuclear

lamina (Pinder, Salsman and Dellaire, 2015). An RFP expressing plasmid is also transfected into cells, which is used as a marker of transfected cells (Figure 4.11A). Therefore, HR efficiency is calculated by quantifying the percentage of RFP expressing cells that have mClover-labelled nuclear lamina (Figure 4.11B). Using this assay, HeLa cells were transfected with either a non-targeting luciferase control, or siRNA-directed towards DIAPH1, BRCA2 or NBS1 and then transfected with a plasmid expressing RFP alone, a plasmid containing the mClover-LMNA/C repair template and a plasmid expressing Cas9 and the LMNA/C sgRNA (Figure 4.12A). BRCA2 and NBS1 were depleted to serve as two positive controls for a HR deficiency. Excitingly, it was found that depletion of DIAPH1 lead to a significant reduction in the percentage of RFP-positive nuclei with GFP-Lamin nuclear rings, which were reduced to levels similar to that of cells depleted of either BRCA2 or NBS1 (Figure 4.12B-C). Collectively, this these results demonstrate that loss/depletion of DIAPH1 reduces the efficiency of HR-dependent DSB repair.

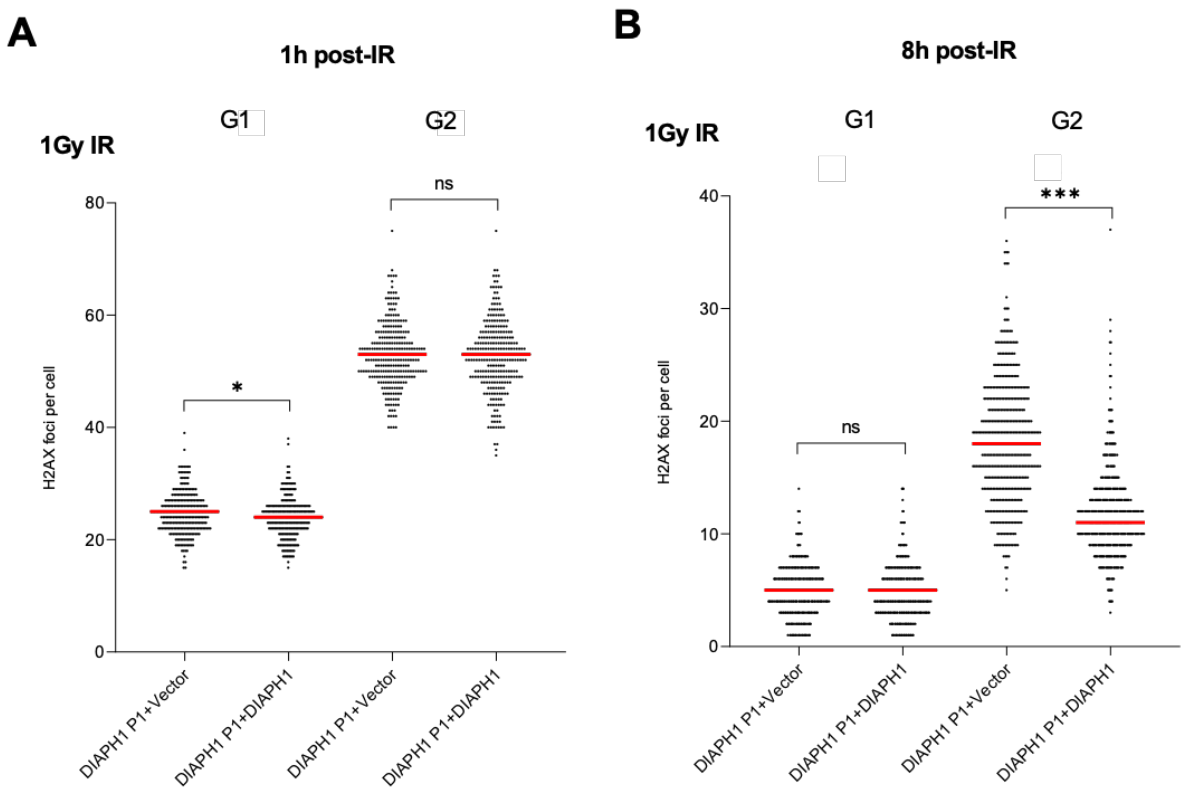


Figure 4.7 - Quantification of individual γ-H2AX foci per CENPF positive P1+Vector and P1+DIAPH1 fibroblasts following exogenous DNA damage – *P1+Vector and P1+DIAPH1 fibroblast cell lines were seeded onto glass coverslips and left untreated or treated with 1 Gy IR. Coverslips were harvested at specific time-points post treatment (1 h, 8 h) and fixed with 3.6 % paraformaldehyde (PFA). Cells were stained with CENPF to distinguish between G_1 (CENPF negative) and G_2 (CEPF positive) cells* ***A*** *- Quantification of γ-H2AX foci 1 h post-IR.* ***B*** *- Quantification of γ-H2AX foci 8 h post-IR. Data from 3 independent repeats, a minimum of 100 cells counted per condition per repeat. Red line denotes the median. * Indicates statistical significance (p=<0.05), ** indicates statistical significance (p=<0.01), *** indicates statistical significance (p=<0.001). Statistical significance was calculated using a Mann-Whitney rank sum test using GraphPad Prism software.*

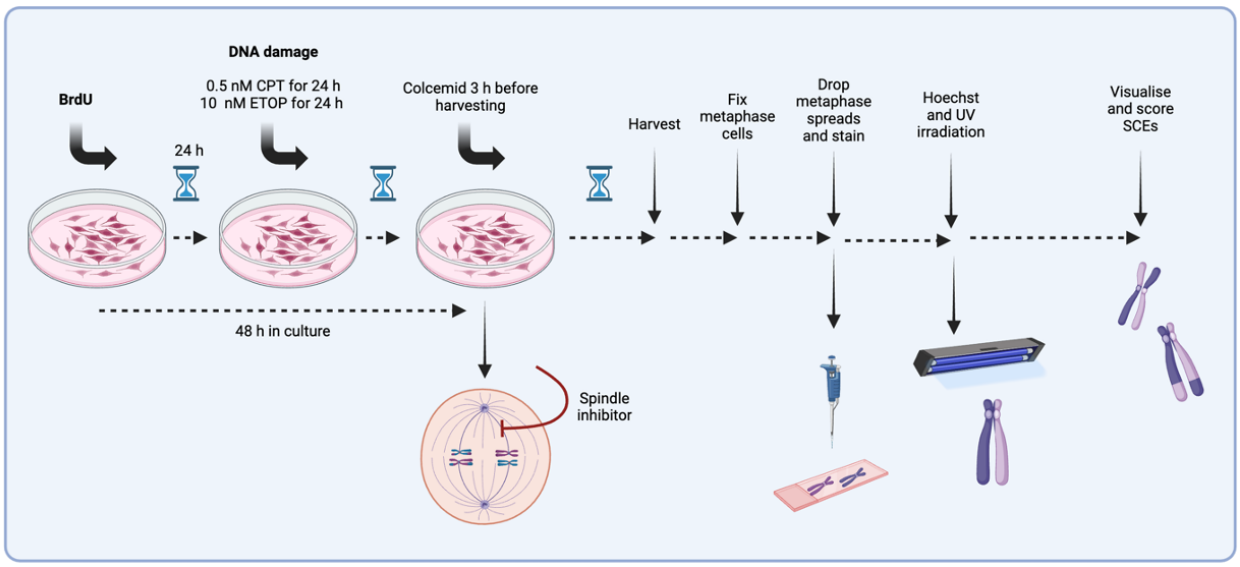


Figure 4.8 – Schematic representation of sister chromatid exchange assay – *For all sister chromatid exchanged (SCE) assays performed cells were cultured in appropriate tissue culture vessels for 48 h in the presence of 10 μM BrdU. 24 h into culture, either 0.5 nM CPT or 10 nM ETOP was added. 3 h prior to harvesting, colcemid was added to cells. Cells were then harvested and fixed in 3:1 methanol: acetic acid. Metaphase cells were dropped into glass microscope slides then incubated with Hoechst and irradiated with UV. Metaphase cells were stained with Giemsa and visualised with Brightfield microscopy. SCEs were scored per metaphase. Created with Biorender.com.*

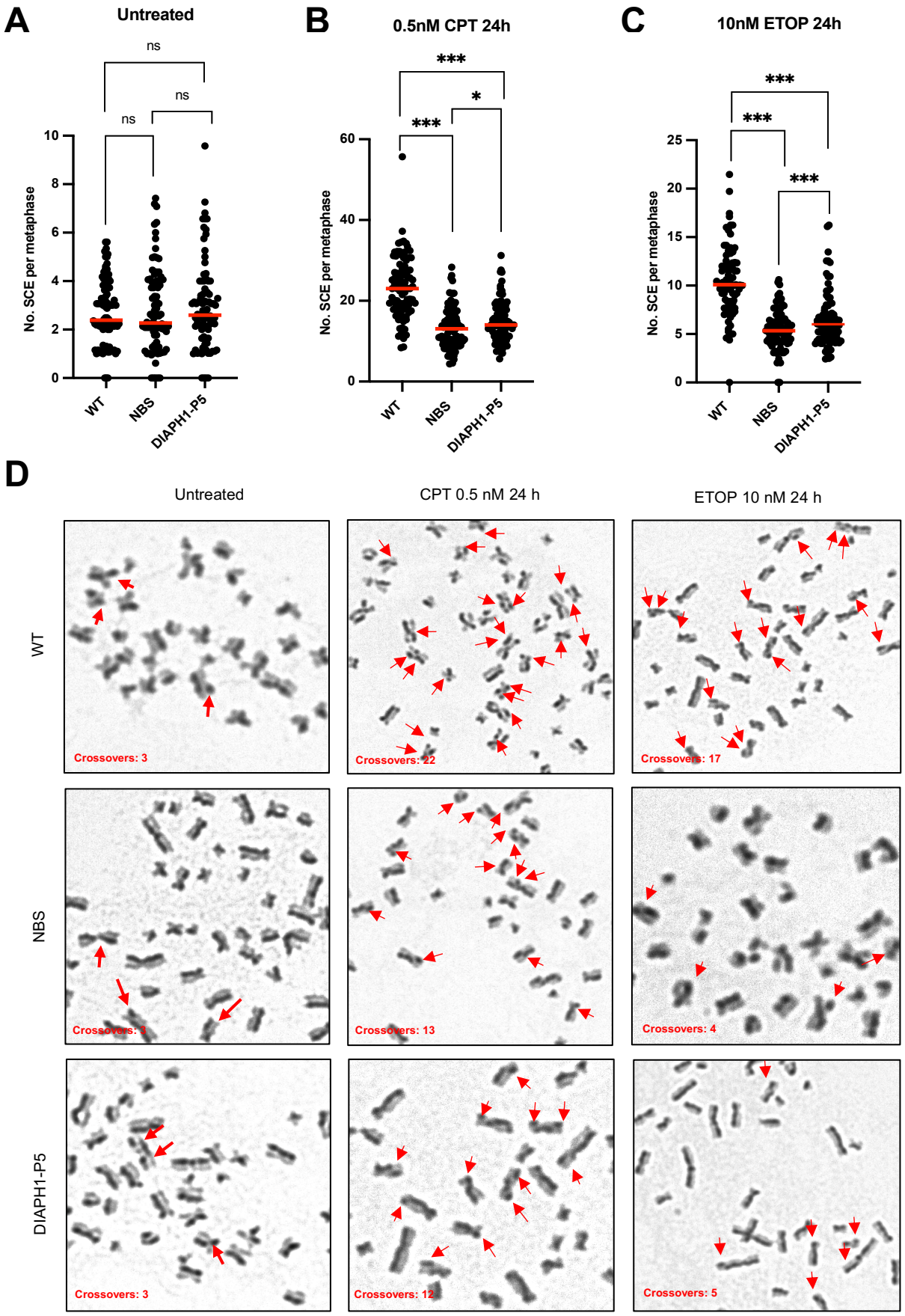

A
Untreated
ns
ns
ns
No. SCE per metaphase
WT
NBS
DIAPH1-P5
B
0.5nM CPT 24h
***
*
***
C
10nM ETOP 24h
***
***
***
D
Untreated
CPT 0.5 nM 24 h
ETOP 10 nM 24 h
WT
NBS
DIAPH1-P5
Crossovers: 3
Crossovers: 22
Crossovers: 17
Crossovers: 13
Crossovers: 4
Crossovers: 12
Crossovers: 5

Figure 4.9 - Quantification of sister chromatid exchanges in DIAPH1 P5 LCLs exposed to DNA damaging agents – *LCLs were cultured in flasks for 48 h in the presence of 10 μM BrdU and either left untreated or at 24 h prior to harvesting, 0.5 nM CPT or 10 nM ETOP was added to flasks. 3 h prior to harvesting, colcemid was added to the cells. Cells were then harvested at 48 h, dehydrated and fixed in 3:1 methanol: acetic acid and dropped onto slides before staining with Giemsa.* ***A*** *- Quantification of SCEs in the absence of exogenous DNA damage.* ***B*** *- Quantification of SCEs in the presence of 0.5 nM CPT.* ***C*** *- Quantification of SCEs in the presence of 10 nM ETOP.* ***D*** *- Representative images metaphase spreads quantified in A-C. Data from 3 independent repeats, a minimum of 30 metaphase spreads counted per condition per repeat. Red line denotes the median. * Indicates statistical significance (p=<0.05), ** indicates statistical significance (p=<0.01), *** indicates statistical significance (p=<0.001). Statistical significance was calculated using a Mann-Whitney rank sum test using GraphPad Prism software.*

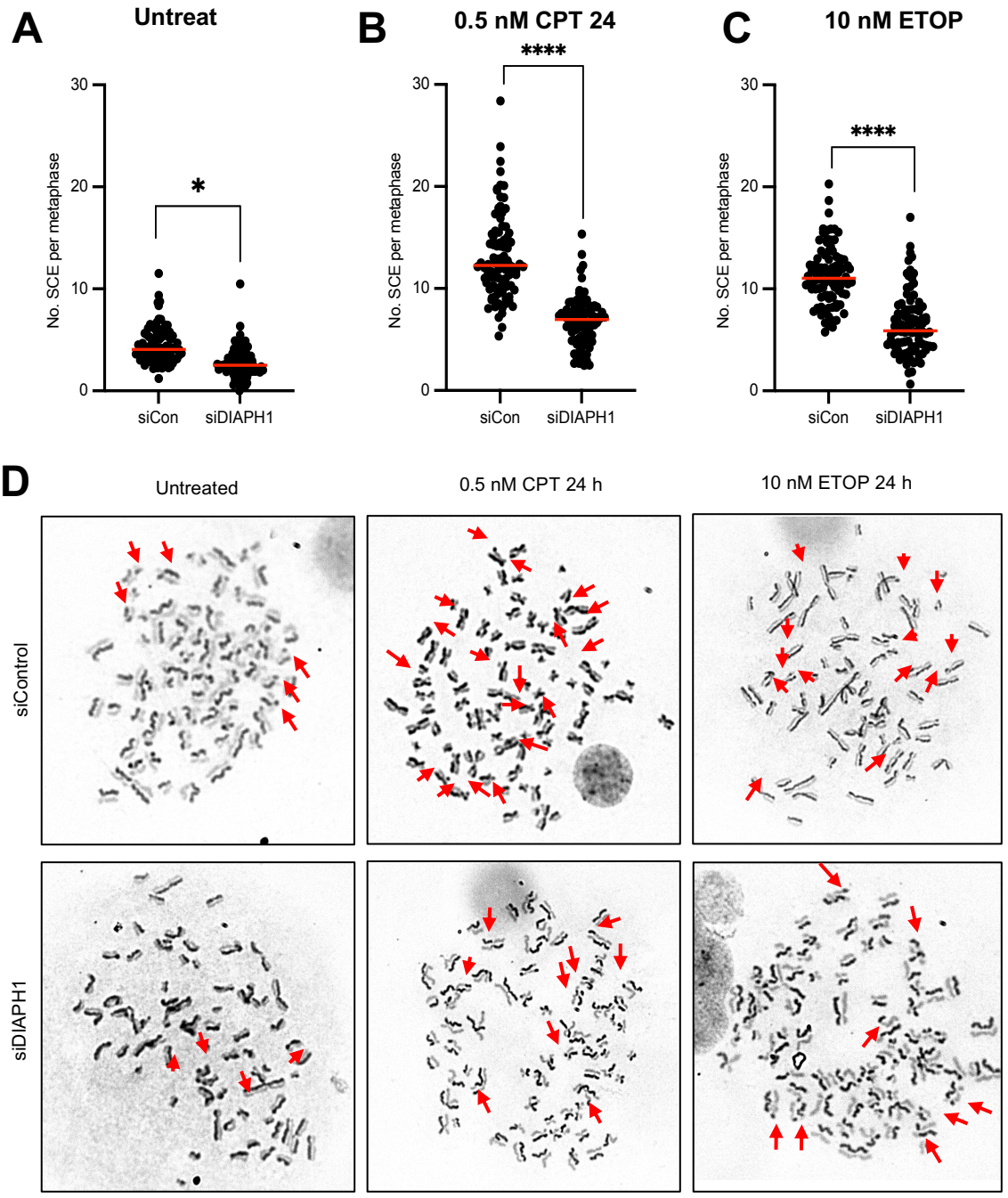


Figure 4.10 - Quantification of sister chromatid exchanges in DIAPH1 depleted HeLa cells exposed to DNA damaging agents – *HeLa subject to siRNA depletion of DIAPH1 or non-targeting luciferase control siRNA were cultured in 10 cm dishes flasks for 48 h in the presence of 10 μM BrdU and either left untreated or at 24 h prior to harvesting, 0.5 nM CPT or 10 nM ETOP was added to flasks. 3 h prior to harvesting, colcemid was added to the cells. Cells were then harvested at 48 h, dehydrated and fixed in 3:1 methanol: acetic acid and dropped onto slides before staining with Giemsa.* ***A*** *- Quantification of SCEs in the absence of exogenous DNA damage.* ***B*** *- Quantification of SCEs in the presence of 0.5 nM CPT.* ***C*** *- Quantification of SCEs in the presence of 10 nM ETOP.* ***D*** *- Representative images of metaphase spreads quantified in A-C. Data from 3 independent repeats, a minimum of 30 metaphase spreads counted per condition per repeat. Red line denotes the median. * Indicates statistical significance (p=<0.05), ** indicates statistical significance (p=<0.01), *** indicates statistical significance (p=<0.001), **** indicates statistical significance (p=<0.0001). Statistical significance was calculated using a Mann-*

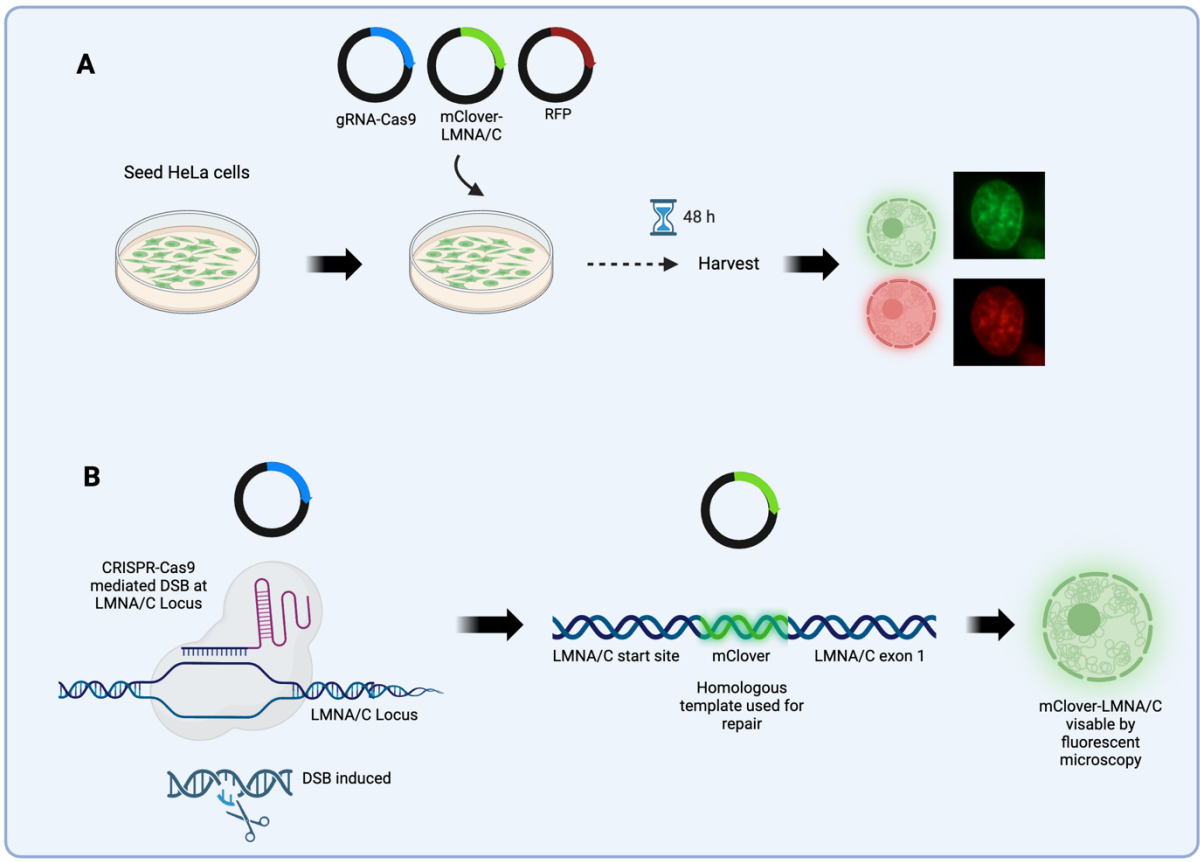


Figure 4.11– Schematic representation of CRISPR Homologous recombination assay – ***A*** *– siRNA depleted HeLa cell were seeded onto glass coverslips and incubated with 3 plasmids; p-gRNA-Cas9-LMNA to generate a DSB at a specific site in the LMNA (Lamin-A locus), pGFP-Lamin donor plasmid to act as a homologous template for the LMNA locus, fused to a GFP-tag and pRFP to serve as a transfection control. Cells were cultured to 48 h then harvested and fixed in 3.6 % PFA.* ***B*** *– Schematic of the DSB generated and GFP-Lamin ring generated that can be visualised by immunofluorescence to indicate HR has taken place.*

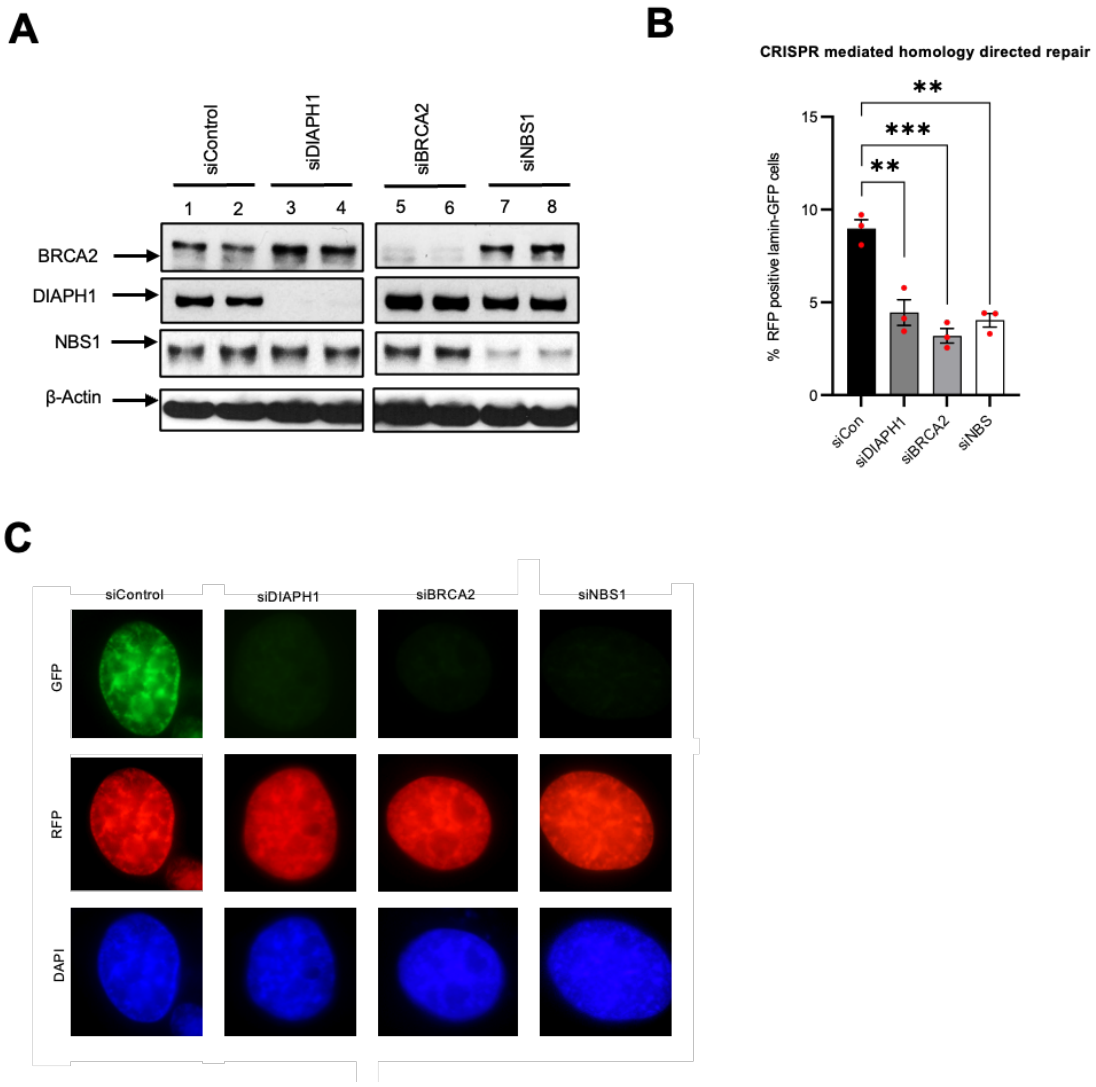


Figure 4.12 - Quantification of Lamin-GFP positive nuclei in RFP positive siDIAPH1 HeLa cells – *HeLa cells subject to siRNA depletion of DIAPH1, NBS or BRCA2 were seeded onto glass coverslips and transfected with pRFP, pLX330-LMNA-gRNA-1 and pCR2.1-Clover-LMNA-Donor. Cells were cultured for 48 h prior to harvesting and then fixed with PFA and mounted onto slides.* ***A*** *– Western blot of cell lysates to show successful siRNA mediated depletion of proteins of interest. β-Actin was used as a loading control.* ***B*** *- Quantification of lamin-GFP positive nuclei in RFP positive HeLa cells.* ***C*** *- Representative images of DAPI positive nuclei from quantification in A. Data from 3 independent repeats, a minimum of 500 cells counted per condition per repeat. Error bars represent standard error of the mean. * Indicates statistical significance (p=<0.05), ** indicates statistical significance (p=<0.01), *** indicates statistical significance (p=<0.001) calculated using an unpaired Students T-test. Statistical significance was calculated using GraphPad Prism software.*

4.3.3 Loss of *DIAPH1* leads to reduced localisation and foci formation of HR factors RPA2, BRCA1 and RAD51 following CPT-induced DNA damage

So far, my data has revealed that loss of DIAPH1 reduces the efficiency of HR, and therefore indicates that DIAPH1 is a novel factor involved in promoting HR-dependent DSB repair. The next step was to investigate where in the HR pathway DIAPH1 functions. To address this, initially HR factors RPA2, BRCA1 and RAD51 that act downstream in the HR pathway after initial processing by upstream proteins were analysed. Following DNA end resection by the MRN-CtIP complex, EXO1 and DNA2 (Chapter 1, Section 1.7.2), RPA (consisting of RPA1/RPA70, RPA2/RPA32 and RPA3/RPA14) rapidly coats the ssDNA generated by this process. BRCA1 functions together with BRCA2 and PALB2 to facilitate the displacement of RPA to allow the loading of RAD51 onto ssDNA. RAD51, being the central recombinase to the HR process, then catalyses strand invasion of the undamaged DNA template (Zhang *et al.*, 2009; Daley and Sung, 2014; Prakash *et al.*, 2015).

To gain insight into where DIAPH1 is functioning, IF was performed first (Figure 4.1) to assess the relocalisation of BRCA1, RPA2 and RAD51 to sites of DNA DSBs in P1+Vector and P1+DIAPH1 cells. Fibroblasts were treated with 100 nM CPT for 1 h, then cells were left in drug-free media until 1 h and 4 h post-CPT treatment and fixed in 3.6 % PFA. To ensure only HR was being assessed, only CPT was used to induce DSBs, as the single-ended DSBs (seDSBs) induced by CPT can only be repaired by HR (Chapter 3, Figure 3.1). Cells were incubated with specific antibodies raised against either BRCA1, RPA2 or RAD51 as well as the G_2/S specific cell cycle phase marker CENPF/Mitosin. When quantifying BRCA1 foci, CENPF positive nuclei were

scored positive for BRCA1 foci if they had >30 foci present. This analysis showed that P1+Vector fibroblast cells displayed a significant reduction in cells with >30 BRCA1 foci at 1 h and 4 h post CPT treatment (Figure 4.13A-B). Similarly, S/G_2-phase cells lacking DIAPH1 exhibited a significant lower level of RPA2 staining when compared to cells re-expressing DIAPH1 at 1 h and 4 h post-CPT treatment (Figure 4.14A-B). Lastly, cells lacking DIAPH1 showed substantially reduced numbers of CPT-induced RAD51 foci when compared to cells expressing DIAPH1 (Figure 4.15A-B). Together these results show that loss of DIAPH1 compromises the relocalisation of key HR factors to sites of DNA DSBs induced by CPT treatment.

To assess this in more detail, the effect of loss of DIAPH1 on recruitment of BRCA1 and RPA2 to individual DSB sites was examined. To do this stochastic optical reconstruction microscopy (STORM) was utilised. This advanced microscopy technique allows for high resolution visualisation of protein localisation (Whelan *et al.*, 2016, Whelan at al., 2018). STORM utilises fluorescent microscopy, where specific wavelengths of laser light induce controlled “blinking” (a state where the fluorophore is either “on” and emits light, or “off” and does not emit light) in individual fluorophores attached to proteins of interest. This controlled blinking ensures that only a subset of the fluorophores are emitting light at any given time. The STORM instrument captures a series of images over time, recording these blinking events as isolated spots of light, allowing for precise determination of each fluorophore's position. The thousands of images captured are then reconstructed into a high-resolution image. This method overcomes the diffraction limit, the inherent resolution limit of conventional light microscopy, by pinpointing the exact location of individual fluorophores to a spatial

resolution of 10-20-nanometre, thereby resolving structural details much smaller than the approximately 200-nanometre threshold typically imposed by the diffraction of light (Xu, Ma and Liu, 2017). A previous study by Whelan *et al*. demonstrated that it is possible to visualise the localisation of individual molecules of BRCA1 and RPA to seDSBs induced by CPT treatment (Whelan *et al.*, 2018). Therefore to investigate a role for DIAPH1 in facilitating the relocalisation of BRCA1 and RPA2 specifically to DSB ends, P1+Vector and P1+DIAPH1 cells were either left untreated or treated with 100 nM CPT for 1 h. Cells were then pulse labelled with EdU for 30 min to detect active replication forks in S-phase cells (Figure 4.16A). In treated cells, this was 30 min into the 1 h CPT treatment. At this dose, previous reports have shown no difference in EdU signal between untreated and CPT treated cells (Saleh-Gohari *et al.*, 2005; Ray Chaudhuri *et al.*, 2012; Whelan *et al.*, 2020). Cells were stained with primary antibodies raised against EdU and BRCA1 or RPA2 followed by incubation with secondary antibodies coupled to different fluorophores that are compatible with STORM. The specific fluorophores used were stimulated by different laser lines to induce fluorophore blinking events. The blinking was then captured in S-phase cells over a 60 second period for each individual laser channel, to enable precise mapping of single molecule localisation of proteins of interest (EdU in green, BRCA1 in red, RPA in blue). The movies captured on the microscope were then reconstructed to produce still images whereby suitable regions of interest (ROI) could be selected for analysis. Selection of the ROIs to be quantified was based on cells in S-phase with pan nuclear distribution of the EdU signal. The EdU signal provides an indirect read-out of CPT-induced damaged replication forks, as EdU has been incorporated into nascent DNA at active replication forks then subsequently damaged by CPT to generate a seDSB

(Figure 4.16A). Then, using specific coding scripts written in MatLab software, the density of both the BRCA1 and RPA2 signal could be cross-correlated with EdU to indicate their proximity to CPT-induced seDSB (Figure 4.16B).

In keeping with the findings from foci quantification using low resolution IF, STORM computational analysis detected a reduction in BRCA1 colocalisation to EdU at 1 h and 4 h post-CPT treatment in P1+Vector cells compared to P1+DIAPH1 cells (Figure 4.17A, E). STORM was also used to assess the amount of chromatin bound BRCA1 in cells with/without DIAPH1. Mirroring the observations in Figure 4.17A, P1+DIAPH1 cells displayed elevated amounts of chromatin bound BRCA1 post-CPT treatment compared to the P1+Vector cells (Figure 4.17B). Similarly, P1+Vector cells displayed a significant reduction in the amount of RPA2 localised at a seDSB or on chromatin following exposure to CPT than the P1+DIAPH1 cells (Figure 4.17C and 4.17D).

Taken together, the results included in this section support the notion that DIAPH1 may play a role in foci formation of BRCA1, RPA2 and RAD51 following CPT treatment. In the absence of DIAPH1, both BRCA1 and RPA2 appear to be recruited less efficiently to CPT-induced seDSB sites and the surrounding chromatin. This suggests that DIAPH1 may function at an early step during the HR-dependent DSB repair pathway required to generate the ssDNA.

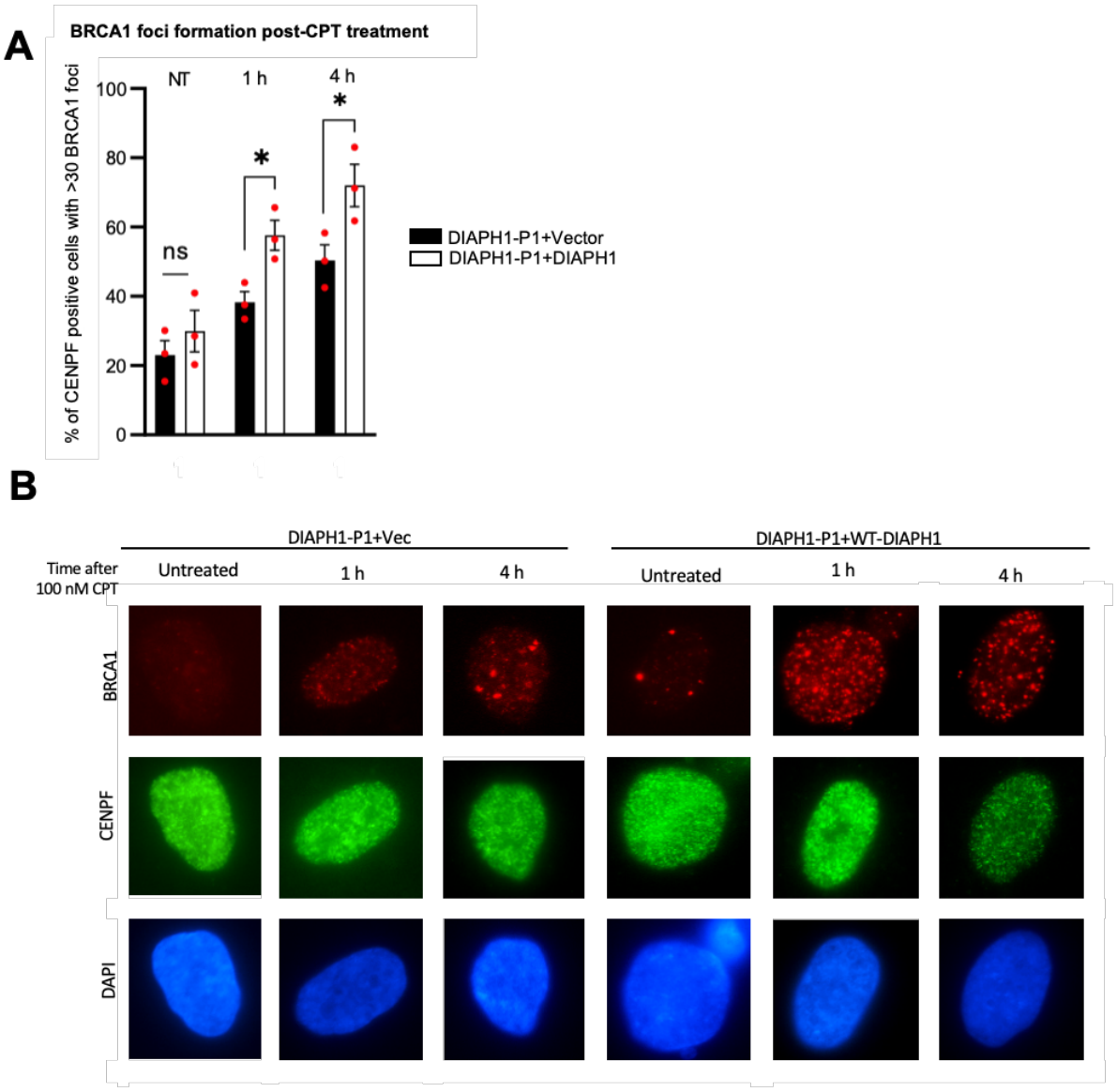


Figure 4.13 - Quantification of BRCA1 foci intensity in P1+DIAPH1 and P1+Vector hTERT immortalised fibroblasts following CPT treatment – *Fibroblasts were seeded onto glass coverslips and left untreated or treated with 100 nM CPT for 1 h. Coverslips were harvested at specific time-points post-treatment (1 h, 4 h) and fixed with paraformaldehyde (PFA).* ***A*** *- Quantification of nuclei with >30 BRCA1 foci in CENPF positive (S/G_2) cells in untreated cells and 1 h and 4 h post-CPT.* ***B*** *- Representative images of CENPF positive cells from quantification in A. Data from 3 independent repeats, a minimum of 300 cells counted per condition per repeat. Error bars represent standard error of the mean. * Indicates statistical significance (p=<0.05), ** indicates statistical significance (p=<0.01), *** indicates statistical significance (p=<0.001), **** indicates statistical significance (p=<0.0001) calculated using an unpaired Student's T-Test. Statistical significance was calculated using GraphPad Prism software.*

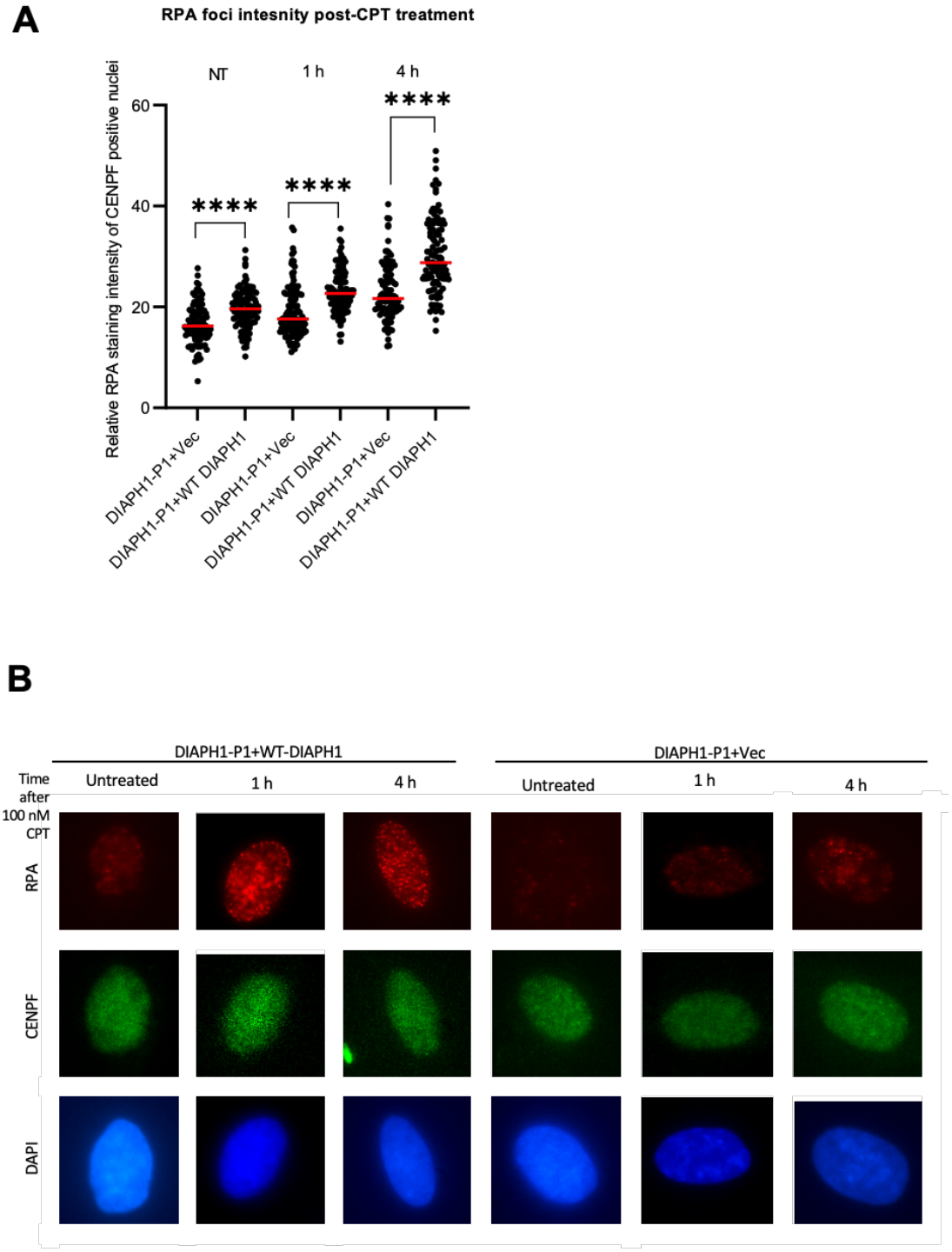
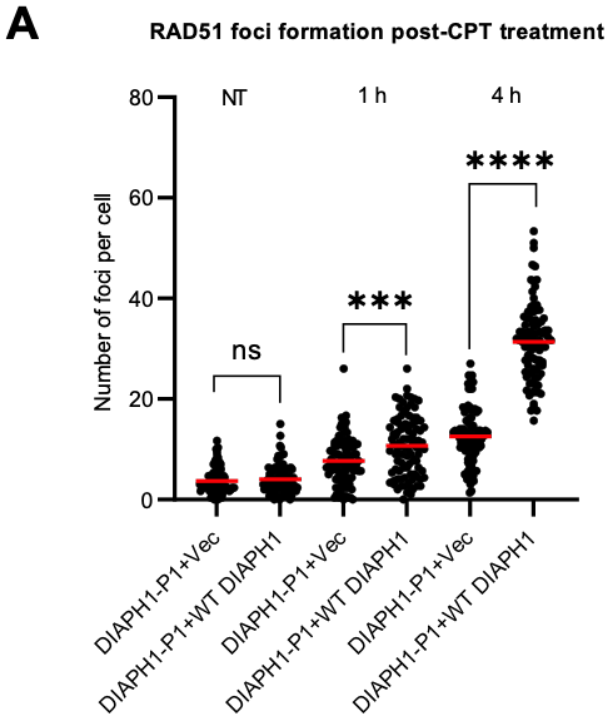


Figure 4.14 - Quantification of RPA2 foci intensity in P1+DIAPH1 and P1+Vector hTERT immortalised fibroblasts following CPT treatment– *Fibroblasts were seeded onto glass coverslips and left untreated or treated with 100 nM CPT for 1 h. Coverslips were harvested at specific time-points post-treatment (1 h, 4 h) and fixed with paraformaldehyde (PFA).* ***A*** *- Quantification of relative RPA2 staining intensity in CENPF positive (S/G_2) cells in untreated cells and 1 h and 4 h post-CPT.* ***B*** *- Representative images of CENPF positive cells from quantification in A. Data from 3 independent repeats, a minimum of 100 cells counted per condition per repeat. RPA foci intensity was quantified in ImageJ. Red line denotes the median. * Indicates statistical significance (p=<0.05), ** indicates statistical significance (p=<0.01), *** indicates statistical significance (p=<0.001), **** indicates statistical significance (p=<0.0001). Statistical significance was calculated using a Mann-Whitney rank sum test using GraphPad Prism software.*



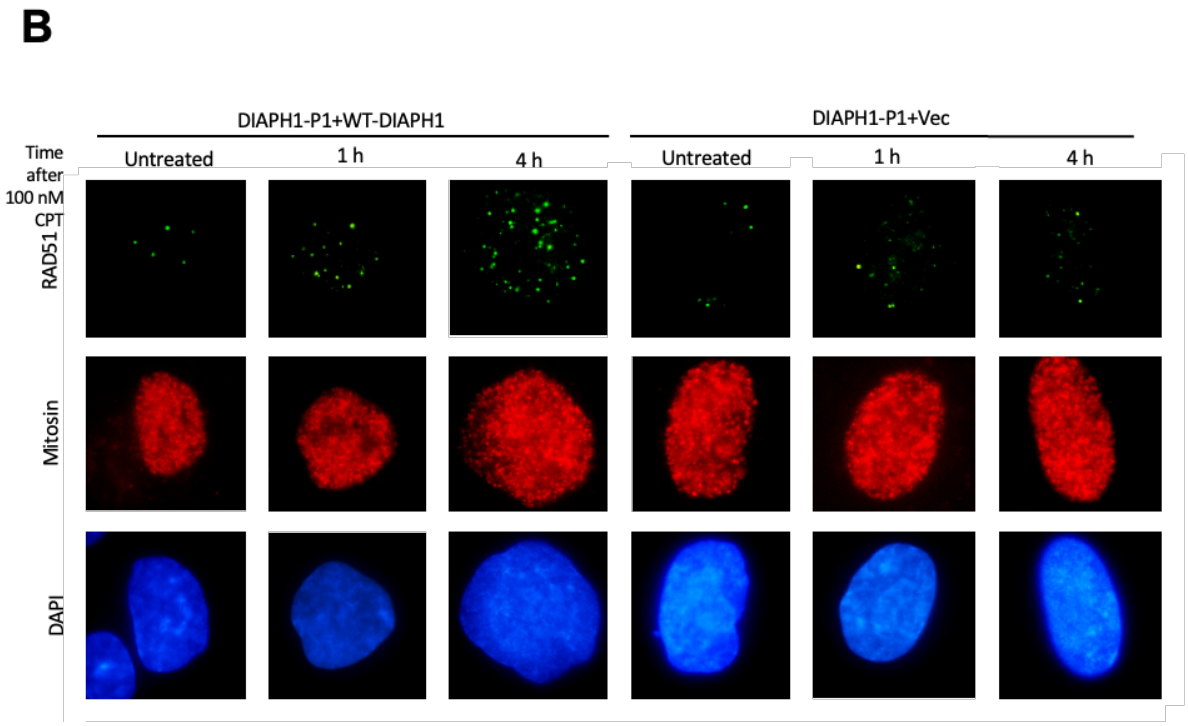


Figure 4.15 - Quantification of RAD51 foci formation P1+DIAPH1 and P1+Vector hTERT immortalised fibroblasts following CPT treatment – *Fibroblasts were seeded onto glass coverslips and left untreated or treated with 100 nM CPT for 1 h. Coverslips were harvested at specific time-points post-treatment (1 h, 4 h) and fixed with paraformaldehyde (PFA).* ***A*** *- Quantification of individual RAD51 foci in Mitosin positive (S/G_2) cells in untreated cells and 1 h and 4 h post-CPT.* ***B*** *- Representative images of Mitosin positive cells from quantification in A. Data from 3 independent repeats, a minimum of 100 cells counted per condition per repeat. RPA foci intensity was quantified in ImageJ. Red line denotes the median. * Indicates statistical significance (p=<0.05), ** indicates statistical significance (p=<0.01), *** indicates statistical significance (p=<0.001), **** indicates statistical significance (p=<0.0001). Statistical significance was calculated using a Mann-Whitney rank sum test using GraphPad Prism software.*

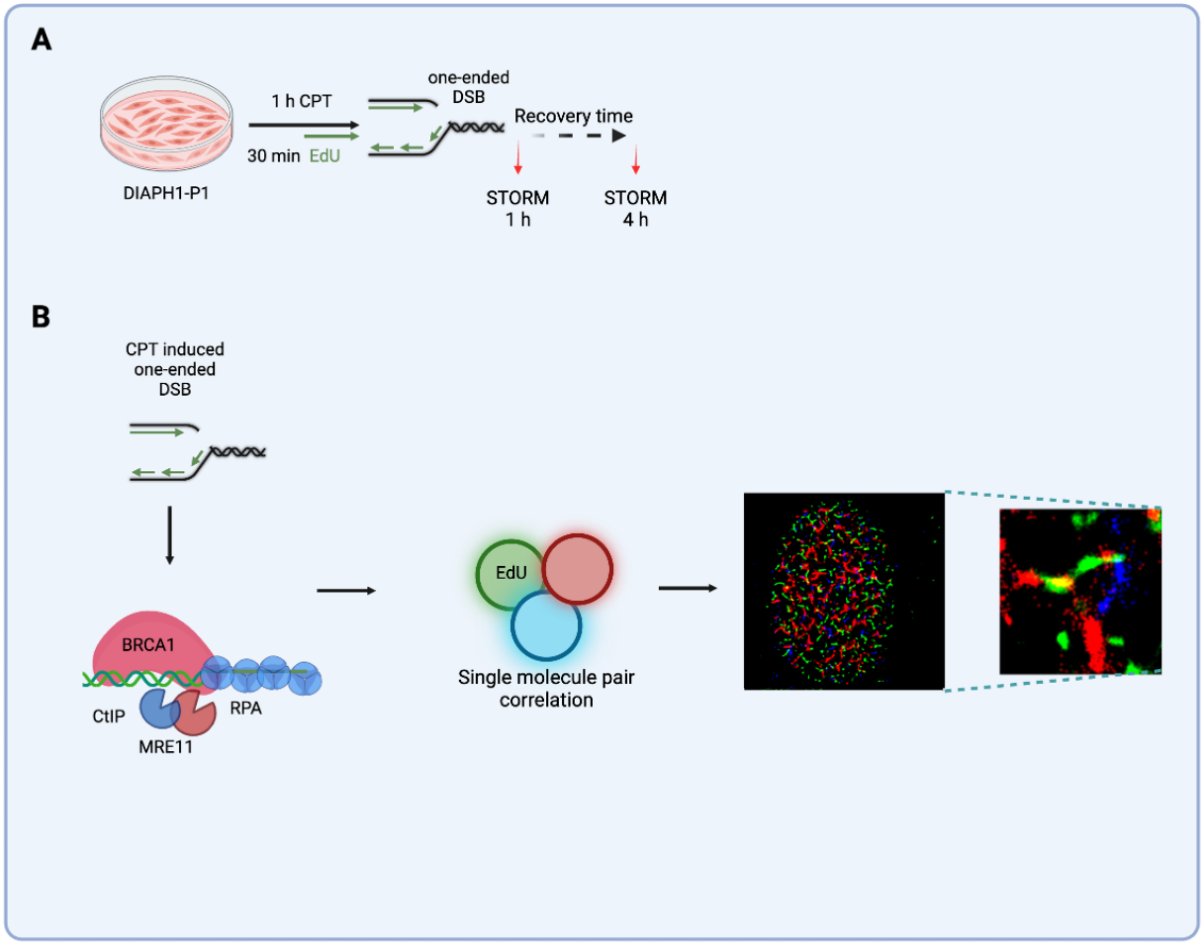


Figure 4.16 - Schematic diagram of STORM – A *–P1+Vector and P1+DIAPH1 fibroblasts were treated with 100 nM CPT for 1 h. 30 min into treatment 10 μM EdU was added to pulse label cells in S-phase so that EdU was incorporated into nascent DNA. Cells were then permeabilised and fixed in 3.6 % PFA 1 h and 4 h post-CPT and stained with antibodies of interest before being imaged on the STORM instrument.* ***B*** *– STORM captures 60 second movies of fluorophore blinking events of antibodies bound to proteins of interest. Blinking events allows for accurate localisation of individual molecules of each protein of interest. The localisation of each protein of interest are then cross correlated to calculate their proximity to each other.*

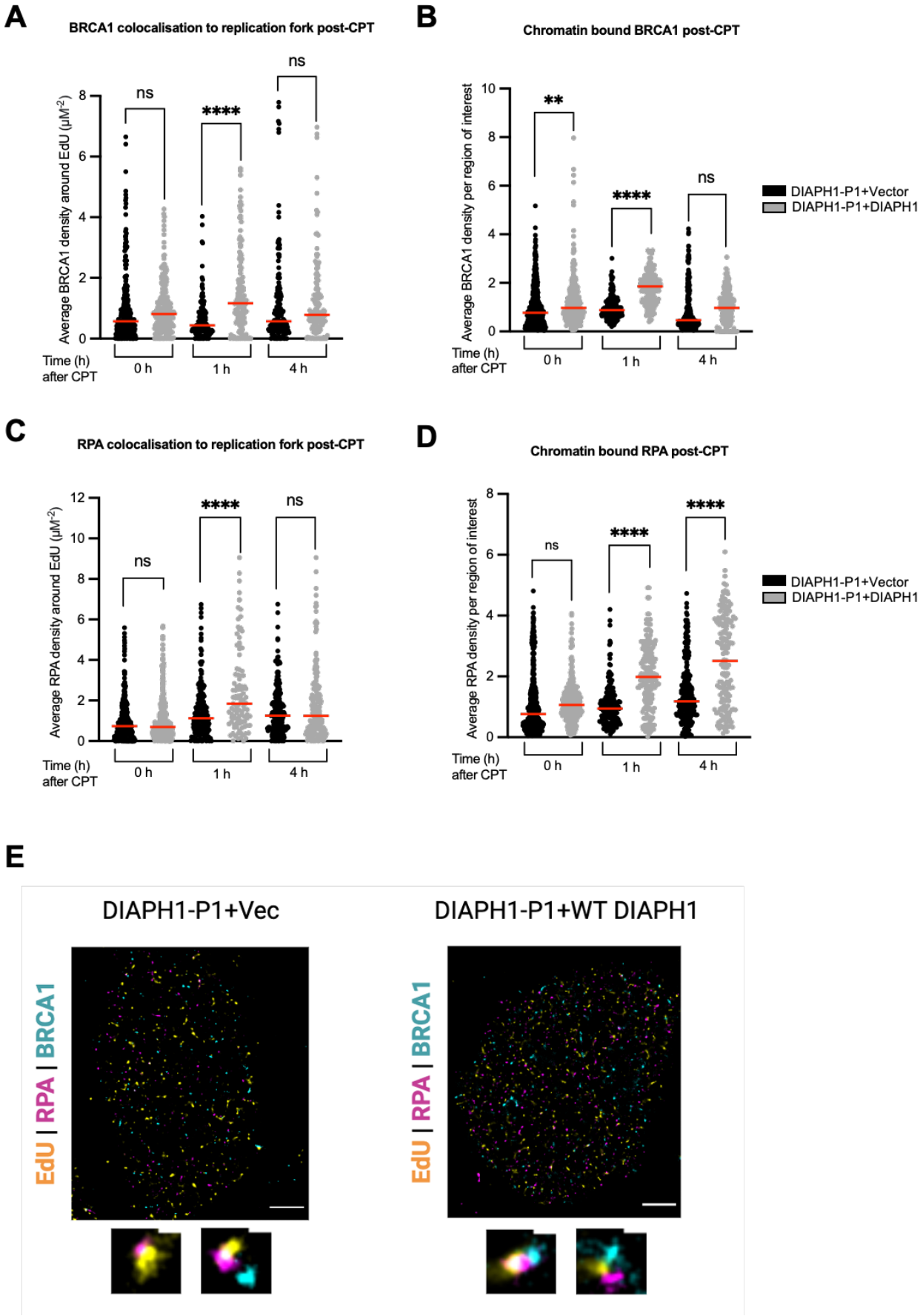

A
BRCA1 colocalisation to replication fork post-CPT
Average BRCA1 density around EdU (μM-2)
ns
****
ns
Time (h) after CPT
0 h
1 h
4 h
B
Chromatin bound BRCA1 post-CPT
Average BRCA1 density per region of interest
**
****
ns
DIAPH1-P1+Vector
DIAPH1-P1+DIAPH1
C
RPA colocalisation to replication fork post-CPT
Average RPA density around EdU (μM-2)
D
Chromatin bound RPA post-CPT
Average RPA density per region of interest
E
DIAPH1-P1+Vec
DIAPH1-P1+WT DIAPH1
EdU | RPA | BRCA1

Figure 4.17 - Quantification of average local density of BRCA1 and RPA2 detected around individual EdU molecules in P1+DIAPH1 and P1+Vector cells - *Fibroblasts were seeded onto glass coverslips and left untreated or treated with 100 nM CPT for 1 h. 30 min into CPT treatment, cells were pulsed with 10 uM EdU for 30 min. Coverslips were harvested at specific time-points post-treatment (1 h, 4 h) and fixed with 3.6 % paraformaldehyde (PFA). Cells were then imaged using stochastic optical reconstruction microscopy (STORM) and regions of interest (ROI) were selected for analysis and single molecule pair correlation of BRCA1 and RPA2 to EdU was calculated using MatLab.* ***A*** *- Average local density of BRCA1 around individual EdU molecules in P1+Vector and P1+DIAPH1 fibroblasts in untreated conditions and 1 h and 4 h post-CPT, fold change has been normalised to untreated controls.* ***B*** *– Average BRCA1 density bound to chromatin in P1+Vector and P1+DIAPH1 fibroblasts in untreated conditions and 1 h and 4 h post-CPT, fold change has been normalised to untreated controls.* ***C*** *- Average local density of RPA2 around individual EdU molecules in P1+Vector and P1+DIAPH1 fibroblasts in untreated conditions and 1 h and 4 h post-CPT, fold change has been normalised to untreated controls.* ***D*** *– Average RPA2 density bound to chromatin in P1+Vector and P1+DIAPH1 fibroblasts in untreated conditions and 1 h and 4 h post-CPT, fold change has been normalised to untreated controls.* ***E*** *- Representative STORM multicolor images of EdU incorporation (orange), BRCA1 (cyan) and RPA2 (magenta). Scale bar 1500 nm. n = 3 independent repeats, for individual ROIs of BRCA1 analysed, n= a minimum of 127. For individual ROIs of RPA2 analysed, n= a minimum of 109. Red line denotes the median. * Indicates statistical significance (p=<0.05), ** indicates statistical significance (p=<0.01), *** indicates statistical significance (p=<0.001), **** indicates statistical significance (p=<0.0001). Statistical significance was calculated using an unpaired Student's T-Test test using GraphPad Prism software.*

f

4.3.4 DIAPH1 plays a role in MRN complex localisation to DSBs and interacts with components of the MRN complex

Next, how loss of DIAPH1 affects recruitment of the MRN complex to DSBs was investigated. As outlined in Chapter 1, Section 1.5.4, the MRN complex, consisting of MRE11, RAD50 and NBS1, possesses both endo- and exo-nuclease activity (Iijima *et al.*, 2008; Blackford and Jackson, 2017; Syed and Tainer, 2018; Bian *et al.*, 2019). A critical decision point in whether a DSB is repaired by NHEJ or HR, is resection of the DSB end, which is initiated by the MRN complex in conjunction with CtIP (Sartori *et al.*, 2007; Liu and Huang, 2016; Zhao *et al.*, 2020). To study recruitment of the MRN complex and CtIP to DSBs in the absence of DIAPH1, STORM was used in combination with specific antibodies to EdU, MRE11 and CtIP (EdU in green, MRE11 in red, CtIP in blue).

Strikingly, P1+Vector cells did not relocalise MRE11 to damaged replication forks as efficiently as P1+DIAPH1 cells at either 1 h or 4 h post-CPT treatment (Figure 4.18A,

C-D). This surprising finding suggests that DIAPH1 is required for the recruitment of the MRN complex to DSBs at early time-points following CPT-induced seDSBs. In keeping with this, STORM was also used to assess density of chromatin bound MRE11 to give an indication of if loss of DIAPH1 affects MRN localisation to chromatin. Mirroring our observations in Figure 4.18A, loss of DIAPH1 reduced the ability of MRE11 to bind to damaged chromatin (Figure 4.18B). Consistent with our observations with MRE11, loss of DIAPH1 reduced the recruitment of CtIP seDSBs and chromatin at 1 h and 4 h post-CPT treatment (Figure 4.19A-B).

To validate our observations using STORM, that DIAPH1 is important for relocalising the MRN complex to DSBs, the ER-mCherry-LacI-FokI-DD inducible nuclease system was used, since the antibodies to MRE11 do not work well for detecting DNA damage-induced foci using low resolution IF. The ER-mCherry-LacI-FokI-DD nuclease system induces DSBs specifically within an integrated Lac-operator array (256 repeats), which are sufficiently clustered to detect the recruitment of specific DNA repair proteins using conventional antibodies and low resolution IF (Figure 4.20) (Shanbhag *et al.*, 2010). LacO-Fok1-mCherry expressing U-2-OS cells were subject to siRNA depletion of DIAPH1 or a non-targeting luciferase control then treated with 1 μM Shield1 and 1 μM 4-Hydroxytamoxifen (4-OHT) for 4 h before fixing in 3.6 % PFA (Figure 4.20A). 4-OHT relocalises the mCherry-*FokI* nuclease from the cytoplasm into the nucleus to generate a single DSB whereas the Shield1 stabilises the nuclease by preventing its proteasomal-mediated degradation. The localisation of the mCherry-*FokI* nuclease to the LacO array can be visualised by IF (Figure 4.20B) (Cho, Lampson and Greenberg, 2017). Consistent with our observations using STORM, U-2-OS cells depleted of

DIAPH1 with siRNA (Figure 4.21A) exhibited a significant defect in the recruitment of MRE11 to FokI-induced DSBs (Figure 4.21B-C). This observation strengthens the notion that DIAPH1 plays a role in the recruitment of the MRN complex to DSB sites.

The next obvious question based on these findings is whether DIAPH1 is directly interacting with components of the MRN complex or any of the other HR proteins studied, or whether it is acting via an indirect mechanism to modulate HR. Since DIAPH1 is largely cytoplasmic, this would support the idea that the role DIAPH1 plays in regulating MRN recruitment to DSB sites is via an indirect mechanism. However, DIAPH1 has been reported to reside in the nucleus albeit in low levels, suggesting that it could interact directly with one or more DNA repair proteins (Baarlink, Wang and Grosse, 2013). To validate the subcellular localisation of DIAPH1 reported by Baarlink *et al*. U-2-OS cells expressing doxycycline (DOX) inducible GFP-tagged DIAPH1 were generated (Baarlink, Wang and Grosse, 2013). These cells were plated onto glass coverslips and treated with DOX for 24 h then either left untreated or treated with 100 nM CPT for 1 h then harvested 1 h post-CPT washout. Cells were incubated with an antibody to γ-H2AX to serve as a marker of DSBs, and the GFP-DIAPH1 signal was visualised by fluorescent microscopy. Consistent with previous reports, DIAPH1 predominantly localised to the cytoplasm but a small amount was visible in the nucleus. However, its localisation did not change following the induction of DSBs (Figure 4.22A). Since DIAPH1 is localised within the nucleus, next whether DIAPH1 binds to any proteins involved in the HR pathway was assessed. To investigate this, GFP-DIAPH1 was overexpressed in HEK293FT cells and GFP-Trap was utilised to affinity purify DIAPH1 containing protein complexes from whole cell extracts. Extracts were then

subject to Western blotting. Given that whole cell extracts were used, it is likely that the majority of the GFP-DIAPH1 protein complexes purified in this technique originated from the cytoplasm. Despite this, an interaction between GFP-DIAPH1 and the HR factors MRE11, NBS1 and RAD51 was detected, but not RPA2 (Figure 4.22B). This suggests that DIAPH1 may function to regulate DNA repair in part through a direct interaction with the MRN complex and RAD51 within the nucleus.

To summarise, this section provides evidence that DIAPH1 may be required for the MRN complex and CtIP to be recruited to DSBs induced by CPT and mCherry-LacI-FokI using STORM and fluorescence microscopy. As a result of this, proteins further downstream in the HR pathway displayed defects in both their localisation to individual DSB sites and recruitment to damaged chromatin in the absence of DIAPH1. These findings suggest that the loss of DIAPH1 leads to defects in the entire HR pathway, which arises due to inefficient processing of DSB ends. Additionally, it has been shown that GFP-DIAPH1 binds to both the MRN complex as well as RAD51. However, it is unclear whether the interaction of DIAPH1 with these HR factors is direct or indirect.

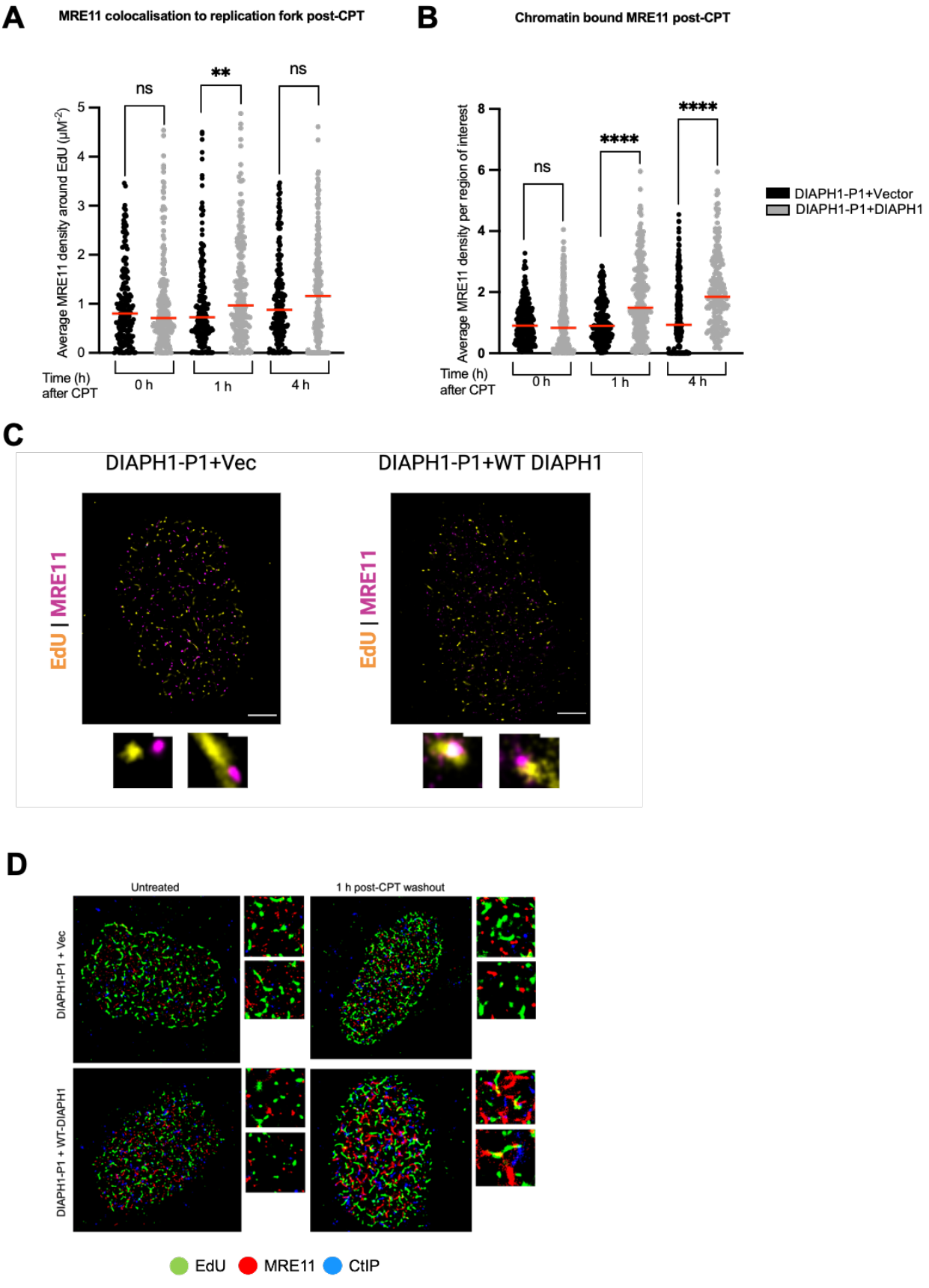

A
MRE11 colocalisation to replication fork post-CPT
Average MRE11 density around EdU (µM-2)
ns
**
ns
Time (h) after CPT
0 h
1 h
4 h
B
Chromatin bound MRE11 post-CPT
Average MRE11 density per region of interest
ns
****
****
DIAPH1-P1+Vector
DIAPH1-P1+DIAPH1
C
DIAPH1-P1+Vec
DIAPH1-P1+WT DIAPH1
EdU | MRE11
D
Untreated
1 h post-CPT washout
DIAPH1-P1 + Vec
DIAPH1-P1 + WT-DIAPH1
EdU
MRE11
CtIP

Figure 4.18 - Quantification of average local density of MRE11 detected around individual EdU molecules in P1+Vector and P1+DIAPH1 cells - *Fibroblasts were seeded onto glass coverslips and left untreated or treated with 100 nM CPT for 1 h. 30 min into CPT treatment, cells were pulsed with 10 uM EdU for 30 min. Coverslips were harvested at specific time-points post-treatment (1 h, 4 h) and fixed with 3.6 % paraformaldehyde (PFA). Cells were then imaged using stochastic optical reconstruction microscopy (STORM) and regions of interest (ROI) were selected for analysis and single molecule pair correlation of MRE11 to EdU was calculated using MatLab.* ***A*** *- Average local density of MRE11 around individual EdU molecules in P1+Vector and P1+DIAPH1 fibroblasts in untreated conditions and 1 h and 4 h post-CPT, fold change has been normalised to untreated controls.* ***B*** *– Average MRE11 density bound to chromatin in P1+Vector and P1+DIAPH1 fibroblasts in untreated conditions and 1 h and 4 h post-CPT, fold change has been normalised to untreated controls. Fold change has been normalised to untreated controls.* ***C*** *- Representative STORM multicolor images of EdU incorporation (orange), MRE11 (magenta).* ***D*** *– Alternative STORM multicolor images of EdU incorporation (green), of MRE11 (red) and CtIP (blue) (Figure 4.19) Representative MRE11 (magenta). Scale bar 1500 nm. n = 3 independent repeats, for individual ROIs of MRE11 analysed, n= a minimum of 199. Red line denotes the median. * Indicates statistical significance (p=<0.05), ** indicates statistical significance (p=<0.01), *** indicates statistical significance (p=<0.001), **** indicates statistical significance (p=<0.0001). Statistical significance was calculated using an unpaired Student's T-Test test using GraphPad Prism software.*

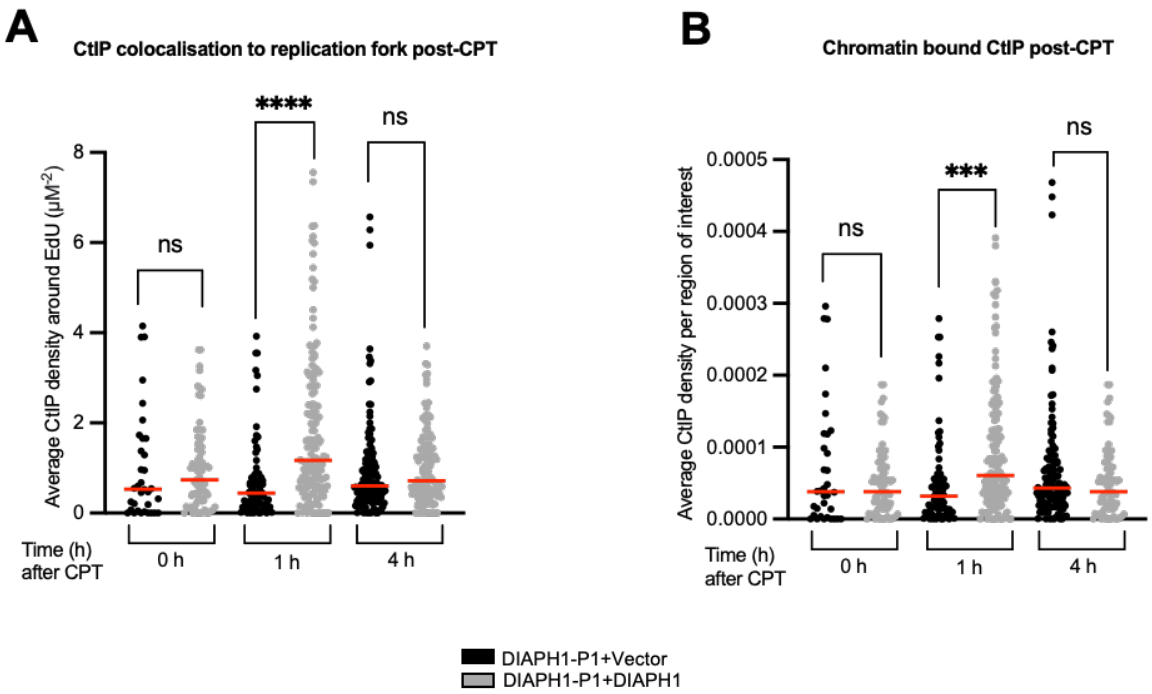


Figure 4.19 - Quantification of average local density of CtIP detected around individual EdU molecules in P1+DIAPH1 and P1+Vector cells - Fibroblasts were seeded onto glass coverslips and left untreated or treated with 100 nM CPT for 1 h. 30 *min into CPT treatment, cells were pulsed with 10 uM EdU for 30 min. Coverslips were harvested at specific time-points post-treatment (1 h, 4 h) and fixed with 3.6 % paraformaldehyde (PFA). Cells were then imaged using stochastic optical reconstruction microscopy (STORM) and rregions of interest (ROI) were selected for analysis and single molecule pair correlation of CtIP to EdU was calculated using MatLab.* ***A*** *- Average local density of CtIP around individual EdU molecules in P1+Vector and P1+DIAPH1 fibroblasts in untreated conditions and 1 h and 4 h post-CPT, fold change has been normalised to untreated controls.* ***B*** *– Average CtIP density bound to chromatin in P1+Vector and P1+DIAPH1 fibroblasts in untreated conditions and 1 h and 4 h post-CPT, fold change has been normalised to untreated controls. Scale bar 1500 nm. n = 3 independent repeats, for individual ROIs of CtIP analysed, n= a minimum of 34. Red line denotes the median. * Indicates statistical significance (p=<0.05), ** indicates statistical significance (p=<0.01), *** indicates statistical significance (p=<0.001), **** indicates statistical significance (p=<0.0001). Statistical significance was calculated using an unpaired Student's T-Test test using GraphPad Prism software.*

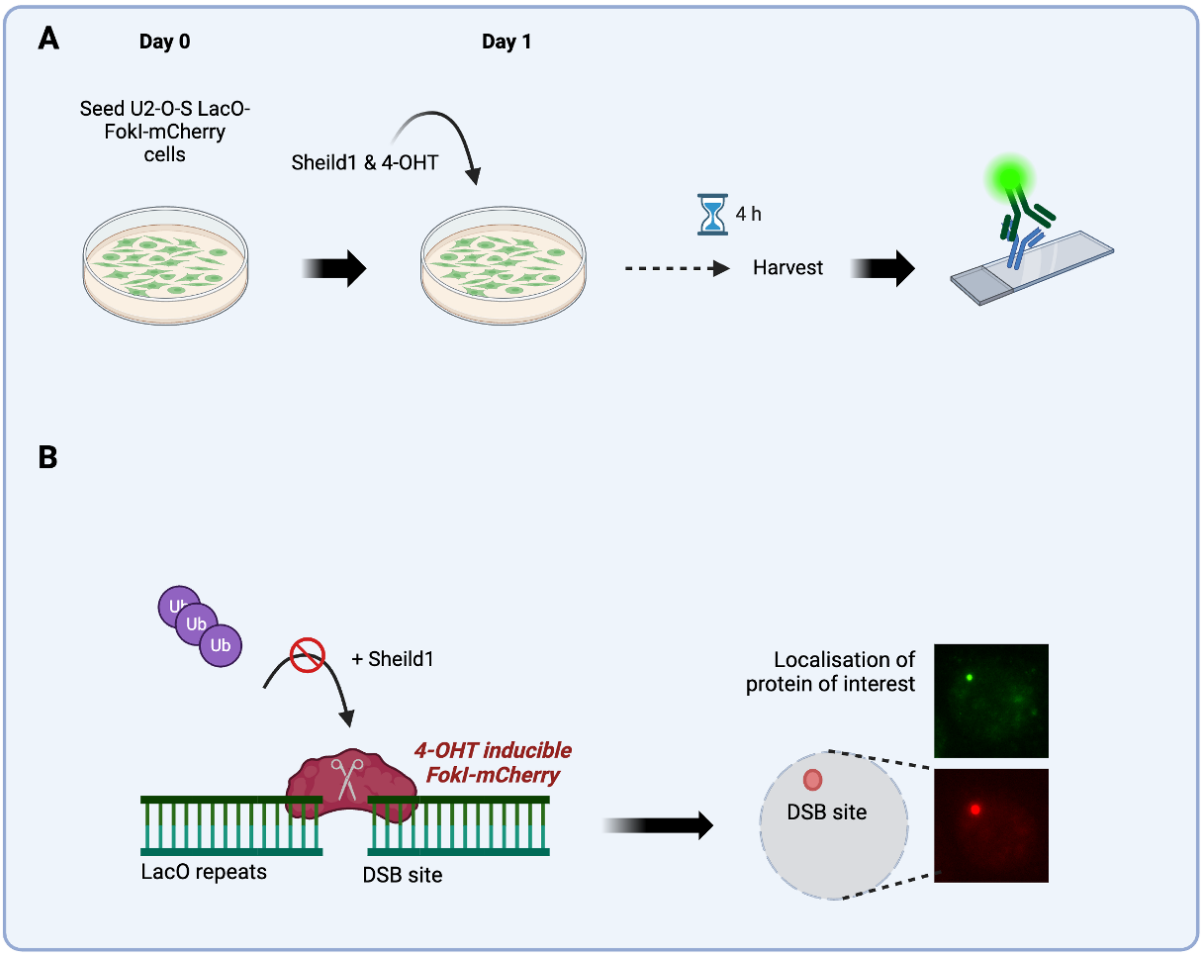


Figure 4.20 – Schematic diagram of mCherry-LacI-FokI-DD nuclease system – A *- mCherry-LacI-FokI-expressing U-2-OS cells depleted of DIAPH1 with siRNA were plated into dishes and cultured for 24 h (Day 0). 24 h later (Day 1), cells were treated with Sheild1 and 4-Hydroxytamoxifen (4-OHT) then harvested and fixed in 3.6 % PF 4 h later. Cells were then subject to IF (Figure 4.1) visualised with fluorescent microscopy.* ***B*** *– 4-OHT treatment induces the mCherry-FokI nuclease to make a DSB at a specific LacO site. Sheild1 prevents degradation of mCherry-FokI. Cells that have been fixed in PFA were incubated with specific antibodies to proteins of interest. Cells were imaged and fluorescent intensity of protein of interest (Green) at mCherry-FokI sites (red) were calculated in ImageJ. Created with Biorender.com.*

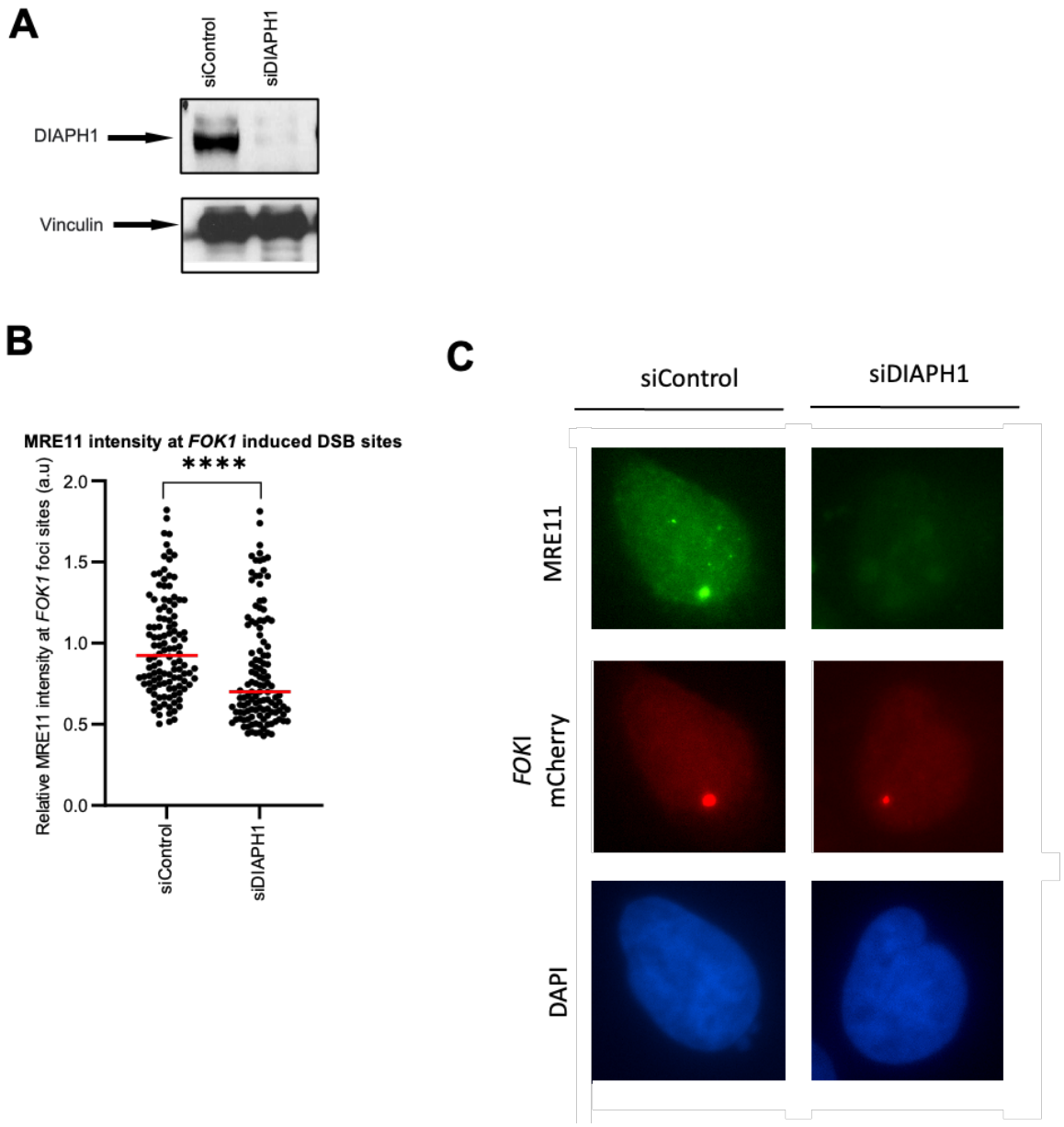


Figure 4.21 – Quantification of MRE11 signal intensity as mCherry-LacO-FokI-induced DSB sites – *mCherry-LacO-FokI expressing U-2-OS cells subject to siRNA depletion of DIAPH1 and a non-targeting luciferase control for 6 h. Cells were then treated with 1 uM Sheild1 and 1 uM 4-OHT for 4 h then harvested and fixed in 3.6 % PFA. Fixed cells were then incubated with specific antibodies raised against MRE11 and imaged with fluorescent microscopy. Images were subject to analysis of MRE11 fluorescent signal intensity at FokI-induced DSB sites.* ***A*** *- Western blot of cell lysates to show successful siRNA mediated depletion of DIAPH1. Vinculin was used as a loading control. This blot has been cropped from a larger blot in Chapter 5 (Figure 5.17).* ***B*** *– MRE11 fluorescent intensity at FokI DSB sites in arbitrary units (a.u).* ***C*** *– Representative image of cells captured in (B). Data from 3 independent repeats, a minimum of 100 cells analysed per condition per repeat. MRE11 intensity was quantified in ImageJ at the FokI site only. Red line denotes the median. * Indicates statistical significance (p=<0.05), ** indicates statistical significance (p=<0.01), *** indicates statistical significance (p=<0.001), **** indicates statistical significance (p=<0.0001). Statistical significance was calculated using a Mann-Whitney rank sum test using GraphPad Prism software.*

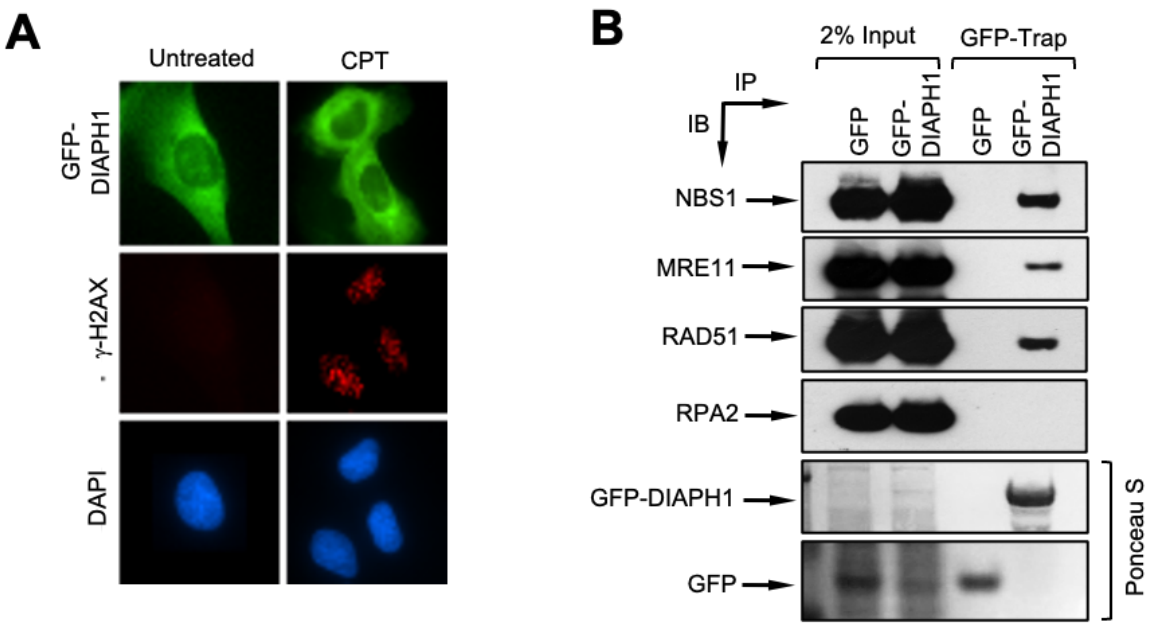


Figure 4.22 – GFP-DIAPH1 nuclear localisation and binding to HR proteins – A *- U-2-OS cells expressing a doxycycline (DOX) inducible GFP-DIAPH1 were treated with 10 mg/ml DOX for 24 h. Cells were then plated on glass coverslips and treated with 100 nM CPT for 1 h, then permeabilised and fixed in 3.6 % PFA 1 h post-CPT. Cells were stained with specific antibodies to γ-H2AX (red), and DAPI (blue) to stain the nucleus and visualised for GFP-DIAPH1 (green) localisation.* ***B*** *- HEK293FT cells were transfected with GFP or GFP-tagged WT DIAPH1 as indicated. GFP-DIAPH1 was purified from cell extracts using GFP-Trap and co-purified proteins were subjected to SDS-Page and Western blotting with the antibodies indicated. Ponceau S stain was used to visualise the affinity purified GFP and GFP-tagged DIAPH1 on the nitrocellulose filter.*

4.3.5 Loss of DIAPH1 leads to reduced resection following DSBs

Following DSB induction, initially MRE11 generates a nick in the DNA proximal to the break, which is then followed by resection in a 3'-5' direction (Sartori *et al.*, 2007; Panier and Boulton, 2014; Anand *et al.*, 2016; Qiu and Huang, 2021). Long-range resection to extend the amount of ssDNA is carried out by EXO1 and DNA2 in a 5'-3' direction. Since DIAPH1 interacts with and is required for the relocalisation of the MRN complex to seDSBs following CPT treatment, whether DIAPH1 is required for the resection step in the HR process was then investigated.

To address this, the native BrdU foci assay was used to examine resection following treatment with 10 Gy IR. This assay involves culturing cells in the presence of BrdU for 24 h, so that BrdU is incorporated into nascent DNA during replication. Following this, cells were treated with 10 Gy IR then permeabilised and fixed in 3.6 % PFA 1 h post-irradiation. Cells were then stained with antibodies to BrdU and CENPF. BrdU that has been incorporated into dsDNA is not accessible to the anti-BrdU antibody unless resection has taken place. Therefore, the amount of native BrdU foci induced by IR is related to the amount of DSB end resection. To quantify DNA end resection, BrdU fluorescent intensity was measured in CENPF-positive cells using fluorescent microscopy and ImageJ (Kilgas, Kiltie and Ramadan, 2021).

HeLa cells were first transfected with siRNA to DIAPH1 or non-targeting luciferase. siRNA depleted cells were then plated into glass coverslips and cultured for 24 h in the presence of BrdU. To act as a positive experimental control, control siRNA treated cells

were treated with mirin, an MRE11 nuclease inhibitor, 1 h prior to IR treatment (Dupré, Boyer-Chatenet and Gautier, 2006; Bian *et al.*, 2019). In control siRNA transfected cells, IR induced a significant increase in BrdU foci formation indicative of DSB end resection (Figure 4.23A-B), which was inhibited in the presence of mirin. In contrast, IR did not induce an appreciable increase in BrdU staining in cells depleted of DIAPH1. This suggests that DIAPH1 is required for MRE11-dependent resection of DSBs.

To confirm that DIAPH1 is required for DSB end resection, *Asi*SI-ER U-2-OS cells coupled with RT-PCR were utilised to analyse the amount of ssDNA generated by resection at two specific loci 335bp and 1618bp away from an *Asi*SI-induced DSB (Figure 4.24) (Zhou *et al.*, 2014). The *Asi*SI-ER U-2-OS cells were subject to siRNA depletion of either DIAPH1 or a non-targeting luciferase control (Figure 4.25A) then were left to grow exponentially for 24 h. 300 nM 4-OHT was added to induce nuclear localisation of *Asi*SI nuclease which then generates a DSB at defined loci containing a 5′-GCGATCGC-3′ sequence (Figure 4.24A) (Zhou *et al.*, 2014). Following this, gDNA was then purified from the cells and incubated with the *BsrGI* restriction enzyme, which digests the gDNA 335bp and 1618bp upstream of the *Asi*SI-DSB loci. If resection has taken place, the gDNA is unable to be digested by *BsrGI* and when RT-PCR is performed, the surrounding gDNA sequence is amplified. In absence of resection, the gDNA is digested by *BsrGI*, which reduces the efficiency of the RT-PCR (Figure 4.24B). Reassuringly, using this assay it was observed that depletion of DIAPH1 resulted in a significant reduction in the amount of ssDNA present at resected DSBs when normalised to the non-targeting siRNA control cells, at both loci located 335bp and 1618bp downstream of the DSB (Figure 4.25B-C). The defect was greater at

335bp suggested the loss of DIAPH1 has a more deleterious impact on short-range resection.

Together, these results provide evidence that DIAPH1 may be required for the resection of DNA DSBs. Preliminary evidence shown in this chapter suggest this may, in part, be due to DIAPH1 playing a role in promoting the relocalisation of the MRN complex to break sites.

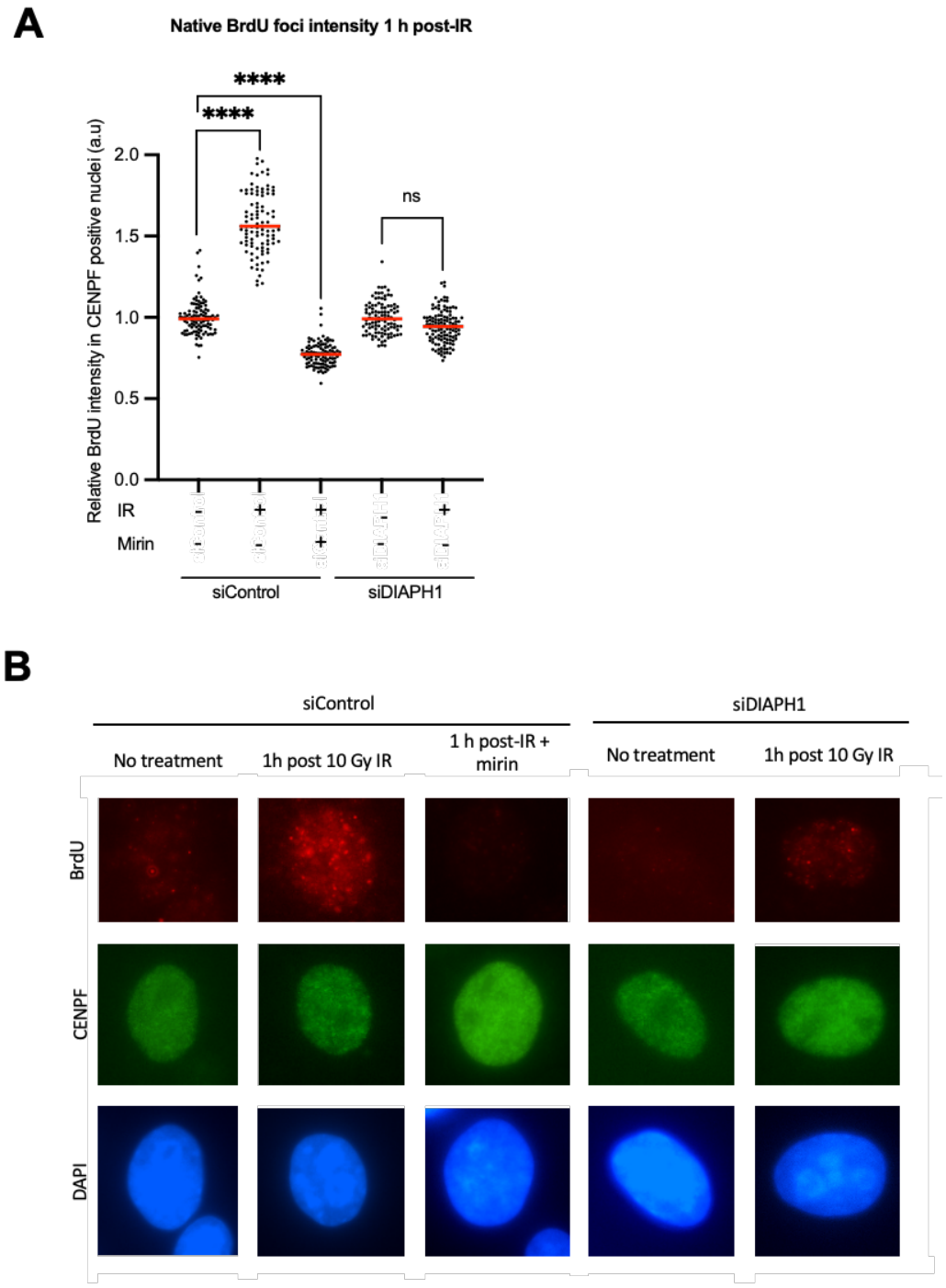


Figure 4.23 – Native BrdU foci intensity in DIAPH1 depleted HeLa cells – *HeLa cells were subject to siRNA depletion of DIAPH1 and a non-targeting luciferase control for 18 h. siRNA treated cells were then incubated with 10 μM BrdU for 24 h. Mirin treated cells were incubated with mirin 1 h prior to IR. Cells were then irradiated with 10 Gy IR and permeabilised and fixed in 3.6 % PFA 1 h post-IR. Cells were then stained with specific antibodies to BrdU and CENPF to mark G_2-phase cells.* ***A*** *– Quantification of native BrdU foci intensity in DIAPH1 depleted HeLa cells.* ***B*** *– Representative image of A. Data from 3 independent repeats, a minimum of 100 cells analysed per condition per repeat. BrdU intensity was quantified in ImageJ in CENPF positive cells only. Fold change has been normalised to untreated controls. Red line denotes the median. * Indicates statistical significance (p=<0.05), ** indicates statistical significance (p=<0.01), *** indicates statistical significance (p=<0.001), **** indicates statistical significance (p=<0.0001). Statistical significance was calculated using a Mann-Whitney rank sum test using GraphPad Prism software.*

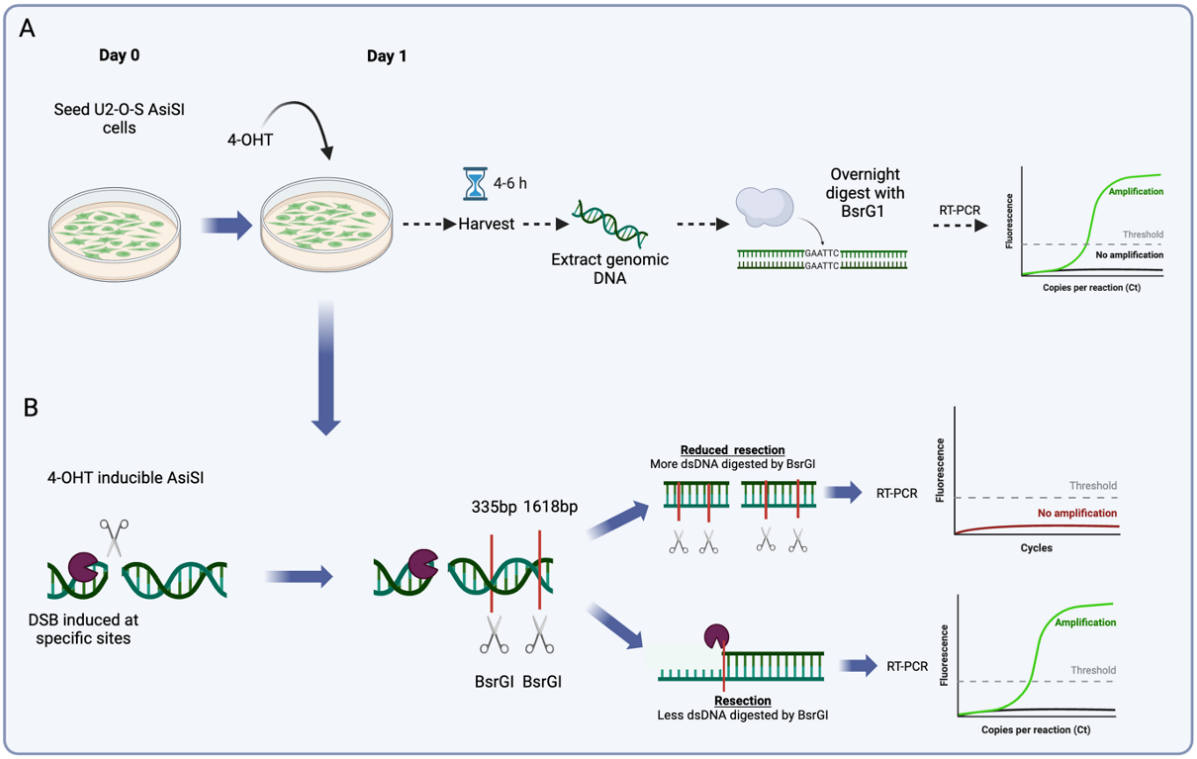


Figure 4.24 – Schematic diagram of AsiSI-end resection assay - A *- AsiSI-U-2-OS expressing cells were subject to siRNA of proteins of interest and plated into 10 cm dishes. Cells were then treated with 4-OHT to induce AsiSI nuclease to induce specific DSB. Genomic DNA was then extracted and incubated overnight with BsrG1 restriction enzymes. DNA was then subject to RT-PCR to examine resection shown in B.* ***B*** *– AsiSI induces DSBs are specific sites and genomic DNA is extracted and subject to DNA digestion by BsrGI resection enzymes. BsrGI digests DNA 335bp and 1618bp upstream of the induced DSB. DNA was then subject to RT-PCR. In cases where resection has been reduced, more dsDNA is digested by BsrGI, meaning less amplification of RT-PCR fluorescent signal. Under normal resection conditions, less dsDNA is available for digestion by BsrGI, therefore more DNA exists for specific primers to bind to, and a greater signal amplitude is produced by RT-PCR.*

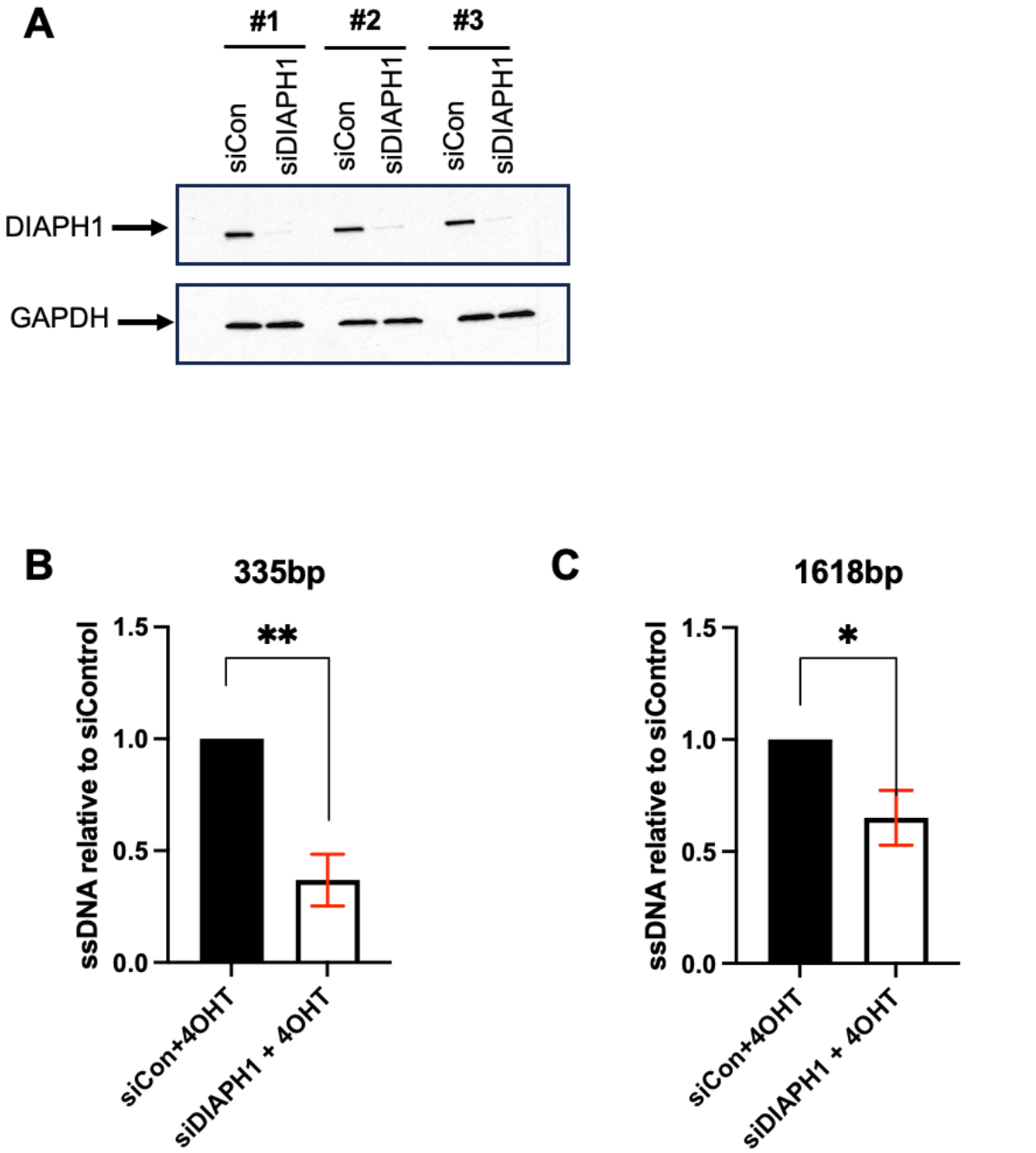


Figure 4.25 – Quantification of DNA end resection using AsiSI-ER U-2-OS reporter assay - *AsiSI-ER expressing U-2-OS were subject to siRNA depletion of DIAPH1 or a non-targeting luciferase control for 6 h.* ***A*** *– Western blot of cell lysates to show successful siRNA mediated depletion of DIAPH1. Vinculin was used as a loading control.* ***B*** *- Quantification of resection of an AsiS1-induced DSB on chromosome 1 at a position 335 bp away from the DSB using RT-PCR in U-2-OS cells transfected with either control of DIAPH1 targeted siRNA.* ***C*** *- Quantification of resection of an AsiS1-induced DSB on chromosome 1 at a position 1618bp away from the DSB using RT-PCR in U-2-OS cells transfected with either control of DIAPH1 targeted siRNA. Relative levels of resection in cells treated with DIAPH1 siRNA were normalised to that present in the control siRNA transfected cells for each experiment and represented as a fold decrease in resection. Data from 3 independent repeats, a minimum of 500 cells counted per condition per repeat. Error bars represent standard error of the mean. * Indicates statistical significance (p=<0.05), ** indicates statistical significance (p=<0.01), *** indicates statistical significance (p=<0.001) calculated using an unpaired Students T-test. Statistical significance was calculated using GraphPad Prism software.*

4.4 Concluding remarks

The data presented within this chapter supports the notion that DIAPH1 is a novel DSB repair factor required for the resection of DSBs. Given the clinical phenotype of patients with homozygous variants in *DIAPH1* sharing many of the clinical features of the DSB repair disorder NBS, it was hypothesised that DIAPH1 is required for DSB repair. DIAPH1 is required specifically for HR repair, where it is needed for the MRN complex to relocalise to DSB break sites. This is the first documentation of an actin nucleating factor being shown to be required upstream of the MRN complex in DSB repair. As DIAPH1 is required for MRN complex function, this provides a mechanistic explanation for why patients with loss of DIAPH1 and NBS patients display a significant clinical overlap. Whilst DIAPH1 patients do exhibit additional clinical features not exhibited by patients with NBS, such as seizures and blindness, the neurodevelopmental and immunological defects could be explained by a failure of the MRN complex to relocalise to DSB sites. Currently it is not clear whether DIAPH1 is regulating the relocalisation of the MRN complex to the sites of damage through direct interaction or that this is mediated by another protein, possibly actin. Interestingly, DIAPH1 can also interact with RAD51, which suggests that DIAPH1 and/or actin also plays a role during the latter stages of HR.

It has been previously proposed that nuclear actin facilitates HR-dependent DSB repair downstream of DNA end resection, via MRE11-dependent recruitment of the WASP and the ARP2/3 complex to DSB sites (Schrank *et al.*, 2018). This process then triggers actin filament formation which promotes DSB mobilisation and subsequent

relocalisation of DSBs to the nuclear periphery (Caridi *et al.*, 2018). It was further proposed that the actin network is involved in a positive feedback loop whereby the DSBs destined for repair by HR are moved and clustered together, which potentiates further resection (Schrank *et al*., 2018). In contrast, the observations presented within this chapter indicate that DIAPH1 and by extension actin, are acting upstream of DNA end resection and promote HR-dependent DNA repair by facilitating the localisation of the MRN complex to sites of DSBs. Notably, whilst the involvement of DIAPH1 as an actin nucleation factor during DNA repair has not been extensively studied, two independent studies ruled out a role for DIAPH1 in this process (Belin, Lee and Mullins, 2015; Caridi *et al*., 2018). Interestingly, in both cases the level of DIAPH1 (or Dia1 in Drosophila) knockdown was not very efficient. This suggests that perhaps the lack of involvement of DIAPH1 in nuclear actin-dependent DSB repair was incorrectly concluded due to sufficient residual protein being present in the cells. Alternatively, in the context studied, the role of actin could be independent of DIAPH1. However, whether DIAPH1 functions to facilitate the repair of DSBs by HR in combination with the ARP2/3 complex and actin remains to be investigated.

In addition to HR, actin has also been implicated in NHEJ by one study, where the authors showed that disruption of actin filament formation disrupted the ability of Ku80 to associate with damaged chromatin, which coincided with a reduced efficiency of NHEJ (Andrin *et al.*, 2012). However, this study, which predominantly used a dominant negative polymerisation deficient actin mutant and a chemical inhibitor of actin polymerisation (Latrunculin) to disrupt actin filament formation, also observed a reduction in the DNA damage-induced chromatin binding of ATM, MRE11 and CHK2,

following actin inhibition. Furthermore, this study did not examine the involvement of any of the known actin nucleating factors, previously implicated in mediating DSB repair, in regulating actin-dependent NHEJ. Whilst this study suggests a role for actin in mediating DNA end-joining, it did not specifically link this with an inability to localise Ku80 to sites of DSBs. In addition, since inhibiting actin polymerisation using inhibitors also affected the recruitment of HR factors, such as ATM and MRE11, to damaged chromatin, it is not clear from this study whether the failure to repair DSBs efficiently when actin polymerisation is chemically inhibited arises from a defect in NHEJ or HR or both. Despite this, our observations are consistent with a requirement for nuclear actin polymerisation to efficiently relocalise the MRE11 complex to sites of DNA DSBs. However, whilst it is possible that loss of DIAPH1 may also affect NHEJ, the observations that loss of DIAPH1 leads to a S/G_2-phase specific DSB repair defect and an inability to repair DSBs-induced by low dose CPT treatment, would strongly indicate that loss of DIAPH1 does not play a major role in regulating NHEJ.

Despite ruling DIAPH1 out as a regulator of NHEJ, similar to NBS patients, loss of DIAPH1 does give rise to immunodeficiency e.g. lymphopenia and reduced immunoglobulins. Many immunodeficiency disorders in humans, such as severe combined immunodeficiency disorder (SCID) arise due to underlying mutations in NHEJ components, including *DCLRE1C* (encoding Artemis), *LIG4* (encoding DNA Lig IV), *XRCC4* and *PRKCD* (encoding DNA-PKcs) (Riballo *et al.*, 2004; Van der Burg *et al.*, 2009; Volk *et al.*, 2015; Fournier *et al.*, 2022). In addition, immunodeficiency can also arise as a consequence of mutating *NBN* or *ATM*, two genes primarily involved in regulating HR-dependent repair. In this case, whilst NBS1 and ATM are not involved

in regulating NHEJ *per se*, they do play roles in the repair of physiologically induced DSBs arising during V(D)J recombination and class-switch recombination. Consistent with DIAPH1 playing a role in the repair of DSBs generated during B and T cell receptor maturation similar to ATM and NBS1, none of the affected patients with DIAPH1 mutations exhibited a SCID phenotype, although there were some minor alterations in B and T cell numbers. In contrast, for the few patients where blood was available, they showed a complete absence of TRECs (T-cell rector excision circles). TRECs are the circularized bits of intervening DNA that are removed during T cell receptor rearrangement and a reduction in these is used as a diagnostic marker of immunodeficiency arising from V(D)J recombination abnormalities. Patients with immunodeficiency caused by mutations in core NHEJ factors, components of the MRN complex or ATM all exhibit a reduction in the levels of TRECs found in their blood (Serana *et al.*, 2013; Patel *et al.*, 2015; Recio *et al.*, 2019; Slatter and Gennery, 2020). As such, a complete absence of TRECs in DIAPH1 mutant patients would be consistent with a defect in either NHEJ- or ATM/MRN-dependent DSB repair during immune receptor rearrangement. Interestingly, no obvious defects in activation of the ATM- or ATR-dependent DNA damage response were observed in the DIAPH1 patient cell lines, indicating that the immunodeficiency and absence of TRECs is not linked to defective ATM signalling. Interestingly, mutations in the actin nucleating factors, WASP, ARPC1B and ARPC5 also give rise to immunodeficiency (Stiehm and McIntosh, 1967; Bouma, Burns and Thrasher, 2009; Brigida *et al.*, 2018; Janssen and Geha, 2019; Papadatou *et al.*, 2021; Chiriaco *et al.*, 2022; Nunes-Santos *et al.*, 2023). Whilst the mechanism of these immunodeficiencies have not been specifically linked with a DNA repair deficiency, given the emerging model of actin, the ARP2/3 complex

and WASP in mediating DSB repair, it is conceivable that the immunodeficiency in these patients may be in part due to the defective repair of physiologically induced DSBs. However, further work is needed to elucidate this precise mechanism of whether DIAPH1's role in DNA repair is actin-dependent or independent and whether defects in this process are linked to the development of immunodeficiency.

Chapter 5: Characterisation of the role of *ACTB* and *ACTG1* in double strand break repair

5.0 Results

5.1 Introduction

The data presented in this thesis, so far, has showed that DIAPH1 is a novel regulator of Homologous recombination (HR) and loss of DIAPH1 in humans gives rise to a double strand break (DSB) repair disorder similar to Nijmegen Breakage Syndrome (NBS). Given that DIAPH1's main role in the cytoplasm is to nucleate linear filaments of actin, the key question that remains is whether DIAPH1's role in DSB repair is direct, such as that it directly binds specific DNA repair proteins or indirect i.e. this function is mediated via the actin network. Data in Chapter 4 demonstrated that DIAPH1 interacts with components of the MRN complex and RAD51 but it was not clear if this interaction is directed by or is mediated by actin.

Actin is the most abundant protein within eukaryotic cells and consequently, it is involved in a diverse array of cellular processes (Chapter 1, Section 1.3). Whilst there are 6 actin paralogs, some of which have tissue-specific expression e.g. α-actin is specifically expressed in smooth and cardiac muscle, the two ubiquitously expressed non-muscle actin isoforms are β- and γ-actin, encoded by *ACTB* and *ACTG1* respectively (Dominguez, 2009). Both β- and γ-actin are primarily expressed in the cytoplasm but are also present in the nucleus at lower levels. β-actin is the predominant form of cellular actin and is required to maintain cell structure and is involved in regulating cell migration and intracellular transport. γ-actin is also expressed in all cell types but is less abundant than β-actin and is important in specialised cell types such

as hair cells in the inner ear, neurons, and muscle cells. γ-actin is particularly important for cell motility and protrusions such as filopodia and lamellipodia (Dugina *et al.*, 2009). Despite the variation in β- and γ-actin function, the amino acid sequence is near identical, differing by only 4 amino acids in the N-terminus (Chapter 1, Figure 1.3A) (Dominguez, 2009; Jeruzalska and Mazur, 2023). However, more often than not, these isoforms play non-redundant roles despite being involved in the same cellular processes. For instance, the activation of DIAPH3 at the cytokinetic furrow promotes the generation of a contractile ring composed of β-actin at the cell equator. Conversely, DIAPH1 localises to the cortex of a mitotic cell, where it promotes assembly of γ-actin filaments, which influences positioning of the cytoplasmic furrow and governs the rate of membrane ingression (Chen *et al.*, 2017, 2021; Jeruzalska and Mazur, 2023).

Patients with *de novo* variants in both *ACTB* and *ACTG1* give rise to Baraitser-Winter Cerebrofrontalfacial (BWCFF) syndrome, which is a rare disorder that causes intellectual disability and distinct facial features. Additional features include short stature and cortical malformations (e.g. lissencephaly and pachygyria) (Yates *et al.*, 2017). Interestingly, despite the extensive clinical variability observed in BWCFF, many of the reported cases exhibit clinical overlap with patients with mutations in *DIAPH1* such as microcephaly, seizures, hearing loss and immunodeficiency (Rivière *et al.*, 2012; Di Donato *et al.*, 2014; Verloes *et al.*, 2015; Cuvertino *et al.*, 2017; Zech *et al.*, 2017; Cabanillas *et al.*, 2018; Latham *et al.*, 2018; Miyajima *et al.*, 2020). Additionally, human diseases associated with the ARP2/3 complex also exhibit some overlap with the clinical deficits exhibited by patient with mutations in *ACTB*, *ACTG1* and *DIAPH1*. Homozygous mutations in *ARPC1B* and *ARPC5* predominantly give rise to

immunodeficiency, whereas *de novo ARPC4* mutations also cause microcephaly (Brigida *et al.*, 2018; Chiriaco *et al.*, 2022; Laboy Cintron *et al.*, 2022; Nunes-Santos *et al.*, 2023). Since all of these features could be caused by an underlying defect in DSB repair, this lead to the hypothesis that actin, DIAPH1 and the ARP2/3 complex may be functioning in the same pathway to promote DSB repair.

5.2 Aims of this chapter

It has been previously suggested that actin and the ARP2/3 complex function in the nucleus to regulate DNA repair by controlling the movement and clustering of DSBs (Caridi *et al.*, 2018; Schrank *et al.*, 2018). Additionally, actin and the ARP2/3 complex have also been shown to play a role in protecting stalled replication forks from nucleolytic degradation during the replication stress response (Lamm *et al.*, 2020; Nieminuszczy *et al.*, 2023; Palumbieri *et al.*, 2023). However, these studies were predominantly carried out using gene knockdown, small molecule inhibitors or the over-expression of dominant acting actin mutants, did not functionally distinguish between β-actin and γ-actin and did not assess the consequences of blocking actin-dependent DNA repair in a cellular model of disease. Therefore, the aim of this chapter is to examine the role of actin in DSB repair in more detail. Using hTERT immortalised fibroblasts derived from patients harbouring mutations in either *ACTB* or *ACTG1* as well as components of the ARP2/3 complex (ARPC1B, ARPC4 and ARPC5), it will be investigated whether disease-associated variants in the two ubiquitously expressed actin paralogs or components of the ARP2/3 give rise to an underlying DSB repair

disorder, which could potentially provide a cellular explanation for some of the clinical features exhibited by these patients.

5.3 Results

5.3.1 Clinical and genetic information of patients with variants in *ACTB, ACTG1* and components of the ARP2/3 complex

BWCFF syndrome is the main disease associated with *ACTB* and *ACTG1* mutations. There is significant heterogeneity associated with BWCFF syndrome which may reflect the vast array of cellular functions and protein-protein interactions mediated by actin. However, given the findings that DIAPH1 gives rise to a novel DSB repair disorder and the clinical overlap with the diseases associated with DIAPH1 and BWCFF syndrome, it was hypothesised that mutations in *ACTB* and *ACTG1* may also give rise to a defect in DSB repair. To investigate this, the Stewart group obtained fibroblasts from a number of BWCFF syndrome patients harbouring different *ACTB* and *ACTG1* mutations as well as from patients with mutations in *ARPC1B, ARPC4* and *ARPC5*.

As previously mentioned, the clinical features and severity of BWCFF syndrome is very heterogenous, which can be explained in part by the differential impact that the individual *de novo* mutations have on protein stability and/or its capacity to be polymerised or depolymerised. The BWCFF syndrome patient mutations analysed within our cohort exhibited a range in clinical severity and presentation (Table 5.1). The specific location of the individual *ACTB* and *ACTG1* mutations tested is shown in

Figure 5.2A-C. For comparison, a summary of the clinical features of both heterozygous and homozygous *DIAPH1* variants are shown to highlight the clinical overlap between DIAPH1 and actin mutations, despite the actin mutations arising sporadically. Since all the *ACTB* and *ACTG1* mutations are *de novo*, this means that have occurred spontaneously during development and have not been inherited. Furthermore, each patient still retains one wild-type allele and as such, the mutations act in either a dominant or haploinsufficient manner. Table 5.1 shows that, of the six *ACTB* patients in this cohort, three exhibit microcephaly (ACTB-P1, P5 and P6), three have intellectual disability (ACTB-P1, P2 and P3), two display hearing loss (ACTB-P3 and ACTB-P4) and two exhibit short stature (ACTB-P2 and ACTB-P6). Notably, only one ACTB patient has immunodeficiency (ACTB-P4) and one patient has seizures (ACTB-P2). Five *ACTG1* patients were included in this cohort. Three of the five affected individuals exhibit microcephaly (ACTG1-P1, P4 and P5), three have hearing loss (ACTG1-P2, P3 and P5), and three display intellectual disability (ACTG-P1, P2 and P4). Only one ACTG1 patient has short stature (ACTG1-P2), and two patients have seizures (ACTG1-P1 and P5) (Table 5.1). None of the ACTG1 patients within our cohort were reported to have developed immunodeficiency. Whilst this cohort of patients is small, most display at least one clinical feature that overlaps with patients with mutations in *DIAPH1*.

There are six patients included in our cohort that have variants in components of the ARP2/3 complex. These include: three patients with homozygous mutations in *ARPC1B* (Table 5.1). The clinical features of the ARPC1B overlap much less with those exhibited by DIAPH1 mutant patients, as none of the three individuals exhibit

microcephaly. However, all of the patients have immunodeficiency, one patient (ARPC1B-P1) has intellectual disability and two patients (ARPC1B-P1 and P3) exhibit short stature. The two *ARPC4* mutant patients included in our cohort are siblings carrying the same *de novo* c.472C>T; p.Arg158Cys mutation. Both siblings exhibit microcephaly and intellectual disability with some additional features outlined in Table 5.1. The final patient within our cohort carries a homozygous c.23C>A; p.Ser8Ter variant in *ARPC5*. This patient presents with intellectual disability and immunodeficiency but no other clinical features that overlap with our DIAPH1 mutant patient cohort.

Table 5.1 Clinical features of patients with *ACTB, ACTG1, ARPC1B, ARPC4* and *ARPC5* with gene variants

			Clinical features							
			Microcephaly	Hearing Loss	Intellectual disability	Short stature/IUGR	Immunodeficiency	Seizures	Other Features	Reference
Heterozygous DIAPH1 patients			No	Yes	No	No	No	No	Thrombocytopenia	Lynch et al.
Homozygous DIAPH1 patient cohort			Yes	No	Yes	Yes	Yes	Yes	Dysmorphic facial features, visual impairements, lymphoid tumours	Ercan-Sencicek et al.
Individual	**Gene mutation**	**Inheritance**								
ACTB-P1 (P42045)	c.474_475DupGG; p.Val159fs	*De novo*	Yes	No	Yes	No	No	No		Not published
ACTB-P2 (P1620)	c.587G>A; p.Arg196His	*De novo*	No	No	Yes	Yes	No	Yes	Muscular hypotonia, scoliosis, constipations, minor facial anomalies (Baraitser-Winter-Cerebrofrontalfacial syndrome)	Verloes et al.
ACTB-P3 (P54667)	c.547C>T; p.Arg183Trp	*De novo*	No	Yes	No	No	No	No	Congenital bilateral deafness, generalized dystonia (dystonia-deafness syndrome)	Zech et al.
ACTB-P4 (P49146)	c.547C>T; p.Arg183Trp	*De novo*	No	Yes	No	No	Yes	No	Constipation	Not published
ACTB-P5 (P49709)	c.992_1008del; p.Ala331Valfs	*De novo*	Yes	No	Yes	No	No		Thrombocytopenia	Latham et al.
ACTB-P6 (P38076)	c.220G>A; p.Gly74Ser	*De novo*	Yes	No	Yes	Yes	No	No	Pachygyria, cleft lip and palate, VSD, minor facial anomalies (Baraitser-Winter-Cerebrofrontalfacial syndrome)	Di Donato et al. and Verloes et al.
ACTG1-P1 (P61760)	c.608C>T; p.Thr203Met	*De novo*	Yes	No	Yes	No	No	Yes	Epilepsy, minor facial anomalies (Baraitser-Winter-Cerebrofrontalfacial syndrome)	Not published
ACTG1-P2 (P55482)	c.611C>G; p.Ala204Gly	*De novo*	No	Yes	Yes	Yes	No	No	ADHD, bilateral hearing loss, intestinal pseudoobstruction at the neonatal period, TPN dependent, periodic tremors, progressive muscle atrophy	Not published
ACTG1-P3 (P64753)	c.548G>A; p.Arg183Gln	*De novo*	No	Yes	No	No	No	No	Progressive bilateral hearing loss, CI at 13y	Cabanillas et al.
ACTG1-P4 (P11422)	c.221G>T; p.Gly74Val	*De novo*	Yes	No	Yes	No	No	No	Agenesis of the corpus callosum, epilepsy, ptosis, renal duplication, liver cirrhosis, Hashimoto thyreoiditis, minor facial anomalies (Baraitser-Winter-Cerebrofrontalfacial syndrome)	Not published
ACTG1-P5 (P64984)	c.760C>T; p.Arg254Trp	*De novo*	Yes	Yes	No	No	No	Yes	Partial agenesis of the corpus callosum, dysgyria, sleep apnoea, minor facial anomalies (Baraitser-Winter-Cerebrofrontalfacial syndrome)	Not published
ARPC1B-P1	c.622G>T; p.Val208Phe (Hom)	Recessive	No	No	Yes	Yes	Yes	No	Cytopenia, thrombocytopenia, hepatosplenomegaly, failure to thrive.	Brigida et al
ARPC1B-P2	c.212_226del; p.Gly71_Asn75del (Hom)	Recessive	No	No	No	No	Yes	No	Persistent eosinophilia, failure to thrive, recurrent infections, mild thrombocytopenia, lymphopenia.	Chiriaco et al
ARPC1B-P3	c.64+1G>A (Hom)	Recessive	No	No	No	Yes	Yes	No	Severe growth failure, eczema, lymphopenia, eosinophilia, thrombocytopenia, recurrent infections	Brigida et al
ARPC4-P1.1	c.472C>T; p.Arg158Cys	*De novo*	Yes	No	Yes	No	No	No	Mild motor delay, delayed speech, ADHD, facial telangiectasia, thumb-in-palm (splinted), strabismus.	Laboy Cintron et al
ARPC4-P1.2	c.472C>T; p.Arg158Cys	*De novo*	Yes	No	Yes	No	No	No	Mild motor delay, delayed speech, ADHD, facial telangiectasia, 5th finger camptodactyly.	Laboy Cintron et al
ARPC5-P4	c.23C>A; p.Ser8Ter (Hom)	Recessive	No	No	Yes	No	Yes	No	Facial dysmorphia, autoimmune haemolytic anaemia, thrombocytopenia, neutrophilia, recurrent infections, scoliosis, hepatosplenomegaly.	Nunes-Santos et al

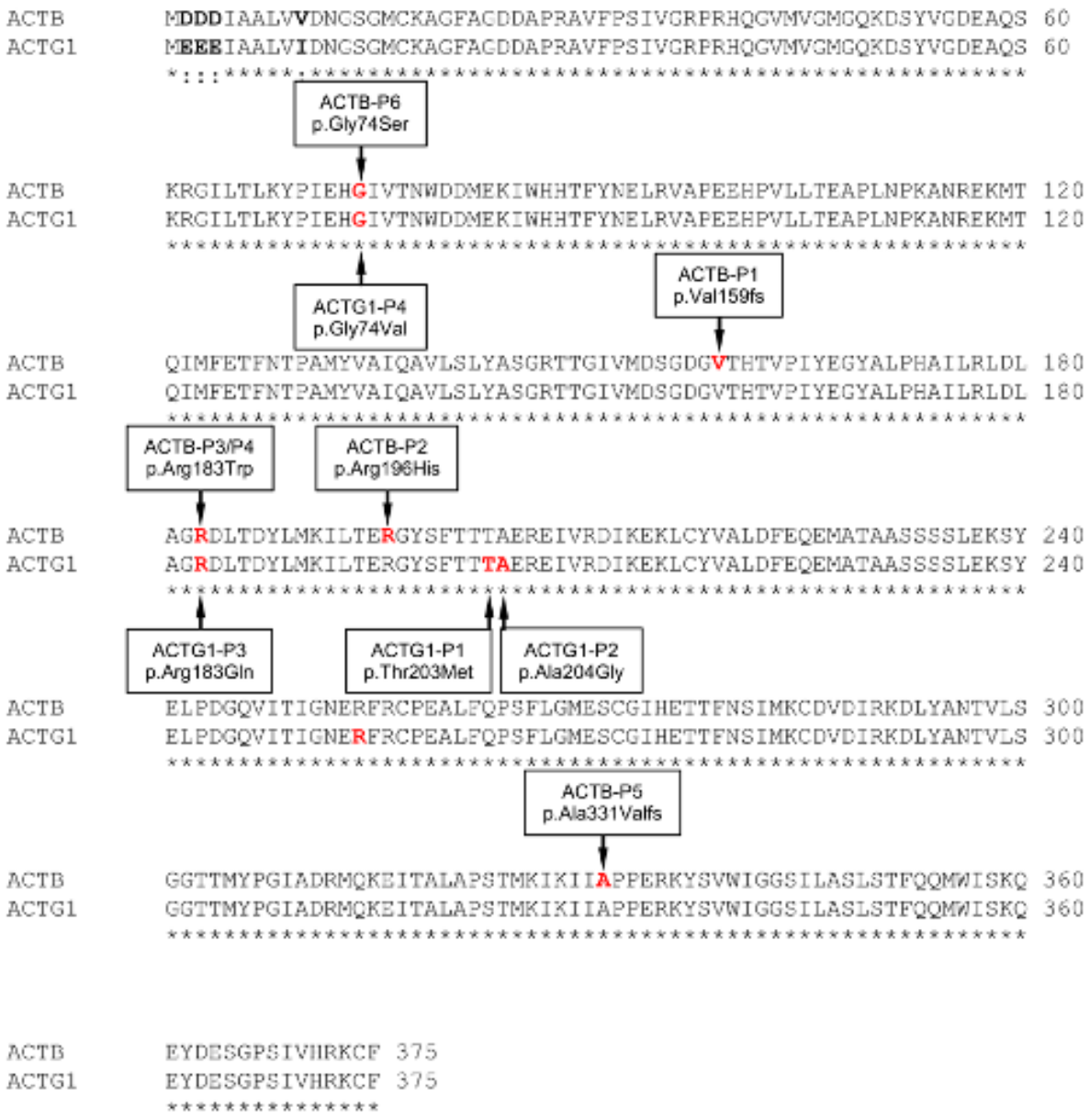


Figure 5.1 – Location of mutations in ACTB and ACTG1 protein in patient cohort – *Full length ACTB and ACTG1 proteins are shown side by side. ACTB-P1 to P6 mutations are shown on ACTB amino acid sequence (upper sequence) and ACTG1 P1-P4 are shown on ACTG1 amino acid sequence (lower sequence). All mutations arise due to de novo heterozygous gene variants in ACTB and ACTG1 respectively.*

5.3.2 Analysis of genome instability following DNA damage in ACTB, ACTG1 and ARP2/3 complex component patient cells

The clinical features exhibited by patients with mutations in *ACTB, ACTG1* and components of the ARP2/3 complex could be indicative of an underlying defect in DNA repair. To investigate this in more detail, micronuclei analysis was performed on patient fibroblasts to assess genome stability following exposure to CPT. Given that loss of DIAPH1 leads to a HR defect and both actin and the ARP2/3 complex have already been shown to play a role in HR, CPT was used initially to induce DSBs since they are only repaired by HR. First, this analysis was performed in the 11 *ACTB* and *ACTG1* patient fibroblasts at 48 h post-CPT treatment. A WT fibroblast was used as a negative control and both an NBS and A-T fibroblast were used as a positive control for defective DSB repair. In untreated conditions, no significant difference in the frequency of micronuclei were observed between the cell lines (Figure 5.2A, E). However, at 48 h post-CPT, the *ACTB* mutant patients displayed no significant increase in micronuclei compared to the WT cell line but strikingly, four out of the five *ACTG1* mutant patient cell lines displayed significantly elevated levels of micronuclei when compared to the WT cell line (Figure 5.2B, E). As expected, both the NBS and A-T fibroblast cell lines exhibited the highest levels of micronuclei. This finding suggests that γ-actin but not β-actin may be required for maintaining genome stability following the induction of DNA damage by CPT.

Next, micronuclei analysis was performed using the ARPC1B, ARPC4 and ARPC5 patient-derived fibroblasts. Again, prior to CPT exposure, no significant increase was

observed between the WT cell line and any of the ARP2/3 complex mutant patient cell lines (Figure 5.3A, C). However, 48 h post-CPT treatment, all of the patient ARP2/3 complex mutant fibroblasts exhibited a significant increase in micronuclei when compared to the WT cell line (Figure 5.3B-C). This suggests that like γ-actin, the ARP2/3 complex is required to maintain genome stability following 888 treatment.

In order to whether the increase in genomic instability was specific to CPT or could be recapitulated with other DSB inducing agents, a selection of patient-derived fibroblasts from each of the ACTB, ACTG1 and ARP2/3 complex cohorts were treated with either IR and ETOP. Again, a WT, NBS and A-T fibroblast cell line were used as controls. Reassuringly, following treatment with either 3 Gy IR or 10 μM ETOP, the same trend was observed. At 24 h post-IR and 48 h post-ETOP treatment, the ACTB patients did not display an increase in micronuclei when compared to the WT cell line but the ACTG1 and ARCP4 mutant cell lines displayed significantly elevated levels of micronuclei after either treatment, albeit this was not as severe as those observed in the NBS or A-T fibroblasts (Figure 5.4B-D). These findings further suggest that γ-actin and the ARP2/3 complex but not β-actin are required for repairing DSBs-induced by a variety of genotoxins.

Whilst my preliminary data suggests that γ-actin but not β-actin is important for DNA repair, it is difficult to make any conclusions since the patient-derived cell lines are not isogenic and the impact of the different *de novo* mutations in either *ACTB* or *ACTG1* on protein stability or its ability to polymerise/depolymerise is unknown. Therefore, to confirm this observation, A375 melanoma lacking ACTB or ACTG1 were utilised

(Figure 5.5A). Two separate clones of each CRISPR-Cas9-mediated knockout (KO) cell line were analysed to confirm that the presence of a specific cellular phenotype was not due to off target affects associated with Cas9 targeting. Micronuclei was again assessed using both KO cell lines along with a parental A375 cell line with WT *ACTB/ACTG1* following exposure to CPT, IR, and ETOP. In unperturbed conditions, there was no significant increase in micronuclei in any of the cell lines tested (Figure 5.5B-G). Consistent with the findings observed in the patient fibroblasts, following treatment with CPT, ETOP or IR, only the two *ACTG* KO clones displayed a significantly elevated level of micronuclei when compared to the WT or the ACTB KO clones. These findings strongly support the notion that γ-actin, but not β-actin, is required to maintain genome stability following the induction of DNA damage.

To confirm that γ-actin, but not β-actin, is required for maintaining genome stability, metaphase spread analysis was used as an alternative assessment of genome stability. ACTB KO and ACTG KO A375 clones were treated with either 5 nM CPT or 50 nM ETOP for 24 h. Whilst there were no observable differences in levels of chromosomal aberrations in untreated conditions between WT, ACTB or ACTG1 KO A375 cell lines (Figure 5.6A, D), following treatment with either CPT or ETOP, the ACTG1 KO clones displayed significantly elevated levels of chromosomal aberrations when compared to the ACTB KO clones and WT parent cell line (Figure 5.6B). Thus, this data provides further evidence that loss of γ-actin is associated with a DNA repair defect. However, one such way to further substantiate these findings would be to perform clonogenic survival studies following exposure to ionising radiation, CPT and

ETOP, which would provide valuable insight into how loss of *ACTB* or *ACTG1* impacts overall cell survival and longer-term effects of DNA damage.

Taken together, the data presented demonstrates that loss of or mutations in *ACTG1* but not *ACTB* lead to an increase in genome instability following the induction of DSBs. Furthermore, these data demonstrate that inherited or *de novo* mutations in components of the ARP2/3 complex also compromise DSB repair.

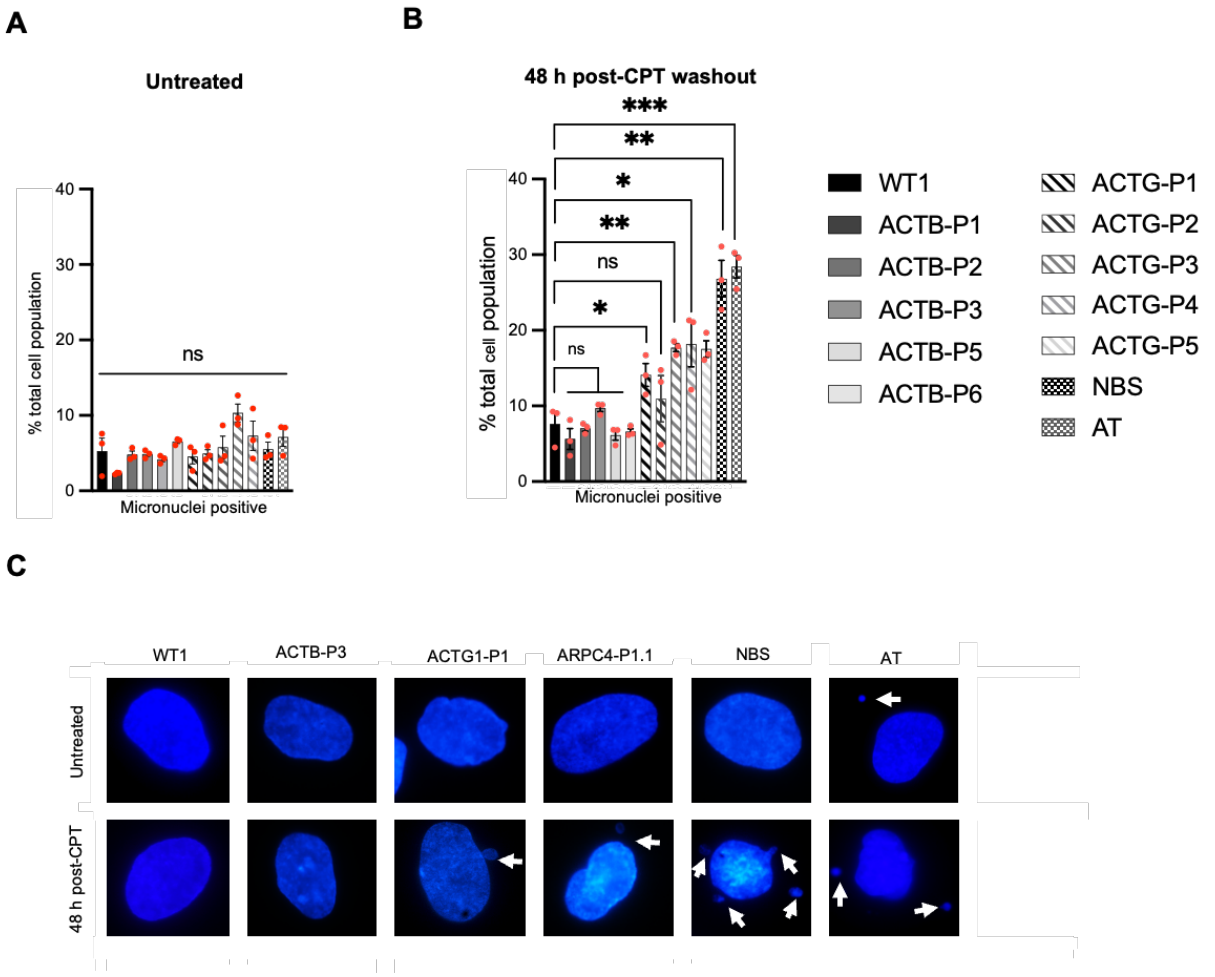


Figure 5.2 - Formation of micronuclei in ACTB and ACTG1 patient-derived hTERT immortalised fibroblasts following treatment with CPT – *Fibroblasts were seeded onto glass coverslips and left untreated or treated with 100 nM CPT for 1 h. Coverslips were harvested at specific time-points post treatment (1 h, 48 h) and fixed with paraformaldehyde (PFA).* ***A*** *- Quantification of micronuclei in the absence of exogenous DNA damage.* ***B*** *- Quantification of micronuclei 48 h post-CPT.* ***C*** *- Representative images of DAPI positive cells from quantification in (A-B). Data from 3 independent repeats, a minimum of 500 cells counted per condition per repeat. Error bars represent standard error of the mean. * Indicates statistical significance (p=<0.05), ** indicates statistical significance (p=<0.01), *** indicates statistical significance (p=<0.001) calculated using an unpaired Students T-test. Statistical significance was calculated using GraphPad Prism software.*

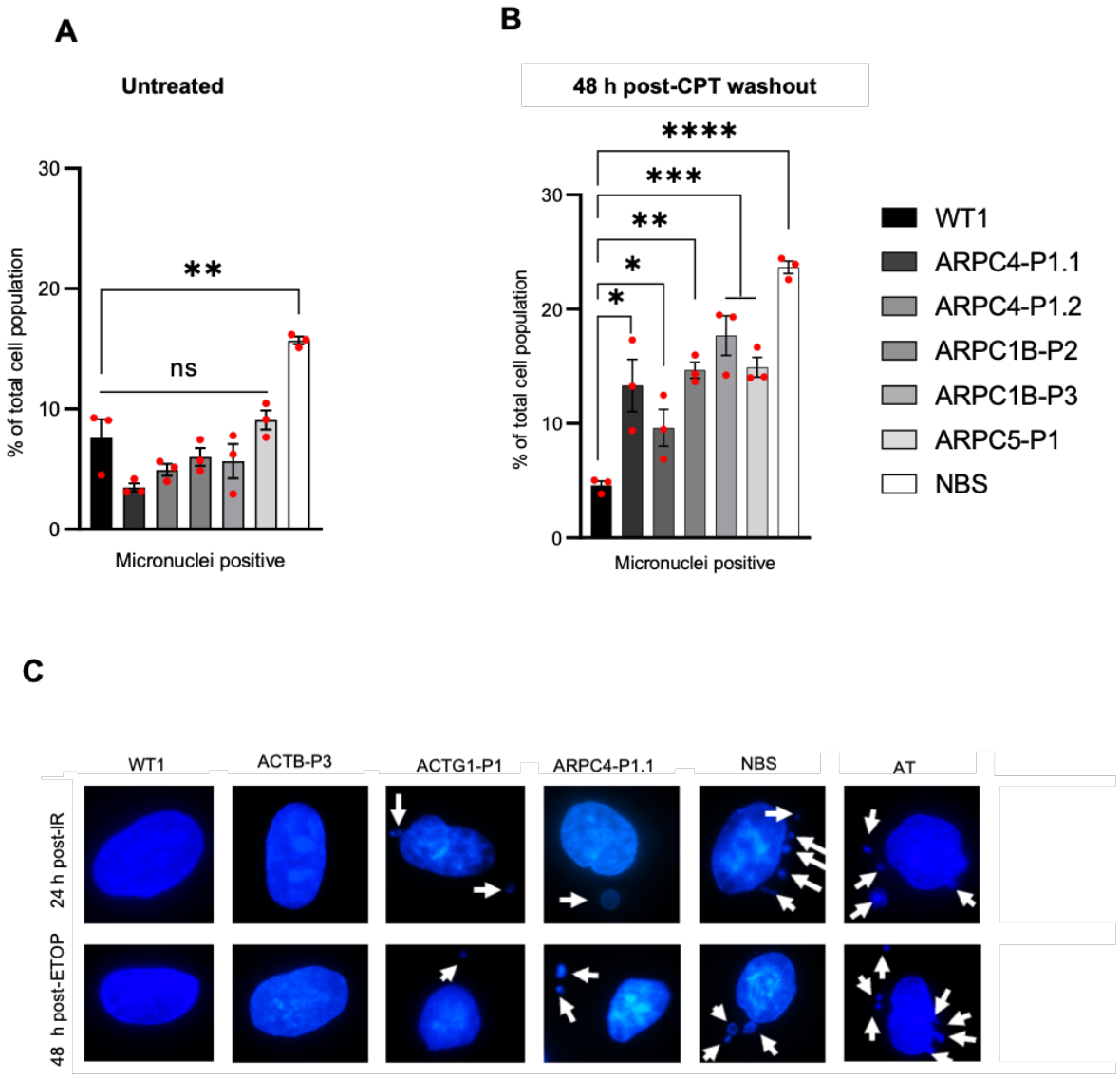


Figure 5.3 - Formation of micronuclei in ARPC1B, ARPC4 and ARPC5 patient-derived hTERT immortalised fibroblasts following treatment with CPT – *Fibroblasts were seeded onto glass coverslips and left untreated or treated with 100 nM CPT for 1 h. Coverslips were harvested at specific time-points post treatment (1 h, 48 h) and fixed with paraformaldehyde (PFA).* ***A*** *- Quantification of micronuclei in the absence of exogenous DNA damage.* ***B*** *- Quantification of micronuclei 48 h post-CPT.* ***C*** *- Representative images of DAPI positive cells from quantification in (A-B). Data from 3 independent repeats, a minimum of 500 cells counted per condition per repeat. Error bars represent standard error of the mean. * Indicates statistical significance (p=<0.05), ** indicates statistical significance (p=<0.01), *** indicates statistical significance (p=<0.001) calculated using an unpaired Students T-test. Statistical significance was calculated using GraphPad Prism software.*

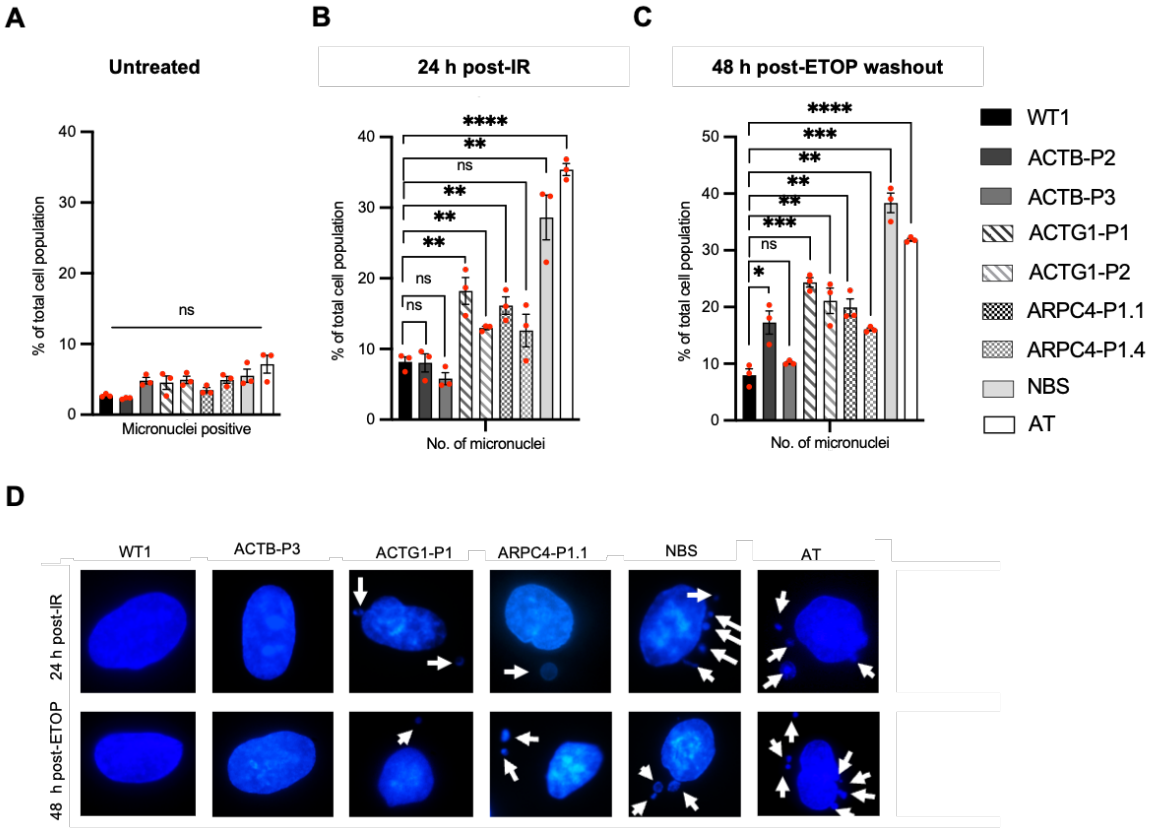


Figure 5.4 - Formation of micronuclei in ACTB, ACTG1 and ARPC1B patient-derived hTERT immortalised fibroblasts following exposure to DNA damage – *Fibroblasts were seeded onto glass coverslips and left untreated or treated with 3 Gy IR or 10 μM ETOP for 30 min. Coverslips were harvested at specific time-points post treatment (0 h, 24 h (IR), 48 h (ETOP)) and fixed with paraformaldehyde (PFA).* ***A*** *- Quantification of micronuclei in the absence of exogenous DNA damage.* ***B*** *- Quantification of micronuclei 24 h post-IR.* ***C*** *- Quantification of micronuclei 48 h post-ETOP.* ***D*** *- Representative images of DAPI positive cells from quantification in (B-c). Data from 3 independent repeats, a minimum of 500 cells counted per condition per repeat. Error bars represent standard error of the mean. * Indicates statistical significance (p=<0.05), ** indicates statistical significance (p=<0.01), *** indicates statistical significance (p=<0.001) calculated using an unpaired Students T-test. Statistical significance was calculated using GraphPad Prism software.*

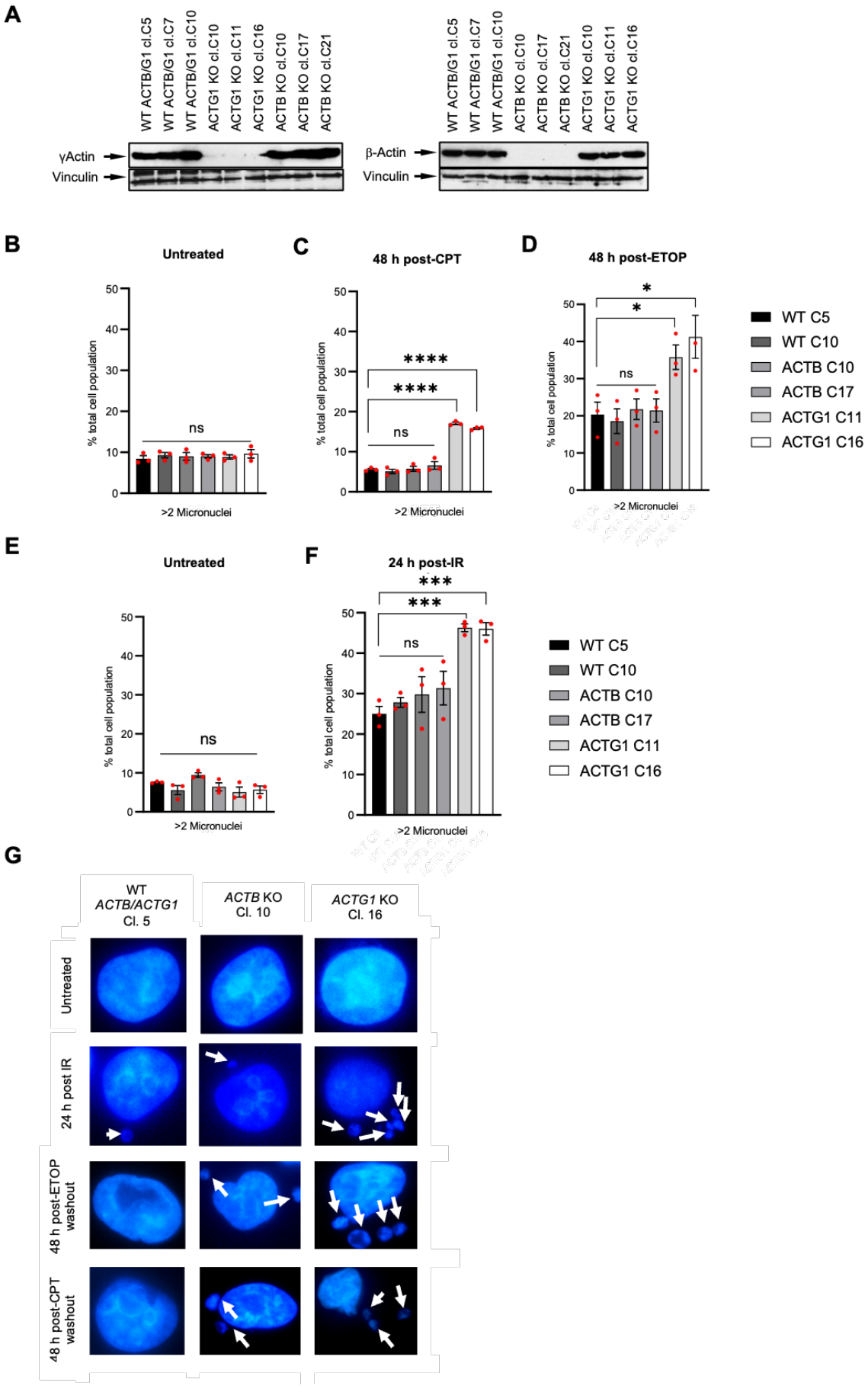

A
WT ACTB/G1 cl.C5
WT ACTB/G1 cl.C7
WT ACTB/G1 cl.C10
ACTG1 KO cl.C10
ACTG1 KO cl.C11
ACTG1 KO cl.C16
ACTB KO cl.C10
ACTB KO cl.C17
ACTB KO cl.C21
γActin
Vinculin
β-Actin
Vinculin
B
Untreated
% total cell population
ns
>2 Micronuclei
C
48 h post-CPT
****
****
ns
D
48 h post-ETOP
*
*
ns
WT C5
WT C10
ACTB C10
ACTB C17
ACTG1 C11
ACTG1 C16
E
Untreated
F
24 h post-IR
***
***
ns
G
WT ACTB/ACTG1 Cl. 5
ACTB KO Cl. 10
ACTG1 KO Cl. 16
Untreated
24 h post IR
48 h post-ETOP washout
48 h post-CPT washout

Figure 5.5 - Quantification of micronuclei formation in A375 cells following DNA damage – A *- Western blot of cell lysates from A375 cell lines to show knock out of proteins indicated. Vinculin was used as a loading control.* ***B-F*** *- WT, ACTB KO and ACTG1 KO A375 cells were seeded onto glass coverslips and left untreated or treated with 100 nM CPT for 1 h, 10 uM ETOP or 3 Gy IR. Coverslips were harvested at specific time-points post treatment (0 h, 24 h, 48 h) and fixed with paraformaldehyde (PFA).* ***B*** *- Quantification of micronuclei in the absence of exogenous DNA damage.* ***C*** *- Quantification of micronuclei 48 h post-CPT.* ***D*** *- Quantification of micronuclei 48 h post-ETOP.* ***E*** *- Quantification of micronuclei in the absence of exogenous DNA damage.* ***F*** *- Quantification of micronuclei 24 h post-IR.* ***G*** *- Representative images of DAPI positive cells from quantification in (A-C). Data from 3 independent repeats, a minimum of 500 cells counted per condition per repeat. Error bars represent standard error of the mean. * Indicates statistical significance (p=<0.05), ** indicates statistical significance (p=<0.01), *** indicates statistical significance (p=<0.001) calculated using an unpaired Students T-test. Statistical significance was calculated using GraphPad Prism software.*

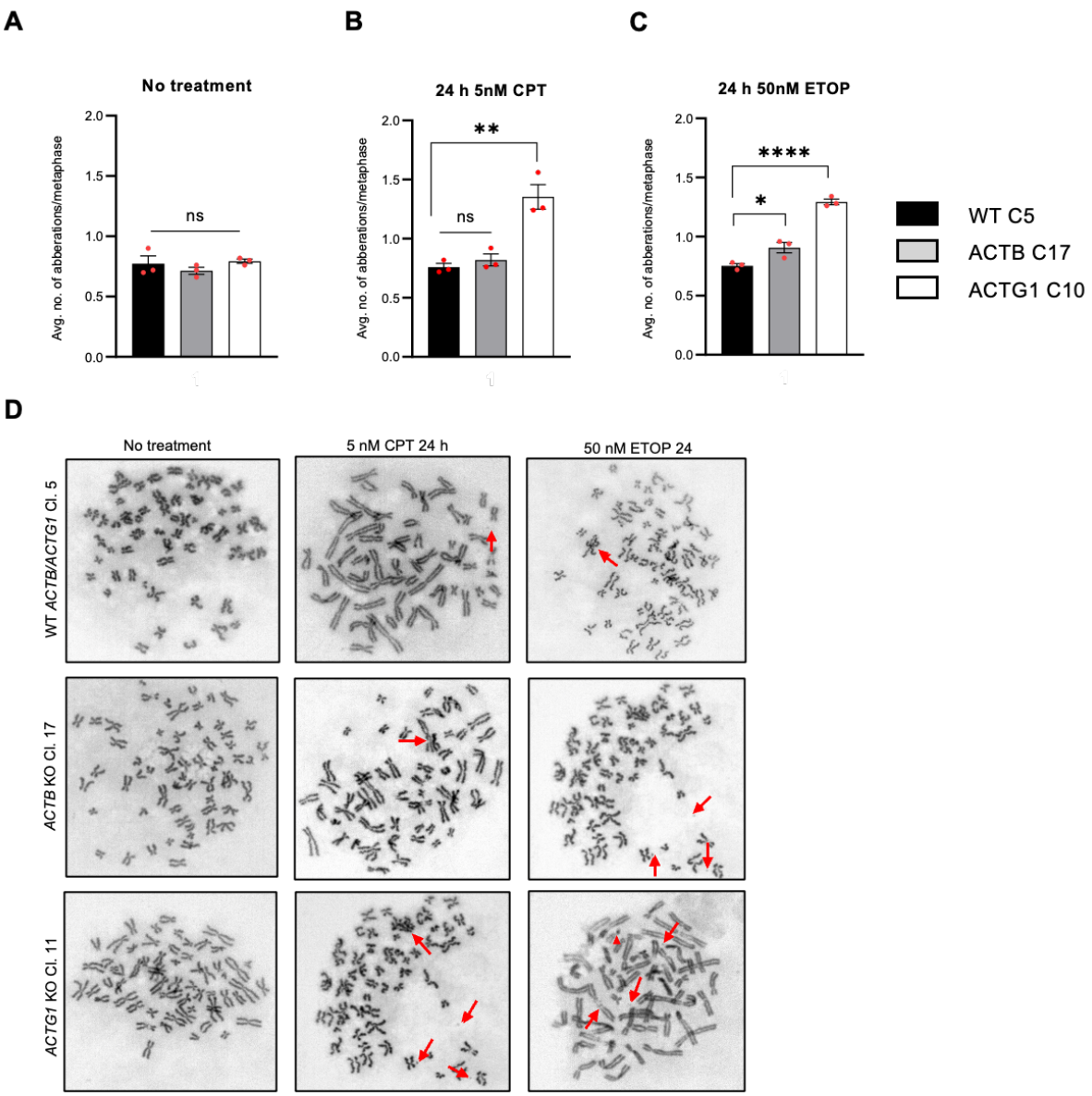


Figure 5.6 - Quantification of chromosomal aberrations in A375 cells following DNA damage– *WT, ACTB KO and ACTG1 KO A375 cells were seeded into 10 cm dishes and either left untreated or cultured in the presence of either 10 nM CPT or 50 nM ETOP for 24 h hours. 3 h prior to harvesting, colcemid was added to the cells. Cells were harvested at 24 h, dehydrated and fixed in 3:1 ethanol:acetic acid and dropped onto slides before staining with Giemsa.* ***A*** *- Quantification of chromosomal aberrations in the absence of exogenous DNA damage.* ***B*** *- Quantification of chromosomal aberrations in the presence of CPT.* ***C*** *- Quantification of chromosomal aberrations in the presence of ETOP.* ***D*** *- Representative images of metaphase spreads quantified in A, B and C. Data from 3 independent repeats, a minimum of 50 metaphase spreads counted per condition per repeat. Error bars represent standard error of the mean. * Indicates statistical significance (p=<0.05), ** indicates statistical significance (p=<0.01), *** indicates statistical significance (p=<0.001) calculated using an unpaired Students T-test. Statistical significance was calculated using GraphPad Prism software.*

5.3.3 Analysis of γ-H2AX/53BP1 foci formation following DNA damage in ACTB, ACTG1 and ARP2/3 complex component patient-derived cells

To investigate a role for γ-actin in DSB in more detail, IF was used to assess DSB repair kinetics by analysing γ-H2AX/53BP1 foci formation, as previously described in Chapter 4, Section 4.3.1. To do this, *ACTB* and *ACTG1* mutant fibroblasts were either left untreated or treated with 100 nM CPT for 1 h, then harvested at 1 h and 24 h post-CPT. Cells were then incubated with specific antibodies to γ-H2AX/53BP1 coupled to different fluorophores and γ-H2AX/53BP1 foci were analysed by fluorescence microscopy. Again, WT, NBS and A-T patient-derived fibroblasts were included as controls.

In untreated conditions, there were no significant increases in γ-H2AX/53BP1 foci in any of the patient-derived fibroblasts when compared to the WT cell line. At 1 h post-CPT, all cell lines displayed an elevation in γ-H2AX/53BP1 foci as expected (Figure 5.7A-B, D-E). Notably however, at 24 h post-CPT, only the ACTG1, NBS and A-T mutant fibroblasts displayed significantly elevated levels of γ-H2AX/53BP1 foci (Figure 5.7C, F). Interestingly, both ACTB-P3 and ACTG1-P3 have a mutation in the same codon, with arginine residue at position 183 being substituted for a tryptophan in ACTB-P3 (c.547C>T; p.Arg183Trp *ACTB*) and a glutamine in ACTG1-P3 (c.548G>A p.Arg183Gln *ACTG1*). However, only a DSB repair defect was observed in the ACTG1 mutant cell line. This re-enforces the importance of which actin paralog is mutated rather than the position of the mutation.

The same analysis was performed in the ARP2/3 complex mutant cell lines. Again, all patients displayed significantly elevated levels of γ-H2AX/53BP1 foci at 24 h post-CPT, in keeping with a role for the ARP2/3 complex in facilitating DSB repair (Figure 5.8A-C).

To verify that the observed inability of ACTG1 and ARP2/3 complex mutant cell lines to repair DSBs was not specific to CPT exposure, a selection of ACTB, ACTG1 and ARPC4 patient-derived fibroblasts were exposed to either 3 Gy IR or 10 μM ETOP for 30 min and harvested at 0 h, 1 h and 24 h post-treatment. Again, no significant differences in γ-H2AX/53BP1 foci were observed between the cell lines prior to treatment and 1 h post-treatment (Figure 5.9A, B, D, E and Figure 5.10A, B, D and E). However, mirroring the observations following CPT exposure, both the ACTG1 and ARPC4 mutant fibroblasts displayed significantly elevated levels of γ-H2AX/53BP1 foci at 24 h post-irradiation or ETOP treatment (Figure 5.9C, F and Figure 5.10C, F). However, whilst ACTB mutant cell lines displayed some variable responses to IR and ETOP (Figure 5.10B-C), overall the ACTB mutant cell lines did not display any consistent defects in resolving DSBs-induced by these two genotoxins.

To substantiate these observations, γ-H2AX/53BP1 foci were analysed in the ACTB KO and ACTG KO A375 cell lines following exposure to either 100 nM CPT for 1 h, 10 μM ETOP for 30 min or 3 Gy IR. Again, cells were harvested at 1 h or 24 h post-treatment. Whilst no substantial alterations in γ-H2AX/53BP1 foci were observed in any of the cell lines prior to treatment or one hour post-exposure (Figure 5.11A, B, D, F-G and Figure 5.12A-B, D), at 24 h post-exposure the two ACTG KO clones reproducibly

displayed significantly elevated levels of γ-H2AX/53BP1 foci when compared to both the WT and ACTB$^{-/-}$ KO cell lines (Figure 5.11C, E, Figure 5.12C-D). This data confirms that loss of ACTG1 results in a failure to repair DSBs induced by CPT, ETOP or IR.

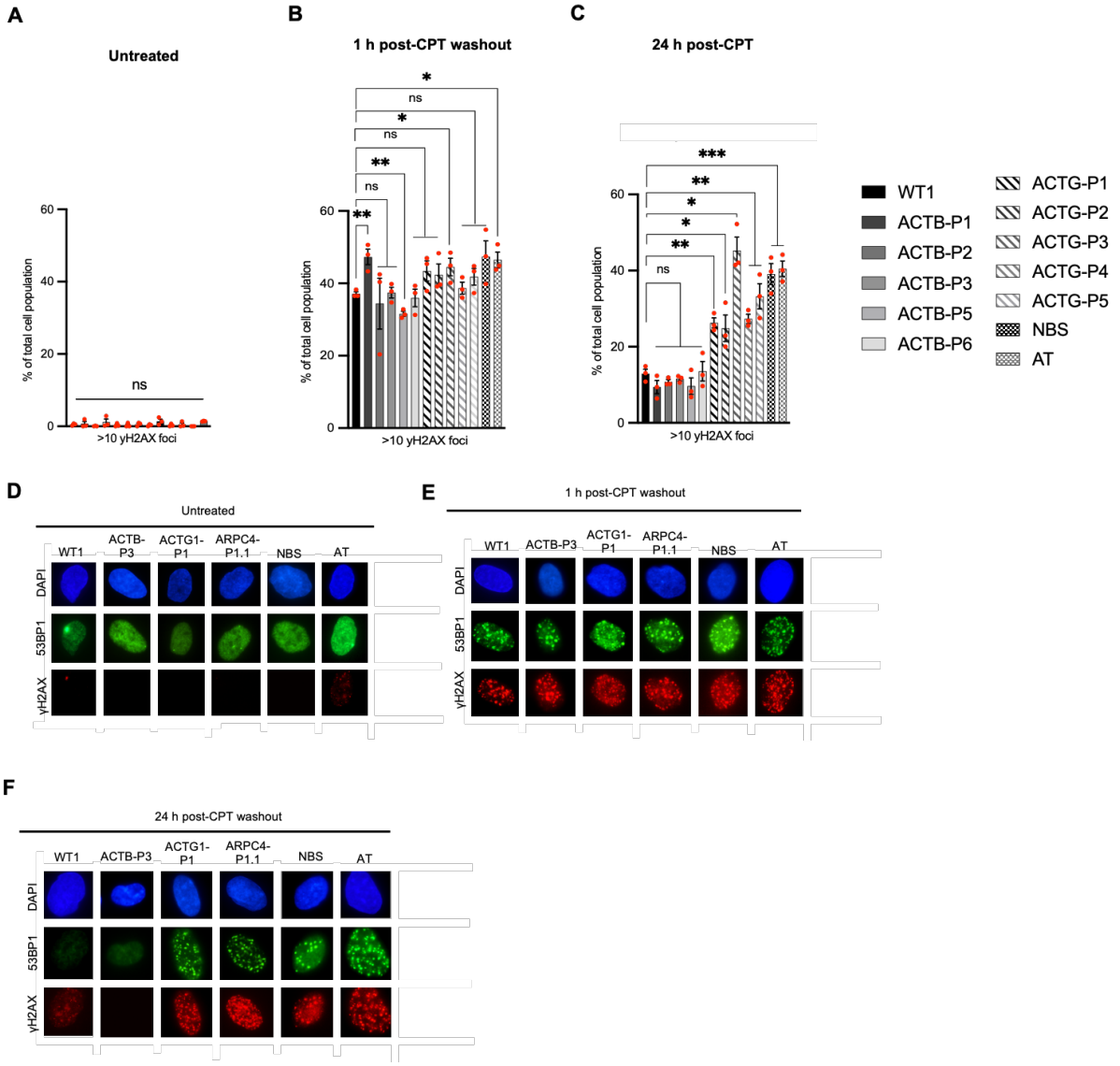


Figure 5.7 - Quantification of γ-H2AX/53BP1 foci formation in ACTB and ACTG1 patient-derived hTERT immortalised fibroblasts following treatment with CPT – *Fibroblasts were seeded onto glass coverslips and left untreated or treated with 100 nM CPT for 1 h. Coverslips were harvested at specific time-points post treatment (1 h, 24 h) and fixed with 3.6 % paraformaldehyde (PFA).* ***A*** *- Quantification of γ-H2AX/53BP1 foci in the absence of exogenous DNA damage.* ***B*** *- Quantification of γ-H2AX/53BP1 foci 1 h post-CPT.* ***C*** *- Quantification of γ-H2AX/53BP1 foci 24 h post-CPT.* ***D*** *- Representative images of DAPI positive cells from quantification in (A).* ***E*** *- Representative images of DAPI positive cells from quantification in (B).* ***F*** *- Representative images of DAPI positive cells from quantification in (C). Data from 3 independent repeats, a minimum of 500 cells counted per condition per repeat. Error bars represent standard error of the mean. * Indicates statistical significance (p=<0.05), ** indicates statistical significance (p=<0.01), *** indicates statistical significance (p=<0.001) calculated using an unpaired Students T-test. Statistical significance was calculated using GraphPad Prism software.*

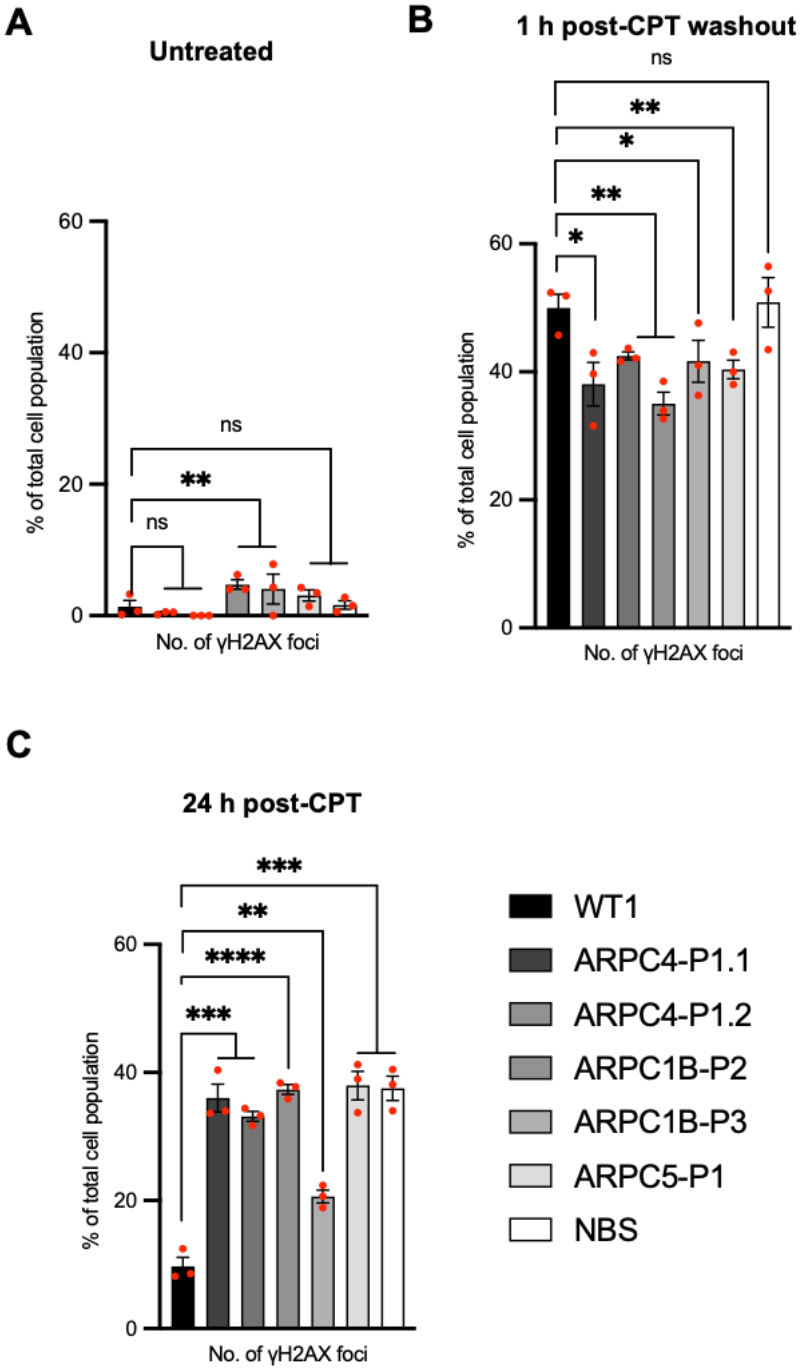


Figure 5.8 - Quantification of γ-H2AX/53BP1 foci formation in ARPC1B, ARPC4 and ARPC5 patient-derived hTERT immortalised fibroblasts following treatment with CPT – *Fibroblasts were seeded onto glass coverslips and left untreated or treated with 100 nM CPT for 1 h. Coverslips were harvested at specific time-points post treatment (1 h, 24 h) and fixed with 3.6 % paraformaldehyde (PFA).* ***A*** *- Quantification of* γ-H2AX/53BP1 *foci in the absence of exogenous DNA damage.* ***B*** *- Quantification of* γ-H2AX/53BP1 *foci 1 h post-CPT.* ***C*** *- Quantification of* γ-H2AX/53BP1 *foci 24 h post-CPT. Data from 3 independent repeats, a minimum of 500 cells counted per condition per repeat. Error bars represent standard error of the mean. * Indicates statistical significance (p=<0.05), ** indicates statistical significance (p=<0.01), *** indicates statistical significance (p=<0.001) calculated using an unpaired Students T-test. Statistical significance was calculated using GraphPad Prism software.*

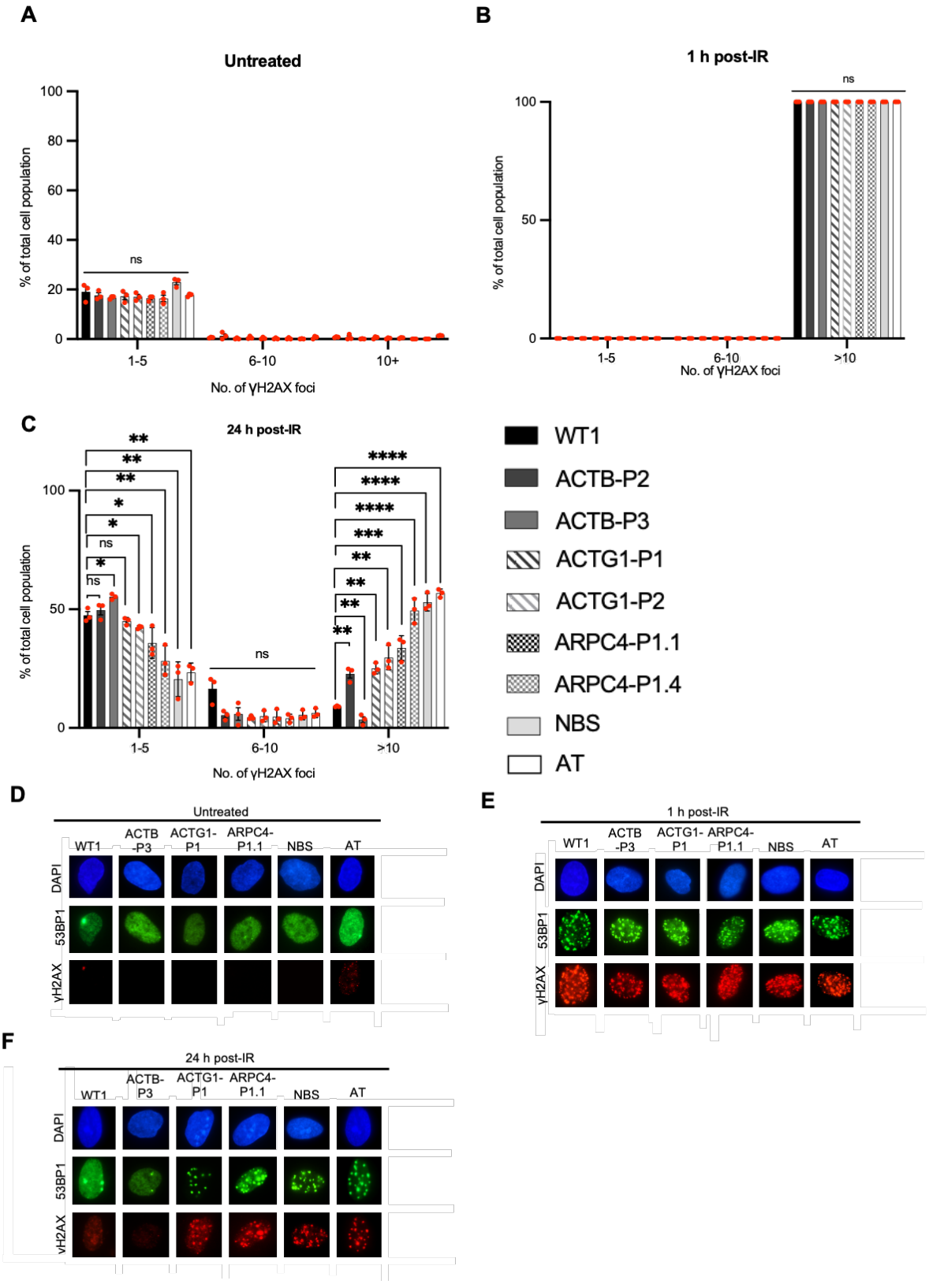

A
Untreated
% of total cell population
100
80
60
40
20
0
ns
1-5
6-10
10+
No. of γH2AX foci
B
1 h post-IR
% of total cell population
100
50
0
ns
1-5
6-10
>10
No. of γH2AX foci
C
24 h post-IR
% of total cell population
100
50
0
**
**
**
*
*
ns
*
ns
ns
**
**
**
****
****
****
***
**
1-5
6-10
>10
No. of γH2AX foci
WT1
ACTB-P2
ACTB-P3
ACTG1-P1
ACTG1-P2
ARPC4-P1.1
ARPC4-P1.4
NBS
AT
D
Untreated
WT1
ACTB -P3
ACTG1- P1
ARPC4- P1.1
NBS
AT
DAPI
53BP1
γH2AX
E
1 h post-IR
WT1
ACTB -P3
ACTG1- P1
ARPC4- P1.1
NBS
AT
DAPI
53BP1
γH2AX
F
24 h post-IR
WT1
ACTB- P3
ACTG1- P1
ARPC4- P1.1
NBS
AT
DAPI
53BP1
γH2AX

Figure 5.9 - Quantification of γ-H2AX/53BP1 foci formation ACTB-P2, ACTB-P3, ACTG1-P1, ACTG1-P2, ARPC4-P1.1, ARPC4-P.14 hTERT immortalised fibroblasts following exogenous DNA damage – A-C *- Fibroblasts were seeded onto glass coverslips and left untreated or treated with 3 Gy IR. Coverslips were harvested at specific time-points post treatment (0 h , 1 h and 24 h) and fixed with paraformaldehyde (PFA).* ***A*** *- Quantification of γ-H2AX/53BP1 foci in the absence of exogenous DNA damage.* ***B*** *- Quantification of γ-H2AX/53BP1 foci 1 h post-3 Gy IR.* ***C*** *- Quantification of γ-H2AX/53BP1 foci 24 h post-3 Gy IR.* ***D*** *- Representative images of DAPI positive cells from quantification in (A).* ***E*** *- Representative images of DAPI positive cells from quantification in (B).* ***F*** *- Representative images of DAPI positive cells from quantification in (C). Data from 3 independent repeats, a minimum of 500 cells counted per condition per repeat. Error bars represent standard error of the mean. * Indicates statistical significance (p=<0.05), ** indicates statistical significance (p=<0.01), *** indicates statistical significance (p=<0.001) calculated using an unpaired Students T-test. Statistical significance was calculated using GraphPad Prism software.*

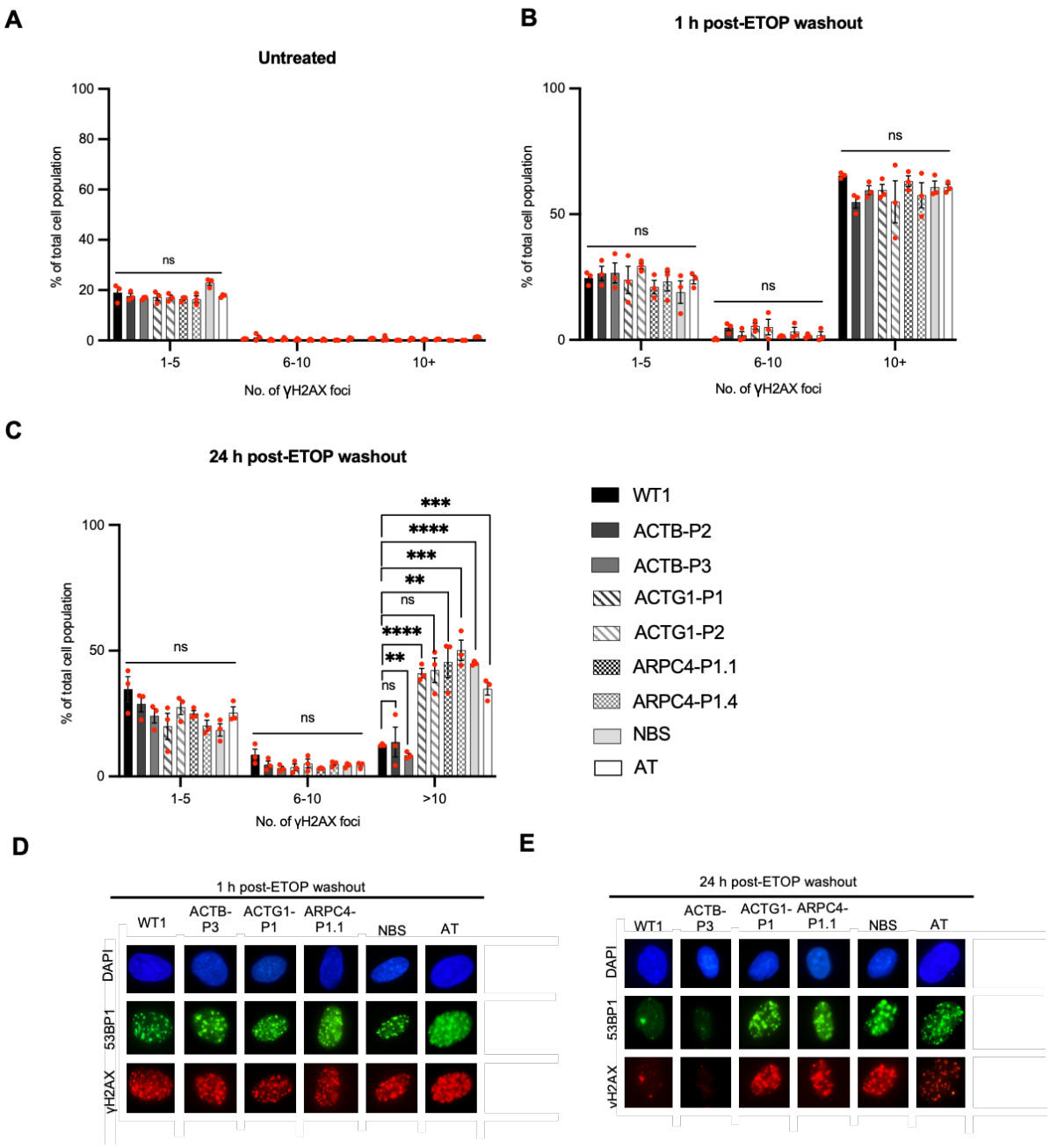


Figure 5.10 - Quantification of γ-H2AX/53BP1 foci formation ACTB-P2, ACTB-P3, ACTG1-P1, ACTG1-P2, ARPC4-P1.1, ARPC4-P.14 hTERT immortalised fibroblasts following exogenous DNA damage – *A-C - Fibroblasts were seeded onto glass coverslips and left untreated or treated with 10 μM ETOP for 30 min. Coverslips were harvested at specific time-points post treatment (0 h, 1 h and 24 h) and fixed with paraformaldehyde (PFA).* ***A*** *- Quantification of γ-H2AX/53BP1 foci in the absence of exogenous DNA damage.* ***B*** *- Quantification of γ-H2AX/53BP1 foci 1 h post-ETOP* ***C*** *- Quantification of γ-H2AX/53BP1 foci 24 h post-ETOP.* ***D*** *- Representative images of DAPI positive cells from quantification in (A).* ***E*** *- Representative images of DAPI positive cells from quantification in (B). Data from 3 independent repeats, a minimum of 500 cells counted per condition per repeat. Error bars represent standard error of the mean. * Indicates statistical significance (p=<0.05), ** indicates statistical significance (p=<0.01), *** indicates statistical significance (p=<0.001) calculated using an unpaired Students T-test. Statistical significance was calculated using GraphPad Prism software.*

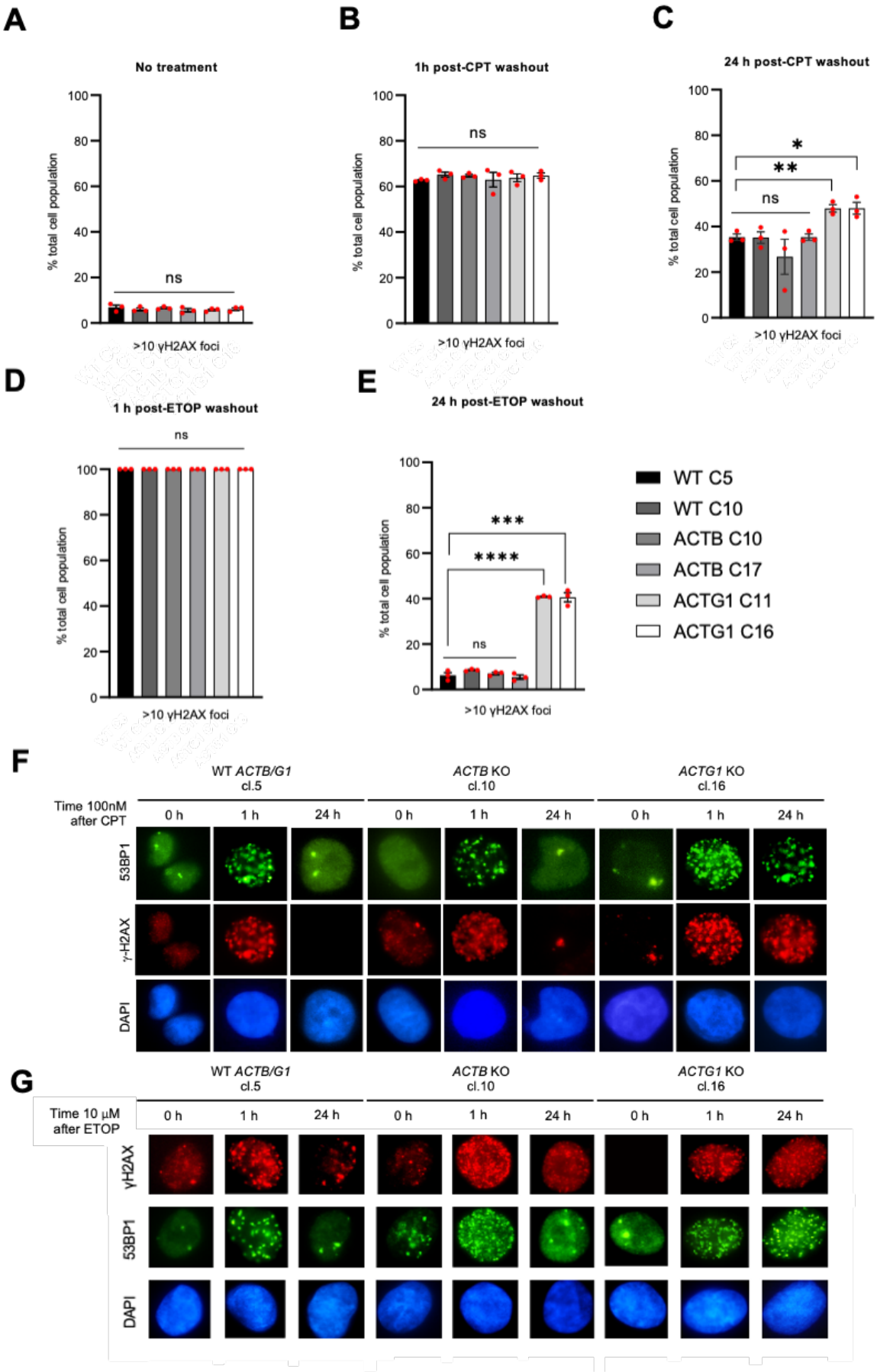

A
No treatment
% total cell population
100
80
60
40
20
0
ns
>10 γH2AX foci
B
1h post-CPT washout
% total cell population
ns
>10 γH2AX foci
C
24 h post-CPT washout
% total cell population
*
**
ns
>10 γH2AX foci
D
1 h post-ETOP washout
ns
% total cell population
>10 γH2AX foci
E
24 h post-ETOP washout
% total cell population
***
****
ns
>10 γH2AX foci
WT C5
WT C10
ACTB C10
ACTB C17
ACTG1 C11
ACTG1 C16
F
WT ACTB/G1 cl.5
ACTB KO cl.10
ACTG1 KO cl.16
Time 100nM after CPT
0 h
1 h
24 h
53BP1
γ-H2AX
DAPI
G
WT ACTB/G1 cl.5
ACTB KO cl.10
ACTG1 KO cl.16
Time 10 µM after ETOP
0 h
1 h
24 h
γH2AX
53BP1
DAPI

Figure 5.11 - Quantification of γ-H2AX/53BP1 foci formation in A375 cells following DNA damage– *WT, ACTB KO and ACTG1 KO A375 cells were seeded onto glass coverslips and left untreated or treated with 100 nM CPT or 10 M ETOP for 1 h and 30 min respectively. Coverslips were harvested at specific time-points post treatment (1 h, 24 h, 48 h) and fixed with paraformaldehyde (PFA).* ***A*** *- Quantification of γ-H2AX/53BP1 foci in the absence of exogenous DNA damage.* ***B*** *- Quantification of γ-H2AX/53BP1 foci 1 h post-CPT.* ***C*** *- Quantification of γ-H2AX/53BP1 foci 24 h post-CPT.* ***D*** *- Quantification of γ-H2AX/53BP1 foci 1 h post-ETOP.* ***E*** *- Quantification of γ-H2AX/53BP1 foci 24 h post-ETOP.* ***F*** *- Representative images of DAPI positive cells from quantification in (A-C).* ***G*** *- Representative images of DAPI positive cells from quantification in (D-E). Data from 3 independent repeats, a minimum of 500 cells counted per condition per repeat. Error bars represent standard error of the mean. * Indicates statistical significance (p=<0.05), ** indicates statistical significance (p=<0.01), *** indicates statistical significance (p=<0.001) calculated using an unpaired Students T-test. Statistical significance was calculated using GraphPad Prism software.*

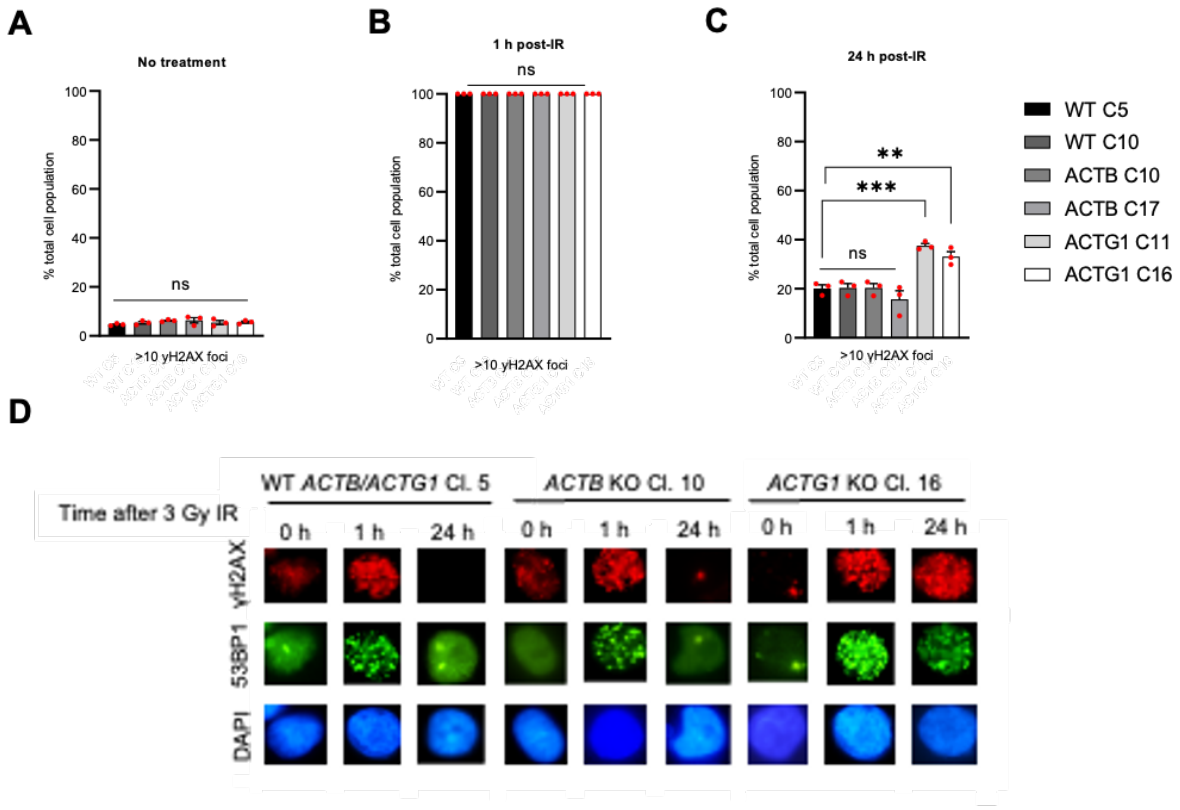


Figure 5.12 - Quantification of γ-H2AX/53BP1 foci formation in A375 cells following exposure to IR *– WT, ACTB KO and ACTG1 KO A375 cells were seeded onto glass coverslips and left untreated or treated with 3 Gy IR. Coverslips were harvested at specific time-points post treatment (1 h, 24 h) and fixed with paraformaldehyde (PFA).* ***A*** *- Quantification of γ-H2AX/53BP1 foci in the absence of exogenous DNA damage.* ***B*** *- Quantification of γ-H2AX/53BP1 foci 1 h post-3 Gy IR.* ***C*** *- Quantification of γ-H2AX/53BP1 foci 24 h post-3 Gy IR.* ***D*** *- Representative images of DAPI positive cells from quantification in (A-C). Data from 3 independent repeats, a minimum of 500 cells counted per condition per repeat. Error bars represent standard error of the mean. * Indicates statistical significance (p=<0.05), ** indicates statistical significance (p=<0.01), *** indicates statistical significance (p=<0.001) calculated using an unpaired Students T-test. Statistical significance was calculated using GraphPad Prism software.*

5.3.4 Loss of *ACTG1* leads to reduced localisation of HR factors BRCA1, RPA2, RAD51 and MRE11 following CPT-induced DNA damage

The findings in Section 5.3.3 suggest that γ-actin is the specific paralog of actin required for DSB repair. Whilst the DSB repair defect in cells lacking γ-actin was observed in response to CPT, ETOP and IR, since CPT-induced breaks are specifically repaired by HR this suggests that γ-actin is required for HR-dependent repair. To address this, IF was performed on ACTB KO and ACTG1 KO A375 cell lines to investigate how loss of the different actin paralogs affect the relocalisation of BRCA1, RPA2 and RAD51 to CPT-induced DSBs. Cells were either left untreated or treated with 100 nM CPT for 1 h and then harvested 1 h and 4 h post-CPT treatment. Cells were then stained with specific antibodies raised against the three proteins of interest in combination with CENPF/Mitosin to distinguish S/G_2-phase cells from G_1-phase cells. BRCA1, RPA2 and RAD51 foci were then quantified in S/G_2-phase cells.

In untreated conditions, there was no difference in BRCA1 foci formation between the WT, ACTB or ACTG1 KO cell lines (Figure 5.13A-B). In keeping with a role for γ-actin in HR, following treatment with CPT, there was a statistically significant decrease in BRCA1 foci formation in the ACTG KO when compared to both the WT and ACTB KO cell lines (Figure 5.13A-B). Consistent with a requirement for γ-actin to relocalise BRCA1 to sites of DSBs, the ACTG1 KO cell line also displayed a significantly reduced ability to form RPA2 and RAD51 foci in response to CPT treatment when compared to the WT and ACTB KO cell lines (Figure 5.14-5.15). To confirm these observations, CPT-induced RAD51 foci formation was examined in a selection of the BWCFF

syndrome and ARP2/3 mutant fibroblast cell lines. Reassuringly, both ACTG1 and ARP2/3 complex mutant patients but not in ACTB patients were unable to efficiently relocalise RAD51 following treatment with CPT (Figure 5.16). Together these results show that γ-actin and the ARP2/3 complex are important in HR-dependent DSB repair.

Previously, my data has demonstrated that DIAPH1 is required early in the HR pathway and its loss compromises recruitment of the MRN complex to DSB sites. To investigate if this was also the case with γ-actin and the ARP2/3 complex, the ER-mCherry-LacI-FokI-DD inducible nuclease system was used once again to assess the relocalisation of MRE11 *FokI*-induced DSBs (Section 4.3.4). Initially, U-2-OS cells expressing the ER-mCherry-LacI-FokI-DD nuclease were transfected with siRNA to deplete either ACTB, ACTG1, ARPC4 or DIAPH1 (Figure 5.17A), the FokI nuclease was then induced and the MRE11 localisation to DSBs was determined by IF. Consistent with the findings in Section 4.3.4 of Chapter 4, depletion of DIAPH1 in U-2-OS cells resulted in a significant reduction in MRE11 foci intensity at FokI-induced DSBs. Strikingly, depletion of both ACTG1 and ARPC4 lead to statistically significant reduction in MRE11 foci formation. However, in contrast depletion of ACTB had very little effect on MRE11 recruitment to sites of DNA damage (Figure 5.17B, C). Together, these data indicate that DIAPH1, γ-actin and the ARP2/3 complex are required for MRN complex localisation to DSBs.

In conclusion, this section provides evidence that γ-actin loss leads to defects in the entire HR pathway from the initial phase of recruitment of the MRN complex to DSB sites to the later stages of the pathway. This implies that γ-actin acts upstream of the

MRN complex, which contrasts with previous reports that the MRN complex is required for ARP2/3 recruitment to DSB sites which in turn triggers actin filament formation. However. whether γ-actin, the ARP2/3 complex and DIAPH1 are functioning together in the same pathway is not yet clear.

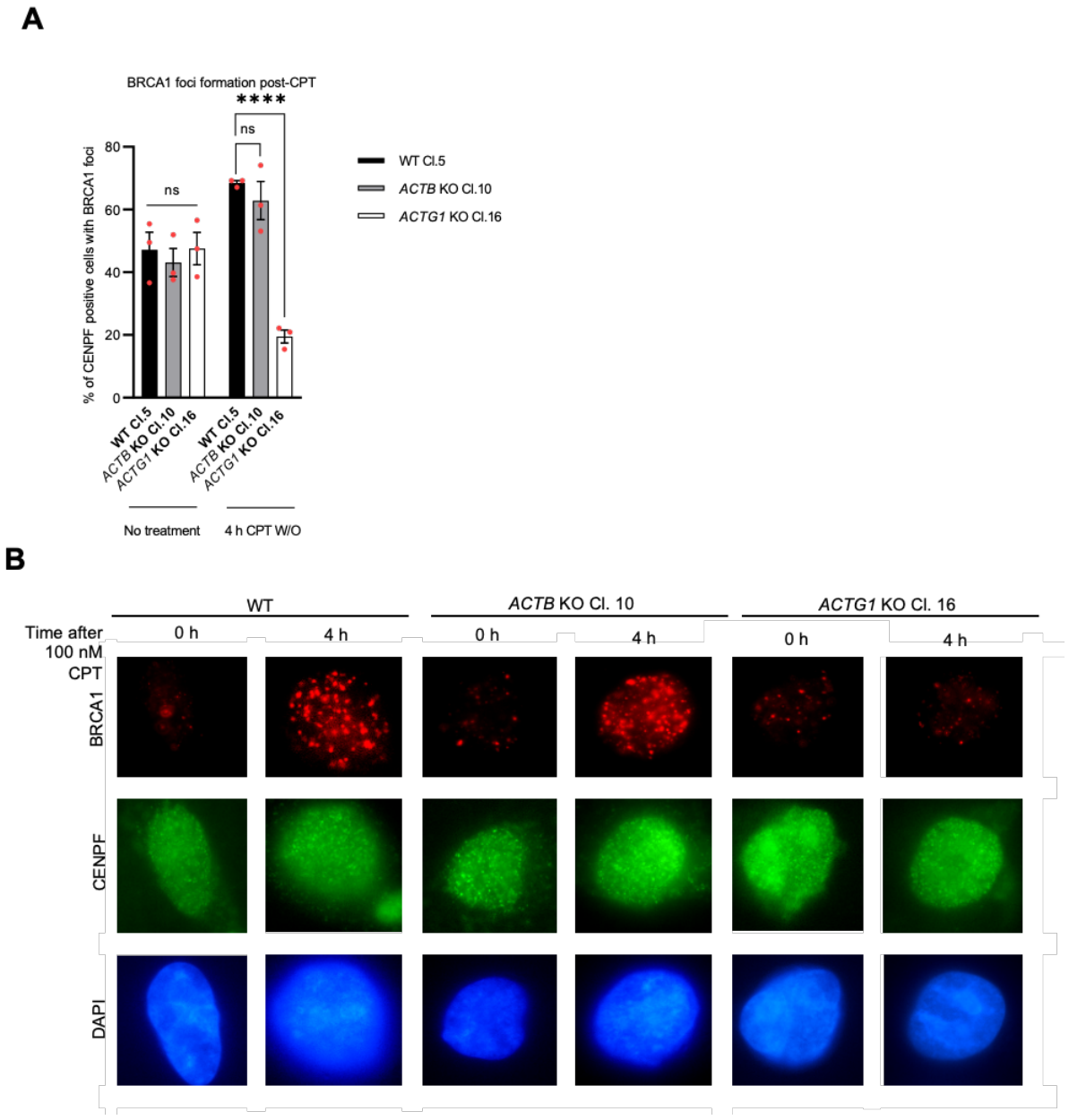


Figure 5.13 - Quantification of BRCA1 foci in A375 cell lines following CPT treatment – *A375 WT, ACTB KO and ACTG1 KO cells were seeded onto glass coverslips and left untreated or treated with 100 nM CPT for 1 h. Coverslips were harvested at 4 h post-CPT treatment and fixed with paraformaldehyde (PFA).* ***A*** *- Quantification of nuclei with >30 BRCA1 foci in CENPF positive (S/G_2-phase) cells in the absence of exogenous DNA damage and 4 h post-CPT treatment.* ***B*** *- Representative images of CENPF positive cells from quantification in (A). Data from 3 independent repeats, a minimum of 300 cells counted per condition per repeat. Error bars represent standard error of the mean. * Indicates statistical significance (p=<0.05), ** indicates statistical significance (p=<0.01), *** indicates statistical significance (p=<0.001), **** indicates statistical significance (p=<0.0001) calculated using an unpaired Student's T-test. Statistical significance was calculated using GraphPad Prism software.*

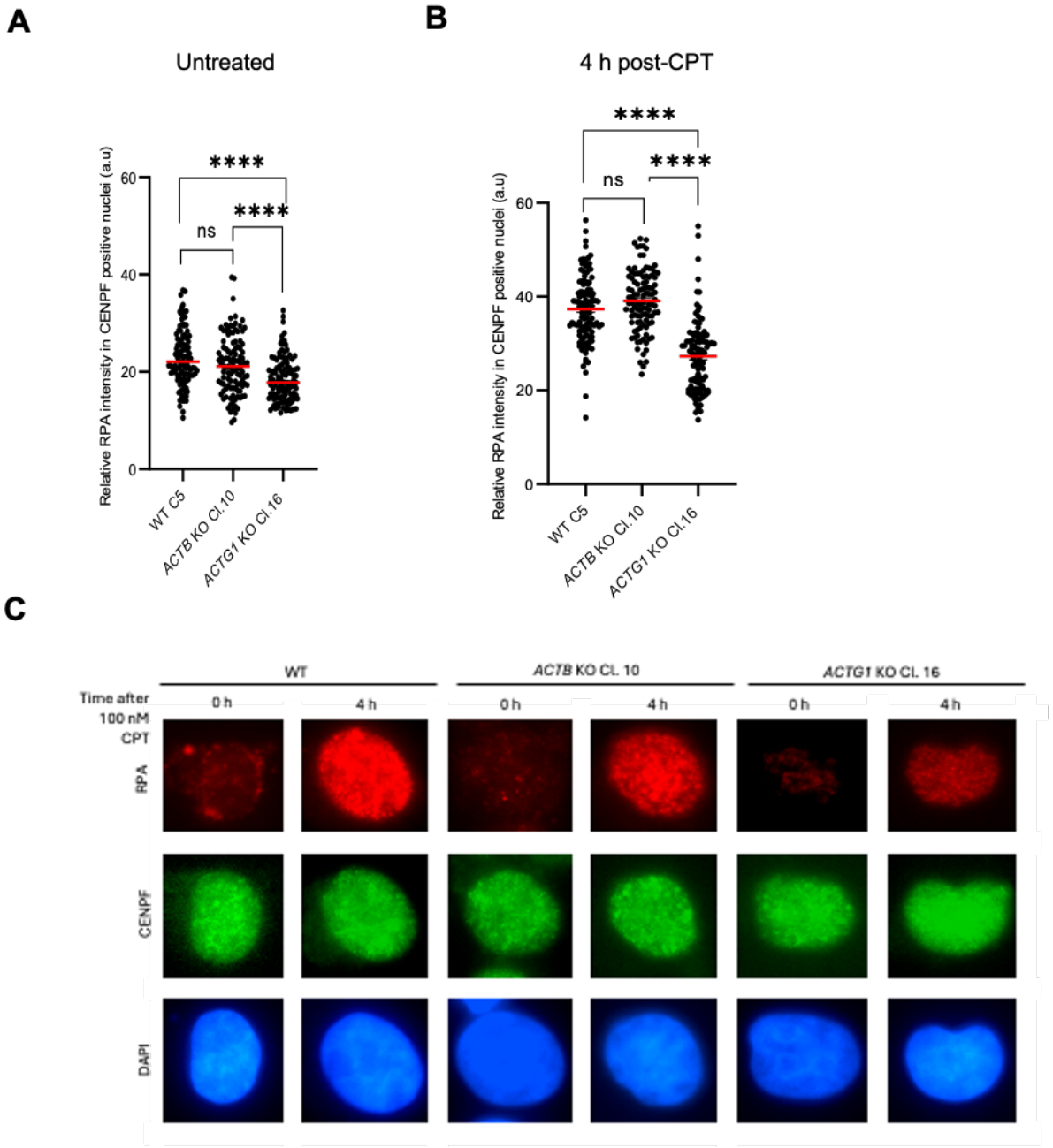


Figure 5.14 - Quantification of RPA2 foci intensity A375 cell lines following CPT treatment – *A375 WT, ACTB KO and ACTG1 KO cells were seeded onto glass coverslips and left untreated or treated with 100 nM CPT for 1 h. Coverslips were harvested at 4 h post-CPT treatment and fixed with paraformaldehyde (PFA).* ***A*** *- Quantification of nuclei with RPA staining intensity in CENPF positive (S/G_2-phase) cells in the absence of exogenous DNA damage.* ***B*** *- Quantification of nuclei with RPA staining intensity in CENPF positive (S/G_2-phase) cells 4 h post-CPT treatment.* ***C*** *- Representative images of CENPF positive cells from quantification in (A-B). Data from 3 independent repeats, a minimum of 100 cells counted per condition per repeat. Error bars represent standard error of the mean. * Indicates statistical significance (p=<0.05), ** indicates statistical significance (p=<0.01), *** indicates statistical significance (p=<0.001), **** indicates statistical significance (p=<0.0001) calculated using an unpaired Mann-Whitney-U test. Foci intensity was measured using ImageJ software. Statistical significance was calculated using GraphPad Prism software.*

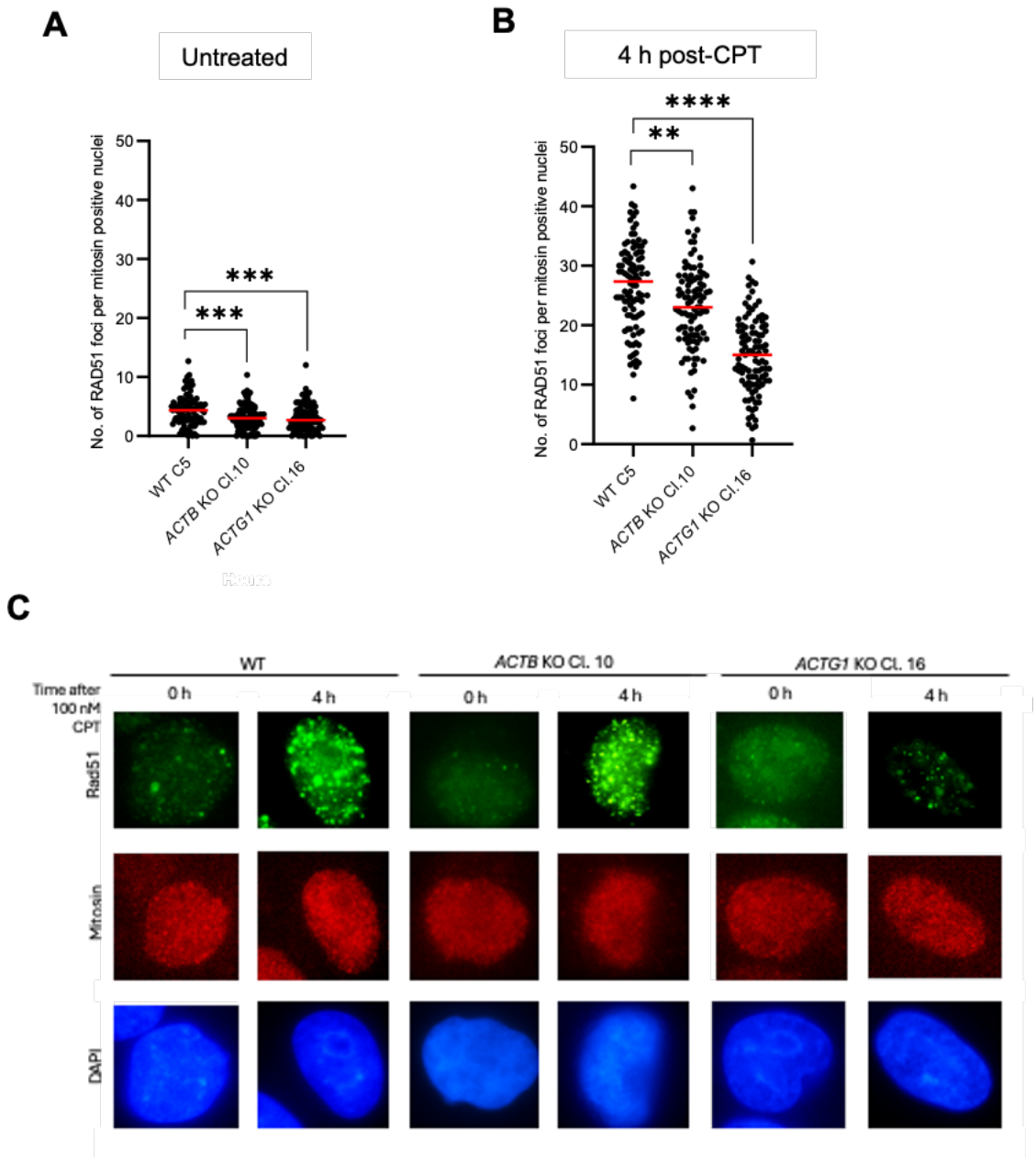


Figure 5.15 - Quantification of RAD51 foci A375 cell lines following CPT treatment – *A375 WT, ACTB KO and ACTG1 KO cells were seeded onto glass coverslips and left untreated or treated with 100 nM CPT for 1 h. Coverslips were harvested at 4 h post-CPT treatment and fixed with paraformaldehyde (PFA).* ***A*** *- Quantification of nuclei with RAD51 foci in mitosin positive (S/G_2-phase) cells in the absence of exogenous DNA damage.* ***B*** *- Quantification of nuclei with RAD51 foci in mitosin positive (S/G_2-phase) cells 4 h post-CPT treatment.* ***C*** *- Representative images of mitosin positive cells from quantification in (A-B). Data from 3 independent repeats, a minimum of 100 cells counted per condition per repeat. Error bars represent standard error of the mean. * Indicates statistical significance (p=<0.05), ** indicates statistical significance (p=<0.01), *** indicates statistical significance (p=<0.001), **** indicates statistical significance (p=<0.0001) calculated using an unpaired Mann-Whitney-U test. Statistical significance was calculated using GraphPad Prism software.*

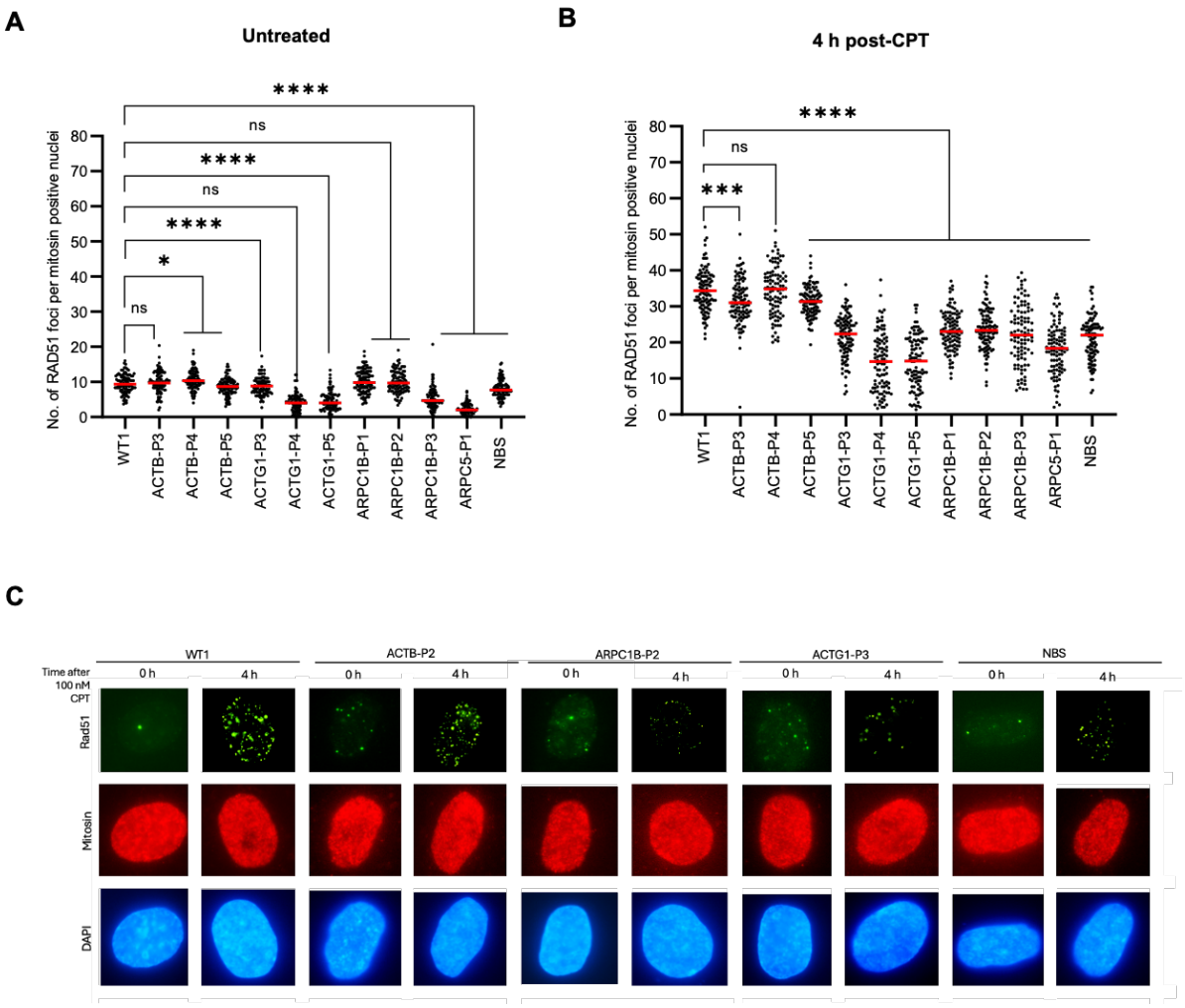


Figure 5.16 - Quantification of RAD51 foci in ACTB, ACGT1, ARPC1B, ARPC4 and APRC5 hTERT immortalised fibroblasts following CPT treatment – *Patient-derived fibroblasts were seeded onto glass coverslips and left untreated or treated with 100 nM CPT for 1 h. Coverslips were harvested at 4 h post-CPT treatment and fixed with paraformaldehyde (PFA).* ***A*** *- Quantification of nuclei with RAD51 foci in mitosin positive (S/G_2-phase) cells in the absence of exogenous DNA damage.* ***B*** *- Quantification of nuclei with RAD51 foci in mitosin positive (S/G_2-phase) cells 4 h post-CPT treatment.* ***C*** *- Representative images of mitosin positive cells from quantification in (A-B). Data from 3 independent repeats, a minimum of 100 cells counted per condition per repeat. Error bars represent standard error of the mean. * Indicates statistical significance (p=<0.05), ** indicates statistical significance (p=<0.01), *** indicates statistical significance (p=<0.001), **** indicates statistical significance (p=<0.0001) calculated using an unpaired Mann-Whitney-U test. Statistical significance was calculated using GraphPad Prism software.*

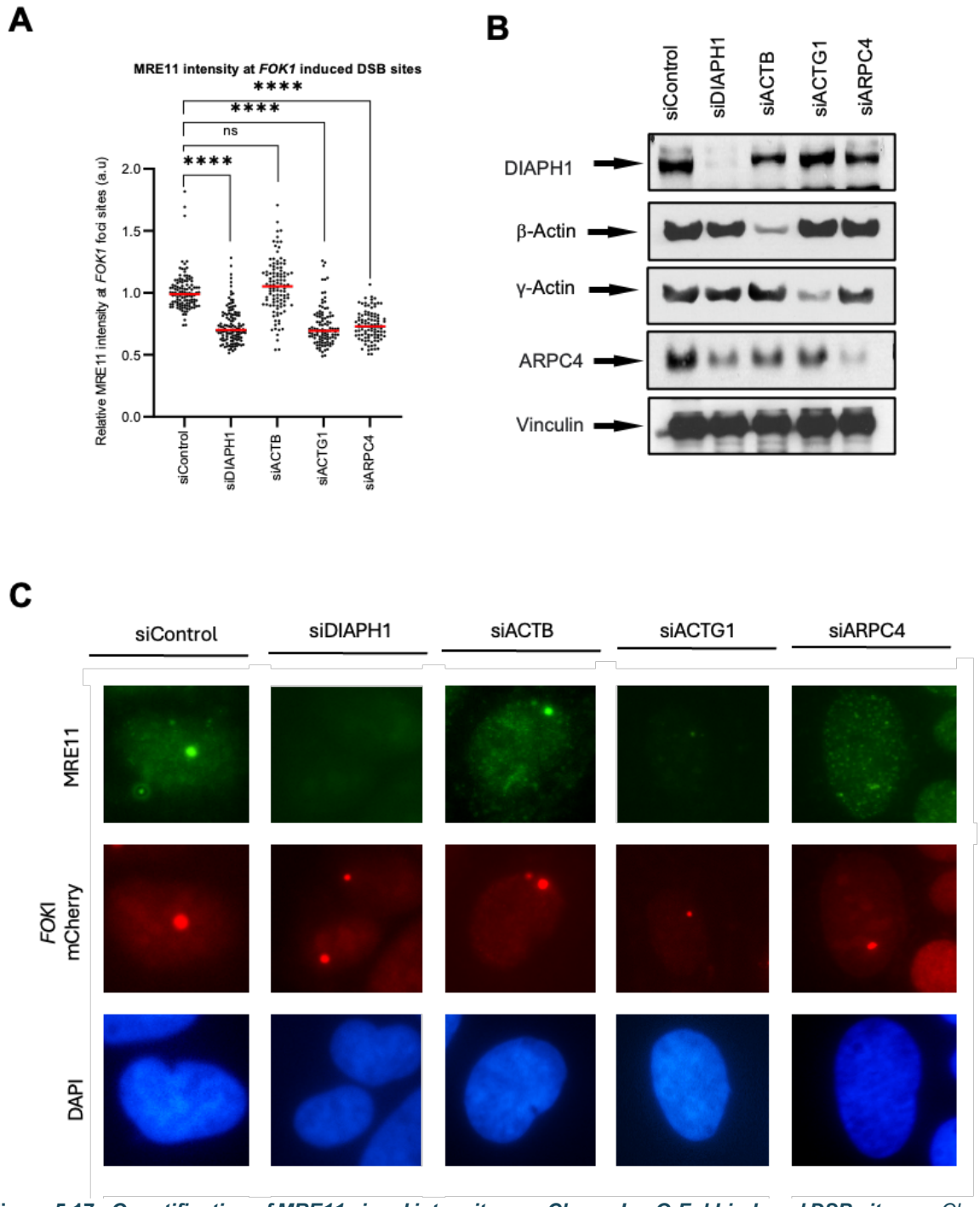


Figure 5.17 - *Quantification of MRE11 signal intensity as mCherry-LacO-FokI-induced DSB sites –* *mCherry-LacO-FokI expressing U-2-OS cells subject to siRNA depletion of DIAPH1, ACTB, ACTG1, ARPC4 and a non-targeting luciferase control for 6 h. Cells were then treated with 1 uM Sheild1 and 1 uM 4-OHT for 4 h then harvested and fixed in 3.6 % PFA. Fixed cells were then incubated with specific antibodies raised against Mre11 and imaged with fluorescent microscopy. Images were subject to analysis of MRE11 fluorescent signal intensity at FokI induced DSB sites.* ***A*** *- Western blot of cell lysates to show successful siRNA mediated depletion of proteins indicated. Vinculin was used as a loading control.* ***B*** *– MRE11 fluorescent intensity at Foki DSB sites in arbitrary units (a.u).* ***C*** *– Representative image of cells captured in B. Data from 3 independent repeats, a minimum of 100 cells analysed per condition per repeat. MRE11 intensity was quantified in ImageJ at the FokI site only. Red line denotes the median. * Indicates statistical significance (p=<0.05), ** indicates statistical significance (p=<0.01), *** indicates statistical significance (p=<0.001), **** indicates statistical significance (p=<0.0001). Statistical significance was calculated using a Mann-Whitney rank sum test using GraphPad Prism software.*

5.3.5 DIAPH1, γ-actin and the ARP2/3 complex function within the same HR pathway

To investigate whether DIAPH1, γ-actin and the ARP2/3 complex function together in the same pathway to regulate HR-dependent DSB repair, epistasis analysis were carried out. To assess HR efficiency, the CRISPR-based homologous recombination assay targeting GFP into the *LMNA* locus was utilised (Chapter 4, Section 4.3.2). HeLa cells were transfected with siRNA to deplete DIAPH1, ACTG1, ACTB and ARPC4 alone or in combination (Figure 5.18A). A non-targeting control and NBS1 siRNA were used as negative and positive controls respectively. Cells were then transfected with plasmids encoding Cas9 and the *LMNA*-targeted sgRNAs as well as a plasmid containing a GFP gene flanked by regions of homology to the *LMNA* locus and a plasmid encoding RFP (which is used to control for transfection efficiency). Using this assay, depletion of either DIAPH1, ACTG1 or ARPC4 alone lead to a significant reduction in HR efficiency comparable to that of depletion of NBS. In contrast, depletion of ACTB did not cause a significant reduction in HR efficiency. Strikingly, co-depletion of DIAPH1 in combination with either ACTG1 or ARPC4 did not exacerbate the HR defect, suggesting the proteins function in the same pathway in HR (Figure 5.18B, C). Reassuringly, depletion of DIAPH1 in combination with ACTB resulted in a HR defect comparable to depletion of DIAPH1 alone.

To confirm the observation that DIAPH1 is functioning within the same HR pathway was both γ-actin and the ARP2/3 complex, IF was used to monitor RAD51 foci formation following CPT-treatment in cells depleted of DIAPH1 together with either

ACTG1, ACTB or ARPC4. Cells were also treated with mirin to assess whether inhibition of the nuclease activity of MRE11 was epistatic with a loss of the DIAPH1-actin-dependent DSB repair pathway. As expected, in untreated conditions, there was very little difference between the number of RAD51 foci present following depletion of DIAPH1, ACTB, ACTG1 or ARPC4 (Figure 5.19A, C). Following CPT treatment, depletion of DIAPH1, ACTG1 or ARPC4 lead to a significant reduction in RAD51 foci. Interestingly, depletion of ACTB resulted in a slight decrease in RAD51 foci when compared to non-targeting siRNA but this was not as severe as the reduction observed in cells depleted of DIAPH1, ACTG1 or ARPC4. Reassuringly, co-depleting DIAPH1 with both ACTG1 and ARPC4 did not exacerbate the RAD51 relocalisation defect, supporting the idea that they are functioning within the same pathway, whereas co-depletion of DIAPH1 and ACTB lead to a dramatic reduction in Rad51 foci number, comparable to the depletion of DIAPH1 alone (Figure 5.19B, C). Notably, mirin treatment resulted in a severe defect in RAD51 foci formation following CPT exposure, which was not further exacerbated when DIAPH1, ACTG1, ACTB or ARPC4 were depleted.

Lastly, the impact of co-depleting DIAPH1 in combination with ACTG1, ACTB or ARPC4 on DNA end resection was investigated. My previous findings indicate that DIAPH1, the ARP2/3 complex and γ-actin all act upstream of the MRN complex and are required for MRN complex recruitment to DSB sites. The MRN complex is critical for initiating the end resection process of HR to enable later phase proteins to carry out their functions. Since I have shown that DIAPH1 is critical for initiating DNA end

resection, it is reasonable to hypothesize that loss of ACTG1 or the ARP2/3 complex would also give rise to a defect in DNA end resection.

To assess DSB end resection, native BrdU foci analysis was used as a measure of DSB end resection following exposure to ionising radiation. HeLa cells were transfected with siRNA to DIAPH1, ACTG1, ACTB or ARPC4 alone or in combination, irradiated with 10 Gy IR to induce DSBs and harvested at 1 h post-IR. Control siRNA transfected cells were cultured in the presence or absence of mirin to serve as a positive control for loss of MRE11-dependent DSB end resection. In control siRNA transfected cells, IR treatment induced a significant increase in native BrdU foci formation, which was significantly reduced in the presence of mirin (Figure 5.20). In contrast, depletion of DIAPH1, ACTG1 or ARPC4 lead to a marked reduction in IR-induced native BrdU foci, indicative of a DSB end resection defect. Consistent with previous observations, depletion of ACTB did not significantly affect BrdU foci formation following exposure to IR. Reassuringly, co-depletion of DIAPH1 with ACTG1 or ARPC4 did not significantly affect the defect in IR-induced BrdU foci indicating that these proteins function in the same pathway (Figure 5.20). However, co-depletion of DIAPH1 with ACTB lead to a defect comparable to depletion of DIAPH1 alone (Figure 5.20).

Taken together, the data in this section supports the premise that DIAPH1, γ-actin and the ARP2/3 complex function in the HR pathway to promote MRE11-dependent DNA end resection. In addition to this, these data highlight the presence of a subset of

BWCFF syndrome patients have an underlying DNA repair defect, which is specifically caused by mutations in *ACTG1* but not *ACTB*.

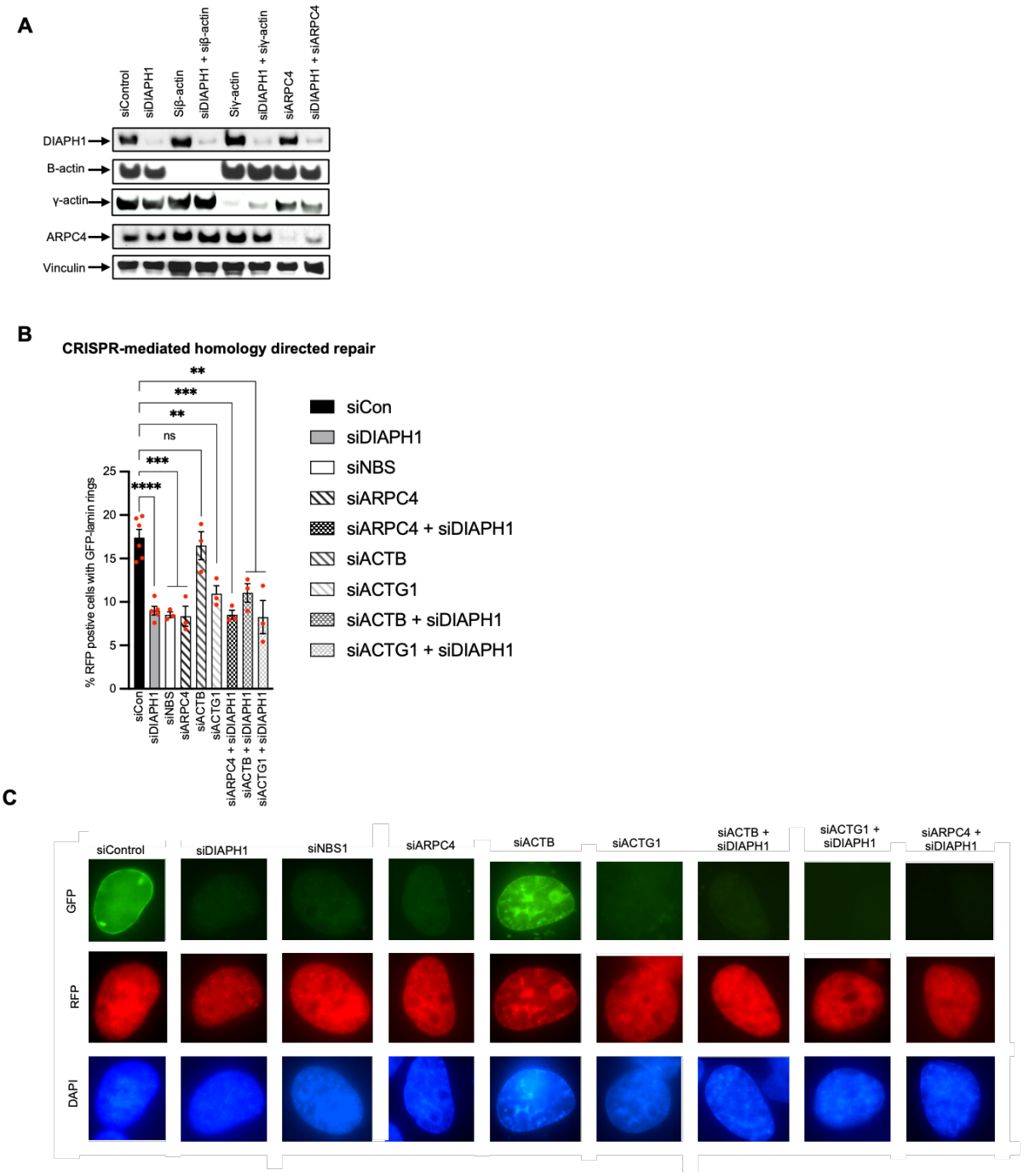


Figure 5.18 - Quantification of Lamin-GFP positive nuclei in RFP positive siRNA depleted HeLa cells – *HeLa cells subject to siRNA depletion of DIAPH1, NBS, ARPC4, ACTB, and ACTG1 were seeded onto glass coverslips and transfected with pRFP, pLX330-LMNA-gRNA-1 and pCR2.1-Clover-LMNA-Donor. Cells were cultured for 48 h prior to harvesting and then fixed with PFA and mounted onto slides.* ***A*** *– Western blot of cell lysates to show successful siRNA mediated depletion of proteins of shown. Vinculin was used as a loading control.* ***B*** *- Quantification of lamin-GFP positive nuclei in RFP positive HeLa cells.* ***C*** *- Representative images of DAPI positive cells from quantification in (A). Data from 3 independent repeats, a minimum of 500 cells counted per condition per repeat. Error bars represent standard error of the mean. * Indicates statistical significance (p=<0.05), ** indicates statistical significance (p=<0.01), *** indicates statistical significance (p=<0.001) calculated using an unpaired Students T-test. Statistical significance was calculated using GraphPad Prism software.*

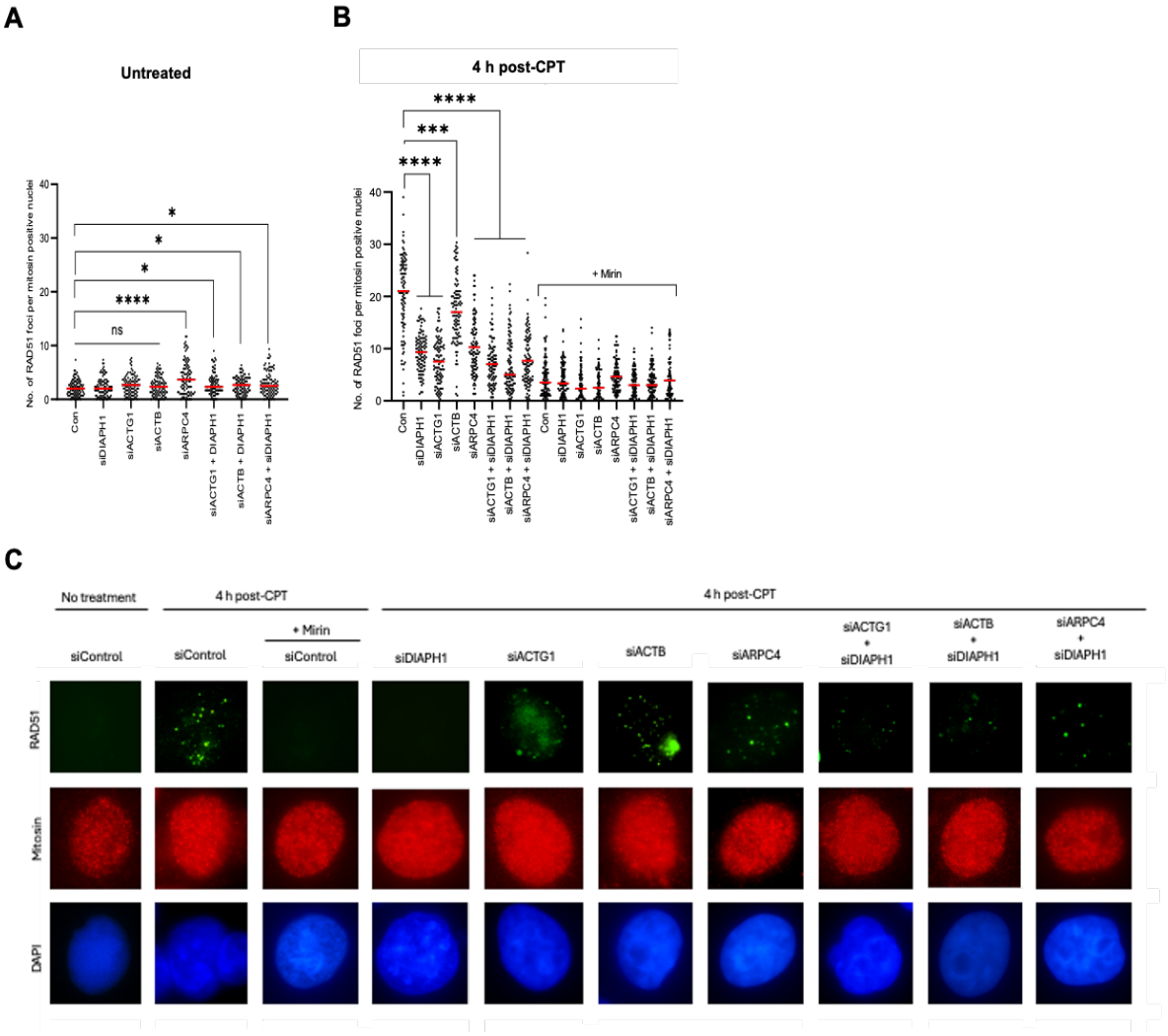


Figure 5.19 - Quantification of RAD51 foci siRNA depleted HeLa cells following CPT treatment– *HeLa cells subject to siRNA depletion of DIAPH1, NBS, ARPC4, ACTB, and ACTG1 were seeded onto glass coverslips and either left untreated or treated with 100 nM CPT for 1 h. Coverslips were harvested at 4 h post-CPT treatment and fixed with paraformaldehyde (PFA).* ***A*** *- Quantification of nuclei with RAD51 foci in mitosin positive (S/G_2-phase) cells in the absence of exogenous DNA damage.* ***B*** *- Quantification of nuclei with RAD51 foci in mitosin positive (S/G_2-phase) cells 4 h post-CPT treatment in the absence or presence of 50 μM mirin.* ***C*** *- Representative images of mitosin positive cells from quantification in (A-B). Data from 3 independent repeats, a minimum of 100 cells counted per condition per repeat. Error bars represent standard error of the mean. * Indicates statistical significance (p=<0.05), ** indicates statistical significance (p=<0.01), *** indicates statistical significance (p=<0.001), **** indicates statistical significance (p=<0.0001) calculated using an unpaired Mann-Whitney-U test. Statistical significance was calculated using GraphPad Prism software.*

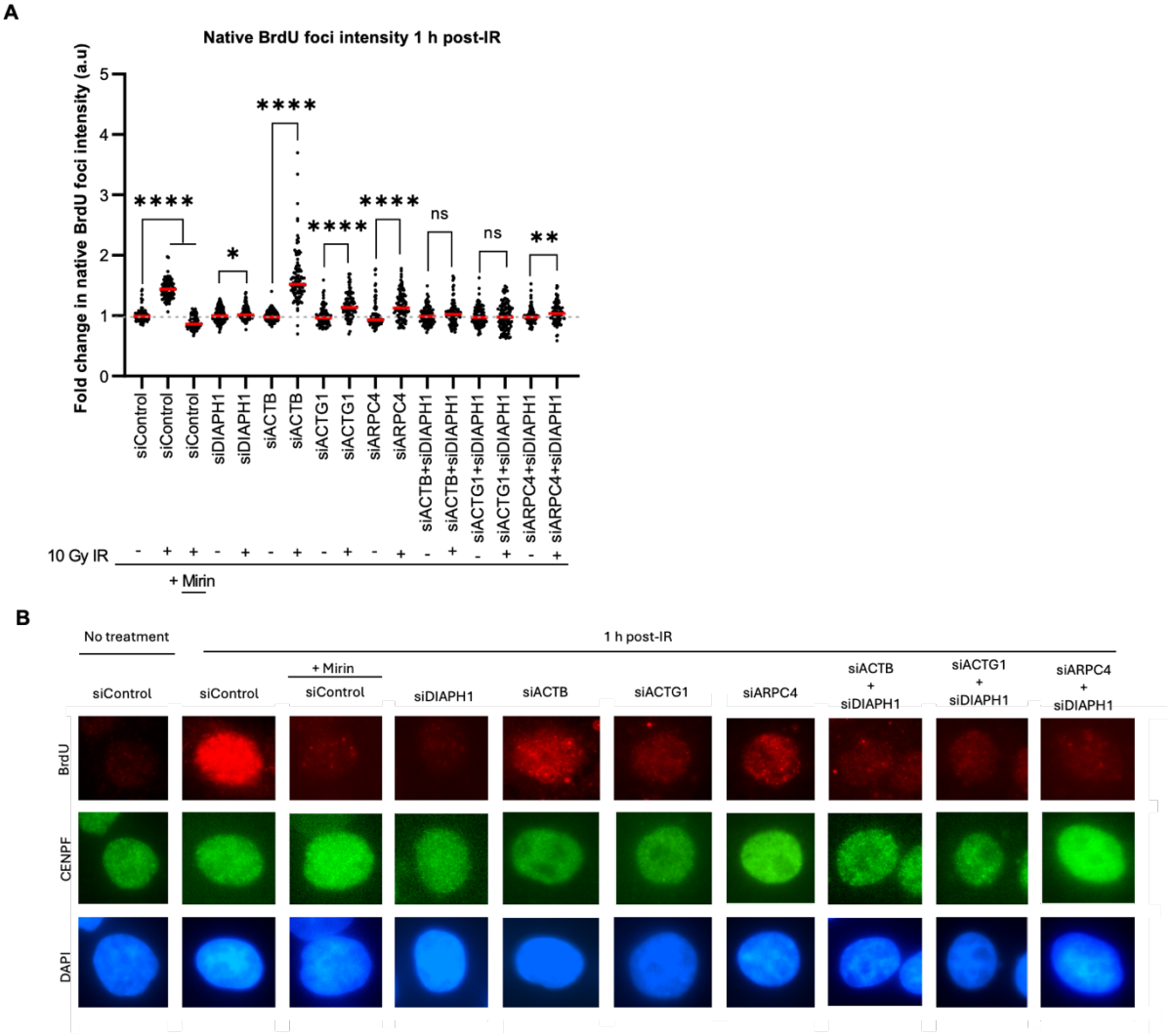


Figure 5.20 – Native BrdU foci intensity in siRNA depleted HeLa cells – *HeLa cells were subject to siRNA depletion of DIAPH1, ACTB, ACTG1, ARPC4 and a non-targeting luciferase control for 18 h. siRNA treated cells were then incubated with 10 μM BrdU for 24 h. Mirin treated cells were incubated with 50 μM mirin 1 h prior to IR. Cells were then irradiated with 10 Gy IR and permeabilised and fixed in 3.6 % PFA 1 h post-IR. Cells were then stained with specific antibodies to BrdU and CENPF to mark S/G_2-phase cells.* ***A*** *– Quantification of native BrdU foci intensity in siRNA depleted HeLa cells.* ***B*** *– Representative image of (A). Data from 3 independent repeats, a minimum of 100 cells analysed per condition per repeat. BrdU intensity was quantified in ImageJ in CENPF positive cells only. Fold change was normalised to the untreated control. Red line denotes the median. * Indicates statistical significance (p=<0.05), ** indicates statistical significance (p=<0.01), *** indicates statistical significance (p=<0.001), **** indicates statistical significance (p=<0.0001). Statistical significance was calculated using a Mann-Whitney rank sum test using GraphPad Prism software.*

5.3.6 Actin-binding defective DIAPH1 gives rise to a DSB repair defect and DIAPH1 preferentially interacts with γ-actin

To strengthen the functional link between DIAPH1 and actin in regulating HR-dependent DSB repair, DIAPH1 P1 fibroblasts were transduced with a lentivirus expressing either empty vector, WT-DIAPH1 or a mutant of DIAPH1 incapable of binding actin (I862A) (Figure 5.21A). This point mutation is located within the FH2 domain of DIAPH1 and renders DIAPH1 unable to nucleate actin, serving as a useful tool to assess the impact of an actin nucleation defective DIAPH1 on genome stability and DSB repair (Thompson *et al.*, 2013; Chen *et al.*, 2021).

Initially to assess whether the actin nucleation defective DIAPH1 mutant compromises DSB repair, micronuclei analysis following CPT treatment was performed. DIAPH1-P1 fibroblasts expressing empty vector, WT DIAPH1 or the I862A DIAPH1 mutant were either left untreated or exposed to 100 nM CPT for 1h and harvested at 48 h post-CPT treatment. Prior to CPT treatment, both the P1+Vector cells and P1+I862A-DIAPH1 cells displayed higher levels of spontaneously arising micronuclei when compared to P1+WT-DIAPH1 cells (Figure 5.21B, D). Following treatment with CPT, both the P1+Vector and P1+I862A-DIAPH1 fibroblasts displayed significantly higher levels of micronuclei than the P1+WT-DIAPH1 fibroblasts, with the P1-I862A-DIAPH1 cells being most severely affected (Figure 5.21C, D). This suggests that the ability of DIAPH1 to maintain genome stability is regulated by its function in actin nucleation. Furthermore, these data imply that the expression of a nucleation-dead mutant of

DIAPH1 may have a more deleterious impact on genome stability than a complete loss of DIAPH1.

To assess the functional relationship between DIAPH1 and its ability to nucleate actin on DSB repair more directly, IF was used to quantify γ-H2AX/53BP1 foci formation following CPT treatment. P1+Vector, P1+WT-DIAPH1 and P1+I862A-DIAPH1 expressing fibroblasts were either left untreated or treated with 100 nM CPT and harvested at 1 h post-CPT and 24 h post-CPT. γ-H2AX/53BP1 foci were analysed by staining cells with specific antibodies to both proteins and foci were visualised by fluorescent microscopy. Intriguingly, prior to CPT exposure, the P1+I862A-DIAPH1 cells displayed significantly elevated levels of cells with >10 γ-H2AX/53BP1 foci, indicating a spontaneous DSB repair defect that is not seen in P1+Vector or P1+WT-DIAPH1 expressing cells. This supports the notion that expression of an actin nucleation defective DIAPH1 is more detrimental on DSB repair than a complete lack of DIAPH1 (Figure 5.22A, D). At 1 h post-CPT, there was no significant difference in γ-H2AX/53BP1 foci between the P1+Vector and P1+WT-DIAPH1 expressing cells. However, in comparison the P1+I862A-DIAPH1 cells displayed elevated levels of γ-H2AX/53BP1 foci (Figure 5.22B, D). Mirroring the observations seen with the micronuclei analysis, both P1+Vector and P1+I862A-DIAPH1 expressing cells retained a significant number of γ-H2AX/53BP1 foci at 24 h post-CPT exposure, when compared to P1+WT-DIAPH1 expressing cells. To link this phenotype more specifically to a defect in HR, RAD51 foci were also quantified in these three isogenic cell lines following CPT treatment. In keeping with the γ-H2AX/53BP1 foci data, whilst no dramatic increases in RAD51 foci in untreated conditions were observed between the

cell lines, at 4 h post-CPT, both the P1+Vector and P1+I862A-DIAPH1 expressing cells exhibited a significant reduction in RAD51 foci formation when compared to the P1+WT-DIAPH1 expressing cell line (Figure 5.23). Together, the findings of these experiments therefore confirm that the role of DIAPH1 in HR is, at least in-part, regulated by its ability to nucleate actin filaments.

Finally, given the overwhelming evidence demonstrating that γ-actin is the actin paralog that functions with DIAPH1 to promote DSB repair, this selectively could be explained if DIAPH1 preferentially binds γ-actin over β-actin. To address this, GFP-DIAPH1 was overexpressed in HEK293FT cells and GFP-Trap was utilised to affinity purify DIAPH1-containing protein complexes from whole cell extracts. Strikingly, despite reports that β-actin is expressed at higher levels in cells than γ-actin, purified DIAPH1 exhibited a preferential interaction with γ-actin versus β-actin (Figure 5.24)

In summary, this section provides evidence that the role DIAPH1 plays in promoting efficient HR and genome stability maintenance is likely due to its role as an actin nucleating factor. Whilst Chapter 4 demonstrated that DIAPH1 interacts with HR proteins, it is likely that this is mediated by γ-actin. This suggests that γ-actin and DIAPH1 share a functional relationship in promoting HR-dependent repair of DSBs and provides mechanistic insight into why patients with mutations in *DIAPH1* and actin exhibit some overlapping clinical features.

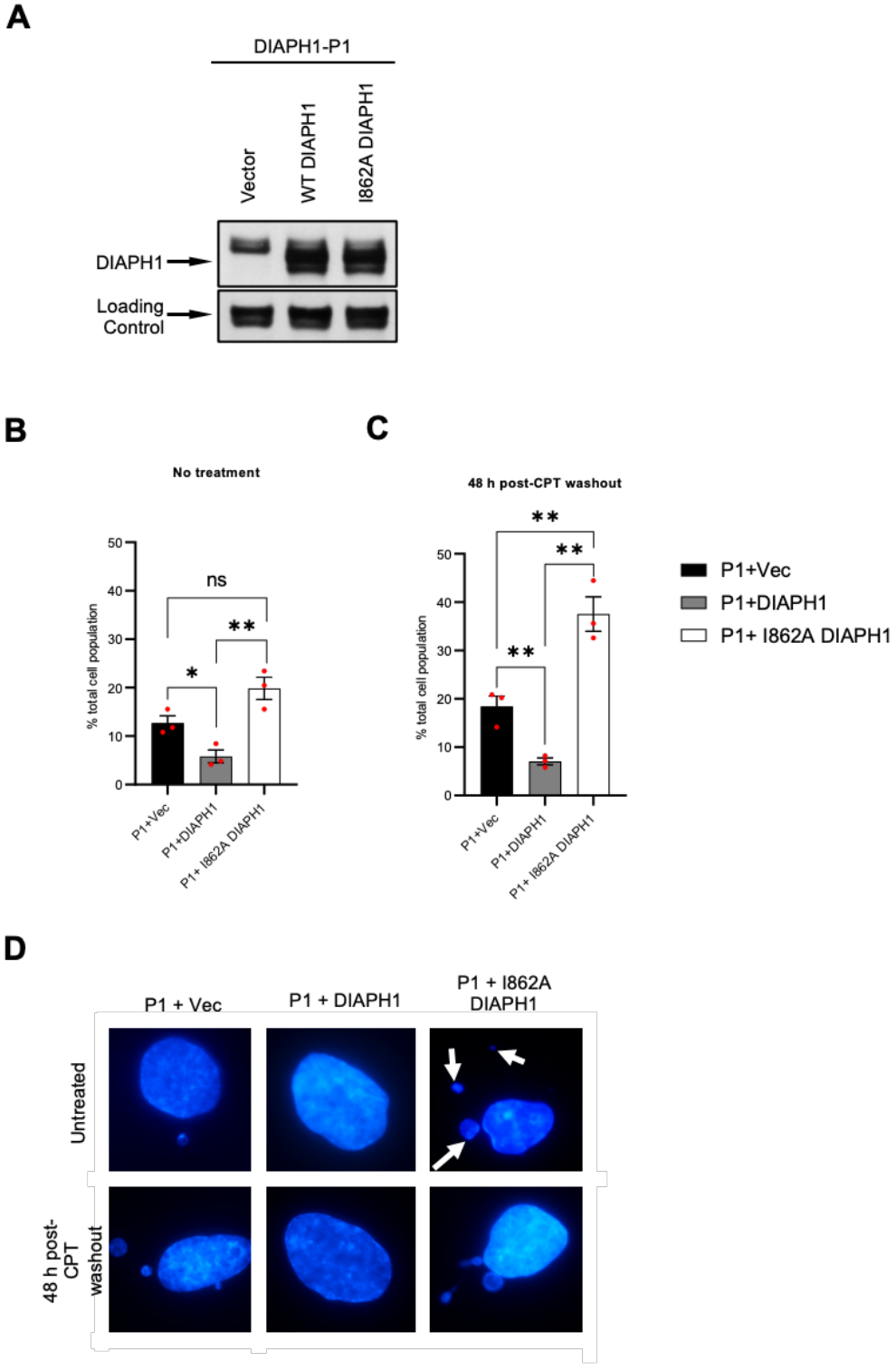


Figure 5.21 - Formation of micronuclei in DIAPH1-P1 patient hTERT immortalised fibroblasts following exposure to DNA damage – *DIAPH1 P1 fibroblasts were transduced with a lentivirus expressing either an empty vector, WT-DIAPH1 or an actin-nucleation defective I862A-DIAPH1. Fibroblasts were seeded onto glass coverslips and left untreated or treated with 100 nM CPT for 1 h. Coverslips were harvested at 48 h post treatment and fixed with paraformaldehyde (PFA).* ***A*** *- Western blot of cell lysates to show re-expression of DIAPH1 in DIAPH1 P1 fibroblasts. A non-specific cross-reactive band was used as a loading control.* ***B*** *- Quantification of micronuclei in the absence of exogenous DNA damage.* ***C*** *- Quantification of micronuclei 48 h post-CPT.* ***D*** *- Representative images of DAPI positive cells from quantification in (B-C). Data from 3 independent repeats, a minimum of 500 cells counted per condition per repeat. Error bars represent standard error of the mean. * Indicates statistical significance (p=<0.05), ** indicates statistical significance (p=<0.01), *** indicates statistical significance (p=<0.001) calculated using an unpaired Students T-test. Statistical significance was calculated using GraphPad Prism software.*

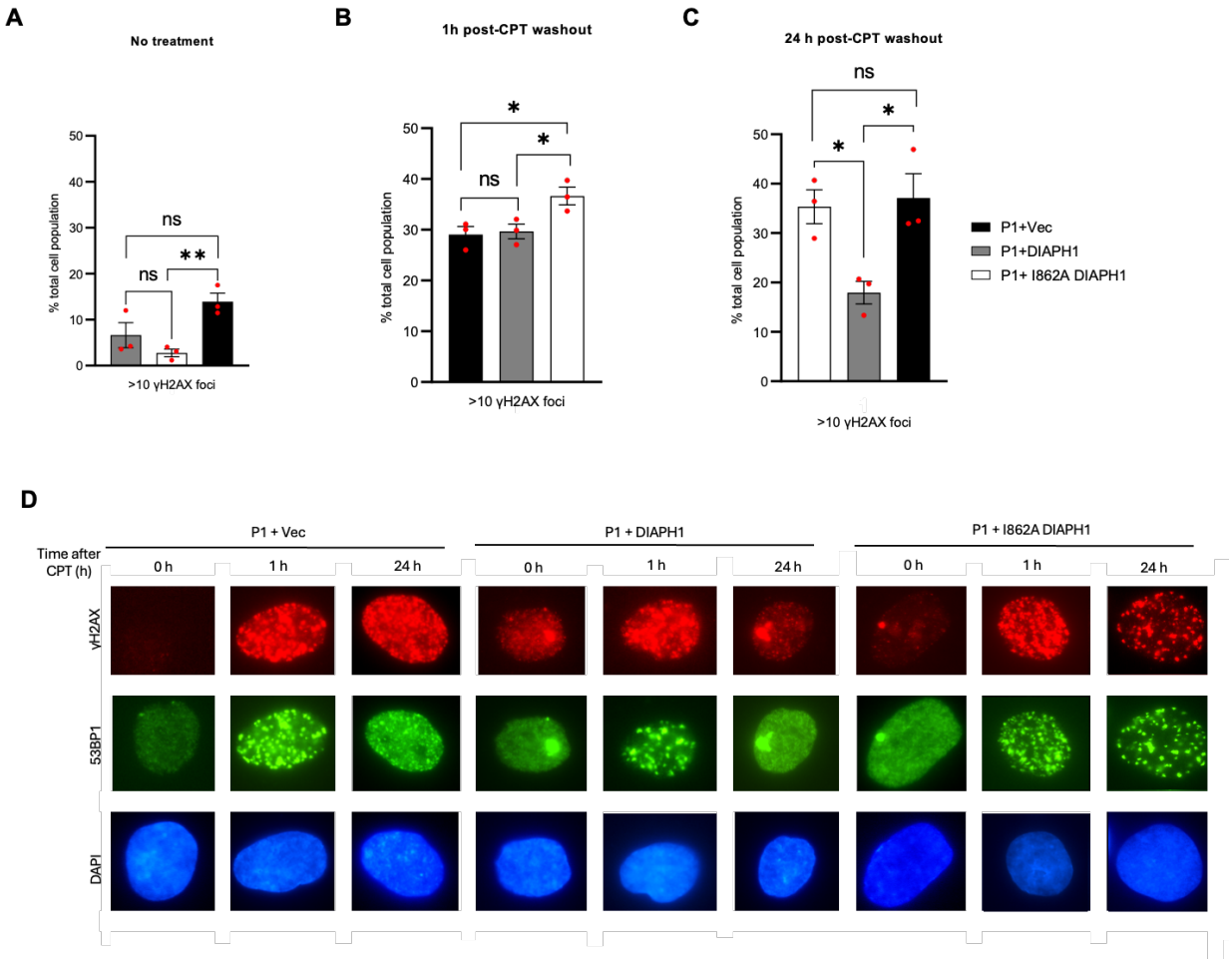


Figure 5.22 - Quantification of γ-H2AX/53BP1 foci formation in DIAPH1-P1 hTERT immortalised fibroblasts following DNA damage – *DIAPH1 P1 fibroblasts were transduced with a lentivirus expressing either an empty vector, WT-DIAPH1 or an actin-nucleation defective I862A-DIAPH1. Fibroblasts were seeded onto glass coverslips and left untreated or treated with 100 nM CPT for 1 h. Coverslips were harvested at 1 h and 24 h post treatment and fixed with paraformaldehyde (PFA).* ***A*** *- Quantification of γ-H2AX/53BP1 foci in the absence of exogenous DNA damage.* ***B -*** *Quantification of γ-H2AX/53BP1 foci 1 h post-CPT.* ***C*** *- Quantification of γ-H2AX/53BP1 foci 24 h post-CPT.* ***D*** *- Representative images of DAPI positive cells from quantification in (A-C). Data from 3 independent repeats, a minimum of 500 cells counted per condition per repeat. Error bars represent standard error of the mean. * Indicates statistical significance (p=<0.05), ** indicates statistical significance (p=<0.01), *** indicates statistical significance (p=<0.001) calculated using an unpaired Students T-test. Statistical significance was calculated using GraphPad Prism software.*

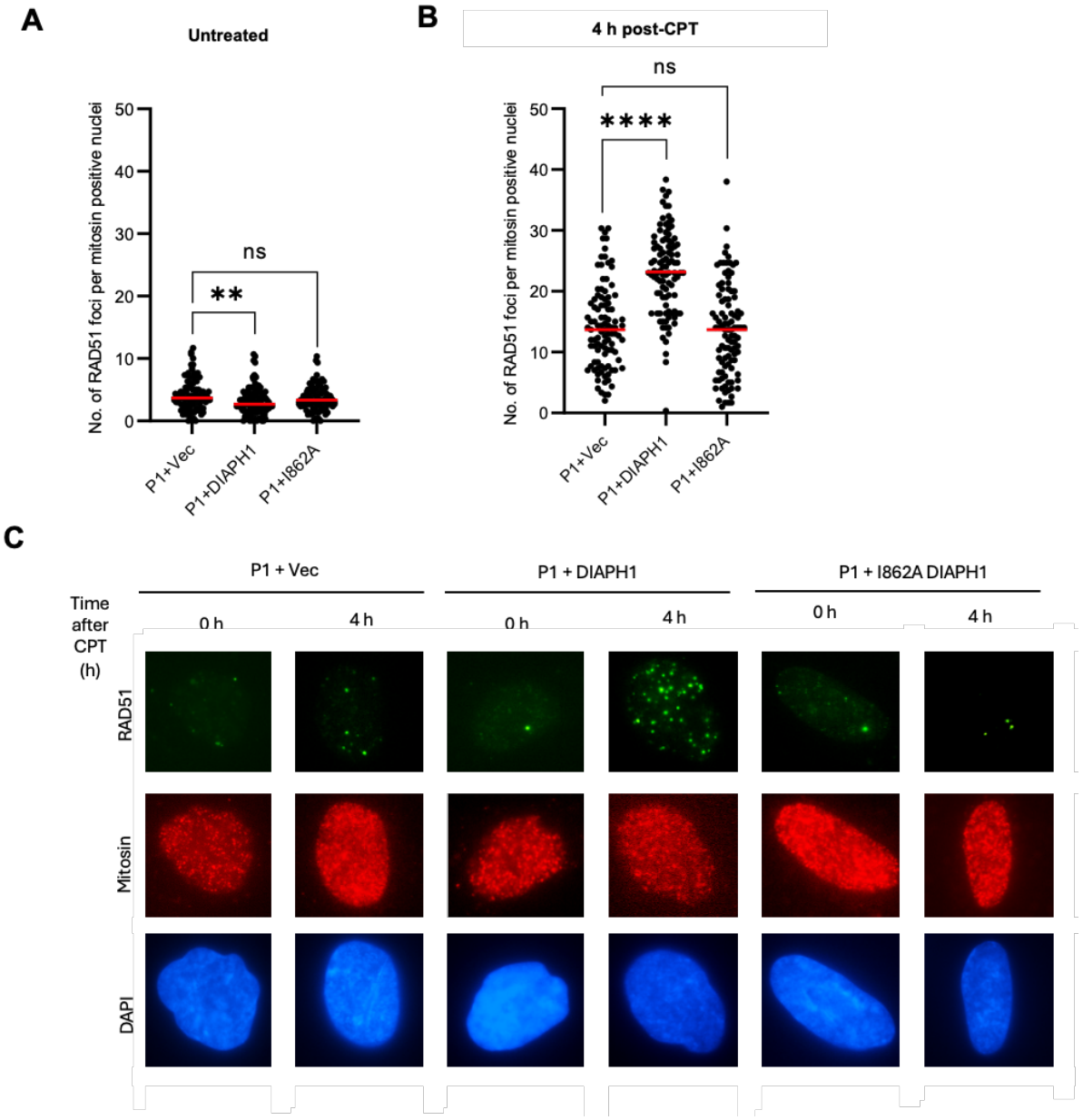


Figure 5.23 - Quantification of RAD51 foci in DIAPH1-P1 hTERT immortalised fibroblasts following DNA damage – *DIAPH1 P1 fibroblasts were transduced with a lentivirus expressing either an empty vector, WT-DIAPH1 or an actin-nucleation defective I862A-DIAPH1. Fibroblasts were seeded onto glass coverslips and left untreated or treated with 100 nM CPT for 1 h. Coverslips were harvested at 1 h and 24 h post treatment and fixed with paraformaldehyde (PFA).* ***A*** *- Quantification of nuclei with RAD51 foci in mitosin positive (S/G_2-phase) cells in the absence of exogenous DNA damage.* ***B*** *- Quantification of nuclei with RAD51 foci in mitosin positive (S/G_2-phase) cells 4 h post-CPT treatment.* ***C*** *- Representative images of mitosin positive cells from quantification in (A-B). Data from 3 independent repeats, a minimum of 100 cells counted per condition per repeat. Error bars represent standard error of the mean. * Indicates statistical significance (p=<0.05), ** indicates statistical significance (p=<0.01), *** indicates statistical significance (p=<0.001), **** indicates statistical significance (p=<0.0001) calculated using an unpaired Mann-Whitney-U test. Statistical significance was calculated using GraphPad Prism software.*

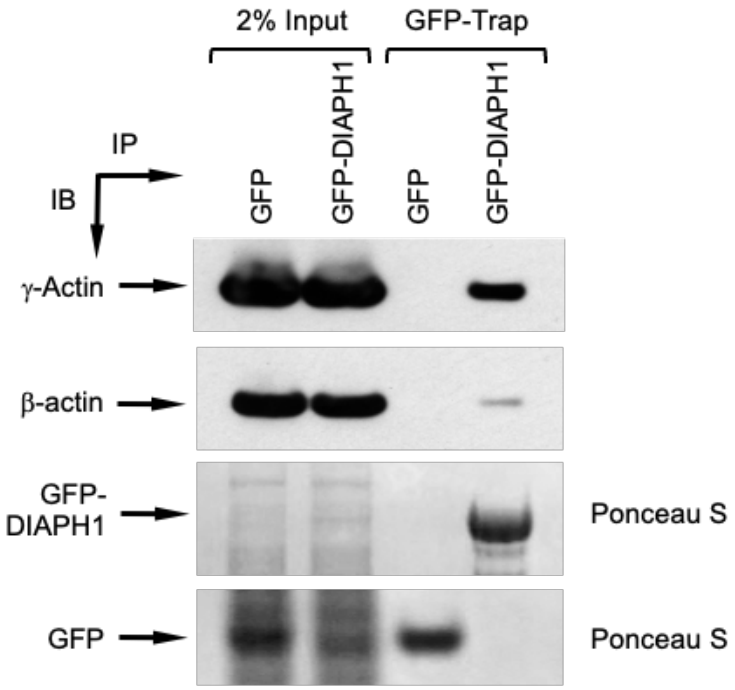


Figure 5.24 – GFP-DIAPH1 nuclear localisation and binding to actin isoforms – *HEK293FT cells were transfected with GFP or GFP-tagged WT DIAPH1 as indicated. GFP-DIAPH1 was purified from cell extracts using GFP-Trap and co-purified proteins were subjected to SDS-Page and Western blotting with the antibodies indicated. Ponceau S stain was used to visualise the affinity purified GFP and GFP-tagged DIAPH1 on the nitrocellulose filter.*

5.4 Concluding remarks

The findings presented here in Chapter 5 offer a novel insight into how the actin network regulates HR and functions in maintaining genome stability. Whilst a role for actin and the ARP2/3 complex in HR has been previously reported, there has been no link reported between actin and DIAPH1 in this process, with DIAPH1 being actively ruled out by two independent studies (Belin, Lee and Mullins, 2015; Caridi *et al.*, 2018). Furthermore, this is the first demonstration that the primary actin paralog that regulates genome stability and DSB repair is γ-actin. This therefore provides some mechanistic insight to explain why some BWCFF syndrome patients exhibit overlapping clinical features with those typically associated with a DSB repair defects, such as microcephaly, short stature, intellectual disability, and facial dysmorphia. Consistent with this, the clinical features of these patients also overlap with the DIAPH1 patient cohort present in Chapter 3.

BWCFF syndrome patient-derived fibroblasts used within this study were selected at random to encompass a range of clinical phenotypes and disease severity. There were no distinct patterns in the clinical phenotypes between *ACTB* and *ACTG1* patients. Patients with mutations in either gene displayed features such as microcephaly, short stature, and intellectual disability but this was not ubiquitous or unique to either *ACTB* or *ACTG1* mutations. Whilst there was some overlap between the clinical phenotypes associated with *DIAPH1* mutations and BWCFF syndrome to suggest the genes may be functioning in the same pathway, the patient cohort sampled was too small and the clinical phenotypes too varied to be able to conclude whether a specific clinical

phenotype may be caused by a DSB repair defect. Given the high degree of heterogeneity and differential effects of *ACTB* and *ACTG1* mutations on protein stability, polymerisation, depolymerisation and interactions with other proteins, it will be difficult to make any genotype-phenotype correlations without a systematic analysis of DSB repair in all documented cases of *ACTB* and *ACTG1* mutant patients (Rivière *et al.*, 2012; Di Donato *et al.*, 2014; Verloes *et al.*, 2015; Cuvertino *et al.*, 2017; Yates *et al.*, 2017; Zech *et al.*, 2017; Cabanillas *et al.*, 2018; Latham *et al.*, 2018; Miyajima *et al.*, 2020).

Interestingly, despite the varied clinical phenotypes, at the cellular level, data from patient-derived fibroblasts shows a clear indication that *ACTG1* mutations are associated with a defect in DSB repair. Data from the *ACTB* mutant cell lines was more variable but suggested that this protein is not involved in promoting the repair of DSBs. This variability could be due to the fact that all of the actin patients used in this study carry *de novo* mutations, which must act in either a dominant or haploinsufficient manner. As such, it is not clear whether the presence of a dominant acting mutant protein is more detrimental to DSB repair than reducing the pool of actin by 50%. Furthermore, since each mutation can have differential impacts on either protein stability and/or its function, this will also affect DSB repair in different ways. Lastly, it is not clear if there is some redundancy between *ACTB* and *ACTG1* and whether one paralog is better at functionally compensating for the loss of the other i.e. *ACTB* is better at compensating for loss of *ACTG1* since it is the dominant actin paralog whereas *ACTG1* cannot compensate as well for loss of *ACTB*. Taken together, it is clear that there are many environmental, genetic and epigenetic factors that may

dictate why some patients display a more severe clinical phenotype than others and why the cellular response of patient-derived fibroblasts to specific genotoxins may vary. Thus, the presence or absence of specific clinical features is not sufficient to predict if BWCFF syndrome may have an underlying DNA DSB repair defect and as such, may be hypersensitive to IR and other chemotherapeutic agents. Moreover, the presence of some of the clinical features, such as microcephaly, which are often associated with a DNA repair defect, could also be caused by compromising actin's role in other pathways such as DNA replication and mitosis (Jeruzalska and Mazur, 2023). However, despite the inherent variability associated with using non-isogenic patient fibroblasts with different hypomorphic actin paralog mutations, the observation that *ACTG1* but not *ACTB* mutations give rise to a DSB defect was recapitulated in the A375 *ACTB* and *ACTG1* KO cells. Therefore, the cellular evidence presented here is strong enough to warrant a larger BWCFF syndrome patient cohort being examined for DSB repair competency.

There is a substantial amount of evidence that nuclear actin polymerisation is critical for repairing DSBs but it is not clear which actin, or which nucleators are involved and in what cellular contexts. Several studies show disrupting actin polymerisation affects HR, NHEJ and SSA-dependant DSB repair (Caridi *et al.*, 2018; Schrank *et al.*, 2018; Pfitzer *et al.*, 2019; T. Wang *et al.*, 2021). Despite this, my data indicates that DIAPH1, γ-actin and the ARP2/3 complex function upstream of the MRN complex to facilitate its localisation to and/or stabilisation at DSB sites and initiation of DNA end resection (Caridi *et al.*, 2018; Schrank *et al.*, 2018). As a result, a new model has emerged from this data: DIAPH1 binds to the MRN complex to localise/stabilise it to DSB sites, which

is facilitated by formation of γ-actin filaments. This process then serves to promote end resection and stimulate the recruitment of the ARP2/3 complex, which initiates branching of γ-actin filaments. The branching filaments then may facilitate mobilisation and clustering of DSBs, proposed by previous work, but the branching may also promote the relocalisation of other repair factors to DNA damage sites, such as the SMC5/6 complex (Schrank *et al.*, 2018). Furthermore, other actin-related proteins such as myosins, which are reported to have a roles in genome stability, could also fit into this model (Caridi *et al.*, 2018; Shi *et al.*, 2023). Interestingly, an interaction between DIAPH1 and RAD51 was detected in Chapter 4, indicating that DIAPH1, and potentially γ-actin, may play additional roles later on within the repair process potentially involved in seeding and/or stabilising RAD51 filament formation. As a collective, Chapter 5 brings together an emerging role of the γ-actin network and its nucleating factors and how it could be functioning not only upstream of the MRN complex but functioning throughout the process of DNA repair. However, why this process appears to be entirely dependent on γ-actin over β-actin is not yet clear.

Interestingly, loss of *Actb* in mice is embryonic lethal, but *Actg1* null animals survive, despite having severely stunted growth and decreased survival into adulthood. This suggests that *Actb* is an essential gene but *Actg1* is not (Patrinostro *et al.*, 2018). Further to this, in some tissues, the two actin proteins appear to play distinct roles but can also be dispensable for one another, depending on the context. Examples of this include in auditory hair cell development; both actins play redundant roles during development and are dispensable for each other but seem to perform distinct post-development functions. This has been proposed by Perrin et al. whereby the authors

demonstrated that knockout of either *Actb*$^{-/-}$ and *Actg1*$^{-/-}$ in mice does not affect stereocilia development, but a double knockout of both *Actb*$^{-/-}$ and *Actg1*$^{-/-}$ together did not develop stereocilia at all. Furthermore following development, the single knock out of either *Actb*$^{-/-}$ and *Actg1*$^{-/-}$ developed distinct stereocilia pathology and each has a distinct pattern of progressive hearing loss (Perrin, Sonnemann and Ervasti, 2010; Patrinostro *et al.*, 2018). *Actg1*$^{-/-}$ mice developed fast progressing hearing loss at all frequencies whereas *Actb*$^{-/-}$ mice developed high frequency hearing loss that did not progress rapidly, suggesting γ-actin has a critical hair-cell specific function that cannot be compensated for by *Actb* (Perrin, Sonnemann and Ervasti, 2010). This may explain why there are overlapping and variable clinical features between patients with mutations in *ACTB* and *ACTG1*, whereby the two genes are functionally redundant in some tissues but not in others. However, in the case of DSB repair, β-actin does not seem to be able to compensate for loss of γ-actin function in this pathway.

The finding that DIAPH1 preferentially interacts with γ-actin can explain why DSB repair requires γ-actin but not β-actin. This is also consistent with previous reports that DIAPH1 and γ-actin function together in mitosis (Chen *et al.*, 2021; Jeruzalska and Mazur, 2023). Intriguingly, both γ-actin and β-actin share a near identical amino acid sequence differing by only 4 amino acids at the N-terminus, which is the region where the FH2 domain of DIAPH1 binds to actin to carry out its nucleation function. Interestingly, the amino acids that differ between the two actin proteins are not chemically very different. β-actin has three aspartic acid residues at positions 2-4 whereas γ-actin has glutamic acid residues. At position 10, both proteins have aliphatic residues, β-actin having valine and γ-actin having isoleucine. Consequently, these

sequence differences do not have a dramatic effect on protein structure but are significant enough to alter its binding preference for specific nucleating factors. This may explain why in mitosis, DIAPH1 functions with γ-actin whereas DIAPH3 preferentially binds β-actin. Interestingly, whilst both DIAPH1 and DIAPH3 are part of the same Formin protein family, their amino acid sequences differ considerably. Both share anf FH2 domain that interacts with actin, but unpublished data from Andrew Wilde's group at the University of Toronto, suggest the specificity of DIAPH1/3 for γ- or β-actin may be due to a sequence difference in the linker region of the FH2 domain. However, further work is needed to validate this claim (Zhu, 2019). Whilst, data presented here provides further evidence that both DIAPH1 and γ-actin function together within the nucleus to regulate DSB repair, it is not clear why this process utilises DIAPH1 and γ-actin over DIAPH3 and β-actin. It is unlikely that γ-actin and β-actin filaments look fundamentally different structurally, but the specificity may be linked with the myosins that transport cargo along the different actin filaments. Further work is needed to completely rule out a role for β-actin and/or DIAPH3 in DNA repair. It is conceivable that these proteins play a more specialised role in DNA repair, but this may be linked with the repair of specific types of breaks.

With regards to the ARP2/3 complex, hypomorphic mutations in A*RPC1B*, *ARPC4* and *ARPC5* all give rise to a DSB repair defect, but the clinical phenotypes are more consistent with Wiskott-Aldrich Syndrome (WAS) than BWCFF syndrome or DIAPH1 homozygous mutations in this study. The underlying mechanism for this variability between the clinical phenotypes caused by ARP2/3 complex mutations and loss of DIAPH1 is unclear, it could be possible that the ARP2/3 complex is only playing a minor

role in DIAPH1 and γ-actin-dependent DSB repair. Conversely, it could be that the ARP2/3 complex in conjunction with the WASP homolog WASH, predominantly functions to promote NHEJ or heterochromatic DSB repair, which are likely to be more prominent in non-proliferating lymphocytes rather than HR (Caridi *et al.*, 2018; Schrank *et al.*, 2018; T. Wang *et al.*, 2021).

In conclusion, patients with mutations in *ACTG1* and components of the ARP2/3 complex, *ARPC1B, ARPC4* and *ARPC5*, display a DSB repair defect but currently this cannot be linked with the presence of any specific clinical features exhibited by the patients. Despite this, my data demonstrates that DIAPH1, γ-actin and the ARP2/3 complex, but not β-actin, function together in the same pathway to facilitate HR and initiate DNA end resection, which is upstream of the MRN complex. These findings are critical for our understanding of how actin and actin nucleating factors regulate DNA repair, as well as our understanding of how gene variants in actin, DIAPH1 and the ARP2/3 complex components give rise to disease in humans.

Chapter 6: Loss of DIAPH1 lead to defects in DNA replication and mitosis

6.0 Results

6.1 Introduction

The data presented in Chapter 3-5 characterised a role for *DIAPH1* in double strand break (DSB) repair, which provides an explanation for some of the clinical symptoms exhibited by patients with homozygous variants in *DIAPH1*. Further to this, DIAPH1 was identified to function specifically with γ-actin and the ARP2/3 complex, acting upstream of the MRN complex to initiate homologous recombination (HR) repair. However, the increase in spontaneous γ-H2AX signal and a reduction in the phosphorylation of RPA2 pS4/S8 after treatment with hydroxyurea (HU) in cells lacking DIAPH1 (Chapter 3; Figure 3.5, Figure 3.7, Figure 3.8) suggests that loss of DIAPH1 may also give rise to a replication defect. As previously mentioned, neurodevelopmental defects can be caused by abnormal DNA replication and/or aberrant progress through mitosis as well as defective DSB repair. Since, previous reports have already implicated actin in regulating the replication stress response and mitosis, it was hypothesised that cells from DIAPH1 mutant patients may also display defects in these processes (Lamm *et al.*, 2020; Chen *et al.*, 2021; Nieminuszczy *et al.*, 2023; Palumbieri *et al.*, 2023; Shi *et al.*, 2023).

6.2 Aims of this chapter

To investigate the hypothesis that loss of DIAPH1 gives rise to defects in DNA replication and mitosis, preliminary experiments were performed using the DNA fibre

analysis and immunofluorescence (IF). The DNA fibre technique provides an effective way to observe changes in replication dynamics in cells at the single molecule level (Tuduri, Tourrière and Pasero, 2010; Quinet *et al.*, 2017; Técher *et al.*, 2017). The impact of agents that induce replication stress can be analysed through the sequential labelling of nascent DNA with two thymidine analogues: 5-chloro-2′-deoxyuridine (CldU) and 5-iodo-2′-deoxyuridine (IdU). Cells can be treated with replication stress inducing agents at different points during the labelling process to assess their impact on replication dynamics. Preliminary experiments were performed to assess the ability of cells lacking DIAPH1 to replicate in the presence of replication stress (Figure 6.1A), their ability to restart replication after the removal of 5 mM HU to halt DNA replication (Figure 6.1B) and the ability to protect stalled forks from nucleolytic degradation (Figure 6.1C). The final aim was to assess spontaneous mitotic defects in the absence of DIAPH1 using IF techniques.

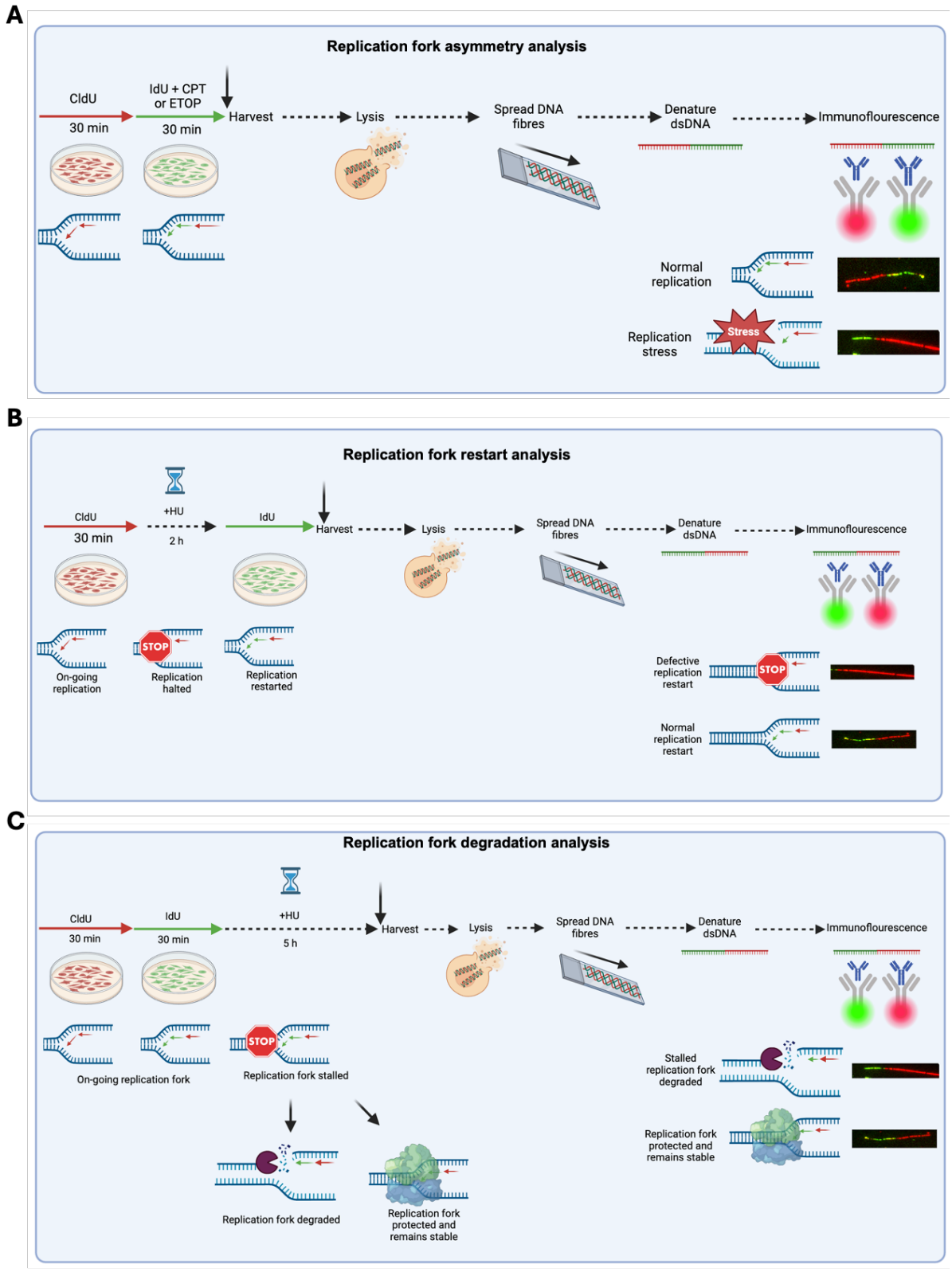


Figure 6.1 – Schematic representation of DNA fibre analysis to assess replication dynamics *– **A** – DNA fibre analysis to assess replication in the presence of replication stress inducing agents. **A** - Reduced ratio of 2nd to 1st label indicates defective replication in the presence of the genotoxin. **B** – DNA fibre analysis to assess replication fork restart after HU-induced replication fork stalling between the 1st and 2nd label. **C** - DNA fibre analysis to assess replication fork degradation in the presence of HU after incubation with both labels. A shortened 2nd label indicates replication fork nucleolytic degradation. Abbreviations: HU – hydroxyurea, CPT – camptothecin, ETOP – etoposide, CldU - 5-chloro-2'-deoxyuridine, IdU - 5-iodo-2'-deoxyuridine, dsDNA – double stranded DNA. Created with Biorender.com.*

6.3 Results

6.3.1 Loss of DIAPH1 causes defects in DNA replication and the DNA replication stress response

Data presented in Chapter 3 indicated that loss of DIAPH1 gives rise to signs of spontaneous genome instability. To investigate whether the source of this was due to a DNA replication defect, DNA fibre analysis was performed in the presence and absence of 2 mM HU using DIAPH1-P1 fibroblasts complemented with either an empty vector or WT-DIAPH1. Following nascent DNA labelling (Figure 6.2A), quantification of DNA structures including on-going replication forks, stalled forks and new origins were analysed (Figure 6.2B). Interestingly, in the absence of exogenous replication stress, P1+Vector fibroblasts displayed a reduction in on-going forks when compared to P1+WT-DIAPH1 cells and an elevation of stalled forks (Figure 6.2C-D). Following a 2 h treatment with 2 mM HU, there was a further increase in stalled forks / 1st label termination (Figure 6.2D) in the P1+Vector fibroblasts when compared to WT-DIAPH1 complemented counterpart. Interestingly, following HU treatment, there was a significant increase in the presence of new origins in P1+Vector cells when compared to P1+WT-DIAPH1 cells (Figure 6.2E). Given that in the presence of replication stress, ATR signalling should supress new origin firing, this implies there may be a defect in the ATR-dependent replication checkpoint in cells lacking DIAPH1 (Saldivar, Cortez and Cimprich, 2017). Reassuringly, the same replication phenotypes were observed in U-2-OS cells depleted of DIAPH1 using siRNA (Figure 6.3).

Next, transient HU exposure was used to investigate if DIAPH1 is required to restart stalled replication forks (Figure 6.4A). In untreated conditions, there was no change in the ratio of the two thymidine labels suggesting that in the absence of exogeneous replication stress, on-going replication forks progress normally (Figure 6.4B). However, following a 2 h exposure to HU, P1+Vector fibroblasts failed to restart stalled replication efficiently when compared to P1+WT-DIAPH1 fibroblasts (Figure 6.4C). Again, this phenotype was recapitulated in U-2-OS cells depleted of DIAPH1 with siRNA (Figure 6.5).

The next preliminary investigation into how DIAPH1 impacts replication dynamics was to assess how loss of DIAPH1 impacts the ability of stalled forks to be protected from nucleolytic degradation. To do this, U-2-OS cells depleted of DIAPH1 with siRNA were labelled with CldU and IdU in succession, followed by treatment with 4 mM HU for 5 h. The ratio of Idu:CldU was then measured as a direct way of assessing if on-going forks stalled by HU treatment had been degraded (Figure 6.1C). In keeping with results reported in a study by Nieminuszczy et al. using DIAPH1-P1 complemented fibroblasts, depletion of DIAPH1 lead to a modest reduction in the ratio of IdU:CldU, indicating a mild defect in the ability of cells lacking DIAPH1 to protect stalled forks from degradation (Figure 6.6) (Nieminuszczy *et al.*, 2023). Finally, the ability of DIAPH1 null cells to undergo DNA replication in the presence of replication stress induced by the topoisomerase inhibitors CPT and ETOP was next investigated (Figure 6.1A). The mechanism of action of these genotoxins is outlined in Chapter 3, Figure 3.1 but both function at the replication fork and induce DSBs coupled to a DPC. In DIAPH1 depleted U-2-OS cells (Figure 6.7A), the ratio of IdU:CldU was reduced in the presence of either

CPT or ETOP, which was comparable to the depletion of NBS1 (Figure 6.7B-C). These data suggest that DIAPH1 is required to maintain replication fork progression in the presence of abortive TOPI/II complexes and increased topological stress.

Taken together, this section provides some preliminary evidence that DIAPH1 is required for normal replication and has a role in the replication stress response. However, the exact mechanism of this and whether this function is dependent on actin is yet to be elucidated.

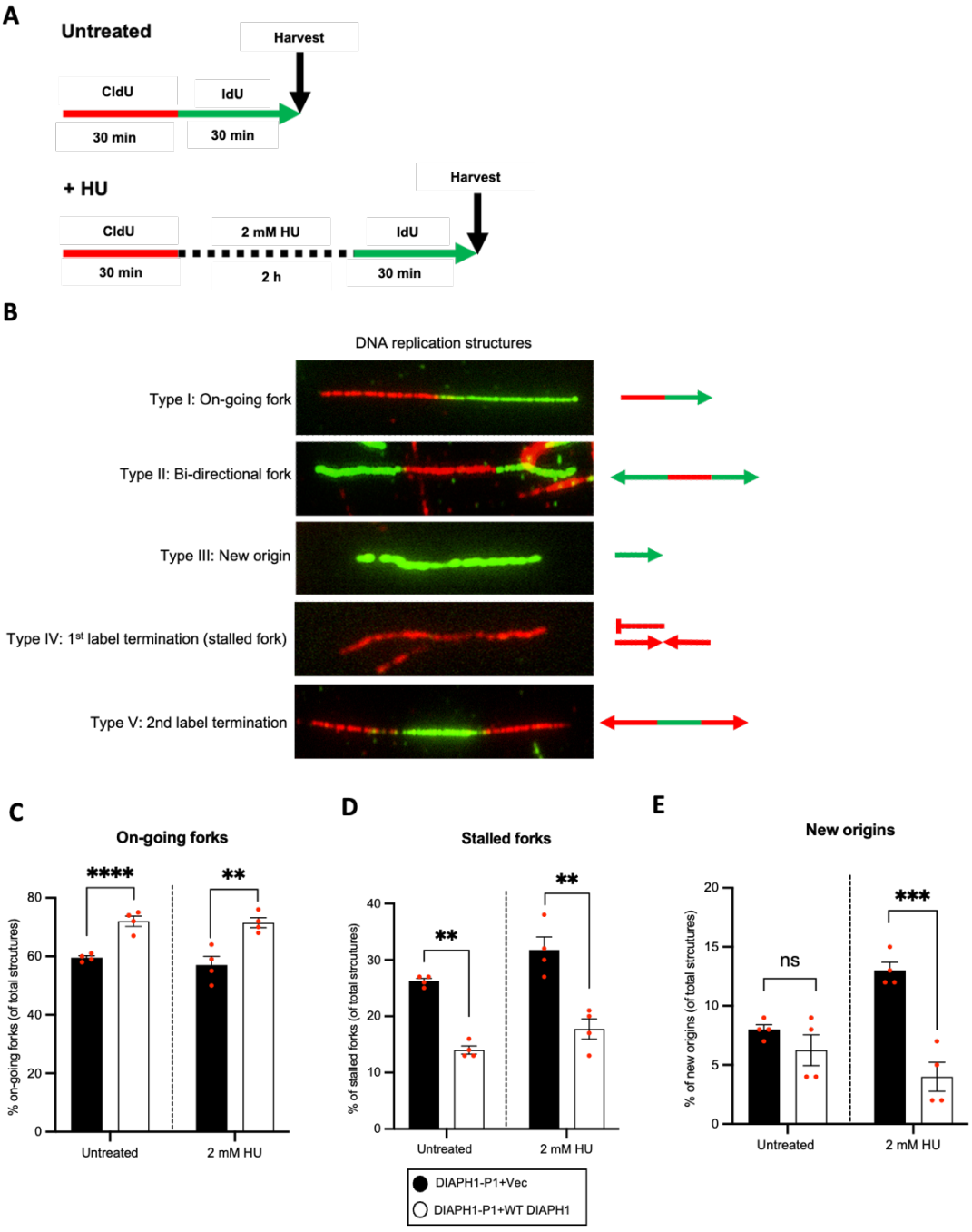


Figure 6.2 - Quantification of DNA fibre structures in HU treated DIAPH1 P1 hTERT fibroblasts – A *– Representative image of subsequent labelling with CldU and IdU thymidine analogues, each for 30 minutes before harvesting. HU was added between the two labels for 2 h.* ***B*** *- Representative images structures analysed in (C-E).* ***C*** *- % of on-going fork structures scored in P1+DIAPH1 and P1+Vector cells.* ***D*** *- % of stalled fork structures scored in P1+DIAPH1 and P1+Vector cells.* ***E*** *- % of new origin structures scored in P1+DIAPH1 and P1+Vector cells. Data from 4 independent repeats. A minimum of 250 structures were analysed per repeat. Error bars represent standard error of the mean. * Indicates statistical significance (p=<0.05), ** indicates statistical significance (p=<0.01), *** indicates statistical significance (p=<0.001) calculated using an unpaired Students T-test. Statistical significance was calculated using GraphPad Prism software.*

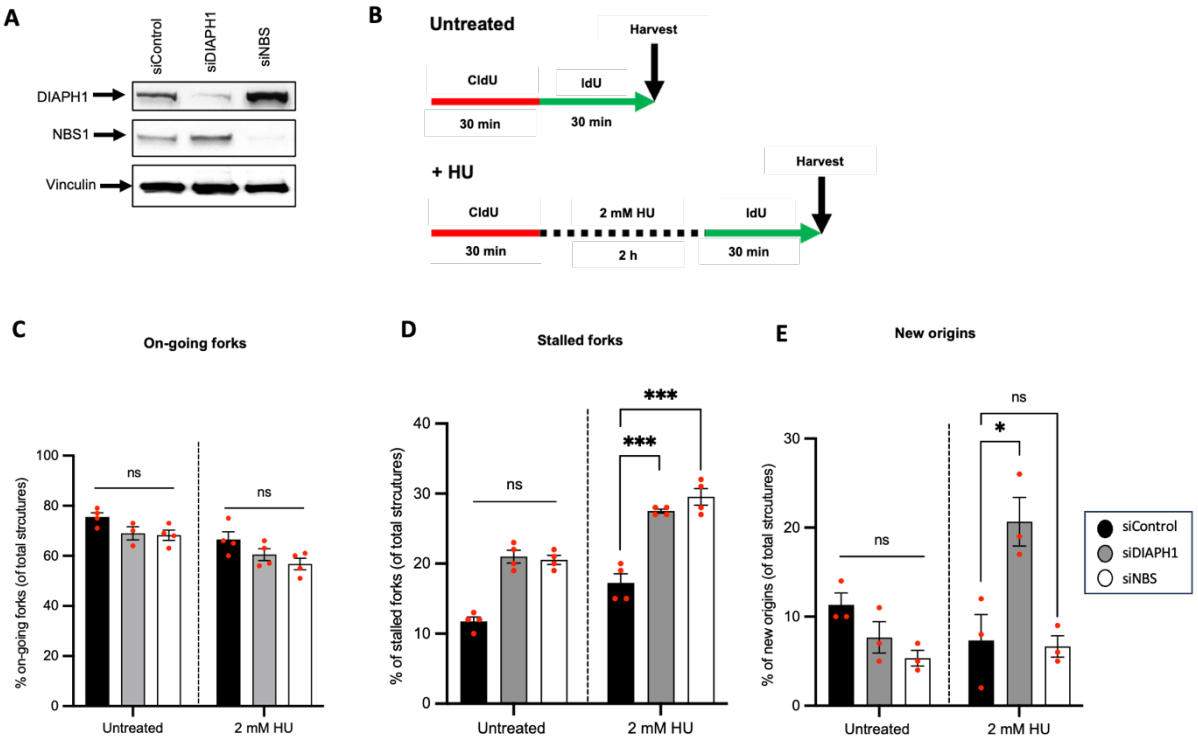


Figure 6.3 - Quantification of DNA fibre structures in HU treated siRNA depleted U-2-OS cell lines – A *– Western blot analysis of cell lysates from U-2-OS cells subject to siRNA treatment to either a non-targeting control (luciferase) or indicated proteins. Vinculin was used as a loading control.* ***B*** *- Representative image of subsequent labelling with CldU and IdU thymidine analogues, each for 30 minutes before harvesting. HU was added between the two labels for 2 h. C - % of on-going fork structures scored in siControl, siDIAPH1 and siNBS cells.* ***D*** *- % of stalled fork structures scored in siControl, siDIAPH1 and siNBS1 cells.* ***E*** *- % new origin structures scored in siControl, siDIAPH1 and siNBS1 cells. Data from 3 independent repeats. A minimum of 250 structures were analysed per repeat. Error bars represent standard error of the mean. * Indicates statistical significance (p=<0.05), ** indicates statistical significance (p=<0.01), *** indicates statistical significance (p=<0.001) calculated using an unpaired Students T-test. Statistical significance was calculated using GraphPad Prism software.*

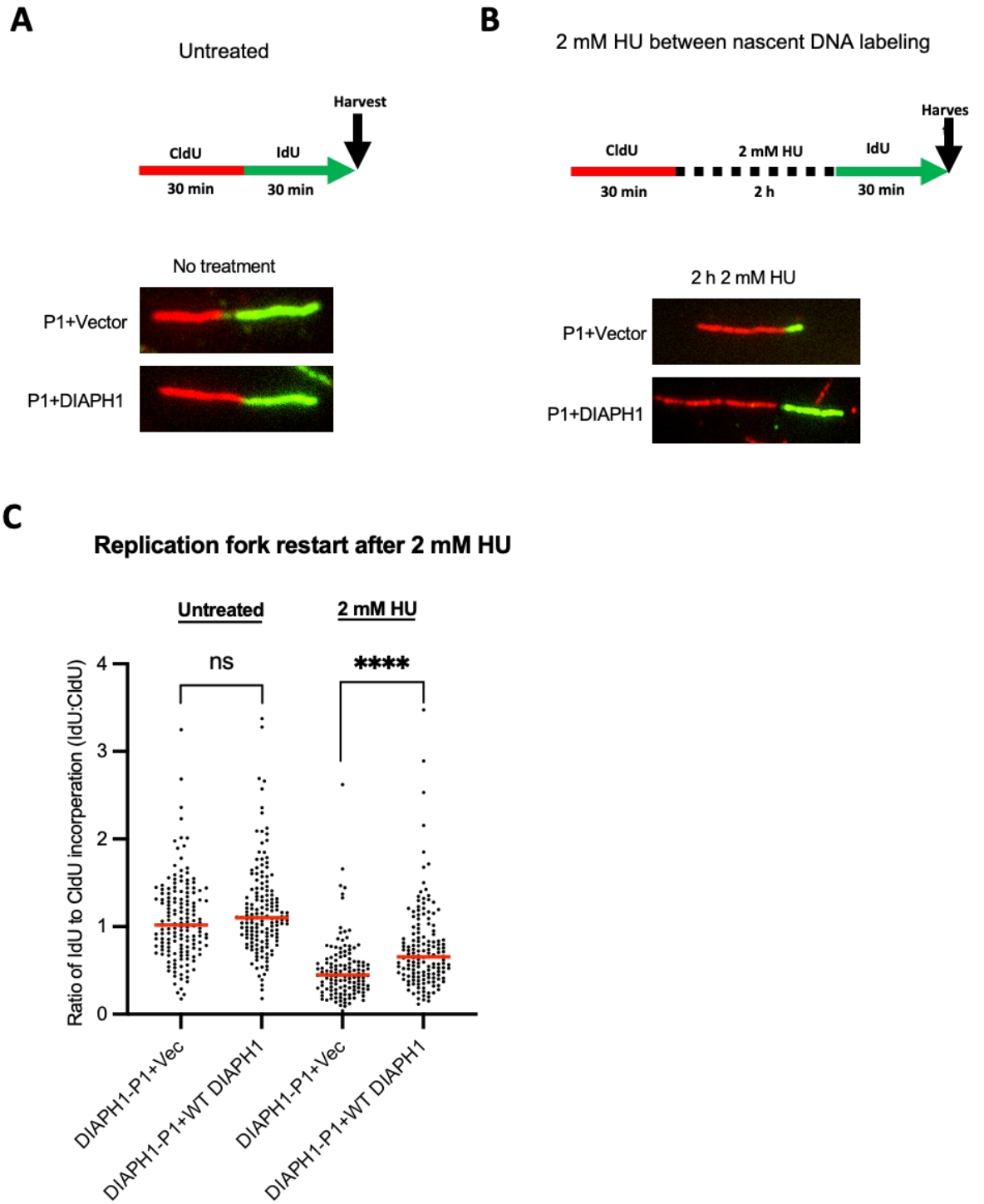


Figure 6.4 - Ratio of IdU and CldU tract length in DIAPH1 P1 fibroblasts after release from HU treatment - *CldU and IdU lengths were measured at on-going replication forks, with a median value of 1 indicating no change in restart efficiency between CldU and IdU incorporation.* ***A*** *- Schematic of labelling regime for untreated cells.* ***B*** *- Schematic of labelling regime for HU treated cells.* ***C*** *- The ratio of IdU to CldU was calculated in hTERT immortalised P1 fibres transduced with WT-DIAPH1 or an empty vector either left untreated or after release from 2 h HU treatment. A minimum of 100 forks were analysed per repeat. Data from 4 independent repeats. Error bars represent standard error of the mean. * Indicates statistical significance (p=<0.05), ** indicates statistical significance (p=<0.01), *** indicates statistical significance (p=<0.001) calculated using an unpaired 2-tailed Mann-Whitney U Test, Statistical significance was calculated using GraphPad Prism software.*

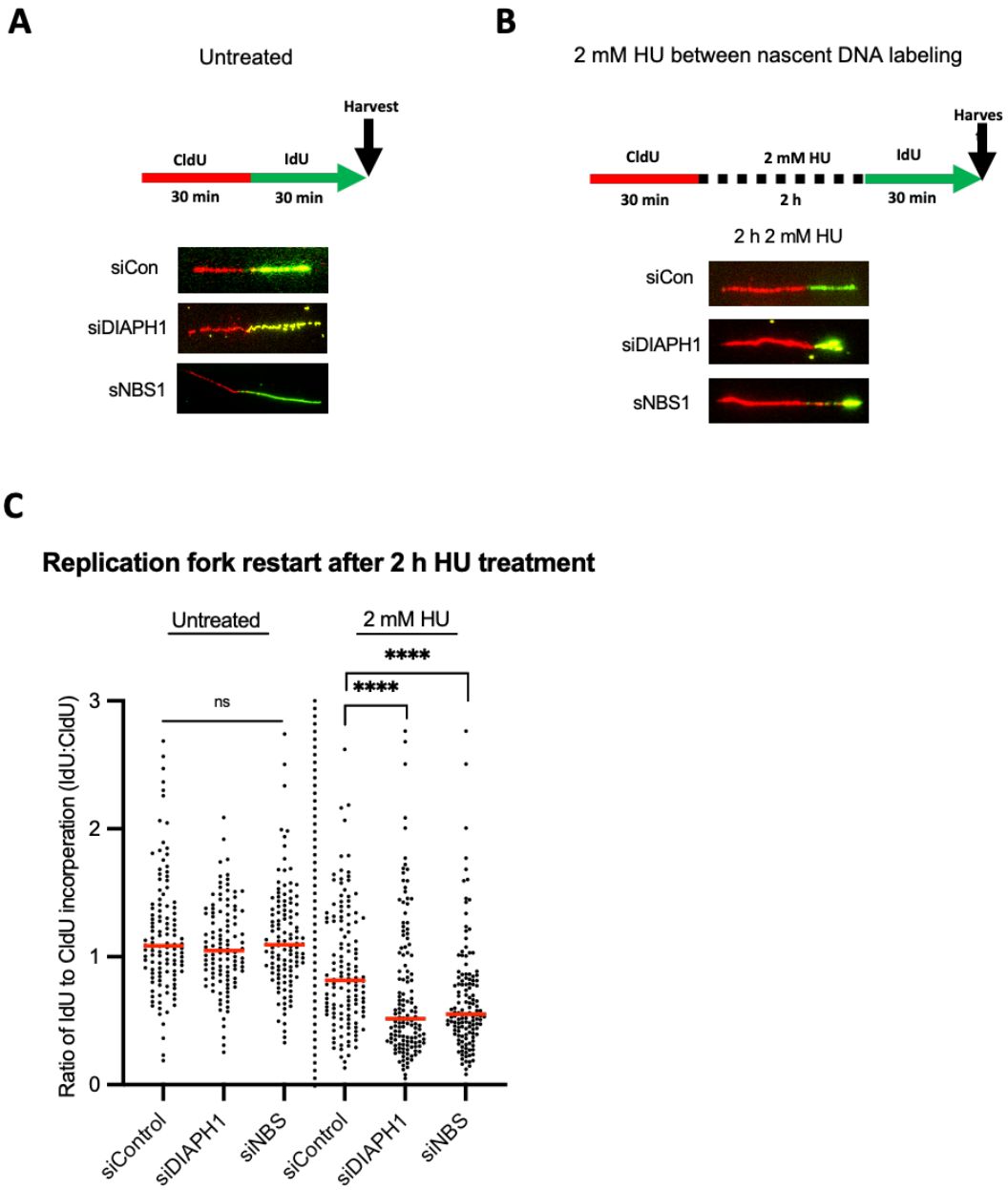


Figure 6.5 - Ratio of IdU and CldU tract length in siDIAPH1 U-2-OS after release from HU treatment - *CldU and IdU lengths were measured at on-going replication forks, with a median value of 1 indicating no change in restart efficiency between CldU and IdU incorporation.* ***A*** *- Schematic of labelling regime for untreated cells.* ***B*** *- Schematic of labelling regime for HU treated cells.* ***C*** *- The ratio of IdU to CldU was calculated U-2-OS siRNA depleted with control siRNA (luciferase), siDIAPH1 or siNBS either left untreated or after release from 2 h HU treatment. A minimum of 100 on-going forks were analysed per repeat. Data from 4 independent repeats. Error bars represent standard error of the mean. * Indicates statistical significance (p=<0.05), ** indicates statistical significance (p=<0.01), *** indicates statistical significance (p=<0.001) calculated using an unpaired 2-tailed Mann-Whitney U Test, Statistical significance was calculated using GraphPad Prism software.*

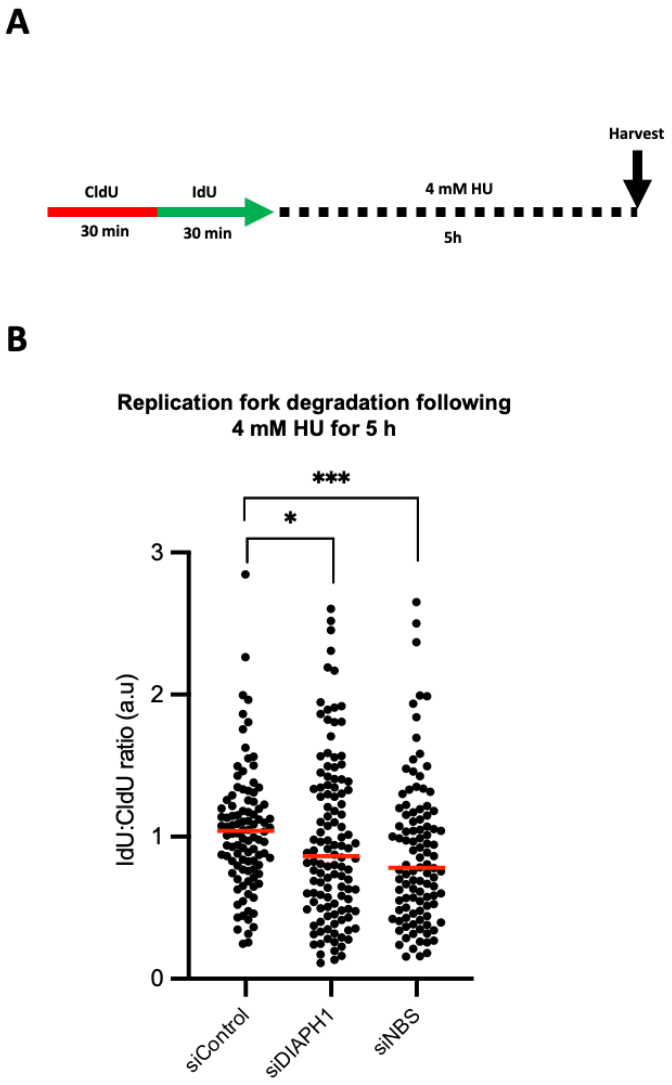


Figure 6.6 - Quantification of replication fork stability in siDIAPH1 U-2-OS after 5 h HU treatment - *CldU and IdU lengths were measured at on-going replication forks, with a median value of 1 indicating no change in tract length between CldU and IdU incorporation. After subsequent labelling with CldU and IdU thymidine analogues for 30 min each, cells were treated with 4 mM HU for 5 h to assess replication fork stability.* ***A*** *- Schematic of labelling regime for HU treated cells.* ***B*** *- The ratio of IdU to CldU was calculated U-2-OS siRNA depleted with control siRNA (luciferase), siDIAPH1 or siNBS after 5 h HU. A minimum of 100 on-going forks were analysed per repeat. Data from 4 independent repeats. Error bars represent standard error of the mean. * Indicates statistical significance (p=<0.05), ** indicates statistical significance (p=<0.01), *** indicates statistical significance (p=<0.001) calculated using an unpaired 2-tailed Mann-Whitney U Test, Statistical significance was calculated using GraphPad Prism software.*

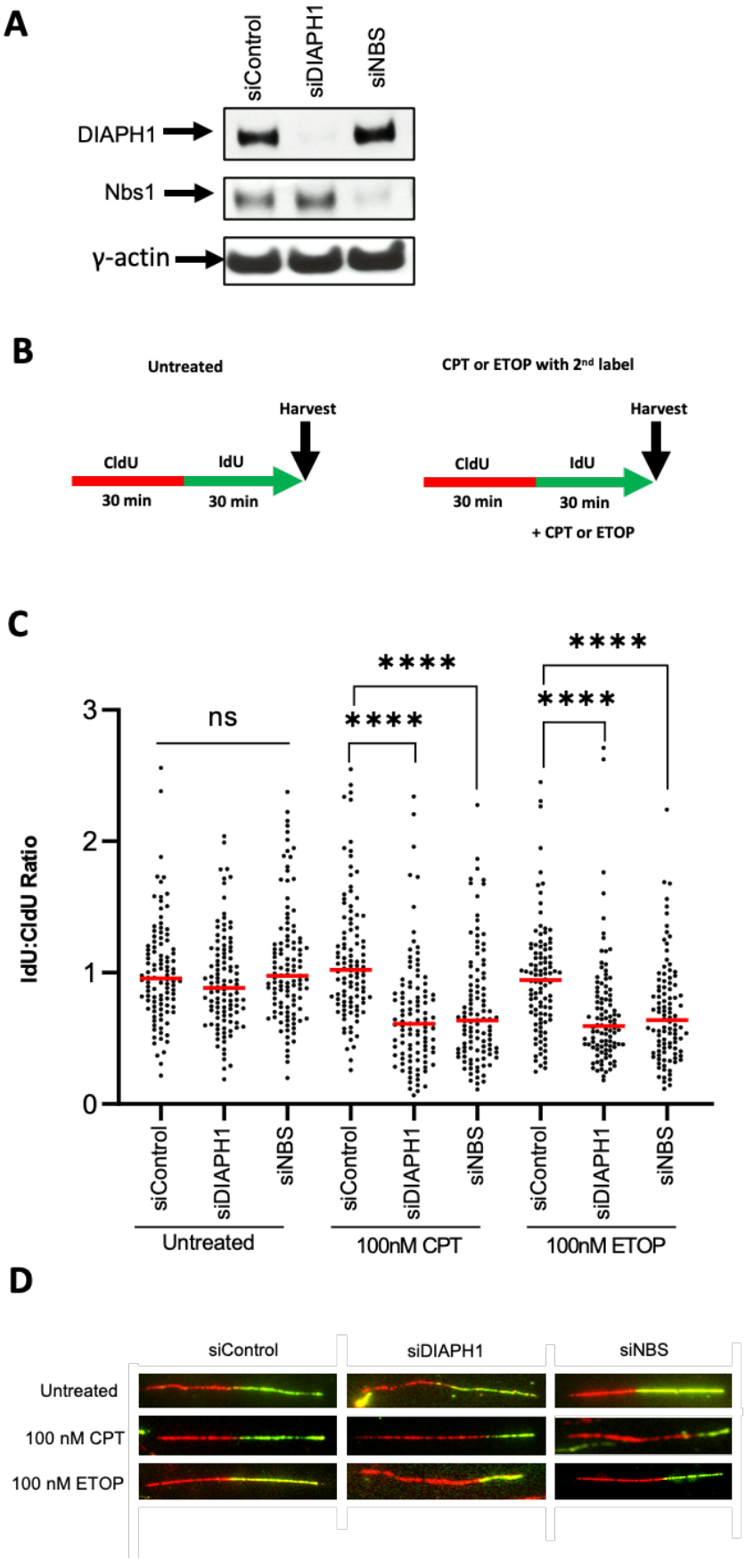

A
siControl
siDIAPH1
siNBS
DIAPH1
Nbs1
γ-actin
B
Untreated
Harvest
CldU
IdU
30 min
30 min
CPT or ETOP with 2nd label
Harvest
CldU
IdU
30 min
30 min
+ CPT or ETOP
C
IdU:CldU Ratio
3
2
1
0
ns
****
****
****
****
siControl
siDIAPH1
siNBS
siControl
siDIAPH1
siNBS
siControl
siDIAPH1
siNBS
Untreated
100nM CPT
100nM ETOP
D
siControl
siDIAPH1
siNBS
Untreated
100 nM CPT
100 nM ETOP

Figure 6.7 - Ratio of IdU and CldU tract length in siDIAPH1 U-2-OS in the presence of replication stress – ***A*** *– Western blot analysis of cell lysates from U-2-OS cells subject to siRNA treatment to either a non-targeting control (luciferase) or indicated proteins. Vinculin was used as a loading control.* ***B*** *- Schematic of subsequent labelling with CldU and IdU thymidine analogues, each for 30 mins before harvesting. In treated cells, either 100 nM CPT or 100 nM ETOP was present during the incubation with the second label.* ***C*** *- The ratio of IdU to CldU was calculated in siRNA treated U-2-OS either left untreated or after treatment with CPT or ETOP with the second (IdU) label.* ***D*** *– Representative image of DNA fibres analysed in (C). Data from 3 independent repeats. A minimum of 100 DNA fibres were analysed per condition per repeat. Error bars represent standard error of the mean. * Indicates statistical significance (p=<0.05), ** indicates statistical significance (p=<0.01), *** indicates statistical significance (p=<0.001) calculated using an unpaired 2-tailed Mann-Whitney U Test, Statistical significance was calculated using GraphPad Prism software.*

6.3.2 Loss of DIAPH1 causes defects in mitosis

The final investigation in this study was to examine whether loss of DIAPH1 gives rise to defects in mitosis in patient-derived fibroblasts. This study so far has extensively investigated the role of DIAPH1 in DSB repair and preliminarily shown DIAPH1 also plays a role in DNA replication. It was already known that DIAPH1 has a role in mitosis, so to confirm a defect could be seen in patient-derived fibroblasts lacking DIAPH1, IF was performed in untreated P1+Vector and P1+WT-DIAPH1 complemented fibroblasts. Mitotic cells were stained with specific antibodies to CDK5/RAP2 and α-tubulin, which were used as markers of centrosomes and the mitotic spindle respectively (Tolić, 2018; X. Wang *et al.*, 2021).

Mitotic cells in all phases of mitosis were included in this analysis (Figure 6.8A) and mitotic defects quantified are outlined in Figure 6.8D. In keeping with a role for DIAPH1 in mitosis, loss of DIAPH1 increased the frequency of aberrant mitotic cells, which included lagging chromosomes, increased centrosomes, centrosome fragmentation and misaligned telophases (Figure 6.8B). These findings were recapitulated in HeLa cells depleted of DIAPH1 with siRNA. However, unexpectedly the telophase defect observed in the fibroblasts was not recapitulated in these cells (Figure 6.8C-D). Whilst

the underlying reason for this is not clear, a similar phenotype was reported by Miao *et al*. who depleted DIAPH1 in HT29 and HCT-116 colorectal cancer cell lines, suggesting that these mitotic defects are caused by loss of DIAPH1 function (Miao *et al.*, 2021).

In summary, in untreated conditions, loss of DIAPH1 leads to multiple mitotic defects, providing a potential further explanation for clinical symptoms exhibited by the DIAPH1 patient cohort.

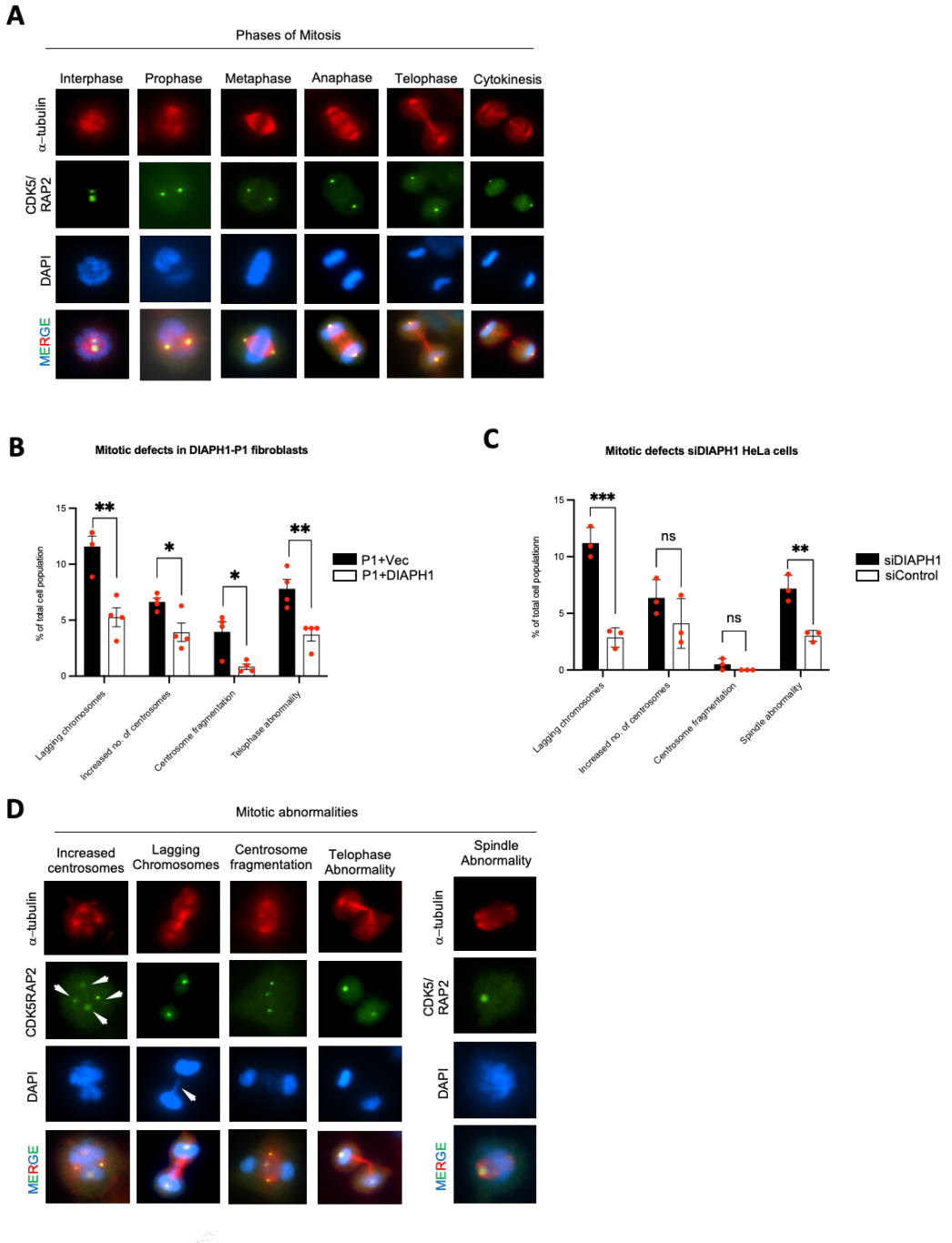


Figure 6.8 - Quantification of mitotic defects in cells lacking DIAPH1 – *P1+Vector and P1 + DIAPH1 fibroblasts and DIAPH1 depleted HeLa cells were seeded onto glass coverslips and left untreated for 48 h. At 48 h, cells were fixed in ice-cold methanol and stained with antibodies against α-tubulin (spindle marker) and CDK5RAP2 (centrosome marker).* ***A*** *- Representative images of each phase of mitosis.* ***B*** *- Quantification of mitotic defects in the absence of exogenous DNA damage in DIAPH1-P1 fibroblasts.* ***C*** *- Quantification of mitotic defects in the absence of exogenous DNA damage in siRNA mediated DIAPH1 depleted HeLa cells.* ***D*** *- Representative images of DAPI positive cells from quantification in (B). Data from 4 independent repeats, a minimum of 200 cells counted per condition per repeat. Error bars represent standard error of the mean. * Indicates statistical significance (p=<0.05), ** indicates statistical significance (p=<0.01), *** indicates statistical significance (p=<0.001) calculated using an unpaired Students T-test. Statistical significance was calculated using GraphPad Prism software.*

6.4 Concluding remarks

This chapter provides an exciting avenue for further study, suggesting that not only does DIAPH1 play a critical role in regulating HR and DNA end resection defined in detail in Chapters 3-5, but it also may function during normal DNA replication, the replication stress response and mitosis. The idea that DIAPH1 regulates multiple genome stability maintenance pathways could explain why homozygous loss of DIAPH1 gives rise to severe clinical deficits indicative of underlying genome instability, such as microcephaly, short stature, immunodeficiency and intellectual disability.

F-actin polymerisation is induced by replication stress, and both WASP and the ARP2/3 complex have been shown to regulate this response, in conjunction with ATR and other proteins including IQGAP1 and LIM (Lamm *et al.*, 2020). Interestingly, IQGAP1 has been shown to regulate DIAPH1 nucleation activity in the cytoplasm and within mitosis, so whilst Lamm et al. did not study DIAPH1's role in replication stress induced actin polymerisation, the data presented in this chapter suggests it may be functioning within this pathway (Chen *et al.*, 2020, 2021). The preliminary findings presented here also fit in with the model of how actin regulates the replication stress response proposed by Nieminuszcz et al. by protecting stalled replication forks from nucleolytic degradation. However, if this function of DIAPH1 also requires γ-actin is unclear. Other studies demonstrating a role for actin in the replication stress response did not specify which isoform was being studied, which poses the question whether both predominant actin paralogs play distinct roles in replication as they do in DSB repair and if DIAPH1 is important for nucleating only γ-actin. Further work is needed to

dissect how the actin network functions across these different genome stability maintenance pathways.

In mitosis, DIAPH1 and γ-actin are required for metaphase cortical stiffness and in anaphase, DIAPH1 activity is inhibited at the poles to relax γ-actin filaments and aid in the generation of the β-actin contractile rings at the cell equator (Chen *et al.*, 2021). The data in this chapter examining mitosis indicates a defect in this process in patient-derived fibroblasts cells, consistent with work by Chen et al. but further work is required to assess how mitotic defects contribute to the clinical features exhibited by patients lacking DIAPH1.

In conclusion, this chapter is important for showing how DIAPH1 functions in multiple genome stability maintenance pathways beyond DNA repair, providing further potential mechanistic insight to explain why the patient cohort have such severe clinical features consistent with underlying genome stability. However, it is not yet clear whether the role for DIAPH1 in DNA replication and mitosis is solely dependent on γ-actin. Nonetheless, these preliminary findings provide an exciting indication that not only does loss of DIAPH1 give rise to a novel DSB repair disorder in humans but more broadly a novel replication and a mitotic disorder also. Characterisation of the precise roles of DIAPH1 in each of these pathways is required to elucidate how DIAPH1 functions in multiple genome stability pathways.

Chapter 7: Discussion

7.0 Discussion

7.1 Introduction

Much of what we know about cellular function has come from studying human disease. Examining the clinical and cellular deficits that arise when an individual has a gene mutation, affecting protein expression and/or protein function, has helped piece together our understanding of cellular pathways and how they underpin human health and wellbeing. More often than not, the clinical features of a genetic disease are directly related to an underlying cellular inability to carry out normal functions, impacting not only single cells but how they work within a tissues and organ system; thus having detrimental effects on overall health. Cellular genome stability maintenance pathways, encompassing DNA repair, DNA replication and mitosis, are extremely important to ensure faithful transmission of genetic information from generation to generation (Wang and Lindahl, 2016). Without genome stability being maintained correctly, the consequences are devastating, ranging from severe and life limiting diseases to cell death and tumour development. Diseases associated with an underlying inability to maintain genome stability highlight this very clearly. Individuals with pathogenic variants in genes that have a role in one or more of these genome stability pathways are severely impacted.

A host of clinical symptoms are associated with underlying genome instability including neurodevelopmental defects, skeletal and facial abnormalities, immunodeficiencies and cancer predisposition; demonstrating how maintaining genome integrity is critical

in multiple organ systems during development and beyond. Well characterised genome instability disorders including Nijmegen Breakage Syndrome (NBS) and Warsaw Breakage Syndrome (WABS). NBS and WABS share overlapping clinical features, such as microcephaly and short stature, representing their shared functions in genome maintenance pathways. However, both these syndromes also have distinct features, for example hearing loss is unique to WABS, which suggest that the encoded gene products have their specialised functions, perhaps outside of the various genome stability pathways.

This study adds to our understanding of important regulators of genome stability and how the actin network functions within DNA repair. The data presented here highlights how detrimental the loss of a functioning actin network is on individual cells and their ability to repair DNA double strand breaks (DSBs), providing an explanation for why patients with homozygous loss of DIAPH1 have severe disease, affecting neurodevelopment, immune function, the visual system and skeletal development. Furthermore, it provides an understanding for why these patient's clinical features heavily overlap with known syndromes like NBS, as the genes function within the same pathways. Moreover, studying BWCFF syndrome patients with *de novo* mutations in *ACTB* and *ACTG1* and patients with pathogenic variants in *ARPC1B, ARPC4* and *ARPC5* has uncovered the specific actin paralog required during DSB repair and shed light on how DIAPH1, γ-actin and the ARP2/3 complex regulate this process. One consistent clinical feature of DIAPH1 patients, and some of the ACTB and ACTG1 patients, is seizures. Whilst seizures is not a typical feature of a genome stability disorder, this deficit may be explained by defects in the cytoplasmic roles of actin and

DIAPH1, distinct from their role in DNA repair, whereby loss of a functional actin network (either through DIAPH1 loss or loss of normal actin function) has an impact on intracellular trafficking of neurotransmitters, neurotransmitter reuptake and release into synapses. Whilst this feature is not indicative of an issue with DNA repair, it highlights how critical these proteins are for multiple cellular functions beyond those in the nucleus. Regardless of the extensive clinical features displayed by patients, this study has provided the underlying mechanism of a novel DSB repair disorder and has deepened our understanding of how actin functions in DNA repair, combining data from five genes that function within the same pathway. This provides an exciting avenue for further study for additional novel DNA repair deficiency syndromes with important clinical implications.

7.2 The actin network and genome stability

Actin has long been known as one of the most highly conserved and abundant proteins in eukaryotic cells. Actin has roles in a host of fundamental cellular functions, and is a key component of the cytoskeleton with roles in maintaining cell structure, motility, mitosis, cellular signalling and intracellular trafficking (Dominguez and Holmes, 2011). Many historic studies detected actin structures in the nucleus but only recently has it become more clear that actin has precise and regulated functions expanding beyond maintaining nuclear structure, including DNA repair and genome stability maintenance (Lane, 1969; Kelpsch and Tootle, 2018; Caridi *et al.*, 2019; Wollscheid and Ulrich, 2023). Despite this, very little is known about how actin regulates DNA repair. To this end, this study provides a novel perspective on where the actin network functions and

the detrimental impact to human health when this becomes dysregulated. Previously, Cobb et al. showed that actin is required to serve as a scaffold platform following DNA damage, but data presented in Chapter 3-5 provide evidence that actin and actin nucleating factors function directly at sites of DSBs, interacting with DNA repair factors to promote efficient repair. The proposed mechanism of this study is that the actin nucleating factor, DIAPH1, may be required to facilitate localisation of the MRN complex to specific DSB sites and stabilise it at DSB sites. DIAPH1 does this by nucleating linear branches of γ-actin to bring the repair factors where they are required. DIAPH1 co-localises with the MRN complex, showing that the actin network functions closely with DNA repair proteins to facilitate their localisation and function. In the absence of DIAPH1, not only is MRN complex relocalisation affected, but DNA end resection, and recruitment of factors throughout the HR process, as RPA2, BRCA1 to RAD51 in the later stages, are also affected. This is an important finding as the role of DIAPH1 in the initial stages has a knock-on effect throughout the pathway, compromising efficient HR. This defect equates to impacting entire organ systems, giving rise to a multisystemic human syndrome. The ARP2/3 complex fits into this model by being required to nucleate branches of γ-actin.

Together, these factors nucleate both linear and branched chain actin filaments to aid the localisation of repair factors around the nucleus. Given that actin is required for cellular trafficking and transport in the cytoplasm, this proposed model fits into actins known cytoplasmic role as a cellular trafficking protein. In the nucleus, this study proposes that actin is also required as an intercellular trafficking network to promote movement of specific repair factors to ensure DNA damage is repaired in a precise

and timely manner (Figure 7.1A). Further to this, the findings of this study fit into the already existing field of actin and DNA repair as the actin filaments are required for clustering of DSBs, aiding in bringing both DSBs in euchromatin and DNA repair factors together (Figure 7.1B) (Caridi *et al.,* 2018). DIAPH1 and the ARP2/3 complex facilitate this process through providing a carefully coordinated network of filaments to cluster DSBs (Figure 7.1C) (Schrank *et al.*, 2018). Furthermore, this model fits with previous findings that actin is required to relocalise heterochromatic DSBs away from repetitive sequences to the nuclear periphery, where other repair factors have also been implicated including the SMC5/6 complex and myosins I and V (Caridi *et al.*, 2018). Myosin VI, the only myosin that moves 'backwards' along actin filaments, was recently shown to function in the replication stress response, so again, our model fits with this data that many actin-related proteins are required to contribute to genome stability as a collective nuclear trafficking system (Shi *et al.*, 2023).

In keeping with this, Chapter 4 also showed that DIAPH1 may also interact with later HR proteins including RAD51, suggesting that actin may also facilitate localisation of other repair factors, not just early factors that initiate DNA repair, such as the MRN complex. Once again, this is in keeping with actin's role as an intercellular trafficking network, that all repair factors must be actively aided in getting to sites of damage in a coordinated manner. This model provides an explanation for why patients lacking DIAPH1, being the key nucleator in facilitating linear actin polymerisation, are so severely affected by DIAPH1 loss. The underlying defect is that DNA DSBs cannot be repaired due to a failing of the actin network to localise DNA repair factors to DSB sites. It is likely that other DNA repair and nuclear functions are also affected by this but as

DSBs are the most toxic to cells, the clinical deficits are most severe and could be masking a defect in other repair pathways also. Alternatively, other nucleating factors play a dominant role over DIAPH1 in alternative DNA repair pathways. In the case of DSB repair, it seems DIAPH1 is required, but different nucleating factors may be operating in other nuclear contexts, for example, DIAPH2 has been linked with short stature and primary ovarian failure in humans. Based on this, it could be speculated that DIAPH2 functions in specific DNA repair processes, such as during meiotic recombination, where it performs a similar nucleating role to DIAPH1 (Bione *et al.*, 1998; Genesio *et al.*, 2015; Qin *et al.*, 2015). DIAPH3 may also function in specific cellular contexts; whilst there are no reported cases of humans with variants in *DIAPH3* with clinical symptoms suggestive of genome instability, mouse models of Diaph3$^{-/-}$ KO have microcephaly (Damiani *et al.*, 2016). This could mean DIAPH3 is also required for maintaining genome stability in humans too, but its role is distinct from DIAPH1. Both DIAPH1 and γ-actin and DIAPH3 and β-actin perform distinct and paired roles in mitosis. The same could also be said for their roles in DNA repair and perhaps DNA replication too (Chen *et al.*, 2021). This notion could then explain why clinical features of BWCFF syndrome arising from either *ACTB* and *ACTG1* mutations in patients overlap not only with each other but *DIAPH1* mutations, and genome stability disorders overall. Both genes could be performing specific roles in all genome stability maintenance pathways, where a highly regulated actin network is required to relocalise proteins to sites of DNA repair and active or stressed replication forks. Further to this, this could provide some explanation for the extensive clinical heterogeneity of BWCFF syndrome patients, whereby specific mutations impact actin's ability to function in certain pathways and not others.

One of the most interesting findings that emerged from this study was that γ-actin was the specific actin required for HR function. The near identical sequence of γ-actin and β-actin meant this was surprising, particularly because there were no real differential features between patients with *ACTB* and *ACTG1* mutations. Nonetheless, a very clear cellular DSB repair defect in the absence of normal γ-actin function emerged. It is important to note that the *de novo* mutations in *ACTB* or *ACTG1* can act in either a dominant or haploinsufficient manner, which can have differential effects on protein stability and function, making clinical features difficult to predict. What the clinical features of these patients may tell us is that whilst β-actin does not have an essential function in DSB repair, it could be functioning in other genome stability and DNA repair pathways where γ-actin is less important. In keeping with this idea, actin has documented roles in NHEJ, SSA, and the replication stress response (Andrin *et al.*, 2012; T. Wang *et al.*, 2021; Han *et al.*, 2022; Nieminuszczy *et al.*, 2023; Palumbieri *et al.*, 2023). Many of these studies did not specify which isoform of actin was being studied, which further strengthens the model being proposed by this study: specific actin networks generated by different actin nucleators and alternative actin paralogs aid the recruitment of individual repair factors to sites of DNA breaks or damaged replication forks. Notably, NHEJ is the dominant repair mechanism utilised in the developing immune system to repair DSBs generated during V(D)J recombination (Woodbine, Gennery and Jeggo, 2014). Patients with DIAPH1 mutations and either *ARPC1B, ARPC4* or *ARPC5* mutations exhibit immunodeficiency of varying severity, so it could be speculated they may also have a NHEJ defect but that is restricted to certain cell types or specific processes. Regardless, at least in the context of HR, there

is evidence that this is solely dependent on DIAPH1 and γ-actin. Thus, whilst NHEJ was not investigated in this study, it is likely that actin and its nucleating factors could have a similar or opposing roles in NHEJ, SSA, other DNA repair pathways and replication stress response, where proteins need to be localised to a specific site. This may be regulated specifically by one actin paralog over another, but further study is needed to clarify this. Preliminary data from Chapter 6, suggests DIAPH1 plays a key role in the response to replication stress, fitting with data already supporting a role for actin in replication stress, but whether this is also dependent on either one or both of γ-actin, and β-actin needs to be investigated further.

Moreover, the two actin genes could compensate for each other in certain nuclear contexts and not others. Where this has been proven to be the case already is during development of the auditory system in mice. During auditory development, the two actin paralogs can compensate for the loss of the other. Replacing *Actb*$^{-/-}$ KO with *Actg1* had no real effect on auditory development that is typical of *Actb*$^{-/-}$ KO models (Perrin, Sonnemann and Ervasti, 2010; Patrinostro *et al.*, 2018). Interestingly, this was not the case in the post-development functions and distinct patterns of *Actb*-dependent hearing loss developed, suggesting Actg1 could not compensate in this specific, post-development context (Patrinostro *et al.*, 2018). As already alluded to, actin interacts with thousands of proteins, and performs many functions, so it will be extremely difficult to dissect the precise functions of γ-actin and β-actin in genome stability maintenance pathways. Despite this, this study provides pivotal data showing that in HR, γ-actin is specifically required and *ACTG1* is a novel DSB repair gene in humans. *ACTB* may also be a DSB repair gene, as suggested by some of the clinical features exhibited by

patients. However, whilst β-actin is not a gene required for HR, it may play a more critical role in NHEJ or during mitosis to maintain genome stability.

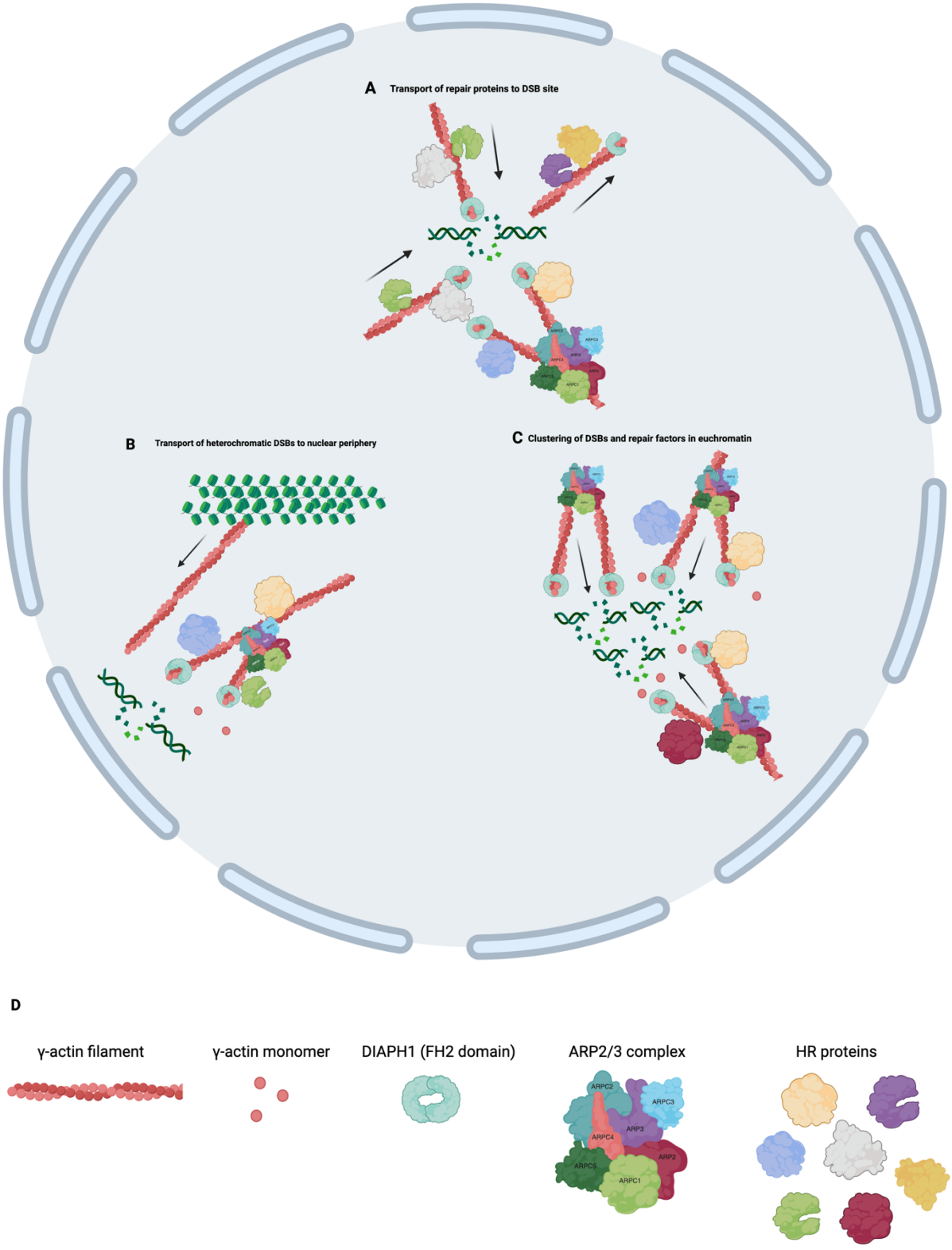


Figure 7.1 – Schematic diagram of the working model of actin's role in DSB repair proposed by this study – A - *This study proposes that γ-actin and actin nucleating factors, DIAPH1 and the ARP2/3 complex are required as a nuclear trafficking network to transport HR proteins to and from sites of DSBs in a timely and coordinated fashion.* ***B*** *– the actin trafficking network is also required to relocalise heterochromatic DSBs to the nuclear periphery away from repetitive sequences.* ***C*** *– The γ-actin network is required to cluster DSBs together in euchromatin.* ***D*** *– Representative key for factors depicted in (A-C). Created with Biorender.com.*

7.3 The future applications of this study

The identification of *DIAPH1* as a novel DSB repair gene has many clinical and future implications. This study demonstrates that *DIAPH1* may function as a tumour suppressor gene (TSG) as loss of DIAPH1 gives rise to genome instability. Actin and DIAPH1 have been implicated in tumour development by many groups, but this is the first time that DIAPH1 has been directly linked to a genome stability function to explain a human syndrome (Yang and Lin, 2018; Izdebska *et al.*, 2020; Miao *et al.*, 2021; Suresh and Diaz, 2021; Yang *et al.*, 2021; Zhang *et al.*, 2022). It is reasonable that the actin network becomes dysregulated in the cytoplasm to facilitate invasion and metastasis given actin is required for filopodia and lamellipodia formation and cell motility (Arjonen, Kaukonen and Ivaska, 2011). However, dysregulation of the actin network in DNA repair may also contribute to tumour development. Whilst only two individuals in our DIAPH1 patient cohort have developed lymphoid tumours, the underlying mechanism for the tumour development is unclear. Whether loss of DIAPH1 and actin's role in genome stability facilitates the tumourigenic process is not known. However, patients with homozygous mutations in *DIAPH1* should be monitored closely for tumour development and clinicians treating patients should consider increasing the frequency of surveillance. Additionally, any oncological management for these patients will now have to consider that the underlying DSB repair defect may cause possible adverse reactions to ionising radiation and specific chemotherapeutic agents. Interestingly, the fact DIAPH1 loss gives rise to a HR defect potentially means that these patients may benefit from PARP inhibitor treatment; but this needs to be investigated thoroughly *in vivo* first. Ideally this could be done using a clonogenic

survival assays to assess cellular survival after PARP inhibitor treatment. The same principles may also apply to patients with *ACTG1* mutations and on the whole, mutations in genes that function in the actin network, including the ARP2/3 complex components. These individuals may also carry an increased risk of tumour development if genome stability is compromised. Extending beyond this, patients with tumours that have acquired a loss or gain of function or overexpression of γ-actin, DIAPH1 or ARP2/3 complex components may also be suitable candidates for PARP inhibitor treatment based on their role in regulating HR. Key future work should include understanding how gain of function variants, and overexpression of these factors impacts genome stability, providing an exciting avenue for study with many clinical applications in oncology and understanding how the actin network could be exploited therapeutically either with PARP inhibitors or specific inhibitors.

On a broader level, many unanswered questions remain about whether multiple pathways are functioning together to enable the actin network to function in DSB repair and genome stability. It is possible that actin and actin related proteins are operating on multiple levels, including relocalisation and stability of proteins at specific sites as well as the wider nuclear matrix and nucleoskeletal organisation, chromatin dynamics and nuclear import/export. This system could exhibit separation of function, with specific mutations having a differing effect on nuclear actin function, with a specific mutation impacting multiple levels of actin nuclear function, from wider nuclear organisation to its ability to interact with a specific actin nucleator and/or DNA repair protein. Elucidating whether this may be the case, could be addressed with further work on characterising the specific impacts of each mutation in the actin patient cohort.

Additionally, future would need to clarify in more detail which DNA repair proteins actin and DIAPH1 interact with and in what contexts are such interactions required. Data presented in this study may suggest a role for DIAPH1 at the beginning of, and during later stages of HR. However, the data does not provide clarity on what the precise function DIAPH1 is performing, what is regulating this interaction, what it is dependent on and whether this is a direct or indirect mechanism. Further study is needed to understand this and address how the actin network regulates DNA repair and genome stability and whether this is multifactorial process.

7.4 Final conclusion

In conclusion, this study provides a detailed mechanistic explanation for the clinical deficits exhibited by patients with homozygous loss of *DIAPH1* and why they overlap with the known DSB repair deficiency disorder, NBS. Loss of DIAPH1 results in a DSB repair defect, specifically due to a cellular inability to carry out HR efficiently. DIAPH1, γ-actin and the ARP2/3 complex function within HR to localise early and late repair factors to DSB sites, thus acting as a nuclear trafficking system. Preliminary data also supports this may be the case in wider genome stability pathways including DNA replication and mitosis. Overall, the actin network is a key component in regulating genome stability and loss of this network manifests clinically with features that are typically associated with genome instability disorders like NBS and WABS. Future work should focus on dissecting which actin isoforms and nucleating factors are required in specific contexts in genome stability, to provide a further mechanistic explanation for

the BWCFF syndrome clinical symptoms and increase our understanding of how the actin network regulates genome stability and DNA repair.

Chapter 8: References

8.0 References

Ackerson, S.M. *et al.* (2021) 'To Join or Not to Join: Decision Points Along the Pathway to Double-Strand Break Repair vs. Chromosome End Protection', *Frontiers in Cell and Developmental Biology*, 9.

Ahn, J.Y. *et al.* (2000) 'Threonine 68 phosphorylation by ataxia telangiectasia mutated is required for efficient activation of Chk2 in response to ionizing radiation', *Cancer Research*, 60(21), pp. 5934–5936.

Allerston, C.K. *et al.* (2015) 'The structures of the SNM1A and SNM1B/Apollo nuclease domains reveal a potential basis for their distinct DNA processing activities', *Nucleic Acids Research*, 43(22), pp. 11047–11060.

Al-Maawali, A. *et al.* (2016) 'Novel loss-of-function variants in DIAPH1 associated with syndromic microcephaly, blindness, and early onset seizures', *American Journal of Medical Genetics. Part A*, 170A(2), pp. 435–440.

Anand, R. *et al.* (2016) 'Phosphorylated CtIP Functions as a Co-factor of the MRE11-RAD50-NBS1 Endonuclease in DNA End Resection', *Molecular Cell*, 64(5), pp. 940–950.

Andrin, C. *et al.* (2012) 'A requirement for polymerized actin in DNA double-strand break repair', *Nucleus*, 3(4), pp. 384–395.

Antala, S. *et al.* (2021) 'ARPC1B Mutation Manifesting as Recurrent Hematemesis With Metaplasia', *JPGN Reports*, 2(3), p. e095.

Arjonen, A., Kaukonen, R. and Ivaska, J. (2011) 'Filopodia and adhesion in cancer cell motility', *Cell Adhesion & Migration*, 5(5), pp. 421–430.

Aymard, F. *et al.* (2014) 'Transcriptionally active chromatin recruits homologous recombination at DNA double strand breaks', *Nature structural & molecular biology*, 21(4), pp. 366–374.

Baarlink, C. *et al.* (2017) 'A transient pool of nuclear F-actin at mitotic exit controls chromatin organization', *Nature Cell Biology*, 19(12), pp. 1389–1399.

Baarlink, C. and Grosse, R. (2014) 'Formin' actin in the nucleus', *Nucleus*, 5(1), pp. 15–20.

Baarlink, C., Wang, H. and Grosse, R. (2013) 'Nuclear Actin Network Assembly by Formins Regulates the SRF Coactivator MAL', *Science*, 340(6134), pp. 864–867.

Bass, T.E. *et al.* (2016) 'ETAA1 acts at stalled replication forks to maintain genome integrity', *Nature Cell Biology*, 18(11), pp. 1185–1195.

Belin, B.J. *et al.* (2013) 'Visualization of actin filaments and monomers in somatic cell nuclei', *Molecular Biology of the Cell*, 24(7), pp. 982–994.

Belin, B.J., Lee, T. and Mullins, R.D. (2015) 'DNA damage induces nuclear actin filament assembly by Formin-2 and Spire-1/2 that promotes efficient DNA repair', *eLife*. Edited by P. Lappalainen, 4, p. e07735.

Belin, B.J., Lee, T. and Mullins, R.D. (no date) 'DNA damage induces nuclear actin filament assembly by Formin-2 and Spire-1/2 that promotes efficient DNA repair', *eLife*, 4.

Bennardo, N. *et al.* (2008) 'Alternative-NHEJ is a mechanistically distinct pathway of mammalian chromosome break repair', *PLoS genetics*, 4(6), p. e1000110.

Bhargava, R., Onyango, D.O. and Stark, J.M. (2016) 'Regulation of Single Strand Annealing and its role in genome maintenance', *Trends in genetics : TIG*, 32(9), pp. 566–575.

Bhattacharya, R. *et al.* (2023) 'AGE-RAGE axis culminates into multiple pathogenic processes: a central road to neurodegeneration', *Frontiers in Molecular Neuroscience*, 16.

Bian, L. *et al.* (2019a) 'MRE11-RAD50-NBS1 complex alterations and DNA damage response: Implications for cancer treatment', *Molecular Cancer*, 18.

Bione, S. *et al.* (1998) 'A human homologue of the Drosophila melanogaster diaphanous gene is disrupted in a patient with premature ovarian failure: evidence for conserved function in oogenesis and implications for human sterility.', *American Journal of Human Genetics*, 62(3), pp. 533–541.

Blackford, A.N. and Jackson, S.P. (2017) 'ATM, ATR, and DNA-PK: The Trinity at the Heart of the DNA Damage Response', *Molecular Cell*, 66(6), pp. 801–817.

Blundred, R.M. and Stewart, G.S. (2011) 'DNA double-strand break repair, immunodeficiency and the RIDDLE syndrome', *Expert Review of Clinical Immunology*, 7(2), pp. 169–185.

Boder, E. and Sedgwick, R.P. (1958) 'Ataxia-telangiectasia; a familial syndrome of progressive cerebellar ataxia, oculocutaneous telangiectasia and frequent pulmonary infection', *Pediatrics*, 21(4), pp. 526–554.

Bohgaki, T., Bohgaki, M. and Hakem, R. (2010) 'DNA double-strand break signaling and human disorders', *Genome Integrity*, 1, p. 15.

Bouma, G., Burns, S.O. and Thrasher, A.J. (2009) 'Wiskott–Aldrich Syndrome: Immunodeficiency resulting from defective cell migration and impaired immunostimulatory activation', *Immunobiology*, 214(9), pp. 778–790.

Bouwman, P. *et al.* (2010) '53BP1 loss rescues BRCA1 deficiency and is associated with triple-negative and BRCA-mutated breast cancers', *Nature Structural & Molecular Biology*, 17(6), pp. 688–695.

Breitsprecher, D. and Goode, B.L. (2013) 'Formins at a glance', *Journal of Cell Science*, 126(1), pp. 1–7.

Brigida, I. *et al.* (2018) 'T-cell defects in patients with ARPC1B germline mutations account for combined immunodeficiency', *Blood*, 132(22), pp. 2362–2374.

Brinkley, B.R., Stubblefield, E. and Hsu, T.C. (1967) 'The effects of Colcemid inhibition and reversal on the fine structure of the mitotic apparatus of Chinese hamster cells *in vitro*', *Journal of Ultrastructure Research*, 19(1), pp. 1–18.

Brown, E.J. and Baltimore, D. (2000) 'ATR disruption leads to chromosomal fragmentation and early embryonic lethality', *Genes & Development*, 14(4), pp. 397–402.

Buchbinder, D., Nugent, D.J. and Fillipovich, A.H. (2014) 'Wiskott–Aldrich syndrome: diagnosis, current management, and emerging treatments', *The Application of Clinical Genetics*, 7, pp. 55–66.

Bunting, S.F. *et al.* (2010) '53BP1 inhibits homologous recombination in Brca1-deficient cells by blocking resection of DNA breaks', *Cell*, 141(2), pp. 243–254.

Burg, M. van der *et al.* (2009) 'A *DNA-PKcs* mutation in a radiosensitive $T^{-}B^{-}$ SCID patient inhibits Artemis activation and nonhomologous end-joining', *The Journal of Clinical Investigation*, 119(1), pp. 91–98.

Cabanillas, R. *et al.* (2018) 'Comprehensive genomic diagnosis of non-syndromic and syndromic hereditary hearing loss in Spanish patients', *BMC medical genomics*, 11(1), p. 58.

Cai, E.D. *et al.* (2017) 'Postzygotic Mutations in Beta-Actin Are Associated with Becker's Nevus and Becker's Nevus Syndrome', *Journal of Investigative Dermatology*, 137(8), pp. 1795–1798.

Campellone, K.G. and Welch, M.D. (2010) 'A nucleator arms race: cellular control of actin assembly', *Nature Reviews. Molecular Cell Biology*, 11(4), pp. 237–251.

Caridi, C.P. *et al.* (2018) 'Nuclear F-actin and myosins drive relocalization of heterochromatic breaks', *Nature*, 559(7712), pp. 54–60.

Caridi, C.P. *et al.* (2019) 'Nuclear actin filaments in DNA repair dynamics', *Nature Cell Biology*, 21(9), pp. 1068–1077.

Ceppi, I. *et al.* (2020) 'CtIP promotes the motor activity of DNA2 to accelerate long-range DNA end resection', *Proceedings of the National Academy of Sciences*, 117(16), pp. 8859–8869.

Chakraborty, S. *et al.* (2018) 'SMARCAD1 Phosphorylation and Ubiquitination Are Required for Resection during DNA Double-Strand Break Repair', *iScience*, 2, pp. 123–135.

Chang, H.H.Y. *et al.* (2017) 'Non-homologous DNA end joining and alternative pathways to double-strand break repair', *Nature Reviews Molecular Cell Biology*, 18(8), pp. 495–506.

Chang, H.H.Y. and Lieber, M.R. (2016) 'Structure-Specific nuclease activities of Artemis and the Artemis: DNA-PKcs complex', *Nucleic Acids Research*, 44(11), pp. 4991–4997.

Chatterjee, N. and Walker, G.C. (2017) 'Mechanisms of DNA damage, repair and mutagenesis', *Environmental and molecular mutagenesis*, 58(5), pp. 235–263.

Chavakis, T., Bierhaus, A. and Nawroth, P.P. (2004) 'RAGE (receptor for advanced glycation end products): a central player in the inflammatory response', *Microbes and Infection*, 6(13), pp. 1219–1225.

Chen, A. *et al.* (2017) 'Cytokinesis requires localized β-actin filament production by an actin isoform specific nucleator', *Nature Communications*, 8(1), p. 1530.

Chen, A. *et al.* (2020) 'The scaffold-protein IQGAP1 enhances and spatially restricts the actin-nucleating activity of Diaphanous-related formin 1 (DIAPH1)', *Journal of Biological Chemistry*, 295(10), pp. 3134–3147.

Chen, A. *et al.* (2021) 'Inhibition of polar actin assembly by astral microtubules is required for cytokinesis', *Nature Communications*, 12(1), p. 2409.

Chen, L. *et al.* (2003) 'WRN, the protein deficient in Werner syndrome, plays a critical structural role in optimizing DNA repair', *Aging Cell*, 2(4), pp. 191–199.

Chen, L. *et al.* (2008) 'Cell cycle-dependent complex formation of BRCA1.CtIP.MRN is important for DNA double-strand break repair', *The Journal of Biological Chemistry*, 283(12), pp. 7713–7720.

Chiereghin, C. *et al.* (2022) 'Role of Cytoskeletal Diaphanous-Related Formins in Hearing Loss', *Cells*, 11(11), p. 1726.

Chiriaco, M. *et al.* (2022) 'Radiosensitivity in patients affected by ARPC1B deficiency: a new disease trait?', *Frontiers in Immunology*, 13.

Chiruvella, K.K., Liang, Z. and Wilson, T.E. (2013) 'Repair of Double-Strand Breaks by End Joining', *Cold Spring Harbor Perspectives in Biology*, 5(5), p. a012757.

Cho, N.W., Lampson, M.A. and Greenberg, R.A. (2017) 'In vivo imaging of DNA double-strand break induced telomere mobility during alternative lengthening of telomeres', *Methods (San Diego, Calif.)*, 114, pp. 54–59.

Clapperton, J.A. *et al.* (2004) 'Structure and mechanism of BRCA1 BRCT domain recognition of phosphorylated BACH1 with implications for cancer', *Nature Structural & Molecular Biology*, 11(6), pp. 512–518.

Cleaver, J.E. (1968) 'Defective repair replication of DNA in xeroderma pigmentosum', *Nature*, 218(5142), pp. 652–656.

Coleman, K.E. *et al.* (2022) 'USP1-trapping lesions as a source of DNA replication stress and genomic instability', *Nature Communications*, 13(1), p. 1740.

Conrad, S., Künzel, J. and Löbrich, M. (2011) 'Sister chromatid exchanges occur in G2-irradiated cells', *Cell Cycle*, 10(2), pp. 222–228.

Cooper, G.M. (2000) ‘Structure and Organization of Actin Filaments’, *The Cell: A Molecular Approach. 2nd edition* [Preprint].

Copeland, S.J. *et al.* (2007) ‘The Diaphanous Inhibitory Domain/Diaphanous Autoregulatory Domain Interaction Is Able to Mediate Heterodimerization between mDia1 and mDia2 *’, *Journal of Biological Chemistry*, 282(41), pp. 30120–30130.

Cortez, D. *et al.* (1999) ‘Requirement of ATM-dependent phosphorylation of brca1 in the DNA damage response to double-strand breaks’, *Science (New York, N.Y.)*, 286(5442), pp. 1162–1166.

Craxton, A. *et al.* (2015) ‘XLS (c9orf142) is a new component of mammalian DNA double-stranded break repair’, *Cell Death and Differentiation*, 22(6), pp. 890–897.

Cruz-García, A., López-Saavedra, A. and Huertas, P. (2014) ‘BRCA1 Accelerates CtIP-Mediated DNA-End Resection’, *Cell Reports*, 9(2), pp. 451–459.

Cuvertino, S. *et al.* (2017) ‘ACTB Loss-of-Function Mutations Result in a Pleiotropic Developmental Disorder’, *The American Journal of Human Genetics*, 101(6), pp. 1021–1033.

Daley, J.M. *et al.* (2014) ‘Regulation of DNA Pairing in Homologous Recombination’, *Cold Spring Harbor Perspectives in Biology*, 6(11), p. a017954.

Daley, J.M. and Sung, P. (2014) ‘53BP1, BRCA1, and the Choice between Recombination and End Joining at DNA Double-Strand Breaks’, *Molecular and Cellular Biology*, 34(8), pp. 1380–1388.

Damiani, D. *et al.* (2016) ‘Lack of Diaph3 relaxes the spindle checkpoint causing the loss of neural progenitors’, *Nature Communications*, 7, p. 13509.

Dewar, J.M., Budzowska, M. and Walter, J.C. (2015) ‘The mechanism of DNA replication termination in vertebrates’, *Nature*, 525(7569), pp. 345–350.

Di Donato, N. *et al.* (2014) ‘Severe forms of Baraitser-Winter syndrome are caused by ACTB mutations rather than ACTG1 mutations’, *European journal of human genetics: EJHG*, 22(2), pp. 179–183.

Dialynas, G., Delabaere, L. and Chiolo, I. (2019) ‘Arp2/3 and Unc45 maintain heterochromatin stability in Drosophila polytene chromosomes’, *Experimental Biology and Medicine (Maywood, N.J.)*, 244(15), pp. 1362–1371.

Ding, Q. *et al.* (2003) ‘Autophosphorylation of the Catalytic Subunit of the DNA-Dependent Protein Kinase Is Required for Efficient End Processing during DNA Double-Strand Break Repair’, *Molecular and Cellular Biology*, 23(16), pp. 5836–5848.

Dominguez, R. (2009) ‘Actin filament nucleation and elongation factors – structure-function relationships’, *Critical reviews in biochemistry and molecular biology*, 44(6), pp. 351–366.

Dominguez, R. and Holmes, K.C. (2011) ‘Actin Structure and Function’, *Annual review of biophysics*, 40, pp. 169–186.

Dong, B. *et al.* (2013) 'Mammalian Diaphanous-Related Formin 1 Regulates GSK3β-Dependent Microtubule Dynamics Required for T Cell Migratory Polarization', *PLOS ONE*, 8(11), p. e80500.

Dos Remedios, C.G. *et al.* (2003) 'Actin Binding Proteins: Regulation of Cytoskeletal Microfilaments', *Physiological Reviews*, 83(2), pp. 433–473.

Dueva, R. and Iliakis, G. (2020) 'Replication protein A: a multifunctional protein with roles in DNA replication, repair and beyond', *NAR Cancer*, 2(3).

Dugina, V. *et al.* (2009) 'Beta and gamma-cytoplasmic actins display distinct distribution and functional diversity', *Journal of Cell Science*, 122(Pt 16), pp. 2980–2988.

Dugina, V.B., Shagieva, G.S. and Kopnin, P.B. (2022) 'Cytoplasmic Beta and Gamma Actin Isoforms Reorganization and Regulation in Tumor Cells in Culture and Tissue', *Frontiers in Pharmacology*, 13.

den Dunnen, J.T. *et al.* (2016) 'HGVS Recommendations for the Description of Sequence Variants: 2016 Update', *Human Mutation*, 37(6), pp. 564–569.

Dupré, A., Boyer-Chatenet, L. and Gautier, J. (2006) 'Two-step activation of ATM by DNA and the Mre11-Rad50-Nbs1 complex', *Nature Structural & Molecular Biology*, 13(5), pp. 451–457.

Durocher, D. *et al.* (1999) 'The FHA domain is a modular phosphopeptide recognition motif', *Molecular Cell*, 4(3), pp. 387–394.

Eisenmann, K.M. *et al.* (2007) 'T Cell Responses in Mammalian Diaphanous-related Formin mDia1 Knock-out Mice *', *Journal of Biological Chemistry*, 282(34), pp. 25152–25158.

Elbakry, A. and Löbrich, M. (2021) 'Homologous Recombination Subpathways: A Tangle to Resolve', *Frontiers in Genetics*, 12.

Ensminger, M. and Löbrich, M. (2020) 'One end to rule them all: Non-homologous end-joining and homologous recombination at DNA double-strand breaks', *The British Journal of Radiology*, 93(1115), p. 20191054.

Ercan-Sencicek, A.G. *et al.* (2015) 'Homozygous loss of DIAPH1 is a novel cause of microcephaly in humans', *European journal of human genetics: EJHG*, 23(2), pp. 165–172.

Falck, J., Coates, J. and Jackson, S.P. (2005) 'Conserved modes of recruitment of ATM, ATR and DNA-PKcs to sites of DNA damage', *Nature*, 434(7033), pp. 605–611.

Fantini, C. *et al.* (1998) 'Sister chromatid exchanges and DNA topoisomerase II inhibitors: effect of low concentrations of etoposide (VP-16) in ataxia telangiectasia lymphoblastoid cell lines', *Mutation Research/Genetic Toxicology and Environmental Mutagenesis*, 412(1), pp. 1–7.

Feng, S. *et al.* (2016) 'Ewing Tumor-associated Antigen 1 Interacts with Replication Protein A to Promote Restart of Stalled Replication Forks', *The Journal of Biological Chemistry*, 291(42), pp. 21956–21962.

Foo, T.K. *et al.* (2021) 'ATR/ATM-mediated phosphorylation of BRCA1 T1394 promotes homologous recombinational repair and G2/M checkpoint maintenance', *Cancer research*, 81(18), pp. 4676–4684.

Fournier, B. *et al.* (2022) 'Inborn errors of immunity caused by defects in the DNA damage response pathways: Importance of minimizing treatment-related genotoxicity', *Pediatric Allergy and Immunology*, 33(6), p. e13820.

Ganaha, A. *et al.* (2017) 'Progressive macrothrombocytopenia and hearing loss in a large family with DIAPH1 related disease', *American Journal of Medical Genetics. Part A*, 173(10), pp. 2826–2830.

Gao, Y. *et al.* (2000) 'Interplay of p53 and DNA-repair protein XRCC4 in tumorigenesis, genomic stability and development', *Nature*, 404(6780), pp. 897–900.

Garcia, V. *et al.* (2011) 'Bidirectional resection of DNA double-strand breaks by Mre11 and Exo1', *Nature*, 479(7372), pp. 241–244.

Gell, D. and Jackson, S.P. (1999) 'Mapping of protein-protein interactions within the DNA-dependent protein kinase complex', *Nucleic Acids Research*, 27(17), pp. 3494–3502.

Genesio, R. *et al.* (2015) 'Short stature and primary ovarian insufficiency possibly due to chromosomal position effect in a balanced X;1 translocation', *Molecular Cytogenetics*, 8, p. 50.

Goley, E.D. and Welch, M.D. (2006) 'The ARP2/3 complex: an actin nucleator comes of age', *Nature Reviews. Molecular Cell Biology*, 7(10), pp. 713–726.

Goodarzi, A.A. *et al.* (2006) 'DNA-PK autophosphorylation facilitates Artemis endonuclease activity', *The EMBO journal*, 25(16), pp. 3880–3889.

Goode, B.L. and Eck, M.J. (2007) 'Mechanism and Function of Formins in the Control of Actin Assembly', *Annual Review of Biochemistry*, 76(1), pp. 593–627.

Grand, R.J.A. and Reynolds, J.J. (2018) *DNA Repair and Replication: machanisms and clinical significance*. 1st edn. Garland Science.

Gudimchuk, N.B. and McIntosh, J.R. (2021) 'Regulation of microtubule dynamics, mechanics and function through the growing tip', *Nature Reviews Molecular Cell Biology*, 22(12), pp. 777–795.

Guo, Z. *et al.* (2010) 'ATM activation by oxidative stress', *Science (New York, N.Y.)*, 330(6003), pp. 517–521.

Gupta, C.M., Ambaru, B. and Bajaj, R. (2020) 'Emerging Functions of Actins and Actin Binding Proteins in Trypanosomatids', *Frontiers in Cell and Developmental Biology*, 8, p. 1109.

Haahr, P. *et al.* (2016) 'Activation of the ATR kinase by the RPA-binding protein ETAA1', *Nature Cell Biology*, 18(11), pp. 1196–1207.

Haga, R.B. and Ridley, A.J. (2016) 'Rho GTPases: Regulation and roles in cancer cell biology', *Small GTPases*, 7(4), pp. 207–221.

Hakem, R. (2008) 'DNA-damage repair; the good, the bad, and the ugly', *The EMBO Journal*, 27(4), pp. 589–605.

Han, S.-S. *et al.* (2022) 'WASp modulates RPA function on single-stranded DNA in response to replication stress and DNA damage', *Nature Communications*, 13(1), p. 3743.

Hanawalt, P.C. (2015) 'Historical Perspective on the DNA Damage Response', *DNA repair*, 36, pp. 2–7.

Higgs, H.N. (2005) 'Formin proteins: a domain-based approach', *Trends in Biochemical Sciences*, 30(6), pp. 342–353.

Huang, Y., Zhang, S. and Park, J.-I. (2022) 'Nuclear Actin Dynamics in Gene Expression, DNA Repair, and Cancer', *Results and problems in cell differentiation*, 70, pp. 625–663.

Hudson, B.I. *et al.* (2008) 'Interaction of the RAGE Cytoplasmic Domain with Diaphanous-1 Is Required for Ligand-stimulated Cellular Migration through Activation of Rac1 and Cdc42', *The Journal of Biological Chemistry*, 283(49), pp. 34457–34468.

Iijima, K. *et al.* (2008) 'Dancing on Damaged Chromatin: Functions of ATM and the RAD50/MRE11/NBS1 Complex in Cellular Responses to DNA Damage', *Journal of Radiation Research*, 49(5), pp. 451–464.

Isono, M. *et al.* (2017) 'BRCA1 Directs the Repair Pathway to Homologous Recombination by Promoting 53BP1 Dephosphorylation', *Cell Reports*, 18(2), pp. 520–532.

Izdebska, M. *et al.* (2020) 'Involvement of Actin and Actin-Binding Proteins in Carcinogenesis', *Cells*, 9(10), p. 2245.

Jackson, S.P. and Bartek, J. (2009) 'The DNA-damage response in human biology and disease', *Nature*, 461(7267), pp. 1071–1078.

Jang, S.-M. *et al.* (2020) 'Regulation of cell cycle drivers by Cullin-RING ubiquitin ligases', *Experimental & Molecular Medicine*, 52(10), pp. 1637–1651.

Janssen, E. and Geha, R.S. (2019) 'Primary immunodeficiencies caused by mutations in actin regulatory proteins', *Immunological Reviews*, 287(1), pp. 121–134.

Jean, F., Stuart, A. and Tarailo-Graovac, M. (2020) 'Dissecting the Genetic and Etiological Causes of Primary Microcephaly', *Frontiers in Neurology*, 11.

Jeruzalska, E. and Mazur, A.J. (2023) ‘The Role of non-muscle actin paralogs in cell cycle progression and proliferation’, *European Journal of Cell Biology*, 102(2), p. 151315.

Jiang, H., Panda, S. and Gekara, N.O. (2019) ‘Chapter Eighteen - Comet and micronucleus assays for analyzing DNA damage and genome integrity’, in J. Sohn (ed.) *Methods in Enzymology*. Academic Press (DNA Sensors and Inflammasomes), pp. 299–307.

Justiz Vaillant, A.A. and Qurie, A. (2024) ‘Immunodeficiency’, in *StatPearls*. Treasure Island (FL): StatPearls Publishing.

Kahr, W.H.A. *et al.* (2017) ‘Loss of the Arp2/3 complex component ARPC1B causes platelet abnormalities and predisposes to inflammatory disease’, *Nature Communications*, 8(1), p. 14816.

Kang, T.-H. *et al.* (2016) ‘A novel missense variant in the *DIAPH1* gene in a Korean family with autosomal dominant nonsyndromic hearing loss’, *Genes & Genetic Systems*, 91(5), pp. 289–292.

Kaustio, M. *et al.* (2021) ‘Loss of *DIAPH1* causes SCBMS, combined immunodeficiency, and mitochondrial dysfunction’, *Journal of Allergy and Clinical Immunology*, 148(2), pp. 599–611.

Kelpsch, D.J. and Tootle, T.L. (2018) ‘Nuclear actin: from discovery to function’, *Anatomical record (Hoboken, N.J. : 2007)*, 301(12), pp. 1999–2013.

Kent, T. *et al.* (2015) ‘Mechanism of microhomology-mediated end-joining promoted by human DNA polymerase θ’, *Nature Structural & Molecular Biology*, 22(3), pp. 230–237.

Keszthelyi, A., Minchell, N.E. and Baxter, J. (2016) ‘The Causes and Consequences of Topological Stress during DNA Replication’, *Genes*, 7(12), p. 134.

Kilgas, S., Kiltie, A.E. and Ramadan, K. (2021) ‘Immunofluorescence microscopy-based detection of ssDNA foci by BrdU in mammalian cells’, *STAR Protocols*, 2(4), p. 100978.

Kim, D. *et al.* (2016) ‘mDia1 regulates breast cancer invasion by controlling membrane type 1-matrix metalloproteinase localization’, *Oncotarget*, 7(14), pp. 17829–17843.

Kitagawa, R. *et al.* (2004) ‘Phosphorylation of SMC1 is a critical downstream event in the ATM–NBS1–BRCA1 pathway’, *Genes & Development*, 18(12), pp. 1423–1438.

Kolinjivadi, A.M. *et al.* (2017) ‘Smarcal1-Mediated Fork Reversal Triggers Mre11-Dependent Degradation of Nascent DNA in the Absence of Brca2 and Stable Rad51 Nucleofilaments’, *Molecular Cell*, 67(5), pp. 867-881.e7.

Kramara, J., Osia, B. and Malkova, A. (2018) ‘Break-Induced Replication: The Where, The Why, and The How’, *Trends in genetics: TIG*, 34(7), pp. 518–531.

Kuijpers, T.W. *et al.* (2017) ‘Combined immunodeficiency with severe inflammation and allergy caused by ARPC1B deficiency’, *The Journal of Allergy and Clinical Immunology*, 140(1), pp. 273-277.e10.

Kundishora, A.J. *et al.* (2021) 'DIAPH1 Variants in Non-East Asian Patients With Sporadic Moyamoya Disease', *JAMA neurology*, 78(8), pp. 993–1003.

Labat-de-Hoz, L. and Alonso, M.A. (2021) 'Formins in Human Disease', *Cells*, 10(10), p. 2554.

Laboy Cintron, D. *et al.* (2022) 'A recurrent, de novo pathogenic variant in ARPC4 disrupts actin filament formation and causes microcephaly and speech delay', *HGG advances*, 3(1), p. 100072.

Lamarche, B.J., Orazio, N.I. and Weitzman, M.D. (2010) 'The MRN complex in Double-Strand Break Repair and Telomere Maintenance', *FEBS letters*, 584(17), pp. 3682–3695.

Lambert, S. *et al.* (2010) 'Homologous recombination restarts blocked replication forks at the expense of genome rearrangements by template exchange', *Molecular Cell*, 39(3), pp. 346–359.

Lamm, N. *et al.* (2020) 'Nuclear F-actin counteracts nuclear deformation and promotes fork repair during replication stress', *Nature Cell Biology*, 22(12), pp. 1460–1470.

Lammers, M. *et al.* (2008) 'Specificity of Interactions between mDia Isoforms and Rho Proteins', *The Journal of Biological Chemistry*, 283(50), pp. 35236–35246.

Lane, N.J. (1969) 'Intranuclear fibrillar bodies in actinomycin D-treated oocytes', *The Journal of Cell Biology*, 40(1), pp. 286–291.

Latham, S.L. *et al.* (2018) 'Variants in exons 5 and 6 of ACTB cause syndromic thrombocytopenia', *Nature Communications*, 9(1), p. 4250.

Lau, E.O.-C. *et al.* (2021) 'DIAPH3 deficiency links microtubules to mitotic errors, defective neurogenesis, and brain dysfunction', *eLife*. Edited by J.G. Gleeson and J.A. Cooper, 10, p. e61974.

Lee, J.-H. and Paull, T.T. (2004) 'Direct activation of the ATM protein kinase by the Mre11/Rad50/Nbs1 complex', *Science (New York, N.Y.)*, 304(5667), pp. 93–96.

Lee, J.-H. and Paull, T.T. (2005) 'ATM activation by DNA double-strand breaks through the Mre11-Rad50-Nbs1 complex', *Science (New York, N.Y.)*, 308(5721), pp. 551–554.

Lee, W.T.C. *et al.* (2021) 'Single-molecule imaging reveals replication fork coupled formation of G-quadruplex structures hinders local replication stress signaling', *Nature Communications*, 12(1), p. 2525.

Lempiäinen, H. and Halazonetis, T.D. (2009) 'Emerging common themes in regulation of PIKKs and PI3Ks', *The EMBO journal*, 28(20), pp. 3067–3073.

Leung, G. *et al.* (no date) 'ARPC1B binds WASP to control actin polymerization and curtail tonic signaling in B cells', *JCI Insight*, 6(23), p. e149376.

Li, R. *et al.* (2012) 'A distinct response to endogenous DNA damage in the development of Nbs1-deficient cortical neurons', *Cell Research*, 22(5), pp. 859–872.

Li, X. and Heyer, W.-D. (2008) 'Homologous recombination in DNA repair and DNA damage tolerance', *Cell Research*, 18(1), pp. 99–113.

Li, Z. *et al.* (2014) 'Mammalian diaphanous-related formin 1 is required for motility and invadopodia formation in human U87 glioblastoma cells', *International Journal of Molecular Medicine*, 33(2), pp. 383–391.

Liao, H. *et al.* (1995) 'CENP-F is a protein of the nuclear matrix that assembles onto kinetochores at late G2 and is rapidly degraded after mitosis', *The Journal of Cell Biology*, 130(3), pp. 507–518.

Lieber, M.R. (2010) 'The Mechanism of Double-Strand DNA Break Repair by the Nonhomologous DNA End-Joining Pathway', *Annual Review of Biochemistry*, 79(1), pp. 181–211.

Liu, Q. *et al.* (2000) 'Chk1 is an essential kinase that is regulated by Atr and required for the G(2)/M DNA damage checkpoint', *Genes & Development*, 14(12), pp. 1448–1459.

Liu, S. *et al.* (2012) 'Distinct roles for DNA-PK, ATM and ATR in RPA phosphorylation and checkpoint activation in response to replication stress', *Nucleic Acids Research*, 40(21), pp. 10780–10794.

Liu, T. and Huang, J. (2016) 'DNA End Resection: Facts and Mechanisms', *Genomics, Proteomics & Bioinformatics*, 14(3), pp. 126–130.

Lopez-Girona, A. *et al.* (2001) 'Serine-345 is required for Rad3-dependent phosphorylation and function of checkpoint kinase Chk1 in fission yeast', *Proceedings of the National Academy of Sciences of the United States of America*, 98(20), pp. 11289–11294.

Lovejoy, C.A. and Cortez, D. (2009) 'Common mechanisms of PIKK regulation', *DNA repair*, 8(9), pp. 1004–1008.

Lynch, E.D. *et al.* (1997) 'Nonsyndromic Deafness DFNA1 Associated with Mutation of a Human Homolog of the Drosophila Gene diaphanous', *Science*, 278(5341), pp. 1315–1318.

Magdalou, I. *et al.* (2014) 'The causes of replication stress and their consequences on genome stability and cell fate', *Seminars in Cell & Developmental Biology*, 30, pp. 154–164.

Mahaney, B.L., Meek, K. and Lees-Miller, S.P. (2009) 'Repair of ionizing radiation-induced DNA double-strand breaks by non-homologous end-joining', *The Biochemical Journal*, 417(3), pp. 639–650.

Malek, N. *et al.* (2021) 'The origin of the expressed retrotransposed gene ACTBL2 and its influence on human melanoma cells' motility and focal adhesion formation', *Scientific Reports*, 11(1), p. 3329.

Manke, I.A. *et al.* (2003) 'BRCT repeats as phosphopeptide-binding modules involved in protein targeting', *Science (New York, N.Y.)*, 302(5645), pp. 636–639.

Mankouri, H.W., Ashton, T.M. and Hickson, I.D. (2011) 'Holliday junction-containing DNA structures persist in cells lacking Sgs1 or Top3 following exposure to DNA damage', *Proceedings of the National Academy of Sciences of the United States of America*, 108(12), pp. 4944–4949.

Maréchal, A. and Zou, L. (2013) 'DNA Damage Sensing by the ATM and ATR Kinases', *Cold Spring Harbor Perspectives in Biology*, 5(9), p. a012716.

Mateos-Gomez, P.A. *et al.* (2015) 'Mammalian polymerase θ promotes alternative NHEJ and suppresses recombination', *Nature*, 518(7538), pp. 254–257.

Matsuoka, S. *et al.* (2000) 'Ataxia telangiectasia-mutated phosphorylates Chk2 in vivo and in vitro', *Proceedings of the National Academy of Sciences of the United States of America*, 97(19), pp. 10389–10394.

Matsuoka, S., Huang, M. and Elledge, S.J. (1998) 'Linkage of ATM to cell cycle regulation by the Chk2 protein kinase', *Science (New York, N.Y.)*, 282(5395), pp. 1893–1897.

McClendon, A.K. and Osheroff, N. (2007) 'DNA Topoisomerase II, Genotoxicity, and Cancer', *Mutation research*, 623(1–2), pp. 83–97.

McKinnon, P.J. (2013) 'Maintaining Genome Stability in the Nervous System', *Nature neuroscience*, 16(11), pp. 1523–1529.

Melchionna, R. *et al.* (2000) 'Threonine 68 is required for radiation-induced phosphorylation and activation of Cds1', *Nature Cell Biology*, 2(10), pp. 762–765.

Miao, S. *et al.* (2021) 'DIAPH1 regulates chromosomal instability of cancer cells by controlling microtubule dynamics', *European Journal of Cell Biology*, 100(3), p. 151156.

Mirman, Z. and de Lange, T. (2020) '53BP1: a DSB escort', *Genes & Development*, 34(1–2), pp. 7–23.

Miyajima, H. *et al.* (2020) 'Novel ACTG1 mutations in patients identified by massively parallel DNA sequencing cause progressive hearing loss', *Scientific Reports*, 10, p. 7056.

Miyoshi, T. *et al.* (2022) 'Human deafness-associated variants alter the dynamics of key molecules in hair cell stereocilia F-actin cores', *Human Genetics*, 141(3), pp. 363–382.

Morita, K. *et al.* (2006) 'HAN11 binds mDia1 and controls GLI1 transcriptional activity', *Journal of Dermatological Science*, 44(1), pp. 11–20.

Motycka, T.A. *et al.* (2004) 'Physical and functional interaction between the XPF/ERCC1 endonuclease and hRad52', *The Journal of Biological Chemistry*, 279(14), pp. 13634–13639.

Moulding, D.A. *et al.* (2013) 'Actin cytoskeletal defects in immunodeficiency', *Immunological Reviews*, 256(1), pp. 282–299.

Muñoz, M.C. *et al.* (2012) 'Ring Finger Nuclear Factor RNF168 Is Important for Defects in Homologous Recombination Caused by Loss of the Breast Cancer Susceptibility Factor BRCA1', *The Journal of Biological Chemistry*, 287(48), pp. 40618–40628.

Murakami, H. and Keeney, S. (2008) 'Regulating the formation of DNA double-strand breaks in meiosis', *Genes & Development*, 22(3), pp. 286–292.

Musiałek, M.W. and Rybaczek, D. (2021) 'Hydroxyurea—The Good, the Bad and the Ugly', *Genes*, 12(7), p. 1096.

Neal, J.A. *et al.* (2011) 'Inhibition of Homologous Recombination by DNA-Dependent Protein Kinase Requires Kinase Activity, Is Titratable, and Is Modulated by Autophosphorylation ▿ ', *Molecular and Cellular Biology*, 31(8), pp. 1719–1733.

Neelsen, K.J. and Lopes, M. (2015) 'Replication fork reversal in eukaryotes: from dead end to dynamic response', *Nature Reviews Molecular Cell Biology*, 16(4), pp. 207–220.

Neuhaus, C. *et al.* (2017) 'Extension of the clinical and molecular phenotype of DIAPH1-associated autosomal dominant hearing loss (DFNA1)', *Clinical Genetics*, 91(6), pp. 892–901.

Nieminuszczy, J. *et al.* (2023) 'Actin nucleators safeguard replication forks by limiting nascent strand degradation', *Nucleic Acids Research*, p. gkad369.

Nimonkar, A.V. *et al.* (2011) 'BLM-DNA2-RPA-MRN and EXO1-BLM-RPA-MRN constitute two DNA end resection machineries for human DNA break repair', *Genes & Development*, 25(4), pp. 350–362.

Nishimura, K. *et al.* (2019) 'Cdk1-mediated DIAPH1 phosphorylation maintains metaphase cortical tension and inactivates the spindle assembly checkpoint at anaphase', *Nature Communications*, 10(1), p. 981.

Nitiss, J.L. (2009) 'Targeting DNA topoisomerase II in cancer chemotherapy', *Nature Reviews Cancer*, 9(5), pp. 338–350.

Nunes-Santos, C.J. *et al.* (2023) 'Inherited ARPC5 mutations cause an actinopathy impairing cell motility and disrupting cytokine signaling', *Nature Communications*, 14(1), p. 3708.

Nunoi, H. *et al.* (1999) 'A heterozygous mutation of β-actin associated with neutrophil dysfunction and recurrent infection', *Proceedings of the National Academy of Sciences*, 96(15), pp. 8693–8698.

Ochi, T. *et al.* (2015) 'DNA repair. PAXX, a paralog of XRCC4 and XLF, interacts with Ku to promote DNA double-strand break repair', *Science (New York, N.Y.)*, 347(6218), pp. 185–188.

Ochi, T., Gu, X. and Blundell, T.L. (2013) 'Structure of the Catalytic Region of DNA Ligase IV in Complex with an Artemis Fragment Sheds Light on Double-Strand Break Repair', *Structure(London, England:1993)*, 21(4), pp. 672–679.

O'Driscoll, M. *et al.* (2001) 'DNA Ligase IV Mutations Identified in Patients Exhibiting Developmental Delay and Immunodeficiency', *Molecular Cell*, 8(6), pp. 1175–1185.

Okada, K. *et al.* (2010) 'Adenomatous polyposis coli protein nucleates actin assembly and synergizes with the formin mDia1', *The Journal of Cell Biology*, 189(7), pp. 1087–1096.

Olson, E. *et al.* (2007) 'The Mre11-Rad50-Nbs1 Complex Acts Both Upstream and Downstream of Ataxia Telangiectasia Mutated and Rad3-related Protein (ATR) to Regulate the S-phase Checkpoint following UV Treatment*', *Journal of Biological Chemistry*, 282(31), pp. 22939–22952.

Ovejero, S., Bueno, A. and Sacristán, M.P. (2020) 'Working on Genomic Stability: From the S-Phase to Mitosis', *Genes*, 11(2), p. 225.

Palumbieri, M.D. *et al.* (2023) 'Nuclear actin polymerization rapidly mediates replication fork remodeling upon stress by limiting PrimPol activity', *Nature Communications*, 14(1), p. 7819.

Pan, J. *et al.* (2014) 'The formin DIAPH1 (mDia1) regulates megakaryocyte proplatelet formation by remodeling the actin and microtubule cytoskeletons', *Blood*, 124(26), pp. 3967–3977.

Panier, S. and Boulton, S.J. (2014) 'Double-strand break repair: 53BP1 comes into focus', *Nature Reviews Molecular Cell Biology*, 15(1), pp. 7–18.

Papadatou, I. *et al.* (2021) 'Case Report: A Novel Synonymous ARPC1B Gene Mutation Causes a Syndrome of Combined Immunodeficiency, Asthma, and Allergy With Significant Intrafamilial Clinical Heterogeneity', *Frontiers in Immunology*, 12, p. 634313.

Passemard, S., Kaindl, A.M. and Verloes, A. (2013) 'Chapter 13 - Microcephaly', in O. Dulac, M. Lassonde, and H.B. Sarnat (eds) *Handbook of Clinical Neurology*. Elsevier (Pediatric Neurology Part I), pp. 129–141.

Patel, J.P. *et al.* (2015) 'Nijmegen Breakage Syndrome Detected by Newborn Screening for T Cell Receptor Excision Circles (TRECs)', *Journal of Clinical Immunology*, 35(2), pp. 227–233.

Patrinostro, X. *et al.* (2018) 'Essential nucleotide- and protein-dependent functions of Actb/β-actin', *Proceedings of the National Academy of Sciences of the United States of America*, 115(31), p. 7973.

Perrin, B.J., Sonnemann, K.J. and Ervasti, J.M. (2010) 'β-Actin and γ-Actin Are Each Dispensable for Auditory Hair Cell Development But Required for Stereocilia Maintenance', *PLoS Genetics*, 6(10), p. e1001158.

Perry, J. and Kleckner, N. (2003) 'The ATRs, ATMs, and TORs are giant HEAT repeat proteins', *Cell*, 112(2), pp. 151–155.

Petermann, E. *et al.* (2010) 'Hydroxyurea-Stalled Replication Forks Become Progressively Inactivated and Require Two Different RAD51-Mediated Pathways for Restart and Repair', *Molecular Cell*, 37(4), pp. 492–502.

Pfitzer, L. *et al.* (2019) 'Targeting actin inhibits repair of doxorubicin-induced DNA damage: a novel therapeutic approach for combination therapy', *Cell Death & Disease*, 10(4), pp. 1–14.

Pinder, J., Salsman, J. and Dellaire, G. (2015) 'Nuclear domain "knock-in" screen for the evaluation and identification of small molecule enhancers of CRISPR-based genome editing', *Nucleic Acids Research*, 43(19), pp. 9379–9392.

Pommier, Y. (2006) 'Topoisomerase I inhibitors: camptothecins and beyond', *Nature Reviews Cancer*, 6(10), pp. 789–802.

Pommier, Y. *et al.* (2022) 'Human topoisomerases and their roles in genome stability and organization', *Nature Reviews Molecular Cell Biology*, 23(6), pp. 407–427.

Porter-Goff, M.E. and Rhind, N. (2009) 'The Role of MRN in the S-Phase DNA Damage Checkpoint Is Independent of Its Ctp1-dependent Roles in Double-Strand Break Repair and Checkpoint Signaling', *Molecular Biology of the Cell*, 20(7), pp. 2096–2107.

Prakash, R. *et al.* (2015) 'Homologous Recombination and Human Health: The Roles of BRCA1, BRCA2, and Associated Proteins', *Cold Spring Harbor Perspectives in Biology*, 7(4).

Pryor, J.M. *et al.* (2015) 'Essential role for polymerase specialization in cellular nonhomologous end joining', *Proceedings of the National Academy of Sciences of the United States of America*, 112(33), pp. E4537–E4545.

Qin, Y. *et al.* (2015) 'Genetics of primary ovarian insufficiency: new developments and opportunities', *Human Reproduction Update*, 21(6), pp. 787–808.

QIU, S. and HUANG, J. (2021) 'MRN complex is an essential effector of DNA damage repair', *Journal of Zhejiang University. Science. B*, 22(1), pp. 31–37.

Quinet, A. *et al.* (2017) 'DNA Fiber Analysis: Mind the Gap!', *Methods in Enzymology*, 591, pp. 55–82.

Ramasamy, R., Shekhtman, A. and Schmidt, A.M. (2022) 'The RAGE/DIAPH1 Signaling Axis & Implications for the Pathogenesis of Diabetic Complications', *International Journal of Molecular Sciences*, 23(9), p. 4579.

Rashi-Elkeles, S. *et al.* (2011) 'Transcriptional modulation induced by ionizing radiation: p53 remains a central player', *Molecular Oncology*, 5(4), pp. 336–348.

Rattner, J.B. *et al.* (1993) 'CENP-F is a .ca 400 kDa kinetochore protein that exhibits a cell-cycle dependent localization', *Cell Motility and the Cytoskeleton*, 26(3), pp. 214–226.

Ray Chaudhuri, A. *et al.* (2012) 'Topoisomerase I poisoning results in PARP-mediated replication fork reversal', *Nature Structural & Molecular Biology*, 19(4), pp. 417–423.

Recio, M.J. *et al.* (2019) 'Extreme Phenotypes With Identical Mutations: Two Patients With Same Non-sense NHEJ1 Homozygous Mutation', *Frontiers in Immunology*, 9, p. 2959.

Riballo, E. *et al.* (2004) 'A Pathway of Double-Strand Break Rejoining Dependent upon ATM, Artemis, and Proteins Locating to γ-H2AX Foci', *Molecular Cell*, 16(5), pp. 715–724.

Ribeiro, J.H. *et al.* (2023) 'DNA damage and repair: underlying mechanisms leading to microcephaly', *Frontiers in Cell and Developmental Biology*, 11.

Rivière, J.-B. *et al.* (2012) 'De novo mutations in the actin genes ACTB and ACTG1 cause Baraitser-Winter syndrome', *Nature Genetics*, 44(4), pp. 440–444.

Robinson, R.C. *et al.* (2001) 'Crystal structure of Arp2/3 complex', *Science (New York, N.Y.)*, 294(5547), pp. 1679–1684.

Rothenberg, E. *et al.* (2008) 'Human Rad52-mediated homology search and annealing occurs by continuous interactions between overlapping nucleoprotein complexes', *Proceedings of the National Academy of Sciences of the United States of America*, 105(51), pp. 20274–20279.

Rothkamm, K. *et al.* (2003) 'Pathways of DNA Double-Strand Break Repair during the Mammalian Cell Cycle', *Molecular and Cellular Biology*, 23(16), p. 5706.

Ruiz, H.H. *et al.* (2021) 'AGE/RAGE/DIAPH1 axis is associated with immunometabolic markers and risk of insulin resistance in subcutaneous but not omental adipose tissue in human obesity', *International Journal of Obesity*, 45(9), pp. 2083–2094.

Sakata, D. *et al.* (2007) 'Impaired T lymphocyte trafficking in mice deficient in an actin-nucleating protein, mDia1', *Journal of Experimental Medicine*, 204(9), pp. 2031–2038.

Saldivar, J.C., Cortez, D. and Cimprich, K.A. (2017) 'The essential kinase ATR: ensuring faithful duplication of a challenging genome', *Nature Reviews Molecular Cell Biology*, 18(10), pp. 622–636.

Saleh-Gohari, N. *et al.* (2005) 'Spontaneous homologous recombination is induced by collapsed replication forks that are caused by endogenous DNA single-strand breaks', *Molecular and Cellular Biology*, 25(16), pp. 7158–7169.

Sallmyr, A. and Tomkinson, A.E. (2018) 'Repair of DNA double-strand breaks by mammalian alternative end-joining pathways', *The Journal of Biological Chemistry*, 293(27), pp. 10536–10546.

Sartori, A.A. *et al.* (2007) 'Human CtIP promotes DNA end resection', *Nature*, 450(7169), pp. 509–514.

Saxena, S. and Zou, L. (2022) 'Hallmarks of DNA replication stress', *Molecular Cell*, 82(12), pp. 2298–2314.

Schär, P. (2001) 'Spontaneous DNA Damage, Genome Instability, and Cancer—When DNA Replication Escapes Control', *Cell*, 104(3), pp. 329–332.

van Schie, J.J.M. *et al.* (2020) 'Warsaw Breakage Syndrome associated DDX11 helicase resolves G-quadruplex structures to support sister chromatid cohesion', *Nature Communications*, 11(1), p. 4287.

Schiller, C.B. *et al.* (2012) 'Structural biology of the Mre11:Nbs1 complex structure yields insights into ataxia–telangiectasia–like disease mutations and DNA damage signaling', *Nature structural & molecular biology*, 19(7), pp. 693–700.

Schoen, C.J. *et al.* (2010) 'Increased activity of Diaphanous homolog 3 (DIAPH3)/diaphanous causes hearing defects in humans with auditory neuropathy and in Drosophila', *Proceedings of the National Academy of Sciences of the United States of America*, 107(30), pp. 13396–13401.

Schrank, B.R. *et al.* (2018a) 'Nuclear ARP2/3 drives DNA break clustering for homology-directed repair', *Nature*, 559(7712), pp. 61–66.

Scully, R. *et al.* (2019) 'DNA double-strand break repair-pathway choice in somatic mammalian cells', *Nature Reviews Molecular Cell Biology*, 20(11), pp. 698–714.

Sefer, A.P. *et al.* (2023) 'A Rare Immunodeficiency As a Cause of Inflammatory Bowel Disease; ARPC1B Deficiency', *Clinical Immunology*, 250, p. 109587.

Senatus, L. *et al.* (2023) 'DIAPH1 mediates progression of atherosclerosis and regulates hepatic lipid metabolism in mice', *Communications Biology*, 6(1), p. 280.

Serana, F. *et al.* (2013) 'Use of V(D)J recombination excision circles to identify T- and B-cell defects and to monitor the treatment in primary and acquired immunodeficiencies', *Journal of Translational Medicine*, 11(1), p. 119.

Setiaputra, D. and Durocher, D. (2019) 'Shieldin - the protector of DNA ends', *EMBO reports*, 20(5), p. e47560.

Shagieva, G.S. *et al.* (2020) 'Divergent Impact of Actin Isoforms on Division of Epithelial Cells', *Biochemistry. Biokhimiia*, 85(9), pp. 1072–1063.

Shanbhag, N.M. *et al.* (2010) 'ATM-dependent chromatin changes silence transcription in cis to DNA double-strand breaks', *Cell*, 141(6), pp. 970–981.

Shi, J. *et al.* (2023) 'Nuclear myosin VI maintains replication fork stability', *Nature Communications*, 14(1), p. 3787.

Shibata, A. *et al.* (2014) 'DNA Double Strand Break Repair Pathway Choice Is Directed by Distinct MRE11 Nuclease Activities', *Molecular cell*, 53(1), pp. 7–18.

Shibata, A. and Jeggo, P.A. (2021) 'ATM's Role in the Repair of DNA Double-Strand Breaks', *Genes*, 12(9), p. 1370.

Shiloh, Y. (2003) 'ATM and related protein kinases: safeguarding genome integrity', *Nature Reviews. Cancer*, 3(3), pp. 155–168.

Sibanda, B.L. *et al.* (2001) 'Crystal structure of an Xrcc4-DNA ligase IV complex', *Nature Structural Biology*, 8(12), pp. 1015–1019.

Singleton, B.K. *et al.* (1999) 'The C terminus of Ku80 activates the DNA-dependent protein kinase catalytic subunit', *Molecular and Cellular Biology*, 19(5), pp. 3267–3277.

Sitar, T. *et al.* (2011) 'Molecular architecture of the Spire–actin nucleus and its implication for actin filament assembly', *Proceedings of the National Academy of Sciences*, 108(49), pp. 19575–19580.

Slatter, M.A. and Gennery, A.R. (2020) 'Update on DNA-Double Strand Break Repair Defects in Combined Primary Immunodeficiency', *Current Allergy and Asthma Reports*, 20(10), p. 57.

So, E.Y. *et al.* (2011) 'Phosphorylation of SMC1 by ATR is required for desferrioxamine (DFO)-induced apoptosis', *Cell Death & Disease*, 2(3), p. e128.

So, S., Davis, A.J. and Chen, D.J. (2009) 'Autophosphorylation at serine 1981 stabilizes ATM at DNA damage sites', *The Journal of Cell Biology*, 187(7), pp. 977–990.

Somech, R. *et al.* (2017) 'Disruption of Thrombocyte and T Lymphocyte Development by a Mutation in ARPC1B', *Journal of Immunology (Baltimore, Md.: 1950)*, 199(12), pp. 4036–4045.

Spycher, C. *et al.* (2008) 'Constitutive phosphorylation of MDC1 physically links the MRE11–RAD50–NBS1 complex to damaged chromatin', *Journal of Cell Biology*, 181(2), pp. 227–240.

Stiehm, E.R. and McIntosh, R.M. (1967) 'Wiskott-Aldrich syndrome: review and report of a large family', *Clinical and Experimental Immunology*, 2(2), pp. 179–189.

Stinson, B.M. and Loparo, J.J. (2021) 'Repair of DNA Double-Strand Breaks by the Non-homologous End Joining Pathway', *Annual review of biochemistry*, 90, pp. 137–164.

Straccia, G. *et al.* (2022) 'ACTB gene mutation in combined Dystonia-Deafness syndrome with parkinsonism: Expanding the phenotype and highlighting the long-term GPi DBS outcome', *Parkinsonism & Related Disorders*, 104, pp. 3–6.

Stritt, S. *et al.* (2016) 'A gain-of-function variant in DIAPH1 causes dominant macrothrombocytopenia and hearing loss', *Blood*, 127(23), pp. 2903–2914.

Stucki, M. *et al.* (2005) 'MDC1 directly binds phosphorylated histone H2AX to regulate cellular responses to DNA double-strand breaks', *Cell*, 123(7), pp. 1213–1226.

Stüven, T., Hartmann, E. and Görlich, D. (2003) 'Exportin 6: a novel nuclear export receptor that is specific for profilin·actin complexes', *The EMBO Journal*, 22(21), pp. 5928–5940.

Sun, Q. *et al.* (2021) 'MCM7 Ubiquitination Regulates CMG Helicase Disassembly in Human'.

Suresh, R. and Diaz, R.J. (2021) 'The remodelling of actin composition as a hallmark of cancer', *Translational Oncology*, 14(6), p. 101051.

Syed, A. and Tainer, J.A. (2018) 'The MRE11-RAD50-NBS1 Complex Conducts the Orchestration of Damage Signaling and Outcomes to Stress in DNA Replication and Repair', *Annual Review of Biochemistry*, 87, pp. 263–294.

Symington, L.S. (2002) 'Role of RAD52 Epistasis Group Genes in Homologous Recombination and Double-Strand Break Repair', *Microbiology and Molecular Biology Reviews*, 66(4), pp. 630–670.

Tammaro, M. *et al.* (2013) 'Replication-Dependent and Transcription-Dependent Mechanisms of DNA Double-Strand Break Induction by the Topoisomerase 2-Targeting Drug Etoposide', *PLoS ONE*, 8(11), p. e79202.

Técher, H. *et al.* (2017) 'The impact of replication stress on replication dynamics and DNA damage in vertebrate cells', *Nature reviews. Genetics*, 18(9), pp. 535–550.

Thompson, M.E. *et al.* (2013) 'FMNL3 FH2-actin structure gives insight into formin-mediated actin nucleation and elongation', *Nature Structural & Molecular Biology*, 20(1), pp. 111–118.

Tolić, I.M. (2018) 'Mitotic spindle: kinetochore fibers hold on tight to interpolar bundles', *European Biophysics Journal*, 47(3), pp. 191–203.

Tuduri, S., Tourrière, H. and Pasero, P. (2010) 'Defining replication origin efficiency using DNA fiber assays', *Chromosome Research: An International Journal on the Molecular, Supramolecular and Evolutionary Aspects of Chromosome Biology*, 18(1), pp. 91–102.

Tumini, E. and Aguilera, A. (2021) 'The Sister-Chromatid Exchange Assay in Human Cells', *Methods in Molecular Biology (Clifton, N.J.)*, 2153, pp. 383–393.

Tyler, J.J., Allwood, E.G. and Ayscough, K.R. (2016) 'WASP family proteins, more than Arp2/3 activators', *Biochemical Society Transactions*, 44(5), pp. 1339–1345.

Ueyama, T., Ninoyu, Y., Nishio, S.-Y., *et al.* (2016) 'Constitutive activation of DIA1 (DIAPH1) via C-terminal truncation causes human sensorineural hearing loss', *EMBO molecular medicine*, 8(11), pp. 1310–1324.

Ueyama, T., Ninoyu, Y., Nishio, S., *et al.* (2016) 'Constitutive activation of DIA1 (DIAPH1) via C-terminal truncation causes human sensorineural hearing loss', *EMBO Molecular Medicine*, 8(11), pp. 1310–1324.

Uziel, T. *et al.* (2003) 'Requirement of the MRN complex for ATM activation by DNA damage', *The EMBO Journal*, 22(20), pp. 5612–5621.

Valikhani, M. *et al.* (2021) 'Involvement of classic and alternative non-homologous end joining pathways in hematologic malignancies: targeting strategies for treatment', *Experimental Hematology & Oncology*, 10(1), p. 51.

Vandekerckhove, J. and Weber, K. (1978) 'At least six different actins are expressed in a higher mammal: an analysis based on the amino acid sequence of the amino-terminal tryptic peptide', *Journal of Molecular Biology*, 126(4), pp. 783–802.

Velkova, A. *et al.* (2010) 'Identification of Filamin A as a BRCA1-interacting protein required for efficient DNA repair', *Cell Cycle (Georgetown, Tex.)*, 9(7), pp. 1421–1433.

Verloes, A. *et al.* (2015) 'Baraitser-Winter cerebrofrontofacial syndrome: delineation of the spectrum in 42 cases', *European journal of human genetics: EJHG*, 23(3), pp. 292–301.

Volk, T. *et al.* (2015) 'DCLRE1C (ARTEMIS) mutations causing phenotypes ranging from atypical severe combined immunodeficiency to mere antibody deficiency', *Human Molecular Genetics*, 24(25), pp. 7361–7372.

Volpi, S. *et al.* (2019) 'A combined immunodeficiency with severe infections, inflammation, and allergy caused by ARPC1B deficiency', *Journal of Allergy and Clinical Immunology*, 143(6), pp. 2296–2299.

Walworth, N.C. and Bernards, R. (1996) 'rad-dependent response of the chk1-encoded protein kinase at the DNA damage checkpoint', *Science (New York, N.Y.)*, 271(5247), pp. 353–356.

Wang, H. *et al.* (2013) 'The Interaction of CtIP and Nbs1 Connects CDK and ATM to Regulate HR–Mediated Double-Strand Break Repair', *PLOS Genetics*, 9(2), p. e1003277.

Wang, J. and Lindahl, T. (2016) 'Maintenance of Genome Stability', *Genomics, Proteomics & Bioinformatics*, 14(3), pp. 119–121.

Wang, T. *et al.* (2021) 'WASH interacts with Ku to regulate DNA double-stranded break repair', *iScience*, 25(1), p. 103676.

Wang, X. *et al.* (2021) 'Centromeric chromatin integrity is compromised by loss of Cdk5rap2, a transcriptional activator of CENP-A', *Biomedicine & Pharmacotherapy = Biomedecine & Pharmacotherapie*, 138, p. 111463.

Watanabe, N. *et al.* (1997) 'p140mDia, a mammalian homolog of Drosophila diaphanous, is a target protein for Rho small GTPase and is a ligand for profilin.', *The EMBO Journal*, 16(11), pp. 3044–3056.

Waters, C.A. *et al.* (2014) 'Nonhomologous end joining: A good solution for bad ends', *DNA Repair*, 17, pp. 39–51.

Weston, L., Coutts, A.S. and La Thangue, N.B. (2012) 'Actin nucleators in the nucleus: an emerging theme', *Journal of Cell Science*, 125(15), pp. 3519–3527.

Whelan, D.R. *et al.* (2016) 'Single Molecule Localization Microscopy of DNA Damage Response Pathways in Cancer.', *Microscopy and Microanalysis*, 22(S3), pp. 1016–1017.

Whelan, D.R. *et al.* (2018) 'Spatiotemporal dynamics of homologous recombination repair at single collapsed replication forks', *Nature Communications*, 9(1), p. 3882.

Whelan, D.R. *et al.* (2020) 'Super-resolution visualization of distinct stalled and broken replication fork structures', *PLOS Genetics*, 16(12), p. e1009256.

White, D.E. *et al.* (2006) 'KAP1, a Novel Substrate for PIKK Family Members, Colocalizes with Numerous Damage Response Factors at DNA Lesions', *Cancer Research*, 66(24), pp. 11594–11599.

Williams, R.M. and Zhang, X. (2021) 'Roles of ATM and ATR in DNA double strand breaks and replication stress', *Progress in Biophysics and Molecular Biology*, 161, pp. 27–38.

Wollscheid, H.-P. and Ulrich, H.D. (2023) 'Chromatin meets the cytoskeleton: the importance of nuclear actin dynamics and associated motors for genome stability', *DNA Repair*, 131, p. 103571.

Woodbine, L., Gennery, A.R. and Jeggo, P.A. (2014) 'The clinical impact of deficiency in DNA non-homologous end-joining', *DNA repair*, 16, pp. 84–96.

Wu, L. and Hickson, I.D. (2003) 'The Bloom's syndrome helicase suppresses crossing over during homologous recombination', *Nature*, 426(6968), pp. 870–874.

Wyatt, D.W. *et al.* (2016) 'Essential Roles for Polymerase θ-Mediated End Joining in the Repair of Chromosome Breaks', *Molecular Cell*, 63(4), pp. 662–673.

Xing, M. *et al.* (2015) 'Interactome analysis identifies a new paralogue of XRCC4 in non-homologous end joining DNA repair pathway', *Nature Communications*, 6, p. 6233.

Xu, J., Ma, H. and Liu, Y. (2017) 'Stochastic optical reconstruction microscopy (STORM)', *Current protocols in cytometry*, 81, p. 12.46.1-12.46.27.

Xu, Y., Wu, X. and Her, C. (2015) 'hMSH5 Facilitates the Repair of Camptothecin-induced Double-strand Breaks through an Interaction with FANCJ', *The Journal of Biological Chemistry*, 290(30), pp. 18545–18558.

Yamana, N. *et al.* (2006) 'The Rho-mDia1 Pathway Regulates Cell Polarity and Focal Adhesion Turnover in Migrating Cells through Mobilizing Apc and c-Src', *Molecular and Cellular Biology*, 26(18), pp. 6844–6858.

Yang, J. *et al.* (2021) 'DIAPH1 Promotes Laryngeal Squamous Cell Carcinoma Progression Through Cell Cycle Regulation', *Frontiers in Oncology*, 11, p. 3801.

Yang, X. and Lin, Y. (2018) 'Functions of nuclear actin-binding proteins in human cancer', *Oncology Letters*, 15(3), pp. 2743–2748.

Yates, L.A. *et al.* (2018) 'A structural and dynamic model for the assembly of Replication Protein A on single-stranded DNA', *Nature Communications*, 9(1), p. 5447.

Yates, T.M. *et al.* (2017) 'Baraitser-Winter cerebrofrontofacial syndrome', *Clinical Genetics*, 92(1), pp. 3–9.

Yin, Y. *et al.* (2021) 'A basal-level activity of ATR links replication fork surveillance and stress response', *Molecular Cell*, 81(20), pp. 4243-4257.e6.

Yin, Y., Lee, W.T.C. and Rothenberg, E. (2019) 'Ultrafast data mining of molecular assemblies in multiplexed high-density super-resolution images', *Nature Communications*, 10(1), p. 119.

Yin, Y. and Rothenberg, E. (2016) 'Probing the Spatial Organization of Molecular Complexes Using Triple-Pair-Correlation', *Scientific Reports*, 6, p. 30819.

Yu, X. *et al.* (2003) 'The BRCT domain is a phospho-protein binding domain', *Science (New York, N.Y.)*, 302(5645), pp. 639–642.

Yuan, Y. and Shen, Z. (2001) 'Interaction with BRCA2 suggests a role for filamin-1 (hsFLNa) in DNA damage response', *The Journal of Biological Chemistry*, 276(51), pp. 48318–48324.

Zech, M. *et al.* (2017) 'Molecular diversity of combined and complex dystonia: insights from diagnostic exome sequencing', *Neurogenetics*, 18(4), pp. 195–205.

Zeman, M.K. and Cimprich, K.A. (2014) 'Causes and Consequences of Replication Stress', *Nature cell biology*, 16(1), pp. 2–9.

Zglejc-Waszak, K., Mukherjee, K. and Juranek, J.K. (2021) 'The cross-talk between RAGE and DIAPH1 in neurological complications of diabetes: A review', *European Journal of Neuroscience*, 54(6), pp. 5982–5999.

Zhang, B. *et al.* (2022) 'Diaphanous-related formin subfamily: Novel prognostic biomarkers and tumor microenvironment regulators for pancreatic adenocarcinoma', *Frontiers in Molecular Biosciences*, 9, p. 910950.

Zhang, F. *et al.* (2009) 'PALB2 Links BRCA1 and BRCA2 in the DNA-Damage Response', *Current biology : CB*, 19(6), pp. 524–529.

Zhao, F. *et al.* (2020) 'DNA end resection and its role in DNA replication and DSB repair choice in mammalian cells', *Experimental & Molecular Medicine*, 52(10), pp. 1705–1714.

Zhao, J.H., Tohda, H. and Oikawa, A. (1992) 'Camptothecin-induced sister-chromatid exchange dependent on the presence of bromodeoxyuridine and the phase of the cell cycle', *Mutation Research Letters*, 282(1), pp. 49–54.

Zhao, S. *et al.* (2000) 'Functional link between ataxia-telangiectasia and Nijmegen breakage syndrome gene products', *Nature*, 405(6785), pp. 473–477.

Zheng, L. *et al.* (2020) 'Multiple roles of DNA2 nuclease/helicase in DNA metabolism, genome stability and human diseases', *Nucleic Acids Research*, 48(1), pp. 16–35.

Zhou, Y. *et al.* (2014) 'Quantitation of DNA double-strand break resection intermediates in human cells', *Nucleic Acids Research*, 42(3), p. e19.

Zhou, Z.-W. *et al.* (2013) 'An essential function for the ATR-activation-domain (AAD) of TopBP1 in mouse development and cellular senescence', *PLoS genetics*, 9(8), p. e1003702.

Zhu, L.Y. (2019) *Dissecting the Aactin Isoform Specificity of the Formin DIAPH3*. Thesis.

Zou, L., Cortez, D. and Elledge, S.J. (2002) 'Regulation of ATR substrate selection by Rad17-dependent loading of Rad9 complexes onto chromatin', *Genes & Development*, 16(2), pp. 198–208.

Anyway, hope that makes sense,
no worries if not.

Appendices

RECON syndrome is a genome instability disorder caused by mutations in the DNA helicase RECQL1

Bassam Abu-Libdeh,[1] Satpal S. Jhujh,[2] Srijita Dhar,[3] Joshua A. Sommers,[3] Arindam Datta,[3] Gabriel M.C. Longo,[4] Laura J. Grange,[2] John J. Reynolds,[2] Sophie L. Cooke,[2] Gavin S. McNee,[2] Robert Hollingworth,[2] Beth L. Woodward,[2] Anil N. Ganesh,[2] Stephen J. Smerdon,[2] Claudia M. Nicolae,[5] Karina Durlacher-Betzer,[6] Vered Molho-Pessach,[7] Abdulsalam Abu-Libdeh,[1] Vardiella Meiner,[6] George-Lucian Moldovan,[5] Vassilis Roukos,[4] Tamar Harel,[6] Robert M. Brosh Jr.,[3] and Grant S. Stewart[2]

[1]Department of Pediatrics and Genetics, Makassed Hospital and Al-Quds Medical School, East Jerusalem, Palestine. [2]Institute for Cancer and Genomic Sciences, University of Birmingham, Birmingham, United Kingdom. [3]Translational Gerontology Branch, National Institute on Aging, NIH, Baltimore, Maryland, USA. [4]Institute of Molecular Biology (IMB), Mainz, Germany. [5]Department of Biochemistry and Molecular Biology, The Pennsylvania State University College of Medicine, Hershey, Pennsylvania, USA. [6]Department of Genetics and [7]Paediatric Dermatology Service, Department of Dermatology, Hadassah Medical Center, Faculty of Medicine, Hebrew University of Jerusalem, Jerusalem, Israel.

Despite being the first homolog of the bacterial RecQ helicase to be identified in humans, the function of RECQL1 remains poorly characterized. Furthermore, unlike other members of the human RECQ family of helicases, mutations in RECQL1 have not been associated with a genetic disease. Here, we identify 2 families with a genome instability disorder that we have named RECON (RECql ONe) syndrome, caused by biallelic mutations in the *RECQL* gene. The affected individuals had short stature, progeroid facial features, a hypoplastic nose, xeroderma, and skin photosensitivity and were homozygous for the same missense mutation in RECQL1 (p.Ala459Ser), located within its zinc binding domain. Biochemical analysis of the mutant RECQL1 protein revealed that the p.A459S missense mutation compromised its ATPase, helicase, and fork restoration activity, while its capacity to promote single-strand DNA annealing was largely unaffected. At the cellular level, this mutation in RECQL1 gave rise to a defect in the ability to repair DNA damage induced by exposure to topoisomerase poisons and a failure of DNA replication to progress efficiently in the presence of abortive topoisomerase lesions. Taken together, RECQL1 is the fourth member of the RecQ family of helicases to be associated with a human genome instability disorder.

Introduction

DNA helicases are ubiquitous enzymes found in most uni- and multicellular organisms and function to unwind DNA in an ATP-dependent and direction-specific manner. The ability to unwind DNA is an essential step in many fundamental cellular processes, such as DNA replication, recombination, repair, and transcription. The RecQ family of helicases represents one of the most highly conserved groups of 3′–5′ DNA helicases and is named after the prototype *Escherichia coli* RecQ. Although bacteria and yeast only express one RecQ-type helicase, higher eukaryotes possess multiple homologs that are highly conserved. The RecQ helicase family has 5 known homologs in humans: RECQL (also known as RECQ1 or RECQL1), WRN, BLM, RECQL4, and RECQL5. Strikingly, biallelic mutations in 3 of 5 of these RecQ homologs — *WRN*, *BLM*, and *RECQL4* — have been associated with rare genetic disorders in humans, characterized by chromosomal instability and cancer predisposition (1, 2). Notably, however, these genetic disorders are distinct, with each syndrome exhibiting a unique set of clinical and cellular features. This serves to highlight that although each of these enzymes is structurally and functionally related, they perform distinct tasks within the cell.

WRN is mutated in Werner syndrome (WS), which is a progeroid syndrome associated with premature aging, type 2 diabetes, osteoporosis, cataracts, graying and loss of hair, skin atrophy, and cancer predisposition. Cells from individuals with WS characteristically undergo premature replicative senescence associated with increased telomere erosion and have been reported to be hypersensitive to replication stress–inducing genotoxic agents, such as camptothecin (CPT), methylmethane sulfonate (MMS), and G-quadruplex (G4) stabilizers (3). In contrast, Bloom syndrome (BS), which is caused by mutations in *BLM*, is a developmental disorder that typically includes microcephaly, short stature, immunodeficiency, skin hyper- or hypopigmentation, photosensitivity, facial erythema, and an increased predisposition for developing cancer (4). The BLM helicase has been implicated in repairing DNA double-stranded breaks (DSBs), restarting damaged replication forks, and resolving homologous recombination (HR) intermediates, including those present in mitosis as a result of underreplicated DNA transiting through the cell cycle (5). Consequently, cells devoid of BLM are hypersensitive to replication stress–inducing genotoxins such as camptothecin (CPT), hydroxyurea (HU), and aphidicolin (APH) and exhibit a characteristic increase in spontaneous sister chromatid exchanges (SCEs). Last, mutations in *RECQL4* have been associ-

Authorship note: BAL, SSJ, SD, and JAS contributed equally to this work.
Conflict of interest: The authors have declared that no conflict of interest exists.
Copyright: © 2022, Abu-Libdeh et al. This is an open access article published under the terms of the Creative Commons Attribution 4.0 International License.
Submitted: January 8, 2021; **Accepted:** January 11, 2022; **Published:** March 1, 2022.
Reference information: *J Clin Invest*. 2022;132(5):e147301.
https://doi.org/10.1172/JCI147301.

ated with 3 distinct, albeit overlapping, genetic disorders: Rothmund-Thomson syndrome (RTS), RAPADILINO syndrome, and Baller-Gerold syndrome (BGS). While patients with these disorders display some unique clinical features, e.g., poikiloderma (RTS) or craniosynostosis (BGS), the vast majority of affected individuals exhibit a constellation of developmental abnormalities, such as growth retardation, aplastic/absent thumbs, aplastic/absent patellae, aplastic/absent bones in the forearms, skin hypo-/hyperpigmentation, cleft palate, and an increased predisposition for developing cancer (6). Unlike WRN or BLM, RECQL4 is a constitutive component of the replication machinery involved in regulating replication origin firing (7). However, RECQL4 has also been suggested to play a role in repairing oxidative base damage and DSBs by HR (8, 9). Accordingly, cells lacking RECQL4 function are hypersensitive to both DSB- and replication stress–inducing agents, e.g., ionizing radiation (IR), CPT, HU and H_2O_2.

Although RECQL1 was the first RecQ family helicase to be identified in humans, it remains the most functionally enigmatic (10). In vitro RECQL1 can unwind a variety of DNA structures in a 3′–5′ direction, particularly those with a 3′ ssDNA tail, e.g., replication fork structures. It can also catalyze branch migration of Holliday junctions and D-loops, unwind G4 structures, and promote single-strand DNA annealing (SSA). However, unlike other human RecQ helicases, it acts poorly to unwind RNA:DNA hybrids or displace Rad51 bound to ssDNA (11, 12). Despite its demonstrated biochemical activities, mice devoid of this enzyme are phenotypically normal (13). To date, there are reports suggesting that RECQL1 is required to repair DSBs induced by IR, CPT, and etoposide (ETOP) (13, 14), although the underlying mechanism is not clear. More recently, it has been proposed that a major function of RECQL1 is to promote the restart of stalled replication forks induced by the inhibition of topoisomerase 1 and that this activity is inhibited by poly-ADP-ribose polymerase 1 (PARP1), allowing the damaged forks time to repair (14). However, whether the role of RECQL1 in promoting the restart of reversed forks caused by abortive topoisomerase activity is solely dependent on PARP1 or whether RECQL1 plays a more fundamental role in this process remains to be clarified.

While *RECQL* has not been previously associated with a defined human chromosomal instability disorder, monoallelic germline mutations have been associated with a moderately increased risk of breast cancer (15, 16). Interestingly, Sun et al. (16) identified two *BRCA1/2*-negative breast cancer families with missense variants in the zinc binding domain (ZBD) of RECQL1 (p.Arg455Cys and p.Met458Lys) that completely abolished its helicase activity. Moreover, functional analysis of conserved cysteine residues within this domain demonstrated that cysteine residues 453, 475, and 478 are critical for RECQL1 to hydrolyze ATP and unwind dsDNA but not to promote SSA (17). Combined, these observations serve to highlight the functional significance of the ZBD of RECQL1 and its importance in relation to its ability to act as a DNA helicase.

Here, we demonstrate that biallelic *RECQL* mutations are associated with a human genome instability syndrome, which we propose to name RECON (RECql ONe) syndrome. Notably, individuals from both affected, but seemingly unrelated, families carried a homozygous missense mutation (p.Ala459Ser, referred to as p.A459S) in the ZBD of RECQL1. Clinically, this *RECQL* mutation was associated with a distinct disorder characterized by striking progeroid facial features, a tiny, pinched nose, apparent skin photosensitivity, xeroderma, and slender, elongated thumbs. Functionally, the p.A459S mutation significantly compromised the ATPase/helicase activity of RECQL1 and modestly affected its ability to bind DNA. However, its capacity to promote SSA was unaffected. At the cellular level, this mutation gave rise to a modest defect in repairing abortive topoisomerase 1 (TOP1) and topoisomerase 2 (TOP2) cleavage complexes and a reduced ability to replicate in the presence of CPT- or ETOP-induced DNA damage. Furthermore, cells expressing the p.A459S mutant RECQL1 also failed to efficiently restart replication following exposure to HU and MMS, indicating that the role that RECQL1 plays in restarting damaged replication forks is not just limited to those associated with abortive TOP1/2 complexes. Taken together, these data suggest that, while it is not essential (13), RECQL1 has nonredundant functions with other RecQ helicases and that its loss compromises genome stability and normal embryonic development.

Results

Clinical phenotype of individuals affected by RECQL1 mutations. The proband of family A (family A, III-2) was a female evaluated at age 9 years, 8 months for short stature, dysmorphism, and dryness of the skin and eyes. She was the second of 5 children born to parents of Middle Eastern descent, who were double first cousins (Figure 1A). The pregnancy and delivery were uncomplicated. The proband was born at term with a birth weight of approximately 3000 grams. Her developmental milestones, including motor, speech, and communication skills, were age appropriate. At 18 months of age, medical evaluation was sought, since her nose remained exceptionally small compared with the rest of her face, her eyes remained open while sleeping, and she had xerophthalmia (dry eyes) and xeroderma (dry skin) with scaling. Eruption of the proband's primary teeth was age appropriate, however, eruption of her permanent teeth was delayed. The parents reported that their child had photosensitivity. Physical examination of the girl at 9 years, 8 months revealed a height of 123.8 cm (*z* score, –1.98), a weight of 22.5 kg (*z* score, –2.05), and a head circumference of 50 cm (*z* score, –1.64). A negative *z* score represents the number of standard deviations below the population mean for each clinical measurement. The proband's dysmorphic features included a round face, redness of eyes, a tiny, pinched nose with anteverted nares, prominent premaxilla, and a smooth philtrum (Figure 1B). Her thumbs were slender and elongated, with hyperconvex nails. She had slight hyperextension of the elbows but no joint laxity in the fingers. The proband also had livedo reticularis and keratosis pilaris (Table 1).

A younger sister of the proband (family A, III-4), examined at 4 years of age, presented with similar clinical features. The pregnancy and delivery were uncomplicated, and the girl's developmental milestones were age appropriate. Physical examination revealed a height of 96.4 cm (*z* score, –1.02), a weight of 13.9 cm (*z* score, –1.05), and a head circumference of 47.8 cm (*z* score, –1.18). She had dysmorphism including a somewhat aged (progeroid) appearance with little subcutaneous fat, red eyes, a tiny, pinched

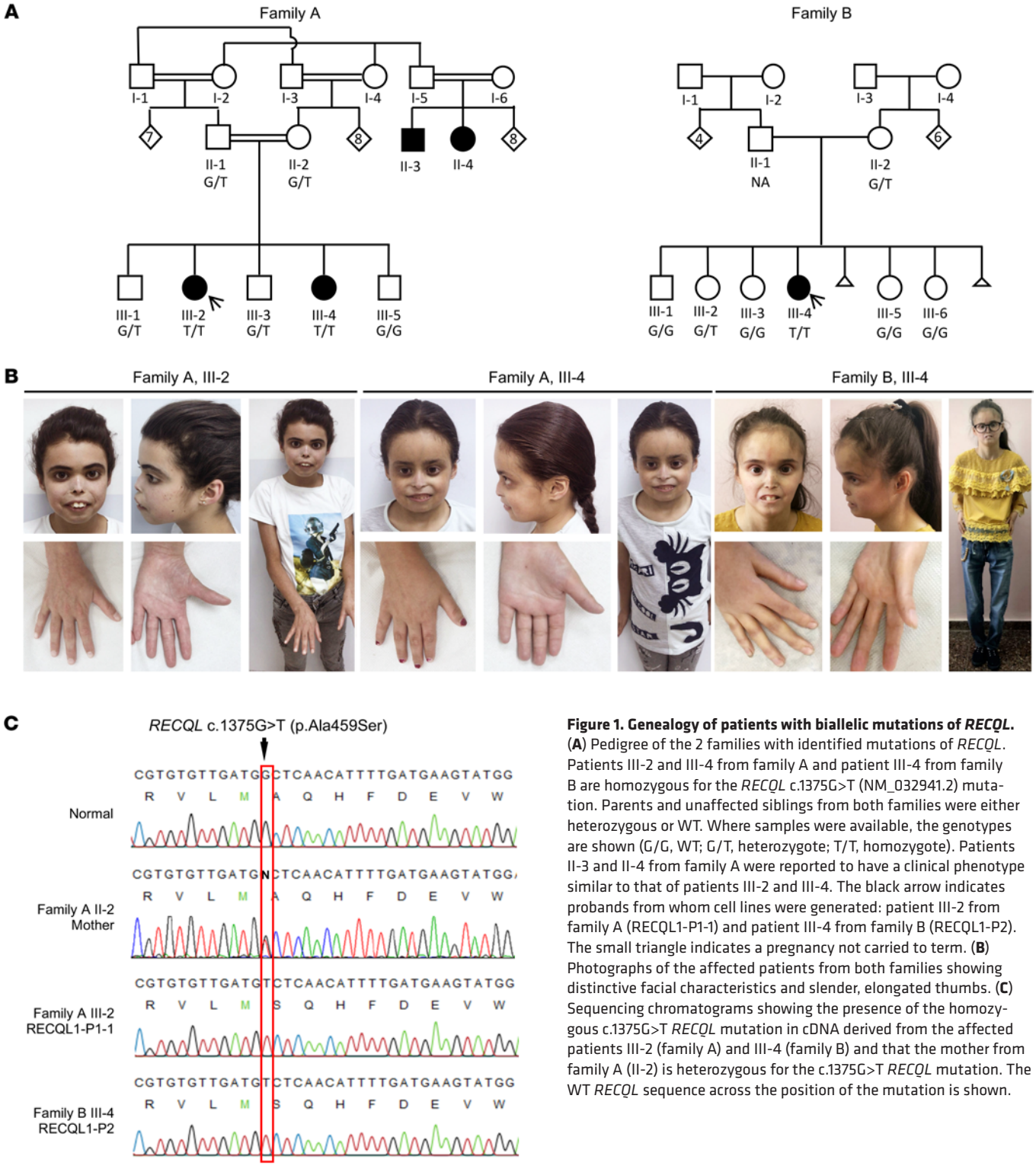


Figure 1. Genealogy of patients with biallelic mutations of *RECQL*. (**A**) Pedigree of the 2 families with identified mutations of *RECQL*. Patients III-2 and III-4 from family A and patient III-4 from family B are homozygous for the *RECQL* c.1375G>T (NM_032941.2) mutation. Parents and unaffected siblings from both families were either heterozygous or WT. Where samples were available, the genotypes are shown (G/G, WT; G/T, heterozygote; T/T, homozygote). Patients II-3 and II-4 from family A were reported to have a clinical phenotype similar to that of patients III-2 and III-4. The black arrow indicates probands from whom cell lines were generated: patient III-2 from family A (RECQL1-P1-1) and patient III-4 from family B (RECQL1-P2). The small triangle indicates a pregnancy not carried to term. (**B**) Photographs of the affected patients from both families showing distinctive facial characteristics and slender, elongated thumbs. (**C**) Sequencing chromatograms showing the presence of the homozygous c.1375G>T *RECQL* mutation in cDNA derived from the affected patients III-2 (family A) and III-4 (family B) and that the mother from family A (II-2) is heterozygous for the c.1375G>T *RECQL* mutation. The WT *RECQL* sequence across the position of the mutation is shown.

nose with anteverted nares, prominent premaxilla, and a smooth philtrum (Figure 1B). Her thumbs were long and slender with proximal insertion, and she had mild hirsutism of the back. We noted minor joint laxity of the fingers (Table 1). The family history was also positive for 2 common adult first cousins of the parents who had similar clinical features. Unfortunately, these relatives were not available for genetic evaluation or a detailed medical workup.

The proband of family B (family B, III-4) was a female and the fourth of 6 children born to parents of Middle Eastern descent with no known consanguinity (Figure 1A). She was referred for evaluation for the first time at the age of 5 years, 10 months for dysmorphism and dryness of skin. The pregnancy and delivery were uncomplicated. She was born at term, with a birth weight of 3500 grams. Her developmental milestones, including motor,

Table 1. Clinical description of the patients with the *RECQL* mutation

	Family A		Family B
Patient	III-2 (RECQL1-P1-1)	III-4 (RECQL1-P1-2)	III-4 (RECQL1-P2)
Variant (homozygous)	c.1375G>T; p.Ala459Ser	c.1375G>T; p.Ala459Ser	c.1375G>T; p.Ala459Ser
Cell line	RECQL1-P1-1	RECQL1-P1-2	RECQL1-P2
Sex	Female	Female	Female
Clinical features			
Gestation (wk)	Term	Term	Term
Age at last evaluation	9 yr 8 mo	4 yr 0 mo	14 yr 9 mo
Head circumference – birth	NA	NA	NA
Head circumference – current (*z* score)	50 cm (–1.64)	47.8 cm (–1.18)	50.8 cm (–2.92)
Length – birth	NA	NA	NA
Height – current (*z* score)	123.8 cm (–1.98)	96.4 cm (–1.02)	138.4 cm (–3.59)
Weight – birth	~3 kg	~3 kg	3.5 kg
Weight – current (*z* score)	22.5 kg (–2.05)	13.9 kg (–1.05)	22.1 kg (–8.47)
Growth retardation	Yes	No	Yes
Learning difficulties	No	No	No
Skin abnormalities	Photosensitivity; livedo reticularis; keratosis pilaris; xeroderma	Photosensitivity; xeroderma	Photosensitivity; thin skin; scaling; hirsutism; xeroderma
Facial abnormalities	Round face; redness of eyes; tiny, pinched nose with anteverted nares; prominent premaxilla; smooth philtrum; progeroid appearance	Redness of eyes; tiny, pinched nose with anteverted nares; prominent premaxilla; smooth philtrum; progeroid appearance	Mask, senile-like face (progeroid); deep-set eyes; absent lower-lid eyelashes; small ears with small, attached earlobes; prominent nasal bridge with a tiny, pinched nose with hypoplastic alae nasi; prominent premaxilla; thin lips; smooth philtrum
Eye abnormalities	Xerophthalmia; eyes remain open during sleep	Xerophthalmia	Deep-set eyes; hypoplastic/absent eyelashes
Skeletal abnormalities	Slender, elongated thumbs with hyperconvex nails; slight hyperextension of elbows	Slender, elongated thumbs with proximal insertion; hirsutism of the back; minor joint laxity	Slender, elongated thumbs with hyperconvex nails; arachnodactyly; slight hyperextension of elbows; severe wasting of muscles
Other abnormalities	Delayed eruption of permanent teeth		Irregular, crowded teeth with delayed eruption of permanent teeth
Immunology			
Recurrent infections	No	No	Early childhood; resolved
Anemia	No	No	Yes
Neutropenia	No	No	No
Immunoglobulins	NA	NA	NA
Other			Thrombocytopenia

NA, not available.

speech, and communication skills, were age appropriate. Her other medical problems at that time were thrombocytopenia of undetermined cause and recurrent chest infections. The parents reported that their child was photosensitive. Physical examination revealed a height of 110 cm (*z* score, –0.7), a weight of 13.5 kg (*z* score, –3.4), and a head circumference of 47 cm (*z* score, –2.9). Dysmorphic features included a mask senile-like face (progeroid), deep-set eyes, absent lower lid eyelashes, small ears with small, attached earlobes, a prominent nasal bridge with a tiny, pinched nose with hypoplastic alae nasi, prominent premaxilla, thin lips, and a smooth philtrum (Figure 1B). The proband had bilateral arachnodactyly, and her thumbs were slender and elongated, with hyperconvex nails. She had hirsutism of the lower limbs, and we observed thin, dry skin (xeroderma) with areas of desquamation (scaling), mainly on exposed body parts, suggestive of photosensitivity. The proband had thin extremities with hypoplastic muscles and subcutaneous fat. Follow-up measurements at age 14 years, 9 months revealed a height of 138.4 cm (*z* score, –3.59), a weight of 22.1 kg (*z* score, –8.47), and a head circumference of 50.8 cm (*z* score, –2.92) (Table 1). Neither family reported any history of breast cancer or other cancers. Genetic testing included chromosome analysis, chromosome breakage studies with diepoxybutane, and Sanger sequencing for mutations in *ERCC6* and *ERCC8*, all of which were normal.

Whole-exome sequencing identified a homozygous missense mutation of RECQL. To identify the genetic cause of the disorder found in family A, we performed whole-exome sequencing on DNA from the proband (III-2) of family A. After exclusion of nonauthentic variants and inconsistent mutations, data mining identified a predicted pathogenic variant in *RECQL* (chr12:21626557[hg19]: NM_032941.2; c.1375G>T; p.Ala459Ser — referred to as p.A459S) as the primary candidate (Figure 1C). This variant affects a highly

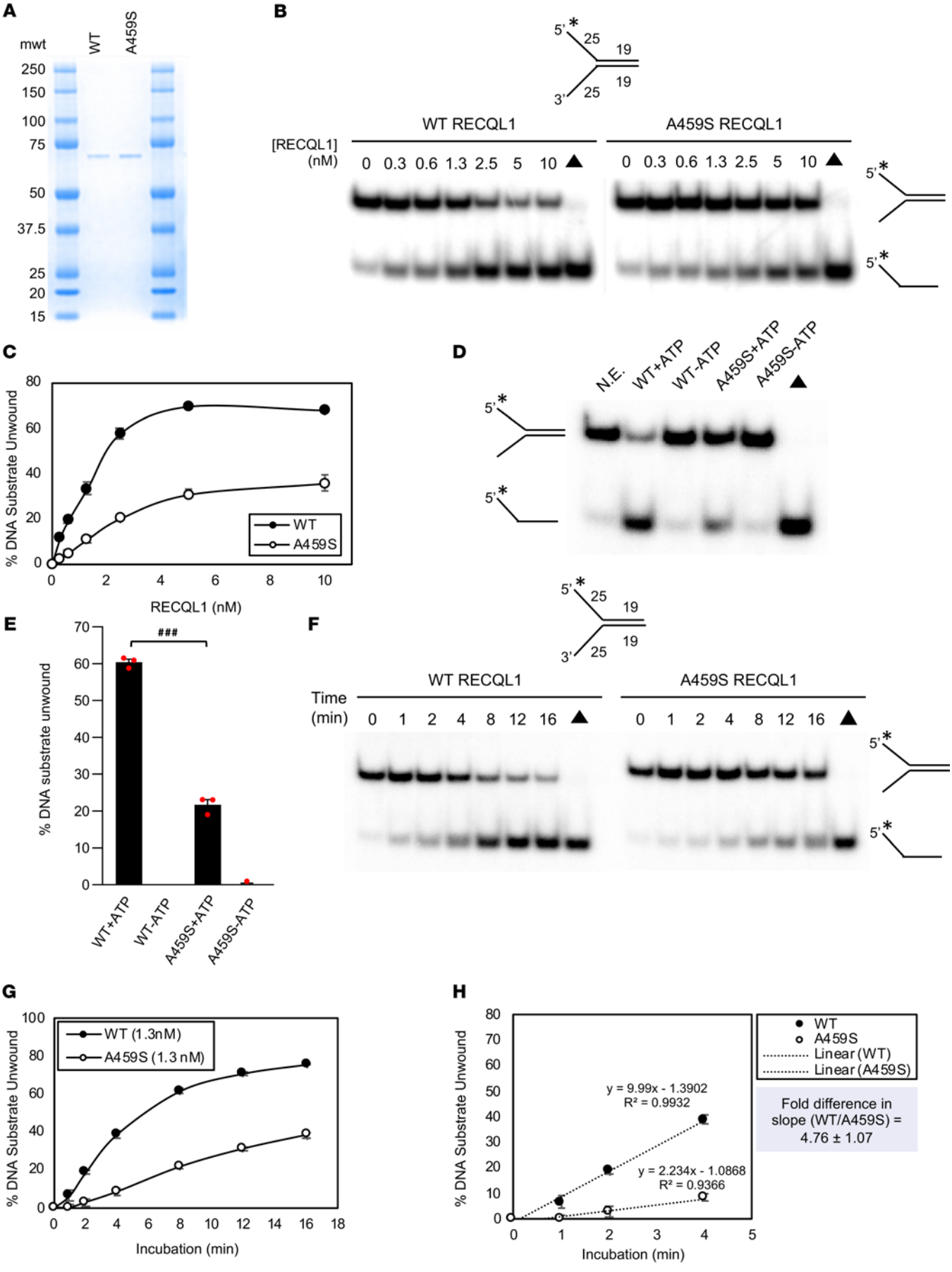

A
mwt
WT
A459S
250
150
100
75
50
37.5
25
20
15
B
5'*
25
19
19
3'
25
WT RECQL1
A459S RECQL1
[RECQL1] (nM)
0 0.3 0.6 1.3 2.5 5 10
0 0.3 0.6 1.3 2.5 5 10
5'*
5'*
C
% DNA Substrate Unwound
RECQL1 (nM)
WT
A459S
D
N.E.
WT+ATP
WT-ATP
A459S+ATP
A459S-ATP
5'*
5'*
E
% DNA substrate unwound
###
WT+ATP
WT-ATP
A459S+ATP
A459S-ATP
F
5'*
25
19
19
3'
25
WT RECQL1
A459S RECQL1
Time (min)
0 1 2 4 8 12 16
0 1 2 4 8 12 16
5'*
5'*
G
% DNA Substrate Unwound
WT (1.3nM)
A459S (1.3 nM)
Incubation (min)
H
% DNA Substrate Unwound
y = 9.99x - 1.3902
R² = 0.9932
y = 2.234x - 1.0868
R² = 0.9366
WT
A459S
Linear (WT)
Linear (A459S)
Fold difference in slope (WT/A459S) = 4.76 ± 1.07
Incubation (min)

Figure 2. The p.A459S mutation compromises RECQL1 helicase activity. (**A**) SDS polyacrylamide gel stained with Coomassie showing recombinant human WT RECQL1 and RECQL1-A459S (500 ng each). mwt, molecular weight. (**B**) The specified RECQL1 concentrations were tested for unwinding a radiolabeled 19 bp forked duplex DNA substrate (0.5 nM) in 15 minutes. Representative gels are shown. The asterisk indicates a 5′ radiolabel on the 19 bp forked duplex DNA substrate. The black triangle indicates the heat-denatured DNA substrate control used as a marker for duplex unwinding. (**C**) Quantitation of DNA unwinding from 3 independent experiments, with the SEM shown. AUC: WT (mean ± SEM: 578.3 ± 8.01); A459S (mean ± SEM: 254.3 ± 18.63). WT versus A459S AUC: $P < 0.0001$, by unpaired *t* test. (**D**) Representative gels showing analysis of helicase activity catalyzed by RECQL1 (2.5 nM) on a 19 bp forked DNA substrate in the presence or absence of 5 mM ATP. N.E., no enzyme. (**E**) Quantitation of DNA unwinding from 3 independent experiments, with the SEM shown. $^{###}P < 0.001$, by unpaired *t* test.(**F**) Kinetics analyses of unwinding by WT RECQL1 or RECQL1-A459S. Representative gel images show analysis of reaction mixtures containing 1.3 nM WT RECQL1 or RECQL1-A459S helicase incubated with a 19 bp forked duplex DNA substrate for the indicated durations. (**G**) Quantitation of DNA unwinding from 3 independent experiments, with the SEM shown. (**H**) Quantitation of DNA unwinding showing a linear trendline and slope of unwinding from 3 independent experiments. The SEM is shown. AUC: WT (mean ± SEM: 830.3 ± 11.35); A459S (mean ± SEM: 316.1 ± 10.3). WT versus A459S AUC: $P < 0.0001$, by unpaired *t* test.

conserved alanine residue (GERP score, 6.04) that lies within the ZBD of the RECQL1 protein (Supplemental Figure 1, A–C; supplemental material available online with this article; https://doi.org/10.1172/JCI147301DS1). Moreover, this variant is not found in the gnomAD or Greater Middle East (GME) variome databases, nor in our local databases of approximately 10,000 exomes. It is predicted to be pathogenic by several bioinformatics algorithms including combined annotation-dependent depletion (CADD) (score, 25.9), MutationTaster (score, 1.0), PolyPhen-2 (score, 0.846), and deleterious annotation of genetic variants using neural networks (DANN) (score, 0.9977). Notably, monoallelic alteration of the adjacent amino acid 458 (p.Met458Lys) has previously been linked with an increased predisposition for developing breast cancer. Moreover, functional studies of this mutation revealed that it significantly compromised the helicase activity of RECQL1 (14). Family B was identified because of the striking similarity of clinical features exhibited by the proband (III-4) and the 2 affected siblings from family A. Segregation analysis by Sanger sequencing of genomic DNA (gDNA) from both families confirmed segregation of this variant with the clinical phenotype (Figure 1A). All 3 affected individuals (III-2 and III-4 from family A and III-4 from family B) were homozygous for this variant, whereas the available parents and 8 healthy siblings were either heterozygous or WT [the logarithm of the odds (LOD) score ($\theta = 0$) was $Z = 3.311$].

To determine what impact the p.A459S mutation had on RECQL1 protein stability, we performed Western blotting on whole-cell extracts generated from lymphoblastoid cell lines (LCLs) derived from RECQL1 patient III-2 from family A (RECQL1-P1-1) and RECQL1 patient III-4 from family B (RECQL1-P2). We observed no obvious differences in the expression of RECQL1 protein in LCLs from the 2 affected patients when compared with the expression of RECQL1 in LCLs from 2 normal individuals (Supplemental Figure 1C). Moreover, the p.A459S mutant RECQL1 protein localized normally to the nucleus in the presence or absence of DNA damage and was still able to associate with PARP1, a known RECQL1 binding protein (ref. 14 and Supplemental Figure 1, D–F). Therefore, to gain insight into the pathogenesis of RECON syndrome, we used biochemical and cell biological approaches to study the effects of the p.A459S mutation on the enzymatic activity of RECQL1 and its roles in regulating the cellular DNA damage response.

RECQL1-A459S displays significantly reduced DNA unwinding activity on a preferred forked duplex DNA substrate. Given that it had been previously shown that mutating the residue preceding alanine-459 (methionine-458) to a lysine abolished helicase activity (16), this prompted us to biochemically characterize RECQL1-A459S and compare its properties with WT RECQL1. Initially, recombinant WT RECQL1 and mutant RECQL1 were expressed and purified from insect cells to near homogeneity (Figure 2A). Following this, using a 19 bp forked duplex as a substrate to measure its helicase activity, a simple protein titration of the WT and mutant RECQL1 proteins revealed that the p.A459S mutation substantially reduced its helicase activity. At a protein concentration of 2.5 nM, WT RECQL1 unwound nearly 60% of the DNA substrate compared with approximately 20% for mutant RECQL1 (Figure 2, B and C). To ascertain whether the DNA unwinding by RECQL1-A459S was ATP dependent, we incubated the mutant protein with the 19 bp forked duplex DNA substrate in the presence or absence of ATP. As predicted, RECQL1-A459S failed to unwind the DNA substrate when ATP was absent, consistent with the behavior of WT RECQL1 (Figure 2, D and E).

Kinetics analysis of RECQL1-dependent unwinding of the 19 bp forked DNA duplex showed a 2.6-fold reduction in the rate catalyzed by the p.A459S mutant compared with WT at a protein concentration of 0.3 nM (Supplemental Figure 2, A–C). Using a 4-fold greater concentration of RECQL1 protein (1.2 nM), the rate of helicase activity was reduced 4.8-fold for RECQL1-A459S (Figure 2, F–H), suggesting that the reduction in the unwinding rate on the short 19 bp forked duplex was in part protein concentration dependent.

RECQL1, like the other human RecQ helicases, shows significantly compromised helicase activity on longer duplex DNA substrates, suggesting that the enzyme lacks processivity (18, 19). This led us to assess helicase-catalyzed DNA unwinding by the WT and mutant RECQL1 proteins on a longer 31 bp forked duplex DNA substrate. As shown in Supplemental Figure 3, A and B, RECQL1-A459S displayed significantly reduced helicase activity on the 31 bp forked duplex compared with WT RECQL1. Approximately 3-fold less DNA substrate was unwound by RECQL1-A459S compared with WT RECQL1 at a protein concentration of 40 nM. This led us to perform a kinetics analysis of the WT and p.A459S RECQL1 proteins on the 31 bp forked duplex with 2 different concentrations of RECQL1. At a 30 nM RECQL1 concentration, we observed a 3.8-fold difference in the rate of unwinding (Supplemental Figure 3, C–E). We observed a similar reduction in the rate of unwinding by the p.A459S mutant at a RECQL1 protein concentration of 40 nM (Supplemental Figure 3, F–H).

Altogether, the findings from these helicase studies demonstrate that the p.A459S amino acid substitution in the ZBD of RECQL1 compromised its DNA unwinding activity, a result that was consistent with those of previous studies assessing the impact of other RECQL1 ZBD mutations on its helicase activity (16, 17).

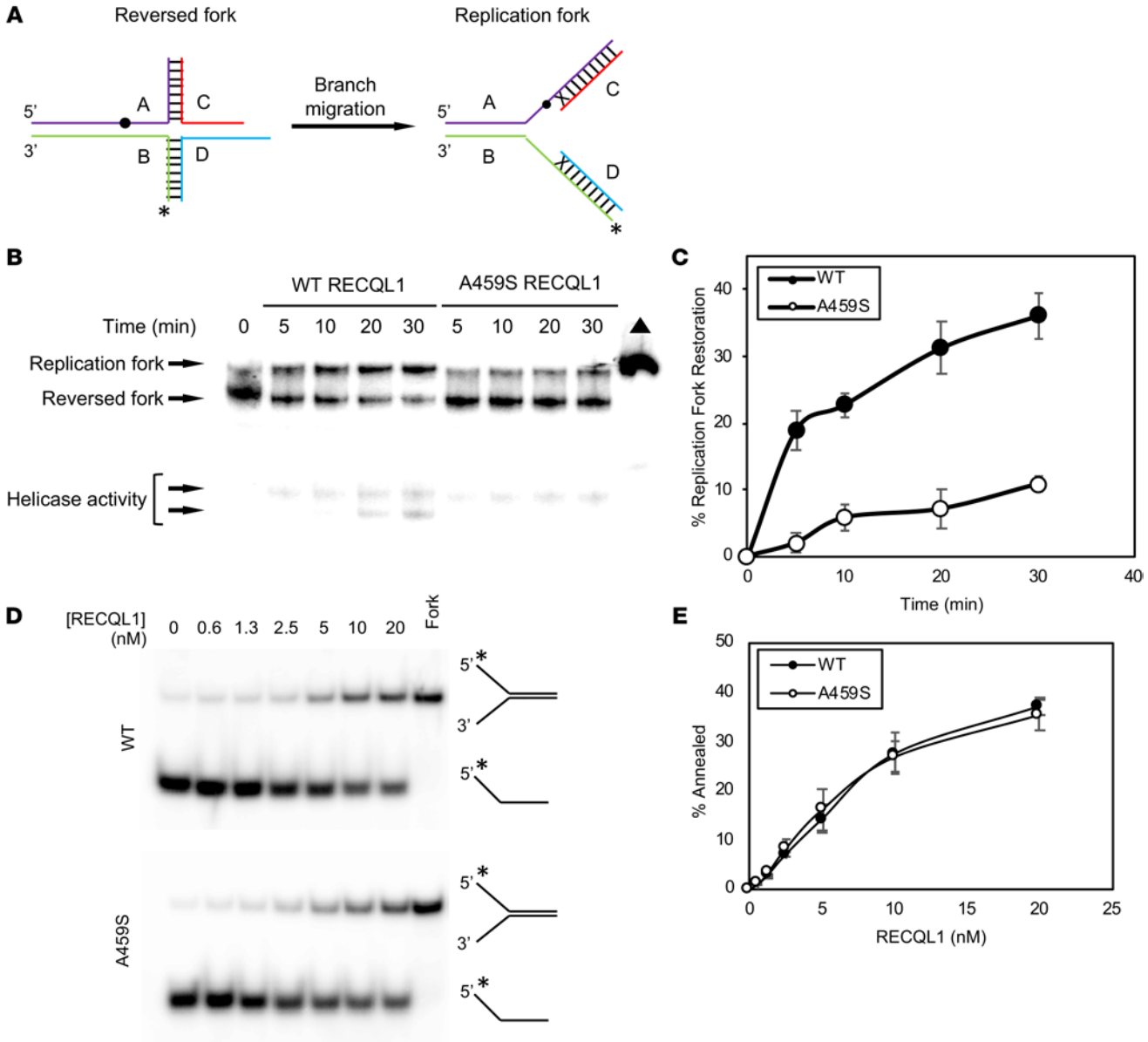


Figure 3. The p.A459S mutation compromises the ability of RECQL1 to remodel reversed replication forks but not its ability to catalyze SSA. (**A**) Depiction of the reversed and replication fork substrates used in this experiment. The black dot and "X" in the figure represent an isocytosine base and mismatched bases, respectively. These were added to minimize spontaneous conversion of the reversed fork into a replication fork. The asterisk indicates the 5′ end of the oligonucleotide that was radiolabeled with ^{32}P. (**B**) WT or A459S RECQL1 (20 nM) was incubated with 2 nM radiolabeled reversed fork substrate at 37°C for the indicated durations. A radiolabeled replication fork (2 nM, black triangle) was included as a marker. A representative gel is shown. (**C**) Quantitation of DNA unwinding from 3 independent experiments, with the SEM shown. AUC: WT (mean ± SEM: 709.5 ± 35.23); A459S (mean ± SEM: 174.4 ± 23.91). WT versus A459S AUC: $P < 0.0002$, by unpaired *t* test. (**D** and **E**) RECQL1 strand annealing activity was assessed by the formation of a 19 bp forked duplex DNA molecule from 2 partially complementary single-stranded oligonucleotides as a function of increasing RECQL1 concentration. (**D**) Two partially complementary oligonucleotides (1 radiolabeled at the 5′ end and the other unlabeled; 0.5 nM of each was incubated with the indicated concentrations of RECQL1 for 15 minutes at 37°C in the absence of ATP). A 19 bp forked duplex was loaded as a marker. Representative gel images are shown. (**E**) Quantitation of strand annealing activity from 3 independent experiments, with the SEM shown.

p.A459S RECQL1 poorly restores a replication fork from its regressed state. Since RECQL1 has been previously shown to restore replication forks that have been regressed (14), we used a reversed fork structure (Figure 3A) as a substrate in our in vitro RECQL1 enzymatic assays to assess whether the p.A459S mutation affected the ability of RECQL1 to remodel a reversed fork. Over a 30-minute time course, the p.A459S mutant RECQL1 consistently had a reduced ability to restore the replication fork compared with WT RECQL1 (Figure 3, B and C). We observed as much as a 7-fold difference in fork restoration at the 5-minute time point and at least a 3.5-fold difference at later time points in the reaction (Figure 3, B and C). Interestingly, we also observed a small but detectable amount of helicase activity using the reversed fork structure as a substrate (Figure 3B), and this activity was also reduced by the p.A459S mutation. This indicates that the p.A459S mutation not only compromises the ability of RECQL1 to unwind forked duplex DNA structures but also to remodel reversed forks in vitro.

Table 2. Comparison of the k_{cat} (s^{-1}), K_m (μM), and V_{max} (nM/s) for ATP hydrolysis by WT RECQL1 and RECQL1-A459S

Protein	k_{cat} (s^{-1})[A]	K_m (μM)[B]	V_{max} (nM/s)
WT RECQL1	103.5 ± 7.7	95.3 ± 8.2	28.3 ± 5.7
RECQL1-A459S	37.3 ± 13.3	48.4 ± 16.4	8.4 ± 2.8

[A]Reaction mixtures contained M13mp18 ssDNA (32 mM nucleotide phosphate), 1 mM ATP, and 20 nM RECQL1. [B]Reaction mixtures contained M13mp18 (32 mM nucleotide phosphate), 31.3 μM to 2 mM ATP range, and 40 nM RECQL1.

RECQL1-A459S retains SSA activity comparable to that of WT RECQL1. Purified human recombinant RECQL1 protein is also known to display potent strand annealing activity (19). To determine whether this activity is also affected by the p.A459S mutation, we examined the ability of mutant and WT RECQL1 proteins to anneal 2 partially complementary oligonucleotides to form a 19 bp forked DNA duplex. These experiments were performed in the absence of ATP to prevent helicase-catalyzed unwinding of the annealed forked duplex, which would normally serve as a canonical substrate for the RECQL1 helicase activity. As shown in Figure 3, D and E, the strand annealing activity of WT and mutant RECQL1 proteins was nearly identical over a range of protein concentrations, indicating that, despite the compromised helicase activity of RECQL1-A459S, its strand annealing activity remained intact.

RECQL1-A459S displays modestly reduced DNA substrate binding compared with WT RECQL1. Given that RECQL1-A459S has reduced helicase but proficient strand annealing activity compared with WT RECQL1, we wanted to examine their relative DNA binding capacities using EMSA, a sensitive technique that allows both visual evidence and quantitative assessment of nucleic acid binding. Although RECQL1 binds to various DNA substrates, it has been shown to preferentially bind a forked DNA duplex molecule over single-stranded or fully duplexed DNA molecules (11, 19). Therefore, we chose to study the DNA binding capabilities of WT and mutant RECQL1 proteins using the 19 bp forked duplex DNA substrate we had tested in the helicase assays. In this case, we omitted ATP or included ATPγS in the binding mixtures to prevent helicase activity. From these assays, we found that both mutant and WT RECQL1 proteins could bind the forked duplex DNA molecule, shifting the free radiolabeled DNA to 3 specific slower-migrating bands presumably representing the DNA substrate bound by monomeric and multimeric species (Supplemental Figure 4, A and B). However, quantitative assessment of the DNA binding isotherm data from binding incubations conducted in the absence of ATP indicated a 1.5-fold greater apparent K_D for RECQL1-A459S compared with WT RECQL1 (Supplemental Figure 4A), suggesting a modest decrease in the affinity of RECQL1-A459S for the forked duplex DNA compared with WT RECQL1. We detected a similar increase of 1.4-fold in the K_D value for RECQL1-A459S in the presence of ATPγS when compared with WT (Supplemental Figure 4B).

To further study the apparent difference in DNA binding between WT RECQL1 and RECQL1-A459S, we performed DNA binding assays in which a competitor oligonucleotide was used as a challenging agent after preincubation of the RECQL1 protein with the radiolabeled forked duplex DNA molecule (Supplemental Figure 5A). Both the mutant and WT RECQL1 proteins showed a similar reduction in DNA binding with an increasing concentration of unlabeled competitor (Supplemental Figure 5, B and C), suggesting that the stability of the preformed forked duplex–RECQL1 protein complex was similar for the WT and mutant forms of RECQL1.

Effect of the RECQL1-A459S mutation on kinetic parameters for ATP hydrolysis. To determine the ability of RECQL1-A459S to bind and hydrolyze ATP, we conducted a series of ATPase assays to measure the turnover rate constant (k_{cat}), the Michaelis constant (K_m), and the maximum velocity (V_{max}) for ATP hydrolysis. In kinetics assays with an ATP concentration of 1 mM, WT RECQL1 had a nearly 3-fold higher k_{cat} for ATP hydrolysis in the presence of the M13mp18 ssDNA effector compared with RECQL1-A459S (Table 2). In ATPase assays at varying ATP concentrations, WT RECQL1 had a 3-fold greater maximum velocity (V_{max}) and a 2-fold greater K_m compared with RECQL1-A459S (Table 2), suggesting that the diminished turnover of ATP catalyzed by the RECQL1-A459S mutant was not reflected by reduced nucleotide binding.

RECQL1-A459S protein retains its ability to oligomerize. To examine the effect of the RECQL1-A459S mutation on its ability to oligomerize, we performed size exclusion chromatography. As seen in previous studies (20, 21), the WT RECQL1 protein eluted from the column in 2 distinct peaks in the absence of ATP (Supplemental Figure 6). The RECQL1-A459S protein also eluted as 2 peaks at similar volumes, indicating that the mutant protein behaved similarly to the WT RECQL1 protein.

The hypomorphic p.A459S RECQL1 mutation causes a defect in the repair of abortive TOP1/2 lesions. Since RECQL1 was previously shown to be important for the repair of DNA damage caused by poisoning TOP1/2 (14, 22), and since the p.A459S mutation significantly compromised the helicase activity of RECQL1 (this study), it was conceivable that cell lines derived from the affected patients would exhibit aberrant repair of DNA breaks induced by exposure to CPT or ETOP. To investigate this, a skin fibroblast cell line was derived from patient III-2 from family A (named RECQL1-P1-1), immortalized with hTERT, and complemented with either an empty vector or a vector expressing WT or p.A459S-mutant RECQL1. We verified the expression of the exogenous RECQL1 by Western blotting (Supplemental Figure 7A). Following this, we exposed the cell lines to low-dose CPT or ETOP for a short period of time and then incubated them in drug-free media to allow time for repair to occur. To monitor DNA DSB induction and repair, we quantified 53BP1 foci over a 24-hour time course (Figure 4A and Supplemental Figure 7B). Consistent with a role for RECQL1 in the repair of TOP1/2-associated DSBs, patients' cells expressing either the empty vector or the p.A459S-mutant RECQL1 had higher numbers of 53BP1 foci in cells throughout a 24-hour time course following exposure to CPT or ETOP than did cells expressing WT RECQL1, despite equal levels of DNA damage being induced in all 3 cell lines and no obvious differences in the cell-cycle profile observed throughout this time course (Figure 4A and Supplemental Figure 7C). Interestingly, even in the absence of DNA-damaging agents, cells containing the empty vector or expressing the p.A459S RECQL1 mutant exhibited higher numbers of spontaneous 53BP1 foci compared with cells expressing WT RECQL1 (Figure 4A and Supplemental Figure

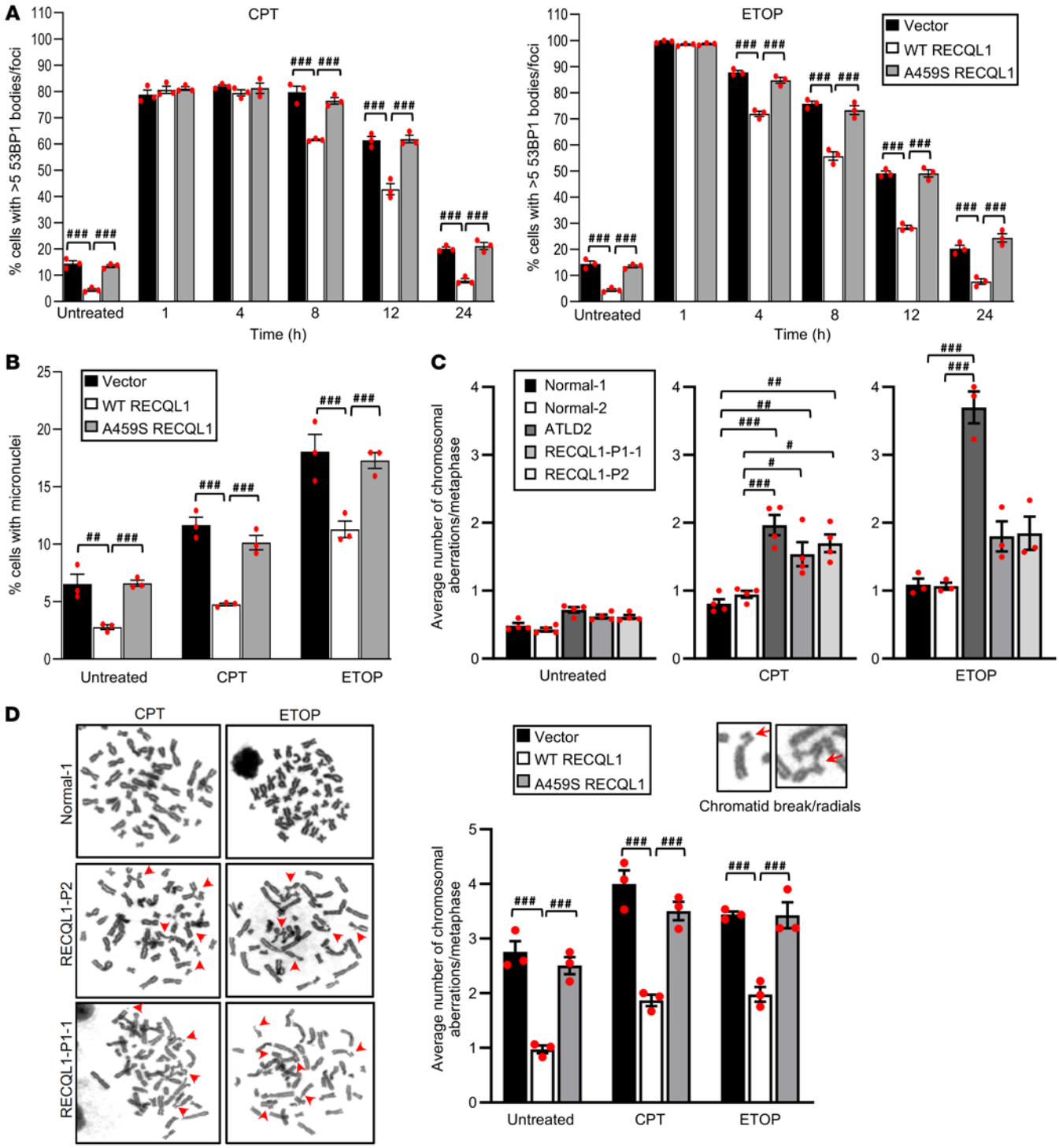


Figure 4. Complementation of RECQL1-P1-1 fibroblasts with WT RECQL1 restores normal repair of DNA damage induced by CPT or ETOP. (**A**) Quantification of 53BP1 foci in complemented patient RECQL1-P1-1 fibroblasts before and after treatment with 100 nM CPT (1 h) or 1 μM ETOP (30 min). 53BP1 foci in untreated cells and cells 24 hours after DNA damage induction were quantified in the G_1 phase only (mitosin negative) to assess the amount of replication damage induced by CPT or ETOP that had transited into the following cell cycle. 53BP1 foci in cells 1 to 12 hours after DNA damage induction were quantified in the S/G_2 phase only (mitosin positive) to monitor the kinetics of repair in damaged S/G_2-phase cells. The mean of 3 independent experiments is shown with the SEM. A minimum of 300 cells were counted per time point. $^{###}P < 0.001$, by 2-way ANOVA with Tukey's multiple-comparison test. (**B**) Micronuclei were quantified from cells described in **A**, before and 24 hours after exposure to CPT or ETOP. The mean of 3 independent experiments is shown with the SEM. A minimum of 500 cells were counted per time point. $^{##}P < 0.01$ and $^{###}P < 0.001$, by 2-way ANOVA with Tukey's multiple-comparison test. (**C** and **D**) Quantification of chromosome aberrations in (**C**) 2 normal LCLs, 2 RECQL-mutant LCLs, and an ATLD LCL and (**D**) complemented patient RECQL1-P1-1 fibroblasts before and 24 hours after chronic exposure to low-dose CPT (5 nM) or ETOP (50 nM). Chromosome aberrations include chromatid/chromosome gaps and breaks, chromatid/chromosome fragments, and chromosome radials and exchanges. Representative images of each type of aberration are shown. Data show the mean ± SEM of 3 independent experiments. A minimum of 50 metaphases were counted per cell line in each experiment. $^{#}P < 0.05$, $^{##}P < 0.01$, and $^{###}P < 0.001$, by 2-way ANOVA with Tukey's multiple-comparison test (**C** and **D**).

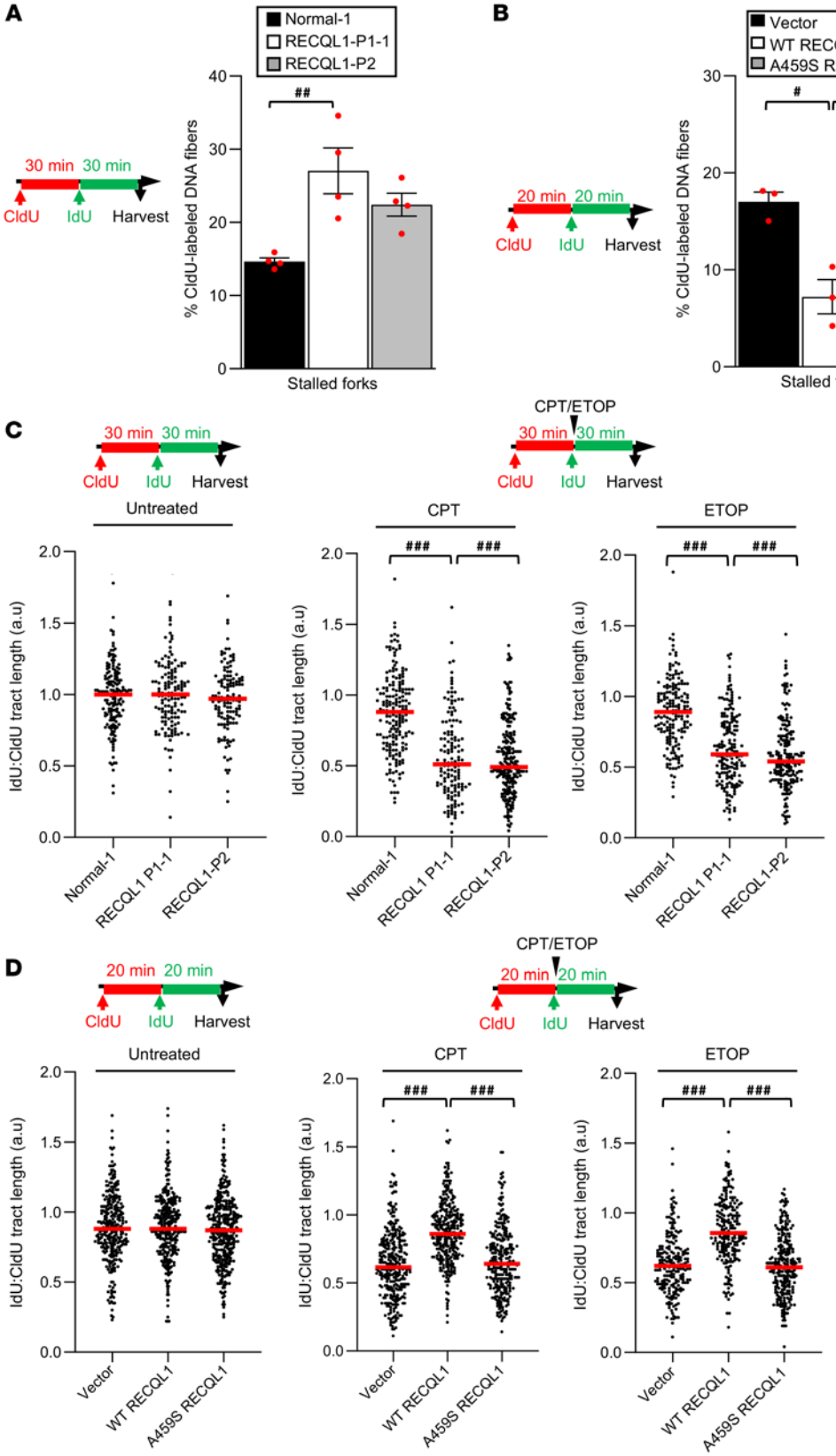


Figure 5. Cells from a patient with RECON syndrome display a reduced efficiency of replication in the presence of TOP1/2 inhibitors. (**A**) LCLs and (**B**) complemented RECQL1-P1-1 patient fibroblasts were sequentially labeled with CldU (red) and IdU (green) as shown. Stalled forks (red-only tracks) were quantified. The mean of 4 independent experiments is shown. A minimum of 200 forks were counted per condition. $^{\#}P < 0.05$ and $^{\#\#}P < 0.01$, by 1-way ANOVA with Tukey's multiple-comparison test. (**C**) LCLs and (**D**) complemented fibroblasts were sequentially labeled with CldU and IdU (with or without 50 nM CPT or ETOP) as shown. The length of the CldU and IdU tracks of dual-labeled DNA fibers (>150 per condition) was measured, and the ratio of IdU/CldU track length was calculated, which represents the efficiency of replication in the presence or absence of CPT or ETOP. The median of 3 independent experiments is shown (red line). $^{\#\#\#}P < 0.001$, by Kruskal-Wallis test with Dunn's multiple comparison.

7B). To further validate these observations, we quantified the formation of micronuclei as a marker of genome stability in all 3 cell lines, before and after exposure to CPT or ETOP. In keeping with the 53BP1 quantification results, cells containing the empty vector or expressing p.A459S-mutant RECQL1 exhibited significantly greater numbers of spontaneous and CPT- or ETOP-induced micronuclei than did their WT RECQL1–expressing counterparts (Figure 4B). Consistent with this, RECQL1 CRISPR-KO

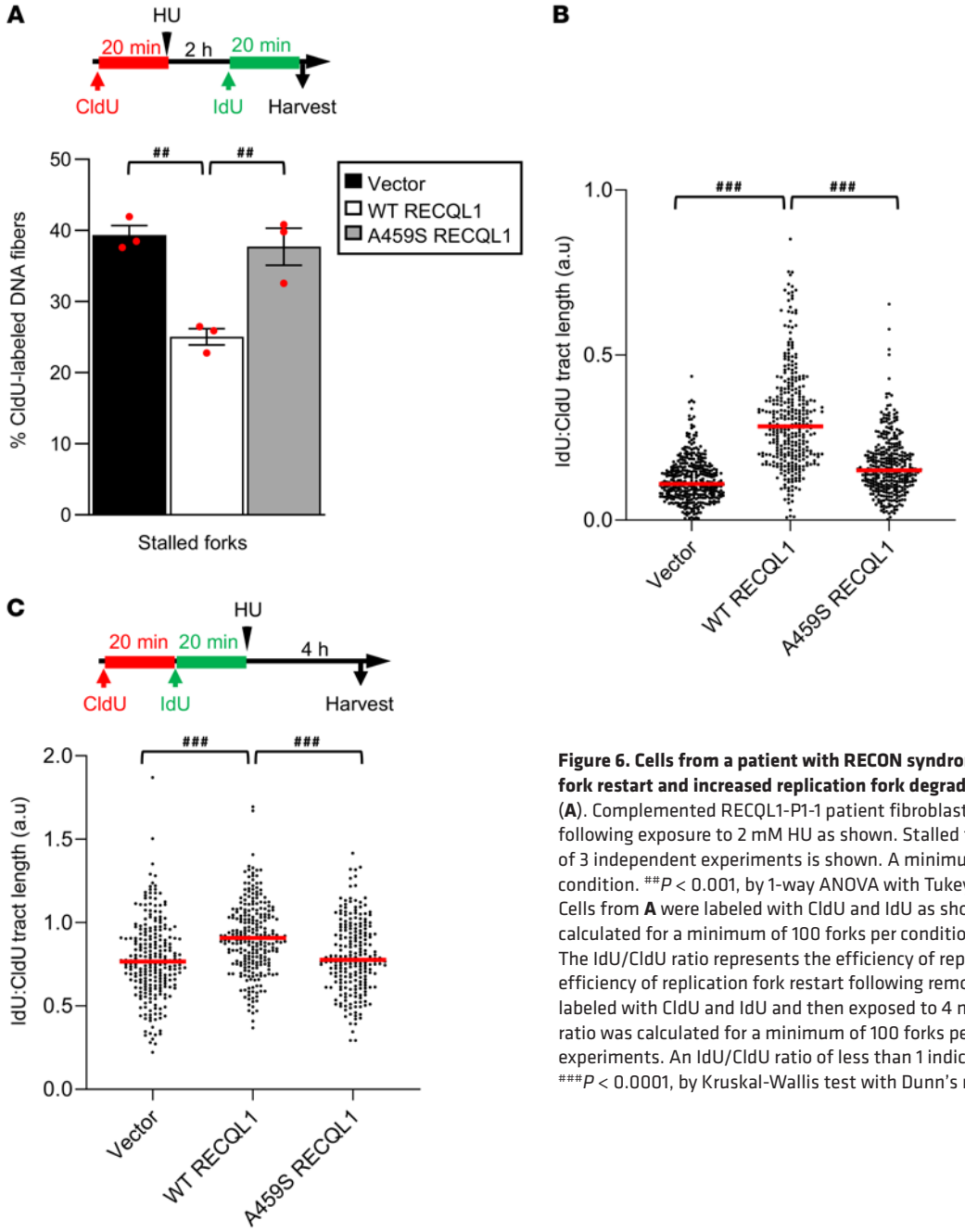


Figure 6. Cells from a patient with RECON syndrome exhibit reduced replication fork restart and increased replication fork degradation following exposure to HU. (**A**). Complemented RECQL1-P1-1 patient fibroblasts were labeled with CldU and IdU following exposure to 2 mM HU as shown. Stalled forks were quantified. The mean of 3 independent experiments is shown. A minimum of 200 forks were counted per condition. $^{\#\#}P < 0.001$, by 1-way ANOVA with Tukey's multiple-comparison test. (**B**) Cells from **A** were labeled with CldU and IdU as shown in **A**. The IdU/CldU ratio was calculated for a minimum of 100 forks per condition from 3 independent repeats. The IdU/CldU ratio represents the efficiency of replication in the absence HU and the efficiency of replication fork restart following removal of HU. (**C**) Cells from **A** were labeled with CldU and IdU and then exposed to 4 mM HU as shown. The IdU/CldU ratio was calculated for a minimum of 100 forks per condition from 3 independent experiments. An IdU/CldU ratio of less than 1 indicates replication fork degradation. $^{\#\#\#}P < 0.0001$, by Kruskal-Wallis test with Dunn's multiple comparison (**B** and **C**).

HeLa cells complemented with empty vector or mutant RECQL1 showed a similar increase in residual 53BP1 foci and micronuclei 24 hours after exposure to CPT or ETOP when compared with KO cells complemented with WT RECQL1 (Supplemental Figure 8, A–C). However, under the growth conditions used in this study, RECQL1-KO HeLa cells did not show significant hypersensitivity to either CPT or ETOP as assessed by a colony survival assay (Supplemental Figure 8D, 8E), suggesting that more sensitive methods of measuring DNA damage repair are required to assess the impact of RECQL1 deficiency on genome stability.

To evaluate more directly what affect the p.A459S RECQL1 mutation had on DNA repair and genome stability, we quantified chromosome breakage by analysis of metaphase spreads from LCLs derived from patients RECQL1-P1-1 and RECQL1-P2. In keeping with our previous observations quantifying 53BP1 foci, the RECQL1-P1-1 and RECQL1-P2 LCLs had higher levels of spontaneous and CPT- or ETOP-induced chromosome breakage than did 2 normal LCLs. Notably, the chromosome breakage phenotype observed in the 2 RECQL1-mutant LCLs was comparable to that seen in a LCL derived from a patient with ataxia telangiectasia–like disorder (ATLD) carrying a hypomorphic homozygous truncating mutation in *MRE11A* (22), following exposure to CPT, but was significantly lower than that seen in the ATLD cell line following exposure to ETOP (Figure 4C). We observed a similar pattern when quantifying spontaneous and CPT- or ETOP-induced chromosome radial exchanges in these cell lines (Supplemental Figure 9A). Important-

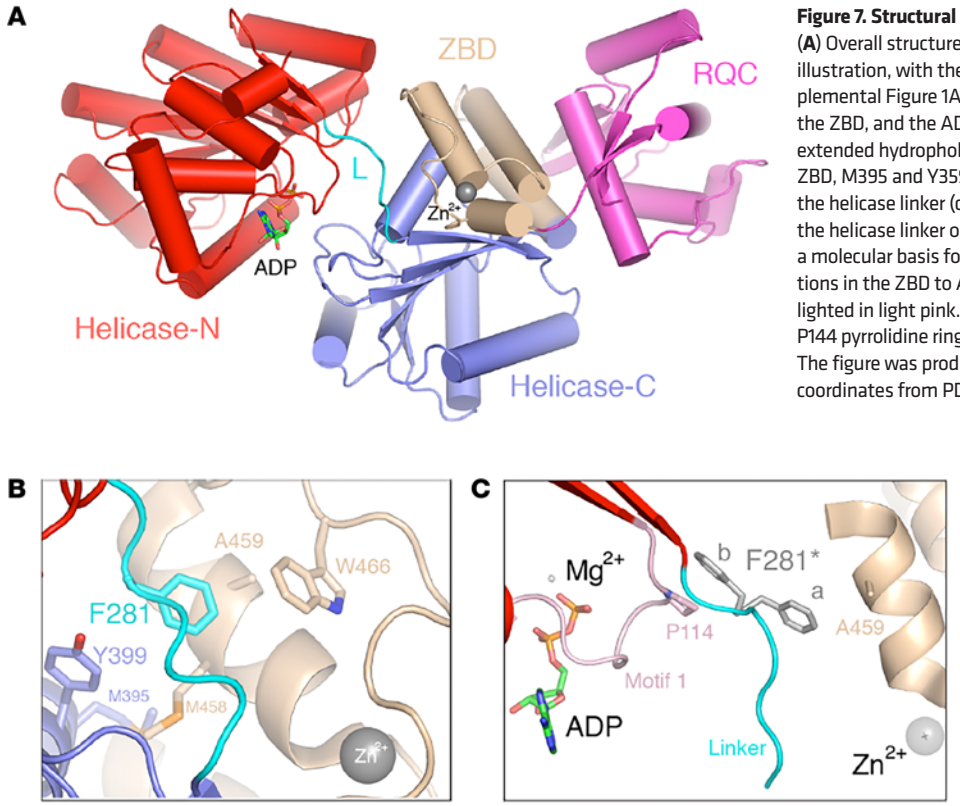


Figure 7. Structural modeling of the RECQL1 p.A459S mutation. (**A**) Overall structure of the RECQL1 monomer shown in a ribbons illustration, with the individual domains colored according to Supplemental Figure 1A. The gray sphere represents the Zn^{2+} ion within the ZBD, and the ADP is shown as sticks. (**B**) A459 forms part of an extended hydrophobic cluster involving W466 and M458 from the ZBD, M395 and Y359 from the helicase-C domain, and F281 from the helicase linker (cyan). (**C**) Two conformations of F281 within the helicase linker observed in the ADP-bound structure suggest a molecular basis for the dynamic coupling of structural perturbations in the ZBD to ATPase/helicase activity. The P-loop is highlighted in light pink. Conformation "b" of F281 stacks against the P144 pyrrolidine ring, while conformation "a" packs against A459. The figure was produced using PyMOL (https://pymol.org/2/) and coordinates from PDB accessions 2V1X and 2WWY (37, 47).

ly, both the increased spontaneous and CPT- or ETOP-induced chromosome breakages were also observed in fibroblasts from patient RECQL1-P1 and could be complemented by the expression of exogenous WT but not mutant A459S RECQL1 (Figure 4D).

While the precise mechanism in which RECQL1 functions to mediate DSB repair is unclear, several reports have suggested that, like other RecQ helicases, RECQL1 regulates HR by affecting the interaction of the strand exchange protein Rad51 with DNA during repair (13, 23). To ascertain whether the underlying DNA repair defect in patient-derived cell lines could be caused by aberrant regulation of Rad51, we exposed the isogenic complemented fibroblasts to CPT or ETOP and then fixed and stained them with antibodies against Rad51 and mitosin (a marker of S/G_2 cells). Quantification of Rad51 foci in S/G_2 cells by fluorescence microscopy revealed that, although the cells containing an empty vector or expressing mutant RECQL1 had higher levels of spontaneous Rad51 than did the cells complemented with WT RECQL1 (Supplemental Figure 9B), we observed no difference between the 3 cell lines in the percentage of S/G_2 cells with more than 10 Rad51 foci following exposure to either CPT or ETOP at both early and late time points (Supplemental Figure 9C). Consistent with the increased spontaneous Rad51 foci in the RECQL1-mutant fibroblasts, LCLs derived from both RECQL1-P1-1 and RECQL1-P2 exhibited a mild increase in spontaneous and DNA damage–induced sister chromatid exchanges (Supplemental Figure 9D). Similar observations were reported for *Recql*-KO mouse embryo fibroblasts exposed to ionizing radiation (13). Importantly, this phenotype was recapitulated in the RECQL1 CRISPR-KO HeLa cells and could be complemented by reexpression of WT but not p.A459S-mutant RECQL1 (Supplemental Figure 9E). Taken together, these results suggest that the defective repair of CPT- or ETOP-induced DNA damage may arise because of defective DNA damage response (DDR) signaling and/or an inability of the replisome to progress past these lesions, resulting in the transiting of underreplicated DNA through the cell cycle to the following G_1 phase. To investigate the first possibility, LCLs from 2 normal individuals and the 2 affected RECQL1-mutant patients (RECQL-P1-1 and RECQL1-P2) were transiently exposed to CPT or ETOP, and, following the induction of DNA damage, early and late time points were set to examine the activation of the DDR by Western blotting using phosphorylated ATM (p-ATM), p-SMC1, p-Nbs1, p-Chk1, p-RPA2, and p-H2AX as markers. Despite some mild variability in the level of the DDR induced by CPT or ETOP, both RECQL1-mutant cell lines showed robust activation of the ATM-dependent DDR (Supplemental Figure 10), suggesting that defective DDR signaling is not the underlying cause of compromised repair of CPT- or ETOP-induced DNA lesions in RECQL1-mutant cells.

An inability to repair TOP2-associated DSBs in cells derived from patients with RECON syndrome does not compromise the induction or repair of DSBs within the MLL locus. It is known that TDP2, MRE11, and components of the NHEJ DSB repair pathway are critical for the repair of TOP2-induced DSBs, especially within the *MLL* locus, which frequently undergoes chromosomal translocation if misrepaired (24, 25). Given the inability of cells from patients with RECON syndrome to efficiently repair ETOP-induced DSBs, we sought to investigate whether the hypomorphic p.A459S RECQL1 mutation present in these cells was associated with aberrant repair of DSBs within the *MLL* locus. Using C-Fusion 3D, a high-throughput imaging methodology to probe chromosomal breakage and rare translocations in single cells (25), we exposed 2 normal LCLs,

LCLs from a patient with a TDP2 mutation, and the LCLs from 2 patients with RECON syndrome to ETOP and monitored *MLL* locus breakage and translocation to the *ENL* locus. Notably, while the TDP2 mutant LCL displayed a high frequency of breakage of the *MLL* gene locus and translocation to the *ENL* locus following exposure to ETOP, we did not observe this in either of the RECQL1-mutant LCLs (Supplemental Figure 11, A and B). These results suggest that RECQL1 does not play a major role in the repair of TOP2-dependent DSBs located within the *MLL* locus.

Cells from patients with RECON syndrome exhibit a reduced ability to replicate in the presence of abortive topoisomerase lesions. It was reported that RECQL1 is required to restart stalled replication forks following the pharmacological inhibition of TOP1 and that cells lacking RECQL1 activity accumulate reversed forks in the presence of CPT (14). To investigate the impact of the RECQL1 p.A459S mutation on replication, we carried out DNA fiber analysis using LCLs from the affected RECQL1 patients in the presence or absence of CPT or ETOP. Interestingly, even in the absence of exposure to genotoxins, both RECQL1 LCLs had an increase in spontaneously stalled forks indicative of higher levels of endogenous replication stress (Figure 5A). Although our analysis cannot distinguish between stalled and reversed forks, as they would both give rise to CldU-only fibers, it is plausible that our observations are consistent with a previous study demonstrating that depletion of RECQL1 results in an increase in reversed forks, even in the absence of exogenously induced DNA damage (26, 27). Following exposure to either CPT or ETOP, our DNA fiber analysis also revealed that both patient RECQL1-mutant cell lines were unable to efficiently replicate in the presence of abortive TOP1 or TOP2-induced DNA lesions, despite the lack of gross alterations in replication fork speed or new origin firing prior to treatment (Figure 5C and Supplemental Figure 12, A and B). Notably, both the spontaneous and CPT- or ETOP-induced replication phenotypes were also observed in the patient-derived fibroblasts and could be complemented by the expression of WT, but not mutant p.A459S, RECQL1 (Figure 5, B and D, and Supplemental Figure 12, C and D). Taken together, these data suggest that the clinically relevant p.A459S mutation in the RECQL1 ZBD, which perturbs its catalytic activity, compromises the ability of RECQL1 to restart reversed replication forks.

Cells from individuals with RECON syndrome exhibit a reduced ability to efficiently restart HU- and MMS-damaged replication forks. It was previously determined that RECQL1, like other helicases such as WRN (26), DNA2 (26), and BLM (28), plays a role in promoting the restart of HU-stalled forks (29). To determine whether the cell lines derived from patients with RECON syndrome exhibit a global inability to restart replication forks that is not just restricted to forks stalled by abortive topoisomerase cleavage complexes, we performed DNA fiber analysis with RECQL-P1-1–complemented fibroblasts following a transient exposure to high-dose HU. Interestingly, this analysis demonstrated that the p.A459S mutation significantly compromised the ability of replication forks transiently stalled by HU to restart efficiently (Figure 6A). Importantly, this phenotype was also recapitulated in the RECQL1 CRISPR-KO HeLa cells complemented with either an empty vector or the p.A459S RECQL1 mutant (Supplemental Figure 12E). Furthermore, we found that the efficiency of replication progression for those forks that did manage to restart following release from HU was also severely affected in the RECQL-P1-1 fibroblasts complemented with an empty vector or the p.A459S mutant compared with those complemented with WT RECQL1 (Figure 6B). These data suggest that RECQL1 may be important for the restart of all types of stalled replication forks, irrespective of the causative DNA lesion. In keeping with this, the p.A459S mutant also compromised the ability of cells to restart replication in the presence of DNA alkylation damage induced by MMS exposure, accompanied by increased chromosome breakage and cell death (Supplemental Figure 13).

Last, it has been suggested that RECQL1, in a manner similar to that of WRN and DNA2 (26), also functions to protect stalled forks from uncontrolled nucleolytic degradation. Therefore, to assess whether the inability of the p.A459S-mutant RECQL1 protein to efficiently restart HU-stalled forks is due to excessive fork degradation, we sequentially labeled the 3 isogenic complemented fibroblast cell lines with CldU and IdU and then exposed them to 4 mM HU for 5 hours. We then quantified replication fork stability by calculating the ratio of CldU- to IdU-labeled fibers. As shown in Figure 6C, RECQL-P1-1 fibroblasts complemented with empty vector and the p.A459S exhibited a mild increase in replication fork degradation after prolonged exposure to HU that could be complemented following the expression of WT RECQL1. This suggests that the replication fork restart defect present in the cells derived from patients with RECON syndrome was not only due to an inability of the mutant RECQL1 to remodel reversed forks but also resulted from the degradation of stalled forks.

Discussion

Despite the cloning of *RECQL* over 25 years ago (10), the role that it plays within the cell to maintain genome stability remains relatively unclear. In contrast, functional insight into how other RecQ helicase family members, such as BLM, WRN, and RECQL4, protect the genome from deleterious DNA damage has been greatly facilitated by the identification of human disorders caused by mutations in these genes. However, even with the rapid advances in whole-exome/genome sequencing technology, mutations of the 2 remaining RecQ helicase genes (*RECQL* and *RECQL5*) have yet to be linked to an inherited chromosomal instability syndrome. Here, we describe the identification of a human chromosomal instability disorder, which we named RECON syndrome (RECql ONe), caused by biallelic missense mutations of *RECQL*. Notably, although it has been suggested that the function of RECQL1 may be redundant with other RecQ helicases such as BLM (30), the individuals affected by the RECQL1 p.A459S mutation exhibit a clinical phenotype distinct from that of BS, WS, and the 3 RECQL4-associated disorders, suggesting that RECQL1 is not redundant with WRN, BLM, or RECQL4 and has unique functions during human development.

Although individuals with BS or one of the RECQL4-associated disorders are clinically distinguishable, they do exhibit an overlap of symptoms, such as pre- and postnatal growth retardation, facial erythema that worsens upon sun exposure, poikiloderma, skin hypo- and hyperpigmentation, alopecia, and an increased predisposition for cancer, which is probably reflective of common cellular processes that the encoded proteins have been reported to take part in, e.g., DSB end-resection and DNA replication (7, 8, 28, 31). In comparison with the clinical features of patients with BS,

RTS, RAPADILINO, or BGS, those with RECON syndrome only share postnatal growth retardation, even though RECQL1 is also implicated in regulating DSB repair and processing replication intermediates (14, 26, 29, 32).

In contrast, individuals with BS can be differentiated by the presence of microcephaly, immunodeficiency, and type 2 diabetes, whereas patients with a RECQL4-associated disorder can be identified by absent or hypoplastic thumbs, radial ray defects, absent or hypoplastic patellae, limb malformations, cataracts, reduced bone density, anemia, neutropenia, and craniosynostosis.

It appears that the defining clinical features of RECON syndrome include skin photosensitivity, xeroderma, and a progeroid-like facial appearance with a tiny, pinched nose and prominent premaxilla. Interestingly, the progeroid-like facial appearance, growth retardation, and muscle wasting are somewhat reminiscent of WS, and although it is likely that the affected patients are currently too young to ascertain whether they have any other clinical signs of premature aging, it is tempting to speculate that this represents another progeroid syndrome (33, 34).

Although it is apparent that the clinical phenotype exhibited by the affected individuals carrying *RECQL* mutations is relatively mild when compared with other RecQ-associated disorders, it should be noted that these individuals are not null for RECQL1 and that the severity of the resulting clinical symptoms is likely to be tempered by the presence of some residual protein function. In addition, it is possible that some of the features of the disease are specific to this particular *RECQL* mutation and/or were modified by the similar genetic background of the 2 affected families. As such, the range and severity of the clinical symptoms linked with RECQL1 dysfunction will only be properly determined following the identification of additional patients. In relation to this, it has been reported by 2 laboratories that heterozygous mutations of *RECQL* are associated with an increased risk of breast cancer (15, 16), although this association has been disputed by several other groups (35, 36). Interestingly, one of the identified breast cancer–associated variants in *RECQL* altered the amino acid residue proximal to the RECON syndrome *RECQL* mutation. Despite this, none of the heterozygous carriers of the p.A459S mutation in either family A or B has reported developing breast cancer. Thus, it is plausible that this *RECQL* variant might not be associated with an increased cancer predisposition, albeit the carrier frequency for the p.A459S mutation is extremely low. However, since we have not directly compared the pathogenic impact of the syndrome and cancer-associated mutations of *RECQL* on its enzymatic activities and roles in regulating DNA replication, we acknowledge that it is difficult to make any conclusions regarding whether the p.A459S mutation may predispose individuals to breast cancer. As such, further studies to address the genotype-phenotype relationship linking the molecular, cellular, and clinical characteristics of individual RECQL1 mutations are warranted.

It has been suggested that the main function of RECQL1 is to promote the restart of reversed replication forks induced by abortive TOP1-cleavage complexes, which in turn is inhibited via an interaction of RECQL1 with PARP1 (14, 26). Interestingly, we detected a replication defect in cells from patients with RECON syndrome by DNA fiber analysis following the pharmacological inhibition of either TOP1 or TOP2, without a requirement to suppress PARP1 activity. This finding suggests that RECQL1 plays a more prominent role in regulating the restart of replication forks in the presence of abortive topoisomerase complexes than was perhaps thought and that this function is only partly dependent on PARP1.

The ability of RECQL1 to restart forks through branch migration of a reversed fork was shown to require its ATPase activity (14). While the p.A459S mutation lies outside the RECQL1 helicase domain, it has been previously demonstrated that mutating conserved cysteine residues within the ZBD compromises both its ATPase and DNA unwinding activities (11, 12). In keeping with this, we have shown that the p.A459S mutation also substantially reduced the ATPase, DNA unwinding, and branch-migrating activities of RECQL1. Examination of the available crystal structures of human RECQL1 showed that the ZBD is spatially juxtaposed with the helicase ATP-binding cleft, which is located between the 2 N-terminal domains (Figure 7A). Interestingly, A459 contacts F281 located within the linker region between the 2 helicase domains that appears to adopt 2 conformations in the GDP-bound structure (37), one of which packs directly against P114 within the P-loop/Walker A/Motif1 region. Since A459 itself forms part of a hydrophobic cluster within the ZBD core that is likely perturbed by mutation to a more polar and bulkier serine residue, the presence of the serine residue may affect the ability of F281 to adopt these different conformations, thus potentially offering a molecular explanation for the effects of the p.A459S mutation on both ATPase and helicase activity (Figure 7, B and C). In a manner similar to the RECQL1 p.A459S mutation, disease-causing missense mutations in the ZBD of BLM also compromise its ATP hydrolysis and DNA-unwinding activities (38, 39). However, unlike RECQL1, BLM also contains a helicase and RNase C-terminal (HRDC) domain, which is required for Holliday junction dissolution (40). Therefore, even though pathogenic missense mutations have been identified in the conserved ZBD of BLM and RECQL1, the functional impact and clinical consequences of these mutations are likely to be distinct, given the unique structural architecture of the respective RecQ helicases.

Taken together, it is likely that the replication defects we observed in cells from patients with RECON syndrome are attributed to an inability of RECQL1 to restart reversed forks due to compromised ATP-dependent helicase/branch migration activity. Fork reversal is thought to be a ubiquitous response to most types of replication stress and is essential for both the repair and restart of damaged replication forks. Therefore, if RECON syndrome represents a disease of failed replication restart, it is not clear why the clinical symptoms exhibited by the affected patients do not have more of a developmental component similar, for example, to that of patients with Schimke immuno-osseous dysplasia (SIOD), which is caused by mutations in the fork remodeling factor SMARCAL1 (41, 42). This suggests that perhaps the fork restart function of RECQL1 is essential in some cell types but not in others or is restricted to a subset of forks.

Interestingly, in addition to RECQL1, other disease-associated DNA helicases involved in replication fork processing and homologous recombination, such as DNA2, WRN, BLM, FANCJ, and FANCM (43), have also been implicated in suppressing the nucleolytic degradation of stalled replication forks and promoting their restart once repaired. Notably, of these, the cellular replication response to CPT and HU damage in cells lacking WRN is most sim-

ilar to that observed in RECON syndrome cells, i.e., both RECON syndrome and WS cells display increased fork degradation and a reduced efficiency with which replication can proceed in the presence of abortive TOP1 complexes or following HU exposure (26, 44). The similar cellular phenotypes of WS and RECON cells may explain the progeroid-like features of both disorders. However, the increased severity of clinical symptoms exhibited by individuals with WS when compared with patients with RECON syndrome may arise as a consequence of loss of specific enzymatic activities and/or functions of the WRN protein, e.g., the exonuclease activity, that are not conserved in RECQL1. In this regard, it remains to be determined whether RECQL1 also plays a role in promoting telomeric replication by dissembling G-quadruplex structures or repairing oxidative damage in a manner similar to WRN.

In summary, we demonstrate that mutations in *RECQL* are the underlying cause of an inherited chromosomal instability syndrome that shares some clinical and cellular phenotypic similarities with WS. Thus, to our knowledge, RECQL1 represents the fourth RecQ helicase to be implicated in genetically inherited disease characterized by genome stability defects.

Methods

Further information can be found in Supplemental Methods.

Exome analysis. We performed exome analysis using DNA extracted from whole blood of the proband in family A (Figure 1A). Exonic sequences from DNA were enriched with the Agilent V5 Kit (Agilent Technologies). Sequences were generated on a HiSeq2500 (Illumina) as 125 bp paired-end runs. Read alignment and variant calling were performed with DNAnexus using default parameters with the human genome assembly hg19 (GRCh37) as a reference. Exome analysis of the proband yielded 60.95 million reads, with a mean coverage of 88.83×.

Segregation analysis. An amplicon containing the *RECQL* variant was amplified by conventional PCR of genomic DNA derived from the probands and all available parents and siblings. PCR amplicons were analyzed by Sanger sequencing. The genomic DNA primer sequences used for *RECQL* PCR amplification were as follows: *RECQL* forward, 5′-TTAGCCTATAAAGGTTTACAAAACA-3′ and *RECQL* reverse, 5′-GGTAATATTATGGCAGTTATAGGAAGC-3′. The primers used to sequence *RECQL* cDNA were as follows: *RECQL* forward, 5′-TGCAGGTCGAGATGACATGA-3′ and *RECQL* reverse, 5′-AGCATGTTTGCAGCCTTCTTC-3′.

Data availability. The *RECQL* gene variant data are available in the NCBI's ClinVar archive (accession number SCV001364447.1).

Cell culture and generation of cell lines. Dermal primary fibroblasts were grown from skin-punch biopsies and maintained in DMEM (Thermo Fisher Scientific) supplemented with 20% FCS, 5% L-glutamine, and 5% penicillin-streptomycin antibiotics (Merck). Primary fibroblasts were immortalized with a lentivirus expressing human telomerase reverse transcriptase (hTERT) that was generated by transfecting 293FT cells (Thermo Fisher Scientific) with the plasmids pLV-hTERT-IRES-hygro (Addgene no. 85140), psPax2 (Addgene no. 12260), and pMD2.G (Addgene no. 12259). Selection was performed using hygromycin (Thermo Fisher Scientific) at 70 μg/mL. All LCLs were routinely grown in RPMI-1640 (Thermo Fisher Scientific) supplemented with 10% FCS, 5% L-glutamine, and 5% penicillin-streptomycin. *RECQL*-KO HeLa cells were routinely grown in DMEM supplemented with 10% FCS, 5% L-glutamine, and 5% penicillin-streptomycin. Fibroblast and HeLa cell complementation was carried out using the pLVX-IRES-Neo lentiviral vector (Takara Bio) encoding 2xHA-tagged *RECQL*. All cell lines were routinely tested for mycoplasma.

Genotoxic agents. Camptothecin (Merck), etoposide (Merck), hydroxyurea (MilliporeSigma), and methylmethane sulfonate (MilliporeSigma) were used as indicated.

Immunoblot analysis, immunoprecipitation, and antibodies. Whole-cell extracts were prepared and subjected to immunoblotting as previously described (23). Immunoblotting was performed using antibodies against pS1981 ATM (AF1655) from R&D Systems; ATM (A300-299A), pS824-KAP1 (A300-767A), KAP1 (A300-274A), pS966-SMC1 (A300-050A), SMC1 (A300-055A), pS4/S8-RPA2 (A300-245A), and RECQL1 (A300-450A) from Bethyl Laboratories; pS345-CHK1 (2341) from Cell Signaling Technology; CHK1 (sc-8408) and PARP1 (sc-8007) from Santa Cruz Biotechnology; H2A (07-146), γ-H2AX (05-636), RPA2 (NA18), and HA (H9658) from Merck; pS343-NBS1 (47272) from Abcam; and Nbs1 (GTX70224) from GeneTex. Co-immunoprecipitation was carried out as previously described (23), with the exception that EDTA was excluded, and 250 units/mL benzonase (Merck) and 1.5 mM $MgCl_2$ were added to the lysis buffer. Anti-RECQL1 antibody (5 μg, A300-450A) or a nonspecific IgG (Dako) coupled with protein A agarose beads (GE Healthcare) were used to isolate protein complexes from 5 mg whole-cell extract.

Immunofluorescence microscopy. Cells were seeded onto coverslips 24 hours before extraction and fixation. Cytochalasin B (2 μg/mL, MilliporeSigma) was added to the media for 24 hours to delete micronuclei. Cells were preextracted for 5 minutes on ice with ice-cold buffer (25 mM HEPES, pH 7.4, 50 mM NaCl, 1 mM EDTA, 3 mM $MgCl_2$, 300 mM sucrose, and 0.5% Triton X-100) and then fixed with 4% paraformaldehyde for 10 minutes. Fixed cells were stained with primary antibodies against γ-H2AX (Merck, 05-636), RAD51 (Merck, PC130), 53BP1 (Novus Biologicals, NB100-904), RECQL1 (Abcam, ab151501), and mitosin (BD Transduction Laboratories, 610768), with secondary antibodies conjugated to Alexa Fluor 488 and Alexa Fluor 594 (Life Technologies, Thermo Fisher Scientific), and then with DAPI (VectaLabs). Images were visualized using a Nikon Eclipse Ni microscope with NIS-Elements software (Nikon Instruments) and captured using a 100× oil immersion objective.

DNA fiber–spreading assay. Cells were pulse-labeled with 25 μM CldU for 20 to 30 minutes, washed with PBS, pulse-labeled with 250 μM IdU with or without 50 nM CPT or 50 nM ETOP for 20 to 30 minutes, and then harvested. For replication restart experiments, cells were labeled with CldU, washed in warm PBS, and incubated in media containing 2 mM HU or 0.02% MMS for 2 hours or 20 minutes, respectively. Cells were washed again in warm PBS and then incubated with IdU for the indicated duration. DNA fiber analysis was carried out as previously described (45).

Metaphase spreads. Giemsa-stained metaphase spreads were prepared as previously described (45). Briefly, Colcemid (KaryoMAX, Thermo Fisher Scientific) was added at a final concentration of 0.2 μg/mL for 3 hours. Cells were then harvested by trypsinization, subjected to hypotonic shock for 30 minutes at 37°C in hypotonic buffer (10 mM KCl, 15% FCS), and fixed in 3:1 ethanol/acetic acid solution. Cells were dropped onto acetic acid–humidified slides, stained for 15 minutes in a Giemsa-modified solution (Merck; 5% vol/vol in water), and washed in water for 5 minutes before visualization by light microscopy.

DNA helicase assays. DNA helicase assays were performed as previously described (19). Briefly, reactions were carried out in a 20 μL volume with 20 mM Tris (pH 7.4), 10 mM KCl, 5 mM ATP, 5 mM $MgCl_2$, 10% glycerol, and 80 ng/μL BSA for 15 minutes at 37°C. Reaction mixtures containing a forked duplex DNA substrate (19 bp or 31 bp) were incubated with the indicated concentrations of WT RECQL1 or RECQL1-A459S helicase proteins. Reactions were quenched with an equal volume of 2× stop dye (18 mM EDTA, 0.6% SDS, 25% glycerol, 0.4% bromophenol blue, 0.4% xylene cyanol, and 0.1 mg/mL proteinase K) and incubated for an additional 15 minutes at 37°C to remove bound RECQL1 protein. Reaction products were resolved by electrophoresis on native 12% polyacrylamide gels at 200 V for 1.5 hours. Radiolabeled DNA products were visualized with a phosphoimager and quantified using ImageQuant software (Cytiva). For kinetics analysis of DNA unwinding, 19 bp or 31 bp forked duplex DNA substrates were incubated with the specified RECQL1 concentration and incubated for the indicated durations at 37°C. The rates of helicase-catalyzed DNA unwinding were determined by linear regression analysis.

Strand annealing assays. Strand annealing assays were performed as previously described (19). Briefly, the specified concentration of WT RECQL1 or RECQL1-A459S helicase protein was incubated with 0.5 nM each of 5′-end radiolabeled oligonucleotide and partially complementary unlabeled oligonucleotide. Strand annealing reactions (20 μL) were carried out in helicase reaction buffer (20 mM Tris-HCl [pH 7.5], 10 mM KCl, 8 mM dithiothreitol, 5 mM $MgCl_2$) and quenched by addition of an equal volume of 2× stop dye (18 mM EDTA, 0.6% SDS, 25% glycerol, 0.4% bromophenol blue, 0.4% xylene cyanol and 0.1 mg/mL proteinase K) and incubated for an additional 15 minutes at 37 °C to remove bound RECQL1 protein. Reaction products were electrophoresed on native 12% polyacrylamide gels at 200 V for 1.5 hours. Radiolabeled products were visualized and quantified as described above.

Fork restoration kinetics assay. WT or A459S RECQL1 (20 nM) was incubated with 2 nM radiolabeled reversed fork substrate, 2 mM ATP, 15 mM phosphocreatine, and 30 u/mL creatine phosphokinase in reaction salts (35 mM Tris-HCl, pH 7.5, 20 mM KCl, 5 mM $MgCl_2$, 0.1 mg/mL BSA, 2 mM DTT, 5% glycerol) in 100 μL reactions at 37°C. Aliquots of 20 μL were removed at the indicated times and were quenched by the addition of 10 μL 3X stop buffer (1.2% SDS, 30% glycerol and proteinase K), followed by incubation for at least 10 minutes at room temperature. Separate reactions containing either a reversed fork and replication fork structure without RECQL1 were incubated for 30 minutes at 37 °C followed by addition of the 3× stop buffer. Samples were immediately loaded onto an 8% polyacrylamide 1× TBE gel and electrophoresed for 4 hours at 200 V and 4°C. Gels were exposed to a phosphoimager screen overnight and then imaged using a Typhoon FLA 9500 imager (Cytiva). Gel images were quantified using ImageQuant TL software (Cytiva), and raw data were processed using Microsoft Excel. The percentage fork restoration was calculated by dividing the volume of the replication fork band by the total volume at each time point and subtracting the percentage of the fork restored in the no-enzyme control from each time point. Data representing 3 replicates of the assay were averaged and graphed.

Study approval. Written informed consent to publish clinical information and photographs of the affected individuals was obtained from the families prior to their involvement in this study, in accordance with the IRB-approved protocol 0306-10-HMO from the Hadassah Medical Center (Jerusalem, Israel). Further approval for this research was obtained from the West Midlands, Coventry, and Warwickshire Research Ethics Committee (Coventry, United Kingdom; REC: 20/WM/0098).

Author contributions

TH, VMP, AAL, and BAL identified the patients with the RECQL1 mutation and provided clinical information and photographs of the affected individuals. TH and VM analyzed the whole-exome sequencing data. KDB performed segregation analysis and established patient-derived LCLs. SSJ, SLC, and AD performed DNA fiber analysis. LJG, JJR, and RH performed flow cytometric, SCE, and chromosome breakage analyses. BLW performed growth and cytotoxicity assays on LCLs. GSM performed chromatin fractionation and immunofluorescence. SJS performed structural modeling. CNM and GLM generated the RECQL1 CRISPR-KO HeLa cell line. GSS generated complemented cell lines, carried out immunofluorescence and co-immunoprecipitation studies, and performed Western blotting. SD and JAS purified recombinant RECQL1 and performed in vitro protein biochemical assays. SD and AD performed cell-based DNA damage sensitivity assays and the comet assay. ANG generated RECQL1 expression vectors. GMCL and VR carried out C-Fusion 3D high-throughput imaging. GSS, SSJ, and RMB planned and supervised the study and wrote the manuscript.

Acknowledgments

We would like to thank the parents and patients from the 2 families for taking part in this study and generously donating tissue samples. We would also like to thank Fay Stewart for help with statistical analysis. GSS, RH, GSM, SLC, AG are funded by a CR-UK Programme grant (C17183/A23303). SSJ is supported by a project grant funded by the Great Ormond Street Hospital Children's Charity and Sparks (V5019). LJG is supported by a joint funded University of Birmingham and CR-UK PhD studentship (C17422/A25154). BLW is supported by a CR-UK Clinical Academic Training Programme award (C11497/A31309). The VR laboratory is supported by funding from the Deutsche Forschungsgemeinschaft (DFG, German Research Foundation, project IDs 393547839-SFB 1361 and 402733153-SPP 2202) and the DFG Major Research Instrumentation Programme (INST 247/845-1 FUGG). JJR is supported by the University of Birmingham. SD, JAS, AD, and RMB are supported in part by the NIH Intramural Research Program of the National Institute on Aging (1Z1AAG000741-19). A collaboration to study the identified *RECQL* variant was established via GeneMatcher (46).

Address correspondence to: Grant S. Stewart. Phone: 121.414.9168; Email: g.s.stewart@bham.ac.uk. Or to: Robert M. Brosh Jr. Phone: 410.558.8578; Email: broshr@mail.nih.gov. Or to: Tamar Harel. Phone: 972.2.6776329; Email: tamarhe@hadassah.org.il.

1. Chu WK, Hickson ID. RecQ helicases: multifunctional genome caretakers. *Nat Rev Cancer*. 2009;9(9):644–654.
2. Croteau DL, et al. Human RecQ helicases in DNA repair, recombination, and replication. *Annu Rev Biochem*. 2014;83:519–552.
3. Oshima J, et al. Werner syndrome: clinical features, pathogenesis and potential therapeutic interventions. *Ageing Res Rev*. 2017;33:105–114.

4. Cunniff C, et al. Bloom's syndrome: clinical spectrum, molecular pathogenesis, and cancer predisposition. *Mol Syndromol*. 2017;8(1):4–23.
5. Chan KL, Hickson ID. New insights into the formation and resolution of ultra-fine anaphase bridges. *Semin Cell Dev Biol*. 2011;22(8):906–912.
6. Dongliang M, et al. Human RecQL4 helicase plays multifaceted roles in the genomic stability of normal and cancer cells. *Cancer Lett*. 2018;413:1–10.
7. Sangrithi MN, et al. Initiation of DNA replication requires the RECQL4 protein mutated in Rothmund-Thomson syndrome. *Cell*. 2005;121(6):887–898.
8. Lu H, et al. RECQL4 promotes DNA end resection in repair of DNA double-strand breaks. *Cell Rep*. 2016;16(1):161–173.
9. Schurman SH, et al. Direct and indirect roles of RECQL4 in modulating base excision repair capacity. *Hum Mol Genet*. 2009;18(18):3470–3483.
10. Seki M, et al. Molecular cloning of cDNA encoding human DNA helicase Q1 which has homology to Escherichia coli Rec Q helicase and localization of the gene at chromosome 12p12. *Nucleic Acids Res*. 1994;22(22):4566–4573.
11. Popuri V, et al. The Human RecQ helicases, BLM and RECQ1, display distinct DNA substrate specificities. *J Biol Chem*. 2008;283(26):17766–17776.
12. Liu NN, et al. Endogenous Bos taurus RECQL is predominantly monomeric and more active than oligomers. *Cell Rep*. 2021;36(10):109688.
13. Sharma S, et al. RECQL, a member of the RecQ family of DNA helicases, suppresses chromosomal instability. *Mol Cell Biol*. 2007;27(5):1784–1794.
14. Berti M, et al. Human RECQ1 promotes restart of replication forks reversed by DNA topoisomerase I inhibition. *Nat Struct Mol Biol*. 2013;20(3):347–354.
15. Cybulski C, et al. Germline *RECQL* mutations are associated with breast cancer susceptibility. *Nat Genet*. 2015;47(6):643–646.
16. Sun J, et al. Mutations in RECQL gene are associated with predisposition to breast cancer. *PLoS Genet*. 2015;11(5):e1005228.
17. Sami F, et al. Site-directed mutants of human RECQ1 reveal functional importance of the zinc binding domain. *Mutat Res*. 2016;790:8–18.
18. Cui S, et al. Analysis of the unwinding activity of the dimeric RECQ1 helicase in the presence of human replication protein A. *Nucleic Acids Res*. 2004;32(7):2158–2170.
19. Sharma S, et al. Biochemical analysis of the DNA unwinding and strand annealing activities catalyzed by human RECQ1. *J Biol Chem*. 2005;280(30):28072–28084.
20. Banerjee T, et al. Catalytic strand separation by RECQ1 is required for RPA-mediated response to replication stress. *Curr Biol*. 2015;25(21):2830–2838.
21. Muzzolini L, et al. Different quaternary structures of human RECQ1 are associated with its dual enzymatic activity. *PLoS Biol*. 2007;5(2):e20.
22. Stewart GS, et al. The DNA double-strand break repair gene hMRE11 is mutated in individuals with an ataxia-telangiectasia-like disorder. *Cell*. 1999;99(6):577–587.
23. Sharma S, et al. Human RECQ1 is a DNA damage responsive protein required for genotoxic stress resistance and suppression of sister chromatid exchanges. *PLoS One*. 2007;110(7):2390–2398.
24. Canela A, et al. Topoisomerase II-induced chromosome breakage and translocation is determined by chromosome architecture and transcriptional activity. *Mol Cell*. 2019;75(2):252–266.
25. Gothe HJ, et al. Spatial chromosome folding and active transcription drive DNA fragility and formation of oncogenic MLL translocations. *Mol Cell*. 2019;75(2):267–283.
26. Thangavel S, et al. DNA2 drives processing and restart of reversed replication forks in human cells. *J Cell Biol*. 2015;208(5):545–562.
27. Zellweger R, et al. Rad51-mediated replication fork reversal is a global response to genotoxic treatments in human cells. *J Cell Biol*. 2015;208(5):563–579.
28. Davies SL, et al. Role for BLM in replication-fork restart and suppression of origin firing after replicative stress. *Nat Struct Mol Biol*. 2007;14(7):677–679.
29. Benedict B, et al. The RECQL helicase prevents replication fork collapse during replication stress. *Life Sci Alliance*. 2020;3(10):e202000668.
30. Wang W, et al. Functional relation among RecQ family helicases RecQL1, RecQL5, and BLM in cell growth and sister chromatid exchange formation. *Mol Cell Biol*. 2003;23(10):3527–3535.
31. Nimonkar AV, et al. BLM-DNA2-RPA-MRN and EXO1-BLM-RPA-MRN constitute two DNA end resection machineries for human DNA break repair. *Genes Dev*. 2011;25(4):350–362.
32. Parvathaneni S, et al. Human RECQ1 interacts with Ku70/80 and modulates DNA end-joining of double-strand breaks. *PLoS One*. 2013;8(5):e62481.
33. Schnabel F, et al. Premature aging disorders: a clinical and genetic compendium. *Clin Genet*. 2021;99(1):3–28.
34. Foo MXR, et al. Premature aging syndromes: From patients to mechanism. *J Dermatol Sci*. 2019;96(2):58–65.
35. Bogdanova N, et al. Analysis of a *RECQL* splicing mutation, c.1667_1667+3delAGTA, in breast cancer patients and controls from central Europe. *Fam Cancer*. 2017;16(2):181–186.
36. Li N, et al. Mutations in RECQL are not associated with breast cancer risk in an Australian population. *Nat Genet*. 2018;50(10):1346–1348.
37. Pike ACW, et al. Structure of the human RECQ1 helicase reveals a putative strand-separation pin. *Proc Natl Acad Sci U S A*. 2009;106(4):1039–1044.
38. Bahr A, et al. Point mutations causing Bloom's syndrome abolish ATPase and DNA helicase activities of the BLM protein. *Oncogene*. 1998;17(20):2565–2571.
39. Neff NF, et al. The DNA helicase activity of BLM is necessary for the correction of the genomic instability of bloom syndrome cells. *Mol Biol Cell*. 1999;10(3):665–676.
40. Wu L, et al. The HRDC domain of BLM is required for the dissolution of double Holliday junctions. *EMBO J*. 2005;24(14):2679–2687.
41. Boerkoel CF, et al. Mutant chromatin remodeling protein SMARCAL1 causes Schimke immunoosseous dysplasia. *Nat Genet*. 2002;30(2):215–220.
42. Poole LA, Cortez D. SMARCAL1 and telomeres: replicating the troublesome ends. *Nucleus*. 2016;7(3):270–274.
43. Tye S, et al. A fork in the road: where homologous recombination and stalled replication fork protection part ways. *Semin Cell Dev Biol*. 2021;113:14–26.
44. Iannascoli C, et al. The WRN exonuclease domain protects nascent strands from pathological MRE11/EXO1-dependent degradation. *Nucleic Acids Res*. 2015;43(20):9788–9803.
45. Higgs MR, et al. BOD1L is required to suppress deleterious resection of stressed replication forks. *Mol Cell*. 2015;59(3):462–477.
46. Sobreira N, et al. GeneMatcher: a matching tool for connecting investigators with an interest in the same gene. *Hum Mutat*. 2015;36:928–930.
47. Pike ACW, et al. Human RECQ1 helicase-driven DNA unwinding, annealing, and branch migration: insights from DNA complex structures. *Proc Natl Acad Sci U S A*. 2015;112(14):4286–4291.

Published online 24 May 2023

Nucleic Acids Research, 2023, Vol. 51, No. 12 ***6337–6354***
https://doi.org/10.1093/nar/gkad369

Actin nucleators safeguard replication forks by limiting nascent strand degradation

Jadwiga Nieminuszczy[1,†], Peter R. Martin[1,†], Ronan Broderick[1], Joanna Krwawicz[1], Alexandra Kanellou[1], Camelia Mocanu[1], Vicky Bousgouni[1], Charlotte Smith[1], Kuo-Kuang Wen[2], Beth L. Woodward[3], Chris Bakal[1], Fiona Shackley[4], Andrés Aguilera[5], Grant S. Stewart[3], Yatin M. Vyas[2,*] and Wojciech Niedzwiedz[1,*]

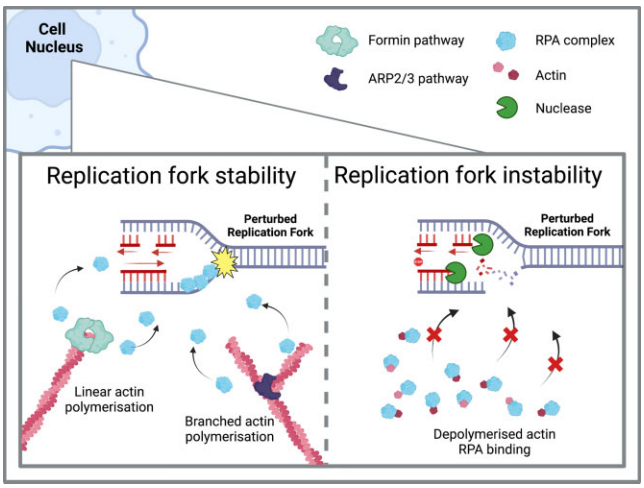
[1]Division of Cancer Biology, The Institute of Cancer Research, London SW3 6JB, UK, [2]Department of Pediatrics, Division of Pediatric Hematology-Oncology, Penn State College of Medicine, Penn State Health Children's Hospital, Hershey, PA 17033, USA, [3]Genome Stability and Human Disease Laboratory, Institute of Cancer and Genomic Sciences, University of Birmingham, Birmingham B15 2TT, UK, [4]Paediatric Immunology, Allergy and Infectious Diseases, Sheffield Children's Hospital NHS Foundation Trust, Sheffield, UK and [5]Centro Andaluz de Biología Molecular y Medicina Regenerativa CABIMER, Universidad de Sevilla-CSIC-Universidad Pablo de Olavide, Seville, Spain

Received October 13, 2022; Revised April 17, 2023; Editorial Decision April 23, 2023; Accepted May 11, 2023

ABSTRACT

Accurate genome replication is essential for all life and a key mechanism of disease prevention, underpinned by the ability of cells to respond to replicative stress (RS) and protect replication forks. These responses rely on the formation of Replication Protein A (RPA)-single stranded (ss) DNA complexes, yet this process remains largely uncharacterized. Here, we establish that actin nucleation-promoting factors (NPFs) associate with replication forks, promote efficient DNA replication and facilitate association of RPA with ssDNA at sites of RS. Accordingly, their loss leads to deprotection of ssDNA at perturbed forks, impaired ATR activation, global replication defects and fork collapse. Supplying an excess of RPA restores RPA foci formation and fork protection, suggesting a chaperoning role for actin nucleators (ANs) (i.e. Arp2/3, DIAPH1) and NPFs (i.e, WASp, N-WASp) in regulating RPA availability upon RS. We also discover that β-actin interacts with RPA directly *in vitro,* and *in vivo* a hyper-depolymerizing β-actin mutant displays a heightened association with RPA and the same dysfunctional replication phenotypes as loss of ANs/NPFs, which contrasts with the phenotype of a hyper-polymerizing β-actin mutant. Thus, we identify components of actin polymerization pathways that are essential for preventing ectopic nucleolytic degradation of perturbed forks by modulating RPA activity.

GRAPHICAL ABSTRACT



INTRODUCTION

Faithful genome duplication during cell division ensures accurate transmission of genetic information to daughter cells. This process relies on the replication of the entire genetic material during S-phase by thousands of replication forks (RFs) emanating from numerous origins of

*To whom correspondence should be addressed. Tel: +44 2071535507; Email: wojciech.niedzwiedz@icr.ac.uk
Correspondence may also be addressed to Yatin M. Vyas. Tel: +1 717 5316701; Email: yvyas@pennstatehealth.psu.edu
†The authors wish it to be known that, in their opinion, the first two authors should be regarded as Joint First Authors.

© The Author(s) 2023. Published by Oxford University Press on behalf of Nucleic Acids Research.
This is an Open Access article distributed under the terms of the Creative Commons Attribution License (http://creativecommons.org/licenses/by/4.0/), which permits unrestricted reuse, distribution, and reproduction in any medium, provided the original work is properly cited.

replication. However, replication is constantly challenged by endogenous and exogenous insults that may damage RFs (1–3). To respond to replicative stress or to prevent stalled forks from collapsing into DNA double-strand breaks (DSBs), or to ascertain that a mutagenic lesion is repaired correctly, cells have evolved intricate genome surveillance mechanisms underpinned by the ATR and ATM kinases (2,4–5). Mutations in genes involved in the DNA replication and repair (DDR) pathway lead to human disorders that clinically manifest in developmental abnormalities and cancer, underscoring their importance to human health (1,6–7).

A key step in the replication stress response (RSR) is the formation of RPA-coated single stranded DNA (RPA-ssDNA) complex at sites of RF damage. Replication protein A (RPA) is a heterotrimeric complex (RPA1, RPA2, RPA3) with essential roles in several aspects of DNA metabolism, with conservation from yeast to humans. During DNA replication, RPA protects ssDNA transiently formed at perturbed forks against nucleolytic degradation and serves as a platform for recruitment and regulation of several DDR factors, including ATR (8,9). Interestingly, work in yeast *Saccharomyces cerevisiae* (Sc) and Xenopus showed that cells actively control the ability of RPA to associate with ssDNA, suggesting an importance of this process for DNA-associated transactions and genome stability (10,11). Indeed, dysregulation of RPA expression has been implicated in tumour progression, chemotherapy-resistance, or DNA-damage tolerance (12–14). Accordingly, we have recently identified a novel function for the Wiskott-Aldrich syndrome protein (WASp), a regulator of ARP2/3-mediated actin nucleation, in promoting the assembly of RPA-ssDNA complexes in *cis* via its direct interaction with RPA (15). Interestingly however, several other factors involved in actin dynamics, for example N-WASp (nucleation-promoting factor, NPF) or ARP2/3 and Formins (actin nucleators, ANs) have all been shown to participate in a range of responses essential for genome maintenance, including DNA replication, centromere maintenance, or DSB repair (16–23).

Here we find that besides WASp, another member of the NPF family, N-WASp, as well as the ANs ARP2/3 and DIAPH1, collectively referred to hence after as (NPF/ANs), are recruited to RFs and function to facilitate the formation/stability of RPA-ssDNA complexes and safeguard genome duplication. Consequently, their loss triggers defective ATR activation, global RF dysfunction and genome instability. Significantly, we discover that monomeric actin (G-actin) interacts directly with RPA, and cells expressing a hyper-depolymerization β-actin (G13R) mutant phenocopy defects associated with NPF/ANs loss i.e. impaired RPA foci formation, impaired ATR activation and fork stability. In contrast, cells expressing a hyper-polymerization β-actin (S14C) mutant do not show replication defects, likely implying a more direct role of actin polymerisation in RF protection**.** In conclusion, we propose that the association of NPF/ANs with perturbed RFs plays a critical role, either directly or indirectly through actin state changes, in facilitating formation of RPA-ssDNA complexes essential for fork protection.

MATERIALS AND METHODS

Cell lines and drug treatments

HeLa cells were a generous gift from Dr F. Esashi. U2OS cells and U2OS over expressing RPA (Super RPA) cells were a kind gift of Dr L. I. Toledo. These cell lines were cultured in Dulbecco's modified Eagle's medium (DMEM) supplemented with 10% fetal bovine serum (FBS) and standard antibiotics. Primary dermal fibroblasts were maintained in Dulbecco's modified Eagle's medium (DMEM; Life Technologies) supplemented with 20% fetal calf serum (FCS), 5% L-glutamine, and 5% penicillin-streptomycin (Invitrogen) antibiotics. Primary fibroblasts were immortalized with 293FT (Invitrogen)-derived supernatant containing a human telomerase reverse transcriptase (TERT) lentivirus that was generated with the plasmids pLV-hTERT-IRES-hygro (gift from Tobias Meyer; Addgene #85140) (24), psPax2 (gift from Didier Trono; Addgene #12260), and pMD2.G (gift from Didier Trono; Addgene #12259). Selection was performed with hygromycin (Invitrogen) at 70 μg/ml. Fibroblast complementation was carried out using a lentiviral vector (pLVX-IRES-Neo; TakaraBio) that encoded 3xHA-tagged DIAPH1 in combination with the lentiviral packaging plasmids described above. Selection was performed with geneticin (Invitrogen) at 400 μg/ml. Expression of HA-tagged DIAPH1 was validated by Western blotting. All cell lines were routinely tested for mycoplasma. Cells were treated with hydroxyurea (Sigma-Aldrich) with indicated doses. Where indicated cells were pre-treated with 100 μM ARP2/3i (CK-666, Sigma-Aldrich) for 1 hour prior to further drug treatment or harvesting.

Plasmids

Plasmids encoding YFP NLS Beta-Actin, YFP NLS Beta-Actin S14C and YFP NLS Beta-Actin G13R were a gift from Primal de Lanerolle (Addgene plasmid # 60613; http://n2t.net/addgene:60613;RRID:Addgene_60613; Addgene plasmid # 60614; http://n2t.net/addgene:60614;RRID:Addgene_60614; Addgene plasmid # 60615; http://n2t.net/addgene:60615;RRID:Addgene_60615 respectively) (25). p11d-tRPA (123) plasmid was a kind gift from David Cortez.

Immunoblotting

Cell lysis was carried out in urea buffer (9 M urea, 50 mM Tris–HCl, pH 7.5, 150 mM β-mercaptoethanol) followed by sonication using a soniprep 150 (MSE) probe sonicator or in RIPA buffer (Sigma-Aldrich), supplemented with 1× SIGMAFAST protease inhibitors (Sigma-Aldrich), and 1xPhosStop phosphatase inhibitors (Roche), on ice for 15 min followed by centrifugation at 1.2 × 10^3 rpm for 20 min followed by collection of supernatant containing cell lysate. Cell lysates were prepared in SDS loading buffer (2% SDS, 10% (v/v) glycerol, 2% 2-Mercaptoethanol and 62.5 mM Tris–HCl, pH 6.8) followed by boiling at 95°C for 10 min. Protein concentrations were determined by spectrophotometry using a DeNovix DS-11 FX+ device (DeNovix) or by the Bradford assay. Samples were resolved by

SDS-PAGE and transferred to PVDF or nitrocellulose followed by blocking in 5% low fat milk in 1× TBS/ 0.1% Tween-20 for 1 h at room temperature. Membranes were washed 3 × 5 min in 1× TBS/ 0.1% Tween-20 and incubated overnight at 4°C in the indicated primary antibodies in 5% low fat milk in 1x TBS/ 0.1% Tween-20. Membranes were subsequently washed 3 × 5 min in 1× TBS/ 0.1% Tween-20 and incubated in 5% low fat milk in 1× TBS/ 0.1% Tween-20 containing secondary antibodies for 1 h at room temperature. Membranes were subsequently washed 3 × 5 min in 1× TBS/ 0.1% Tween-20 and developed using Immobilon Western HRP Substrate (Millipore, WBKLS0S00) and imaged using the Azure C280, 300 or 600 instruments (Azure biosystems). Primary antibodies used were: α-Tubulin (Sigma, B-5-1-2; T5168, 1:100 000), MCM2 (Abcam, ab4461, 1:10 000), Lamin-B1 (Santa Cruz, sc-30264, 1:1000), N-WASp (Abcam ab187527, 1:1000), DIAPH1 (Bethyl, A300-077A-T, 1:1000; Santa Cruz, sc-373807, 1:500), CHK1 – phospho S345 (Cell Signalling, 133D3; 2348, 1:1000), CHK1 (Santa Cruz, sc-8408, 1:1000), RPA1 (Abcam ab79398), RPA2 (Abcam ab2175; 1:500), Actin (Sigma, A2066, 1:1000), GFP (Roche, 11 814 460 001, 1:500), SMARCAL1 (Santa Cruz, sc-376377, 1:1000), BRCA2 (Millipore, OP-95, 1:500), Secondary antibodies used were anti-mouse IgG-HRP (Dako, P0447, 1:2000) and anti-rabbit IgG-HRP (Dako, P0448, 1:5000).

Rapid, efficient and practical (REAP) cellular fractionation

To fractionate cytoplasmic and nuclear compartments of the cell we carried out REAP fractionation as described previously (26). HeLa cells grown to 70–90% confluence in a 10 cm tissue-culture dish were washed 2 times in ice cold 1x PBS. Then, 1 ml ice cold PBS was added to a 10 cm tissue culture dish and cells were scraped and collected in 1.5 ml microcentrifuge tubes. Microcentrifuge tubes were pulse spun for 10 s and the supernatant was discarded. Cell pellets were then pipetted up and down 5 times in 1 ml ice cold 0.1% NP-40/ 1x PBS and pulse spun for 10 s in a microcentrifuge. The supernatant was then transferred to a new microcentrifuge tube (Cytoplasmic fraction). The cell pellet was then resuspended by pipetting up and down 5 times in 1 ml ice cold 0.1% NP-40/ 1x PBS and pulse spun and the supernatant was discarded. The nuclear pellet was then resuspended in 50 μl of PBS and sonicated for 30 s at 10% amplitude using a soniprep 150 (MSE) probe sonicator. The protein concentration of the cytoplasmic and nuclear fractions were then quantified by Bradford assay and processed by SDS-PAGE and western blot transfer in advance of immunoblot analysis.

YFP-NLS-β-actin mammalian expression construct transfection for immunofluorescence microscopy

For YFP-NLS-β-actin mammalian expression construct transfection, 2×10^5 cells were seeded into a well of a 6-well tissue culture plate. Cells were incubated at 37°C for 24 h to allow them to adhere. Per condition, 0.75 μg of YFP-NLS-β-Actin mammalian expression construct was transfected following the Lipofectamine 3000 manufacturer's protocol. Cells were then incubated at 37°C for 24 h and treated with hydroxyurea at the indicated doses before harvesting cells for down-stream assays.

Cell survival assay

Alamar Blue survival assays were performed in accordance with the manufacturer's recommendations (Bio Rad). Briefly, 500 cells per well in 96-well plates were plated and untreated or treated with indicated doses of hydroxyurea, *cis*-platin or Mitomycin C and incubated for 7 days. Alamar blue reagent was added to each well and fluorometric measurements taken after 4 h incubation at 37°C.

RNAi treatment

Small interfering RNA used in this study were as follows: siWASp – 5′-GAGUGGCUGAGUUACUUGC-3′ and ON-TARGETplus Human WAS siRNA smart pool (LQ-028294-00-0005, Dharmacon); siN-WASp – ON-TARGETplus Human WASL siRNA smart pool (L-006444-00-0005, Dharmacon), 5′-CAGCAGAUCGGAACUGUAU-3′ (J-006444-07, Dharmacon), 5′-UAGAGAGGGUGCUCAGCUA-3′ (J-006444-08, Dharmacon); siDIAPH1-ON-TARGETplus Human DIAPH1 siRNA smart pool (L-010347-00-0005, Dharmacon); siRNA targeting luciferase— 5′-CGTACGCGGAATACTTCGA-3′ (27) was used as control siRNA. Oligonucleotides were transfected using HiPerfect reagent (Qiagen) at 25 nM concentration, according to the manufacturer's protocol. First pulse of siRNA was followed with second pulse after 24 h and all experiments were performed at maximum knock down-efficiency 72 h post first siRNA pulse.

Immunofluorescence microscopy

Cells were grown and treated on circular 13 mm diameter coverslips, thickness 1.5 mm. For visualization of 53BP1, RAD51 foci and Cyclin A, cells were fixed with 4% paraformaldehyde in PBS for 10 min at room temperature, washed twice in PBS and permeabilised with 0.2% Triton X-100 in PBS for 10 min at room temperature. Coverslips were washed 3 × in PBS cells and were blocked in 10% FBS in PBS for 1 h at room temperature before incubation with primary antibodies in 0.1% FBS in PBS overnight at 4°C. Coverslips were then washed 4 × 5 min in PBS followed by incubation with secondary antibodies for 1 h at room temperature. Slides were then washed 4 × 5 min in PBS and subsequently mounted with Vectashield mounting medium (Vector Laboratories) with DAPI. Micronuclei were quantified by assessing DAPI stained nuclei. For visualization of RPA2 foci and BrdU foci cells were pre-extracted on ice for 2 min in CSK buffer (10 mM PIPES pH6.8, 300 mM sucrose, 100 mM NaCl, 1.5 mM $MgCl_2$, 0.5% Triton X-100), washed with PBS and fixed with 4% paraformaldehyde in PBS for 10 min at room temperature. Coverslips were then blocked and processed as above. Primary antibodies employed for immunofluorescence were as follows: 53BP1 (MAB3802, Millipore, 1:1000), Cyclin A (ab19150, Abcam, 1:500), RPA2 (NA-18, Calbiochem, 1:200), RAD51 (ab133534, Abcam 1:500), BrdU (BU-1;

RPN202 GE Healthcare Life Sciences 1:200). Secondary antibodies for immunofluorescence were as follows: Alexa Fluor 488 anti-rabbit (A21206, Invitrogen, 1:200) and Alexa Fluor 555 anti-mouse (A31570, Invitrogen, 1:400). Images were acquired using a Leica SP8 confocal microscope with a 63x oil objective, using a Zeiss Axio Observer Z1 Marianas™ Microscope attached with a CSU-W spinning disk unit using either a Hamamatsu Flash 4 CMOS camera or a Photometrics Prime 95b sCMOS camera built by Intelligent Imaging Innovations (3i) or a Zeiss Axio Observer Z1 Marianas™ Microscope attached with a CSUX1 spinning disk unit and Hamamatsu Flash 4 CMOS camera built by Intelligent Imaging Innovations (3i). Quantification was carried out using FIJI (ImageJ) software and CellProfiler (Broad Institute).

iPOND

iPOND was performed as decribed previously (28). Briefly, logarithmically growing HeLa S3 cells (1×10^6 per ml) or HEK293TN cells were incubated with 10 μM EdU for 10 or 15 min respectively. Following EdU labeling, cells were fixed in 1% formaldehyde, quenched by adding glycine to a final concentration of 0.125 M and washed three times in PBS. Collected cell pellets were frozen at −80°C and cells were permeabilized by resuspending $1.0–1.5 \times 10^7$ cells per ml in ice cold 0.25% Triton X-100 in PBS and incubating for 30 min. Before the Click reaction, samples were washed once in PBS containing 0.5% BSA and once in PBS. Cells were incubated for 2 h at room temperature in Click reaction buffer containing 10 μM azide-PEG(3 + 3)-*S*-*S*-biotin conjugate (Click ChemistryTools, cat. no AZ112-25), 10 mM sodium ascorbate, and 1.6 mM copper (II) sulfate ($CuSO_4$) in PBS. The 'no Click' reaction contained DMSO instead of biotin-azide. Following the Click reaction, cells were washed once in PBS containing 0.5% BSA and once in PBS. Cells were resuspended in lysis buffer (50 mM Tris–HCl pH 8.0, 1% SDS) containing protease inhibitor cocktail (Sigma) and sonicated. Samples were centrifuged at 14 500 rcf. at 4°C for 30 min and the supernatant was diluted 1:3 with TNT buffer (50 mM Tris pH 7.5, 200 mM NaCl and 0.3% Triton X-100) containing protease inhibitors. An aliquot was taken as an input sample. Streptavidin–agarose beads (Novagen) were washed three times in TNT buffer containing protease inhibitor cocktail. Two hundred microliters of bead slurry was used per 1 × 108 cells. The streptavidin–agarose beads were resuspended 1:1 in TNT buffer containing protease inhibitors and added to the samples, which were then incubated at 4°C for 16 h in the dark. Following binding, the beads were then washed two times with 1 ml TNT buffer, two times with TNT buffer containing 1 M NaCl, two times with TNT buffer and protein–DNA complexes were eluted by incubating with 5 mM DTT in TNT buffer. Cross-links were reversed by incubating samples in SDS sample buffer at 95°C for 20 min. Proteins were resolved on SDS-PAGE and detected by immunoblotting using specific antibodies.

iPOND in ND1 cells was performed as described (29) with some modifications. Briefly, T cells (∼80 million cells per sample) were incubated with 20 μM EdU in 30 ml culture medium at 37°C for 20 min and then washed with fresh medium at 37°C. For HU or thymidine pluse, cells were resuspended either with 30 ml fresh medium at 37°C as the control or 4 mM HU or 20 μM thymidine in fresh medium. These cells were further cultured at 37°C for another 2 h. After labeling/treatments, each cell samples were washed with PBS, and crossed-linked in 1% formaldehyde in PBS for 20 min at RT, quenched with glycine at the final concentration of 0.125 M for another 5 min, and washed 2 times in PBS. Cell pellets were permeabilized with 10 ml permeabilizing buffer (0.3% Triton-X/0.5% BSA in PBS) 30 min at RT and washed with 0.5% BSA/PBS. Each cell pellet was resuspended in 10 ml PBS as the control, or 10 ml fresh prepared Click buffer (10 mM Sodium ascorbate, 2 mM $CuSO_4$, and 20 μM Biotin-dPEG7-azide) and incubated for 1–2 h at room temperature (RT). Cells were washed with 0.5% BSA/PBS and then pellets either frozen at -80°C or immediately used for lysis. Each cell pellet was resuspended in 0.8 ml lysis buffer (25 mM NaCl, 2 mM EDTA, 50 mM Tris pH 8, 1% Igepal CA630, 0.2% SDS, 0.5% sodium deoxycholate, and 1× Halt protease and phosphatase inhibitor cocktail (Thermo Fisher)) and incubated for 10 min on ice. Samples were sonicated with a Branson 250 using the settings, 20–25 W, 20 s constant pulse, and 40 s pauses for a total of 4 min on ice. Cell lysates were centrifuged at 1.8×10^3 rcf for 10 min at RT. The supernatants were collected and diluted with the dilution buffer (the lysis buffer without SDS or sodium deoxycholate). Streptavidin-agarose beads (Millipore Sigma) (80 μl/sample) were washed with the dilution buffer 3 times, and then incubated with the diluted samples overnight at 4°C. The beads were again washed 3 times with RIPA buffer. Captured proteins were separated from beads by incubating beads in 50 μl 2× Laemmli Sample Buffer (Bio-Rad) at 95°C for 25 min. The supernatant was collected, and proteins resolved on 4–15% SDS-PAGE and detected by immunoblotting.

EdU labeling of nascent DNA and proximity ligation assay

Analysis of the association of proteins to nascent DNA by EdU labelling and the Proximity Ligation Assay was carried out as previously described (28,30). Briefly, cells grown on coverslips were labeled with 10 mM EdU for 10 min followed by treatment with 1 mM or 4 mM hydroxyurea at various timepoints as indicated. Fixation was carried out with 3% formaldehyde, 2% sucrose in PBS for 10 min at room temperature. Slides were then washed twice with PBS and incubated with blocking solution (3% BSA in PBS) for 30 min. Following this, slides were washed 2× in PBS before EdU-Biotin Azide conjugation by click chemistry using the Click-iT reaction (Click-iT assay kit (Thermo Fisher, according to the manufacturer's instructions). Coverslips were washed 2× with PBS before primary antibody incubation overnight at 4°C in 1% BSA/0.1% saponin in PBS. Following primary antibody incubation coverslips were washed 2× in PBS and then the proximity ligation assay was carried out (Duolink *In Situ* Red Starter kit (Sigma Aldrich) according to the manufacturer's instructions). Coverslips were mounted using Vectashield containing DAPI. Antibodies employed for the PLA assay were as follows: Biotin (Bethyl Laboratories, A150-109A, 1:3000), (Biotin (Jackson Immunoresearch, 200-002-211, 1:1000), WASp (Santa Cruz, sc-5300, 1:500), N-WASp (Abcam, ab187527,

1:500), PCNA (Santa Cruz, sc-56, 1:500), PCNA (Abcam, ab18197, 1:500) and RAD51 (Sigma Aldrich, PC130). Images were acquired using a Zeiss Axio Observer Z1 Marianas™ Microscope attached with a CSU-W spinning disk unit using either a Hamamatsu Flash 4 CMOS camera or a Photometrics Prime 95b sCMOS with a 63× objective. Image analysis was carried out with FIJI (ImageJ) software. PLA foci positive cells were scored as cell nuclei with equal or greater than one PLA foci within them.

DNA fibre analysis

DNA fibre assay was performed as described previously with some modifications (28,31,32). In brief, exponentially growing cells were first incubated with 25 μM iododeoxyuridine (IdU) and then with 125 μM chlorodeoxyuridine (CldU) for the indicated times. Fibre spreads were prepared from 0.5 × 10^6 cells/ml. Slides were stained as described previously (31,32). Images were acquired with Leica SP8 or Carl Zeiss LSM 710 Meta confocal microscope using a 63x oil objective. Analysis was performed using the ImageJ software package (National Institutes of Health). A minimum of 100 fibres from three, unless stated otherwise, independent experiments were scored. Mann–Whitney test was used to determine statistical significance.

qPCR

RNA extraction and cDNA synthesis were performed using the RNeasy mini kit (Qiagen) and High Capacity cDNA Reverse Transcription Kit (Applied Biosystems). QPCR analysis was performed with QuantStudio™ 6 Flex Real-Time PCR System (Applied Biosystems) using SYBR Green PCR Master Mix (Life Technologies) and the following primers 5′-GTCCTACTTCATCCGCCTTTAC-3′ and 5′-TCGTCTGCAAAGTTCAGCC-3′ for WASP and 5′-GGCATGGACTGTGGTCATGAG-3′ and 5′-TGCACC ACCAACTGCTTAGC-3′ for GAPDH.

RPA complex expression, purification and *in vitro* pull down

RPA complex was expressed from a plasmid (a kind gift from David Cortez (Vanderbilt University, Nashville, Tennessee, US) (33,34) encoding 6xHis-tagged RPA1 (70 kDa), tagless RPA2 (32 kDa), and 6xHis-tagged RPA3 (14 kDa) in BL21 (D3) *E. coli* cells for 2 h at 37°C in LB medium with 100 μM/ml ampicillin after induction with 1 mM IPTG. Cells were harvested and lysed in buffer containing 50 mM Tris–HCl, pH 8.0, 400 mM NaCl, 1 mM PMSF, 10 μM $ZnCl_2$, 5% glycerol and protease inhibitor cocktail (Sigma, #S8830). Supernatant was applied to a HisTrap HP 5 ml column (DE Healthcare) calibrated in 5 volumes of calibration buffer containing 20 mM Tris–HCl, pH 8.0, 500 mM NaCl, 1 mM PMSF, 10 μM $ZnCl_2$ and 5% glycerol. Next, the column was washed in 10 column volumes with washing buffer: 20 mM Tris–HCl, pH 7.6, 500 mM NaCl, 20 mM imidazole, 10 μM $ZnCl_2$ and 5% glycerol. Then, the proteins were eluted from column with the linear imidazole gradient in final concertation as follow, 20 mM Tris–HCl, pH 7.5, 100 mM NaCl, 300 mM imidazole, 10 μM $ZnCl_2$ and 5% glycerol. The RPA complex of three proteins was bound to the column and was eluted from it by high imidazole concentration (about 250 mM). The eluate was diluted to bring the NaCl concentration down to 50 mM. It was then applied to a HiTrap Heparin HP 5 ml column (GE Healthcare) in 20 mM Tris–HCl, pH 7.5, 50 mM NaCl, 1 mM PMSF, 10 μM $ZnCl_2$ and 5% glycerol, and eluted with 10 volumes of 50–1000 mM NaCl linear gradient. The fractions containing all three proteins were joined together and purified RPA complex was rebuffered into storage buffer (50 mM Tris–HCl, pH 8.0, 100 mM NaCl, 1 mM DTT, 5% glycerol), aliquoted and frozen in –80°C. The complex composition was confirmed by western blot using antibodies recognizing His-tag peptide and RPA2 protein and by binding RPA complex to ssDNA and lack of biding it to dsDNA. Interaction of RPA complex with monomeric actin was analysed using G-Actin Sepharose beads (Hypermol). Reaction was performed in a buffer containing (10 mM Tris–HCl pH7.5, 150 mM NaCl, 1 mM DTT, 5% glycerol, 0.1% NP-40). Complexes were extensively washed with IP buffer before elution in 2× SDS sample buffer and subsequently boiled for 3 min followed by centrifugation. The resultant supernatant fraction was retained as the eluate.

YFP-NLS-β-actin co-immunoprecipitations

YFP-NLS-β-actin expression constructs were transfected into HEK293TN cells using lipofectamine 2000 (Thermo Scientific) following manufacturer's instructions. HEK293TN cells were harvested 48 h post transfection from a 70–80% confluent 15 cm tissue culture dish by trypsinisation, inactivation with serum containing media, centrifugation at 1500 rpm for 5 min, followed by the removal of the supernatant. Cells were washed twice in phosphate-buffered saline and lysed in IP buffer 1 (100 mM NaCl, 0.2% Igepal CA-630, 1 mM $MgCl_2$, 10% glycerol, 5 mM NaF, 50 mM Tris–HCl, pH 7.5), supplemented with SigmaFAST Protease Inhibitor Cocktail, EDTA free (Sigma-Aldrich, S8830) and 25 U ml^{-1} Benzonase (Novagen). After nuclease digestion, NaCl and EDTA concentrations were adjusted to 200 and 2 mM, respectively, and lysates were cleared by centrifugation (16 000 × g for 25 min). Lysates were incubated for 1 h with 20 μl of agarose binding control beads (ChromoTek), equilibrated in IP buffer 2 (200 mM NaCl, 0.2% Igepal CA-630, 1 mM $MgCl_2$, 10% glycerol, 5 mM NaF, 2 mM EDTA 50 mM Tris–HCl, pH 7.5) to pre-clear. The agarose binding control beads were pelleted by centrifugation at 2000 × g for 2 min and total protein quantified by the Bradford assay. Lysates were then incubated with 20 μl of GFP-Trap agarose beads (ChromoTek), equilibrated in IP buffer 2, for 2 h with end-to-end mixing at 4°C at a concentration of 1mg/ml. Complexes were washed 4× in IP buffer 2 before resuspension in 2 × SDS sample buffer and elution by boiling at 95°C for 10 min.

String analysis

Gene accession codes from iPOND analysis were input into the multiple protein search function of STRING (https://string-db.org/cgi/input?sessionId=b5U7THWxoyjd&input_page_active_form=

multiple_identifiers) (35) with the detected organisms selected as *Homo sapiens*. The network was then exported from STRING and imported into Cytoscape (v3.8.2). Functional enrichment network analysis was then conducted using the STRING plug-in, with the network to be set as background set to genome. The STRING Enrichment tab was selected, and the generated network was filtered by GO Biological processes. GO Biological processes associated with all the actin related processes were selected and exported as a new network. The subsequently generated network was saved, and the file was uploaded to STRING (https://string-db.org/cgi/input?sessionId=b5U7THWxoyjd&input_page_show_search=on). Active interaction sources settings were adjusted to display links associated with only experiments and databases. The minimum required interaction score was adjusted to high confidence (0.700) and the network was updated. GO terms GO:0034314 Arp2/3 complex-mediated actin nucleation and GO:0008154 Actin polymerization or depolymerization were selected in the analysis tab functional enrichment biological process list.

Statistics and reproducibility

Statistical analyses were done using GraphPad Prism 9 (GraphPad Software Inc.) or Microsoft Excel. Unpaired Students' *t*-test or Mann–Whitney test were used to determine statistical significance as indicated in the figure legends.

Contact for reagent and resource sharing

Further information and requests for resources and reagents should be directed to the Lead Contact, Wojciech Niedzwiedz (wojciech.niedzwiedz@icr.ac.uk).

RESULTS

NPF/AN family proteins are enriched at perturbed replication forks

To address the possible role of NPF/ANs during normal and stressed DNA replication we performed a deep mining of our iPOND (isolation of proteins on nascent DNA) data set (28,36,37) combined with STRING analysis (http://string-db.org) (35) performed with or without hydroxyurea (HU)-mediated replicative stress (RS) in HeLa cells. This analysis identified a cluster of proteins involved in actin polymerisation, including the ARP2/3 complex, WASp family proteins, and members of the formin family of actin nucleators (DIAPH1, 2 and 3), but not Spire family proteins, the latter known to nucleate actin polymers directly without ARP2/3 (Figure 1A). We validated the presence of these factors at replication forks (RFs) in two ways: a) iPOND/Western blot (WB) analysis and b) EdU-based proximity ligation assay (PLA), aka quantitative *in situ* analysis of protein interaction at RFs (SIRF) (15,38,39). Using iPOND/WB analysis we could readily detect WASp, N-WASp, and DIAPH1, as well as RPA2 (control) enriched at HU-perturbed RFs in both human T cells and HEK293TN cells (Supplementary Figure S1A-C). Notably, a thymidine chase decreased their association with nascent DNA as compared to HU treated samples, which indicates that these factors are likely recruited specifically to RFs in a RSR-dependent manner (29,40) (Supplementary Figure S1A–C). Accordingly, utilizing PLA we could also readily detect proximity of the NPFs (N-WASp, WASp) to newly-synthesised DNA (monitored by EdU labelling of nascent DNA marking RFs) in HeLa cells. The nuclear PLA signal for N-WASp and WASp was significantly enriched upon HU-induced RS compared to untreated as well as control samples (Figure 1B). Upon 4 mM/3 h HU treatment, which is known to induce replication fork collapse (29,41), we observed a decrease in the PLA signal when compared to 1 mM/1 h. This is consistent with the fact that fork collapse leads to dissociation of RF associated factors (29,41). Finally, thymidine addition resulted in a significant decrease in PLA signal between N-WASp or WASp and nascent DNA (Figure 1C), which is in support of our iPOND data. To ascertain that the observed phenotype is not restricted to EdU labelling we repeated these analyses using an antibody against PCNA—an established marker of RFs. Again, we readily detected association between PCNA and N-WASp or WASp (Supplementary Figure S1D and E) confirming their proximity to sites of DNA replication, which is in line with our recent analysis demonstrating WASp localisation to RFs in human T and B cells (15). Taken together, these data suggest that members of the NPF/AN family of proteins enrich at perturbed RFs in human immune and nonimmune cells, malignant or non-malignant.

Deficiency in NPF/ANs provokes global replication dysfunction

To address the mechanism by which NPF/ANs manage RS, we employed the DNA fibre assay to analyse various aspects of stressed DNA replication (42,43). Strikingly, replicative stress induced by HU resulted in a significant reduction in the average fork velocity in cells transiently depleted of N-WASp, DIAPH1 or WASp by RNA interference relative to WT control (Figure 2A, Supplementary Figure S2A–C). To validate the specificity of siRNA data we recapitulated these observations using (i) multiple different siRNAs against N-WASp or WASp (Supplementary Figure S2D), (ii) patient-derived DIAPH1-deficient cell-line and a complemented control cell line (Figure 2B), as well as (iii) a specific ARP2/3 inhibitor (CK-666; Supplementary Figure S2E). In addition, loss of WASp, N-WASp or DIAPH1 significantly impaired fork restart upon HU treatment (Figure 2C). WASp family members function as positive regulators of ARP2/3-mediated generation of short branched F-actin filaments (44) whereas formins, of the DIAPH-family, nucleate long unbranched F-actin filaments (45). Thus, given the striking similarity of the replication phenotypes we observed in the tested NPF/ANs, we next tested if these factors function in a single or parallel pathway(s) to manage RS. To this end, we tested the impact on DNA replication (measured as fork speed) of either WASp or DIAPH1 depletion alone or together with an ARP2/3 inhibitor under HU-induced stress. Targeting either WASp or ARP2/3 alone as well as inhibiting both together resulted in a similar replication defect, indicating that WASp and ARP2/3

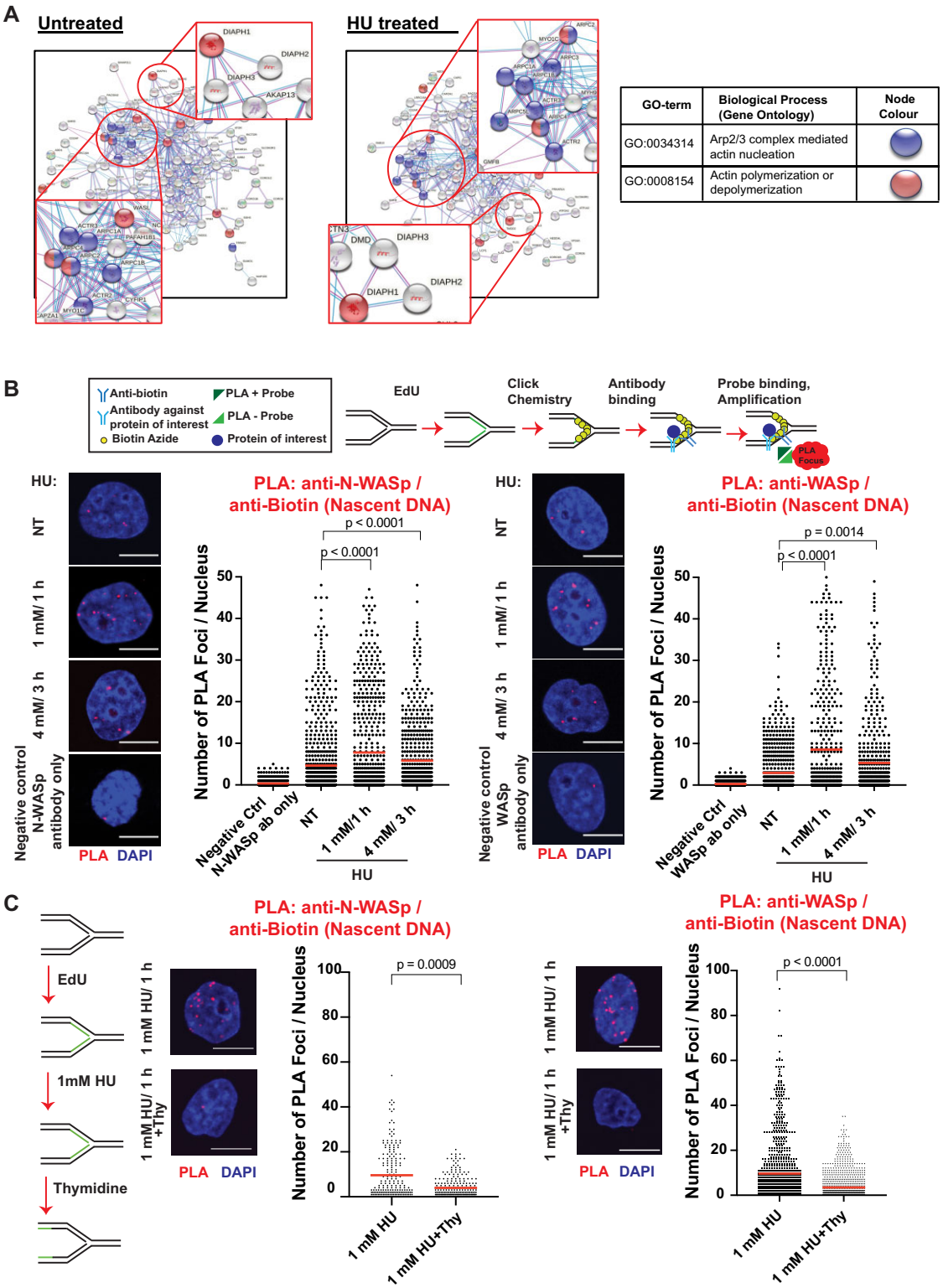


Figure 1. WASp, N-WASp and DIAPH1 associate with replication forks. (**A**) STRING analysis of iPOND/MS data in untreated and HU treated HeLa S3 cells. (**B**) Representative images and dot plots of the number of N-WASp/Biotin (nascent DNA) and WASp/Biotin (Nascent DNA) PLA foci per nucleus in HeLa cells upon HU treatment as indicated (red lines indicate mean values). Dot plots represent data pooled from three independent experiments. Statistical significance was determined using the Mann–Whitney test (left panel median values negative Ctrl N-WASp ab only [0] $n = 524$, NT [1] $n = 731$, 1 mM/1 h [2] $n = 594$, 4 mM/3 h [2] $n = 561$; right panel median values Negative Ctrl WASp ab only [0] $n = 545$, NT [0] $n = 649$, 1 mM/1 h [1] $n = 557$, 4 mM/3 h [0] $n = 620$). (**C**) Representative images and dot plots of number of N-WASp/Biotin (Nascent DNA) and WASp/Biotin (Nascent DNA) PLA foci per nucleus in HeLa cells treated with 1 mM HU for 1 h, followed or not by thymidine chase as indicated (red lines indicate mean values). Dot plots represent data pooled from two independent experiments. Statistical significance was determined using the Mann–Whitney test (Left panel median values 1 mM/1 h [4] $n = 139$, 1 mM/1 h Thy [2] $n = 244$; right panel median values 1 mM/1 h [5] $n = 1012$, 1 mM/1 h Thy [0.5] $n = 1084$).

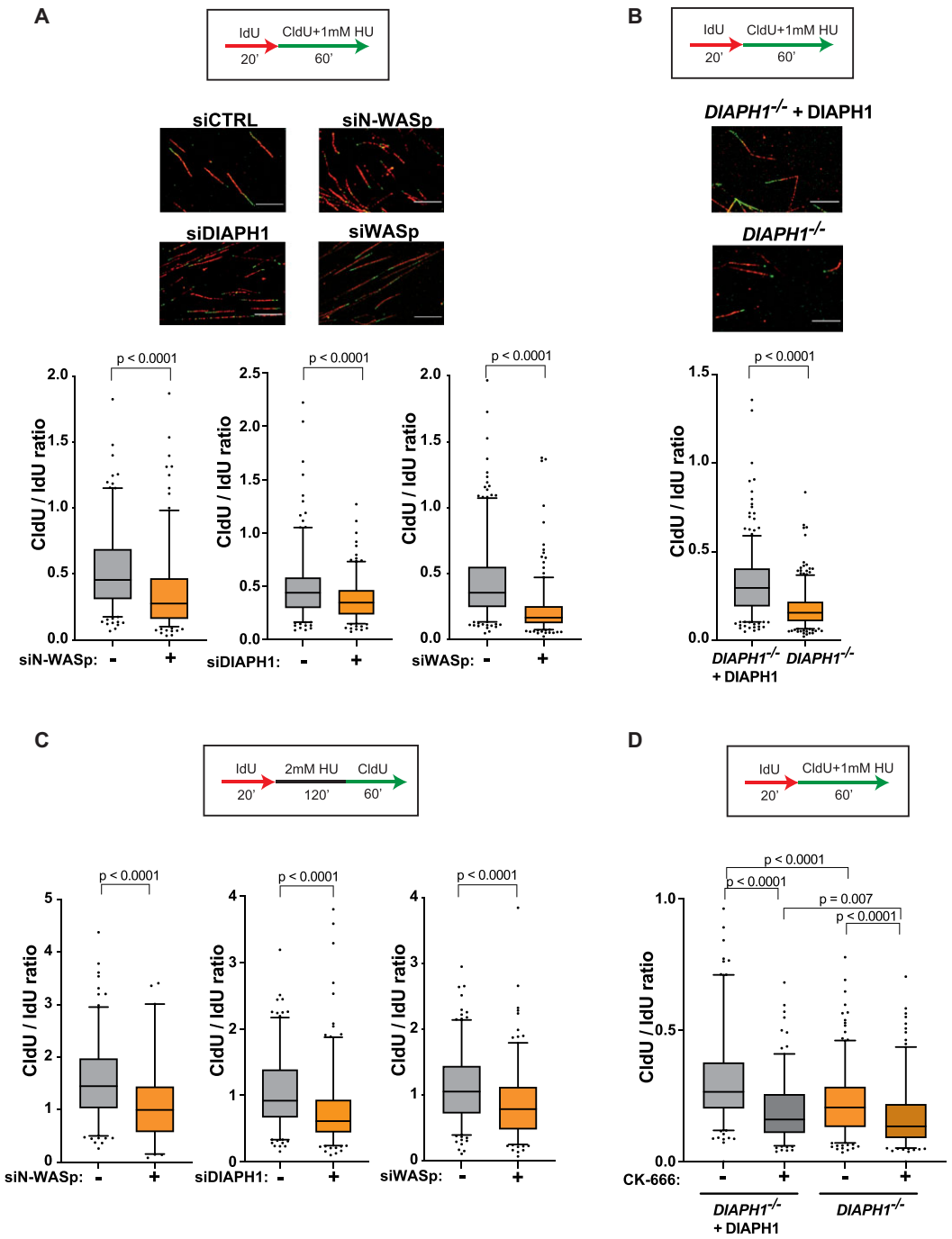


Figure 2. WASp, N-WASp, ARP2/3 and DIAPH1 are required for intact replication dynamics under condition of replicative stress. (**A**) Representative DNA fibre images and box plots of CldU/IdU tract ratios from HeLa cells treated with control siRNA (–) or siRNA against WASp, N-WASp or DIAPH1(+) and exposed to 1 mM HU during CldU labelling pulse. Whiskers indicate 5–95 percentile. Box plots represent data pooled from three (siWASp) or two (siN-WASp and siDIAPH1) independent experiments. Statistical significance was determined using the Mann–Whitney test (left panel siCTRL $n =$ 223; siN-WASp $n = 218$; central panel siCTRL $n = 222$; siDIAPH1 $n = 218$; right panel siCTRL $n = 311$, siWASp $n = 282$). (**B**) Box plots of CldU/IdU tract ratios from DIAPH1-deficient patient-derived cells treated with 1 mM HU during CldU labelling pulse. Whiskers indicate 5–95 percentile. Box plots represent data pooled from three independent experiments. Statistical significance was determined using the Mann–Whitney test (DIAPH1-/-+DIAPH1 $n = 379$; DIAPH1-/- $n = 374$). (**C**). Box plots of CldU/IdU tract ratios of HeLa cells treated with control siRNA (–) or siRNA against N-WASp, DIAPH1 or WASp (+). After IdU pulse, cells were exposed to 2 mM HU for 2 h followed by release into CldU for 60 min. Whiskers indicate 5–95 percentile. Box plots represent data pooled from two independent experiments. Statistical significance was determined using the Mann–Whitney test (left panel siCTRL $n = 166$; siN-WASp $n = 64$; central panel siCTRL $n = 199$; siDIAPH1 $n = 205$; right panel siCTRL $n = 204$, siWASp $n = 198$). (**D**) Box plots of CldU/IdU tract ratios from DIAPH1-deficient patient-derived cells treated with CK-666 (ARP2/3 inhibitor) (+) or DMSO (–). During CldU labelling pulse, cells were exposed to 1 mM HU. Whiskers indicate 5–95 percentile. Box plots represent data pooled from two independent experiments. Statistical significance was determined using the Mann–Whitney test (*DIAPH1*$^{-/-}$+DIAPH1 $n = 210$; *DIAPH1*$^{-/-}$+DIAPH1 + ARP2/3i $n = 173$; *DIAPH1*$^{-/-}$ $n =$ 245, *DIAPH1*$^{-/-}$+ARP2/3i $n = 211$).

both function in the same pathway to manage RS (Supplementary Figure S3A). In contrast, inhibition of ARP2/3 in DIAPH1-deficient cells led to a significantly greater replication defect than the defect displayed by DIAPH1-deficient cells alone (Figure 2D), indicating an additive effect between branched and unbranched actin polymerisation pathways in promoting DNA replication. Taken together, these data suggest that WASp/ARP2/3- and DIAPH1 (formin)-mediated actin signalling is required to facilitate fork stability and global RF dynamics.

Interfering with actin polymerisation elicits replication-associated DNA damage

Unstable RFs are prone to collapse into single-ended DSBs. Thus, to determine the fate of HU-stalled RFs when actin nucleation is impaired, we analysed the formation of 53BP1 foci (a canonical marker of DSB) in cells depleted for either N-WASp, WASp or DIAPH1, either in unperturbed conditions, after 1 mM/ 1h HU treatment (mild RS associated with fork stalling) or 4 mM/ 3h HU treatment (high RS, associated with elevated RF collapse) (46). We noticed a significant increase in the number of 53BP1 foci in cyclin A-positive (S/G2-phase) cells after depleting either of the three proteins as compared to their respective controls, most likely due to extensive fork collapse (Figure 3A). Notably, we reproduced these findings in cells treated with an ARP2/3 inhibitor (CK-666) and in the patient-derived DIAPH1-deficient cells (Supplementary Figure S3B). Fork collapse is known to induce genome instability resulting in the increased formation of micronuclei, which are particularly prominent in cancer cell models (e.g. HeLa) that display an intrinsically high levels of replicative stress. Consistently, loss of WASp, N-WASp, or DIAPH1 as well as inhibition of ARP2/3 resulted in increased levels of micronuclei compared to control cells even in the absence of any exogenous replication stressors (Figure 3B and Supplementary Figure S3C). This observation further underscores the role of NPF/ANs in preventing genome-instability not only in response to exogenous genotoxic insults but also those arising from endogenous sources of RS, including but not limited to R loops (RNA-DNA hybrids), transcription–replication (T–R) conflicts, etc. (15,17). Collectively, these data support the notion that NPF/ANs promote recovery of perturbed RFs and suppress replication-associated genome instability under normal growth conditions as well as in response to exogenous replicative stress.

Actin nucleation protects replication forks from uncontrolled degradation by promoting RPA localisation to ssDNA

Since unstable RFs undergo excessive nucleolytic degradation (47–50), we tested whether loss of NPF/ANs influences this process by employing a modified DNA fibre protocol (28). Interestingly, depletion of N-WASp, DIAPH1 or WASp in HeLa cells, resulted in a significant shortening of the CldU tracts (in the IdU > CIdU > HU labelling scheme) compared to controls (Figure 4A). This data indicate that pathological nucleolytic degradation of HU-perturbed forks is not restricted to WASp deficiency or to human T and B lymphocytes, but is a more general phenotype associated with depletion of multiple NPF/AN proteins (15). As pathological fork resection is attributed to the unrestrained activity of the MRE11 or DNA2 nucleases, we monitored fork degradation in cells treated with the MRE11 inhibitor mirin, or siRNA targeting DNA2. Treatment with mirin or depletion of DNA2 supressed excessive fork degradation observed in cells depleted of NPF/ANs (Supplementary Figure S3D). Moreover, depletion of SMARCAL1 (SWI/SNF related, matrix associated, actin dependent regulator of chromatin, subfamily A like 1) also rescued excessive fork degradation in cells depleted of N-WASp, WASp or DIAPH1 suggesting a role in fork protection downstream to RF reversal (Figure 4B and Supplementary Figure S3E). Since pathological fork resection is attributed to fork deprotection (51) and we have shown that WASp-deficient immune cells (T and B cells) display defective ssDNA-RPA complex formation (15), we tested if depletion of other NPF/ANs would have a similar function in non-immune cells (i.e. HeLa) as well. Remarkably, depletion of either N-WASp or DIAPH1 or WASp alone led to defective RPA foci formation upon HU-induced RS (Figure 4C, Supplementary Figure S4A). To discount the possibility of off-target effects associated with siRNA, we again validated the specificity of our data by recapitulating these observations in two ways: (i) employing different siRNAs against N-WASp or WASp (Supplementary Figure S4B) as well as (ii) utilising a specific ARP2/3 inhibitor (CK-666; Figure S4C). In line with this, loading of RAD51 at perturbed/collapsed RFs, an event dependent on RPA-ssDNA formation (8) was also defective in WASp and DIAPH1 depleted cells, as measured by the PLA assay between nascent DNA (EdU labelling) and RAD51 (Figure 5A). Furthermore, the number of RAD51 foci detected by IF after HU treatment upon WASp depletion was also significantly reduced when compared to those treated with control siRNA (Supplementary Figure S4D), thus supporting our PLA-based analysis. Formation of RPA-ssDNA is required for ATR activation and consequently, we have shown recently that WASp is required for this response in T and B cells (15). To ascertain whether other members of the NPF/ANs family are similarly required for this response we analysed the efficiency of ATR signalling in cells depleted for N-WASp or DIAPH1. Again, and in line with the defective RPA loading onto ssDNA, ATR activity was significantly compromised as evidenced by impaired phosphorylation of CHK1 (pSer345) in N-WASp, WASp and DIAPH1 depleted HeLa cells, and increased replication origin firing in N-WASp or WASp depleted HeLa cells and in DIAPH1-deficient cells (Figure 5B and C).

Since impaired formation of RPA foci and defective DNA replication was not restricted to WASp deficiency alone, but was observed with loss of multiple other members of the NPF/ANs protein family, we considered that this phenotype could arise through at least three distinct mechanisms: (i) an overall decrease in the levels of RPA expression in cells, (ii) defective nucleolytic processing of HU-perturbed forks failing to generate ssDNA, and/or (iii) defects in a downstream process that promotes RPA association with ssDNA. To distinguish between these possibilities, we first analysed total RPA2 protein levels in cells depleted of NPF/ANs, which indicated that loss of these factors does

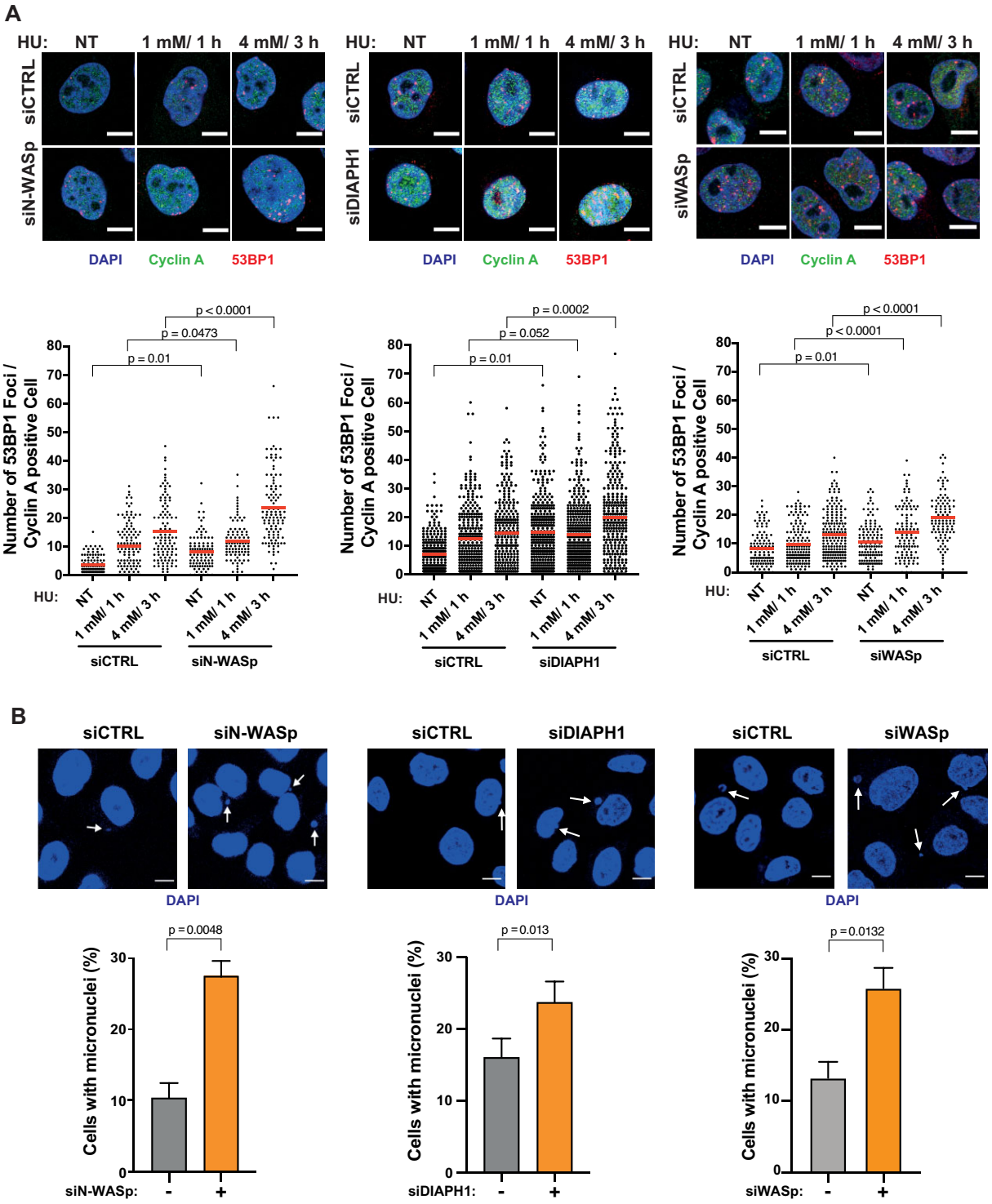


Figure 3. Depletion of WASp, N-WASp or DIAPH1 leads to increase in replication fork collapse. (**A**) Representative images and dot plots of the number of 53BP1 foci per cyclin A positive HeLa cells treated with control siRNA (siCTRL) or siRNA targeting N-WASp, DIAPH1 or WASp upon HU treatment. Dot plots represent data pooled from three independent experiments (red lines indicate mean values). Statistical significance was determined using the Mann–Whitney test (Left panel median values siCTRL NT [2] $n = 104$, siCTRL 1 mM/1 h [10] $n = 125$, siCTRL 4 mM.3 h [13] $n = 110$, siN-WASp NT [8] $n = 102$, siN-WASp 1 mM/1 h [11] $n = 89$, siN-WASp 4 mM/3 h [20.5] $n = 110$; middle panel median values siCTRL NT [6] $n = 252$, siCTRL 1 mM/1 h [10] $n = 297$, siCTRL 4 mM/3 h [13] $n = 277$, siDIAPH1 NT [13] $n = 362$, siDIAPH1 1 mM/1 h [11] $n = 372$, siDIAPH1 4 mM/3 h [18] $n = 327$; right panel median values siCTRL NT [7] $n = 109$, siCTRL 1 mM/1 h [8] $n = 151$, siCTRL 4 mM/3 h [11.5] $n = 186$, siWASp NT [9] $n = 122$, siWASp 1 mM/1 h [12.5] $n = 108$, siWASp 4 mM/3 h [18] $n = 102$). (**B**) Representative images and quantification of micronuclei formation in HeLa cells treated with control siRNA (–) or siRNA targeting N-WASp, DIAPH1 or WASp (+). Bar plots represent data pooled from at three (N-WASp, DIAPH1) or four (WASp) independent experiments with 100 cells per condition per experiment analysed. Bar charts represent mean ± SEM of three or four experiments and statistical significance was determined using *t* test.

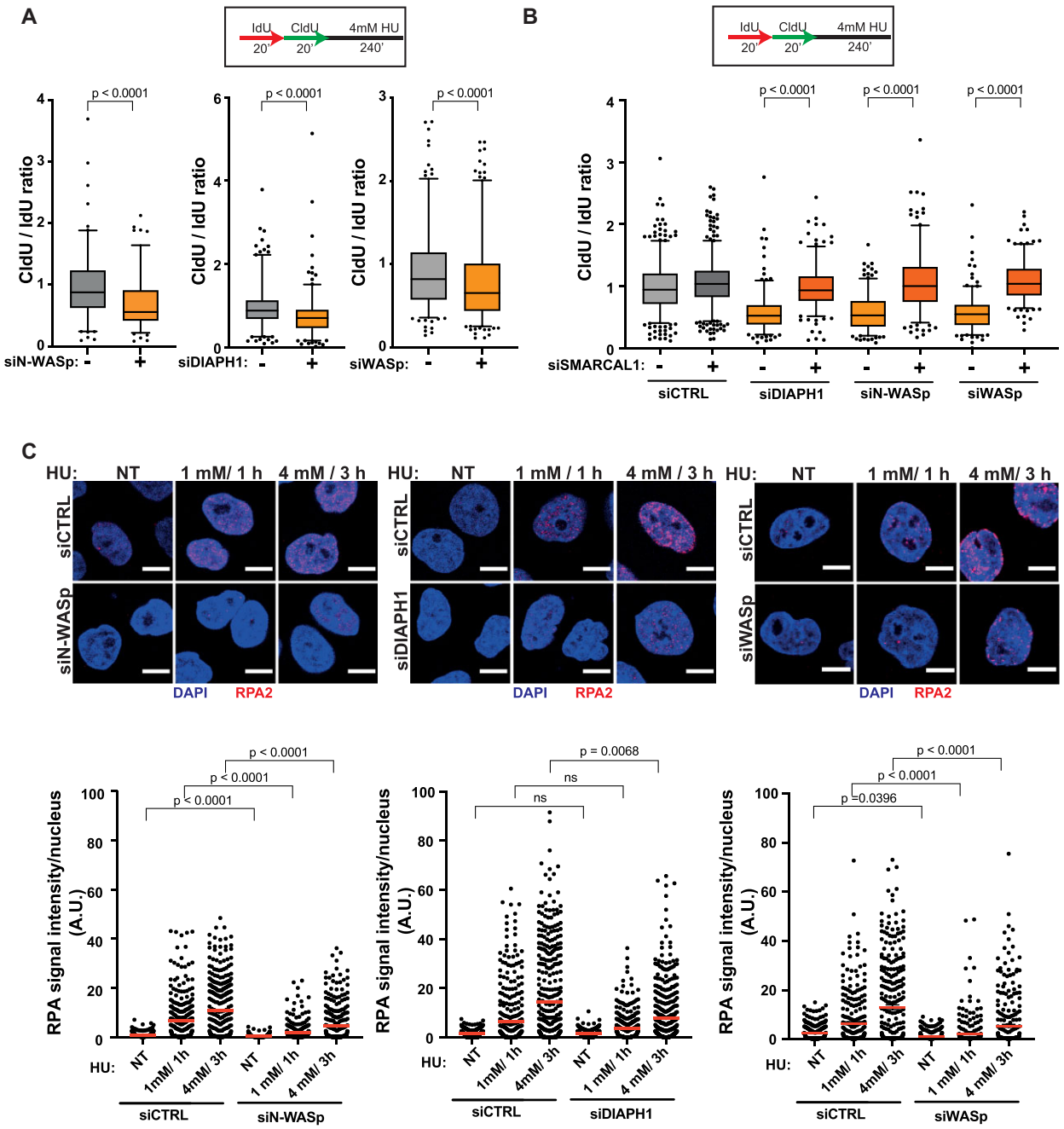


Figure 4. Depletion of WASp, N-WASp or DIAPH1 leads to increased degradation of nascent DNA and defects in RPA recruitment to perturbed replication forks. (**A**) Box plots of CldU/IdU tract ratios from HeLa cells treated with control siRNA(-) or siRNA targeting N-WASp, DIAPH1 or WASp (+). CldU/IdU pulse labelling was followed by treatment with 4 mM HU for 4h. Whiskers indicate 5–95 percentile. Box plots represent data pooled from four (siWASp), or two (siN-WASp, siDIAPH1) independent experiments. Statistical significance was determined using the Mann–Whitney test (left panel siCTRL $n = 123$; siN-WASp $n = 116$; central panel siCTRL $n = 210$; siDIAPH1 $n = 204$; right panel siCTRL $n = 232$, siWASp $n = 259$). (**B**). Box plots of CldU/IdU tract ratios from HeLa cells treated with control siRNA or siRNA targeting N-WASp, DIAPH1 or WASp and SMARCAL1. CldU/IdU pulse labelling was followed by treatment with 4 mM HU for 4 h. Whiskers indicate 5–95 percentile. Box plots represent data pooled from two independent experiments. Statistical significance was determined using the Mann–Whitney test (siCTRL $n = 452$, siSMARCAL1 $n = 499$, siDIAPH1 $n = 235$, siDIAPH1/siSMARCAl1 $n = 248$, siN-WASp $n = 231$, siN-WASp/siSMARCAL1 $n = 235$, siWASp $n = 232$, siWASp/siSMARCAL1 $n = 230$). (**C**) Representative images and dot plots of RPA signal intensity per nucleus of Hela cells treated with control siRNA or siRNA targeting N-WASp, WASp or DIAPH1 upon HU treatment as indicated (red lines indicate mean values). Dot plots represent data pooled from three independent experiments. Statistical significance was determined using the Mann–Whitney test (left panel median values siCTRL NT [0.4295] $n = 300$, siCTRL 1 mM/1 h [2.4368] $n = 300$, siCTRL 4 mM/3 h [6.1924] $n = 300$, siN-WASp NT [0.1678] $n = 300$, siN-WASp 1 mM/1 h [0.2192] $n = 300$, siN-WASp 4 mM/3 h [0.4568] $n = 300$; middle panel median values siCTRL NT [1.2417] $n = 373$, siCTRL 1 mM/1 h [1.3593] $n = 395$, siCTRL 4 mM/3 h [3.9828] $n = 407$, siDIAPH1 NT [1.1798] $n = 392$, siDIAPH1 1 mM/1 h [1.1713], siDIAPH1 4 mM/3 h [2.6214] $n = 439$; right panel median values siCTRL NT [0.5790] $n = 300$, siCTRL 1 mM/1 h [0.8026] $n = 300$, siCTRL 4 mM/3 h [1.7282] $n = 300$, siWASp NT [0.5426] $n = 300$, siWASp 1 mM/1 h [0.4892] $n = 300$, siWASp 4 mM/3 h [0.5701] $n = 300$.

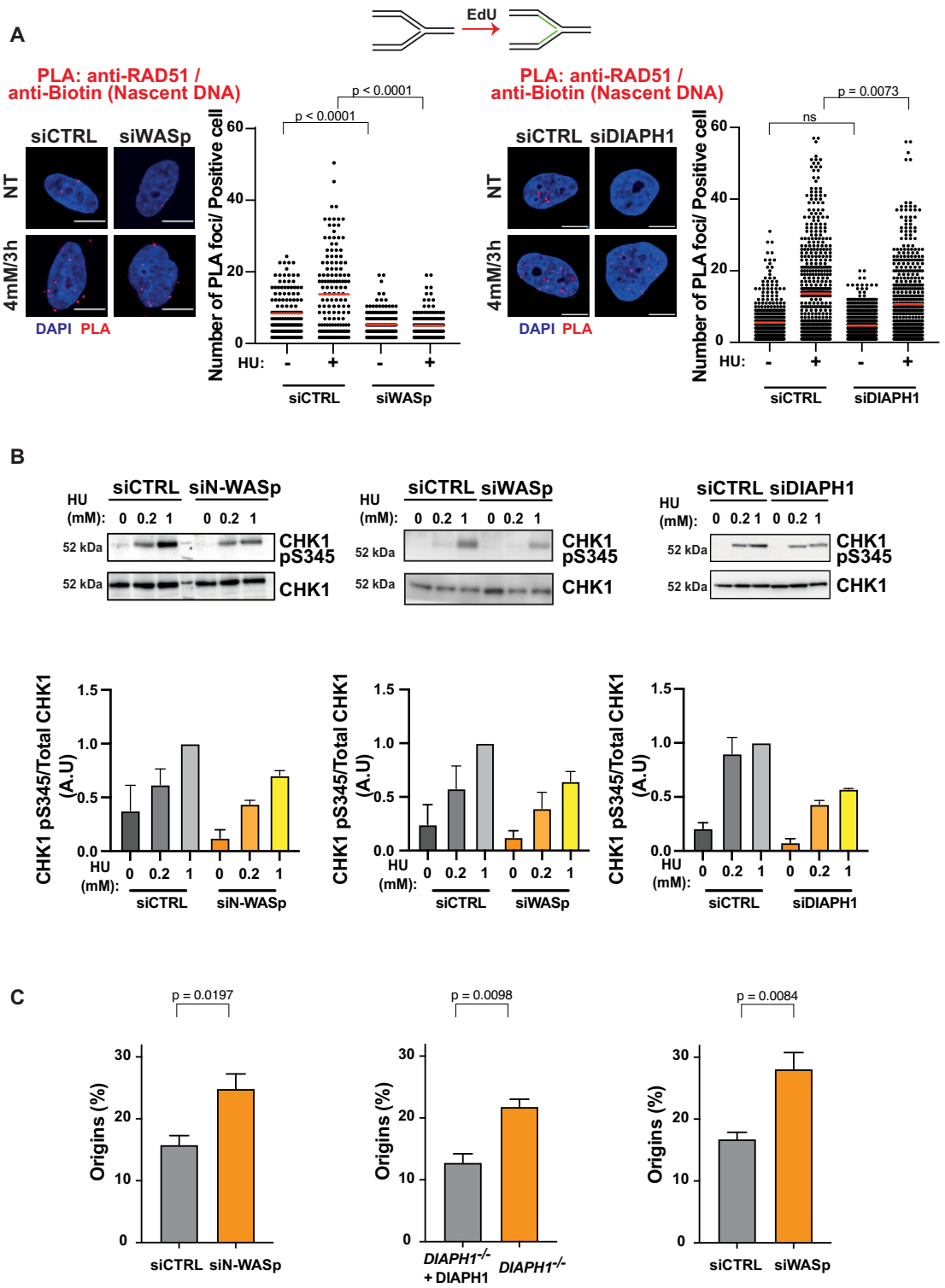


Figure 5. Depletion of WASp, N-WASp or DIAPH1 leads to defects in ATR signalling activation. (**A**) Dot plots of number of RAD51/Biotin (nascent DNA) PLA foci per nucleus in HeLa cells treated with control siRNA or siRNA against WASp upon treatment with 4 mM HU for 3 h. Dot plots represent data pooled from two independent experiments (red lines indicate mean values). Statistical significance was determined using the Mann–Whitney test (left panel median values siCTRL NT [7] $n = 145$, siCTRL 4 mM/3 h [12] $n = 147$, siWASp NT [3] $n = 151$, siWASp 4 mM/3 h [3] $n = 129$; right panel median values siCTRL NT [4] $n = 393$, siCTRL 4 mM/3 h [9.5] $n = 516$, siDIAPH1 NT [4] $n = 545$, siDIAPH1 4 mM/3 h [7] $n = 518$. (**B**). WB showing CHK1 phosphorylation in HeLa cells with or without indicated HU treatment for 1 h, treated with control siRNA (siCTRL) or siRNA targeting N-WASp or WASp as well as the same analysis in DIAPH1-deficient patient-derived cells and the corresponding control cells. Bar charts represent mean ± SEM of three experiments and statistical significance was determined using *t* test. (**C**) Quantification of the frequency of origin firing in HeLa cells treated with control siRNA or siRNA against N-WASp, WASp or DIAPH1. Bar charts represent mean ± SEM of four (siN-WASp and siWASp) or three (DIAPH1) independent experiments. Statistical significance was determined using t test.

not affect RPA2 levels (Figure 6A), as we previously showed in WASp-deficient T cells (15). We also used sub-cellular fraction and WB to confirm that the cytoplasmic and nuclear pools of RPA1 and 2 did not alter upon depletion of NPF/ANs (Supplementary Figure S5A). Next, we analysed efficiency of ssDNA generation at HU-perturbed RFs by BrdU staining under non-denaturing condition. Here too, we did not observe a decrease in ssDNA generation (end-resection) at perturbed RFs upon depletion of these factors (Figure 6B). Thus, we considered it likely that NPF/ANs may function as RPA 'chaperones' facilitating RPA loading and/or stability at RFs both, in *cis* as in the case of WASp (15) but also in *trans*, likely via modulating the actin state, i.e. G-actin (monomeric) versus F-actin (polymeric).

A simple prediction from this model would be that a surplus of RPA may be enough to overcome limitation associated with suboptimal RPA chaperoning in NPF/AN-deficient cells. To test this hypothesis, we utilised the previously characterised SuperRPA U2OS cells generated in the Lukas lab, that display a modest two-fold excess of all three RPA subunits. Importantly, these cells retain a normal cell-cycle profile and do not show spontaneous defects in either DNA replication or ATR activation (52). Strikingly, RPA over-expression largely restored RPA loading/stability at HU-perturbed forks in DIAPH1- or WASp-deficient cells (Supplementary Figure S5B), as well as restored global RF dynamics (Supplementary Figure S5C and D) with a concomitant rescue of ectopically-increased fork collapse – as measured by 53BP1 foci formation (Supplementary Figure S6A and B). To examine the specificity of the rescue phenotype we tested if a surplus of RPA can rescue, in general, any phenotype associated with RF instability. To this end, we analysed DNA replication in SuperRPA cells depleted for BRCA2, since BRCA2-depletion confers a strong defect in fork stability (48,53). In support of a specific role for NPF/ANs in facilitating RPA association with ssDNA and RF stability, we did not observe a similar rescue of BRCA2-associated replication phenotype in SuperRPA cells (Supplementary Figure S6C-E).

Actin polymerisation mutants recapitulate the phenotypes associated with loss of NPF/ANs

Our above results suggest that actin nucleators, i.e. components of ARP2/3 or formin-dependent pathways, act early in the RSR pathway to promote the localisation of RPA to perturbed forks, stimulating efficient RPA-ssDNA complex formation both, directly through WASp-RPA interaction (15) but also indirectly through another putative mechanism. Indeed, a recent report by Pfitzer *et al.* (54) demonstrated that RPA2 coimmunoprecipitates (co-IPs) with nuclear actin, which proposes a model that G-actin/F-actin state itself may somehow influence the ability of RPA to form RPA-ssDNA complexes. To test this hypothesis, we first show that sepharose-coated monomeric G-actin directly binds purified RPA complex (Figure 7A and Supplementary Figure S7A) by *in-vitro* pull-down assays, suggesting that the *in vivo* RPA:G-actin association is also likely to be a direct interaction. Furthermore, we show that actin co-IPs with RPA2 in human cells spontaneously (without HU-induced replication stress), however, upon HU treatment, this RPA:actin interaction is decreased (Supplementary Figure S7B). Notably, and in direct support of the role of NPF/ANs in 'chaperoning' RPA-ssDNA complex formation, we observe that a hyper-depolymerising G13R β-actin mutant (YFP-NLS-β-actin^{G13R}) (55,56) preferentially interacts with RPA2 in co-IP analyses from human HEK293TN cell extracts, when compared to WT (YFP-NLS-β-actin^{WT}) or the S14C hyper-polymerising mutant of β-actin (YFP-NLS-β-actin^{S14C}) (Figure 7B) (56). Accordingly, cells over-expressing an actin polymerization-incompetent (YFP-NLS-β-actin^{G13R}) mutant that preferentially associates with RPA phenocopy the abnormal phenotypes associated with the loss of NPF/ANs i.e. defective RPA foci formation, ATR activation as well as global impairment in DNA replication (Figure 7C, D, Supplementary Figure S7C). In contrast, cells expressing actin polymerization-hypercompetent S14C mutant (YFP-NLS-β-actin^{S14C}) showed phenotypes similar to cells expressing the control YFP-NLS-β-actin^{WT} (Figure 7C, D)

Note, WT and S14C mutant have a similar RPA foci phenotype (Figure 7C), suggesting a rate-limiting step within the actin pathway that may be distinct from actin filament formation, especially since we also show that all 3 actins (WT, S14C, G13R) are expressed at a similar level (Figure 7E). Thus, our data suggest a unique functional and co-operative interaction between RPA, actin and NPF/ANs, where a combination of *cis* and *trans*, actin-state dependent mechanisms calibrate RPA activity at the forks to safeguard DNA replication (Model, Figure 7F).

DISCUSSION

The RPA-ssDNA-protein complex plays a key role in protecting ssDNA generated during DNA metabolism, including at RFs, as well as acting as a 'platform' for recruitment/signalling/regulation of a plethora of DNA repair factors. However, increased RPA levels can be toxic likely due to excessive formation of RPA–ssDNA complexes (13,52,57–59). Our recent report (15) as well as work in yeast *Saccharomyces cerevisiae* (Sc) and Xenopus together point to active mechanisms employed by cells to dynamically control the ability of RPA to associate/dissociate with ssDNA (10,11).

Here, we have shown that not only WASp, but also other members of the NPF/ANs protein family such as N-WASp, ARP2/3 or DIAPH1 as well as actin itself, promote efficient localisation of RPA to perturbed forks and by doing so promote ATR activation and supress ectopic fork resection. In line with this, we show that NPF/ANs involved in ARP2/3 or formin-dependent actin polymerisation are specifically enriched at perturbed forks and their loss preclude RPA localisation to ssDNA resulting in defective activation of ATR, excessive fork degradation and ultimately RF collapse. The extensive fork degradation that we observed is likely due to increased fork regression since this phenotype can be rescued by SMARCAL1 depletion, however the amount of ssDNA generated at perturbed RFs seems to be similar between WT and NPFs/ANs mutants. Therefore, we conclude that the kinetics of resection that is required to generate ssDNA at the fork is unaffected, but fork regression coupled with fork deprotection (lack of

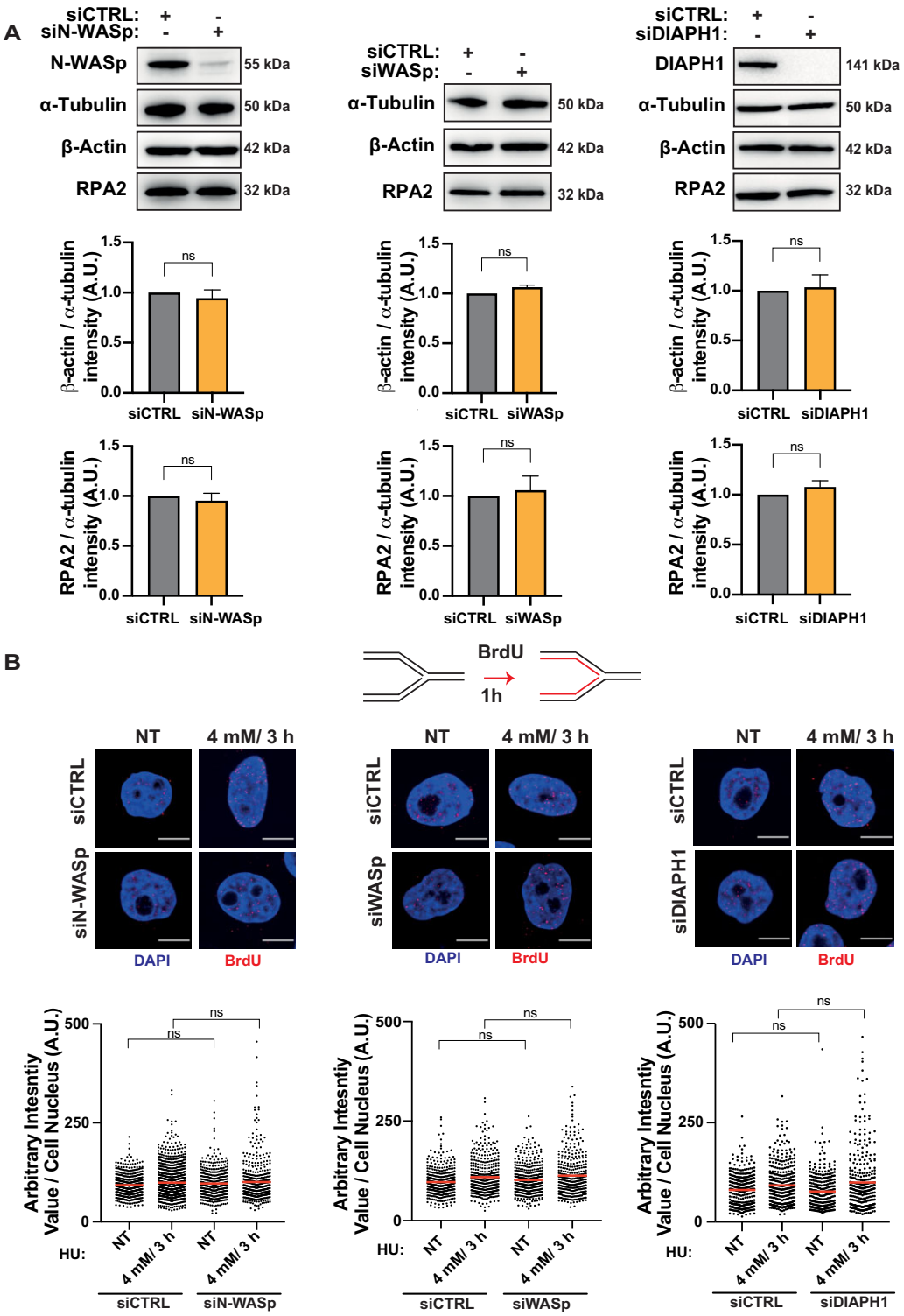


Figure 6. Depletion of WASp, N-WASp or DIAPH1 neither affects RPA or β-actin protein expression nor ssDNA formation. (**A**) WB and quantitation showing protein levels of RPA2 and β−actin upon depletion of N-WASp, DIAPH1 or WASp. Bar charts represent mean ± SEM of three experiments and statistical significance was determined using *t* test. (**B**) Representative images and dot plots of BrdU signal intensity per nucleus of Hela cells treated with control siRNA (siCTRL) or siRNA targeting N-WASp, DIAPH1 or WASp upon HU treatment at the indicated dose/duration (red lines indicate mean values). Cells were incubated with BrdU (10 μM) for 1 h prior to HU treatment. Dot plots represent data pooled from two independent experiments. Statistical significance was determined using the Mann–Whitney test. n.s., nonsignificant (left panel median values siCTRL NT [88.90] $n = 585$, siCTRL 4 mM/3 h [92.01] $n = 1038$, siN-WASp NT [91.53] $n = 431$, siN-WASp 4 mM/3 h [86.23] $n = 479$; middle panel median values siCTRL NT [93.11] $n = 435$, siCTRL 4 mM/3 h [99.71] $n = 435$, siWASp NT [94.31] $n = 425$, siWASp 4 mM/3 h [97.60] $n = 380$; right panel median values siCTRL NT [83.70] $n = 368$, siCTRL 4 mM/3 h [82.89] $n = 371$, siDIAPH1 NT [70.80] $n = 319$, siDIAPH1 4 mM/3 h [81.44] $n = 371$).

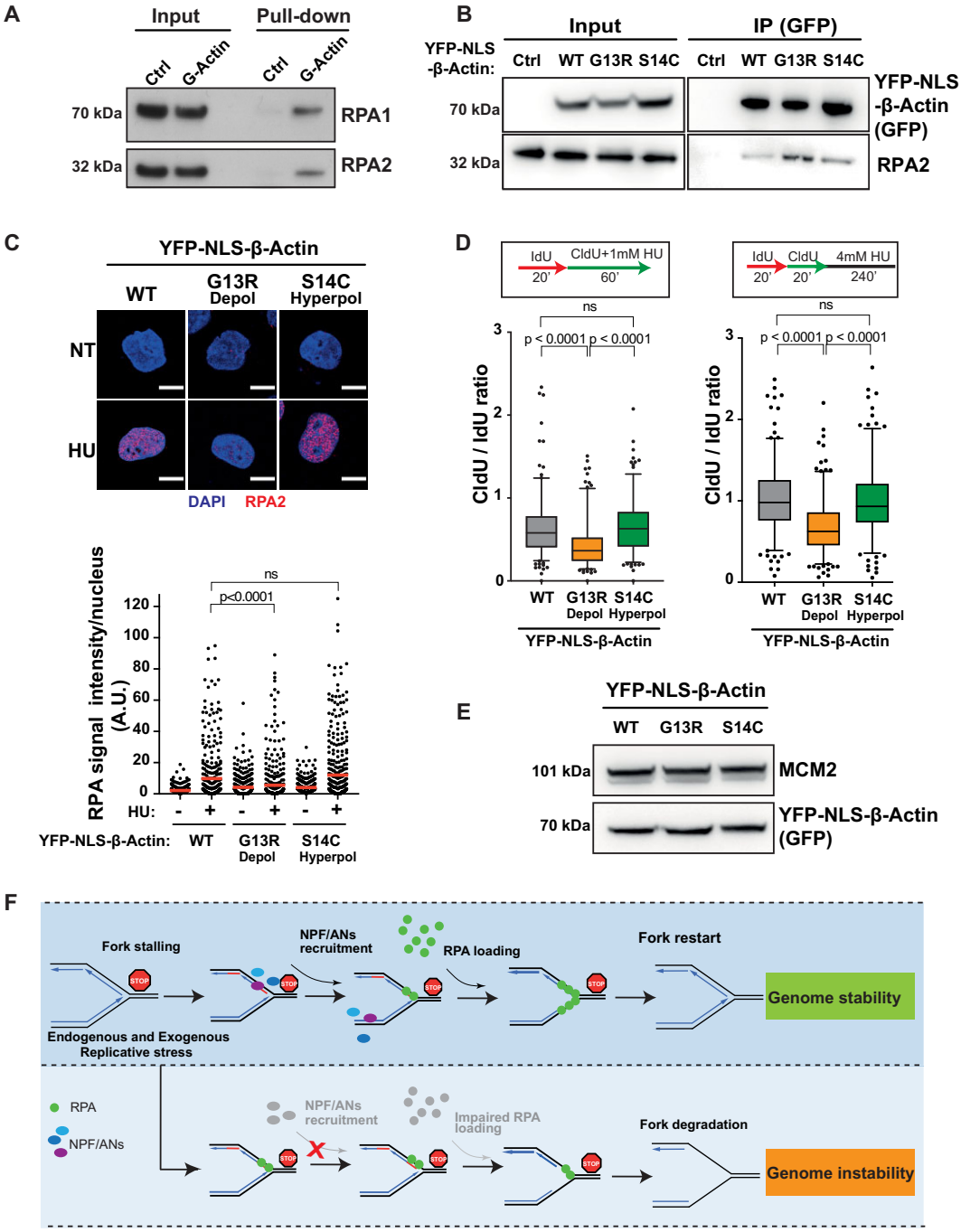


Figure 7. Monomeric actin directly binds RPA and actin polymerization is required for efficient RPA deposition at perturbed replication forks. (**A**) RPA directly binds G-actin. WB of RPA *in vitro* pull down with G-actin conjugated sepharose beads. Ctrl, control. (**B**) WB of immunoprecipitation (IP) experiments in HEK293TN cells expressing YFP-NLS-β-actin WT, G13R or S14C mutant. (**C**) Representative images and dot plot of RPA signal intensity in HeLa cells expressing YFP- NLS-β-actin WT, G13R or S14C mutant upon 1mM HU treatment for 1h. Dot plots represent data pooled from three independent experiments (red lines indicate mean values). Statistical significance was determined using the Mann–Whitney test. ns, nonsignificant, (median values WT NT [1.2965] $n = 337$, WT 4 mM/3 h [2.4615] $n = 359$, G13R NT [1.5587] $n = 365$, G13R 4 mM/3 h [1.0400] $n = 392$, S14C NT [2.6205] $n = 401$, S14C 4 mM/3 h [2.9104] $n = 432$). (**D**) Box plots of CldU/IdU tract ratios of HeLa cells expressing YFP-NLS-β-actin WT, G13R or S14C mutant proteins treated with 1 mM HU during CldU labelling pulse (left panel) or CldU/IdU pulse labelling was followed by treatment with 4 mM HU for 4 h (right panel). Whiskers indicate 5–95 percentile. Box plots represent data pooled from two independent experiments. Statistical significance was determined using the Mann–Whitney test. ns, nonsignificant (left panel WT $n = 225$; G13R $n = 194$; S14C $n = 196$; right panel WT $n = 227$; G13R $n = 227$; S14C $n = 206$). (**E**) Representative WB showing levels of expression of YFP-NLS-β-actin WT, G13R or S14C in HeLa cells from C and D. (**F**) Proposed model for the role of NPF/ANs in the replicative stress response. Replicative stress leads to fork stalling and generation of ssDNA, subsequently the association of actin nucleators (ANs) and nucleation promoting factors (NPFs) with sites of ongoing replication facilitates RPA deposition, either directly (via WASp) or indirectly (via actin polymerization), in order to protect ssDNA generated at perturbed forks. This allows for an efficient fork restart and promotes genome stability. Depletion of NPF/ANs and/or interference with actin polymerization impairs RPA loading/stability on ssDNA leading to extensive nascent strand degradation and ultimately genome instability.

RPA loading) drives extensive fork degradation of nascent DNA strands. Defective RPA loading is associated with impaired RAD51 localization upon replicative stress, accordingly we observe a decreased RAD51 signal at perturbed RFs, as measured by both, IF and PLA assay. Thus, we conclude that NPF/ANs loss effects RAD51 recruitment to perturbed RFs compromising their stability (15,16). Indeed, WASp and DIAPH1 deficient cells show increased frequency of DSB formation upon HU-treatment as compared with WT, consistent with the role of RAD51 in promoting fork stability (8). Furthermore, factors from the two actin polymerisation pathways (branched and unbranched) appear to act in parallel, as combined disruption of both pathways results in an increased inability of cells to protect RFs. Accordingly, our work reveals an unexpected yet highly significant association between actin nucleation and the ability of cells to respond to replicative stress. Notably, our data indicate that actin interacts directly with RPA and overexpression of a nuclear-localizing actin mutant that impedes its polymerisation (G13R) (56) leads to defective RPA foci formation and replication fork instability, while the polymerization-hypercompetent actin mutant (S14C) does not (55,60). Our findings with G-actin (G13R) and F-actin (S14C) mutants on RPA foci formation, ATR activation, and efficiency of DNA replication (Figure 7 and Supplementary Figure S7C) suggest that the role of NPF/ANs in this process may be at least by two complementary mechanisms: (i) in *trans*, via control of the actin polymerisation and (ii) in *cis*, via WASp-RPA binding (15). Since β-actin is a sub-unit of multiple chromatin-remodelling complexes,(61–63) and their disruption causes global chromatin reorganization, this proposes an additional mechanism that may potentially contribute to the dysfunctional replication stress response (RSR) in cells lacking NPF/ANs.

Accordingly, our findings propose a model in which localized actin assembly at replication forks provides a spatiotemporal coordination of the RSR by delivering a pool of RPA at the right time (replicative stress) and at the right place (perturbed RFs). This could perhaps involve a 'hand-off' like mechanism to transfer RPA from low-affinity sites on polymerized actin (F-actin) to high-affinity sites on ssDNA. Equally, it is possible that monomeric actin (G-actin) serves as an RPA rheostat, limiting the pool of free RPA to suppress toxicity associated with supra-physiological loading of RPA onto ssDNA. Upon fork stalling (RSR signaling) change in actin state (actin polymerization) may drive the dissociation of G-actin-bound RPA, which increases the pool of RPA available for binding to ssDNA and facilitates, both *in cis* and *in trans*, the efficient formation of RPA-ssDNA complexes, essential for fork protection and robust checkpoint activation (15). As such, a role for ATR in promoting nuclear actin filament formation has been established (19). In this context, our findings raise an intriguing possibility that an ATR-dependent feed-forward loop links the control of RPA assembly with the severity of replicative stress. Such a mechanism would allow for 'discreet' activation of the replication checkpoint, facilitating 'local' versus 'global' responses. Indeed, the key function of checkpoint signaling is to control the global surplus of nuclear RPA, shielding RFs from catastrophic breakage (64). Our findings insert NPF/ANs into this fundamental process in both immune and non-immune cell types.

Patient phenotypes with mutations in actin polymerisation pathways closely resemble those found in genetic disorders with defects in replication/DNA repair pathways i.e. increased cancer risk, failure of the hematopoietic system (immunodeficiency), microcephaly, neurodegeneration, developmental delay, or premature aging (20,65–68). The severity and broad spectrum of these phenotypes likely reflect context- and cell-dependent variability, including the high redundancy within these complimentary mechanisms, as well as potential functions of NPF/ANs outside of the RSR/DDR pathways. Indeed, disruption of WASp:ARP2/3- and DIAPH1-dependent actin polymerisation pathways confers a stronger replication defect than loss of a single pathway.

Altogether, our findings shed new light on the molecular mechanism by which actin nucleators and nucleation-promoting factors facilitate efficient DNA replication and suppress genome instability during the RSR, and further clarify the pathophysiology of human disorders linked to WASp and DIAPH1 deficiencies.

Limitations of the study

This study demonstrates that depletion or loss of NPF/ANs leads to an impairment in the loading of RPA and RAD51 at perturbed RFs. Throughout this study we use the replication inhibitor HU, a ribonucleotide reductase inhibitor (69), to induce replicative stress. However, HU is known to promote RF stalling, regression and dynamic conversion to collapsed RFs, therefore our analysis assays the recruitment of proteins to a mixture of perturbed fork structures (46,70). Furthermore, analysis of 53BP1foci formation (an indirect marker of DSB formation) highlights that NPF/ANs limit replication fork collapse (35) in response to replicative stress induced by HU.

DATA AVAILABILITY

Unprocessed imaging files generated for this study and source data for STRING analysis of iPOND have been deposited on Figshare (doi:10.6084/m9.figshare.21312300).

SUPPLEMENTARY DATA

Supplementary Data are available at NAR Online.

ACKNOWLEDGEMENTS

We thank L.I. Toledo (University of Copenhagen) for U2OS SuperRPA cell line, M. Seidman and M. Bellini (NIH, Baltimore, USA) for scholarly input, M. Dylewska for technical assistance, and the Flow Cytometry & Light Microscopy Facility at the ICR (K. Betteridge, A. Stojiljkovic, H. Ale and M. Guelbert) for assistance with microscopy and flow cytometry cell sorting. Graphical abstract created using BioRender.com (licence number WN2599OAUC).

Author contributions: W.N. and Y.M.V. conceived the project. W.N., J.N. and P.M. designed and analysed the

experiments with contribution from R.B.. J.N., P.M. and R.B. performed most of the experiments. J.K., A.K., C.M., C.S., V.B. and K.K.W. contributed with specific experiments. A.A. provided advice on project design and data analysis. C.B. provided assistance with visualisation of actin polymers and high content imaging. G.S.S. provided advice on project design and carried out initial analysis and complementation of DIAPH1 cell line with assistance from B.L.W.; F.S. provided the DIAPH1 cell line. W.N. wrote the manuscript with inputs from Y.M.V., and editing contributions from J.N., P.M., R.B., A.A. and G.S.S., and all authors reviewed it.

FUNDING

Work in W.N.'s laboratory is funded by CR-UK Programme [A24881] and the CR-UK RadNet Programme; P.M. was supported by the BBSRC fellowship [BB/T009608/1]; G.S.S. is funded by a CR-UK Programme Grant [C17183/A23303]; Y.M.V. research was funded by grants from National Institutes of Health (NIH), National Institute of Allergy and Infectious Diseases (NIAID) [R01AI146380]; endowment from the Penn State THON & Children's Miracle Network; A.A. was funded by the European Research Council [ERC2014 AdG669898 TARLOOP]; B.L.W. is supported through the CR-UK Clinical Academic Training Programme award [C11497/A31309]. Funding for open access charge: ICR Intramural Grant.
Conflict of interest statement. None declared.

REFERENCES

1. Jackson,S.P. and Bartek,J. (2009) The DNA-damage response in human biology and disease. *Nature*, **461**, 1071–1078.
2. Zeman,M.K. and Cimprich,K.A. (2014) Causes and consequences of replication stress. *Nat. Cell Biol.*, **16**, 2–9.
3. Kotsantis,P., Petermann,E. and Boulton,S.J. (2018) Mechanisms of Oncogene-Induced Replication Stress: jigsaw Falling into Place. *Cancer Discov.*, **8**, 537–555.
4. Cimprich,K.A. and Cortez,D. (2008) ATR: an essential regulator of genome integrity. *Nat. Rev. Mol. Cell Biol.*, **9**, 616–627.
5. Neelsen,K.J. and Lopes,M. (2015) Replication fork reversal in eukaryotes: from dead end to dynamic response. *Nature reviews. Mol. Cell Biol.*, **16**, 207–220.
6. Ciccia,A. and Elledge,S.J. (2010) The DNA damage response: making it safe to play with knives. *Mol. Cell*, **40**, 179–204.
7. Kass,E.M., Moynahan,M.E. and Jasin,M. (2016) When genome maintenance goes badly awry. *Mol. Cell*, **62**, 777–787.
8. Bhat,K.P. and Cortez,D. (2018) RPA and RAD51: fork reversal, fork protection, and genome stability. *Nat. Struct. Mol. Biol.*, **25**, 446–453.
9. Saldivar,J.C., Cortez,D. and Cimprich,K.A. (2017) The essential kinase ATR: ensuring faithful duplication of a challenging genome. *Nat. Rev. Mol. Cell Biol.*, **18**, 622–636.
10. Jullien,D., Görlich,D., Laemmli,U.K. and Adachi,Y. (1999) Nuclear import of RPA in Xenopus egg extracts requires a novel protein XRIPα but not importin α. *EMBO J.*, **18**, 4348–4358.
11. Li,S., Xu,Z., Xu,J., Zuo,L., Yu,C., Zheng,P., Gan,H., Wang,X., Li,L. and Sharma,S. (2018) Rtt105 functions as a chaperone for replication protein A to preserve genome stability. *EMBO J.*, **37**, e99154.
12. Marechal,A. and Zou,L. (2015) RPA-coated single-stranded DNA as a platform for post-translational modifications in the DNA damage response. *Cell Res.*, **25**, 9–23.
13. Deng,S.K., Gibb,B., de Almeida,M.J., Greene,E.C. and Symington,L.S. (2014) RPA antagonizes microhomology-mediated repair of DNA double-strand breaks. *Nat. Struct. Mol. Biol.*, **21**, 405–412.
14. VanderVere-Carozza,P.S., Gavande,N.S., Jalal,S.I., Pollok,K.E., Ekinci,E., Heyza,J., Patrick,S.M., Masters,A., Turchi,J.J. and Pawelczak,K.S. (2022) *In Vivo* Targeting Replication Protein A for Cancer Therapy. *Front Oncol.*, **12**, 826655.
15. Han,S.-S., Wen,K.-K., García-Rubio,M.L., Wold,M.S., Aguilera,A., Niedzwiedz,W. and Vyas,Y.M. (2022) WASp modulates RPA function on single-stranded DNA in response to replication stress and DNA damage. *Nat. Commun.*, **13**, 3743.
16. Schrank,B.R., Aparicio,T., Li,Y., Chang,W., Chait,B.T., Gundersen,G.G., Gottesman,M.E. and Gautier,J. (2018) Nuclear ARP2/3 drives DNA break clustering for homology-directed repair. *Nature*, **559**, 61–66.
17. Sarkar,K., Han,S.S., Wen,K.K., Ochs,H.D., Dupre,L., Seidman,M.M. and Vyas,Y.M. (2018) R-loops cause genomic instability in T helper lymphocytes from patients with Wiskott-Aldrich syndrome. *J. Allergy Clin. Immunol.*, **142**, 219–234.
18. Caridi,C.P., D'Agostino,C., Ryu,T., Zapotoczny,G., Delabaere,L., Li,X., Khodaverdian,V.Y., Amaral,N., Lin,E., Rau,A.R. *et al.* (2018) Nuclear F-actin and myosins drive relocalization of heterochromatic breaks. *Nature*, **559**, 54–60.
19. Lamm,N., Read,M.N., Nobis,M., Van Ly,D., Page,S.G., Masamsetti,V.P., Timpson,P., Biro,M. and Cesare,A.J. (2020) Nuclear F-actin counteracts nuclear deformation and promotes fork repair during replication stress. *Nat. Cell Biol.*, **22**, 1460–1470.
20. Hurst,V., Shimada,K. and Gasser,S.M. (2019) Nuclear actin and actin-binding proteins in DNA repair. *Trends Cell Biol.*, **29**, 462–476.
21. Caridi,C.P., Plessner,M., Grosse,R. and Chiolo,I. (2019) Nuclear actin filaments in DNA repair dynamics. *Nat. Cell Biol.*, **21**, 1068–1077.
22. Liu,C., Zhu,R. and Mao,Y. (2018) Nuclear actin polymerized by mDia2 confines centromere movement during CENP-A loading. *Iscience*, **9**, 314–327.
23. Parisis,N., Krasinska,L., Harker,B., Urbach,S., Rossignol,M., Camasses,A., Dewar,J., Morin,N. and Fisher,D. (2017) Initiation of DNA replication requires actin dynamics and formin activity. *EMBO J.*, **36**, 3212–3231.
24. Hayer,A., Shao,L., Chung,M., Joubert,L.M., Yang,H.W., Tsai,F.C., Bisaria,A., Betzig,E. and Meyer,T. (2016) Engulfed cadherin fingers are polarized junctional structures between collectively migrating endothelial cells. *Nat. Cell Biol.*, **18**, 1311–1323.
25. Chang,L., Godinez,W.J., Kim,I.H., Tektonidis,M., de Lanerolle,P., Eils,R., Rohr,K. and Knipe,D.M. (2011) Herpesviral replication compartments move and coalesce at nuclear speckles to enhance export of viral late mRNA. *Proc. Natl. Acad. Sci. U.S.A.*, **108**, E136–E144.
26. Suzuki,K., Bose,P., Leong-Quong,R.Y., Fujita,D.J. and Riabowol,K. (2010) REAP: a two minute cell fractionation method. *BMC Res. Notes*, **3**, 294.
27. Tuschl,T. (2006) Cotransfection of luciferase reporter plasmids with siRNA duplexes. *CSH Protoc.*, **2006**, pdb.prot4342.
28. Nieminuszczy,J., Broderick,R., Bellani,M.A., Smethurst,E., Schwab,R.A., Cherdyntseva,V., Evmorfopoulou,T., Lin,Y.L., Minczuk,M., Pasero,P. *et al.* (2019) EXD2 protects stressed replication forks and is required for cell viability in the absence of BRCA1/2. *Mol. Cell*, **75**, 605–619.
29. Sirbu,B.M., Couch,F.B., Feigerle,J.T., Bhaskara,S., Hiebert,S.W. and Cortez,D. (2011) Analysis of protein dynamics at active, stalled, and collapsed replication forks. *Genes Dev.*, **25**, 1320–1327.
30. Taglialatela,A., Alvarez,S., Leuzzi,G., Sannino,V., Ranjha,L., Huang,J.W., Madubata,C., Anand,R., Levy,B., Rabadan,R. *et al.* (2017) Restoration of replication fork stability in BRCA1- and BRCA2-deficient cells by inactivation of SNF2-family fork remodelers. *Mol. Cell*, **68**, 414–430.
31. Nieminuszczy,J., Schwab,R.A. and Niedzwiedz,W. (2016) The DNA fibre technique - tracking helicases at work. *Methods*, **108**, 92–98.
32. Schwab,R.A. and Niedzwiedz,W. (2011) Visualization of DNA replication in the vertebrate model system DT40 using the DNA fiber technique. *J. Vis. Exp.*, **56**, e3255.
33. Bhat,K.P., Betous,R. and Cortez,D. (2015) High-affinity DNA-binding domains of replication protein A (RPA) direct SMARCAL1-dependent replication fork remodeling. *J. Biol. Chem.*, **290**, 4110–4117.
34. Henricksen,L.A., Umbricht,C.B. and Wold,M.S. (1994) Recombinant replication protein A: expression, complex formation, and functional characterization. *J. Biol. Chem.*, **269**, 11121–11132.
35. Szklarczyk,D., Gable,A.L., Lyon,D., Junge,A., Wyder,S., Huerta-Cepas,J., Simonovic,M., Doncheva,N.T., Morris,J.H., Bork,P.

et al. (2019) STRING v11: protein-protein association networks with increased coverage, supporting functional discovery in genome-wide experimental datasets. *Nucleic Acids Res.*, **47**, D607–D613.
36. Higgs,M.R., Reynolds,J.J., Winczura,A., Blackford,A.N., Borel,V., Miller,E.S., Zlatanou,A., Nieminuszczy,J., Ryan,E.L., Davies,N.J. *et al.* (2015) BOD1L is required to suppress deleterious resection of stressed replication forks. *Mol. Cell*, **59**, 462–477.
37. Coquel,F., Silva,M.J., Techer,H., Zadorozhny,K., Sharma,S., Nieminuszczy,J., Mettling,C., Dardillac,E., Barthe,A., Schmitz,A.L. *et al.* (2018) SAMHD1 acts at stalled replication forks to prevent interferon induction. *Nature*, **557**, 57–61.
38. Roy,S., Luzwick,J.W. and Schlacher,K. (2018) SIRF: quantitative in situ analysis of protein interactions at DNA replication forks. *J. Cell Biol.*, **217**, 1521–1536.
39. Roy,S. and Schlacher,K. (2019) SIRF: a single-cell assay for in situ protein interaction with nascent DNA replication forks. *Bio-protocol*, **9**, e3377–e3377.
40. Dungrawala,H. and Cortez,D. (2015) Purification of proteins on newly synthesized DNA using iPOND. *Methods Mol. Biol.*, **1228**, 123–131.
41. Dungrawala,H. and Cortez,D. (2015) In: *The Nucleus*. Springer, pp. 123–131.
42. Schwab,R.A., Nieminuszczy,J., Shah,F., Langton,J., Lopez Martinez,D., Liang,C.C., Cohn,M.A., Gibbons,R.J., Deans,A.J. and Niedzwiedz,W. (2015) The Fanconi anemia pathway maintains genome stability by coordinating replication and transcription. *Mol. Cell*, **60**, 351–361.
43. Blackford,A.N., Nieminuszczy,J., Schwab,R.A., Galanty,Y., Jackson,S.P. and Niedzwiedz,W. (2015) TopBP1 interacts with BLM to maintain genome stability but is dispensable for preventing BLM degradation. *Mol. Cell*, **57**, 1133–1141.
44. Pollard,T.D. (2016) Actin and actin-binding proteins. *Cold Spring Harb. Perspect. Biol.*, **8**, a018226.
45. Baarlink,C., Plessner,M., Sherrard,A., Morita,K., Misu,S., Virant,D., Kleinschnitz,E.-M., Harniman,R., Alibhai,D. and Baumeister,S. (2017) A transient pool of nuclear F-actin at mitotic exit controls chromatin organization. *Nat. Cell Biol.*, **19**, 1389–1399.
46. Petermann,E., Orta,M.L., Issaeva,N., Schultz,N. and Helleday,T. (2010) Hydroxyurea-stalled replication forks become progressively inactivated and require two different RAD51-mediated pathways for restart and repair. *Mol. Cell*, **37**, 492–502.
47. Hashimoto,Y., Ray Chaudhuri,A., Lopes,M. and Costanzo,V. (2010) Rad51 protects nascent DNA from Mre11-dependent degradation and promotes continuous DNA synthesis. *Nat. Struct. Mol. Biol.*, **17**, 1305–1311.
48. Schlacher,K., Christ,N., Siaud,N., Egashira,A., Wu,H. and Jasin,M. (2011) Double-strand break repair-independent role for BRCA2 in blocking stalled replication fork degradation by MRE11. *Cell*, **145**, 529–542.
49. Karanja,K.K., Lee,E.H., Hendrickson,E.A. and Campbell,J.L. (2014) Preventing over-resection by DNA2 helicase/nuclease suppresses repair defects in Fanconi anemia cells. *Cell Cycle*, **13**, 1540–1550.
50. Lachaud,C., Moreno,A., Marchesi,F., Toth,R., Blow,J.J. and Rouse,J. (2016) Ubiquitinated Fancd2 recruits Fan1 to stalled replication forks to prevent genome instability. *Science*, **351**, 846–849.
51. Berti,M., Cortez,D. and Lopes,M. (2020) The plasticity of DNA replication forks in response to clinically relevant genotoxic stress. *Nat. Rev. Mol. Cell Biol.*, **21**, 633–651.
52. Toledo,L.I., Altmeyer,M., Rask,M.B., Lukas,C., Larsen,D.H., Povlsen,L.K., Bekker-Jensen,S., Mailand,N., Bartek,J. and Lukas,J. (2013) ATR prohibits replication catastrophe by preventing global exhaustion of RPA. *Cell*, **155**, 1088–1103.
53. Chaudhuri,A.R., Callen,E., Ding,X., Gogola,E., Duarte,A.A., Lee,J.E., Wong,N., Lafarga,V., Calvo,J.A., Panzarino,N.J. *et al.* (2016) Replication fork stability confers chemoresistance in BRCA-deficient cells. *Nature*, **535**, 382–387.
54. Pfitzer,L., Moser,C., Gegenfurtner,F., Arner,A., Foerster,F., Atzberger,C., Zisis,T., Kubisch-Dohmen,R., Busse,J., Smith,R. *et al.* (2019) Targeting actin inhibits repair of doxorubicin-induced DNA damage: a novel therapeutic approach for combination therapy. *Cell Death. Dis.*, **10**, 302.
55. Chang,L., Godinez,W.J., Kim,I.-H., Tektonidis,M., De Lanerolle,P., Eils,R., Rohr,K. and Knipe,D.M. (2011) Herpesviral replication compartments move and coalesce at nuclear speckles to enhance export of viral late mRNA. *Proc. Natl. Acad. Sci. U.S.A.*, **108**, E136–E144.
56. Posern,G., Sotiropoulos,A. and Treisman,R. (2002) Mutant actins demonstrate a role for unpolymerized actin in control of transcription by serum response factor. *Mol. Biol. Cell*, **13**, 4167–4178.
57. Brosh,R.M. Jr (2013) DNA helicases involved in DNA repair and their roles in cancer. *Nat. Rev. Cancer*, **13**, 542–558.
58. Velegzhaninov,I.O., Belykh,E.S., Rasova,E.E., Pylina,Y.I., Shadrin,D.M. and Klokov,D.Y. (2020) Radioresistance, DNA damage and DNA repair in cells with moderate overexpression of RPA1. *Front Genet*, **11**, 855.
59. Zhang,Y. and Yu,C. (2020) Distinct expression and prognostic values of the replication protein A family in gastric cancer. *Oncol. Lett.*, **19**, 1831–1841.
60. Baarlink,C., Wang,H. and Grosse,R. (2013) Nuclear actin network assembly by formins regulates the SRF coactivator MAL. *Science*, **340**, 864–867.
61. Kapoor,P., Chen,M., Winkler,D.D., Luger,K. and Shen,X. (2013) Evidence for monomeric actin function in INO80 chromatin remodeling. *Nat. Struct. Mol. Biol.*, **20**, 426–432.
62. Kapoor,P. and Shen,X. (2014) Mechanisms of nuclear actin in chromatin-remodeling complexes. *Trends Cell Biol.*, **24**, 238–246.
63. Klages-Mundt,N.L., Kumar,A., Zhang,Y., Kapoor,P. and Shen,X. (2018) The nature of actin-family proteins in chromatin-modifying complexes. *Front. Genet.*, **9**, 398.
64. Toledo,L., Neelsen,K.J. and Lukas,J. (2017) Replication catastrophe: when a checkpoint fails because of exhaustion. *Mol. Cell*, **66**, 735–749.
65. Simon,D.N., Zastrow,M.S. and Wilson,K.L. (2010) Direct actin binding to A- and B-type lamin tails and actin filament bundling by the lamin A tail. *Nucleus*, **1**, 264–272.
66. Ercan-Sencicek,A.G., Jambi,S., Franjic,D., Nishimura,S., Li,M., El-Fishawy,P., Morgan,T.M., Sanders,S.J., Bilguvar,K., Suri,M. *et al.* (2015) Homozygous loss of DIAPH1 is a novel cause of microcephaly in humans. *Eur. J. Hum. Genet.*, **23**, 165–172.
67. Al-Maawali,A., Barry,B.J., Rajab,A., El-Quessny,M., Seman,A., Coury,S.N., Barkovich,A.J., Yang,E., Walsh,C.A., Mochida,G.H. *et al.* (2016) Novel loss-of-function variants in DIAPH1 associated with syndromic microcephaly, blindness, and early onset seizures. *Am. J. Med. Genet. A*, **170A**, 435–440.
68. Moulding,D.A., Record,J., Malinova,D. and Thrasher,A.J. (2013) Actin cytoskeletal defects in immunodeficiency. *Immunol. Rev.*, **256**, 282–299.
69. Yarbro,J.W. (1992) In: *Seminars in Oncology*. Vol. **19**, pp. 1–10.
70. Zellweger,R., Dalcher,D., Mutreja,K., Berti,M., Schmid,J.A., Herrador,R., Vindigni,A. and Lopes,M. (2015) Rad51-mediated replication fork reversal is a global response to genotoxic treatments in human cells. *J. Cell Biol.*, **208**, 563–579.